Estimating planetary heat flow from a shallow subsurface heat flow measurement

Thesis

MARC ANDREW CORNWALL

MSc: Space Studies

BSc (Hons): Astronomy, Space Science and Astrophysics

ESTIMATING PLANETARY HEAT FLOW FROM A SHALLOW SUBSURFACE HEAT FLOW MEASUREMENT

A thesis submitted to the Open University for the degree of Doctor of Philosophy in Planetary Science

March 28, 2014

DATE OF SUBMISSION : 28 MARCH 2014

DATE OF AWARD : 29 APRIL 2015

ProQuest LLC.
789 East Eisenhower Parkway
P.O. Box 1346
Ann Arbor, MI 48106 – 1346

ABSTRACT

This study investigates the feasibility of estimating planetary heat flow from a shallow subsurface heat flow measurement with a Function Specification Inversion (FSI) model. Heat flow is a product of the thermal conductivity and gradient at depth; these are measured and therefore contain errors. The model estimates other parameters, as well as the former, while not explicitly accounting for temperature dependent thermal properties.

The heat flow is decomposed into steady state basal (planetary) and unsteady state (related to the surface temperature variation) heat flow components. Surface heat flow is typically several orders of magnitude higher than the planetary heat flow; therefore unsteady components in a shallow subsurface heat flow measurement may mask the planetary heat flow. The extent of masking positively correlates with the skin depth and amplitude of the surface heat flow, and negatively correlates with the magnitude of the planetary heat flow.

The planetary heat flow is estimated by inverting the temperature measurement and optimising the basal heat flow. The basal heat flow is most effectively optimized from instantaneous measurements, taken when the surface temperature is relatively constant. Long-period measurements, while more accurately optimized, introduce more unsteady temperature gradients, thereby increasing the ill-determinacy and instability of the problem. The model tolerates errors up to 25 % in simultaneous optimization of several unknown parameters, with related errors in the optimized basal heat flow.

On Mars, the heat flow is optimized to within 10 % for measurements over at least twice the skin depth and 0.5 of a Martian year, or at least five times the skin depth and 0.25 of a Martian year. On Mercury, temperature amplitudes control optimized heat flow accuracy; sensor penetration depths well below three skin depths are required. On Vesta, very low heat flows render FSI ineffective with a noise amplitude of 1 mK.

TABLE OF CONTENTS

LIST OF FIGURES

1 INTRODUCTION

1.1 Planetary Heat Flow

The life of a planet is thought to begin in a turbulent rotating disk of gas and dust surrounding a stellar object (e.g. Lissauer, 1993; Völschow et al., 2014). Gravity takes hold in the denser regions of the disk, forcing a runaway process of accretion and heating, the end products of which are planets (e.g. Lissauer, 1993; Zhou et al., 2005; Kashi and Soker, 2011). Through the processes of accretion and merger, the heated balls of material, protoplanets, and their less massive counterparts which feed their growth, planetesimals, go through a process of thermal evolution (Weidenschilling, 2000; Cassen, 2001; Chambers and Wetherill, 2001; Kokubo and Ida, 2002; Chambers, 2004; Leinhardt et al., 2009).

Some planets are large and hot enough to achieve hydrostatic equilibrium. The largest planets evolve into giant balls of gas, ice and rock, with their surface heat loss governed, largely, by convection and radiation (e.g. Pollack et al., 1996; Hubbard et al., 2002). The smaller planets (and planetesimals) maintain a dense rocky profile where their surface heat loss is governed, largely, by its diffusion through a solid surface (e.g. Wetherill, 1985; Kokubo et al., 2006; Quintana and Lissauer, 2006; Kokubo and Ida, 2007; Hansen, 2009; Kokubo and Genda, 2010); volcanism may also play an important role (e.g. Spohn, 1991).

Planetary heat flow quantifies the rate of heat flow from the interior of a planet through its surface – knowledge of the heat flow from a planetary surface can, therefore, shed light on its thermal evolution (e.g. Hagermann, 2005). This study focuses on heat flow from rocky planets[1], and how it can be estimated from a measurement of shallow subsurface temperatures and thermal properties. Discussion of this is continued in Section 1.1.2. It is instructive to begin with a general outline of current theory on the thermal evolution of rocky planets. This will provide further context to the heat flow concept and initial insight into the useful information that can be gained from a heat flow measurement.

[1] Heat flow from rocky planets is also known as heat diffusion which is often dominated by the solid state process of heat conduction.

1.1.1 Thermal Evolution of Rocky Planets

The size of a planet plays a dominant role in its thermal evolution (Hsui and Toksöz, 1977). Larger bodies tend to cool more slowly because their ratio of surface area (for heat to escape) to volume (for heat production) is smaller. The model results of Hsui and Toksöz (1977) show that smaller bodies therefore tend to reach their peak of thermal evolution – i.e. when thermal energy generated equals thermal energy lost – sooner than larger bodies and tend to have thicker crusts due to more rapid heat loss. Internal planetary heat is produced largely by differentiation and the decay of radioisotopes. For a constant volumetric heat production rate and similar surface energy balance, a planet with larger radius therefore has higher heat flow over a given timescale. This explains, in part, why heat flow on Earth averages 65 mW/m^2 on the continents while that on the Moon is estimated at 30 mW/m^2 (e.g. Heiken et al., 1991; also see Section 1.1.3).

The conditions in which a planet forms also play a crucial role in its thermal evolution (e.g. Hsui and Toksöz, 1977; O'Rourke and Korenaga, 2012). Hsui and Toksöz (1977) find that bodies of radius 1000km and less (asteroids and other minor planets) are unlikely to reach a molten state if their initial conditions are cold (500-1500 K) and heat source abundances similar to terrestrial and lunar values are used. Hot initial conditions (1300-1500 K), possibly caused by short half-life radioisotopes such as ^{26}Al (e.g. McKeegan and Davis, 2005; Boss, 2007) or T-Tauri solar wind induction (e.g. Shimazu and Terasawa, 1995), result in these planets achieving a molten state during evolution. This is thought to be the case with the protoplanet Vesta (discussed in Chapter 7), where current thermal models suggest a very low heat flow of the order of $\mu W/m^2$ (e.g. Stubbs and Wang, 2012; Formisano et al., 2013).

The results of Hsui and Toksöz (1977) indicate that, with hot initial conditions, all planets undergo an initial period of rapid heat loss, also achieving a higher thermal state with higher heat flow at far future times than are permitted by cold initial conditions (also see

O'Rourke and Korenaga, 2012).[2] Kaula (1979) cites geophysical evidence for early lunar crust differentiation pointing to hot formation conditions for the Earth-Moon system. Kaula (1979) shows that very large impact events can produce the heat required for hot formation over millions of years, removing the need for unrealistically small accretion times of tens of thousands of years or granular planetesimal sizes to account for early crustal differentiation.

The process of differentiation causes release of energy which further influences planetary thermal evolution. Mantle differentiation results in the formation of a crust when lighter mantle rock is extruded or piped to near surface layers or onto the surface and crystallises (e.g. Spohn, 1991). Spohn (1991) investigates the crustal thickness that results from a purely conductive versus largely volcanic mode of heat transfer from the mantle to the surface. The results of Spohn (1991) indicate that, dependent on other factors such as surface energy balance, radioisotope abundance, and heat flow through the mantle, volcanic heat transfer tends to produce thicker crust while purely conductive heat transfer tends to produce thinner crust.

Crust formation depletes the mantle of heat producing elements (e.g. Spohn, 1991) and insulates the mantle, reducing the vigour of mantle convection. Plate tectonics – e.g. on Earth (Parsons and Sclater, 1977; Sclater et al., 1980; Sclater et al., 1981) and possibly early Mars (Spohn, 1991; Breuer and Spohn, 2003) – cools a planet more efficiently while reintroducing (remixing) some heat producing elements into the mantle at subduction zones, consequently equilibrating temperatures and lowering heat flow. Single plate planets – e.g. present Mars (Breuer and Spohn, 2003; Grott and Breuer, 2010; discussed in Chapter 5) and Mercury (Breuer et al., 2007; discussed in Chapter 6) – form an insulating stagnant lid, leading to less efficient heat loss, higher mantle temperatures and higher heat flow.

[2] A higher thermal state refers to a higher energy state such as with a solid inner, liquid outer core with fluid mantle and volcanic surface like Earth, currently, as opposed to current Mars or asteroids.

Differentiation causes relatively high pressures and densities in larger planets which may lead to core formation. Core formation results in a period of increased heating, with larger or denser cores causing more heating due to release of potential energy into the mantle of the planet. Stevenson et al. (1983) Kleine et al. (2002) and Samuel et al. (2010) explore the thermal interactions of the core and mantle and their relation to planetary dynamos and magnetic fields. Their findings indicate that Earth's magnetic field is powered by a dynamo, which is driven by release of gravitational potential energy, due to nucleation of an inner core, coupled with an outer core interacting with the mantle. They also indicate that other terrestrial planets may have frozen, near solid or liquid cores which drive thermally convective dynamos. The remnant magnetic field of Mars coupled with its thick crust raises important questions about its history of crust growth and core cooling; in particular, whether or not its heat loss process has been dominated by plate cooling or stagnant lid processes[3] (e.g. Breuer and Spohn, 2003). The weak field at Mercury indicates it has an active dynamo, despite its size suggesting that the core should have cooled within the first billion years of its formation (e.g. Benkhoff and Helbert, 2006; Breuer et al., 2007; Hauck et al., 2013).

Comets, Trans-Neptunian Objects (TNOs) including Kuiper Belt Objects (KBOs), and satellites of the outer planets are worth separate consideration. These are composed of significant internal ice and volatile components, which contribute as much to their evolution as their changing surface environments (e.g. Prialnik and Merk, 2008; Prialnik et al., 2008). Ceres is a known icy body (e.g. Coradini et al., 2011; O'Brien and Sykes, 2011) and ice has been detected on other asteroids in the asteroid belt (e.g. Campins et al.,

[3] Plate cooling refers to crustal plate differentiation from a magma ocean, while stagnant lid accounts for a layered lithosphere which includes a crust and a rheological lithosphere, together forming a 'stagnant lid,' atop a convecting mantle which contributes significant heat flow.

[3] The map of Hahn et al. (2011) presents only the crustal component of the heat flow as opposed to total surface heat flow which accounts for both the crustal, mantle and core components of heat flow.

2010). Hydrogen rich areas have been detected on Vesta, which are associated with pitted terrains from which volatiles have degassed (e.g. Denevi et al., 2012; Russell et al., 2013; also see discussion in Chapter 7). The former observations suggest small icy bodies cool quickly and have low heat flow, where comets on approach to the Sun may have a net inward flow of heat. However, certain asteroids show evidence of differentiation and may host internal water reservoirs depending on their internal thermal states (e.g. Seep, 2001; Abramov and Mojzsis, 2011).

The preceding overview presents some of the key roles heat flow plays in the thermal evolution of planets. In summary, surface heat flow partially regulates the internal temperatures of a planet, influencing crust formation and the depletion of radioisotopes from the mantle. The internal temperatures influence mantle convection and, by extension, core properties and potential dynamo formation. Measuring the surface heat flow can therefore place important bounds on the thermal profile at greater depths. Used in conjunction with seismic, radiometric and magnetic information, it can provide bounds on the radioisotope concentration, lithosphere thickness, and the size and state of any mantle and core (e.g. Dehant et al., 2012). For the special case of asteroids, heat flow can provide information on internal temperatures, and whether or not large asteroids are home to internal liquid water environments. In this study, it is shown how the heat flow can be estimated from a local measurement of the temperature gradient and thermal properties of the shallow subsurface of a planet. To this end, heat flow is discussed in further detail in Section 1.1.2. The context of heat flow investigations is established in Section 1.1.3 in terms of their development on Earth and extension to other planets.

1.1.2 Properties of Surface Heat Flow

Heat flow at the surface of a planet varies as the surface is periodically heated in diurnal and seasonal temperature cycles. Surface heat flow is often several orders of magnitude higher than planetary heat flow, except at times where the former passes through zero during the surface heating cycle (Figure 1.1). The surface heat flow can be decomposed into steady state and unsteady state heat flow components. Steady (or basal) heat flow

exhibits very long period or no time variation and is identifiable with the planetary heat flow.[4] Unsteady heat flow quantifies the time-varying surface heat flow component due to diurnal and seasonal temperature cycles.

Surface heat flow depends on regolith porosity, the level of contact between different particulates, the amount of volatiles present and the physical properties of said particulates and volatiles. For porous regolith in vacuum, radiative heat transfer within the pore spaces plays an important role, evidence suggests that it becomes strongly temperature dependent above 200 K (e.g. Linsky, 1966; Prialnik, 1989). Radiative heat transfer is less efficient than purely conductive heat transfer (e.g. Piqueux and Christensen, 2011) resulting in a steeper temperature gradient.[5] Heat flows down the temperature gradient and is therefore always a half of a period out of phase with the temperature variation (see Figure 1.1).

The grain contact coefficient – the Hertz factor (e.g. Seiferlin et al., 1996; Paton et al., 2010) – plays a greater role in loose, porous and/or layered materials, where less grain (or layer) contact reduces the efficiency with which conduction takes place, therefore resulting in a steeper temperature gradient. The presence of volatiles within pores results in areas of constant temperature, where volatiles undergo phase changes. Volatiles transfer heat by advection as well as conduction and radiation. The greater efficiency of advection leads to a shallow temperature gradient along volatile rich layers with well-connected pores (e.g. Benkhoff and Spohn, 1991; Steiner and Komle, 1991).

Regolith physical properties which govern heat flow are thermal conductivity, density and specific heat capacity. Thermal conductivity is most influential in particulate heat transfer and is, therefore, related to the Hertz factor. The density relates to the porosity of the material where denser material is, in principle, less porous. The product of density and

[4] Planets are non-homogeneous bodies; therefore heat flow varies across their surfaces based on local and regional properties.

[5] All temperature (thermal) gradient references are with respect to depth unless otherwise noted.

specific heat capacity is the thermal capacity which dictates how much heat a unit volume of regolith can hold at a particular temperature. The ratio of thermal conductivity to thermal capacity is thermal diffusivity, which quantifies the rate of heat retention of a unit volume of regolith. The effects of the discussed thermal properties are reviewed in detail in Chapter 3. The heat flow is the product of the thermal conductivity and temperature gradient.

Regolith properties highlighted in the previous paragraph, along with the characteristics of surface heating, determine the depth, known as the skin depth, at which the amplitude of the unsteady surface heat flow is reduced to negligible values[6]. Longer period surface heating cycles cause surface heat to flow deeper into the regolith. A lagged and damped periodic signature of unsteady surface heating is preserved in the regolith subsurface (Figure 1.1). The shallow subsurface unsteady heat flow component therefore contains a record of past variations in the surface climate (e.g. Pollack and Huang, 2000). The basal heat flow is consequently more isolated at greater depths, which highlights the fundamental problem being explored in this study: heat flow is most conveniently measured closer to the surface (see Section 1.2), therefore methods must be devised which allow extraction of the basal heat flow from a measurement, which may contain the unsteady heat flow component (discussed in Section 1.3).

Local surface heat flow is affected by the thickness of surrounding regolith. For a columnar section through a planetary crust, the more long lived the heat producing elements (HPEs or radioisotopes – mainly ^{40}K, ^{232}Th, ^{235}U and ^{238}U – e.g. Heiken et al., 1991), the greater the heat produced in the column. This means that regions of thicker crust and/or higher elevation produce more heat than other regions. Surface heat, therefore, preferentially escapes from regions of thinner crust where the heat production and temperature are lower, as the thicker crust effectively acts as an insulating lid.

[6] More, precisely, the skin depth is quantified by the depth at which the unsteady surface temperature amplitude is reduced by a factor e, the natural exponent.

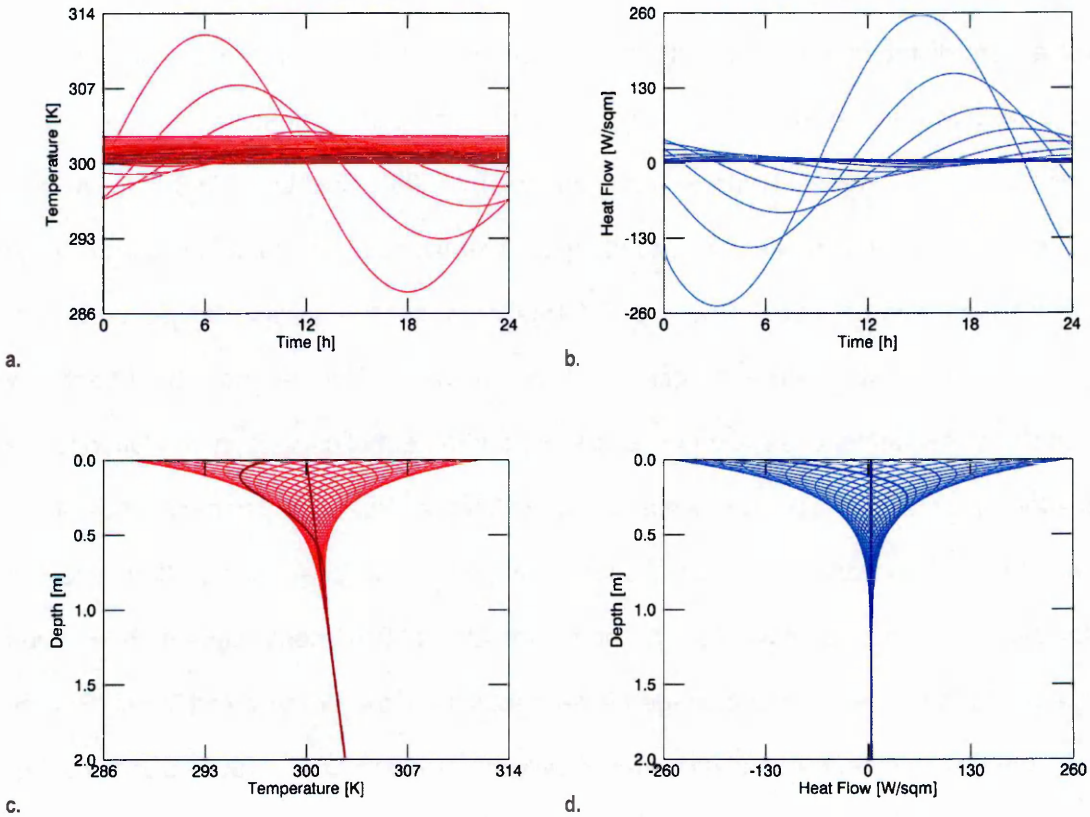

Figure 1.1. Subsurface temperature (right) and heat flow (left) due to a sinusoidal diurnal (24 h) surface temperature of amplitude 12 K and a heat flow of 4 W/m/K. The upper plots show overlays of time dependent temperature at different depths; the lower plots show overlays of depth dependent temperature at different different times. The dark lines in all four plots are the steady components while the dark curves in c and d show the real temperature (steady + unsteady) at the start of the period.

1.1.3 Heat Flow Investigations

1.1.3.1 Heat Flow on Earth

Earth-focused heat flow studies go back to the 1870s and 1880s, where measurements were made of the thermal conductivity (see Section 1.1.3.2) of continental rocks (Bullard, 1945). Preliminary heat flow studies revealed an inverse relationship between heat flow and distance from mid-ocean ridges (e.g. Pettersson, 1949; Revelle and Maxwell, 1952; Bullard, 1954; Bullard et al., 1956; Bullard and Day, 1961; von Herzen and Uyeda, 1963). The discovery provided supporting evidence for the theory of sea floor spreading (e.g. Crook, 1923; Melton, 1925; Holmes, 1931; Turcotte and Oxburgh, 1967; Parsons and Sclater, 1977; Sclater et al., 1980; 1981).

Heat flow measurements have been combined with seismic and petrological data to constrain the distribution of radioisotopes throughout, and vertical extent of, the crust and deeper subsurface (e.g. Roy et al., 1968; Jaupart et al., 1981; Pinet and Jaupart, 1987; Mareschal et al., 1989; Rudnick and Fountain, 1995; Boehler, 1996). Heat flow measurements have also been used to study past surface climatic variations because the shallow subsurface heat flow preserves information about the surface temperature (e.g. Chapman et al., 1992; Shen and Beck, 1992; Wang, 1992). The dependence of heat flow on regolith water content has been used to study hydrothermal circulation in relation to the formation of transitions between oceanic and continental crust, and characteristics of the flanks along mid-ocean ridges (e.g. Fisher et al., 2003; Lucazeau et al., 2010) and soil water content (Béhaegel et al., 2007). Thousands of heat flow measurements have been made on Earth with a derived average global heat loss of the order of 4×10^{13} W (Pollack et al., 1993), or planetary heat flow of ~78 mW/m^2.[7] Heiken et al. (1991) gives a lower value of 63 mW/m^2.

1.1.3.2 Heat Flow on Other Planets

The first in situ heat flow measurements were taken on the Moon by Apollo 15 and 17 astronauts, using heat flow probes (see Section 1.2.2) emplaced into cored lunar regolith up to 1.4 m for 3.5 years, and 2.36 m for 2 years, respectively (e.g. Langseth et al., 1972; 1976; Heiken et al., 1991). Langseth et al. (1976) presents preliminary heat flow estimates of 21 mW/m^2 for the Apollo 15 site (at 26°N 3.6°E[8], known as Hadley Rille) and 14 mW/m^2 for the Apollo 17 site (at 20°N 30.6°E[8], known as Taurus-Littrow), corrected for topographic and equilibration effects. The difference between the two measurements is partially attributed to topographic effects of Hadley Rille (lowers heat flow) and the Appenine Front (increases heat flow) which is also in the region of the Apollo 15 landing site (Figure 1.2). Langseth, et al. (1976) use remotely sensed variations in Th abundance and inferred crustal thicknesses to extrapolate the measurements to a lunar global heat

[7] Based on a total surface area of 5.101×10^{14} m^2 (Wolfram Alpha, 2014).

[8] After Heiken et al. (1991).

flow of 18 mW/m^2. Heiken et al. (1991) use the same Apollo measurements to estimate global lunar heat flow between 20-30 mW/m^2.

The lunar heat flow measurements have been subject to several subsequent revisions, many summarised in Hagermann and Tanaka (2006). These include a focusing effect outlined by Warren and Rasmussen (1987), with revised heat flow of 12 mW/m^2, where heat flows laterally from the highlands to the mare (the probe sites are located at the mare-highland boundary). Hagermann and Tanaka (2006) note that the probe sites are located in the Procellarum KREEP Terrane (PKT)[9]. They show that a Th rich layer (excavated by the Imbrium impactor) contributes a more significant amount to the heat flow at Hadley Rille, located closer to the centre of the Imbrium impact, than at Taurus-Littrow They recommend that a "very long ruler" be used to draw error bars for derived global heat flows (see Appendix 9.8.4 for an investigation of the available Apollo temperature data in the context of this work).

[9] The Procellarum KREEP (K, Rare Earth Elements, P) Terrain is a unique lunar geophysical feature characterised by high concentrations of KREEP, including Th.

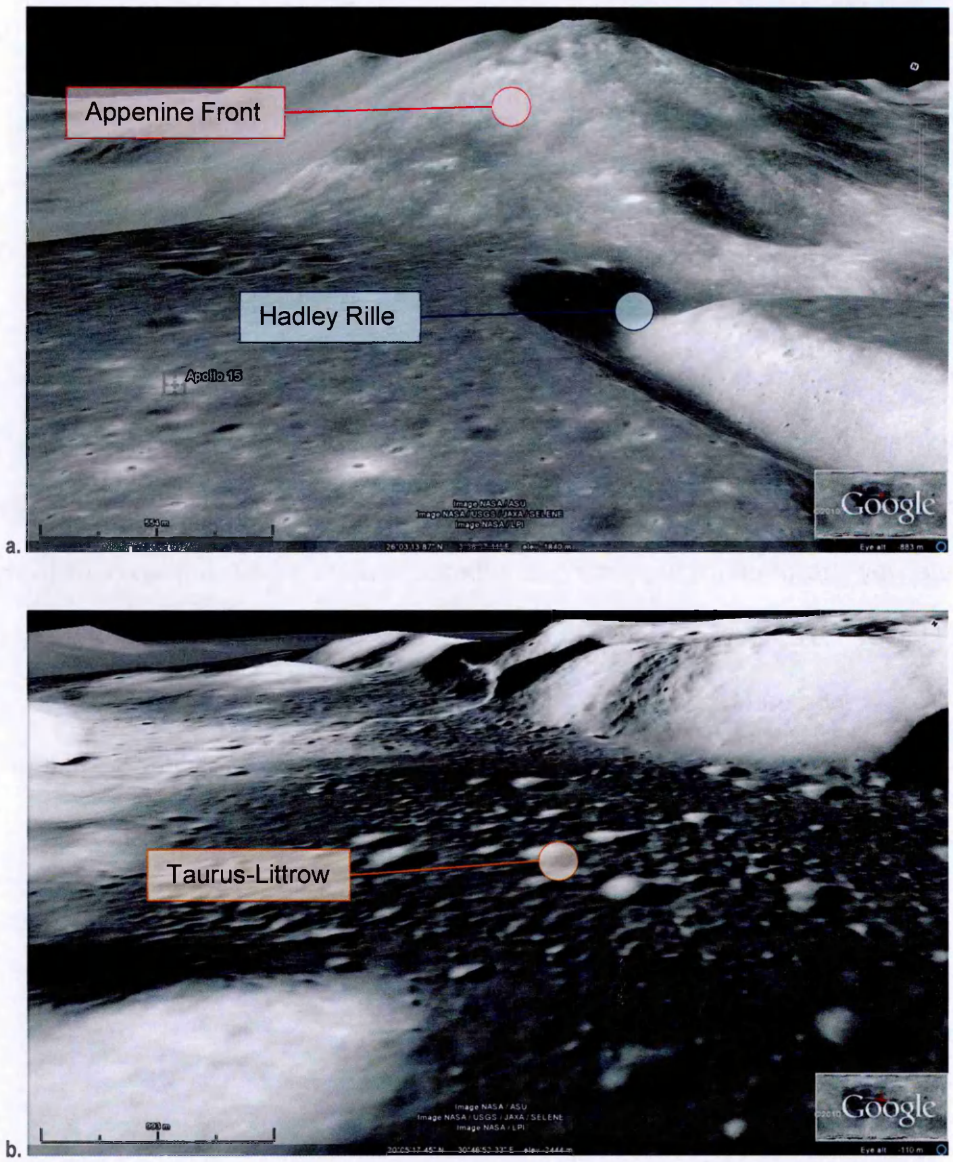

Figure 1.2. Apollo landing site topography: a. Apollo 15 site – the heat flow probes were emplaced towards the centre of the image. Hadley Rille is to the right while the Appenine Front spans the upper region of the image; b. Apollo 17 site –.the Taurus-Littrow Valley is located in heavily cratered terrain (Google, 2010).

The Apollo heat flow measurements illustrate the difficulties inherent in extrapolating single planetary measurements to a global heat flow. The topography of the location must be taken into account due to the effects of lateral heat flow from higher elevations. Global variation in HPEs must be accounted for due to the additive effect of radioisotope heat production to the surface heat flow. The volatile content of the regolith is also important – e.g. a local ice-rich layer may lead to a high local heat flow measurement inapplicable to global estimates due to the high conductivity of water ice (e.g. Grott et al., 2007) and the

advective component of heat transfer (e.g. Steiner and Komle, 1991; Seiferlin et al., 1996). The choice of site(s) for in situ heat flow measurements is, therefore, of critical importance.

On other solar system bodies, heat flow investigations have largely relied on remotely sensed data. The first heat flow estimates of the Moon were achieved by Earth-based sensing of lunar microwave thermal emissions (see e.g. Keihm, 1984; Hagermann, 2005), with derived heat flow of 30-40 mW/m^2 (Heiken et al., 1991). Due to the limited coverage and local bias of in situ measurements, complementary orbital measurements calibrated against in situ measurements allow better global heat flow estimates. However, surface and subsurface scattering processes, along with density gradients, can cause interference which must be accounted for when extracting temperature gradients from brightness temperatures, as discussed in Keihm (1984). On Mars, surface heat flow has been calculated using surface HPE distributions derived from gamma ray spectrometry, and crustal thickness derived from gravity measurements (e.g. Grott and Breuer, 2010; Dehant et al., 2012). Images of surface topography have been used to infer palaeo-heat flow on Mercury (e.g. Watters Watters et al., 2002; Egea-Gonzalez and Ruiz, 2013), Venus (Ruiz, 2007) and Mars (e.g. Grott et al., 2005; Ruiz et al., 2006), in lithosphere elastic strength studies. Naturally, an integration of these methods with in situ measurements can provide the most robust estimates of planetary heat flow.

1.2 Measuring Heat Flow

Hagermann (2005) mentions several potential methods of measuring heat flow; these include penetrators for loose, porous regolith, and blankets for sedimented or impenetrable surfaces. The blanket method is, naturally, restricted to surface heat flow and requires monitoring periods over annual temperature cycles for a reliable basal heat flow estimate. Penetrators (heat flow probes) can potentially avoid the former limitation by penetrating below the skin depth. The heat flow investigations mentioned in Section 1.1.3 are all based on heat flow probe measurements. The latter are the focus of this study.

1.2.1 Earth-bound Heat Flow Probes

Pettersson (1949) mentions an 11 m long "geothermometer" which penetrated the ocean bed to measure the temperature gradient; cores were also taken which allowed for conductivity measurements and consequent heat flow estimates in other studies (e.g. Bullard, 1954). Bullard (1954) mentions the first successful use of a 3 m long probe to take ocean bed heat flow measurements (described in Revelle and Maxwell, 1952), and a similar ~4.7 m long probe (Figure 1.3) with similar capabilities.

Lucazeau et al. (2010) describe the use of a 5 m long, so-called "POGO stick" heat flow probe, which can take several ocean bed heat flow measurements over 2-3 d. The POGO stick probe records thermal conductivities by employing heated temperature sensors (thermistors). A constant power is applied to the latter and the consequent rise in temperature recorded – the temperature rise depends on the thermal conductivity of the soil. Lucazeau et al. (2010) note that cores are taken to enhance the conductivity measurements.

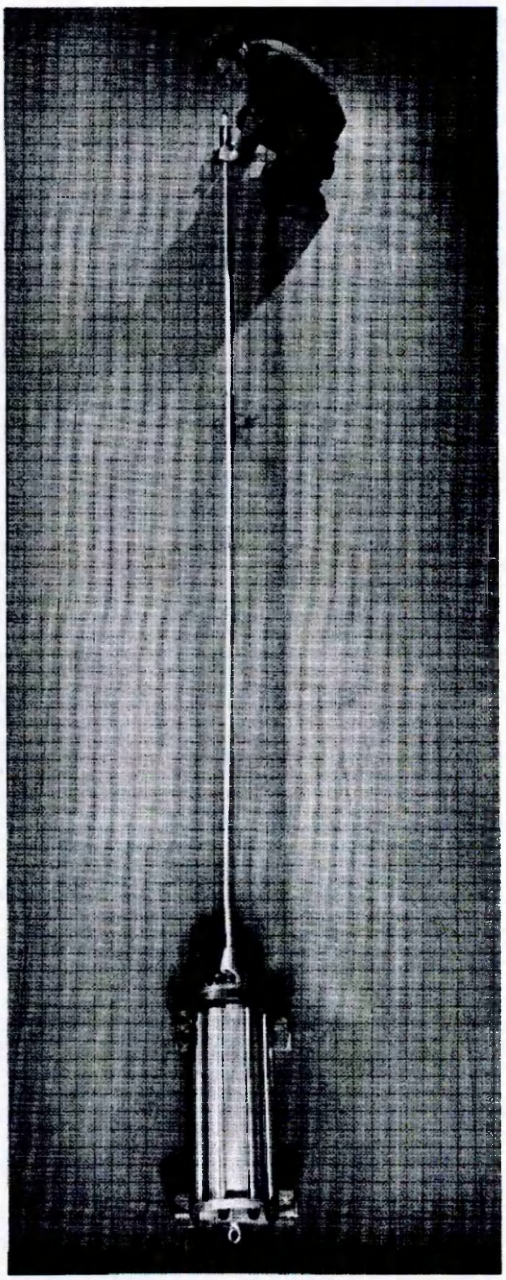

Figure 1.3. Temperature probe after Bullard (1954). The probe was 4.7 m long with two temperature sensors: one at its tip and the other at the base of the bulbous instrument package. The probe was released into the ocean from a vessel where it would sink to the ocean floor and embed itself into the regolith.

1.2.2 Planetary Heat Flow Probes

The heat flow probes used in the Apollo measurements (Langseth et al., 1972; 1976) were approximately 1.1 m long, with four differential temperature sensors[10], paired with

[10] A differential temperature sensor measures a change in temperature, as opposed to absolute temperature.

heaters, along their length. The sensors measured both differential and absolute temperatures, allowing the measuring of the thermal gradient; the heaters function similar to those mentioned in Lucazeau et al. (2010), mentioned at the end of Section 1.2.1. The probes were deployed in pairs (i.e. two per Apollo mission), separated by a distance of about 10 m. The dual configuration was meant to allow for any lateral temperature gradients along the probe-probe vertical plane to be detected (e.g. Langseth et al., 1972; Heiken et al., 1991) which, along with topographic information (see Section 1.1.3.2), is important for the correct interpretation of the recorded heat flows.

In situ heat flow measurements on other planets require robotic probes because of current limitations on the deployment of Apollo-style heat flow probes (or those used on Earth) on other planets (e.g. Stoker et al., 2006). The current generation of planetary heat flow probes are therefore optimised for robotic planetary missions, and are several times smaller than their earlier Earth-bound and lunar counterparts (e.g. Hagermann and Spohn, 1999; Spohn et al., 2001; Hagermann, 2005; Hagermann et al., 2006; Spohn et al., 2007; Paton et al., 2010; Kömle et al., 2011).

PLUTO (Planetary Underground Tool) was on the (failed) Beagle 2 lander of the Mars Express mission. It was to be deployed in a mole configuration capable of burrowing both vertically and laterally into and measuring thermophysical properties of Martian regolith (e.g. Richter et al., 2003; Richter et al., 2006). MUPUS PEN (Multi-Purpose Sensors for Surface and Subsurface Science Penetrator – see one configuration in Figure 1.4a) is part of the MUPUS payload on the Rosetta space probe lander, Philae (Spohn et al., 2007). It is designed to measure the surface heat flow (energy balance) and is due to rendezvous with comet 67P/Churyumov-Gerasimenko (67P/CG) in 2014. HP^3 (Heat flow and Physical Properties Package – see one configuration in Figure 1.4b) is a heat flow probe proposed for deployment in a mole configuration on Mars (e.g. Banerdt et al., 2012; Dehant et al., 2012; Spohn et al., 2012), Mercury (Spohn et al., 2001), and the Moon (Spohn et al., 2010).

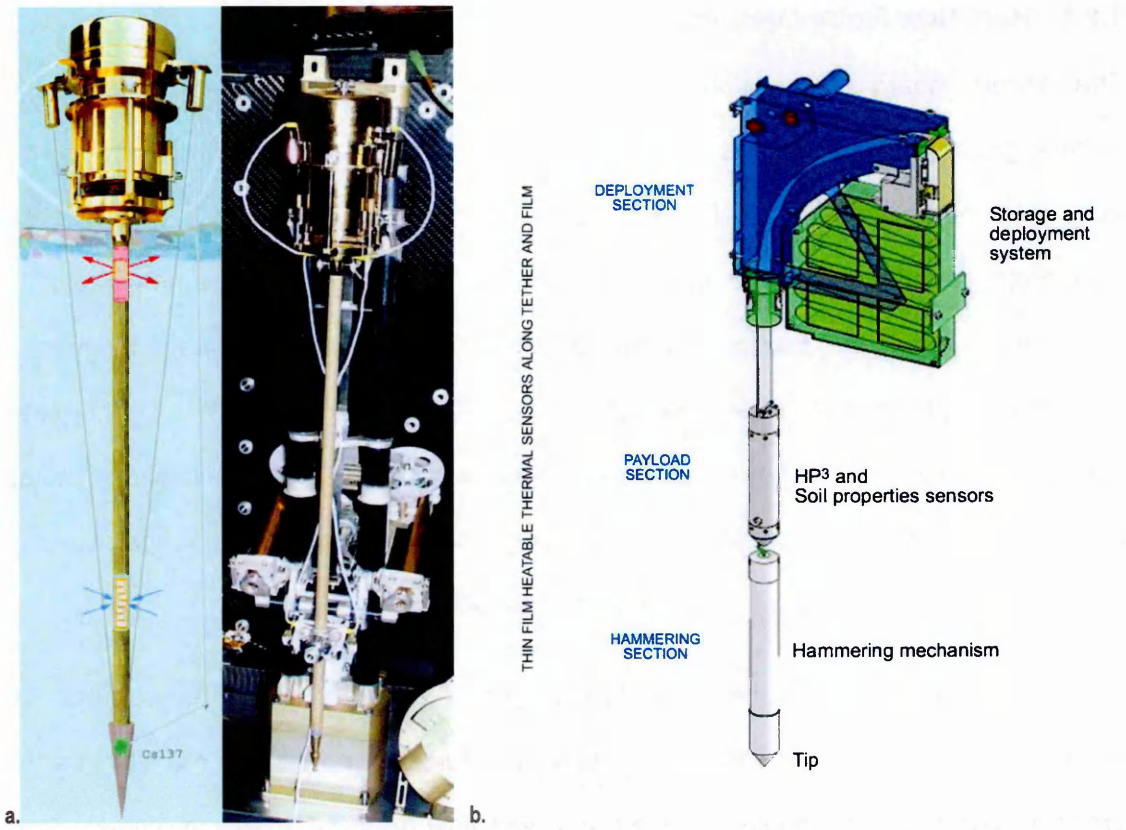

Figure 1.4. Heat flow probes: a. MUPUS-PEN one the left is an illustration of MUPUS-PEN in situ, on the right, MUPUS-PEN housed on the Rosetta Lander Robotic Arm (after Spohn et al., 2007); b. HP³ candidate configuration (after Ambrosi, 2008; also see Spohn et al., 2001; Kömle et al., 2011) – thermal sensors are located along the length of the tether, payload section and hammering section.

While being several times smaller and employing different technologies, the planetary probes mentioned above function on the same base principles as their Earth-bound and Apollo lunar counterparts: they have maximised length to diameter ratios; employ temperature sensors along their length; and possess means of measuring thermal conductivity from the dissipation of heat generated during probe emplacement, or by active heaters. MUPUS PEN, for example, has 16 active temperature sensors which range in length from 1 cm close to the base (surface) to 4 cm close to the tip, and cover a depth range of 32 cm. The design is optimized to measure the steep temperature gradients of the shallowest regions of the regolith and the shallower temperature gradients as depth increases (see Figure 1.1).

1.2.3 Heat Flow Probe Measurements

The sensors aboard a conventional planetary heat flow probe allow a measurement of the thermal gradient along the axis of penetration and an estimate of thermal conductivity, from which heat flow can be calculated. The modern probes mentioned in Section 1.2.2 have the capability to penetrate up to 5 m into planetary regolith (e.g. Spohn et al., 2012). At 5 m the surface solar flux is most likely damped to negligible values on the Moon (see Section 3.6), possibly Mars (see Section 5.3.1), Mercury (see Section 6.3.1) and small bodies like Vesta (see Section 7.3.1). Towards the surface, this is not the case; simulated skin depths of the former bodies lie between ~1 mm for Vestan diurnal temperatures to 1.9 m for Martian annual temperature end member scenarios.

The surface heat flow may be useful in the case of cometary surface energy balance investigations with MUPUS PEN, where there is interest in how the sun influences the emission processes. It should be noted that heat flow from the interior of comets (and possibly volatile rich asteroids) is not necessarily steady state and may vary with a period of the order of the orbital period (e.g. Prialnik and Merk, 2008; Prialnik et al., 2008) which further complicates matters. With asteroids and planets, interest is skewed towards the planetary heat flow which is related to the state of the interior. The superposition of the unsteady heat flow from the surface with the steady heat flow from the interior is, therefore, problematic where the heat flow probe sensor penetration depths are not far enough below the skin depth. As the main aim of this study is the extraction of the basal heat flow in the preceding case, detailed investigations of related scenarios are presented in Chapters 4-8.

The influence of topography is introduced at the end of Section 1.1.2 and its influence on lunar heat flow measurements mentioned in Section 1.1.3.2. Local and regional variation in topography causes lateral heat flow which cannot be quantified by a single heat flow probe measurement. Lateral heat flow modifies the temperature gradient which, unaccounted for, leads to systematic errors in any heat flow estimate (see Section 7.3 for examples with Vesta). Placing two or more probes in a particular configuration, as done

with the Apollo heat flow measurements (e.g. Langseth et al., 1972; Heiken et al., 1991), can allow these effects to be quantified. Each measurement, therefore, requires unique topographic analyses to correct for lateral heat flow. Wang (1992) notes that the horizontal attenuation of heat is similar to the vertical and finds that topography which extends at least the depth of measurement will likely affect all temperatures. Wang (1992) indicates that significant topographic features smaller than the measurement depth (e.g. rocks, diagonal stratigraphy) should be accounted for though gradual changes in topography have small effects. Additional topographic considerations, such as proximity to impact craters and breccia, with residual heat from an impact event or radioisotope enriched impact ejecta, can produce anomalously high heat flows as mentioned in Section 1.1.3.2 (also see Appendix 9.7.2 on Vesta).

Below the surface, unknown regolith composition may produce unexpected effects on the thermal profile; these may be due to refraction from sloping interfaces (subsurface layers or large rocks) of differing thermal diffusivity (see Section 3.3 for a discussion on layering; see Chapter 6 for examples with Mercury). Analysis of substructure profiles from infrared and mircrowave observations may aid the interpretation of any heat flow measurement. The presence of volatiles (ices) may render any measurements difficult to interpret because of high, temperature dependent thermal conductivities (e.g. Seiferlin et al., 1996; Spohn et al., 2001; Grott et al., 2007). Methods exist by which the effect of these can be isolated to some degree by analysis of relationships between volatile content and thermal properties (e.g. Béhaegel et al., 2007).

The process of penetration of a heat flow probe disturbs the regolith along its axis and may alter the physical and thermal properties of the soil. This can, however, be quantified to some degree, with suitable corrections made to heat flow estimates (e.g. Grott et al., 2010). Conduction along the probe axis may smooth the temperature profile where the conductivity of the probe is significantly higher than the regolith conductivity; this effect has been quantified by Hagermann & Spohn (1999) with a solution to recover the prestine temperature distribution.

The preceding phenomena highlight the importance of choosing an appropriate heat flow measurement site. Planetary heat flow probe measurements are suited to dry plains with suitably porous regolith. A trade-off is necessary between sites shadowed from solar influence versus areas exposed to the unsteady solar flux. Sites shadowed from the unsteady solar flux likely have relatively rough topography and high volatile content (with attendant temperature dependence of thermal properties). Dry sites tend to be close to the equator, where the mean temperatures are highest and temperature variation typically largest, resulting in greater masking of the basal heat flow and potentially greater variation of temperature dependent thermal properties. Practical constraints on the measurement depth means that a heat flow measurement will likely display both steady and unsteady components.

The magnitude of the heat flow is also critical to whether or not a heat flow measurement is successful. The current generation of planetary heat flow probes are precise to the order of 1 mK, which is equivalent to a temperature gradient uncertainty of 2 mK/m. The latter represents a lower limit to a temperature gradient which can be measured by the heat flow probes mentioned in this study. Low heat flow bodies like Vesta (see Chapter 7) may, therefore, not be ideal targets for heat flow measurement.

1.3 Modelling Heat Flow

1.3.1 Forward Modelling

Once the thermal influence of the probe itself is removed from the measurement and thermal conductivity determined (e.g. Banaszkiewicz et al., 1997; Hagermann and Spohn, 1999), the basal heat flow may be immediately available where the probe sensors penetrate far enough below the skin depth. Where no more than one sensor accesses the steady temperature gradient, further work is necessary. This involves the creation of a forward model (see Chapter 3) of the heat flow environment of the measurement using the heat flow equation (HFE – see Section 2.1.1).

Forward models developed in 2D or 3D space are more comprehensive. However, these are more complex and, therefore, require more computing resources and development time. A heat flow probe returns a measurement in 1D space over the time period of measurement. Any higher dimensional models require extrapolation of physical and thermal properties beyond the axis of measurement. In this study, the simpler 1D approach is taken.

The HFE can be partitioned into unsteady and steady components, conveniently allowing the steady (basal) and unsteady (surface) heat flow to be handled separately in a model; the steady component requires no time discretization. Where the regolith can be accurately represented by homogeneous (bulk) thermal properties with simple (smooth, continuous) boundary conditions, the forward model may be developed from analytical solutions (e.g. Carslaw and Jaeger, 1986). Numerical development leads to more general models which can handle homogeneous and heterogeneous regolith equivalently, as well as arbitrary boundary conditions (e.g. Patankar, 1980).

The forward model simulates subsurface temperatures during the period of measurement by time stepping from an initial state until the temperatures are equilibrated. Numerical boundary conditions can be heat flow, and/or temperature. Therefore, different basal heat flows (and, if necessary, surface temperatures and thermal properties) can be applied to the forward model until a good fit is obtained with the measured heat flow (conductivity and steady temperature gradient). This is, essentially, Monte Carlo modelling (e.g. Press, 2002). The preceding method, though potentially robust, can be time-consuming. A potentially more efficient route to a best fit solution involves the inversion of the temperature measurement, and optimization of the basal heat flow.

1.3.2 Inverse Modelling

The essential difference between the forward modelling approach and inversion is that in the former, the potential solutions are chosen arbitrarily, while in the latter, the solutions are chosen at the optimal value of a misfit function (see Section 2.3.1). There are several

approaches to inversion (see Menke, 1989 for general discrete theory and Tarantola, 2005 for a generalised functional theory), each of which determines the particular form of the misfit function. However, the misfit functions are all mainly defined by residuals between the temperature measurement and that predicted by a forward model calculation. These residuals are used to define the most efficient path to minimisation (or optimization) of the misfit function.

Shen et al. (1992) compare three methods of inversion, namely function specification (FSI – Shen and Beck, 1991; 1992), spectrum inversion (SI – Wang, 1992) and singular value decomposition (SVD – Mareschal and Vasseur, 1992). FSI and SI are based on the Bayesian inverse theory of Tarantola and Valette (1982) (also see Tarantola, 2005) and allows the optimization of both thermal properties and boundary conditions which are not well known. SVD, on the other hand, does not allow optimization of thermal properties, though these can be implicitly accounted for by discarding parts of the solution which contribute to instability.[11] The greater versatility of the FSI and SI approaches is, therefore, more attractive. In this study, FSI is pursued because it is more straightforwardly transcribed into a general numerical form, which is more accommodating in dealing with different boundary conditions and regolith properties.

It is important to note that inversion of temperature measurements (from boreholes, in particular) is a mature field in Earth-based climate studies: there have been few planetary measurements for the former to be applied to. These inversions are performed in 1D in the majority of cases because the measurements are 1D. A 3D inversion method is presented in Hopcroft et al. (2009). Where there is appreciable lateral variation in physical and thermal properties (which affects the subsurface temperature profile), the method

[11] Singular value decomposition allows for the removal of singular values from the matrix defined by the thermal properties along with associated temperature calculations. This effectively reduces the resolution of the method – more critical where time dependent parameters are being optimized, as opposed to the basal heat flow.

gives more accurate solutions. For the current purposes, a 1D approach is considered sufficient, as noted earlier; however 3D approaches appear to be a worthwhile area for further study.

1.4 Summary

It has been shown how planets form as hot bodies which, over time, lose heat through their surface regions by convection for the giant planets and diffusion (conduction, radiation, and advection) for rocky bodies. The heat loss from the surface regions is balanced by heat input from the planetary surface environment which is dominated by nearby stars. This study focuses on rocky planets. Steady (basal) heat flow quantifies the process of heat loss from the interior of a rocky planet and is dependent on mantle temperatures and the heat generated by radioisotopes in the crust. Unsteady heat flow quantifies the heat input from the planetary surface environment. The steady and unsteady states are superimposed in the surface regions. Measuring the heat flow of these bodies and combining the measurement with petrologic, seismologic, other geophysical data and modelling allows constraints to be placed on the internal processes which generate heat. In turn, this can provide crucial information about the evolution of these planets.

Heat flow measuring probes have been developed and used on Earth. The heat flow measurements have provided support for plate tectonic theory, estimation of crustal thickness, the state of the mantle and core, and the processes by which heat is transported from the interior. Attempts have been made, somewhat successfully, to remotely measure the surface heat flow of other planets using microwave and infrared observations. Lunar heat flow has been measured by probes emplaced by Apollo astronauts, though the measurements suffer from systematic uncertainties and have undergone several reanalyses. A heat flow measurement is due to be made on a comet by MUPUS PEN, a payload on the Rosetta space probe lander. MUPUS PEN is part of a new class of robotic instruments which are optimised for heat flow measurements. HP^3 is

a more capable, modular counterpart to MUPUS PEN and is designed to facilitate heat flow measurement on a variety of terrestrial planets. This study focuses on the recovery of the steady state heat flow from a heat flow probe measurement in the shallow subsurface regions of a planet.

Numerical modelling is the most versatile approach for the recovery of the basal heat flow from a shallow subsurface temperature measurement. Heat flow modelling can be separated into two regimes: forward and inverse modelling. Forward modelling is performed where the boundary conditions (temperature and/or heat flow) of the system are available and the internal (subsurface) temperatures are required. Inverse modelling is performed where a subsurface temperature measurement has been made and the boundary conditions (and/or thermal properties) which generated that temperature state are required. A heat flow probe measurement is returned in 1D space, over time, therefore 1D modelling is deemed sufficient for the current purposes.

In this study, an inverse model is developed which allows the recovery of the basal heat flow from a heat flow probe measurement of the shallow subsurface temperature gradient and thermal conductivity. This model, based on the Function Specification Inversion (FSI) method of Shen and Beck (1991, 1992), allows the (optional) simultaneous optimization of basal heat flow, surface temperature and thermal properties (conductivity, thermal capacity) with the temperature measurement. In Chapter 2, the heat flow theory supporting the forward model, and that behind FSI, are outlined. In Chapter 3, the forward model is presented with synthetic examples. It is an integral part of the inverse model, which is similarly presented in Chapter 4. In Chapters 5-7 the inverse model is applied to end member scenarios on Mars, Mercury and Vesta, respectively. The results are assessed in Chapter 8, and relevant implications outlined.

1.5 References

ABRAMOV, O. & MOJZSIS, S. J. 2011. Abodes for life in carbonaceous asteroids? *Icarus,* 213, 273-279.

AMBROSI, R. M. 2008. X-Gamma, HP^3 Extended:. *In:* BALL, A. J. (ed.) *Heat Flow, Density, Composition and Habitability Below the Martian Surface.* Online.

BANASZKIEWICZ, M., SEIFERLIN, K., SPOHN, T., KARGL, G. & KÖMLE, N. 1997. A new method for the determination of thermal conductivity and thermal diffusivity from linear heat source measurements. *Review of Scientific Instruments,* 68, 4184-4190.

BANERDT, W. B., SMREKAR, S., ALKALAI, L., HOFFMAN, T., WARWICK, R., HURST, K., FOLKNER, W., LOGNONNÉ, P., SPOHN, T., ASMAR, S., BANFIELD, D., BOSCHI, L., CHRISTENSEN, U., DEHANT, V., GIARDINI, D., GOETZ, W., GOLOMBEK, M., GROTT, M., HUDSON, T., JOHNSON, C., KARGL, G., KOBAYASHI, N., MAKI, J., MIMOUN, D., MOCQUET, A., MORGAN, P., PANNING, M., PIKE, W. T., TROMP, J., VAN ZOEST, T., WEBER, R., WIECZOREK, M. & TEAM, I. 2012. InSight: An Integrated Exploration of the Interior of Mars. *In:* Lunar and Planetary Institute Science Conference Abstracts, March 1, 2012 2012. 43, 2838.

BÉHAEGEL, M., SAILHAC, P. & MARQUIS, G. 2007. On the use of surface and ground temperature data to recover soil water content information. *Journal of Applied Geophysics,* 62, 234-243.

BENKHOFF, J. & HELBERT, J. 2006. Thermal infrared spectroscopy to investigate the composition of mercury – The MERTIS instrument on BepiColombo. *Advances in Space Research,* 38, 647-658.

BENKHOFF, J. & SPOHN, T. 1991. Thermal Histories of the Kosi Samples. *Geophysical Research Letters,* 18, 261-264.

BOEHLER, R. 1996. Melting Temperature of the Earth's Mantle and Core: Earth's Thermal Structure. *Annual Review of Earth And Planetary Sciences,* 24, 15-40.

BOSS, A. P. 2007. Evolution of the Solar Nebula. VIII. Spatial and Temporal Heterogeneity of Short-lived Radioisotopes and Stable Oxygen Isotopes. *The Astrophysical Journal,* 660, 1707-1714.

BREUER, D., HAUCK, S., II, BUSKE, M., PAUER, M. & SPOHN, T. 2007. Interior Evolution of Mercury. *Space Science Reviews,* 132, 229-260.

BREUER, D. & SPOHN, T. 2003. Early plate tectonics versus single-plate tectonics on Mars: Evidence from magnetic field history and crust evolution. *Journal of Geophysical Research (Planets),* 108, 5072.

BULLARD, E. 1954. The Flow of Heat through the Floor of the Atlantic Ocean. *Royal Society of London Proceedings Series A,* 222, 408-429.

BULLARD, E. C. 1945. Thermal History of the Earth. *Nature,* 156, 35-36.

BULLARD, E. C. & DAY, A. 1961. The Flow of Heat through the Floor of the Atlantic Ocean. *Geophysical Journal International,* 4, 282-292.

BULLARD, E. C., MAXWELL, A. E. & REVELLE, R. 1956. Heat Flow through the Deep Sea Floor. *Advances in Geophysics,* 3, 153.

CAMPINS, H., HARGROVE, K., PINILLA-ALONSO, N., HOWELL, E. S., KELLEY, M. S., LICANDRO, J., MOTHÉ-DINIZ, T., FERNÁNDEZ, Y. & ZIFFER, J. 2010. Water ice and organics on the surface of the asteroid 24 Themis. *Nature,* 464, 1320-1321.

CARSLAW, H. S. & JAEGER, J. C. 1986. *Conduction of heat in solids,* Oxford, Clarendon.

CASSEN, P. 2001. Nebular thermal evolution and the properties of primitive planetary materials. *Meteoritics & Planetary Science, vol. 36, no. 5,* 671-700.

CHAMBERS, J. E. 2004. Terrestrial Planet Formation. *THE SEARCH FOR OTHER WORLDS: Fourteenth Astrophysics Conference. AIP Conference Proceedings,* 713, 203-212 (2004).

CHAMBERS, J. E. & WETHERILL, G. W. 2001. Planets in the asteroid belt. *Meteoritics & Planetary Science, vol. 36, no. 3,* 381-399.

CHAPMAN, D. S., CHISHOLM, T. J. & HARRIS, R. N. 1992. Combining borehole temperature and meteorologic data to constrain past climate change. *Global and Planetary Change,* 6, 269-281.

CORADINI, A., TURRINI, D., FEDERICO, C. & MAGNI, G. 2011. Vesta and Ceres: Crossing the History of the Solar System. *Space Science Reviews,* 163, 25-40.

CROOK, T. 1923. The Wegener Hypothesis and the Origin of the Oceans. *Nature,* 111, 255-256.

DEHANT, V., BANERDT, B., LOGNONNÉ, P., GROTT, M., ASMAR, S., BIELE, J., BREUER, D., FORGET, F., JAUMANN, R., JOHNSON, C., KNAPMEYER, M., LANGLAIS, B., LE FEUVRE, M., MIMOUN, D., MOCQUET, A., READ, P., RIVOLDINI, A., ROMBERG, O., SCHUBERT, G., SMREKAR, S., SPOHN, T., TORTORA, P., ULAMEC, S. &

VENNERSTRØM, S. 2012. Future Mars geophysical observatories for understanding its internal structure, rotation, and evolution. *Planetary and Space Science,* 68, 123-145.

DENEVI, B. W., BLEWETT, D. T., BUCZKOWSKI, D. L., CAPACCIONI, F., CAPRIA, M. T., DE SANCTIS, M. C., GARRY, W. B., GASKELL, R. W., LE CORRE, L., LI, J.-Y., MARCHI, S., MCCOY, T. J., NATHUES, A., O'BRIEN, D. P., PETRO, N. E., PIETERS, C. M., PREUSKER, F., RAYMOND, C. A., REDDY, V., RUSSELL, C. T., SCHENK, P., SCULLY, J. E. C., SUNSHINE, J. M., TOSI, F., WILLIAMS, D. A. & WYRICK, D. 2012. Pitted Terrain on Vesta and Implications for the Presence of Volatiles. *Science,* 338, 246-.

EGEA-GONZALEZ, I. & RUIZ, J. 2013. Mercurian megaregolith layer and surface heat flows constraints. *In:* EGU General Assembly Conference Abstracts, April 1, 2013 2013. 15, 1788.

FISHER, A. T., DAVIS, E. E., HUTNAK, M., SPIESS, V., ZÜHLSDORFF, L., CHERKAOUI, A., CHRISTIANSEN, L., EDWARDS, K., MACDONALD, R., VILLINGER, H., MOTTL, M. J., WHEAT, C. G. & BECKER, K. 2003. Hydrothermal recharge and discharge across 50km guided by seamounts on a young ridge flank. *Nature,* 421, 618-621.

FORMISANO, M., FEDERICO, C., TURRINI, D., CORADINI, A., CAPACCIONI, F., SANCTIS, M. C. & PAUSELLI, C. 2013. The heating history of Vesta and the onset of differentiation. *Meteoritics and Planetary Science,* 48, 2316-2332.

GOOGLE 2010. Google Earth. *In:* GOOGLE (ed.) *Google Earth.* 5.2 ed. Online: Google.

GROTT, M. & BREUER, D. A. A. 2010. On the spatial variability of the Martian elastic lithosphere thickness: Evidence for mantle plumes? *Journal of Geophysical Research (Planets),* 115, 3005.

GROTT, M., HAUBER, E., WERNER, S. C., KRONBERG, P. & NEUKUM, G. 2005. High heat flux on ancient Mars: Evidence from rift flank uplift at Coracis Fossae. *Geophysical Research Letters,* 32, L21201.

GROTT, M., HELBERT, J. & NADALINI, R. 2007. Thermal structure of Martian soil and the measurability of the planetary heat flow. *J. Geophys. Res.,* 112, E09004.

GROTT, M., KNOLLENBERG, J. & KRAUSE, C. 2010. Apollo lunar heat flow experiment revisited: A critical reassessment of the in situ thermal conductivity determination. *Journal of Geophysical Research (Planets),* 115, 11005.

HAGERMANN, A. 2005. Planetary heat flow measurements. *Royal Society of London Transactions Series A, vol. 363*, 2777-2791.

HAGERMANN, A., BALL, A. J., HATHI, B., LEESE, M. R., LORENZ, R. D., ROSENBERG, P. D., TOWNER, M. C. & ZARNECKI, J. C. 2006. Inferring the composition of the liquid surface on Titan at the Huygens probe landing site from Surface Science Package measurements. *Advances in Space Research,* 38, 794-798.

HAGERMANN, A. & SPOHN, T. 1999. A method to invert MUPUS temperature recordings for the subsurface temperature field of P/Wirtanen. *Advances in Space Research,* 23, 1333-1336.

HAGERMANN, A. & TANAKA, S. 2006. Ejecta deposit thickness, heat flow, and a critical ambiguity on the Moon. *Geophysical Research Letters,* 33, L19203.

HANSEN, B. M. S. 2009. Formation of the Terrestrial Planets from a Narrow Annulus. *The Astrophysical Journal,* 703, 1131-1140 (2009).

HAUCK, S. A., MARGOT, J.-L., SOLOMON, S. C., PHILLIPS, R. J., JOHNSON, C. L., LEMOINE, F. G., MAZARICO, E., MCCOY, T. J., PADOVAN, S., PEALE, S. J., PERRY, M. E., SMITH, D. E. & ZUBER, M. T. 2013. The curious case of Mercury's internal structure. *Journal of Geophysical Research (Planets),* 118, 1204-1220.

HEIKEN, G. H., VANIMAN, D. T., FRENCH, B. M., VANIMAN, D. T. & FRENCH, B. M. 1991. *Lunar sourcebook - A user's guide to the moon.*

HOLMES, A. 1931. Radioactivity and Earth Movements. *Nature,* 128, 496.

HOPCROFT, P. O., GALLAGHER, K., PAIN, C. C. & FANG, F. 2009. Three-dimensional simulation and inversion of borehole temperatures for reconstructing past climate in complex settings. *Journal of Geophysical Research (Earth Surface),* 114, 2019.

HSUI, A. T. & TOKSÖZ, M. N. 1977. Thermal evolution of planetary size bodies. *In: Lunar Science Conference, 8th, Houston, Tex., March 14-18, 1977, Proceedings. Volume 1. (A78-41551 18-91) New York, Pergamon Press, Inc., 1977*, 447-461.

HUBBARD, W. B., BURROWS, A. & LUNINE, J. I. 2002. Theory of Giant Planets. *Annual Review of Astronomy and Astrophysics, Vol. 40*, 103-136 (2002).

JAUPART, C., SCLATER, J. G. & SIMMONS, G. 1981. Heat flow studies: Constraints on the distribution of uranium, thorium and potassium in the continental crust. *Earth and Planetary Science Letters,* 52, 328-344.

KASHI, A. & SOKER, N. 2011. The outcome of the protoplanetary disk of very massive stars. *New Astronomy,* 16, 27-32.

KAULA, W. M. 1979. Thermal Evolution of Earth and Moon Growing by Planetesimal Impacts. *Journal of Geophysical Research,* 84, 999-1008.

KEIHM, S. J. 1984. Interpretation of the lunar microwave brightness temperature spectrum: Feasibility of orbital heat flow mapping. *Icarus,* 60, 568-589.

KOKUBO, E. & GENDA, H. 2010. Formation of Terrestrial Planets from Protoplanets Under a Realistic Accretion Condition. *The Astrophysical Journal Letters,* 714, L21-L25 (2010).

KOKUBO, E. & IDA, S. 2002. The Formation of Protoplanet Systems and the Diversity of Planetary Systems. *The Proceedings of the IAU 8th Asian-Pacific Regional Meeting,* II, held at National Center of Sciences, Hitotsubashi Memorial Hall, Tokyo, July 2 - 5, 2002, Edited by S. Ikeuchi, J. Hearnshaw, and T. Hanawa, the Astronomical Society of Japan, 2002, 47-48.

KOKUBO, E. & IDA, S. 2007. Formation of Terrestrial Planets from Protoplanets. II. Statistics of Planetary Spin. *The Astrophysical Journal,* 671, 2082-2090.

KOKUBO, E., KOMINAMI, J. & IDA, S. 2006. Formation of Terrestrial Planets from Protoplanets. I. Statistics of Basic Dynamical Properties. *The Astrophysical Journal,* 642, 1131-1139.

KÖMLE, N. I., HÜTTER, E. S., MACHER, W., KAUFMANN, E., KARGL, G., KNOLLENBERG, J., GROTT, M., SPOHN, T., WAWRZASZEK, R., BANASZKIEWICZ, M., SEWERYN, K. & HAGERMANN, A. 2011. In situ methods for measuring thermal properties and heat flux on planetary bodies. *Planetary and Space Science,* 59, 639-660.

LANGSETH, M. G., JR., CLARK, S. P., JR., CHUTE, J. L., JR., KEIHM, S. J. & WECHSLER, A. E. 1972. The Apollo 15 Lunar Heat-Flow Measurement. *Moon,* 4, 390-410.

LANGSETH, M. G., KEIHM, S. J. & PETERS, K. 1976. Revised lunar heat-flow values. *In:* KINSLER, D. C., ed. Lunar and Planetary Science Conference Proceedings, April 1, 1976 1976. 7, 3143-3171.

LEINHARDT, Z. M., RICHARDSON, D. C., LUFKIN, G. & HASELTINE, J. 2009. Planetesimals to protoplanets - II. Effect of debris on terrestrial planet formation. *Monthly Notices of the Royal Astronomical Society,* 396, 718-728.

LINSKY, J. L. 1966. Models of the Lunar Surface Including Temperature-Dependent Thermal Properties. *Icarus,* 5, 606-634.

LISSAUER, J. J. 1993. Planet formation. *In: Annual review of astronomy and astrophysics. Vol. 31 (A94-12726 02-90)*, 129-174.

LUCAZEAU, F., LEROY, S., ROLANDONE, F., D'ACREMONT, E., WATREMEZ, L., BONNEVILLE, A., GOUTORBE, B. & DÜSÜNUR, D. 2010. Heat-flow and hydrothermal circulation at the ocean-continent transition of the eastern gulf of Aden. *Earth and Planetary Science Letters,* 295, 554-570.

MARESCHAL, J.-C. & VASSEUR, G. 1992. Ground temperature history from two deep boreholes in Central France. *Palaeogeography, Palaeoclimatology, Palaeoecology,* 98, 185-192.

MARESCHAL, J. C., HAMDANI, Y. & JESSUP, D. M. 1989. Downward continuation of heat flow data. *Tectonophysics,* 164, 129-137.

MCKEEGAN, K. D. & DAVIS, A. M. 2005. *Early Solar System Chronology*

Meteorites, Comets and Planets: Treatise on Geochemistry, Volume 1. Edited by A. M. Davis. Executive Editors: H. D. Holland and K. K. Turekian. ISBN 0-08-044720-1. Published by Elsevier B. V., Amsterdam, The Netherlands, 2005, p.431.

MELTON, F. A. 1925. Scientific Books: The Origin of Continents and Oceans. *Science,* 62, 14-15.

MENKE, W. 1989. *Geophysical Data Analysis: Discrete Inverse Theory,* San Diego, Academic Press.

O'BRIEN, D. & SYKES, M. 2011. The Origin and Evolution of the Asteroid Belt—Implications for Vesta and Ceres. *Space Science Reviews,* 163, 41-61.

O'ROURKE, J. G. & KORENAGA, J. 2012. Terrestrial planet evolution in the stagnant-lid regime: Size effects and the formation of self-destabilizing crust. *Icarus,* 221, 1043-1060.

PARSONS, B. & SCLATER, J. G. 1977. An analysis of the variation of ocean floor bathymetry and heat flow with age. *Journal of Geophysical Research,* 82, 803-827.

PATANKAR, S. V. 1980. *Numerical Heat Transfer and Fluid Flow,* New York, NY, London, Hemisphere.

PATON, M. D., KARGL, G., BALL, A. J., GREEN, S. F., HAGERMANN, A., KÖMLE, N. I., THIEL, M. & ZARNECKI, J. C. 2010. Computer modelling of a penetrator thermal sensor. *Advances in Space Research,* 46, 337-345.

PETTERSSON, H. 1949. Exploring the Bed of the Ocean. *Nature,* 164, 468-470.

PINET, C. & JAUPART, C. 1987. The vertical distribution of radiogenic heat production in the Precambrian crust of Norway and Sweden: Geothermal implications. *Geophysical Research Letters,* 14, 260-263.

PIQUEUX, S. & CHRISTENSEN, P. R. 2011. Temperature-dependent thermal inertia of homogeneous Martian regolith. *Journal of Geophysical Research (Planets),* 116, 7004.

POLLACK, H. N. & HUANG, S. 2000. Climate Reconstruction from Subsurface Temperatures. *Annual Review of Earth And Planetary Sciences,* 28, 339-365 (2000).

POLLACK, H. N., HURTER, S. J. & JOHNSON, J. R. 1993. Heat flow from the earth's interior - Analysis of the global data set. *Reviews of Geophysics,* 31, 267-280.

POLLACK, J. B., HUBICKYJ, O., BODENHEIMER, P., LISSAUER, J. J., PODOLAK, M. & GREENZWEIG, Y. 1996. Formation of the Giant Planets by Concurrent Accretion of Solids and Gas. *Icarus,* 124, 62-85.

PRESS, W. H. 2002. *Numerical Recipes in C++: The Art of Scientific Computing,* Cambridge, Cambridge University Press.

PRIALNIK, D. 1989. Thermal evolution of cometary nuclei. *Advances in Space Research,* 9, 25-40.

PRIALNIK, D. & MERK, R. 2008. Growth and evolution of small porous icy bodies with an adaptive-grid thermal evolution code - I. Application to Kuiper belt objects and Enceladus. *Icarus,* 197, 211-220.

PRIALNIK, D., SARID, G., ROSENBERG, E. D. & MERK, R. 2008. Thermal and chemical evolution of comet nuclei and Kuiper belt objects. *Space Science Reviews,* 138, 147-164.

QUINTANA, E. V. & LISSAUER, J. J. 2006. Terrestrial planet formation surrounding close binary stars. *Icarus,* 185, 1-20.

REVELLE, R. & MAXWELL, A. E. 1952. Heat Flow through the Floor of the Eastern North Pacific Ocean. *Nature,* 170, 199-200.

RICHTER, L., GROMOV, V. V., KOCHAN, H., KOSACKI, K., TOKANO, T. & KIEFFER, H. H. 2003. The Planetary Underground Tool (PLUTO) Experiment on the Beagle 2 Mars Lander. *In:* ALBEE, A. L., ed. Sixth International Conference on Mars, July 1, 2003 2003. 3180.

RICHTER, L. O., COSTE, P. A., GRZESIK, A., KNOLLENBERG, J., MAGNANI, P., NADALINI, R., RE, E., ROMSTEDT, J., SOHL, F. & SPOHN, T. 2006. Instrumented Moles for Planetary Subsurface Regolith Studies. *AGU Fall Meeting Abstracts,* 54, 05.

ROY, R. F., BLACKWELL, D. D. & BIRCH, F. 1968. Heat generation of plutonic rocks and continental heat flow provinces. *Earth and Planetary Science Letters,* 5, 1-12.

RUDNICK, R. L. & FOUNTAIN, D. M. 1995. Nature and composition of the continental crust: A lower crustal perspective. *Reviews of Geophysics,* 33, 267-310.

RUIZ, J. 2007. The heat flow during the formation of ribbon terrains on Venus. *Planetary and Space Science,* 55, 2063-2070.

RUIZ, J., TEJERO, R. & MCGOVERN, P. J. 2006. Evidence for a differentiated crust in Solis Planum, Mars, from lithospheric strength and heat flow. *Icarus,* 180, 308-313.

RUSSELL, C. T., RAYMOND, C. A., JAUMANN, R., MCSWEEN, H. Y., SANCTIS, M. C., NATHUES, A., PRETTYMAN, T. H., AMMANNITO, E., REDDY, V., PREUSKER, F., O'BRIEN, D. P., MARCHI, S., DENEVI, B. W., BUCZKOWSKI, D. L., PIETERS, C. M., MCCORD, T. B., LI, J.-Y., MITTLEFEHLDT, D. W., COMBE, J.-P., WILLIAMS, D. A., HIESINGER, H., YINGST, R. A., POLANSKEY, C. A. & JOY, S. P. 2013. Dawn completes its mission at 4 Vesta. *Meteoritics and Planetary Science,* 48, 2076-2089.

SCLATER, J. G., JAUPART, C. & GALSON, D. 1980. The heat flow through oceanic and continental crust and the heat loss of the earth. *Reviews of Geophysics and Space Physics,* 18, 269-311.

SCLATER, J. G., PARSONS, B. & JAUPART, C. 1981. Oceans and continents - Similarities and differences in the mechanisms of heat loss. *Journal of Geophysical Research,* 86, 11535-11552.

SEEP, N. H. 2001. Habitability of Terrestrial Planets in the Early Solar System. *AGU Fall Meeting Abstracts,* 51, 01.

SEIFERLIN, K., KÖMLE, N. I., KARGL, G. & SPOHN, T. 1996. Line heat-source measurements of the thermal conductivity of porous H_2O ice, CO_2 ice and mineral powders under space conditions. *Planetary and Space Science,* 44, 691-704.

SHEN, P. Y. & BECK, A. E. 1991. Least Squares Inversion of Borehole Temperature Measurements in Functional Space. *J. Geophys. Res.,* 96, 19965-19979.

SHEN, P. Y. & BECK, A. E. 1992. Paleoclimate change and heat flow density inferred from temperature data in the Superior Province of the Canadian sheild. *Palaeogeography, Palaeoclimatology, Palaeoecology,* 98, 143-165.

SHEN, P. Y., WANG, K., BELTRAMI, H. & MARESCHAL, J. C. 1992. A comparative study of inverse methods for estimating climatic history from borehole temperature data. *Palaeogeography, Palaeoclimatology, Palaeoecology,* 98, 113-127.

SHIMAZU, H. & TERASAWA, T. 1995. Electromagnetic induction heating of meteorite parent bodies by the primordial solar wind. *Journal of Geophysical Research,* 100, 16923-16930.

SPOHN, T. 1991. Mantle differentiation and thermal evolution of Mars, Mercury, and Venus. *Icarus,* 90, 222-236.

SPOHN, T., BALL, A. J., SEIFERLIN, K., CONZELMANN, V., HAGERMANN, A., ÖMLE, N. I. & KARGL, G. 2001. A heat flow and physical properties package for the surface of Mercury. *Planetary and Space Science,* 49, 1571-1577.

SPOHN, T., GROTT, M., KNOLLENBERG, J., VAN ZOEST, T., KARGL, G., SMREKAR, S. E., BANERDT, W. B., HUDSON, T. L. & TEAM, H. I. 2012. INSIGHT: Measuring the Martian Heat Flow Using the Heat Flow and Physical Properties Package (HP^3). *In:* Lunar and Planetary Institute Science Conference, 2012. 43, 1445.

SPOHN, T., GROTT, M., RICHTER, L., KNOLLENBERG, J., SMREKAR, S. E. & TEAM, H. I. 2010. Measuring Heat Flow on the Moon -- The Heat Flow and Physical Properties Package HP^3. *LPI Contributions,* 1530, 3016.

SPOHN, T., SEIFERLIN, K., HAGERMANN, A., KNOLLENBERG, J., BALL, A. J., BANASZKIEWICZ, M., BENKHOFF, J., GADOMSKI, S., GREGORCZYK, W., GRYGORCZUK, J., HLOND, M., KARGL, G., KÜHRT, E., KÖMLE, N., KRASOWSKI, J., MARCZEWSKI, W. & ZARNECKI, J. C. 2007. Mupus A Thermal and Mechanical Properties Probe for the Rosetta Lander Philae. *Space Science Reviews,* 128, 339-362.

STEINER, G. & KOMLE, N. I. 1991. A Model of the Thermal-Conductivity of Porous Water Ice at Low Gas-Pressures. *Planetary and Space Science,* 39, 507-513.

STOKER, C. R., LEMKE, L. G., GONZALES, A. A. & STANSBERY, E. 2006. Applications of Burrowing Moles for Planetary and Lunar Subsurface Access. *In:* MACKWELL, S., ed. 37th Annual Lunar and Planetary Science Conference, March 1, 2006 2006. 37, 1542.

STUBBS, T. J. & WANG, Y. 2012. Illumination conditions at the Asteroid 4 Vesta: Implications for the presence of water ice. *Icarus,* 217, 272-276.

TARANTOLA, A. 2005. *Inverse problem theory and methods for model parameter estimation,* Philadelphia, PA, Society for Industrial and Applied Mathematics.

TARANTOLA, A. & VALETTE, B. 1982. Generalized nonlinear inverse problems solved using the least squares criterion. *Reviews of Geophysics,* 20, 219-232.

TURCOTTE, D. L. & OXBURGH, E. R. 1967. Finite amplitude convective cells and continental drift. *Journal of Fluid Mechanics,* 28, 29-42.

VÖLSCHOW, M., BANERJEE, R. & HESSMAN, F. V. 2014. Second generation planet formation in NN Serpentis? *Astronomy and Astrophysics,* 562, 19.

VON HERZEN, R. P. & UYEDA, S. 1963. Heat Flow through the Eastern Pacific Ocean Floor. *Journal of Geophysical Research,* 68, 4219.

WANG, K. 1992. Estimation of Ground Surface Temperatures from Borehole Temperature Data. *J. Geophys. Res.,* 97, 2095-2106.

WARREN, P. H. & RASMUSSEN, K. L. 1987. Megaregolith insulation, internal temperatures, and bulk uranium content of the moon. *Journal of Geophysical Research,* 92, 3453-3465.

WATTERS, T. R., SCHULTZ, R. A., ROBINSON, M. S. & COOK, A. C. 2002. The mechanical and thermal structure of Mercury's early lithosphere. *Geophysical Research Letters,* 29, 1542.

WEIDENSCHILLING, S. J. 2000. *Formation of Planetesimals and Accretion of the Terrestrial Planets*

From Dust to Terrestrial Planets. Proceedings of an ISSI Workshop, held February 15-19, 1999, in Bern, Switzerland. Space Sciences series of International Space Science Institute (ISSI). Edited by W. Benz, R. Kallenbach, and G. W. Lugmair. Published by Kluwer Academic Publishers, P. O. Box 17, 3300 AA Dordrecht, The Netherlands.

WETHERILL, G. W. 1985. Occurrence of giant impacts during the growth of the terrestrial planets. *Science (ISSN 0036-8075), vol. 228, May 17, 1985,* 877-879.

WOLFRAM ALPHA, L. 2014. Wolfram|Alpha. *Wolfram|Alpha.* 1.3.0.4590401 ed. Google Play Store: Wolfram Alpha LLC.

ZHOU, J.-L., AARSETH, S. J., LIN, D. N. C. & NAGASAWA, M. 2005. Origin and Ubiquity of Short-period Earth-like Planets: Evidence for the Sequential Accretion Theory of Planet Formation. *The Astrophysical Journal,* 631, L85-L88.

2 THEORY

2.1 Forward Problem

Heat flow involves several processes within a planet[1] where, as noted in Section 1.1, the focus of this study is heat diffusion. Heat flow leads to an internal temperature distribution, based on internal thermal properties and surface energy balance (see Section 1.1.2). If the internal temperature distribution at a given point in time is required, a theory of heat transfer (defined by a heat flow equation) is solved by applying appropriate boundary and initial conditions – this is the essence of the forward problem.

2.1.1 Heat Flow Equation (HFE)

In this study the HFE is presented in general (superposed) and partitioned (unsteady and steady) forms. These forms are permitted by the analytical solutions (see Section 2.1.2) to the HFE and allow convenient manipulation of the boundary and initial parameters in the forward problem and the inverse problem (Section 2.2), in particular.

2.1.1.1 General HFE

General 1D[2] heat diffusion can be represented by the HFE

$$\rho c \frac{\partial T}{\partial t} - \frac{\partial}{\partial z}\left(k \frac{\partial T}{\partial z}\right) = S, \qquad z \in [z_S, z_B], t \in (t_B, t_E], \tag{2.1}$$

with boundary conditions

---

[1] Heat flow involves transfer of heat by diffusion, convection and fluid flow. Heat diffusion, as introduced in Section 1.1, is the focus of this study; the latter two transfer modes are beyond its scope.

[2] The merits of considering heat flow in 1D, versus 2D or 3D space are discussed in Section 1.3.

[3] The notation applies to a data range where: $c \in (a, b) \Leftrightarrow a < c < b$ (an open interval) and $c \in [a, b] \Leftrightarrow a \leq c \leq b$ (a closed interval).

$$T = T_S, \qquad z = z_S, t \in (t_B, t_E] \tag{2.2}$$

$$-k\frac{\partial T}{\partial z} = F_B, \qquad z = z_B, t \in (t_B, t_E], \tag{2.3}$$

and initial condition

$$T = T^0, \qquad z \in [z_S, z_B], t = t_B. \tag{2.4}$$

Variable t is time (t_B begins the period, t_E ends the period), z is one spatial dimension (depth: z_S is the surface[4], z_B is the base), $T \Leftrightarrow T(z,t)$, is temperature, $F \Leftrightarrow F(z,t)$, is heat flow, $\rho \Leftrightarrow \rho(z)$ is the depth dependent density, $c \Leftrightarrow c(z)$ is specific heat, the product ρc the thermal capacity, $k \Leftrightarrow k(z)$, is thermal conductivity, and $S \Leftrightarrow S(z,t)$ is a term representing heat sources or sinks. Alphanumeric and topical lists of symbols are presented in Appendix 9.1.

2.1.1.2 Unsteady HFE

In the partitioned problem the unsteady component is equivalent to the time varying surface heat fluxes, it may therefore be represented by

$$\rho c\frac{\partial T^U}{\partial t} - \frac{\partial}{\partial z}\left(k\frac{\partial T^U}{\partial z}\right) = S^U, \qquad z \in [z_S, z_B], t \in (t_B, t_E], \tag{2.5}$$

where superscript U denotes unsteady and subscripts carry the same meaning as in Equations 2.1-2.4. The boundary conditions are

$$T^U = T_S^U, \qquad z = z_S, t \in (t_B, t_E], \tag{2.6}$$

$$-k\frac{\partial T^U}{\partial z} = F_B^U, \qquad z = z_B, t \in (t_B, t_E], \tag{2.7}$$

with initial condition

---

[4] Usually defined as $z_S = 0$

$$T^U = 0, \qquad z \in [z_S, z_B], t = t_B. \tag{2.8}$$

Conventionally, $F_B^U = S^U = 0$.[5]

2.1.1.3 *Steady HFE*

The steady component of the partitioned problem is equivalent to the internal heat flux and is defined by

$$-\frac{d}{dz}\left(k\frac{dT^S}{dz}\right) = S^S, \qquad z \in [z_S, z_B], \tag{2.9}$$

where superscript S denotes steady and the boundary conditions are

$$T^S = T_S^S, \qquad z = z_S, \tag{2.10}$$

$$-k\frac{dT^S}{dz} = F_B^S, \qquad z = z_B. \tag{2.11}$$

Equation 2.11 defines the basal steady heat flow F_B^S. The aim of this study is to recover a best estimate of F_B^S from measurements of the temperature at depth. Examining the solutions, and solution methods for these equations, aids in quantifying the challenges posed by the superposition of the steady and unsteady heat flows.

---

[5] In the heat flow problem the initial condition is considered to be steady state with T_S and F_B constant. T_S starts to evolve due to external forcing by a surface heat source, introducing T_S^U into T^U and T^U into T. In the planetary sense F_B remains constant and F_B^U non-existent as the heat flowing into the lower boundary from the interior can be considered constant for medium term scenarios, though there are variations over planetary evolution timescales, and on shorter timescales for small bodies like comets.

2.1.2 Solutions to the HFE

2.1.2.1 Analytical Solutions

The HFE may be solved analytically using integral transforms of Laplace and Fourier type. Fourier analytical methods work best applied to relatively simple heat flow problems with homogeneous thermal properties while Laplace methods are handy when dealing with heterogeneity (e.g Carslaw and Jaeger, 1986). The complexity of analytical solutions increases with the degree of heterogeneity of thermal properties (see Section 2.1.2.3) and nonlinearity of boundary conditions.

2.1.2.1.1 Unsteady Solutions

An analytical solution to the unsteady HFE (Equation 2.5) can be found by treating the planetary surface as a homogeneous, isotropic, semi-infinite solid, to which an arbitrary, repeating boundary surface temperature is applied. Applying (see Appendix 9.2.1.1) the discrete Fourier transform (DFT – e.g. Press, 2002; Arfken and Weber, 2005) gives the solution (Carslaw and Jaeger, 1986)[6]

$$T^U = T_S^{UA} e^{-z\sqrt{\omega_f/2\kappa}} \cos\left(\omega_f t - \varphi - z\sqrt{\omega_f/2\kappa}\right), \qquad 2.12$$

$$z \in [z_S, z_B), t \in (t_B, t_E]$$

where T_S^{UA} is the surface temperature amplitude, ω_f is the frequency of temperature oscillations, $\kappa = k/\rho c$ is the thermal diffusivity, and φ indicates the phase of the surface boundary temperature, the cosine term being the phase shift with depth.

Examination of Equation 2.12 reveals two key characteristics of unsteady heat flow which are noted in Section 1.2.2:

---

[6] Also see Tautz (1971) which arrives at the same solution using the Laplace transform (Hagermann, 2013).

1. the temperature oscillations are attenuated at depth, and are more strongly attenuated with higher frequencies or lower thermal diffusivities – this is characterised by the natural exponent and;
2. the harmonic characteristics of the propagated disturbance are modified by the introduction of a phase lag which increases with depth – this is characterised by the cosine term.

The observations from Equation 2.12 illustrate how information on surface heating is lost with unsteady heat flow into the subsurface, making the problem of determining unsteady surface boundary conditions by inverting a given temperature distribution ill-posed. This also means that the basal heat flow (steady temperature gradient) can be accessed at depths below the unsteady temperature envelope. The temperature profile produced by the solution is illustrated in Section 3.4.1.where the two observations can be confirmed.

2.1.2.1.2 Steady Solutions

An analytical solution to the steady HFE (Equation 2.9) can be found by treating the planetary surface as a homogeneous, isotropic finite solid to give (Appendix 9.2.1.2)

$$T^S = T_S^S - \frac{F_B^S}{k}z + \frac{S^S}{2k}z^2, \qquad z \in [z_S, z_B). \tag{2.13}$$

Key observations from Equation 2.13 are:

1. The basal heat flow F_B^S introduces a linear temperature gradient with depth;
2. the magnitude of the temperature gradient with depth z correlates positively with F_B^S and negatively with k and;
3. the source term S^S has a parabolic effect on the temperature distribution with depth – this is discussed further in Section 3.2.

The steady temperature gradient is positive or negative depending on whether heat is flowing into $F_B^S > 0$) or out of ($F_B^S < 0$) the base of the solid, respectively. In conventional planetary cases the temperature gradient due to F_B^S is positive. The third observation suggests how unknown source distributions can mask the temperature gradient due to F_B^S

and reduce the accuracy with which it can be determined. All three of the preceding observations are illustrated in Section 3.2.

2.1.2.1.3 Superposed Solution

The superposed solution corresponding to the solution of Equation 2.1 is found by summing Equations 2.12 and 2.13 to produce

$$T = T^S + T^U = T_S^S - \frac{F_B^S}{k} + \frac{S^S}{k}z - \frac{S^S}{2k}z^2 + T_S^{UA} e^{-z\sqrt{\omega_f/2\kappa}} \cos\left(\omega_f t - \varphi - z\sqrt{\omega_f/2\kappa}\right), \quad 2.14$$

$$z \in [z_S, z_B), t \in (t_B, t_E].$$

Equation 2.14 quantifies the interaction of the unsteady and steady components of the heat flow with the thermal properties such that:

1. for a given conductivity k (and diffusivity κ) more of the steady temperature is seen with depth z, and less of the unsteady temperature;
2. if k remains constant and κ increases (thermal capacity ρc decreases) the unsteady temperature penetrates deeper and masks more of the steady temperature and;
3. a larger unsteady temperature amplitude T_S^{UA} masks more of the steady temperature for given z.

The former are not the only possible representations of the subsurface temperature due to surface forcing. The heat flow and heat source terms in the steady solution can be modified depending on the distribution of heat sources while the attenuation and phase lag of the unsteady solution can be represented by other functions (e.g. the error function solution; see Carslaw and Jaeger, 1986). The temperature and heat flow distributions of the superposed solution are illustrated in Section 3.5.

2.1.2.2 *Numerical Solutions*

Numerical development of solutions to the HFE possesses notable advantages over analytical development. The numerical solutions are intrinsically tailored to handle heterogeneity (see Section 2.1.2.3) in thermal properties and are relatively conducive to the use of nonlinear boundaries. Numerical solutions converge on the analytical solutions in the limit where the space and time resolutions are infinitesimal (e.g. Davis, 1986; see Section 3.4.1.1 for an illustration).

2.1.2.2.1 Finite Control Volume Method

Numerical methods reduce the equations in Section 2.1.1 to a set of simultaneous equations through discretization. The fully implicit 1D Finite Control Volume (FCV) method (Patankar, 1980; summarised in Appendix 9.2.1.3) is used to discretize Equation 2.1. This produces a set (or grid) of simultaneous equations for N temperatures T_n at M times where

$$a_n T_n - b_n T_{n+1} - c_n T_{n-1} = d_n, \qquad n \in [1, N], \tag{2.15}$$

and (Figure 2.1)

$$\text{a.} \quad b_n = \frac{k_{i+1}}{\delta z_{i+1}}, \qquad i \in [1, N-1],$$

$$\text{b.} \quad c_n = \frac{k_i}{\delta z_i}, \qquad z \in [z_1, z_N),$$

$$\text{c.} \quad a_n^0 = \rho_n c_n \frac{\Delta z_n}{\Delta t_m}, \qquad m \in [0, M-1], \tag{2.16}$$

$$\text{d.} \quad d_n = S_n^C \Delta z_n + a_n^0 T_n^0, \qquad t \in (t_0, t_{M-1}] \ .$$

$$\text{e.} \quad a_n = b_n + c_n + a_n^0 - S_n^T \Delta z_n,$$

The previous two equations show that the temperature at any gridpoint n is due to the balance of energy between it and surrounding gridpoints $n-1$, $n+1$. The temperature coefficients b_n and c_n correspond to the conductance H across the control volume interfaces which is explained in Section 2.1.2.3.

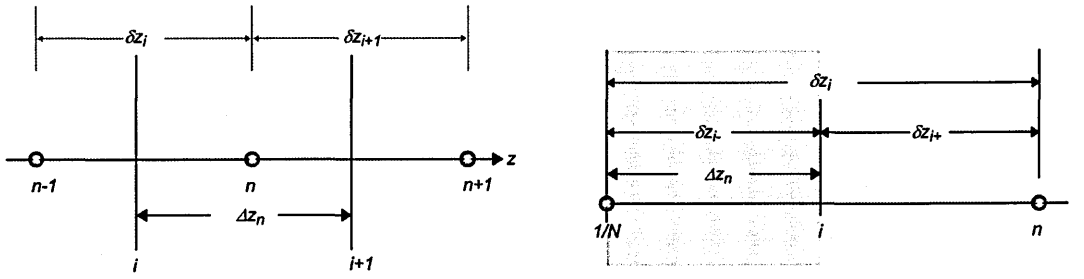

a. b.

Figure 2.1. 1D FCV discretization: a. internal grid with $n \in [1,N]$ $\Delta z_n \times 1 \times 1$ control volumes and interfaces $i \in [1,N-1]$; b. arbitrary boundary point on grid showing half control volume (shaded area). After: Patankar (1980).

The conductivity k_i for the control volume interface i shared by control volumes n and $n+1$ is calculated by interpolating the conductivities k_n, k_{n+1} according to

a. $$k_i = \left(\frac{1-f_i}{k_n} + \frac{f_i}{k_{n+1}}\right)^{-1}, \qquad n \in [1,N], \quad i \in [1,N-1]. \tag{2.17}$$

b. $$f_i = \frac{\delta z_{i+}}{\delta z_i},$$

Patankar (1980) notes that the source term S_n, which is often temperature dependent, can be represented in several ways, a general representation being

$$S_n = S_n^C + S_n^T T_n, \qquad n \in [1,N], \tag{2.18}$$

where S_n represents the average source contribution to the heat flowing out of control volume n, S_n^C represents a constant component of the source term and S_n^T is a temperature dependent component. For numerical stability in the forward problem, any heat sinks, or negative components of S_n, are absorbed into S_n^T while respective positive components are absorbed into S_n^C. In special cases it may be necessary to separate S_n into unsteady and steady components. While it is not conventional to do this it can be used to simulate transient heating effects within the medium. Further details on the representation of k_i and S_n can be found in Appendix 9.2.1.3.

The linear system in compact form is

$$\mathbf{FT} = \mathbf{S} \qquad 2.19$$

where $\mathbf{F}$ is a tridiagonal system of coefficients a_n, b_n, c_n, $\mathbf{T}$ an array of temperatures T_n^m, and $\mathbf{S}$ an array of source-associated terms d_m^n (see Appendix 9.2.1.3 for details). The solution can therefore be represented by

$$\mathbf{T} = \mathbf{F}^{-1}\mathbf{S}. \qquad 2.20$$

The system of equations in 2.15 and 2.19 can be solved using standard numerical methods (e.g. Press, 2002; Collins, 2003).[7] However the tridiagonal form of the equations makes it appropriate for use with the Tri-Diagonal Matrix Algorithm (TDMA – e.g. Patankar, 1980)[8]. The TDMA is used in this study.

2.1.2.2.2 Surface Energy Balance

In planetary cases where surface temperature $T_S = T_S^S + T_S^U$ is not given, it may be calculated from the surface energy balance, which is a nonlinear surface boundary condition given by

$$\frac{S^o}{R^2}(1 - A_B)\cos\varphi_i - \varepsilon\sigma {T_S}^4 = -k\frac{\partial T_S}{\partial z}. \qquad 2.21$$

S^o is the solar constant at the average distance of the body R. This is modified by the surface Bond albedo A_B and solar incidence angle φ_i. The term $\varepsilon\sigma T^4$ is the blackbody

---

[7] The special case of the partitioned unsteady temperature solution T_n^U is obtained by setting the source term S_n in Equation 2.18 to zero leading to the source terms S_n^C and S_n^T vanishing from d_n, and a_n accordingly. The full set of unsteady temperatures T_n^{Um} is obtained by taking timesteps Δt_m from t_0 to t_{M-1}. The steady temperature is attained at the limit where the timestep gets large ($\Delta t_m \to \infty$), therefore the steady temperature solution T_n^S is achieved by setting $\Delta t_m = \infty$ (or some practically large number) such that a_n^0 vanishes.

[8] The TDMA is a special case of the Gaussian Elimination method of solving linear systems.

radiation function where ε is the emittance of the surface of the body and σ is the Stephan-Boltzmann constant. The boundary condition can be incorporated into the HFE by integrating Equation 2.1 over the half control volume defined by Figure 2.1b. This produces a discretization equation

$$a_0 T_0 = b_0 T_1 + d_0 \tag{2.22}$$

where

a. $$b_0 = \frac{k_1}{\delta z_1},$$

b. $$a_0^0 = \rho_0 c_0 \frac{\Delta z_0}{\Delta t_m}, \qquad m \in [0, M-1], \quad t \in (t_0, t_{M-1}] \,. \tag{2.23}$$

c. $$d_0 = S_0^C \Delta z_0 + a_0^0 T_0^0 - \frac{S^o}{R^2}(1-A)\cos\varphi_i,$$

d. $$a_0 = b_0 + a_0^0 - S_0^T \Delta z_0 - \varepsilon\sigma {T_0}^3,$$

Equation 2.22 can be solved through an iterative procedure such that

$$T_0 = \frac{b_0 T_1 + d_0}{a_0} \tag{2.24}$$

This is applied in Section 3.6 and Chapters 6-7.

2.1.2.3 Composites

Composite media can be represented as a collection of N homogeneous, a heterogeneous mix of different granular materials with parametric variation in thermal properties, or a combination of the former and latter. The analytical solutions of Section 2.1.2.1 still hold true in the case of N homogeneous layers but with N of each solution for each layer. The numerical expressions of Section 2.1.2.2 are already in the form of N simultaneous equations and can be more efficiently solved with techniques like the TDMA.

To solve the heat flow problem with composites, the conditions at the internal boundaries must be taken into account, where in the absence of any heat sources or sinks S, the heat flow is continuous across the boundary. This leads to the internal boundary (continuity) condition

$$k_n\left(\frac{\partial T}{\partial z}\right)_n = k_{n+1}\left(\frac{\partial \mathrm{T}}{\partial z}\right)_{n+1}, \qquad n \in [1, N], \tag{2.25}$$

noting that $\left(\frac{\partial T}{\partial z}\right)_n$ is the temperature gradient in layer n,. Equation 2.25 reveals the particular relationship between layers in contact where the ratio of temperature gradients is inversely proportional to the ratio of conductivities. Assuming that the temperature is continuous across the boundaries of layers in perfect contact, leads to a further continuity condition

$$T_{i\_} = T_{i_+}, \qquad i \in [1, N-1], \tag{2.26}$$

where $i_{\mp}$ identifies each temperature to the immediate right or left of the interface as shown in Figure 2.1b. The effect of this on the temperature profile and heat flow is shown in Section 3.3.1. The temperature gradient in the upper layer is 10 times that in the middle layer, which is ten times that in the lower layer, the opposite of the conductivity ratios, as dictated by Equation 2.25. The temperatures are also equal at the layer boundaries as dictated by Equation 2.26.

For layers which are not in perfect contact the temperature may not be continuous across the boundary, therefore Equation 2.26 does not hold. However the heat flow across the boundary is still continuous and proportional to the temperature difference between the two media. Therefore, for heat flowing from layer n to layer $n+1$ (Carslaw and Jaeger, 1986),

$$-k_n\left(\frac{\partial T}{\partial z}\right)_n = H(T_{i\_} - T_{i_+}). \tag{2.27}$$

The term H is a constant which is determined experimentally and is called the heat transfer coefficient or conductance as introduced in the previous Section 2.1.2.2. In this way, Equations 2.25 and 2.26 or 2.25 and 2.27 are used to deal with continuous boundaries or discontinuous boundaries respectively when finding solutions to composite systems.

The interface conductivity k_i (Equation 2.17) in the FCV scheme facilitates any layering within the medium, in cases of perfect layer contact. In cases of imperfect layer contact the extent of contact can be quantified by a given quantity h_i which modifies the interface conductivity k_i to produce k_c where

$$h_i = \frac{A_i}{\delta x_i} = \frac{k_c}{k_i}, \qquad i \in [1, N-1]. \tag{2.28}$$

The quantity h_i is analogous to the Hertz factor of Seiferlin et al. (1996) and Paton et al. (2010) for granular media where A_i represents the layer interface contact area and δx_i the cross sectional area of the layer along the heat flow axis. Instances of perfect layer contact have $h_i = 1$ while instances of imperfect layer contact have $0 < h_i < 1$.

The effect of imperfect layer contact on the temperature profile and heat flow is illustrated in Section 3.3.2. It is evident that while the heat flow and temperature gradients within each layer are unaffected by the imperfect contact, the temperatures in all layers except the surface layer are positively displaced. The heat flow across the boundary can be seen as the instantaneous average of the heat flow of the bordering layers – this is to be expected in the absence of heat sources, to avoid any violation of energy conservation.

2.2 Inverse Problem

The problem of recovering boundary and initial conditions from a given temperature distribution (measurement) is the inverse problem, introduced in Section 1.3.2. Several observations are made, in Section 2.1, which highlight why the inverse heat flow problem is unstable[9] – in summary, these are:

---

[9] In an ideal scenario with perfect knowledge of problem parameters and infinite measurement precision the problem is not necessarily unstable.

1. information on the unsteady surface temperature T_S^U is lost because the propagated signal[10] is lagged and damped, dependent on the magnitude of the temperature variation period P, depth z and thermal properties k, ρ, c. This is quantified by the skin depth $z_{SKIN} = (kP/\rho c\pi)^{1/2}$ which is the depth at which the unsteady temperature amplitude falls to $1/e$ of the surface value;
2. information on the basal heat flow F_B^S may be masked by the propagated unsteady surface temperature signal, dependent on z_{SKIN}, the unsteady surface temperature amplitude, and the magnitude of F_B^S;
3. the temperature distribution may be modified by unaccounted for physical phenomena such as lateral variation and/or temperature dependence of thermal properties or, equivalently, the presence of unknown heat sources and/or sinks S.

Additionally, as noted in Section 1.2.3, heat flow probes return measurements of finite precision, therefore

4. the temperature distribution and thermal properties may contain errors.

Factors 1 and 2 are opposing factors, to some degree. In the case where the main parameter sought from the inversion is surface temperature T_S, less lagging and damping of the T_S^U signal (1) and little or no temperature gradient due to F_B^S (2) over the considered depth z, are ideal. Conversely, where the inversion is mainly concerned with F_B^S – the case in this study – it is better to have a temperature gradient of higher magnitude (2), and greater damping of T_S^U (1). However in the same vein, if T_S is not well known, along with F_B^S, the information in the unsteady subsurface temperature may be useful in estimating both T_S and F_B^S.

[10] Propagated signal refers to the heat flow into the subsurface.

The consequence of the former is that the inverse problem is ill-posed: the loss of information on the surface temperature allows several possible unsteady temperature solutions which can fit a subsurface temperature distribution; likewise, the masking of the basal heat flow by the unsteady temperature allows several possible heat flow solutions; the measurement errors compound these by allowing several possible temperature distributions. Methods therefore need to be employed which help to provide a unique solution to the inverse problem.

2.2.1 General Inverse Theory and Methods

The inverse problem, as described above, leads to a sparse linear system of equations after parametrization, analogous to the form of Equation 2.20. There are numerous approaches to solving sparse linear systems (e.g. Saad, 2003), though particular approaches tend to be suited to particular parametrizations (e.g. Beck and Arnold, 1977; Menke, 1989; Tarantola, 2005). The principal determinacy of the inverse problem for a given measurement[11], as described above, depends on the parameter(s) being sought: for the basal heat flow F_B^S and steady surface temperature T_S^S, the problem is overdetermined; for the thermal properties k, ρ and c, source distribution S, and unsteady surface temperature T_S^U, the determinacy depends on the required depth and time resolution. Three inversion methods, often encountered in the literature, are introduced in Section 1.3.2, Function Specification Inversion (FSI – e.g. Shen and Beck, 1991,1992; Tarantola, 2005), Spectrum Inversion (SI – Wang, 1992) and Singular Value Decomposition (SVD – e.g. Menke, 1989), with noted advantages of FSI and SI (e.g. Shen et al., 1992). FSI and SI are based on Bayesian principles (e.g. Tarantola and Valette, 1982), using a priori information to provide a unique solution, which is useful for systems of any determinacy.

---

[11] In the sense of being underdetermined, mixed determined or overdetermined, and assuming the measurement is taken with two or more sensors.

SVD allows the highly singular parts of a solution to be identified and discarded, reducing the resolving power of the data, but stabilising the solution – this is particularly useful for underdetermined problems. What follows is a general summary of inverse theory and methods, discussing the applicability of particular approaches, and providing some insight into the reasoning behind the final chosen approach of FSI, which is presented in further detail.

2.2.1.1 Model and Data Parameters

In the forward problem the $\mathbf{F}$ matrix and $\mathbf{S}$ vector (Equation 2.20) are well posed, which leads to a unique temperature solution $\mathbf{T}$. The inverse problem stems from using measurements of $\mathbf{T}$ to determine the form of the expression $\mathbf{F}^{-1}\mathbf{S}$, where the parameters in the $\mathbf{F}$ matrix and $\mathbf{S}$ vector are not accurately known. This is stated, generally, as

a. $$\mathbf{d} = \mathbf{g}(\mathbf{m}),$$

b. $$\mathbf{m} = \left[T_S^U, T_S^S, F_B^S, k, \rho, c, S\right]. \qquad 2.29$$

The data vector $\mathbf{d} \leftarrow \mathbf{T}$ is a vector of N measured temperatures (temperature distribution)[12] which can be considered as part of a data space D containing all possible data observations with coordinates $\mathbf{d}_1, \mathbf{d}_2, \ldots, \mathbf{d}_i$. The term $\mathbf{g}(\mathbf{m}) \leftarrow \mathbf{F}^{-1}\mathbf{S}$ is a potentially nonlinear function of model vectors $\mathbf{m}$ which can be considered as part of a model space M containing all possible models with coordinates $\mathbf{m}_1, \mathbf{m}_2, \ldots, \mathbf{m}_i$.

Examination of the HFE with boundary conditions (Equations 2.1-2.4) shows that the model $\mathbf{m}$ may be represented with two components $\mathbf{m} = [\mathbf{m}_B, \mathbf{m}_P]$ where $\mathbf{m}_B = \left[T_S^U, T_S^S, F_B^S\right]$ represents the component with unknown boundary conditions and $\mathbf{m}_P = [k, \rho, c, S]$ represents the component with unknown regolith properties. Solving the forward

[12] For a general inverse problem $\mathbf{d}$ may consist of any measured parameter of an experiment.

problem with elements of $\mathbf{m}_P$ unknown is a nonlinear problem requiring iteration – recalling that forward calculations are used when solving inverse problems it can be seen that this nonlinearity carries over to the inverse problem. For this reason Equation 2.29 is the nonlinear parametrization of the inverse problem and is solved using iterative search methods similar to FSI and SI or sampling methods (e.g. Monte Carlo).

The linear parametrization results when the model component $\mathbf{m}_P = [k, \rho, c, S]$ is – or is assumed – exactly known; the forward problem may then be solved without iteration and the inverse problem stated as

a. $$\mathbf{d} = \mathbf{G}\mathbf{m} \qquad 2.30$$

b. $$\mathbf{m} = \mathbf{m}_B = \left[T_S^U, T_S^S, F_B^S\right]$$

where $\mathbf{G}$ is often referred to as the data kernel. In this form, with $\mathbf{G}$ invertible, the solution to the inverse problem can be stated as

$$\mathbf{m} = \mathbf{G}^{-1}\mathbf{d}. \qquad 2.31$$

The linear inverse problem parametrization is solved according to its determinacy, where Lagrange multipliers can be used to solve the underdetermined problem, least squares to solve the overdetermined problem, or singular value decomposition and least squares to solve problems of mixed determinacy (e.g. Menke, 1989).

The nonlinear and linear inverse problem solution methods mentioned above are discussed in further detail in the following sections. It is important to note the well-known fact that there are several potential viewpoints regarding what constitutes an inverse problem solution (e.g. Beck and Arnold, 1977; Menke, 1989; Tarantola, 2005). Typically, an estimate of the model parameter $\mathbf{m}$ is sought, however this may not always be the case and it may not always be possible to estimate $\mathbf{m}$ accurately. Other information such as the relationships between or the nature of uncertainties associated with different model and data parameters in $\mathbf{d}$ and $\mathbf{m}$ may suffice, or in fact be sought – these are discussed next (also see Section 2.2.3.5).

2.2.1.2 *Parameter Variance and Covariance*

The data in $\mathbf{d}$ has uncertainties depending on the measurement conditions. There may be information of varying quality on the model parameters in $\mathbf{m}$. This initial (a priori) information on the quality of the data, along with any correlation between model parameters and/or model parameters with data parameters, can be quantified in covariance matrices $\mathbf{C_d}$ and $\mathbf{C_m}$, and an a priori model $\mathbf{m}_0$ (e.g. Beck and Arnold, 1977). This a priori information may be pivotal in stabilising the inverse problem, particularly in the nonlinear case covered by Equations 2.29 or where Equation 2.30 is underdetermined. $\mathbf{C_d}$ and $\mathbf{C_m}$ establish the size of the subspaces in M and D which contain probable solutions $\mathbf{d}_I$ and $\mathbf{m}_I$. $\mathbf{C_d}$ and $\mathbf{C_m}$ are represented by square, positive definite arrays (see Section 4.2.3.2 for examples)

a. $$\mathbf{C_d} = \mathbf{C}_{d_0},$$

2.32

b. $$\mathbf{C_m} = \left[\mathbf{C}_{T_S^U}, \mathbf{C}_{T_S^S}, \mathbf{C}_{F_B}, \mathbf{C}_k, \mathbf{C}_\rho, \mathbf{C}_c, \mathbf{C}_S\right].$$

The subscript d_0 in $\mathbf{C_d}$ represents the covariance of the measured temperature, the diagonal of which may be considered a vector of variances σ_n^2, associated with each measured temperature T_n, where the standard deviation σ_n corresponds to the measured temperature error. The lower and upper triangles of $\mathbf{C}_{d_0}$ represent the covariances of pairs of T_n. The variances σ_n^2 vary depending on the measurement scenario: for example, in an ideal measurement scenario it is expected that the variance will decrease exponentially with depth as the unsteady temperature oscillations are damped. The same follows for $\mathbf{C_m}$ such that the diagonal of each model parameter covariance $\mathbf{C}_m$ is a vector of variances σ_m^2 with the off diagonal elements being covariances.

The time dependent nature of unsteady temperature T_S^U means $\mathbf{C}_{T_S^U}$ can be represented with a time component which reflects the time variation of T_S^U, such that the diagonal elements of $\mathbf{C}_{T_S^U}$ are represented by $\sigma_{T_S^U}^2 f(\tau)$, where $f(\tau)$ is a time varying function, and

$\tau = -t$. For example it is expected that information on T_S^U from the remote past – which is in the lower regions of a temperature profile and is asymptotically lost to damping – will have a smaller variance than more recent T_S^U information. Therefore, in the case of a sinusoidal T_S^U (expected in simplified planetary cases), $f(\tau)$ may be represented by a sinc function (e.g. Wang, 1992). Similarly, the potential depth dependent nature of parameters of $\mathbf{m}_P$ allows the introduction of a covariance function $f(z)$ such that the diagonal elements of $\mathbf{C}_m$ are given by $\sigma_m^2 f(z)$. Additional off-diagonal elements $\mathbf{C}_{d_1 d_2}$ and $\mathbf{C}_{m_1 m_2}$ may be explicitly introduced to $\mathbf{C_d}$ and $\mathbf{C_m}$ respectively, to represent correlation (cross-covariances) between different data and model parameters.

With the measurement $\mathbf{d}_0$, the physical model (also called the constraint) $\mathbf{g(m)} \Leftarrow \mathbf{Gm}$ and uncertainties described in the covariances $\mathbf{C_d}$ and $\mathbf{C_m}$, all the information needed to solve the inverse problem is now established – next to be discussed are the different methods of solution.

2.2.1.3 Solution Methods

The solution methods applied to an inverse problem depend, as noted above, on its parametrization. In this study, the basal heat flow F_B^S, is the main model parameter sought, suggesting that a linear parametrization is sufficient for a reliable estimate. However, the potential for inaccuracies in the temperature data in $\mathbf{d}$ and thermal properties in $\mathbf{m}$ warrants an approach which also allows these to be estimated; the nonlinear parametrization satisfies this requirement, and is, in this sense, a more robust approach.

Solutions to the nonlinear problem invariably involve sampling of the joint model and data space $[\mathrm{D}, \mathrm{M}]$ through iteration or random exploration, though in most instances (one

exception being SVD[13]), at each step, the same procedures are carried out as would be the case in the linear problem – i.e. the linear problem can be considered a special case of the nonlinear problem with no iterations. Solutions to the inverse problem from this point are, therefore, primarily discussed in a general nonlinear sense, with the linear problem considered as a special case.

2.2.1.3.1 Misfit Function

Solving the inverse problem involves finding a best-fit set of data $\mathbf{d}_I$ and model $\mathbf{m}_I$ parameters according to the model prediction (or constraint) $\mathbf{g}(\mathbf{m}) = \mathbf{d}$, data observation $\mathbf{d}_0$, a priori model information $\mathbf{m}_0$ and covariances $\mathbf{C}_\mathbf{d}$ and $\mathbf{C}_\mathbf{m}$. In most cases (one exception being SVD), the first step to doing this is defining a misfit function on the joint model and data space $[\mathrm{D}, \mathrm{M}]$, also known as an objective function or cost function, which can be stated as

$$S_\mathbf{m} = \frac{1}{2}\Big[[\mathbf{d} - \mathbf{d}_0]^\mathrm{T}\mathbf{W}_\mathbf{d}[\mathbf{d} - \mathbf{d}_0] + [\mathbf{m} - \mathbf{m}_0]^\mathrm{T}\mathbf{W}_\mathbf{m}[\mathbf{m} - \mathbf{m}_0]\Big]. \qquad 2.33$$

$S_\mathbf{m}$ can be considered the most general (nonlinear) form of the least squares (L_2 – see next paragraph) misfit function, which can be reduced to particular (linear) forms,

---

[13] Singular Value Decomposition (SVD) is an important inversion method, though, as noted in the text, it is restricted to linear problems and therefore cannot estimate internal model parameters ($\mathbf{m}_P$ in Section 2.2.1.1), which is desired in this study. It is addressed here, briefly, for completeness. SVD decomposes the matrix $\mathbf{G}$ in the linear inverse problem such that $\mathbf{G} = \mathbf{U}\boldsymbol{\Lambda}\mathbf{V}^\mathrm{T}$, where matrices $\mathbf{U}$ and $\mathbf{V}$ are respectively orthogonal and orthonormal such that $\mathbf{U}\mathbf{U}^\mathrm{T} = \mathbf{U}^\mathrm{T}\mathbf{U} = \mathbf{I}$ and $\mathbf{V}\mathbf{V}^\mathrm{T} = \mathbf{V}^\mathrm{T}\mathbf{V} = \mathbf{I}$. The diagonal matrix $\boldsymbol{\Lambda}$ is an eigenvalue matrix containing the so-called singular values. The zero or near-zero singular values can be used to identify and discard degenerate parts of the linear system which defines the inverse problem – i.e. null areas of the $\mathbf{G}$ matrix and areas with high measurement error sensitivity. This in turn allows the identification of implicitly underdetermined systems, and a stable solution $\mathbf{m}_I$ according to $\mathbf{m}_I = \mathbf{V}\boldsymbol{\Lambda}^{-1}\mathbf{U}^\mathrm{T}\mathbf{d}$.

depending on the chosen parametrization. For example: with weighted nonlinear least squares $\mathbf{d} = \mathbf{g(m)}$, $\mathbf{W_d} = \mathbf{C_d}^{-1}$ and $\mathbf{W_m} = \mathbf{C_m}^{-1}$; with weighted linear least squares (WLS) $\mathbf{d} = \mathbf{Gm}$, weight $\mathbf{W_d}$ is positive definite ($\mathbf{W_d} = \mathbf{C_d}^{-1}$ for maximum likelihood, ML) and $\mathbf{W_m}$ is null; while with the method of ordinary linear least squares (OLS), $\mathbf{W_d} = \mathbf{I}$, all else remaining the same as WLS.

$S_\mathbf{m}$ is defined from the negative logarithm of a Gaussian probability density function (PDF) $\phi(\mathbf{d}, \mathbf{m}) = \phi(\mathbf{d})\phi(\mathbf{m}) = \phi_0 e^{-S_\mathbf{m}}$ for the probability over $[\mathrm{D}, \mathrm{M}]$ where ϕ_0 is a constant. The form of $S_\mathbf{m}$ – based on the assumption that the data and model parameters display Gaussian statistics – is derived from a weighted L_2 (also least squares) norm. A L_n norm (a norm of order n) is a measure of distance over a space and is defined such that – for a given linear space $\mathrm{E} \ni \mathbf{e} \ni e_p$ and expectation (mean) value $\langle e \rangle$ – a weighted L_n norm over E is denoted $\|\mathbf{e}\|_n = \left[\sum_p \frac{|e_p - \langle e \rangle|^n}{{\sigma_p}^n}\right]^{1/n}$, $n \in [1, \infty]$. The weighting factor is ${\sigma_p}^n$, σ_p being the estimator of dispersion (in L_2, the square root of the variance ${\sigma_p}^2$ – the standard deviation). A PDF utilising the L_2 norm is a Gaussian PDF which is a relatively short tailed distribution and is therefore suited to parameters where the dispersion is large (higher order norms are suited for more accurate data while the L_1 norm is suited for data with large outliers – e.g. Menke, 1989; Tarantola, 2005). $S_\mathbf{m}$ (Equation 2.33) can therefore be stated as $S_\mathbf{m} = \frac{1}{2}[\|\mathbf{d} - \mathbf{d_0}\|_2 + \|\mathbf{m} - \mathbf{m_0}\|_2]$.

2.2.1.3.2 Misfit Function Gradient

With the form of the misfit function $S_\mathbf{m}$ established, the problem becomes one of minimising $S_\mathbf{m}$ with respect to the model parameters in $\mathbf{m}$. This is analogous to a standard problem in elementary calculus and is achieved by setting the derivative of $S_\mathbf{m}$ with

respect to $\mathbf{m}$ – i.e. the Fréchet derivative[14], $\frac{\partial S_{\mathbf{m}}}{\partial \mathbf{m}}$ – to zero. The Fréchet derivative of $S_{\mathbf{m}}$ (Equation 2.33) is

$$\frac{\partial S_{\mathbf{m}}}{\partial \mathbf{m}} = \mathbf{G}^{\mathrm{T}}\mathbf{W}_{\mathbf{d}}[\mathbf{g}(\mathbf{m}) - \mathbf{d}_0] + \mathbf{W}_{\mathbf{m}}[\mathbf{m} - \mathbf{m}_0], \qquad 2.34$$

where $\mathbf{G} = \frac{\partial \mathbf{d}}{\partial \mathbf{m}}$ is the data Fréchet derivative, calculated from the solution to the HFE (e.g. the analytical solution of Equation 2.14 or the numerical solution of Equation 2.20). Therefore, the explicit form of $\mathbf{G}$ depends on the forward parameterization of the problem. For example: Spectrum Inversion (SI – Wang, 1992) is formulated in the Fourier domain, such that $\mathbf{G}$ consists of derivatives of the real and imaginary parts of the Fourier expressions[15]; Functional Space Inversion (FSI – Shen and Beck 1991,1992; Sections 2.2.2-2.2.3) is formulated in a functional space domain, with explicit expressions of the components of $\mathbf{G}$ derived analytically, then discretized using standard methods.

Equation 2.34 is considered a general nonlinear form of the gradient, which can be reduced to particular forms based on the inverse problem parametrization. For example: for linear WLS $\frac{\partial S_{\mathbf{m}}}{\partial \mathbf{m}} = \mathbf{G}^{\mathrm{T}}\mathbf{W}_{\mathbf{d}}[\mathbf{G}\mathbf{m} - \mathbf{d}_0] = 0$, leading to a solution $\mathbf{m}_I = \left[\mathbf{G}^{\mathrm{T}}\mathbf{W}_{\mathbf{d}}\mathbf{G}\right]^{-1}\mathbf{G}^{\mathrm{T}}\mathbf{W}_{\mathbf{d}}\mathbf{d}_0$ ($\mathbf{W}_{\mathbf{d}} = \mathbf{C}_{\mathbf{d}}{}^{-1}$ for ML); and for linear OLS $\frac{\partial S_{\mathbf{m}}}{\partial \mathbf{m}} = \mathbf{G}^{\mathrm{T}}[\mathbf{G}\mathbf{m} - \mathbf{d}_0] = 0$, leading to a solution, $\mathbf{m}_I = \left[\mathbf{G}^{\mathrm{T}}\mathbf{G}\right]^{-1}\mathbf{G}^{\mathrm{T}}\mathbf{d}_0$. A nonlinear parametrization leads to $\mathbf{G}^{\mathrm{T}}\mathbf{W}_{\mathbf{d}}[\mathbf{d}_0 - \mathbf{g}(\mathbf{m})] = \mathbf{W}_{\mathbf{m}}[\mathbf{m} - \mathbf{m}_0]$, which in turn, leads to $\mathbf{m} = \mathbf{W}_{\mathbf{m}}{}^{-1}\mathbf{G}^{\mathrm{T}}\mathbf{W}_{\mathbf{d}}[\mathbf{d}_0 - \mathbf{g}(\mathbf{m})] + \mathbf{m}_0$. Because $\mathbf{g}(\mathbf{m})$ is a function of $\mathbf{m}$, finding an explicit solution is a nontrivial problem, therefore, as noted before, implicit solution methods such as iterative or random exploration of the probability space $[\mathrm{D}, \mathrm{M}]$ are required to arrive at a solution $\mathbf{m}_I$ (e.g. Menke, 1989). Therefore, for

---

[14] Also known as the Jacobian or simply, the gradient.

[15] In this case the unsteady surface temperature is among the model parameters to be determined (see Appendix 9.2.1.1, Equation 9.2.12 for an example of a Fourier domain temperature solution).

example, for a nonlinear maximum likelihood estimate $\mathbf{m}_{i+1} = \mathbf{C}_\mathbf{m}\mathbf{G}^\mathrm{T}\mathbf{C}_\mathbf{d}^{-1}[\mathbf{d}_0 - \mathbf{g}(\mathbf{m}_i)] + \mathbf{m}_i$.

2.2.1.3.3 Optimizing the Nonlinear Misfit Function

The general iterative solution to a nonlinear inverse problem parametrization, can be stated as

$$\mathbf{m}_{i+1} = \mathbf{m}_i - \mu_i \boldsymbol{\gamma}_i, \qquad i \in [0, I-1]. \tag{2.35}$$

This is most efficiently solved by gradient methods of steepest descent where the steepest descent algorithm is terminated at iteration $i = I$ – the maximum likelihood point with solution $\mathbf{m}_I$ at misfit function optimum $S_{\mathbf{m}_I}$. The term μ_i is a relaxation factor, affecting the rate of convergence and $\boldsymbol{\gamma}_i$ the steepest ascent vector, defined by

$$\boldsymbol{\gamma}_i = \mathbf{M}_i \left[\frac{\partial S_\mathbf{m}}{\partial \mathbf{m}}\right]_i, \qquad i \in [0, I-1]. \tag{2.36}$$

The steepest ascent vector establishes a localised direction of maximum gradient in the space $[\mathrm{D}, \mathrm{M}]$ as $S_\mathbf{m}$ is minimised. The metric $\mathbf{M}_i$ introduces a measure of distance between different models $\mathbf{m}_i$ across model space M. $\mathbf{M}_i$ can take many forms; in the simple steepest descent algorithm it is the model covariance matrix $\mathbf{C}_\mathbf{m}$ and in the Newtonian steepest descent algorithm it is the inverse of the Hessian metric which gives the second partial derivative such that $\mathbf{M}_i \left[\frac{\partial S_\mathbf{m}}{\partial \mathbf{m}}\right]_i = \left[\frac{\partial^2 S_\mathbf{m}}{\partial \mathbf{m}^2}\right]_i$ (Tarantola, 2005). $\mathbf{M}_i$ may also incorporate an arbitrary, optional preconditioning operator $\mathbf{P}_i$ such that $\mathbf{M}_i^P = \mathbf{P}_i\mathbf{M}_i$ in which case the optimization is known as a preconditioned steepest descent method. Preconditioning is useful in restricting model estimates to physically meaningful results and can promote more rapid convergence.

Presenting the nonlinear maximum likelihood estimate at the end of Section 2.2.1.3.2 in the form of the steepest descent algorithm with $\mathbf{d}_i = \mathbf{g}(\mathbf{m}_i)$ and $\mu_i = 1$ shows their equivalence with

$$\mathbf{m}_{i+1} = \mathbf{m}_i - \mu_i \left[\mathbf{C_m}\mathbf{G}_i{}^{\mathrm{T}}\mathbf{C_d}^{-1}[\mathbf{d}_i - \mathbf{d}_0] + [\mathbf{m}_i - \mathbf{m}_0]\right], \qquad i \in [0, I-1]. \tag{2.37}$$

In Equation 2.37, the model covariance $\mathbf{C_m} = \mathbf{M}_i$, the metric.

The Hessian of $S_\mathbf{m}$ is given by

$$\frac{\partial^2 S_\mathbf{m}}{\partial \mathbf{m}^2} = \mathbf{G}^{\mathrm{T}}\mathbf{C_d}^{-1}\mathbf{G} + \mathbf{C_m}^{-1} + \frac{\partial \mathbf{G}}{\partial \mathbf{m}}\mathbf{C_d}^{-1}[\mathbf{g}(\mathbf{m}) - \mathbf{d}_0]. \tag{2.38}$$

The rightmost term can be dropped where nonlinearities are small or the data residuals are small, leading to $\frac{\partial^2 S_\mathbf{m}}{\partial \mathbf{m}^2} \approx \mathbf{G}^{\mathrm{T}}\mathbf{C_d}^{-1}\mathbf{G} + \mathbf{C_m}^{-1}$. Setting $\mathbf{M}_i\left[\frac{\partial S_\mathbf{m}}{\partial \mathbf{m}}\right]_i = \left[\frac{\partial^2 S_\mathbf{m}}{\partial \mathbf{m}^2}\right]_i$, the descent algorithm is known as a quasi-Newton algorithm

$$\begin{aligned}\mathbf{m}_{i+1} = \mathbf{m}_i - \mu_i\left[\mathbf{G}_i{}^{\mathrm{T}}\mathbf{C_d}^{-1}\mathbf{G}_i + \mathbf{C_m}^{-1}\right]^{-1} \\ \times \left[\mathbf{G}_i{}^{\mathrm{T}}\mathbf{C_d}^{-1}[\mathbf{d}_i - \mathbf{d}_0] + \mathbf{C_m}^{-1}[\mathbf{m}_i - \mathbf{m}_0]\right], \qquad i \in [0, I-1].\end{aligned} \tag{2.39}$$

Selection of a particular optimization method depends on the ease with which the Hessian can be calculated; the quasi-Newton method is considered the most stable and can be run with $\mu_i = 1$ with rapid convergence. Estimating a suitable value for μ_i in the simple steepest descent algorithm is largely a case of trial and error, particularly where the elements of $\mathbf{m}$ have different dimensions; Tarantola (2005) presents different methods of estimating the parameter. Where the Hessian cannot be directly calculated, so-called variable metric methods use a preconditioning operator $\mathbf{P}_i$ which is iteratively updated to approximate the Hessian. Therefore, the algorithm behaves similar to simple steepest descent at the start and evolves to a quasi-Newton algorithm towards the end.

The optimum of $S_\mathbf{m}$ corresponds to the maximum likelihood point $\phi(\mathbf{d}_I, \mathbf{m}_I)$ where data prediction $\mathbf{d}_I$, close to $\mathbf{d}_0$, maximises data probability density $\phi(\mathbf{d})$ (minimises the weighted data norm $\|\mathbf{d} - \mathbf{d}_0\|$), subject to model estimate $\mathbf{m}_I$, close to $\mathbf{m}_0$, which maximises model parameter probability density $\phi(\mathbf{m})$ (maintains a small weighted model parameter norm $\|\mathbf{m} - \mathbf{m}_0\|$) (e.g. Shen and Beck, 1991; Tarantola, 2005). That is, the algorithm locates the most probably combination of model and data parameters $\mathbf{m}_I$ and

$\mathbf{d}_I$, given all the available information. Figure 2.2 shows an ideal representation of $S_{\mathbf{m}}$ with its component norms $S_{\|\mathbf{d}\|} \Leftrightarrow \|\mathbf{d} - \mathbf{d}_0\|$ and $S_{\|\mathbf{m}\|} \Leftrightarrow \|\mathbf{m} - \mathbf{m}_0\|$.

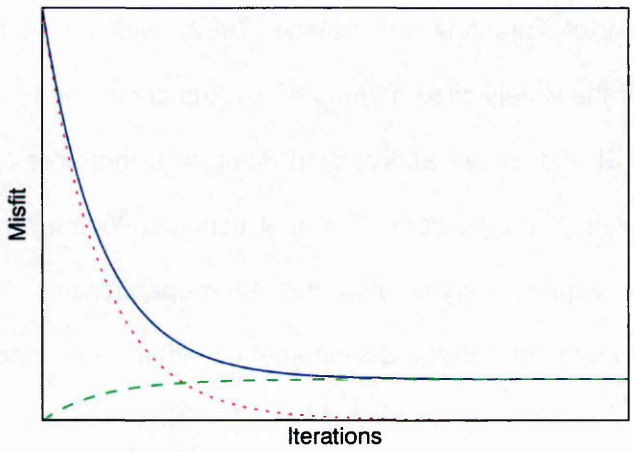

Figure 2.2. Form of misfit function $S_{\mathbf{m}}$. The red (dotted) curve is the data residual norm $S_{\|\mathbf{d}\|}$ and the green (dashed) curve is the model parameter norm $S_{\|\mathbf{m}\|}$.

Examining Equation 2.33 along with Figure 2.2 it can be deduced that the balance of $\mathbf{C_d}$ and $\mathbf{C_m}$ determines the final shape of $S_{\mathbf{m}}$. If $\mathbf{C_m}$ is too small $S_{\|\mathbf{m}\|}$ may dominate $S_{\mathbf{m}}$ as iterations progress leading to increasing $S_{\mathbf{m}}$ and essentially a premature termination of the optimization. The optimal model for that particular initialization with $\mathbf{C_m}$ is actually obtained but would not necessarily be close to the true model (also see Section 2.2.3.5). It is therefore important to appropriately design $\mathbf{C_m}$ and estimate $\mathbf{C_d}$ such that the balance of $S_{\|\mathbf{d}\|}$ and $S_{\|\mathbf{m}\|}$ promote convergence close to the true model parameters (examples can be seen in sections 4.2.1, 4.2.2 and throughout Appendix 9.4).

The preceding summary of general inverse theory has shown that there are several possible approaches to solving the inverse problem for the basal heat flow where $\mathbf{m} = [F_B^S]$, which warrants only a linear parametrization. However, unknown errors in the other parameters may lead to correspondingly inaccurate (and mistaken) estimates of F_B^S. Therefore, the capability to estimate boundary and internal parameters where $\mathbf{m} =$

$[T_S^U, T_S^S, F_B^S, k, \rho, c, S]$ is considered a compelling reason to adapt a generalized nonlinear parametrization.

FSI and SI, the nonlinear methods explored in this study, are both based on the least squares inverse theory of Tarantola and Valette (1982), which is in turn based on the Bayesian principles of the widely cited method of Backus and Gilbert (1970). The forward parametrizations of FSI and SI are approached differently, therefore leading to different expressions for calculating the gradient. The analytical development of FSI is preferred because it promises explicit insights into the interdependencies of different model parameters. It is adapted for further development in this study and is discussed in requisite detail below.

2.2.2 Functional Inverse Theory

2.2.2.1 *Primal Problem*

FSI parameterisation starts from heat flow Equations 2.1, 2.5 and 2.9 where they are written as differential operations allowing the use of unique mathematical concepts in solving the inverse problem. The general HFE (Equation 2.1) takes the form

$$\rho c \frac{\partial T}{\partial t} - \frac{\partial}{\partial z}\left(k \frac{\partial T}{\partial z}\right) = S \equiv \boldsymbol{FT} = \boldsymbol{S}, \qquad z \in [z_S, z_B], t \in [t_B, t_E], \tag{2.40}$$

where $\boldsymbol{F}$ can be considered a primal differential operator – analogous to the matrix $\mathbf{F}$ of Equation 2.19. $\boldsymbol{T}$ is the field of all temperatures in temperature space T (a subspace of dataspace D) which $\boldsymbol{F}$ associates with the field of all source terms $\boldsymbol{S}$ in a source space S ($\boldsymbol{F}$ maps T into S a subspace of model space M – see Shen and Beck, 1991; Tarantola, 2005). Similarly the unsteady (superscript U) and steady (superscript S) components take the forms

$$\boldsymbol{F}^U \boldsymbol{T}^U = \boldsymbol{S}^U, \qquad z \in [z_S, z_B], t \in [t_B, t_E] \tag{2.41}$$

and

$$\boldsymbol{F}^S \boldsymbol{T}^S = \boldsymbol{S}^S, \qquad z \in [z_S, z_B]. \tag{2.42}$$

2.2.2.2 *Dual Problem*

2.2.2.2.1 Introduction to Duality

An important concept for solving the inverse problem is duality (Gottfried and Weisman, 1973; Nocedal and Wright, 1999; Tarantola, 2005). Duality recognises that any problem involving normed spaces may be looked at from dual perspectives and permit easier resolution. For example optimizing the misfit (objective) function of Equation 2.33 can be formulated as minimizing S_m[16] subject to constraint $\boldsymbol{d} = \boldsymbol{g}(\boldsymbol{m})$ or maximizing an analogous function $\hat{S}_{\hat{\boldsymbol{m}}}$ subject to constraint $\hat{\boldsymbol{m}} = \boldsymbol{g}^{\mathrm{T}}(\hat{\boldsymbol{d}})$ (Gottfried and Weisman, 1973; Nocedal and Wright, 1999). Where solutions to both problems exist, then a single solution exists at the optima of S_m and $\hat{S}_{\hat{m}}$, satisfying them both (Tarantola, 2005). The pair are known as primal and dual problems where, in principle, each can respectively be considered the primal while the other the dual. Equations 2.40-2.42, are considered the primal problem as they are physically meaningful.

In the case of FSI, the use of duality allows the Fréchet and Hessian derivatives of the misfit function, as discussed in Section 2.2.1.3.2 and 2.2.1.3.3, to be calculated analytically. Calculating the explicit analytical components of the derivatives, in particular, the thermal properties in $\boldsymbol{m}$ is nontrivial in the primal domain. In SI, for example, Wang (1992) resorts to difference equations, but this approach does not highlight explicit relationships between the different model parameters. Constructing the problem in the dual domain allows for simpler resolution of the derivatives, because the dual problem accepts quiescent boundary conditions (e.g. Equations 2.47-2.49), which simplify the analytical development, as presented below. Note that much of the development presented here follows Shen and Beck (1991,1992) and Tarantola (2005).

---

[16] The italicized notation S_m indicates the functional form as opposed to matrix (discretized) form $\mathrm{S_m}$.

2.2.2.2.2 Dual of the HFE

The spaces T and S associated with Equation 2.40 have respective duals[17] $\hat{\mathrm{T}}$ and $\hat{\mathrm{S}}$ such that scalars $\langle \hat{T}, T \rangle_{\mathrm{T}} = \langle \hat{S}, S \rangle_{\mathrm{S}}$, subject to a transpose[18] operator $\boldsymbol{F}^{\mathrm{T}}$ mapping $\hat{\mathrm{T}}$ into $\hat{\mathrm{S}}$ according to

$$\boldsymbol{F}^{\mathrm{T}} \hat{\boldsymbol{S}} = \hat{\boldsymbol{T}}, \qquad z \in [z_S, z_B], t \in [t_E, t_B],^{19} \tag{2.43}$$

such that, $\langle \boldsymbol{F}^{\mathrm{T}} \hat{S}, T \rangle_{\mathrm{T}} = \langle \hat{S}, \boldsymbol{F} T \rangle_{\mathrm{S}}$.[20] It follows that, while Equation 2.40 involving $\boldsymbol{F}$ is formulated as the primal problem Equation 2.43 involving $\boldsymbol{F}^{\mathrm{T}}$ is consequently the dual problem. It can be shown that in the particular case where S can be identified with $\hat{\mathrm{T}}$ such that $\mathrm{S} \subseteq \hat{\mathrm{T}}$ and $\mathrm{T} \subseteq \hat{\mathrm{S}}$ (Figure 2.3) $\boldsymbol{F}$ and $\boldsymbol{F}^{\mathrm{T}}$ map T into $\hat{\mathrm{T}}$ according to duality relations $\langle \boldsymbol{F}^{\mathrm{T}} T^D, T^P \rangle_{\mathrm{T}} = \langle T^D, \boldsymbol{F} T^P \rangle_{\hat{\mathrm{T}}}$ where $[T^P, T^D] \in \mathrm{T}$ and are appropriately termed the primal and dual temperatures (e.g. Shen and Beck, 1991; Tarantola, 2005). The scalars from the duality relation between S and T can then be defined such that

---

[17] The dual $\hat{\mathrm{M}}$ of any linear space M, is also a linear space and is defined by all linear forms (applications, mappings and/or operators) which associate $m^i \in \boldsymbol{m} \in \mathrm{M}$ with a positive real number $r \in \mathrm{R}^+$, the space of scalars. This can be stated several ways including $\langle \hat{\boldsymbol{m}}, \boldsymbol{m} \rangle_{\mathrm{M}} = \hat{\boldsymbol{m}}^{\mathrm{T}} \boldsymbol{m} = \sum_i \hat{m}_i m^i = r$ (a duality product) where $\hat{m}_i \in \hat{\boldsymbol{m}} \in \hat{\mathrm{M}}$ and $i = 1,2,\ldots$ The dimensions of $\hat{m}_i$ are reciprocal to those of m^i because r are scalars.

[18] Given elements of linear spaces $\boldsymbol{m} \in \mathrm{M}$ and $\boldsymbol{d} \in \mathrm{D}$ with respective duals $\hat{\boldsymbol{m}} \in \hat{\mathrm{M}}$ and $\hat{\boldsymbol{d}} \in \hat{\mathrm{D}}$, a linear operator $\mathbf{G}$ mapping M into D such that $\boldsymbol{d} = \boldsymbol{G}\boldsymbol{m}$ has a transpose $\boldsymbol{G}^{\mathrm{T}}$ which by definition maps $\hat{\mathrm{D}}$ into $\hat{\mathrm{M}}$ such that $\hat{\boldsymbol{m}} = \boldsymbol{G}^{\mathrm{T}} \hat{\boldsymbol{d}}$ according to the duality product $\langle \boldsymbol{G}^{\mathrm{T}} \hat{\boldsymbol{d}}, \boldsymbol{m} \rangle_{\mathrm{M}} = \langle \hat{\boldsymbol{d}}, \boldsymbol{G}\boldsymbol{m} \rangle_{\mathrm{D}}$.

[19] The reversal of the time domain is explained further in the text by Equation 2.50 and the associated discussion.

[20] The order of nomenclature is as follows: a linear space T has associated with it a field $\boldsymbol{T}$ which has an arbitrary element T.

$$\langle S^D, T^P \rangle_{\mathrm{T}} = \langle T^D, S^P \rangle_{\mathrm{S}} = \int_{z_S}^{z_B} dz \int_{t_B}^{t_E} dt\, TS, \tag{2.44}$$

where $[S^P, S^D] \in \mathrm{S}$.

Reintroducing the primal and dual operators and substracting, it can be seen that

$$\langle \boldsymbol{F}^{\mathrm{T}} T^D, T^P \rangle_{\mathrm{T}} - \langle T^D, \boldsymbol{F} T^P \rangle_{\mathrm{S}} = \int_{z_S}^{z_B} dz \int_{t_B}^{t_E} dt\, \boldsymbol{F}^{\mathrm{T}} T^D T^P - T^D \boldsymbol{F} T^P, \tag{2.45}$$

$$z \in [z_S, z_B], t \in [t_B, t_E].$$

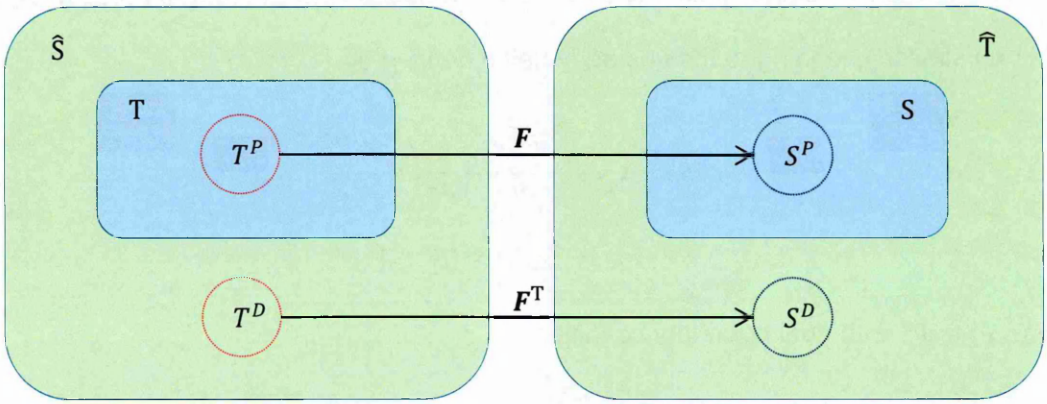

Figure 2.3. Visualization of the primal and dual spaces with S and T as mutual duals. The green rectangles represent the dual spaces, which are infinite. The blue ractangles with their red (temperature) and blue (source) encircled elements represent the primal spaces. The horizontal arrows represent primal-dual function mappings (operators F and F^{T}).

Tarantola (2005) defines the transpose of a linear differential operator and shows that the transpose of the gradient operator is the negative of the divergence operator ($\boldsymbol{\nabla}^{\mathrm{T}} = -\boldsymbol{\nabla}$); likewise, in Shen and Beck (1991) $\boldsymbol{F}^{\mathrm{T}}$, the transpose of the differential operator in Equation 2.40, is shown (see Appendix 9.2.2.1) to take the form

$$\boldsymbol{F}^{\mathrm{T}} T^D = S^D \equiv -\rho c \frac{\partial T^D}{\partial t} - \frac{\partial}{\partial z}\left(k \frac{\partial T^D}{\partial z}\right) = S^D, \qquad z \in [z_S, z_B], t \in [t_E, t_B], \tag{2.46}$$

or $\boldsymbol{F}^{\mathrm{T}} \widehat{\boldsymbol{S}} = \widehat{\boldsymbol{T}}$ with boundary conditions

$$T^P = T^D = 0, \qquad z = z_S, t \in [t_E, t_B], \tag{2.47}$$

$$k\frac{\partial T^P}{\partial z} = k\frac{\partial T^D}{\partial z} = 0, \qquad z = z_B, t \in [t_E, t_B], \tag{2.48}$$

$$T^P = T^D = 0, \qquad z \in [z_S, z_B], t = t_B, t = t_E, \tag{2.49}$$

defining the dual problem. Boundary conditions 2.47-2.49 are known as dual boundary conditions. The dual boundary conditions are chosen to limit the domain of the primal and dual problem such that the expression in Equation 2.45 vanishes – i.e. they enforce the condition of mutual duality between spaces S and T.

The form of the respective unsteady and steady transpose operators (dual problems) are obtained similarly, leading to the unsteady being defined by

$$\boldsymbol{F}^{U^{\mathrm{T}}} T^{DU} = S^{DU} \equiv -\rho c\frac{\partial T^{DU}}{\partial t} - \frac{\partial}{\partial z}\left(k\frac{\partial T^{DU}}{\partial z}\right) = S^{DU}, \tag{2.50}$$
$$z \in [z_S, z_B], t \in [t_E, t_B]$$

or $\boldsymbol{F}^{U^{\mathrm{T}}}\widehat{\boldsymbol{S}}^U = \widehat{\boldsymbol{T}}^U$ with dual boundary conditions

$$T^U = T^{DU} = 0, \qquad z = z_S, t \in [t_B, t_E], \tag{2.51}$$

$$k\frac{\partial T^U}{\partial z} = k\frac{\partial T^{DU}}{\partial z} = 0, \qquad z = z_B, t \in [t_B, t_E], \tag{2.52}$$

$$T^U = T^{DU} = 0, \qquad z \in [z_S, z_B], t = t_B, t = t_E \tag{2.53}$$

and the steady defined by

$$\boldsymbol{F}^{S^{\mathrm{T}}} T^{DS} = S^{DS} \equiv -\frac{\partial}{\partial z}\left(k\frac{\partial T^{DS}}{\partial z}\right) = S^{DS}, \qquad z \in [z_S, z_B], \tag{2.54}$$

or $\boldsymbol{F}^{S^{\mathrm{T}}}\widehat{\boldsymbol{S}}^S = \widehat{\boldsymbol{T}}^S$ with dual boundary conditions

$$T^S = T^{DS} = 0, \qquad z = z_S, \tag{2.55}$$

$$k\frac{\partial T^{S}}{\partial z} = k\frac{\partial T^{DS}}{\partial z} = 0, \qquad z = z_B. \tag{2.56}$$

The duals of the parameter spaces are therefore represented alternatively by Equations 2.46-2.49 or Equations 2.50-2.56 for the separation of steady and unsteady temperatures.

$\boldsymbol{F}^{S^{\mathrm{T}}} = \boldsymbol{F}^{S}$, meaning the steady operator is symmetric. The only difference between $\boldsymbol{F}^{U^{\mathrm{T}}}$ and $\boldsymbol{F}^{U}$ is the introduction of a negative sign in the time component.[21] The negative time component may be interpreted as the dual field of source terms $\widehat{\boldsymbol{S}}$ generating heat which propagates dual temperature fields $\widehat{\boldsymbol{T}}$ backward in time. In fact, simulations have shown that the dual field is unstable when propagated in forward time as the primal field is unstable when propagated in backward time.

2.2.3 Functional Inversion Solutions

2.2.3.1 *Primal Problem Solution*

In solving for the field $\boldsymbol{T}$ Shen and Beck (1991) use the Green's function[22] such that

$$\boldsymbol{T} = \boldsymbol{F}^{-1}\boldsymbol{S} = \boldsymbol{G}\boldsymbol{S}, \tag{2.57}$$

$\boldsymbol{G} \equiv \boldsymbol{G}(z,t;z',t')$, $z,z' \in [z_S, z_B], t,t' \in [t_B, t_E]$, being the Green's operator. The explicit expression of the general Green's function solution to the primal HFE is shown (see Appendix 9.2.2.2) to be

---

[21] Hence the time reversal in the dual problems of Equation 2.43 onward.

[22] The Green's operator $\boldsymbol{G}$ for a linear differential operator $\boldsymbol{F}$ acting on function $\boldsymbol{T}$ according to $\boldsymbol{F}\boldsymbol{T} = \boldsymbol{S}$ is defined by the operation $\boldsymbol{F}\boldsymbol{G} = \delta(z-z';t-t') = \delta_{z,z';t,t'} = \boldsymbol{I} - \delta_{z,z';t,t'}$ being the Kronecker delta function – with the solution $\boldsymbol{T}$ being defined by $\boldsymbol{T} = \int_z dz' \int_t dt' \boldsymbol{G}\boldsymbol{S}$. Therefore $\boldsymbol{G} = \boldsymbol{F}^{-1}$, an integral operator.

$$T = \int_{z_S}^{z_B} dz' \int_{t_B}^{t_E} dt'\, GS + \int_{t_B}^{t_E} dt' k_S \frac{\partial G_S}{\partial z'} T_S - \int_{t_B}^{t_E} dt'\, G_B F_B + \int_{z_S}^{z_B} dz'\, \rho c G^0 T^0, \qquad 2.58$$

$$z, z' \in [z_S, z_B], t, t' \in [t_B, t_E],$$

where the various G are elements of the Green's operator $\boldsymbol{G} \equiv \boldsymbol{G}(z, t; z', t')$. This gives the structure of the Green's operator as $\boldsymbol{G} = [\boldsymbol{G}_{S*}, \boldsymbol{G}_S, \boldsymbol{G}_B, \boldsymbol{G}^0]$ and the source as $\boldsymbol{S} = [S, T_S, F_B, T^0]$ where each element of $\boldsymbol{G}$ is the Green's operator for the corresponding element of $\boldsymbol{S}$.[23] It is clear then that the Green's solution corresponds to the inverse problem $\boldsymbol{d} = \boldsymbol{g}(\boldsymbol{m})$. The field $\boldsymbol{S}$ can therefore be considered as a generalised field of sources which generate the temperature field $\boldsymbol{T}$. In fact, Shen and Beck (1991) use Equation 2.58 with Equation 2.57 to display the temperature field in the useful form $\boldsymbol{T} = \boldsymbol{G}(\boldsymbol{F}^*\boldsymbol{T})\boldsymbol{m}$ where $\boldsymbol{F}^*$ is a nonlinear primal differential operator and $\boldsymbol{S}$ is a nonlinear function of $\boldsymbol{T} = T = T^U + T^S$ and model parameters $\boldsymbol{m} = [T_S^U, T_S^S, F_B, k, \rho, c, S]$. This new form is useful in obtaining the form of the gradient, which is derived in Section 2.2.3.3.

Similar operators can be derived for the unsteady and steady primal and dual problems such that for the unsteady primal

$$\boldsymbol{T}^U = \boldsymbol{G}^U \boldsymbol{S}^U, \qquad 2.59$$

where $\boldsymbol{G}^U \equiv \boldsymbol{G}^U(z, t; z', t')$, $z, z' \in [z_S, z_B], t, t' \in [t_B, t_E]$. Partitioning Equation 2.58 into steady and unsteady components, and applying the primal boundary and initial conditions reveals the unsteady Green's operator as

$$T^U = \int_{t_B}^{t_E} dt' k_S \frac{\partial G_S^U}{\partial z'} T_S^U, \qquad 2.60$$

$$z, z' \in [z_S, z_B], t, t' \in [t_B, t_E],$$

---

[23] Equations 2.57 and 2.58 are analogous to Equations 2.15, 2.16 and 2.19 in the FCV numerical solution of Section 2.1.2.2.

giving the structure of the unsteady Green's operator as $\boldsymbol{G}^U = \boldsymbol{G}_S^U$ and the source as $\boldsymbol{S}^U = T_S^U$. For the steady primal

$$\boldsymbol{T}^S = \boldsymbol{G}^S \boldsymbol{S}^S, \tag{2.61}$$

where $\boldsymbol{G}^S \equiv \boldsymbol{G}^S(z; z')$, $z, z' \in [z_S, z_B]$. The explicit steady solution is

$$T^S = \int_{z_S}^{z_B} dz'\, G^S S^S + k_S \frac{\partial G_S^S}{\partial z'} T_S^S - G_B^S F_B^S \tag{2.62}$$

$$z, z' \in [z_S, z_B],$$

giving the structure of the steady Green's operator as $\boldsymbol{G}^S = \left[\boldsymbol{G}_{S*}^S, \boldsymbol{G}_S^S, \boldsymbol{G}_B^S\right]$ and the source as $\boldsymbol{S}^S = \left[S^S, T_S^S, F_B^S\right]$. It is useful to note that $S = S^S$, $T_S = T_S^U + T_S^S$, $F_B = F_B^S$, $T^0 = T^S$.

2.2.3.2 *Dual Problem Solution*

For the general dual problem

$$\widehat{\boldsymbol{S}} = \boldsymbol{G}^{\mathrm{T}} \widehat{\boldsymbol{T}}. \tag{2.63}$$

To solve for $\widehat{\boldsymbol{S}}$ the same procedure as in Section 2.2.3.1 is carried out for the dual problem (applying the quiescent boundary and initial conditions) to give

$$T^D = \int_{z_S}^{z_B} dz' \int_{t_B}^{t_E} dt'\, G^{\mathrm{T}} S^D, \qquad z, z' \in [z_S, z_B], t, t' \in [t_B, t_E], \tag{2.64}$$

recalling that spaces S ∋ $\boldsymbol{S} \subseteq \widehat{\mathrm{T}}$ and $\widehat{\mathrm{S}} \ni \widehat{\boldsymbol{S}} \subseteq$ T (S and T are mutual duals by definition) with $T^D \in$ T and $S^D \in$ S (also see Figure 2.3). This gives the structure of the dual Green's operator as $\boldsymbol{G}^{\mathrm{T}} = \widehat{\boldsymbol{G}}_{S*}$ and the source as $\widehat{\boldsymbol{T}} = S^D$. For the unsteady

$$\widehat{\boldsymbol{S}}^U = \boldsymbol{G}^{U^{\mathrm{T}}} \widehat{\boldsymbol{T}}^U, \tag{2.65}$$

and solving for $\widehat{\boldsymbol{S}}^U$

$$T^{DU} = \int_{z_S}^{z_B} dz'\, G^{U^{\mathrm{T}}} S^{DU}, \qquad z, z' \in [z_S, z_B], t, t' \in [t_B, t_E], \tag{2.66}$$

giving the structure of the unsteady dual Green's operator as $\boldsymbol{G}^{U^{\mathrm{T}}} = \widehat{\boldsymbol{G}}_{S*}^U$ and the source as $\widehat{\boldsymbol{T}}^U = S^{DU}$. Likewise for the steady

$$\widehat{\boldsymbol{S}}^{S} = \boldsymbol{G}^{S^{\mathrm{T}}}\widehat{\boldsymbol{T}}^{S}, \qquad 2.67$$

and solving for $\widehat{\boldsymbol{S}}^{S}$

$$T^{DS} = \int_{z_S}^{z_B} dz'\, G^{S^{\mathrm{T}}} S^{DS}, \qquad z, z' \in [z_S, z_B], \qquad 2.68$$

giving the structure of the steady dual Green's operator as $\boldsymbol{G}^{S^{\mathrm{T}}} = \widehat{\boldsymbol{G}}^{S}_{S*}$ and the source as $\widehat{\boldsymbol{T}}^{S} = S^{DS}$.

The dual boundary conditions effectively restrict the dual problem to a source solution of the (dual) heat flow model, based on the solution of the physically meaningful primal problem and temperature measurement. The condition of mutual duality associates the relevant primal and dual source and temperature fields such that – with the quiescent dual boundary conditions – a residual field $\delta\boldsymbol{T}$ (or perturbation, disturbance) in the primal problem will produce an equivalent residual field $\delta\widehat{\boldsymbol{T}}$ in the dual problem. In this way, the misfit $\delta T^{P} \in \delta\boldsymbol{T} \triangleq \delta\boldsymbol{d}$ between a calculated primal temperature T^{P} and data measurement $\boldsymbol{d}_0$ can be used as a source to calculate an associated dual temperature residual δT^{D} (see Appendix 9.2.2.3.3). This facilitates the calculation of an adjusted T^{P} which is a closer match to $\boldsymbol{d}_0$ in an iterative fashion. The calculation of an adjusted T^{P} requires the estimation of model residuals $\delta\boldsymbol{m}$ which are shared between the primal and dual spaces. The associated $\delta\boldsymbol{m}$ are derived from a residual heat flow equation which is presented in Appendix 9.2.2.3 – these residuals are used to derive the gradient of misfit function S_m, which is presented in Section 2.2.3.3 below. In this way all concerned parameters are optimized using the data residual $\delta\boldsymbol{d}$ from the primal space as a source in the dual space (also see Figure 2.4).

2.2.3.3 *Fréchet and Hessian Derivatives*

The appropriate misfit function[24] for FSI is equivalent to the general nonlinear least squares form (Equation 2.33), restated here as

$$S_m = \frac{1}{2}\Big[[\boldsymbol{d}-\boldsymbol{d}_0]^{\mathrm{T}}\boldsymbol{C_d}^{-1}[\boldsymbol{d}-\boldsymbol{d}_0] + [\boldsymbol{m}-\boldsymbol{m}_0]^{\mathrm{T}}\boldsymbol{C_m}^{-1}[\boldsymbol{m}-\boldsymbol{m}_0]\Big]$$
$$\equiv \frac{1}{2}\big[\langle \delta\hat{\boldsymbol{d}}, \delta\boldsymbol{d}\rangle_{\mathrm{D}} + \langle \delta\hat{\boldsymbol{m}}, \delta\boldsymbol{m}\rangle_{\mathrm{M}}\big] \qquad 2.69$$

A series expansion of S_m about a point $\boldsymbol{m}_0$ corresponding to model perturbation $\boldsymbol{m}_0 + \delta\boldsymbol{m}$ gives

$$S_{\boldsymbol{m}_0+\delta\boldsymbol{m}} = S_{\boldsymbol{m}_0} + \langle \hat{\boldsymbol{\gamma}}, \delta\boldsymbol{m}\rangle_{\mathrm{M}} + \frac{1}{2}\langle \hat{\boldsymbol{H}}\delta\boldsymbol{m}, \delta\boldsymbol{m}\rangle_{\mathrm{M}} + O(\delta\boldsymbol{m}^3), \qquad 2.70$$

where $O(\delta\boldsymbol{m}^3)$ is negligible, $\hat{\boldsymbol{H}}$ is the Hessian and $\hat{\boldsymbol{\gamma}}$ the Fréchet derivative. The operator $\hat{\boldsymbol{\gamma}} \in \hat{\mathrm{M}}$ is the dual of the steepest ascent vector $\boldsymbol{\gamma} \in \mathrm{M}$ (Equation 2.35) which maps the model space M into the space of real numbers R according to

$$\boldsymbol{\gamma} = \boldsymbol{M}\left[\frac{\partial S_m}{\partial \boldsymbol{m}}\right] = \boldsymbol{M}\hat{\boldsymbol{\gamma}}. \qquad 2.71$$

The inverse metric $\boldsymbol{M}$ of the Hessian $\hat{\boldsymbol{H}} \equiv \frac{\partial \hat{\boldsymbol{\gamma}}}{\partial \boldsymbol{m}}$ is a part of the dual space $\hat{\mathrm{M}}$ and also maps M into $\hat{\mathrm{M}}$. It then follows that $\boldsymbol{G}^{\mathrm{T}}$, the transpose of $\boldsymbol{G} = \frac{\partial \boldsymbol{d}}{\partial \boldsymbol{m}}$, is also a member of $\hat{\mathrm{M}}$ according to $\hat{\boldsymbol{m}} = \boldsymbol{G}^{\mathrm{T}}\hat{\boldsymbol{d}}$. Explicitly differentiating S_m in Equation 2.69 and comparing to Equation 2.70 reveals the forms of the Fréchet derivative and Hessian as (see Appendix 9.2.2.4)

---

[24] When a weighting operator is defined such as the inverse covariance matrix $\boldsymbol{W} = \boldsymbol{C}^{-1}$ the duality relationship $\langle \hat{\boldsymbol{m}}, \boldsymbol{m}\rangle_{\mathrm{M}}$ between a linear space $\mathrm{M} \ni \boldsymbol{m}$ and its dual $\hat{\mathrm{M}} \ni \hat{\boldsymbol{m}}$ may be expressed as $\hat{\boldsymbol{m}} = \boldsymbol{W}\boldsymbol{m} = \boldsymbol{C}^{-1}\boldsymbol{m}$ or $\langle \boldsymbol{C}^{-1}\boldsymbol{m}, \boldsymbol{m}\rangle_{\mathrm{M}}$.

a. $$\hat{\boldsymbol{\gamma}} = \hat{\boldsymbol{\gamma}}^{d} + \hat{\boldsymbol{\gamma}}^{m} = [\boldsymbol{F}^{*}\boldsymbol{T}]^{\mathrm{T}}\boldsymbol{G}^{\mathrm{T}}\delta\hat{\boldsymbol{d}} + \delta\hat{\boldsymbol{m}},$$

b. $$\hat{\boldsymbol{H}} = \hat{\boldsymbol{H}}^{d} + \hat{\boldsymbol{H}}^{m} = [\boldsymbol{F}^{*}\boldsymbol{T}]^{\mathrm{T}}\boldsymbol{G}^{\mathrm{T}}\boldsymbol{C}_{\boldsymbol{d}}{}^{-1}\boldsymbol{G}[\boldsymbol{F}^{*}\boldsymbol{T}] + \frac{\delta[\boldsymbol{F}^{*}\boldsymbol{T}]^{\mathrm{T}}\boldsymbol{G}^{\mathrm{T}}}{\delta\boldsymbol{m}}\delta\hat{\boldsymbol{d}} + \boldsymbol{C}_{\boldsymbol{m}}{}^{-1}, \quad 2.72$$

which corresponds to the discrete form in Equation 2.38. The form of $\hat{\boldsymbol{\gamma}}^{m}$, the component of the gradient dictated explicitly by the model parameters, is $\hat{\boldsymbol{\gamma}}^{m} = \delta\hat{\boldsymbol{m}} = \boldsymbol{C}_{\boldsymbol{m}}{}^{-1}[\boldsymbol{m} - \boldsymbol{m}_{0}]$ and for the Hessian $\hat{\boldsymbol{H}}^{m} = \boldsymbol{C}_{\boldsymbol{m}}{}^{-1}$.

To obtain the explicit forms of the Green's operators $\boldsymbol{G}$ and $\boldsymbol{G}^{\mathrm{T}}$, further spatial transformations are performed to get the explicit forms of $\hat{\boldsymbol{\gamma}}^{d}$ and $\hat{\boldsymbol{H}}^{d}$. To do this, it is important to appreciate the relationships of the spaces $\langle\hat{\mathrm{M}},\mathrm{M}\rangle$ and $\langle\hat{\mathrm{D}},\mathrm{D}\rangle$ to the spaces $\langle\hat{\mathrm{S}},\mathrm{S}\rangle$ and $\langle\hat{\mathrm{T}},\mathrm{T}\rangle$. The spatial relationships (see Figure 2.4) can be inferred from the components of the fields over each space. Reviewing the Green's operator solutions it can be inferred that: $\hat{\mathrm{T}}$ and S are subspaces of M; $\hat{\mathrm{S}}$ and T are subspaces of D. Also $\hat{\mathrm{M}}$ can be identified with D and $\hat{\mathrm{D}}$ identified with M which can be seen by examining the gradient relationships above and in what follows. As highlighted earlier, M and D form a joint space $[\mathrm{D},\mathrm{M}]$ in terms of the objective function and gradients.

With the dual source space $\hat{\mathrm{S}} \subset \mathrm{D} \subset \hat{\mathrm{D}}$ a temperature residual $\delta\boldsymbol{T} \triangleq \delta\boldsymbol{d}$ in D has a dual field corresponding to a source $\delta\hat{\boldsymbol{T}} \triangleq \delta\hat{\boldsymbol{d}} = \boldsymbol{C}_{\boldsymbol{d}}{}^{-1}\delta\boldsymbol{d}$ in $\hat{\mathrm{D}}$ which generates a dual temperature field $\delta\hat{\boldsymbol{S}}$ in $\hat{\mathrm{S}}$ such that $\delta\hat{\boldsymbol{S}} = \boldsymbol{G}^{\mathrm{T}}\delta\hat{\boldsymbol{T}} \Leftrightarrow \delta T^{D} = \boldsymbol{G}^{\mathrm{T}}\delta S^{D}$ (also see Figure 2.4). With this particular case of the data residual $\hat{\boldsymbol{\gamma}}^{d}$ and $\hat{\boldsymbol{H}}^{d}$ can be shown (see Appendix 9.2.2.4) to have components $\hat{\boldsymbol{\gamma}}^{d} = [\hat{\boldsymbol{\gamma}}^{Ts}, \hat{\boldsymbol{\gamma}}^{F_B}, \hat{\boldsymbol{\gamma}}^{k}, \hat{\boldsymbol{\gamma}}^{pc}, \hat{\boldsymbol{\gamma}}^{S}]$ and $\hat{\boldsymbol{H}}^{d} = [\hat{\boldsymbol{H}}^{Ts}, \hat{\boldsymbol{H}}^{F_B}, \hat{\boldsymbol{H}}^{k}, \hat{\boldsymbol{H}}^{pc}, \hat{\boldsymbol{H}}^{S}]$ corresponding to the analogous model residuals $\delta\boldsymbol{m} = [\delta T_S, \delta F_B, \delta k, \delta\rho c, \delta S]$ where $\hat{\boldsymbol{\gamma}}^{d}$ is explicitly

$$\hat{\gamma}^{Ts} = k_S \frac{\partial \delta T_S^D}{\partial z}$$

$$\hat{\gamma}^{F_B} = -\delta T_B^D$$

$$\hat{\gamma}^{k} = -\int_{t_B}^{t_E} dt \frac{\partial T}{\partial z}\frac{\partial \delta T^D}{\partial z} \qquad 2.73$$

$$\hat{\gamma}^{pc} = -\int_{t_B}^{t_E} dt\, \delta T^D \frac{\partial T}{\partial t}$$

$$\hat{\gamma}^{S} = \int_{t_B}^{t_E} dt\, \delta T^D, \qquad z \in [z_S, z_B], t \in [t_B, t_E].$$

and $\hat{\boldsymbol{H}}^{\boldsymbol{d}}$ is

$$\hat{\boldsymbol{H}}^{Ts} = \frac{\partial \hat{\gamma}^{Ts}}{\delta T_S}$$

$$\hat{\boldsymbol{H}}^{F_B} = \frac{\partial \hat{\gamma}^{F_B}}{\delta F_B}$$

$$\hat{\boldsymbol{H}}^{k} = \frac{\partial \hat{\gamma}^{k}}{\delta k} \qquad 2.74$$

$$\hat{\boldsymbol{H}}^{pc} = \frac{\partial \hat{\gamma}^{pc}}{\delta \rho c}$$

$$\hat{\boldsymbol{H}}^{S} = \frac{\partial \hat{\gamma}^{S}}{\delta S}.$$

where the second order term $\frac{\delta(\boldsymbol{F}^*\boldsymbol{T})^{\mathrm{T}}\boldsymbol{G}^{\mathrm{T}}}{\delta \boldsymbol{m}}\delta\hat{\boldsymbol{d}} \approx 0$ in $\hat{\boldsymbol{H}}^{\boldsymbol{d}}$ has been discarded.

In the partitioned problem the boundary derivatives related to $\boldsymbol{m}_B$ and the source derivative related to $\boldsymbol{m}_P$ are separated into their respective steady and unsteady components.

2.2.3.4 FSI Algorithm

Recalling the general steepest descent algorithm as $\boldsymbol{m}_{i+1} = \boldsymbol{m}_i - \mu_i \boldsymbol{\gamma}_i$: $\boldsymbol{\gamma}_i = \boldsymbol{M}_i \hat{\boldsymbol{\gamma}}_i$ and $\boldsymbol{M}_i$ is a metric operator – the covariance matrix $\boldsymbol{C}_{\boldsymbol{m}}$ or the inverse of the Hessian $\hat{\boldsymbol{H}}_i$. The algorithm is terminated at iteration $i = I$, the maximum likelihood point with solution $\boldsymbol{m}_I$ at the minimum $S_{\mathbf{m}_I}$ of the misfit function.

In the case of the simple steepest descent algorithm where $\boldsymbol{M}_i = \boldsymbol{C}_m$

$$\begin{aligned} \boldsymbol{m}_{i+1} &= \boldsymbol{m}_i - \mu_i \boldsymbol{\gamma}_i = \boldsymbol{m}_i - \mu_i \boldsymbol{M}_i \widehat{\boldsymbol{\gamma}}_i = \boldsymbol{m}_i - \mu_i \boldsymbol{C}_m \left[\widehat{\boldsymbol{\gamma}}_i^d + \widehat{\boldsymbol{\gamma}}_i^m\right] \\ &= \boldsymbol{m}_i - \mu_i \left[\boldsymbol{C}_m \widehat{\boldsymbol{\gamma}}_i^d + \boldsymbol{m}_i - \boldsymbol{m}_0\right], \end{aligned} \tag{2.75}$$

recalling that $\widehat{\boldsymbol{\gamma}}^m = \boldsymbol{C}_m{}^{-1}[\boldsymbol{m} - \boldsymbol{m}_0]$. In the case of the quasi-Newtonian descent algorithm where $\boldsymbol{M}_i = \widehat{\boldsymbol{H}}_i{}^{-1}$

$$\begin{aligned} \boldsymbol{m}_{i+1} &= \boldsymbol{m}_i - \mu_i \boldsymbol{\gamma}_i = \boldsymbol{m}_i - \mu_i \widehat{\boldsymbol{H}}_i{}^{-1} \widehat{\boldsymbol{\gamma}}_i = \boldsymbol{m}_i - \mu_i \widehat{\boldsymbol{H}}_i{}^{-1} \left[\widehat{\boldsymbol{\gamma}}_i^d + \widehat{\boldsymbol{\gamma}}_i^m\right] \\ &= \boldsymbol{m}_i - \mu_i \left[\left[\widehat{\boldsymbol{H}}_i^d + \widehat{\boldsymbol{H}}_i^m\right]^{-1} \left[\widehat{\boldsymbol{\gamma}}_i^d + \widehat{\boldsymbol{\gamma}}_i^m\right]\right] \\ &= \boldsymbol{m}_i - \mu_i \left[\left[\widehat{\boldsymbol{H}}_i^d + \boldsymbol{C}_m{}^{-1}\right]^{-1} \left[\widehat{\boldsymbol{\gamma}}_i^d + \boldsymbol{C}_m{}^{-1}[\boldsymbol{m} - \boldsymbol{m}_0]\right]\right]. \end{aligned} \tag{2.76}$$

Equations 2.75 and 2.76 respectively correspond to Equations 2.37 and 2.39 in the discrete theory. In the case of a preconditioned descent algorithm $\boldsymbol{M}_i$ is substituted by $\boldsymbol{M}_i^P = \boldsymbol{P}_i \boldsymbol{M}_i$, $\boldsymbol{P}_i$ being the preconditioning operator.

Figure 2.4 and Table 2.1 summarise the FSI development in terms of spaces and operators and the flow of calculations as the algorithm progresses.

Steps 1-7 are repeated until convergence at the optimum S_{m_I} or when S_m is close enough to S_{m_I} – referred to as the termination point. A suitable termination point is where the Fréchet derivative $\widehat{\boldsymbol{\gamma}} \to 0$ or displays a change in sign indicating the algorithm is close to an optimal point which may correspond to S_{m_I} such that $S_{m_{i+1}} > S_{m_i}$.

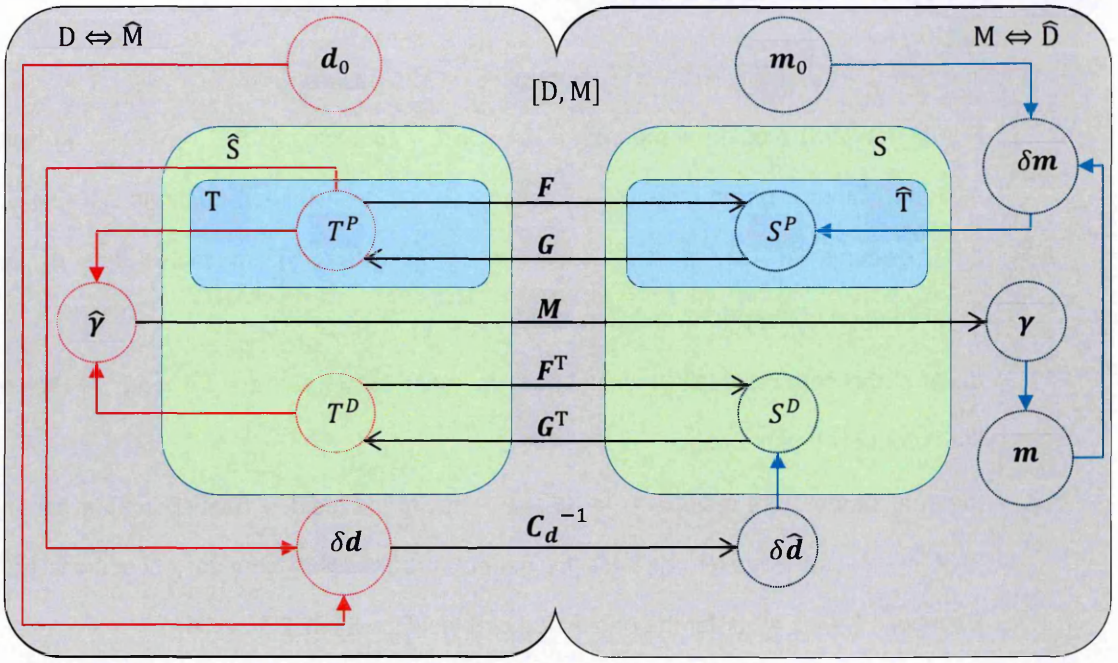

Figure 2.4. FSI spaces, parameters and operators. The joint space [D, M] (grey) and its primal and dual subspaces (see text) are represented by the respective blue nad green rectangles. The black, red and blue arrows represent respective primal-dual mappings, data space operations and model space operations. Note that operator M includes model covariance C_m.

To facilitate a numerical solution the critical equations of the theory must be discretised. Important to note is that the same code can be used to solve the primal and dual problems and can be made general enough to solve both the general problem and the partitioned problem. Therefore the FCV method can be used for steps 1 and 3 with the time reversed in the dual problem. Here, the primal and dual problems are solved using the partitioned model which facilitates easier isolation of the steady heat flow F_B^S which remains the primary model parameter to be estimated. The remainder of the inverse problem is solved using standard algebraic methods for linear systems.

Table 2.1. The FSI Algorithm. This listing can be used as a companion to Figure 2.4.

	FSI CALCULATIONS (also see Figure 2.4)
1.	Primal (forward) problem temperature solution T^P, according to $\boldsymbol{F}T^P = S^P$ with an initial estimate of model parameters $\boldsymbol{m}_0$ – Equations 2.1-2.11 (also see Equations 2.40-2.42);
2.	data residuals $\delta\boldsymbol{d} = \boldsymbol{d} - \boldsymbol{d}_0 \equiv \delta\boldsymbol{T} = T^P - \boldsymbol{d}_0$ resulting from the measured data $\boldsymbol{d}_0$ and initial solution of the primal problem T^P;
3.	duals of the data residuals (residual heat sources) $\delta\widehat{\boldsymbol{d}} = \boldsymbol{C_d}^{-1}\delta\boldsymbol{d} = \delta\widehat{\boldsymbol{T}} \equiv \delta\boldsymbol{S}^D$ facilitating the introduction of the dual;
4.	the dual temperature residual $T^D \in \delta\widehat{\boldsymbol{S}} \equiv \delta\boldsymbol{T}^D$ due to the residual heat sources according to $\boldsymbol{F}^{\mathrm{T}}T^D = S^D$ – Equation 2.46 for the general problem with boundary conditions from Equations 2.47-2.49 or for the partitioned problem Equations 2.50-2.56;
5.	the misfit function derivatives from the dual temperature and the primal temperature
a.	the gradient (Fréchet derivative) $\widehat{\boldsymbol{\gamma}}$ in simple steepest descent – Equation 2.73;
b.	and additionally the Hessian in the Newtonian descent $\widehat{\boldsymbol{H}} = \boldsymbol{M}^{-1}$ – Equation 2.74;
6.	the direction of steepest ascent $\boldsymbol{\gamma} = \boldsymbol{M}\widehat{\boldsymbol{\gamma}}$ for the misfit function – Equations 2.75 in the steepest descent and Equation 2.76 in Newtonian descent;
7.	the model parameter updates by subtracting the direction of steepest ascent and applying the update constant – Equation 2.75 in the steepest descent and Equation 2.76 in Newtonian descent.

2.2.3.5 *Analysing Inversion Results*

The results of the inversion can be quantified using an a posteriori covariance operator $\boldsymbol{C}_{\boldsymbol{m}_I}$, defined as (e.g. Menke, 1989; Shen and Beck, 1991; Tarantola, 2005)

$$\boldsymbol{C}_{\boldsymbol{m}_I} = \boldsymbol{G}_{\boldsymbol{m}}\boldsymbol{C}_{\boldsymbol{m}} \equiv [\boldsymbol{I} - \boldsymbol{R}_{\boldsymbol{d}}]\boldsymbol{C}_{\boldsymbol{m}}. \qquad 2.77$$

$\boldsymbol{G}_{\boldsymbol{m}}$, the resolution operator, determines the contribution of the a priori model $\boldsymbol{m}_0$ and $\boldsymbol{R}_{\boldsymbol{d}}$, the sensitivity operator, determines the contribution of the data measurement $\boldsymbol{d}_0$ to the resolution of the model $\boldsymbol{m}_I$. $\boldsymbol{I}$ is the identity operator. $\boldsymbol{R}_{\boldsymbol{d}}$ is further defined as

$$\boldsymbol{R}_{\boldsymbol{d}} = \boldsymbol{C}_{\boldsymbol{m}}[\boldsymbol{F}^*\boldsymbol{T}^I]^{\mathrm{T}}\boldsymbol{G}_I{}^{\mathrm{T}}[\boldsymbol{G}_I[\boldsymbol{F}^*\boldsymbol{T}^I]\boldsymbol{C}_{\boldsymbol{m}}[\boldsymbol{F}^*\boldsymbol{T}^I]^{\mathrm{T}}\boldsymbol{G}_I{}^{\mathrm{T}} + \boldsymbol{C}_{\boldsymbol{d}}]^{-1}\boldsymbol{G}_I[\boldsymbol{F}^*\boldsymbol{T}^I], \qquad 2.78$$

where $\boldsymbol{G}_I\left[\boldsymbol{F}^*\boldsymbol{T}^I\right]$ corresponds to $\frac{\partial \mathbf{d}_I}{\partial \mathbf{m}_I}$, the data Fréchet derivative evaluated at solution point $\boldsymbol{m}_I$. The closer $\boldsymbol{R}_d$ is to the identity operator, the smaller are $\boldsymbol{G}_m$ and $\boldsymbol{C}_{m_I}$, and therefore the better resolved is the model $\boldsymbol{m}_I$. Matrix identities in Tarantola (2005) show that, $\boldsymbol{C}_{m_I}$ can be reduced to the form

$$\boldsymbol{C}_{m_I} = \left[[\boldsymbol{F}^*\boldsymbol{T}^I]^{\mathrm{T}}\boldsymbol{G}_I{}^{\mathrm{T}}\boldsymbol{C}_d{}^{-1}\boldsymbol{G}_I[\boldsymbol{F}^*\boldsymbol{T}^I] + \boldsymbol{C}_m{}^{-1}\right]^{-1} \equiv \left[\widehat{\boldsymbol{H}}_I^d + \boldsymbol{C}_m{}^{-1}\right]^{-1}, \qquad 2.79$$

corresponding to the inverse Hessian metric $\boldsymbol{M}_I = \widehat{\boldsymbol{H}}_I{}^{-1}$ of Equation 2.76 evaluated at solution point $\boldsymbol{m}_I$. Interpreting $\boldsymbol{C}_{m_I}$ relative to $\boldsymbol{C}_m$ and $\boldsymbol{C}_d$ allows some insight into how much information has been gained on model parameters $\boldsymbol{m}$ in the inversion. It is important to note that the $\boldsymbol{C}_{m_I}$ estimate is not an accurate quantification of the covariance in a nonlinear problem and is strictly true only for the corresponding linear problem. It must therefore be used with some caution (see Chapter 4 for examples).

2.3 Summary

The theory outlining a method for inversion of a subsurface temperature measurement T_n^m is presented (n is the number of temperature sensors over depth z and m represents the number of measurements over time t). This method is based on the theory presented in Tarantola (2005) and largely follows the method of Shen and Beck (1991,1992). The method optimizes data $\boldsymbol{d}_0 = T_n^m$, boundary $\mathbf{m}_B = \left[T_S^U, T_S^S, F_B\right]$ and regolith $\mathbf{m}_P = [k, \rho, c, S]$ parameters simultaneously, in principle, though the steady basal heat flow $F_B \Leftrightarrow F_B^S$ which is identified with the planetary heat flow is the main parameter of interest.

The forward (also direct or primal) problem is presented in Section 2.1.2 with the option of partitioning it into a steady and unsteady problem. Partitioning allows for easier management of the different model parameters – F_B^S in particular, which is identified with the steady partition. Analytical solutions (Sections 2.1.2.1.1-2.1.2.1.3; after Carslaw and Jaeger, 1986), and a Finite Control Volume (FCV) numerical solution (Section 2.1.2.2; after Patankar, 1980) are presented. These are used in the forward model in Chapter 3.

The inverse problem is presented in Section 2.2 as the optimization of $\mathbf{m}_B$ (linear) or $\mathbf{m}_B$ and $\mathbf{m}_P$ (nonlinear) from $\boldsymbol{d}_0$. The inverse problem is unstable because information on the surface unsteady temperature T_S^U is lost due to lagging and damping of the propagated unsteady temperature signal T^U, the superposition of the surface heat flow F_B^U with F_B^S and errors in $\boldsymbol{d}_0$, $\mathbf{m}_B$ and $\mathbf{m}_P$. Some features which cause instability in estimating one parameter may be a benefit for estimating another. The problem can be stabilised by quantifying this information in a priori model parameters using model and data covariances $\boldsymbol{C}_m$ and $\boldsymbol{C}_d$ – a Bayesian approach. $\boldsymbol{C}_m$ and $\boldsymbol{C}_d$ weight the contribution of each model parameter to the resolution of the inverse problem (Section 2.2.1.2).

The linear inverse problem can be solved by least squares minimisation of a misfit function S_m, optionally incorporating normed data and model parameter misfits $S_{\|d\|}$ and $S_{\|m\|}$ or by singular value decomposition (SVD). For the nonlinear problem, the misfit function can be optimized using gradient methods of steepest descent (steepest descent, quasi-Newton, and preconditioned descent are presented) or random search methods such as Monte Carlo. In gradient methods, the Fréchet $\hat{\boldsymbol{\gamma}}$ and Hessian $\widehat{\boldsymbol{H}}$ gradients of S_m are calculated using primal-dual linear spaces where the gradient – a member of the dual space – is calculated from the results of the dual problem using weighted data residuals $\delta\widehat{\boldsymbol{d}} = \boldsymbol{C}_d{}^{-1}\delta\boldsymbol{d}$ as heat sources (Section 2.2.3.3). The relationships are developed analytically using Green's function solutions to the heat flow equation (Sections 2.2.3.1-2.2.3.2, analogous to the forward problem solution of Section 2.1.2.2) and a residual heat flow equation accounting for the misfits (residuals) of the model parameters $\delta\boldsymbol{m}$ due to the data misfit $\delta\boldsymbol{d}$. The dual problem (Section 2.2.2.2) is essentially the primal problem (Section 2.2.2.1), with time reversed (or lagged) such that dual time $\tau = -t$. It has quiescent initial and boundary conditions which permit simpler resolution of the gradients of S_m than in a corresponding primal problem. An a posteriori covariance $\boldsymbol{C}_{m_I}$ is presented which can be used to analyse the results of the inversion (Section 2.2.3.5).

The method, as presented, effectively involves four solutions of the forward problem (unsteady and steady primal, unsteady and steady dual) along with calculations of $\hat{\gamma}$, $\widehat{H}$ and the direction of steepest ascent γ. The primal and dual problems are discretized and solved using the FCV method of Patankar (1980). Gradients $\hat{\gamma}$ and $\widehat{H}$ are calculated by discretizing the terms at the end of Section 2.2.3.3 and γ calculated using standard numerical methods. The method is programmed in Interactive Data Language (IDL; Excelis, 2014). The theory is tested in Chapters 4-7, and overall results are discussed in Chapter 8.

2.4 References

ARFKEN, G. B. & WEBER, H.-J. 2005. *Mathematical Methods for Physicists,* Amsterdam, London, Elsevier Academic.

BACKUS, G. & GILBERT, F. 1970. Uniqueness in the Inversion of Inaccurate Gross Earth Data. *Royal Society of London Philosophical Transactions Series A,* 266, 123-192.

BECK, J. V. & ARNOLD, K. J. 1977. *Parameter Estimation in Engineering and Science,* New York, London, Sydney, Tokyo, John Wiley & Sons.

CARSLAW, H. S. & JAEGER, J. C. 1986. *Conduction of heat in solids,* Oxford, Clarendon.

COLLINS, G. W., II 2003. *Fundamental Numerical Methods and Data Analysis*. George W. Collins, II.

DAVIS, G. D. V. 1986. *Numerical Methods in Engineering & Science,* London, Allen & Unwin.

EXCELIS, V. I. S. 2014. IDL Software. 7.0-8.0 ed.: Excelis Visual Information Solutions.

GOTTFRIED, B. S. & WEISMAN, J. 1973. *Introduction to Optimization Theory,* Englewood Cliffs, Hemel Hempstead, Prentice-Hall.

HAGERMANN, A. 2013. *RE: Forward Solution to the Unsteady Heat Flow Problem.* Type to CORNWALL, M.

MENKE, W. 1989. *Geophysical Data Analysis: Discrete Inverse Theory,* San Diego, Academic Press.

NOCEDAL, J. & WRIGHT, S. J. 1999. *Numerical Optimization,* New York, Springer.

PATANKAR, S. V. 1980. *Numerical Heat Transfer and Fluid Flow,* New York, NY, London, Hemisphere.

PATON, M. D., KARGL, G., BALL, A. J., GREEN, S. F., HAGERMANN, A., KÖMLE, N. I., THIEL, M. & ZARNECKI, J. C. 2010. Computer modelling of a penetrator thermal sensor. *Advances in Space Research,* 46, 337-345.

PRESS, W. H. 2002. *Numerical Recipes in C++: The Art of Scientific Computing,* Cambridge, Cambridge University Press.

SAAD, Y. 2003. Iterative Methods for Sparse Linear Systems. Society of Industrial and Applied Mathematics.

SEIFERLIN, K., KÖMLE, N. I., KARGL, G. & SPOHN, T. 1996. Line heat-source measurements of the thermal conductivity of porous H_2O ice, CO_2 ice and mineral powders under space conditions. *Planetary and Space Science,* 44, 691-704.

SHEN, P. Y. & BECK, A. E. 1991. Least Squares Inversion of Borehole Temperature Measurements in Functional Space. *J. Geophys. Res.,* 96, 19965-19979.

SHEN, P. Y. & BECK, A. E. 1992. Paleoclimate change and heat flow density inferred from temperature data in the Superior Province of the Canadian sheild. *Palaeogeography, Palaeoclimatology, Palaeoecology,* 98, 143-165.

SHEN, P. Y., WANG, K., BELTRAMI, H. & MARESCHAL, J. C. 1992. A comparative study of inverse methods for estimating climatic history from borehole temperature data. *Palaeogeography, Palaeoclimatology, Palaeoecology,* 98, 113-127.

TARANTOLA, A. 2005. *Inverse problem theory and methods for model parameter estimation,* Philadelphia, PA, Society for Industrial and Applied Mathematics.

TARANTOLA, A. & VALETTE, B. 1982. Generalized nonlinear inverse problems solved using the least squares criterion. *Reviews of Geophysics,* 20, 219-232.

TAUTZ, H. 1971. *Wärmeleitung und Temperaturausgleich,* Weinheim, Verlag Chemie.

WANG, K. 1992. Estimation of Ground Surface Temperatures from Borehole Temperature Data. *J. Geophys. Res.,* 97, 2095-2106.

3 FORWARD MODEL

3.1 Introduction

The forward model (the model) is the forward problem of Section 2.1 programmed and solved in IDL using the Finite Control Volume (FCV) discretization method introduced in Section 2.1.2.2.1 (Figure 3.1). The model is partitioned into steady and unsteady components (modules) as with the partitioned forward problem. The model is adapted to the steady state by bypassing[1] the TIME module.

The model is tested against results from the analytical solutions presented in Section 2.1.2.1. Use of the analytical solutions is limited to homogenous problems where the medium properties are constant with depth (and time) or heterogeneous problems with a few layers. Several representative scenarios are used to illustrate the behaviours of the forward model in response to different boundary conditions and regolith properties. The depth scales covered are those that a planetary heat flow probe similar to those discussed in Section 1.2.2 is likely to cover. The tests serve as an initial guide to the range of setups which can be simulated with the inverse model – of which the forward model is a major component – and as a point of reference for specific results from inverse model tests in Chapters 4-7.

[1] A numerical solution to the steady partitioned problem is facilitated by allowing the timestep $\Delta t_m \rightarrow \infty$ and therefore the "thermal capacity" coefficient $a_n^0 \rightarrow 0$ in the general numerical solution. This simply means there is no measurable change in temperature over the simulation time.

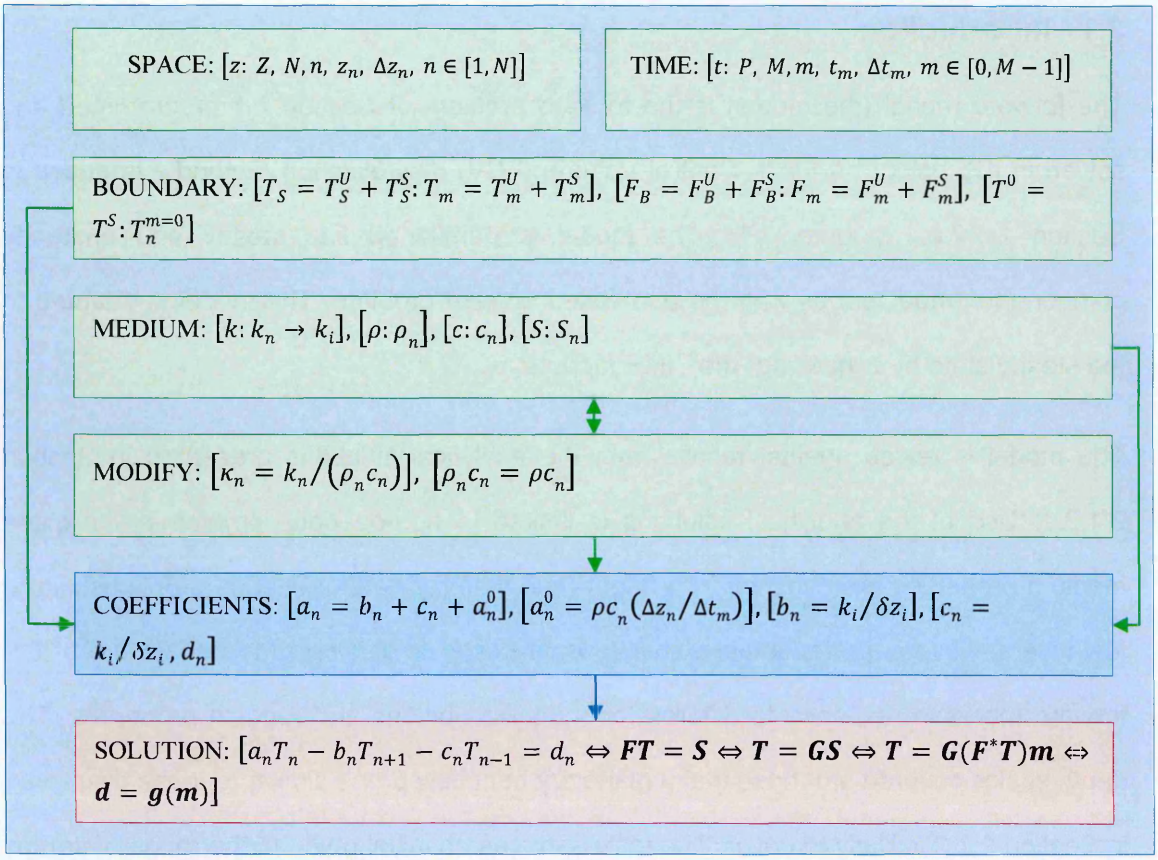

Figure 3.1. Primal (forward) model. Illustrates the implementation of the general primal problem in IDL. The green upper modules (rectangles) represent the initialization of the simulation, including the modification of some medium properties. Much of the initialization can be performed in parallel (green rectangles). The blue module shows the calculation of coefficients and the red module the solution via the TDMA. Note that Δz_n is the control volume size while δz_i is the distance between nodes and k_i is the interface conductivity. Symbol definitions can be found in Appendix 9.1.

3.2 Steady Primal Problem

A few examples serve to verify the steady state model against analytical solutions presented in Section 2.1.2.1. The effects of the steady state model parameters are examined where the specific model relationships (see Chapter 2) can be stated as $\boldsymbol{F}^S\boldsymbol{T}^S = \boldsymbol{S}^S$ (forward) and $\boldsymbol{d}^S = \boldsymbol{g}^S(\boldsymbol{m}) \Leftrightarrow \boldsymbol{T}^S = \boldsymbol{G}^S\boldsymbol{S}^S$ (inverse). $\boldsymbol{T}^S$ and $\boldsymbol{d}^S$ represent temperature data, $\boldsymbol{F}^S$ the forward differential operator, $\boldsymbol{g}^S$ the functional inverse model relationship, $\boldsymbol{G}^S$ the steady Green operator and $\boldsymbol{m} = [T_S^S, F_B^S, k, S^S]$ where T_S^S is the surface steady temperature, F_B^S the basal heat flow, k the conductivity and S^S heat sources and sinks. Typical terrestrial values are used throughout.

3.2.1 Basal Heat Flow F_B^S

Figure 3.2 illustrates the influence of the magnitude of the basal heat flow $F_B^S = 100$, 76 and 50 mW/m^2 on the subsurface steady temperature T^S. A basaltic conductivity $k = 3$ W/m/K (e.g. Wang, 1992) is used with steady surface temperature $T_S^S = 287.15$ K.

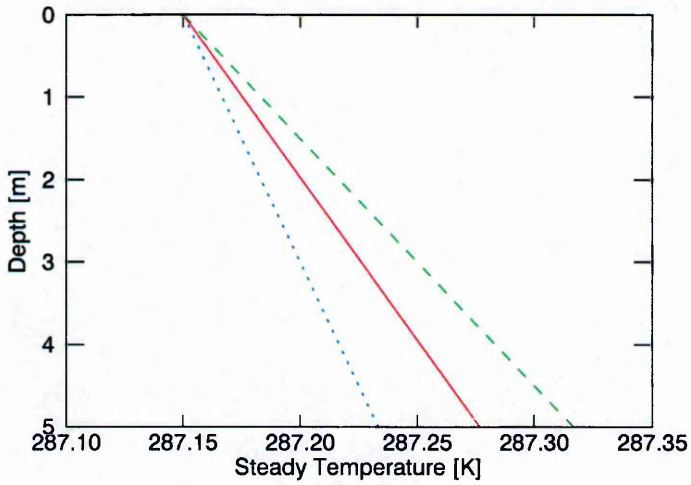

Figure 3.2. Effects of basal heat flow F_B^S. The dashed green, solid red and dotted blue curves respectively have F_B^S of 100, 76 and 50 mW/m^2. The thermal conductivity $k = 3$ W/m/K and steady surface temperature $T_S^S = 287.15$ K. A 10 point homogeneous grid is used in the simulation.

From Figure 3.2, it can be seen that heat flows of higher magnitude produce steeper steady temperature gradients and, equivalently, higher basal temperatures. This is understandable in the sense that heat flows from regions of higher temperature to regions of lower temperature such that a greater temperature difference occurs with greater heat flow. This may be verified by examining the steady heat flow equation (HFE) analytical solution in Section 2.1.2.1.2 which illustrate the direct relationship between F_B^S and T^S.

3.2.2 Conductivity k

Figure 3.3 illustrates the influence of thermal conductivities $k = 2.5$ and 3.5 W/m/K on the subsurface steady temperature T^S, with basal heat flow $F_B^S = 76$ mW/m^2 and steady surface temperature $T_S^S = 287.15$ K.

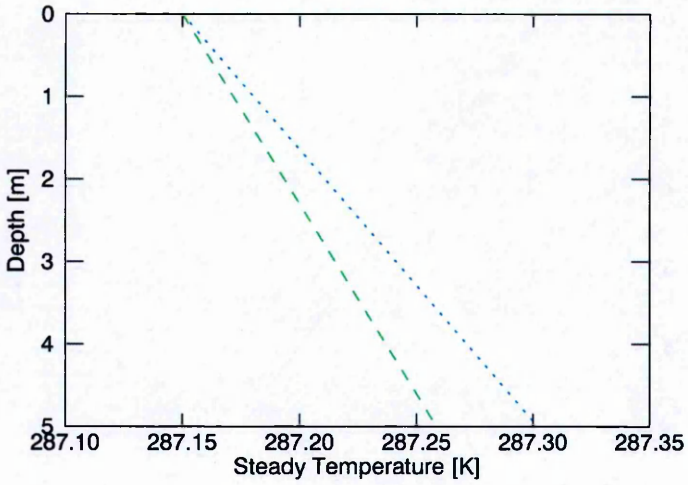

Figure 3.3. Effects of thermal conductivity k. The dashed green and dotted blue curves respectively have k of 3.5 and 2.5 W/m/K. Basal heat flow $F_B^S = 76$ mW/m² and steady surface temperature $T_S^S = 287.15$ K. A 10 point homogeneous grid is used in the simulation.

Figure 3.3 confirms that a higher conductivity produces a smaller temperature gradient. This can be physically understood as the higher conductivity allowing temperatures to reach a greater state of equilibrium due to more heat transfer within the medium. The steady analytical solution of Section 2.1.2.1.2 can be examined to confirm this, where there is an inverse relationship between k and T^S.

3.2.3 Heat Sources and Sinks S^S

Figure 3.4 illustrates the effects of heat sources $S^S = 0$ and 10 mW/m^3 on the subsurface steady temperature T^S with and without a basal heat flow. Thermal conductivity $k = 3$ W/m/K and steady surface temperature $T_S^S = 287.15$ K with basal heat flow $F_B^S = [0,76]$ mW/m^2, t

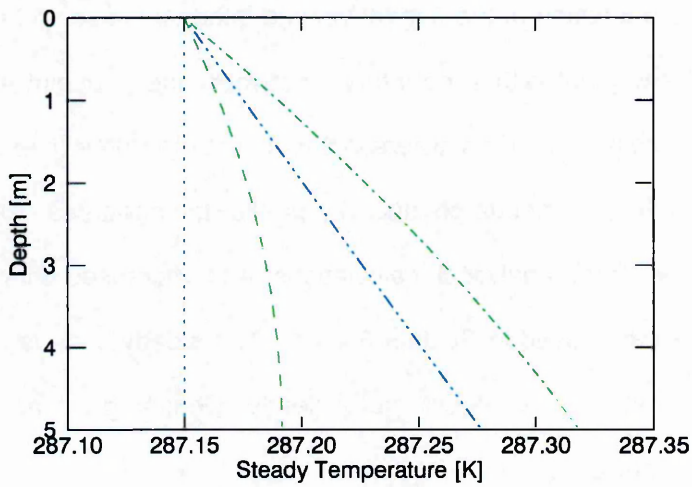

Figure 3.4. Effects of steady heat sources S^S where the blue curves have $S^S = 0$ mW/m^3 and the green curves have $S^S = 10$ mW/m^3 The dotted and dashed curves represent conditions with no heat flow. The dot-dashed and double-dot-dashed curves represent temperature profiles with basal heat flow $F_B^S = 76$ mW/m^2. Thermal conductivity $k = 3$ W/m/K and steady surface temperature $T_S^S = 287.15$ K. A 10 point homogeneous grid is used in the simulation.

Typical terrestrial crustal source heating is of the order of μW/m^3 (e.g. Aurangzeb et al., 2008) which produces no discernible difference in temperature at the depth scale being considered here. A comparatively high value is used in Figure 3.4 to illustrate the nonlinear effect of a constant distribution of heat sources. The analytical solution in Section 2.1.2.1.2 can be examined to verify the results, where the effect of S^S on T^S is second order with depth z.

3.3 Composites

Introduction of layering with FCV discretization is fairly straightforward as outlined in Section 2.1.2.3. However, it is important to note that, with analytical solutions, the temperatures are calculated at the location of a gridpoint, while with FCV discretization, the temperature is calculated based on the flow of heat between control volumes. The flow of heat across control volumes is regulated by the interface conductivity, the value of which is based on the location of the control volume interface. A control volume interface may be located at any point within the interval between one gridpoint and the next, or, equivalently, the gridpoint located anywhere within a control volume (see Section 2.1.2.3). Therefore, with an inhomogeneous conductivity profile, temperatures calculated by FCV discretization diverge from analytical calculations with increased inhomogeneity and courser grids (further discussed in Section 3.4.1.1). The steady state is used to illustrate layering as it demonstrates the effect more clearly. Denser grids are used than the preceding homogeneous cases.

3.3.1 Perfect Contact

Figure 3.5 shows a simulation with perfect layer contact, where the upper, middle, and lower layer respectively have conductivity k of 0.03, 0.3 and 3 W/m/K. Basal heat flow $F_B^S = 76$ mW/m^2 and steady surface temperature $T_S^S = 287.15$ K.

Figure 3.5 illustrates the continuity conditions discussed in Section 2.1.2.3: the heat flow is continuous across, and temperatures equal at, boundaries in perfect contact. Notably, the temperature gradients in each layer (respectively 2.49, 0.25, and 0.025 K/m from upper to lower; see Appendix 9.3.1) correlate inversely with the magnitude of the conductivities: the conductivity increases by a factor of 10 downward in each layer; the temperature gradient decreases by the same factor. Note that the calculated values of steady heat flow F^S and temperature gradient $\frac{\Delta T^S}{\Delta z}$ (see Appendix 9.3.1) do not exactly replicate the theory because the calculation of the interface conductivities (Section 2.1.2.2.1), at the layer boundaries, introduces numerical inaccuracies.

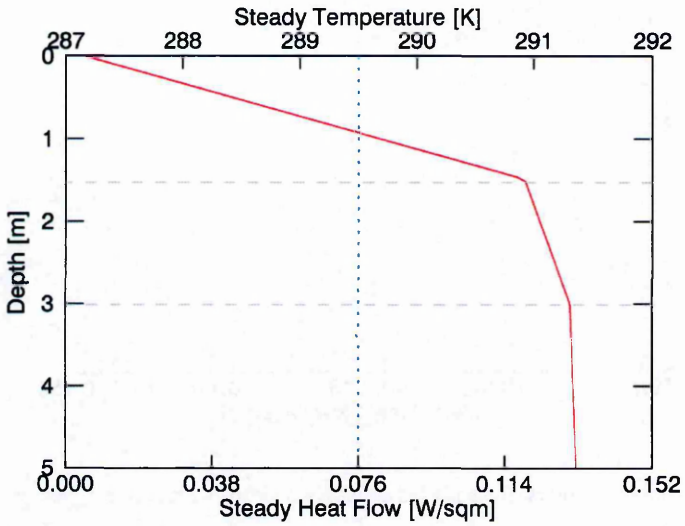

Figure 3.5. Layering with perfect contact. The solid red curve is the steady temperature T^S and the dotted blue curve the steady (basal) heat flow $F^S = F_B^S = 76$ mW/m². The dashed grey lines indicate layer boundaries where the upper, middle, and lower layer respectively have conductivity k of 0.03, 0.3 and 3 W/m/K. Steady surface temperature $T_S^S = 287.15$ K. A 100 point homogeneous grid is used in the simulation.

3.3.2 Imperfect Contact

Figure 3.6 shows a simulation with imperfect layer contact. This shows the effect of the modifying term h_i with values of 0.5 between the upper and middle layers and 0.75, between the middle and lower layers (it is analogous to the so-called Hertz factor, mentioned in Section 2.1.2.3). The upper, middle, and lower layer respectively have conductivity k of 0.03, 0.3 and 3 W/m/K. Basal heat flow $F_B^S = 76$ mW/m^2 and steady surface temperature $T_S^S = 287.15$ K.

As discussed in Section 2.1.2.3, while the heat flow across the boundaries remains continuous, the temperatures differ such that the product of the temperature difference and the conductance H is proportional to the heat flow. Analysis (Appendix 9.3.2) shows that for any interface i, $H_i = k_c = h_i k_i$, where k_i is the interface conductivity and k_c the contact conductivity. The temperature gradient relationship noted in Section 3.3.1 is preserved within each layer.

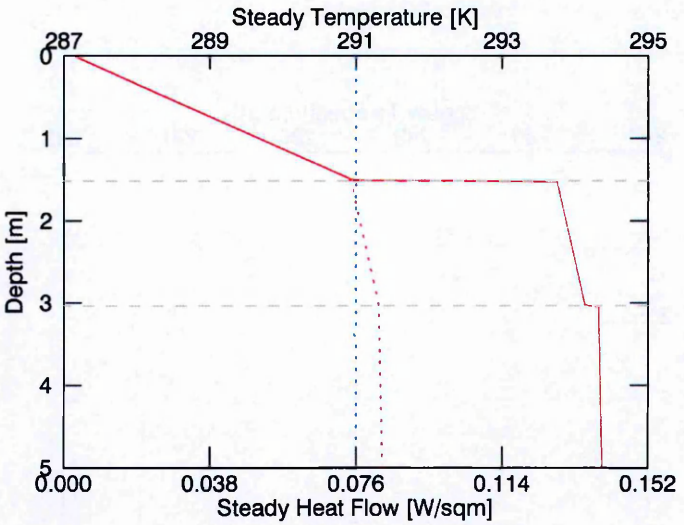

Figure 3.6. Layering with imperfect contact. The solid red curve is the steady temperature T^S and the dotted blue curve the steady (basal) heat flow $F_B^S = 76$ mW/m². The dashed grey lines indicate layer boundaries where the upper, middle, and lower layer respectively have conductivities k of 0.03, 0.3 and 3 W/m/K. At the upper and lower boundary the conductivity is reduced by factors h_i of 0.5 and 0.75, respectively. A 100 point sinusoidal grid is used in the simulation with the grid density increasing towards layer boundaries.

3.3.3 Continuous Layering

In many planetary cases, the variation of thermal properties can be assumed as continuous (Figure 3.7), reflecting the gradual nature of deposition processes. The temperature profile due to an asymptotically increasing conductivity at first glance may be confused with an unsteady temperature profile. This underscores the importance of obtaining accurate thermal conductivity measurements to produce an accurate estimate of the unsteady temperature perturbation due to the surface unsteady temperature. It should be noted, though, that the steady (basal) heat flow F_B^S, in the absence of sources, is constant throughout the medium; therefore, where calculated heat flows show systematic variation, particularly towards the surface, a reasonable conclusion is that the steady temperature is contaminated with the unsteady temperature or there are errors in the measured conductivity.

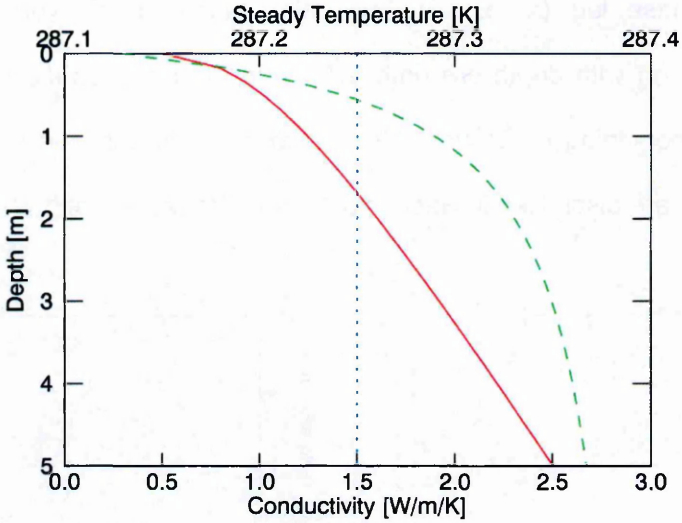

Figure 3.7. Continuous layering. Here the thermal conductivity k (dashed green curve) undergoes a continuous functional variation with depth z according to $k = k_\infty \frac{z+a}{z+b}$ where $k_\infty = 3$ W/m/K is an asymptotic conductivity, and $a = b = 1$ are constants (Grott et al., 2007) such that $k = 0.3$ at $z = 0$. The solid red curve is the steady temperature T^S and the dotted blue curve the steady (basal) heat flow $F_B^S = 76$ mW/m². A 30 point homogeneous grid is used in the simulation.

3.4 Unsteady Primal Problem

The effects of the unsteady model parameters are now explored. The specific model relationships (see Chapter 2) can be stated as $\boldsymbol{F}^U\boldsymbol{T}^U = \boldsymbol{S}^U$ (forward) and $\boldsymbol{d}^U = \boldsymbol{g}^U(\boldsymbol{m}) \Leftrightarrow \boldsymbol{T}^U = \boldsymbol{G}^U\boldsymbol{S}^U$ (inverse). $\boldsymbol{T}^U$ and $\boldsymbol{d}^U$ represent temperature data, $\boldsymbol{F}^U$ the forward differential operator, $\boldsymbol{g}^U$ the functional inverse model relationship, $\boldsymbol{G}^U$ the unsteady Green operator and $\boldsymbol{m} = [T_S^U, F_B^U, k, \rho, c, S^U]$. T_S^U is the surface unsteady temperature, F_B^U the unsteady basal heat flow, which is zero in all cases, ρ and c respectively density and specific heat capacity, the product of which is the thermal capacity, and S^U heat sources and sinks. Typical terrestrial values are used throughout.

3.4.1 Unsteady Surface Temperature T_S^U

Figure 3.8 illustrates the effects of a sinusoidal surface temperature $T_S^U = T_S^{UA} \sin(2\pi t/P)$ with $T_S^{UA} = 12$ K and $P = 86400$ s; the calculations are carried out both numerically (red), using the TDMA (see Section 2.1.2.2.1), and analytically (green) using the analytical solution from Section 2.1.2.1), for comparison. Note that the grid density increases towards the surface to better capture the unsteady temperature variation.

The increasing phase lag (a. and b.) and attenuation of the surface temperature oscillations (c. and d.) with depth are both evident in the plots, as discussed in Section 2.1.2.1.1 and the beginning of Section 2.2. The differences between the analytical and numerical solutions are discussed in Section 3.4.1.1 in the context of grid convergence.

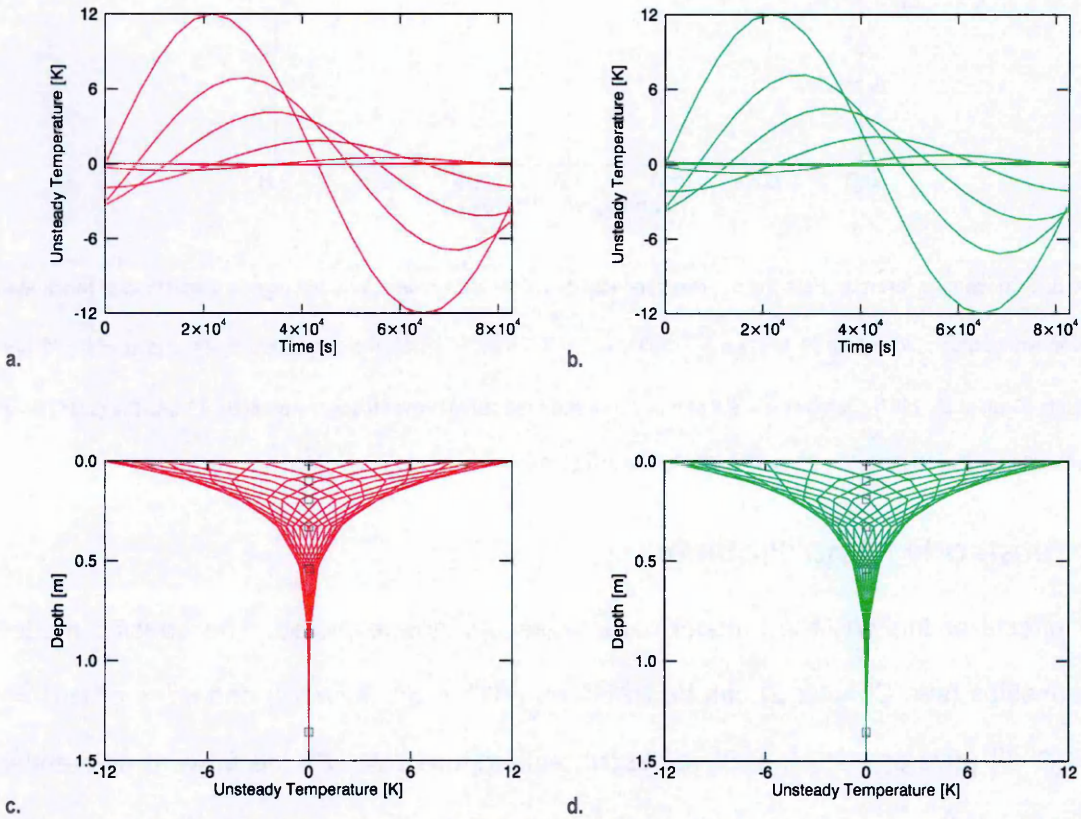

Figure 3.8. Numerical (red, left) and analytical (green ,right) unsteady temperature due to unsteady surface temperature $T_S^U = T_S^{UA} \sin(2\pi t/P)$ with amplitude $T_S^{UA} = 12$ K and period $P = 86400$ s. Thermal conductivity $k = 3.0$ W/m/K, density $\rho = 2700$ kg/m^3 and specific heat capacity $c = 790$ J/kg/K. Timestep $\Delta t_m = 3600$ s and control volumes ($n = 10$) range in size such that 0.01 m $\leq \Delta z_n \leq$ 1.75 m. The parameter of the upper countours (a. and b.) is depth where the temperature amplitude decreases with depth. The parameter of the lower contours (c. and d.) is time where the grey squares represent gridpoints.

3.4.1.1 Grid Convergence

A grid convergence[2] study is performed using the difference between the unsteady analytical T^{UA} and numerical T^{U} temperature calculations, here called the discretization error $\epsilon_A = \sqrt{\sum(\Delta T)^2}$, where $\Delta T = T^U - T^{UA}$. The study is performed using an unsteady surface temperature $T_S^U = T_S^{UA} \sin(2\pi t/P)$ with amplitude $T_S^{UA} = 12$ K and period $P =$ 86400 s in a homogeneous medium where: thermal conductivity k = 3.0 W/m/K; density ρ = 2700 kg/m^3; and specific heat capacity c = 790 J/kg/K. The simulations are performed on a space of eleven homogeneous timesteps (Δt) by ten homogeneous grid spacings (Δz) over a period of 24 h and down to depth 5 m.

Figure 3.9a shows that a general refinement in timestep Δt and grid spacing Δz does not lead to an improved overall solution. With the grid refined in terms of Δz or Δt, the numerical converges on the analytical solution within a limited range, beyond which the solution it diverges. The case of decreasing Δz (or increasing Δt) can be interpreted as the solution tending to the steady state as decreasing Δz decreases the thermal capacity coefficient a_n^0 of the FCV numerical solution. Therefore the calculation is less influenced by the previous temperature T_n^0 as the timesteps progress. Conversely, the case of decreasing Δt (or increasing Δz) effectively increases the thermal capacity coefficient, reducing the transfer of unsteady heat information to deeper control volumes. If Δt is too small, implicit time discretization may become problematic; explicit or Crank-Nicolson time discretization are alternatives.[3]

Figure 3.9b illustrates how the gridding conforms to the Courant principle (e.g. Patankar, 1980), which requires $\Delta t < \rho c\,(\Delta x)^2/2k$. The principle is not strictly applicable in the

---

[2] Grid convergence is achieved when successive refinement of the model grid and timesteps achieves a solution where the errors ϵ_A asymptotically approach zero.

[3] Implicit time discretization assumes that the temperature immediately transitions from T_n^0 to T_n over Δt. Explicit assumes that T_n^0 persists over Δt, while Crank-Nicolson assumes a linear change from T_n^0 to T_n.

implicit time discretization scheme used here (see Appendix 9.2.1.3); it becomes useful in explicit or Crank-Nicolson time discretization, when small Δt makes implicit discretization problematic. The Courant Number ϵ_C is defined as $\epsilon_C = \rho c(\Delta z)^2/(2k\Delta t)$ where the Courant principle stipulates $\epsilon_C > 1$ for stable results. Notably, Figure 3.9b shows that while the implicit discretization scheme becomes more unstable as $\Delta z \to 0$ for a given Δt, the alternative schemes increase in stability.

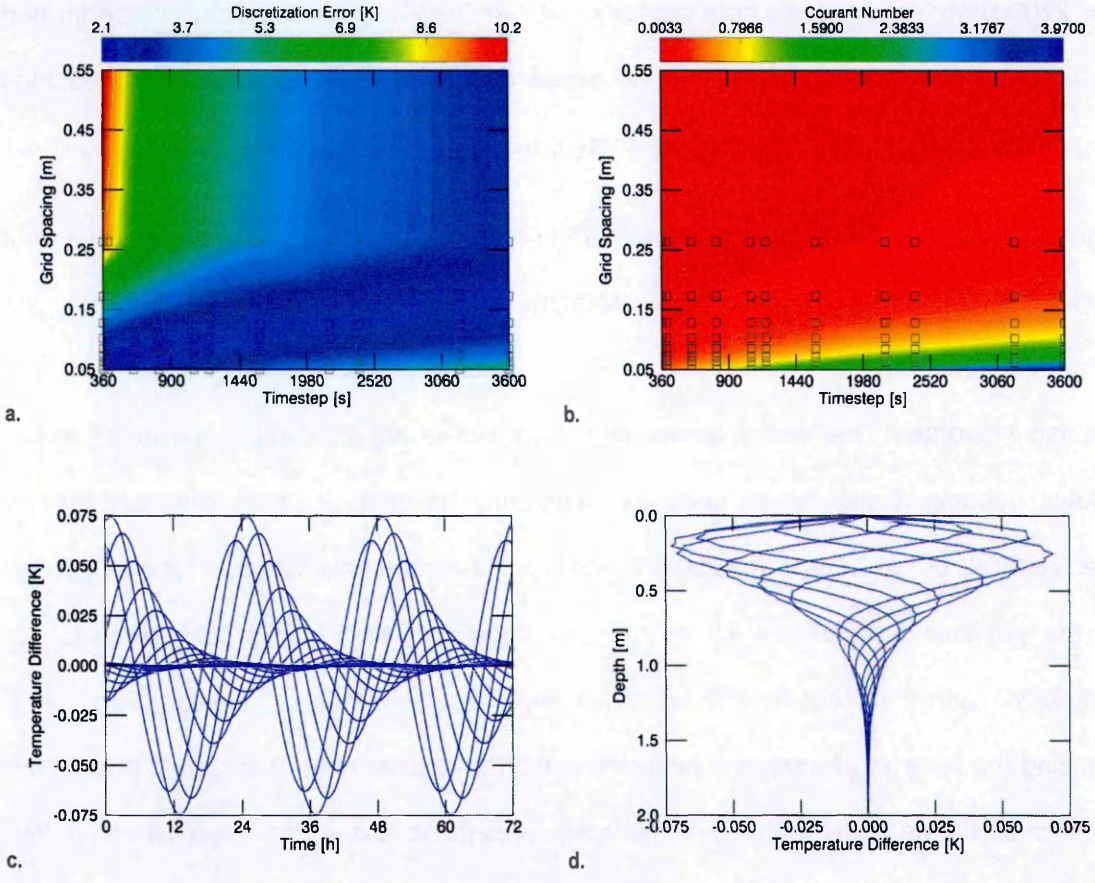

Figure 3.9. Grid convergence study using difference between calculated analytical and numerical temperatures. Contour: a. represents the discretization error relative to grid spacing Δz and timesteps Δt; b. shows the equivalent Courant number (after Patankar, 1980) for the different grids in a. The grey squares show the data points (simulations) from which the contours are interpolated; c. is an overly of the temperature difference ΔT at different depths; d. is an overly of ΔT at different times. For c. and d.: $\Delta t = 360$ s and $\Delta z = 0.05$ m on a homogeneous grid down to 5 m.

In Figure 3.9c and d, the discretization error appears to introduce a phase lag in the numerical solution which increases with depth and the solutions produced are oscillatory. Evidently the errors are largest away from the constraining effect at the boundaries which

can be traced back to the forward and backward substitution processes in solving the TDMA (see Section 2.1.2.2.1; also see e.g. Patankar, 1980) which tend to propagate and inflate numerical errors along the grid.

3.4.1.2 High Frequency Components

In order to examine the stability of the model in cases where the temperature is not a simple sine wave, cases of a surface temperature with high frequency components are tested, starting with square and sawtooth temperature waves (Figure 3.10 and Figure 3.11). The square surface unsteady temperature is defined by T_S^{UA} SGN[sin(2π$(t - \lfloor t \rfloor)/P$)] and the sawtooth unsteady temperature defined by $T_S^{UA}(t/P - \lfloor t/P \rfloor)$.[4]. Amplitude $T_S^{UA} = 12$ K and $P = 86400$s in a homogeneous medium with thermal conductivity $k =$ 3.0 W/m/K, density $\rho =$ 2700 kg/m^3 and specific heat capacity $c =$ 790 J/kg/K. Unsteady basal heat flow $F_B^U = 0$.

It is evident that the high frequency components characterising the discontinuities in the waves are attenuated fairly close to the surface of the medium. As the waves propagate further into the medium their characteristics are increasingly smoothed. Much of the high frequency information in the original surface temperature waves is therefore lost from the subsurface temperature profile. Inverting even an accurately measured subsurface temperature profile will therefore not uniquely reproduce higher frequency components of the original surface temperature. This is reflective of the ill-posed nature of the inverse problem as discussed at the beginning of Section 2.2.

An interesting note is that the square wave propagates marginally deeper into the medium and has a larger temperature envelope[5], this is because it forces more heat into the medium. The relatively smooth profile of the sawtooth wave minimum temperatures with

[4] The operator SGN represents the sign function, which takes the sign (±) of its argument. The operator ⌊ ⌋ represents the floor function, which produces the largest integer less than or equal to its argument.

[5] Defined by the amplitude of the time dependent temperature at a particular depth.

depth (the leftmost extent of the envelope in Figure 3.10d) suggests that unique characteristics can be used to glean information about the specific shape of the unsteady surface temperature.[6] Figure 3.11 compares the form of the sinusoidal, square and sawtooth temperature profiles of Figure 3.10 taken at $t = 0$.

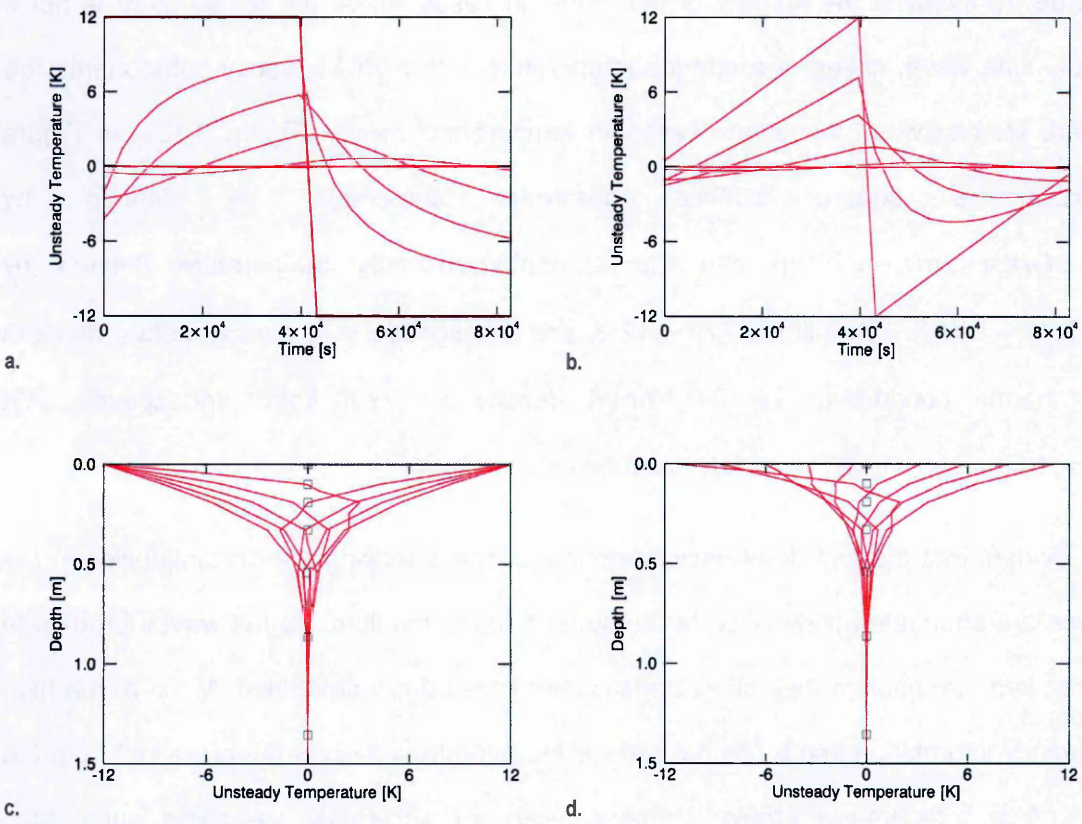

Figure 3.10. Propagation of high frequencies. The left (a. and c.) contours represent a square temperature wave (T_S^{UA} SGN[sin(2π$(t - \lfloor t \rfloor)/P$)]) while the right (b. and d.) contours represent a sawtooth temperature wave ($T_S^{UA}(t/P - \lfloor t/P \rfloor)$). The parameter of the upper countours (a. and b.) is depth where the high frequency components are attenuated with depth. The parameter of the lower contours (c. and d.) is time where the grey squares represent gridpoints.

Much of the information which allows for differentiation of the surface temperature profiles is present in the upper 0.5 m in the particular cases of Figure 3.10 and Figure 3.11. If the main parameter sought is the surface temperature history T_S^U, then the information precludes a unique solution to the inverse problem, without the use of a priori information

[6] This is important when inverting a temperature profile from an instantaneous or short term measurement, where information on the unsteady surface temperature is unknown or incomplete.

(e.g. Section 2.2.1.2). Here the main parameter sought is the basal heat flow F_B^S which is masked by the unsteady temperature oscillations in the subsurface; therefore in this case, attenuation is desirable. However, one parameter which is important in recovering F_B^S is the steady surface temperature T_S^S which is the mean of T_S^U and can only be well determined if the characteristics of T_S^U are well determined; the particular shape of T_S^U tends to bias T_S^S positively or negatively.

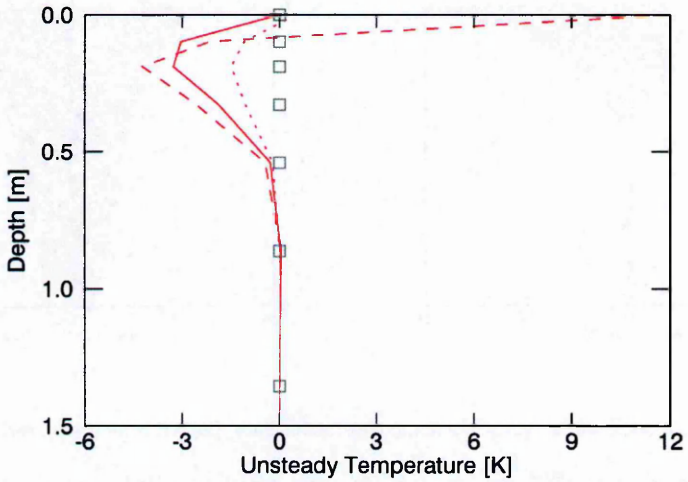

Figure 3.11. Comparison of sinusoidal (solid), square (dashed) and sawtooth (dotted) subsurface temperature profiles of Figure 3.10, taken at time $t = 0$. The grey squares represent gridpoints.

The heat signatures of longer period (lower frequency) and/or greater amplitude surface temperatures will propagate further into the subsurface as illustrated in Figure 3.12. Illustrated are annual (360 d) unsteady temperature cycles in a homogeneous medium with thermal conductivity k = 3.0 W/m/K, density ρ = 2700 kg/m^3 and specific heat capacity c = 790 J/kg/K. One simulation (Figure 3.12, left) contain only annual (low) frequencies according to $T_S^U = 2T_S^{UA} sin(2\pi t/P_0)$ while the other (Figure 3.12, right) contains superimposed diurnal and annual frequencies such that $T_S^U = T_S^{UA}[sin(2\pi t/P_0) + sin(2\pi t/P_1)]$, shown only down to 5 m. Temperature amplitude T_S^{UA} = 12 K, period P_0 = 360 d and P_1 = 86400 s.

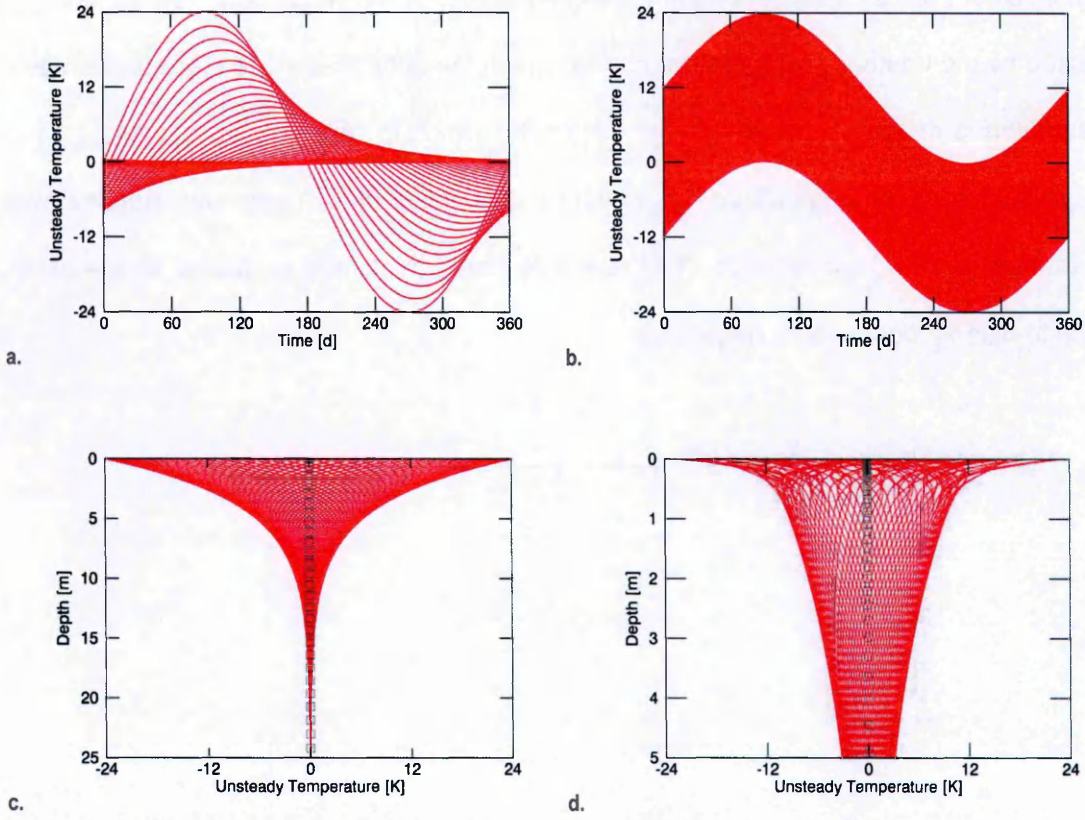

Figure 3.12. Annual unsteady temperature cycles in a homogeneous medium. The left contours (a. and c.) represent a 360 d unsteady surface temperature ($T_S^U = 2T_S^{UA} sin(2\pi t/P_0)$). The right contours (b. and d.) shows superimposed diurnal ($P_1 = 86400$ s) and annual ($P_0 = 360$ d) temperatures such that $T_S^U = T_S^{UA}[sin(2\pi t/P_0) + sin(2\pi t/P_1)]$. The parameter of the upper countours (a. and b.) is depth with larger amplitudes towards the surface and the parameter of the lower contours (c. and d.) is time. The grey squares represent gridpoints.[7]

The annual temperature oscillation simply heats the surface for a longer time period relative to the diurnal temperature ($P_0 > P_1$) and therefore forces more heat into the subsurface, to greater depth z. The effects of the high frequency diurnal components are most evident in the upper 1 m of the medium, as Figure 3.12d shows. A temperature of larger amplitude T_S^{UA} also forces more heat into the subsurface over a given time period P. These effects define the maximum temperature amplitude at depth z (temperature

[7] It is interesting to note that while the primal numerical code solves this setup effectively, an analytical calculation involves calculating the diurnal and annual components separately, then summing the results. This demonstrates the potential time saving features of a strictly numerical approach to solving the problem.

envelope) as seen in Figure 3.12c. The conical shape of the envelope is due to damping and is regulated by the thermal diffusivity $\kappa = k/\rho c$. The effects of varying κ are quantified below with the thermal capacity.

3.4.2 Thermal Capacity ρc

The physical effects of density ρ and specific heat capacity c are illustrated in Figure 3.13 with $\rho = 5100$, 2700 and 1051 kg/m^3 (left) and $c = 1381$, 790 and 395 J/kg/K (right). The surface temperature is a simple sinusoidal surface temperature as used in Section 3.4.1, the thermal conductivity $k = 3.0$ W/m/K, the unsteady basal heat flow $F_B^U = 0$.

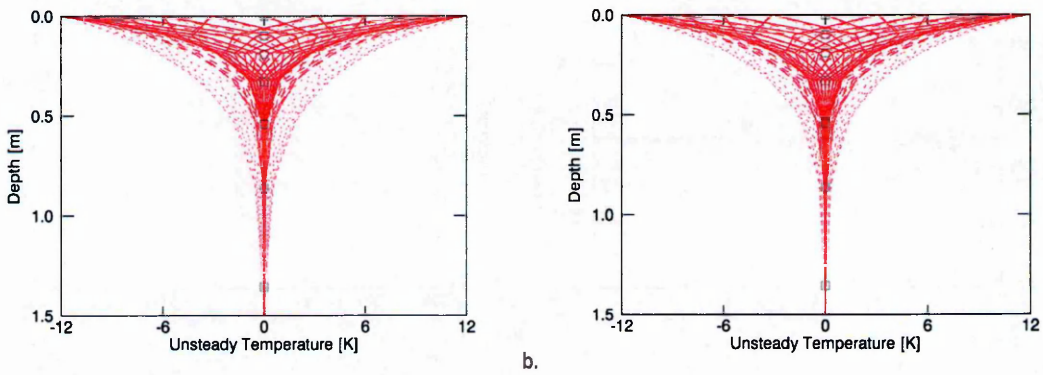

Figure 3.13. Characteristics of thermal capacity. The left countours (a.) illustrate the effects of a change in density. The solid, dashed and dotted contours respectively representing density $\rho = 5100$, 2700 and 1051 kg/m^3. The right countours (b.) illustrate the effects of a change in specific heat capacity. The solid, dashed and dotted contours respectively representing heat capacity $c = 1381$, 790 and 395 J/kg/K. The thermal conductivity $k = 3.0$ W/m/K, the unsteady basal heat flow $F_B^U = 0$. A simple sinusoidal surface temperatue is used. The grey squares represent grid points.

Evidently, higher density and specific heat capacity increase the attenuation of the surface temperature oscillations with depth, which is verified by the analytical solution of Section 2.1.2.1.1. The similar effects of both justify their use in the single thermal capacity term. Similar features are observed with high versus low k, though with inverse effects: higher k causes decreased attenuation with depth. The similar effects of the change in these parameters, and the period P in Section 3.4.1.2, explains their use in calculating the skin depth z_{SKIN}, introduced in Section 2.2.

3.5 Superposed Numerical Solution

The partition of the subsurface temperature into steady and unsteady states is allowed by the solutions to the heat flow equation, they are not partitioned in a temperature measurement. Therefore, it is instructive to illustrate a superposed temperature profile to precisely highlight its characteristics (Figure 3.14). Analytically, this is achieved by summing the steady and unsteady solution for a given problem, as done in Section 2.1.2.1.3. Numerically, it is achieved by applying relevant boundary conditions to the unsteady state.

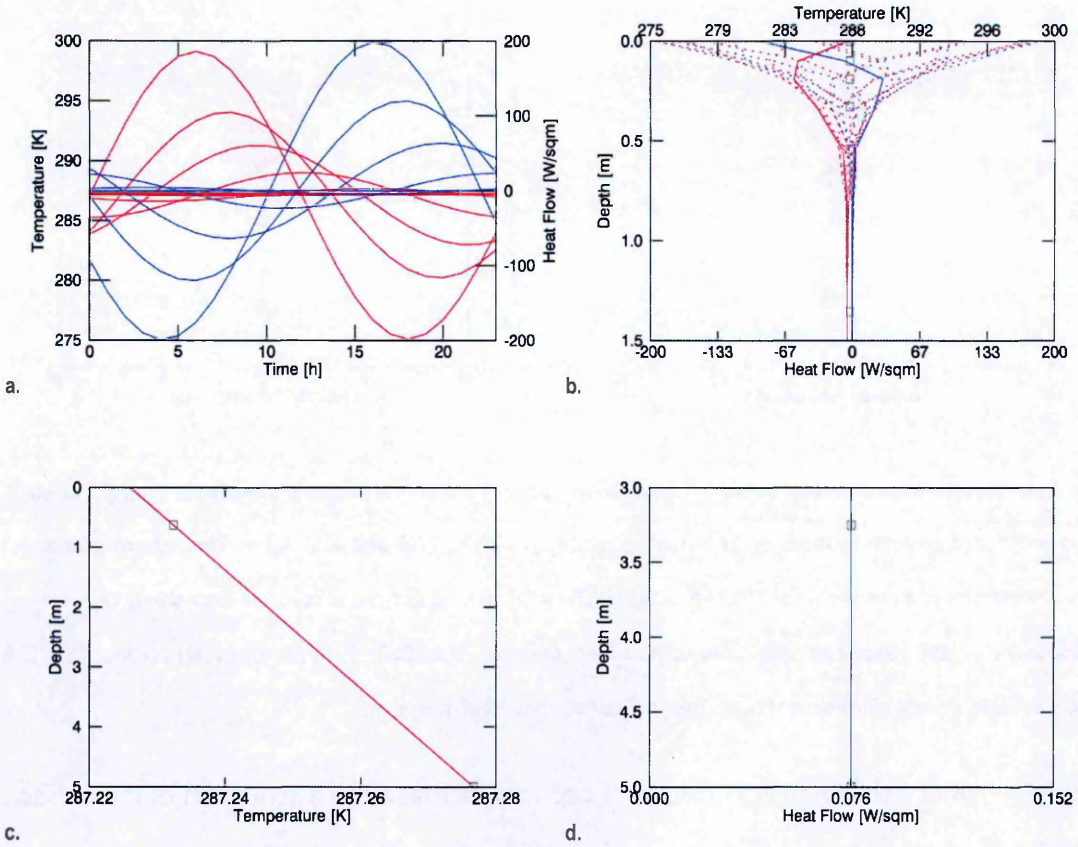

Figure 3.14. Numerical temperature and heat flow. The upper contours show overlays of temperature (red) and heat flow (purple) at: a. different depths; b. different times – the solid curves represent readings at a starting time. The lower plots show: c. zoomed subsurface temperature at depth; d. zoomed heat flow at depth. Thermal conductivity $k = 3.0$ W/m/K, density $\rho = 2700$ kg/m^3 and specific heat capacity $c = 790$ J/kg/K. The grey squares represent gridpoints.

The heat flow is almost half of a period (180° or π radians) out of phase with the temperature. This is to be expected, as heat flows down the temperature gradient. The

slight lag between the heat flow and temperature extremes is reflected in the thermal inertia $I = \sqrt{k\rho c}$ (or equivalently in the thermal diffusivity κ) of the medium, where the lag decreases with an increase in I. The characteristics illustrated with the partitioned steady and unsteady problems are retained, and it is clear that the surface unsteady heat flow is likely to be far larger than the basal heat flow F_B, at an arbitrary point in time.

3.6 Surface Energy Balance

As mentioned in Section 2.1.2.2.2, there are cases where the surface temperature is not known but can be calculated using surface energy balance relationships. The surface energy balance theory in Section 2.1.2.2.2 does not account for an atmosphere, and is therefore not strictly applicable to bodies with atmospheres. Accounting for an atmosphere is a complicated process, which is left up to sophisticated climate models to solve (see Section 5.2.1 for examples). However, for airless bodies, a surface energy balance relationship can provide a first order estimate of surface temperatures, replicating major features of their empirical counterparts.

Figure 3.15 shows Lunar temperatures obtained by applying the surface energy balance relationship of Section 2.1.2.2.2 (see Appendix 9.3.3 for related parameter values). They are compatible with the results of Jones et al. (1975) and the measurements in Langseth et al. (1976). Figure 3.15a shows how the thermal diffusivity κ (or alternatively thermal inertia I – see Section 3.5) dictates surface temperature as heat is adiabatically lost from the surface during lunar night (between 15-27 d). Note the low amplitude annual surface temperature that is evident in Figure 3.15b. This causes a small increase in skin depth evidenced by the slightly larger temperature envelope down to 2.5 m depth.

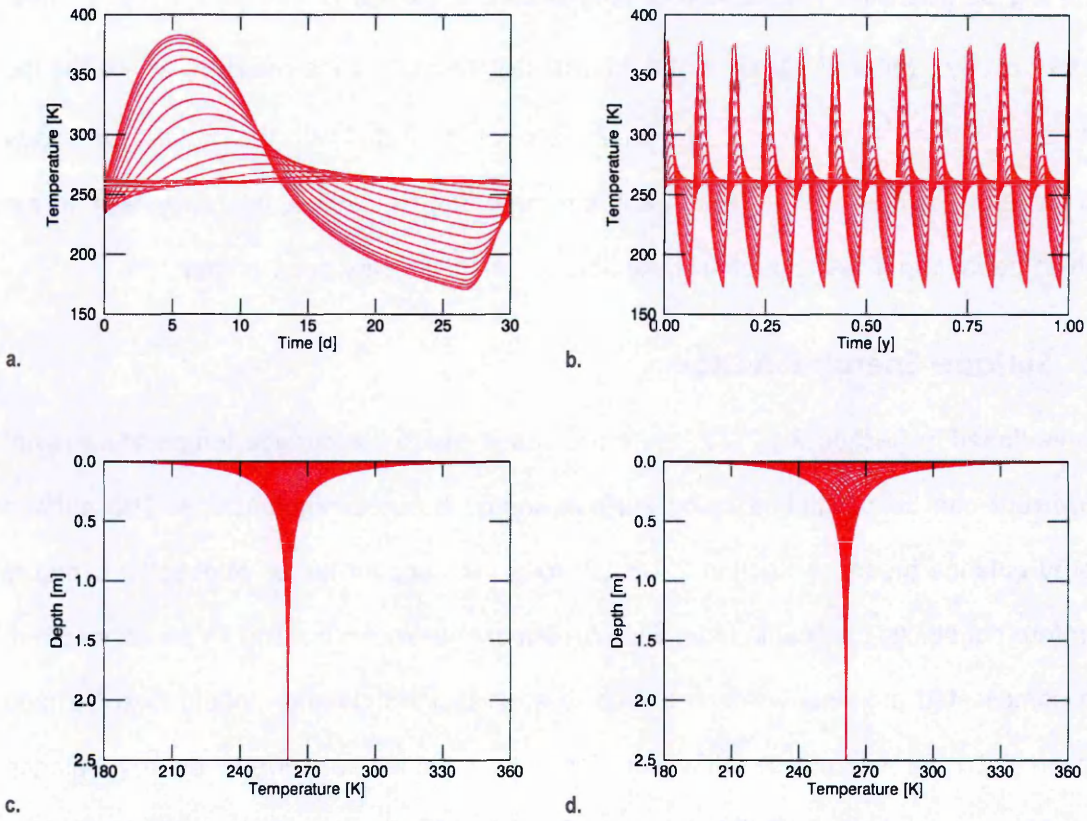

Figure 3.15. Surface energy balance numerical solution for a lunar analogue environment according to $\frac{S^o}{R^2}(1-A)\cos\varphi - \varepsilon\sigma {T_S}^4 = -k\frac{\partial T_S}{\partial z}$ (see Appendix 9.1 for symbol definitions). Plots: a. and b. show the surface temperature over 1 lunation (1 month) and 12 lunations, respectively; c. and. Show the evolution of subsurface temperature profiles over 1 lunation and 12 lunations, respectively. The basal heat flow $F_B^S = 22$ mW/m². A 100 point grid is used with decreasing control volume size towards the surface.

3.7 Summary

A one dimensional forward heat flow model is presented based on the forward modelling theory outlined in Section 2.1. The model is programmed in IDL and contains a steady state and unsteady state module for a partitioned solution to the heat flow problem. It is capable of simulating scenarios using homogeneous or heterogeneous grids and implicit, explicit or Crank-Nicholson time discretization.

The model simulates the temperature distribution in the subsurface, based on conductivity, thermal capacity and heat source distributions. It accepts temperature, heat flow or energy balance boundary conditions. The model is capable of simulating layering

of thermal property values both with perfect and imperfect contact, allowing the 1D simulation of arbitrarily complex composites. The model is a major component of the inverse model which is presented in Chapter 4 and applied in Chapters 5-7; the properties explored here will assist interpreting the inverse model results in subsequent chapters.

3.8 References

AURANGZEB, MEHMOOD, S. & MAQSOOD, A. 2008. Modeling of Effective Thermal Conductivity of Dunite Rocks as a Function of Temperature. *International Journal of Thermophysics,* 29, 1470-1479.

GROTT, M., HELBERT, J. & NADALINI, R. 2007. Thermal structure of Martian soil and the measurability of the planetary heat flow. *J. Geophys. Res.,* 112, E09004.

JONES, W. P., WATKINS, J. R. & CALVERT, T. A. 1975. Temperatures and thermophysical properties of the lunar outermost layer. *Moon,* 13, 475-494.

LANGSETH, M. G., KEIHM, S. & PETERS, K. 1976. The Revised Lunar Heat Flow Values. *In:* Lunar and Planetary Institute Science Conference Abstracts, March 1, 1976 1976. 7, 474.

PATANKAR, S. V. 1980. *Numerical Heat Transfer and Fluid Flow,* New York, NY, London, Hemisphere.

WANG, K. 1992. Estimation of Ground Surface Temperatures from Borehole Temperature Data. *J. Geophys. Res.,* 97, 2095-2106.

4 INVERSE MODEL

4.1 Introduction

The inverse model is the Function Specification Inversion (FSI) problem of Section 2.2 programmed and solved in IDL. The forward model presented in Chapter 3 is a major component of the inverse model. The inverse model consists of four forward model components, or modules – two modules for the partitioned (steady and unsteady) primal problem and two for the partitioned dual problem (Figure 4.1). The dual code is identical to the primal code with the only difference being the time which, for the dual, is run in reverse such that $t^D = -t^P$, P indicating primal and D dual. The primal and dual problems are therefore solved using the same program, but with different inputs.

The other main calculation modules of the model are those for calculations of the residual heat sources, Fréchet and Hessian gradient, direction of steepest ascent, misfit function optimization, and model parameter updates, and a posteriori covariances. The steady and unsteady partitioned problems along with the Fréchet and Hessian gradient may be calculated in parallel. The measurement and a priori model parameter and covariance modules may also be initialized in parallel – they are not modified during the iterations. The model is terminated in the misfit function module once the function value falls below a given constant, or continues to update the model parameters iteratively.

The inverse model is tested in a fairly straightforward manner where a synthetic temperature is generated and inverted to recover the boundary conditions. The synthetic data is generated using the numerical forward module of the inverse model; this is verified against data extracted from analytical forward calculations in Appendix 9.4.9. To make things flow easily, in most cases forward model profiles of Chapter 3 are used. The tests are conducted, in the first instance (Section 4.2), on ideal measurements (with negligible errors) in order to assess the interaction of data and model parameters, without the instabilities caused by data noise. Noisy measurements are introduced in Section 4.3 to assess the impact noise has in obscuring any relationships identified in Section 4.2.

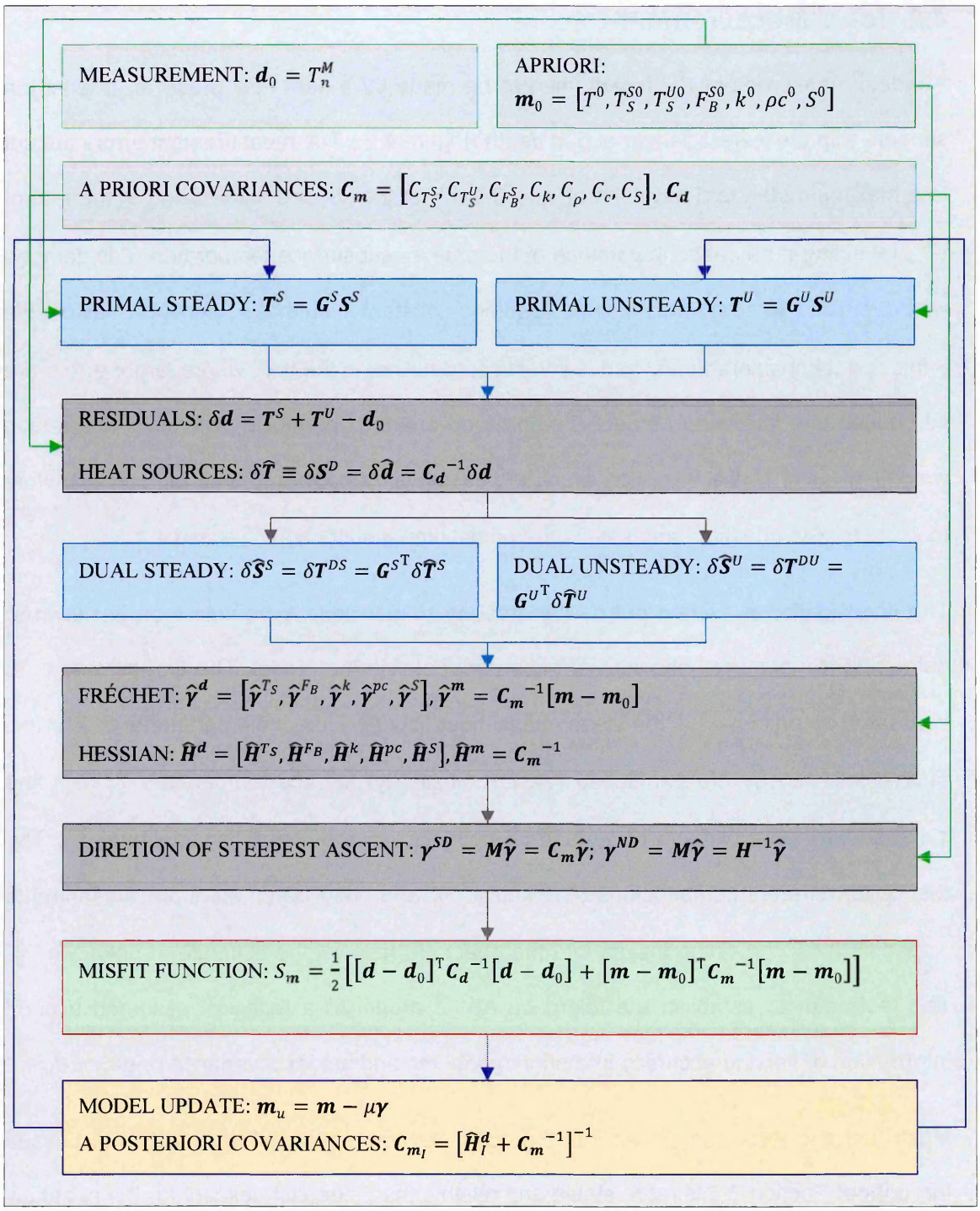

Figure 4.1. Flowchart of the inverse model. The blue bordered modules represent the TDMA module. The green bordered modules represent the modul inputs. The redborder identifies where the model is terminated once the misfit function has been optimized.The different coloured arrows illustrate how output from related modules interact with other model components. A list of defined symbols is presented in Appendix 9.1.

4.2 Ideal Measurement

An ideal measurement $\boldsymbol{d}_0$, is assumed to be made by a heat flow probe of at least ten sensors with the lowest sensor at 5 m depth (Figure 4.2). The measurement errors are set to a maximum standard deviation of $\sigma_\eta = 0.1$ mK at the surface, decreasing at the rate of e^{-z}, reflecting a decrease in variance of the data as subsurface temperature T is damped with depth z. The errors may also be assumed constant such that σ_η persists at all depths – this is not considered ideal and is investigated further in the text, where larger errors are introduced into the measurement. The data covariance operator $\boldsymbol{C}_d$ therefore has a high weighting factor in the inversion which increases with depth (and time lag $\tau = -t$). Note that $\tau \equiv t^D$, the dual time and $t \equiv t^P$, the primal time mentioned in Section 4.1.

The investigation is carried out by first treating single model parameters as unknown to determine the primary behaviour of each parameter in the model. The first parameter to be treated as unknown[1] is the steady basal heat flow F_B^S – the main parameter of interest. This is followed by the partitioned (steady, unsteady) surface temperature T_S^S, T_S^U and subsequently the conductivity k, thermal capacity ρc and steady source term S^S. The results for different combinations of unknown F_B^S and other parameters are presented in Appendix 9.4.7, providing insight into the effect of these on the estimate of unknown F_B^S. The tests aim to establish the tolerance of the model to a range of assumed a priori information of varying accuracy in a priori model $\boldsymbol{m}_0$ and model covariance operator $\boldsymbol{C}_m$.

Much trial and error has shown that the quasi-Newton method of optimization discussed throughout Section 2.2 is more stable and reliable than steepest descent for the heat flow

[1] It should be noted that – in this case – the steady basal heat flow F_B^S is accessed by the four lowest sensors. This means the basal heat flow – which for an arbitrary measurement may or may not include unsteady components – is consistent with the steady basal heat flow. This is a unique case which aims to demonstrate relationships between different model parameters as a first step. Cases where the basal heat flow estimated from the data is not consistent with the (true) steady basal heat flow are investigated further in the text.

problem being considered. This is due, in particular, to the difficulties in determining appropriate stepsizes μ_i as the model progresses through each iteration i in steepest descent. For example, in cases where a fixed μ_i is unstable, μ_i is estimated by curve fitting – i.e. several instances of updated model $\boldsymbol{m}_{i+1}$ and misfit $S_{\boldsymbol{m}_{i+1}}$ are calculated during each iteration using the current ascent vector $\boldsymbol{\gamma}_i$ and a range of μ_i, as mentioned in Tarantola (2005). A parabola is fitted to the resulting values of $S_{\boldsymbol{m}_{i+1}}$, choosing μ_i at the minimum as mentioned in Shen and Beck (1991). The calculation of several model instances makes the process rather inefficient. The quasi-Newton method avoids the former by allowing $\mu_i \approx 1$. The quasi-Newton method is used throughout this presentation and is tested at $\mu_i = 1$ in most instances and occasionally with $\mu_i = 0.5$.

4.2.1 Basal Heat Flow F_B^S

4.2.1.1 Heat Flow Dependence

Basal heat flow F_B^S is first tested in the range of true values from -0.76 to 0.76 W/m^2 which covers the range of values expected from terrestrial bodies of the solar system – all other parameters remain constant (Figure 4.2). This serves to illustrate any symmetries in the behaviour of the model in optimizing F_B^S. The model is run at fixed stepping constant $\mu_i = 1$ in all tests and also at $\mu_i = 0.5$ in a limited number of cases. F_B^S is initialized between 10-100 % inaccurate while the standard deviation $\sigma_{F_B^S}$ is tested in the range $\sigma_{F_B^S} \in [10^{-5}, 10^3]$ W/m^2.

Results show that, in the majority of initializations, the model converges exactly[2] on the true value where, naturally, the most intriguing cases are the minority which failed to converge, given the profile of Figure 4.2. Importantly, no significant differences are

[2] To the number of significant figures (s.f.) of the true value.

observed between results for the different heat flows tested indicating the behaviour of the model is largely independent of the magnitude of F_B^S.[3]

Figure 4.3 shows general trends[4] in the results using measures of F_B^S accuracy ($\epsilon_{F_B^{SI}} = \frac{F_B^{SI}}{F_B^{ST}} - 1$ with optimal estimates F_B^{SI} and true values F_B^{ST}), and optimal misfit function value ($\log_{10} S_{m_I}$), with respect to initial relative error $\epsilon_{F_B^{So}} = \frac{F_B^{So}}{F_B^{ST}} - 1$ of initial estimates F_B^{S0} to F_B^{ST}, and F_B^S standard deviation (SD) $\sigma_{F_B^S}$. The contours illustrate the likelihood of accurate convergence in different regions of the solution space. They are interpolated from 3D scatterplots where the values can be considered as central estimators, not exclusively associated with any single data point.

Figure 4.3 shows that increasing estimates of standard deviation $\sigma_{F_B^S}$ and consequently covariance $\boldsymbol{C}_{F_B^S}$ yield asymptotic improvements on the initial F_B^S estimate. Also, the more accurate the initial F_B^S estimate, the smaller the value of $\sigma_{F_B^S}$ required to achieve an accurate F_B^S estimate. The preceding observations follow the inverse theory outlined in Section 2.2.1.2 where $\boldsymbol{C}_{F_B^S}$ defines the solution space which is explored by the model to locate the maximum likelihood point of the misfit function S_{m_I}; if the space around the initial point is too small, the model does not have enough room to explore and fails to advance.

---

[3] More precisely, the model behaviour is independent in terms of the shape of the F_B^S model space. The studies in Chapters 5-7 do show that results depend on heat flow magnitude, but this is intricately tied to the masking effect of the unsteady temperature, which is not a factor in these tests.

[4] See Appendix 9.4.1 for a discussion of the measures used in the visualizations.

The misfit function value S_{m_I}, compared to the F_B^S relative error, illustrates the sensitivity of the misfit function to the error in the F_B^S estimate.[5] It is interesting to note that the optimized F_B^S from the full range of tests tend toward a delta distribution about the true value as the error in F_B^S decreases (see Appendix 9.4.2), effectively demonstrating that Monte-Carlo techniques can be used to obtain a robust estimate of the true F_B^S.

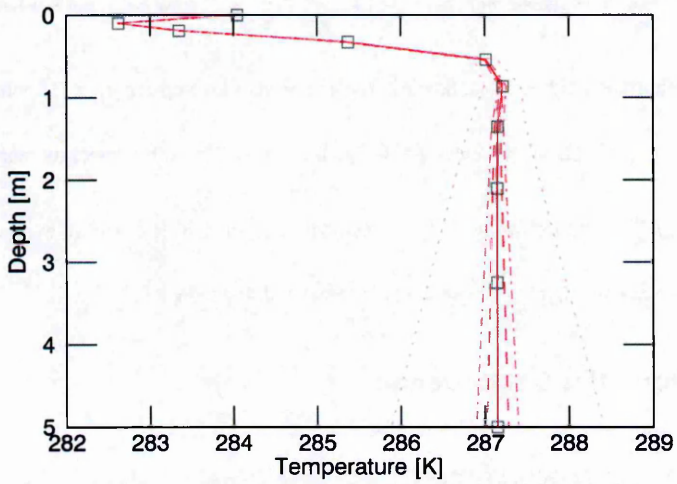

Figure 4.2. Ideal subsurface temperature T profiles with basal heat flow F_B^S of ±0.76 (dotted curves), ±0.152 (dot-dashed curves) ±0.076 (dashed curves), and 0 (solid curve) W/m². This is the temperature profile down to depth $z = 5$ m at time $t =$ 23 hr due to sinusoidal surface temperature $T_S = 12\sin(2\pi t/86400) + 287.15$ K. Thermal conductivity $k = 3.0$ W/m/K, density $\rho = 2700$ kg/m³ and specific heat capacity $c = 790$ J/kg/K. The grey squares represent sensor locations. Symbol definitions can be found in Appendix 9.1.

[5] Note that the misfit function value is dependent on the value of the covariance $C_{F_B^S}$ and also C_d, therefore a comparison between misfit function values is strictly applicable only in the case where the same covariances are used.

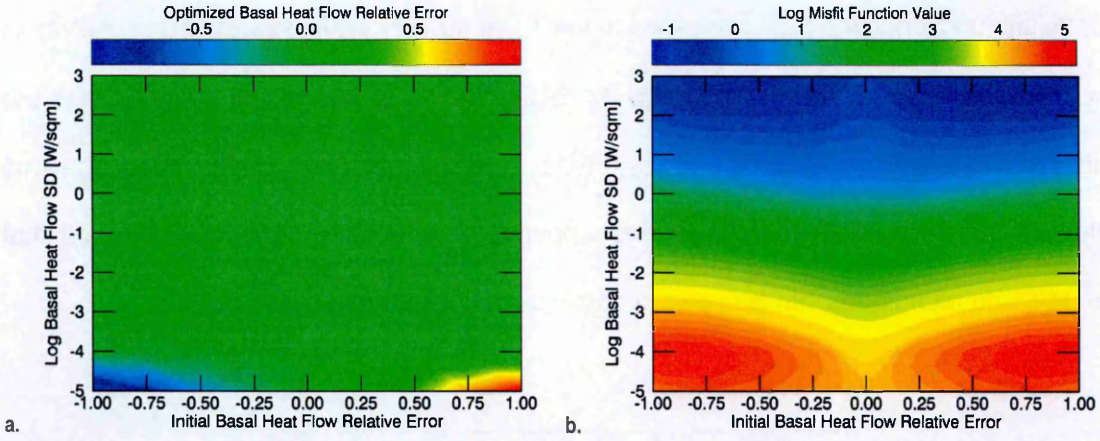

Figure 4.3. Trends in the optimization of basal heat flow F_B^S from ideal data with stepsize $\mu_i = 1$. Contour: a. shows trends in the relative error $\epsilon_{F_B^{SI}} = \frac{F_B^{SI}}{F_B^{ST}} - 1$ of optimal estimates F_B^{SI} to the true value F_B^{ST}, with respect to initial relative error $\epsilon_{F_B^{S0}} = \frac{F_B^{S0}}{F_B^{ST}} - 1$ of initial estimates F_B^{S0} to the true value F_B^{ST}, and standard deviation $\sigma_{F_B^S}$; b. shows trends in the misfit function value ($\log_{10} S_{m_i}$) at the optimal point. Symbol are defined in the text and Appendix 9.1.

4.2.1.2 *Thermal Properties Dependence*

4.2.1.2.1 Instantaneous Measurement

It is discussed in Section 3.4.2 that unsteady heat from the surface boundary flows deeper into a medium with increased conductivity k, resulting in a relatively larger masking effect on steady basal heat flow F_B^S. It is therefore prudent to test how the model responds to a range of k in optimizing F_B^S. Tests are carried out with small deviations of k, 1.5 W/m/K above and below the 3.0 W/m/K tested in Section 4.2.1.1 – the resulting trends are similar to those of Figure 4.3. There are, however, indications of increased instability with higher k, evidenced by increased error in the optimized F_B^S. This is consistent with higher k causing larger masking effects of F_B^S by the unsteady surface heat flow. A larger range of k will illustrate the masking effect more comprehensively but here the thermal properties are being limited to fairly plausible values. The skin depth z_{SKIN} (introduced in Section 2.2) takes account of the thermal properties and unsteady surface temperature in characterising the surface unsteady heat flow penetration depth – it is therefore one of the more useful tools to quantify the extent of masking of F_B^S by the unsteady surface heat flow. To better illustrate the masking effect, tests are performed with an annual

temperature cycle where the surface temperature is defined by $T_S = 12 \times [\sin(2\pi t) + \sin(2\pi t/360)] + 287.15$ K where t is measured in days. This allows for larger skin depth with plausible k in the range 0.3 to 3.0 W/m/K. Measurements are taken from day 360 of the cycle – Figure 4.4 illustrates the resulting temperature and associated measurement profiles.

The resulting trends are similar to the diurnal case down to a limiting skin depth, beyond which there is no meaningful improvement on the initial F_B^S estimate (in several cases the model diverges). This result occurs between $k = 0.6$ and 1.5 W/m/K which corresponds to a skin depth z_{SKIN} between 1.67 and 2.64 m. Skin depths at $z_{SKIN} = 1.67$ m and shallower give acceptable results similar to the diurnal temperature results, while those at $z_{SKIN} = 2.64$ m and below show no useful improvement on initial estimates. These results are improved when frequent measurements are made over extended monitoring periods as discussed below.

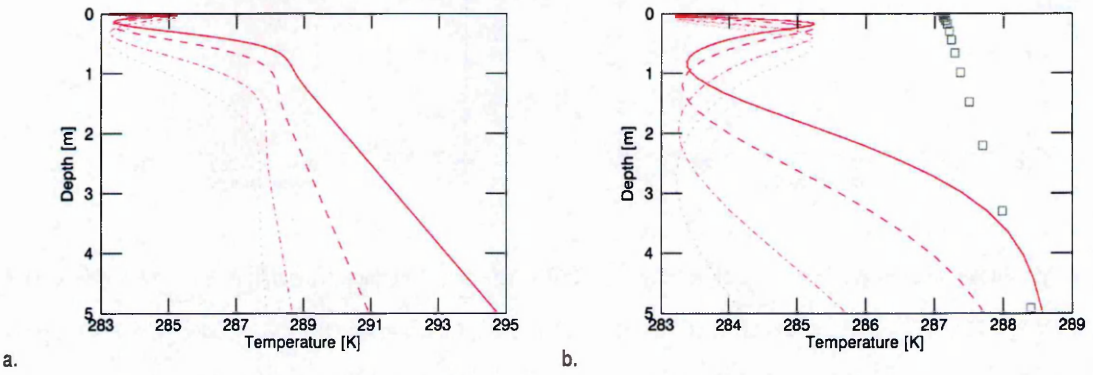

Figure 4.4. Subsurface temperature T profiles from time $t = 358$ d due to sinusoidal surface temperature $T_S = 12 \times [\sin(2\pi t) + \sin(2\pi t/360)] + 287.15$ K with conductivitity k of 0.3 (solid), 0.6 (dashed, 1.5 (dot-dashed) and 3.0 (dotted) W/m/K.. Density $\rho = 2700$ kg/m3 and specific heat capacity $c = 790$ J/kg/K. Contour: a. shows the forward modeled profiles down to depth $z = 30$ m produced on a 100 point grid with smaller control volumes towards the surface; b. shows the profiles down to $z = 5$ m with 15 sensors (grey squares – they follow the steady temperature profile) used for temperature measurements. Symbol are defined in Appendix 9.1.

4.2.1.2.2 Long-Period Measurements and Number of Sensors

The optimization tests presented so far cannot resolve temporal changes in the subsurface unsteady temperature T^U as they invert instantaneous measurements. Of course, measurements may be taken over a period of time which allows changes in T^U and, by extension, the subsurface temperature T, to be recorded. Recording the changes in T^U facilitates more straightforward characterisation of the surface unsteady heat flow and extraction of the steady basal heat flow F_B^S. This is useful, in particular, for cases similar to those in Figure 4.4 where the skin depth is substantial. To quantify the effects of long-period measurements (with recordings at set time intervals), optimization tests involving extended monitoring periods are performed on the same annual temperature profiles used in Figure 4.4 – the full profiles are shown in Figure 4.5 below.

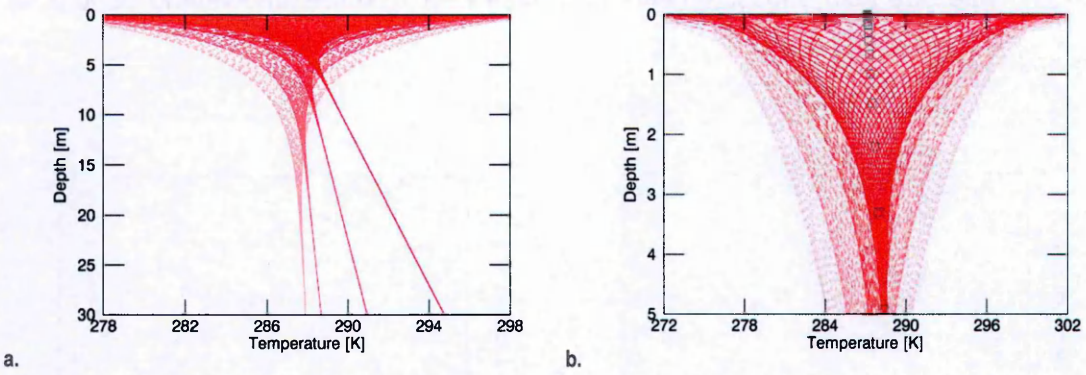

Figure 4.5. Subsurface temperature T profiles due to a 360 d sinusoidal surface temperature $T_S = 12 \times [\sin(2\pi t) + \sin(2\pi t/360)] + 287.15$ K with conductivitity k of 0.3 (solid), 0.6 (dashed, 1.5 (dot-dashed) and 3.0 (dotted) W/m/K – the plots are overlaid in order of decreasing k, with the lowest conductivity (brightest red, solid curves) in front. Density $\rho = 2700$ kg/m^3 and specific heat capacity $c = 790$ J/kg/K. Contour: a. shows the forward modeled profiles down to depth $z = 30$ m produced on a 100 point grid with smaller control volumes towards the surface; b. shows the profiles down to $z = 5$ m with 15 sensors (grey squares) used for temperature measurements. Symbol defined in Appendix 9.1.

Measurements are taken over periods which: 1. cover the 360 d period of the surface unsteady temperature T_S^U with measurement frequencies from 1 per day to 1 every 72 days; 2. cover only 25 % (90 d) of the 360 d T_S^U period with 2 measurements at the beginning and end of the 90 d period. Also, to determine the optimal number of sensors to

use, the measurements are taken using sensor grids of 10, 15, 20 and 25 sensors, though only the 15 sensor grid is shown in Figure 4.5.

The results show a clear improvement in the optimization of F_B^S as the number of measurements increase in a particular scenario (Figure 4.6) with an exception in the 90 d measurement. Interestingly, there is no consistent relationship between the accuracy of the optimized F_B^S and the number of sensors. This follows from the fact that in these tests only F_B^S is unknown. If, for example, T_S^U is not well known, having more sensors to record higher resolution depth profiles of the subsurface temperature T provides more information with which to find T_S^U.

Notably for skin depths below $z_{SKIN} = 2.64$ m (conductivity $k \geq 1.5$ W/m/K), long period measurements with frequencies higher than 1 per 10 days over the full period find F_B^S to within 6 % of the true value ($\left|\epsilon_{F_B^S}\right| \leq 0.06$) in the majority of cases. Recall that equivalent scenarios with instantaneous measurements (Figure 4.4) do not produce any useable results. There is no evidence of improvement in the optimized F_B^S estimate with 2 measurements spaced 90 d apart (0.25 of the T_S^U period) below $z_{SKIN} = 2.64$ m. Figure 4.6 does illustrate instances where the direct correlation between F_B^S accuracy and measurement frequency is not strictly adhered to. For example, with the 90 d measurement, an instantaneous measurement at the beginning of the cycle gives better results than a pair of measurements – one at the beginning of the cycle and another 90 d later. This is because the amplitude of the subsurface unsteady temperature T^U is at a minimum at the beginning of the cycle, minimising the masking of F_B^S, but increases to a maximum 90 d into the cycle (maximising the masking of F_B^S. Therefore the measurement at time $t = 90$ d introduces some instability into the problem.

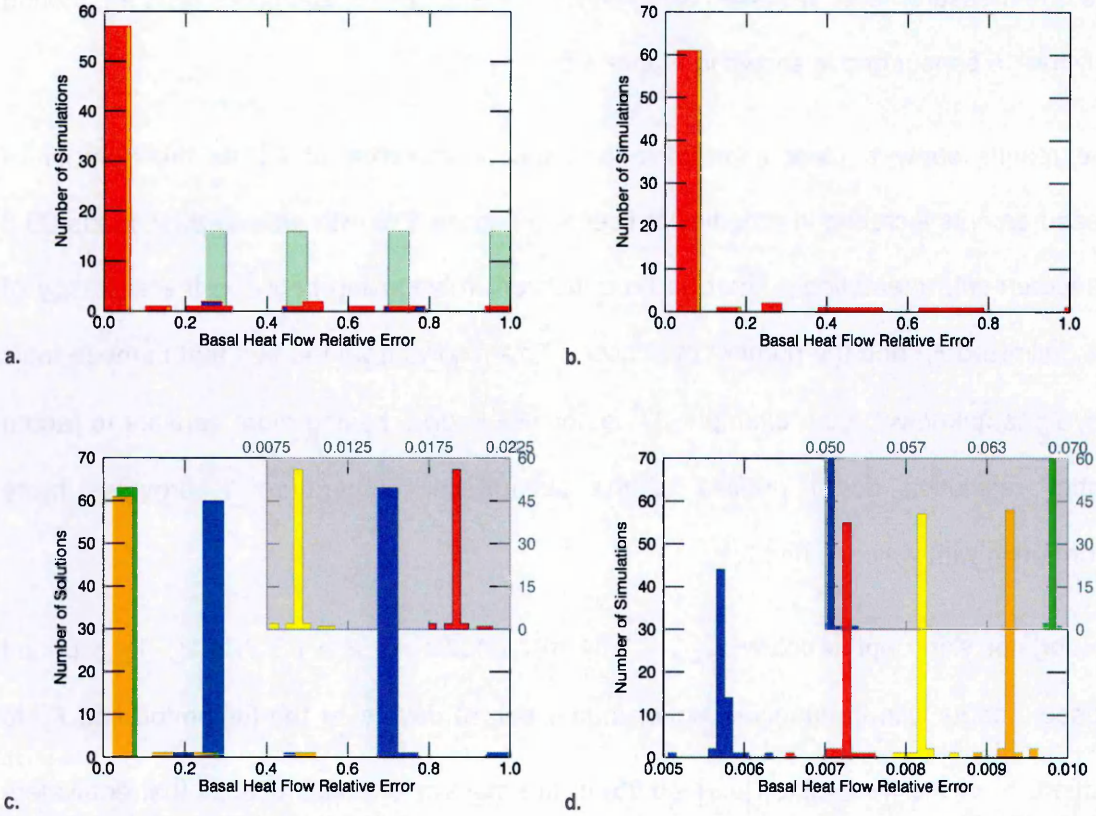

Figure 4.6. Accuracy of optimized basal heat flow $\left|\epsilon_{F_B^S}\right|$ from inversion of subsurface temperature measurement generated by a sinusoidal surface temperature with a 360 d period. Measurement frequencies coordinate with colours according to red (1 per day), orange (1 per 10 days), yellow (1 per 72 days) and green (1 per 360 days) for a monitoring period covering 360 d. Blue corresponds with 2 measurements at the start and end of a 90 d monitoring period (0.25 of the temperature cycle) while violet corresponds to 1 measurement at the end of a 90 d period. Plot: a. is for skin depth z_{SKIN} =3.73 m; b. for z_{SKIN} =2.64 m; c. for z_{SKIN} =1.67 m and; d. for z_{SKIN} =1.18 m. Note that for a. and b. the scale is cut off at $\left|\epsilon_{F_B^S}\right| = 1$ but the missing colours have values greater than 1 – i.e. for those the model diverged. The insets in c. and d. are zooms of $\left|\epsilon_{F_B^S}\right|$ close to zero. The histogram binsize is 0.05 for the main plots in a-c and 5E-4 for the inset plots, and plot d. The light green background histogram in plot a. is the intial distribution of F_B^S error used in all tests (off the scale of plot d).

Investigations show that it is useful to define a ratio of a priori model parameter to data standard deviations such that $r_d^m = \sigma_m/\sigma_d$ as a measure of the stability of a region of the space defined by covariances $\boldsymbol{C_m}$ and $\boldsymbol{C_d}$. Here the stable region is defined by stability ratio $r_d^{F_B^S} = \sigma_{F_B^S}/\sigma_d \geq 1$ W/m^2/K with the most accurate results largely occurring at $r_d^{F_B^S} = 10$ W/m^2/K for the instantaneous measurements and $r_d^{F_B^S} = 1$ W/m^2/K for the long-period

measurement cases. The results suggest that the increased information available from long-period measurements allows σ_d to be less constrained relative to $\sigma_{F_B^S}$.

4.2.1.2.3 Thermal Property Errors

Thermal properties conductivity k and thermal capacity ρc may be unknown to some degree. It is expected that, if the thermal properties contain inaccuracies, then the optimized basal heat flow F_B^S will contain related inaccuracies. The results of optimization tests on thermal properties (see Section 4.2.4) suggest that a significant level of noise may be present in thermal properties without significantly affecting the accuracy of the optimized F_B^S. Also, the results of tests where parameters are optimized simultaneously confirm positive correlation between the accuracy of the optimized F_B^S and the accuracy of the initial k estimate, while showing no correlation between the accuracies of F_B^S and ρc (see Appendices 9.4.7.5-9.4.7.6). These results follow from the direct physical relationship between F_B^S and k and lack of the same between F_B^S and ρc. It is important to note, however, that ρc and all other parameters indirectly, if not directly, affect the optimized F_B^S value in an inversion. Using an incorrect parameter value without accounting for the errors produces an incorrect (or potentially physically implausible) scenario for which there is no correct solution. Considering these points it is important to quantify the relationship between the accuracy of thermal properties which are (incorrectly) assumed known and the accuracy of the optimized F_B^S.

Optimization tests are performed using temperature profiles from the long-period measurement tests in Section 4.2.1.2.2. Specifically measurements are taken which: 1. cover the full period of a 360 d surface unsteady temperature T_S^U cycle with a measurement frequency of 1 per day (Figure 4.5); 2. are from the end of the 360 d T_S^U cycle as an instantaneous measurement (Figure 4.4). The measurements are taken on a 10 sensor grid with spacing increasing with depth. Conductivity k and thermal capacity ρc are initialized within 25-90 % of their respective true values of 0.3 W/m/K and 2.133 MJ/K/m^3 while basal heat flow F_B^S is initialized within 25-100 % of the true value of 76

mW/m^2. The F_B^S standard deviation is tested in the range $\sigma_{F_B^S} \in [10^{-4}, 10^{-2}]$ W/m/K. Tests are conducted with inaccuracies in either k or ρc (but not both simultaneously) to separate the effects of each in the model. This follows the partition of the heat flow problem into steady and unsteady state (see Section 2.1).

The results show positive correlation between the inaccuracies in k and the optimized F_B^S and negative correlation between the inaccuracies in ρc and optimized F_B^S (Figure 4.7). Generally, for all cases, low estimates of k and high estimates of ρc produce low F_B^S estimates; high estimates of k and low estimates of ρc produce high F_B^S estimates. The general result follows from the fact that high or low k respectively produces shallow or steep steady temperature T^S gradients along with higher or lower subsurface unsteady temperatures T^U amplitudes. Likewise, low or high ρc weakly or strongly attenuate heat flowing into a medium from the surface which respectively masks or reveals the T^S gradient with T^U, relative to the true profile (this is illustrated in Figure 4.22). This characteristic is compensated for in the model by respective high and low F_B^S estimates which make the T^S gradient either more steep or more shallow, exposing or masking the T^S gradient relative to the T^U envelope. Recall that thermal diffusivity $\kappa = k/\rho c$ gathers both physical quantities which means the preceding discussion can be explained in the more simple terms of high and low estimates of κ. Figure 4.22 provides example illustrations of the optimized temperature profiles produced with unknown k and ρc, though in the context of a noisy data measurement $\boldsymbol{d}$.

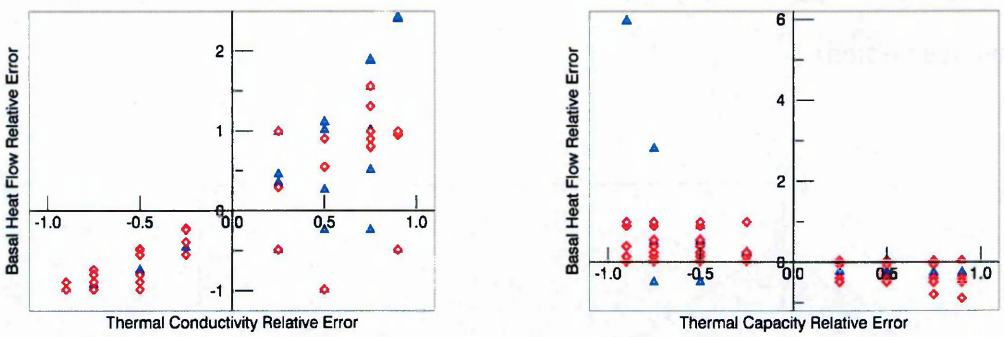

Figure 4.7. Accuracy of optimized F_B^S with inaccurate thermal conductivity k and thermal capacity ρc. F_B^S is optimized from subsurface temperature measurements of different measurement frequencies, generated by a sinusoidal surface temperature with a 360 d period. The red diamonds have measurement frequencies of 1 per day and blue triangles have measurement frequencies of 1 per 360 days for a monitoring period covering 360 d.Plot: a. shows the optimized F_B^S error $\epsilon_{F_B^{SI}}$ relative to the k error ϵ_k; b. shows the optimized F_B^S error $\epsilon_{F_B^{SI}}$ relative to the ρc error $\epsilon_{\rho c}$.

There is a number of outliers in Figure 4.7 which does not conform to the trends identified above. These correspond to cases where the F_B^S standard deviation $\sigma_{F_B^S}$ is too small and the initial F_B^S estimate is below the true value – the model does not significantly change the value of F_B^S leaving the final estimate below the true value. Also, the outliers (and scatter) correspond to thermal property inaccuracies which increase the masking of F_B^S by the subsurface unsteady temperature T_S^U. The scatter in the results is also partially due to the ratio $r_d^{F_B^S} = \sigma_{F_B^S}/\sigma_d$ not being optimal where σ_d is the data standard deviation, which is constant for different initial F_B^S estimates. Here $r_d^{F_B^S} \geq 1$ which produces 20-75 % improvement on initial estimates. The model is designed to optimize thermal properties, if they are unknown; this is performed in Section 4.2.4 (individually) and Appendices 9.4.7.5-9.4.7.6 (simultaneously with F_B^S).

4.2.1.3 Convergence

The expected convergence of the model is discussed in Section 2.2.1.3. Figure 4.8 shows the rate of convergence of the model in terms of misfit function S_m and its component data

$S_{\|d\|}$ and model $S_{\|m\|}$ parameter norms for a single test (compare to Figure 2.2 and see related discussion).

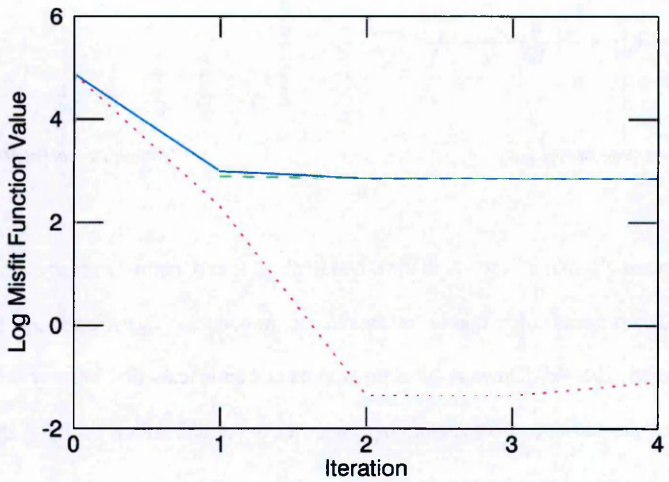

Figure 4.8. Convergence of the model in optimizing F_B^S. The base 10 logarithm of the misfit function S_m (solid blue) and its component data $S_{\|d\|}$ (dotted red) and model $S_{\|m\|}$ (dashed green) parameter norms are used to highlight small changes over the number of iterations i. The model can be terminated after 2-4 iterations. In this simulation standard deviation $\sigma_{F_B^S}$ = 1E-3 W/m², initial relative error $\epsilon_{F_B^{S0}}$ = -0.10 and optimized F_B^S relative error $\epsilon_{F_B^{SI}}$ = 1.25E-5. The general behavior is similar in other convergent simulations.

Figure 4.8 shows that the model converges fairly rapidly and can be terminated after 2-4 iterations around which there is a change of sign in the basal heat flow Fréchet derivative $\widehat{\boldsymbol{\gamma}}_{F_B^S}$ (see Figure 4.1 and Sections 2.2.3.3-2.2.3.4). The result is true for all initializations of F_B^S and covariance $\boldsymbol{C}_{F_B^S}$ in the range referenced by Figure 4.3 with stepsize $\mu_i = 1$. Similar results are obtained with $\mu_i = 0.5$ though with more iterations due to the model taking smaller steps through the joint data and model space $[\mathrm{D}, \mathrm{M}]$. These results are detailed in Appendix 9.4.2. Generally it can be deduced that initializing the model with suitably large standard deviation $\sigma_{F_B^S}$ promotes optimal convergence of the model when optimizing F_B^S.

4.2.2 Steady Surface Temperature T_S^S

4.2.2.1 General Trend Analysis

Optimization tests on T_S^S using the ideal measurement show behaviour similar to but more stable than that of basal heat flow F_B^S in the model. T_S^S is initialized between 10-75 % inaccurate relative to the true value of 287.15 K, while the standard deviation $\sigma_{T_S^S}$ is tested in the range $\sigma_{T_S^S} \in [10^{-3}, 10^5]$ K.

Figure 4.9 shows shows general trends in the results using measures of T_S^S accuracy ($\epsilon_{T_S^{SI}} = \frac{T_S^{SI}}{T_S^{ST}} - 1$ with optimal estimates T_S^{SI} and true values T_S^{ST}), and misfit function value (defined as in Section 4.2.1.1 with Figure 4.3), with respect to initial relative error $\epsilon_{T_S^{S0}} = \frac{T_S^{S0}}{T_S^{ST}} - 1$ of initial estimates T_S^{S0} to T_S^{ST}, and T_S^S standard deviation (SD) $\sigma_{T_S^S}$. The contours illustrate the likelihood of convergence in different regions of the solution space. They are interpolated from 3D scatterplots where the values can be considered as central estimators, not exclusively associated with any single data point.

The model converges exactly on the true T_S^S value in all cases though estimates worsen in the case of small covariance $C_{T_S^S}$ due to low estimates of standard deviation $\sigma_{T_S^S}$. A stable region can be defined by a stability ratio (as with F_B^S) such that $r_d^{T_S^S} = \sigma_{T_S^S}/\sigma_d \geq 10$ though the most accurate results occur at $r_d^{T_S^S} \geq 10^4$. More accurate convergence is achieved with a more accurate initial T_S^S estimate. Here, again the model is run at fixed stepping constant $\mu_i = 1$ – similar results are obtained setting $\mu_i = 0.5$ except with more iterations and marginal improvement at the smallest $\sigma_{T_S^S}$. The former result is attributed to the space being explored in finer detail due to the smaller μ_i. As with F_B^S, the solutions tend toward a delta distribution about the true value (see Appendix 9.4.3).

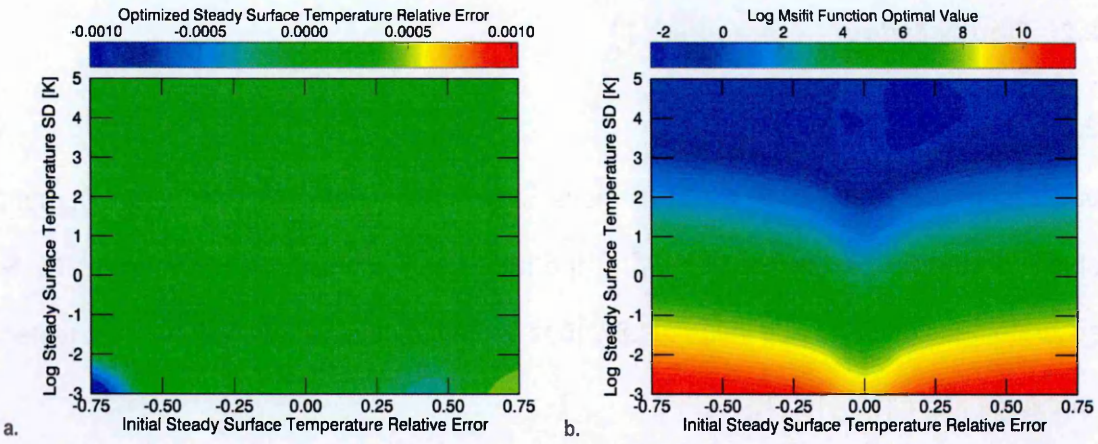

Figure 4.9. Trends in the optimization of steady surface temperature T_S^S from ideal data with stepsize $\mu_t = 1$. Contour: a. shows trends in the relative error $\epsilon_{T_S^{SI}} = \frac{T_S^{SI}}{T_S^{ST}} - 1$ of optimal estimates T_S^{SI} to the true value T_S^{ST}, with respect to initial relative error $\epsilon_{T_S^{S0}} = \frac{T_S^{S0}}{T_S^{ST}} - 1$ of initial estimates T_S^{S0} to the true value T_S^{ST}, and standard deviation $\sigma_{T_S^S}$; b. shows trends in the optimizal misfit function value $\log_{10} S_{m_t}$. Symbol are defined in the text and Appendix 9.1.

4.2.2.2 *Convergence*

Figure 4.10 shows the rate of convergence of the model in terms of misfit function $S_{\boldsymbol{m}}$ and its component data $S_{\|\boldsymbol{d}\|}$ and model $S_{\|\boldsymbol{m}\|}$ parameter norms for a single test (compare to Figure 2.2 and see related discussion). The same rapid convergence of the model is evident as with F_B^S. Also, more stable convergence is achieved with initialisations where the initial T_S^S estimate is less than the true value. These results are detailed in Appendix 9.4.3. Generally it can be stated that initializing the model with suitably large $\sigma_{T_S^S}$ promotes optimal convergence of the model.

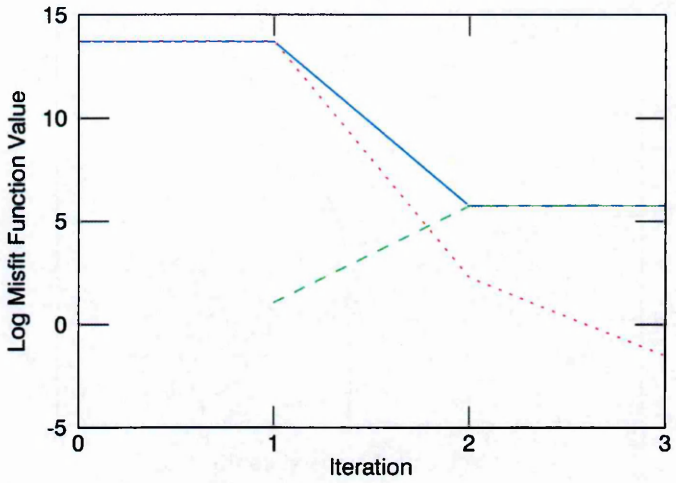

Figure 4.10. Convergence of the model in optimizing T_S^S. The base 10 logarithm of the misfit function S_m (solid blue) and its component data $S_{\|d\|}$ (dotted red) and model $S_{\|m\|}$ (dashed green) parameter norms are used to highlight small changes over the number of iterations i. In this simulation standard deviation $\sigma_{T_S^S} = 1$ K, initial relative error $\epsilon_{T_S^{S0}} = -0.75$ and optimized T_S^S relative error $\epsilon_{T_S^{SI}} = 0$. The general behavior is similar in other convergent cases.

4.2.3 Unsteady Surface Temperature T_S^U

4.2.3.1 Measurements

Optimization tests on T_S^U are performed using ideal measurements from a diurnal sinusoidal temperature profile such that $T_S^U = 12\sin(2\pi t/86400)$ K, chosen at time $t = 23$, 17, 11 and 5 hr into the cycle. Measurements at 23 and 11, and 17 and 5 hr are respectively out of phase by half of a period which allows straightforward interpretation of the behaviour of the model in responding to the different true shapes of T_S^U. Figure 4.11 shows the unsteady temperature profiles down to 1 m – inversions are performed on superposed (containing the steady component) temperature profiles down to 5 m.

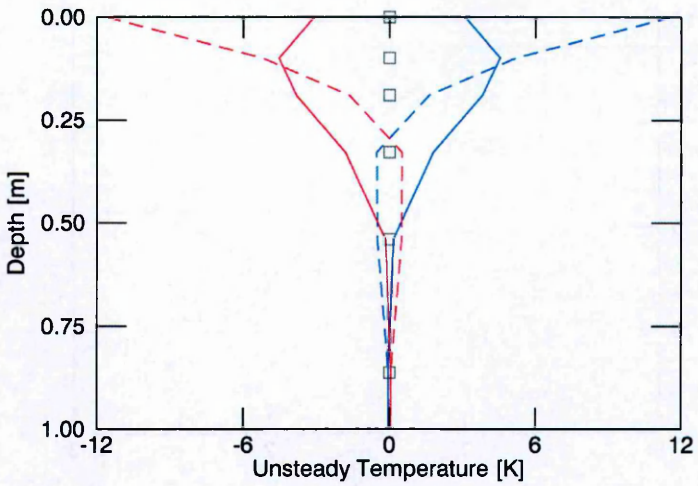

Figure 4.11. Ideal subsurface unsteady temperature profiles T^U down to depth $z = 1$ m at time $t = 23$ (solid red), 17 (dashed red), 11 (solid blue) and 5 (dashed blue) hr into a 24 hr sinusoidal surface unsteady temperature $T_S^U = 12\sin(2\pi t/86400)$ K. Thermal conductivity $k = 3.0$ W/m/K, density $\rho = 2700$ kg/m^3 and specific heat capacity $c = 790$ J/kg/K. The grey squares represent sensor locations. Symbol definitions can be found in Appendix 9.1.

4.2.3.2 A Priori Information

To invert a single measurement related to the profiles in Figure 4.11 a priori information is required for the initial T_S^U estimate based on the time period prior to the measurement being considered. Each pair of temperature profiles out of phase by half of a period (π radians, 180°) is expected to be produced by T_S^U which are likewise out of phase by half of a period (Figure 4.12). If there is no reliable a priori information on T_S^U a constant initial estimate may be used. Of course, if the measurements are taken in succession from 5 to 23 hr, there is already useful a priori information on the peaks and troughs of the generating (sinusoidal) T_S^U and they can be inverted simultaneously.

In the optimization tests presented here, T_S^U is initialized in two ways: 1. constant and 0-12 K above or below the mean value of 0 K, therefore including no a priori information on the

variation of T_S^U; 2. with amplitude 0.25-1.5 times the true value of 12 K, phase 0-π radians out of phase with the true phase of 2π radians and background (mean) value of 0-12 K[6].

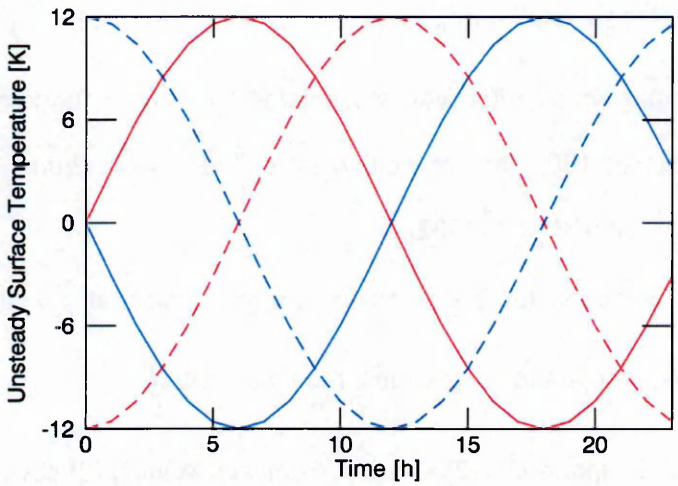

Figure 4.12. Surface unsteady temperatures T_S^U 24 hr before time $t = 23$ (solid red), 17 (dashed red), 11 (solid blue) and 5 (dashed blue) hr into a 24 hr sinusoidal surface unsteady temperature $T_S^U = 12\sin(2\pi t/86400)$ K. The solid and dashed pairs of red and blue curves respectively represent ideal temperature measurements which are π radians out of phase.

A priori information is also introduced with covariance $\boldsymbol{C}_{T_S^U}$ containing a covariance function $\sigma_{T_S^U}^2 f_\tau$ where f_τ is a function of the time lag τ [7]. The standard deviation $\sigma_{T_S^U}$ is tested in the range $\sigma_{T_S^U} \in [10^{-4}, 10^4]$ K. The form of f_τ is limited only by the different shapes of T_S^U that may be encountered and by the requirement that $\boldsymbol{C}_{T_S^U}$ is positive definite. Several covariance functions are tested with:

1. no assumptions on the time variation of T_S^U such that $f_\tau = 1$;

[6] While introducing a background value into T_S^U is effectively introducing an error in steady surface temperature T_S^S investigations show that the inverse model is more stable in optimizing T_S^U when a background value is introduced into the initial T_S^U estimate.

[7] The time lag is time before the measurement was taken.

2. an exponential function[8] $f_\tau = e^{-r\tau}$ where r adjusts the rate of decrease and τ is the time lag, reflecting the damping of subsurface unsteady temperature T^U with depth;
3. a variation on the Hanning function such that $f_\tau = 0.5e^{-r\tau}(1 + \frac{cos\pi\tau}{\tau_c})$ where τ_c is a correlation time which effectively associates T_S^U with a fundamental frequency (Shen and Beck, 1992) and is equivalent to the cut off period in the Spectrum Inversion method of Wang (1992);
4. a sinusoidal variation on the Hanning function such that $f_\tau = 0.5e^{-r\tau}(1 - \frac{cos\pi\tau}{\tau_c})$ which damps the variance of the most recent part of T_S^U.

Figure 4.13 shows the exponential (2) and first modified Hanning (3) covariance functions, illustrating the effects of varying τ_c.

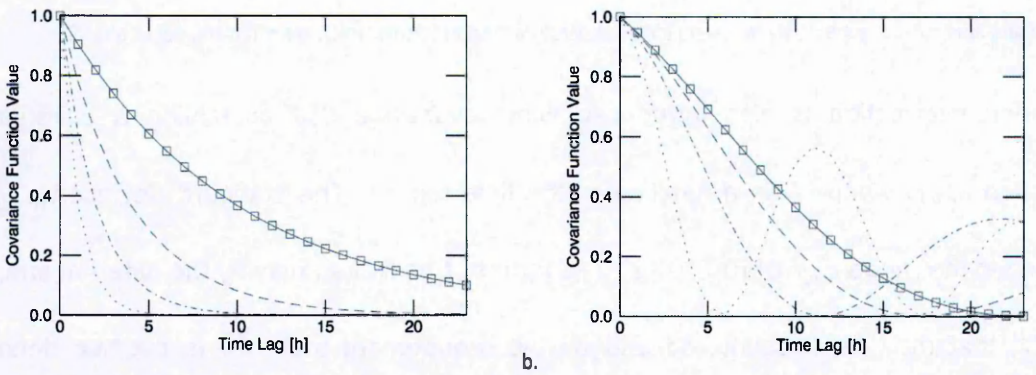

Figure 4.13. Covariance functions f_τ used to introduce apriori information into unsteady surface temperature T_S^U: a. exponential function $f_\tau = e^{-r\tau}$ with $r = 0.1$ (solid), 0.25 (dashed), 0.5 (dot-dashed), 1.0 (dotted); b. modified Hanning function $f_\tau = 0.5e^{-r\tau}(1 + \frac{cos\pi\tau}{\tau_c})$ with r =0.05 and $\tau_c = \tau_{MAX}$ (solid), 0.75 τ_{MAX} (dashed), 0.5 τ_{MAX} (dot-dashed), 0.25 τ_{MAX} (dotted), where τ_{MAX} = 23 hr. The grey squares separate the timesteps.

The larger magnitude of f_τ close to $\tau = 0$ allows the model more freedom to change associated values of the initial T_S^U estimate. More recent times (towards $\tau = 0$) correspond to shallower depths where much of the variation in subsurface unsteady temperature T^U occurs, in scenarios where there are no subsurface unsteady heat sources or sinks.

[8] Exponential functions have been used before, as mentioned in Shen and Beck (1992).

4.2.3.3 Results

The results show that the true unsteady surface temperature T_S^U profile is not well recovered without apropriate a priori information in covariance $\boldsymbol{C}_{T_S^U}$ which complements the initial T_S^U estimate. This is due to the loss of information on T_S^U due to damping and lagging of the surface signal. The model introduces whatever features necessary to T_S^U – within the constraints imposed by $\boldsymbol{C}_{T_S^U}$ – to minimise the misfit between the calculated and measured subsurface unsteady temperature T^U. General features of the true T_S^U profile are reflected in the optimized T_S^U when the a priori information is not too errant. Consistent use of an exponential or Hanning covariance function in $\boldsymbol{C}_{T_S^U}$ where $f_\tau = [e^{-r\tau}, 0.5e^{-r\tau}\left(1+\frac{cos\pi\tau}{\tau_c}\right)]$ respectively and $\tau_c = P$, the period of T_S^U, yield the most accurate results though this is not universally the case. A typical good result for each measurement is shown in Figure 4.14 where the exponential function works best for the S-shaped T_S^U while the second modified Hanning function (4) works best for the valley- and hill-shaped T_S^U.

There are clear inaccuracies in the optimized T_S^U, although examination of the unsteady subsurface temperature profile T^U shows that the fit to the measurements is relatively accurate (see Appendix 9.4.4). While the initial T_S^U estimates in Figure 4.14 are constant, more often than not there is useful a priori information on T_S^U when investigating heat flow on a planetary surface. Results of tests performed which introduce frequency information into the initial T_S^U estimate can be found in Appendix 9.4.4. In the face of uncertainty, however, a constant initial T_S^U estimate is recommended as significantly errant features introduced into the initial T_S^U estimate are likely to persist to some degree in the optimized T_S^U. Care is also needed with the use of τ_c in selecting fundamental frequencies via covariance $\boldsymbol{C}_{T_S^U}$ as the model will tend to introduce oscillations to match high frequency components of a measurement which may be due to noise, or layering.

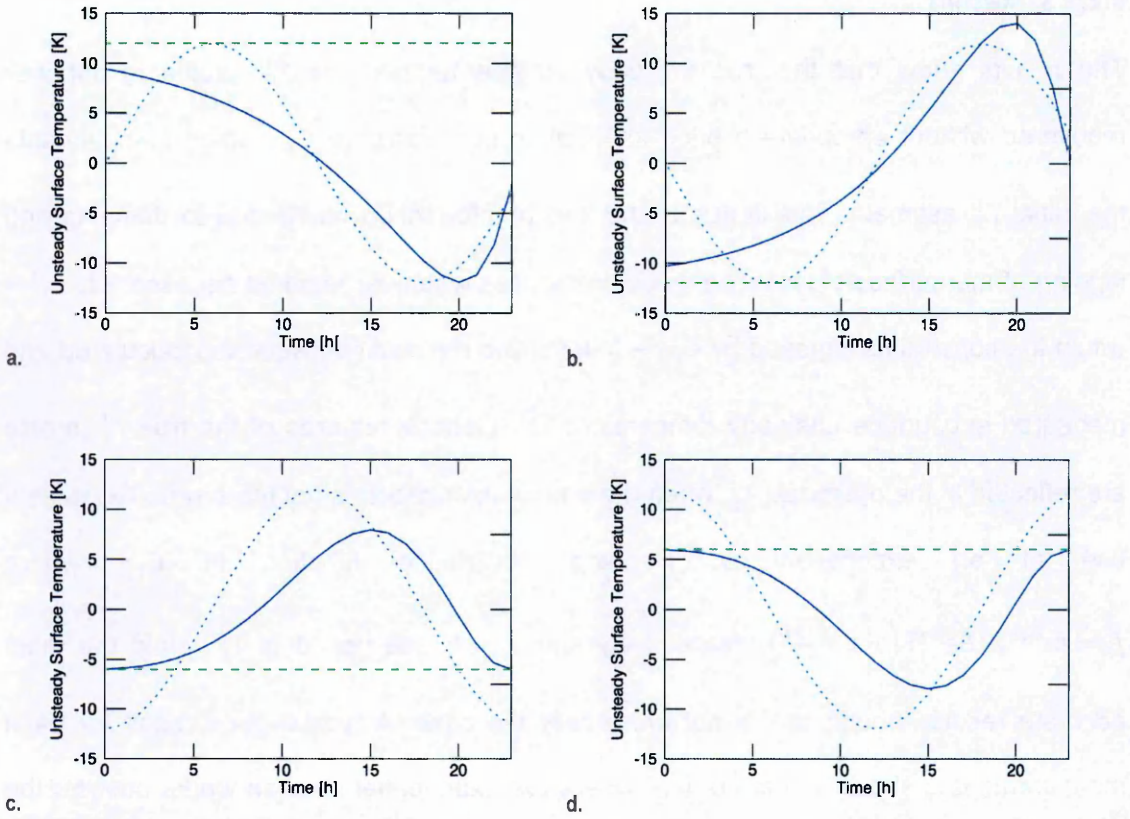

Figure 4.14. Optimization of unsteady surface temperature T_S^U. The dotted blue curves represent the true T_S^U profile, the dashed green curves constant initial T_S^U estimate, and the solid blue curves the optimized T_S^U. Each plot represents a 24 hr profile of T_S^U leading up to a measurement at: a. time $t = 23$ hr into a sinusoidal T_S^U cycle with a covariance function $f_\tau = e^{-4\tau}$; b. time $t = 11$ hr into a sinusoidal T_S^U cycle with $f_\tau = e^{-4\tau}$; c. time $t = 17$ hr into a sinusoidal T_S^U cycle with $f_\tau = 0.5e^{-4\tau}(1 - \frac{5cos\pi\tau}{P})$; d. time $t = 5$ hr into a sinusoidal T_S^U cycle with $f_\tau = 0.5e^{-4\tau}(1 - \frac{2cos\pi\tau}{P})$ where τ is the time lag and P is the period of T_S^U.

A useful means of quantifying the information gained on T_S^U is the a posteriori covariance analysed alongside the a priori covariance. Here this is done in terms of the ratio of a posteriori ($\sigma_{T_S^{UI}}$) to a priori ($\sigma_{T_S^{U0}}$) standard deviations (SD ratio) as presented in Shen and Beck (1992). The SD ratio $r_{\sigma_{T_S^U}} = \sigma_{T_S^{UI}}/\sigma_{T_S^{U0}}$ is interpreted in the relative sense and is used as a guide to the information gain in T_S^U based on the a priori covariance $\boldsymbol{C}_{T_S^U} \equiv \boldsymbol{C}_{T_S^{U0}}$, the data covariance $\boldsymbol{C}_{\boldsymbol{d}} \equiv \boldsymbol{C}_{\boldsymbol{d}_0}$ and the a posteriori covariance matrix $\boldsymbol{C}_{T_S^{UI}}$ (see Section 2.2.3.5). The resolution of T_S^U follows naturally from the form of $\boldsymbol{C}_{T_S^{U0}}$ – elements of $\boldsymbol{C}_{T_S^{U0}}$ which are close to zero express relative certainty in associated values of the initial T_S^U

estimate, therefore leaving them relatively unchanged in the inversion. This is reflected by a relatively large $\sigma_{T_S^{UI}}$ in $\boldsymbol{C}_{T_S^{UI}}$ and a consequently large SD ratio $r_{\sigma_{T_S^U}}$. SD ratios of the sample results of Figure 4.14 are presented in Appendix 9.4.4. The results are similar to those obtained in Shen et al (1992).

Generally, the behaviour of the model with respect to $\boldsymbol{C}_{T_S^U}$ and to a lesser degree the initial T_S^U estimate is similar to that displayed with T_S^S and F_B^S, with suitably large standard deviation $\sigma_{T_S^U}$ and accurate initial T_S^U estimate resulting in smaller errors between the optimized and true T_S^U. The exception occurs where $\sigma_{T_S^U}$ is overestimated and T_S^U is close to the true value, which leads to instability – an indicator of a relatively shallow misfit function gradient around the optimum point. The convergence is initially not smoothly quadratic but generally falls into quadratic optimization after a few iterations. Investigations show the former is due to the model oscillating T_S^U above and below the initial T_S^U estimate within a range $a\sigma_{T_S^U}$ – where a is a function of the unsteady temperature Fréchet derivative $\boldsymbol{\gamma}_{T_S^U}$ (see Figure 4.1 and Sections 2.2.3.3-2.2.3.4) – before settling on a particular shape, either in phase or π radians out of phase with $\boldsymbol{C}_{T_S^U}$. The model reaches the optimum point after a few to several tens of iterations though the general shape of T_S^U is fixed in the first few iterations. Convergence profiles of the sample results of Figure 4.14 are presented in Appendix 9.4.4.

4.2.4 Thermal Properties k, ρc

Optimization of the conductivity k and thermal capacity ρc is tested by inverting the ideal measurement profile of Figure 4.2 with a heat flow of 0.076 W/m^2. The model is initialized with k and ρc between 10-75 % inaccurate relative to the true values of 3 W/m/K and 2.133 MJ/K/m^3, respectively. The standard deviations are tested in the range $\sigma_k \in [10^{-5}, 10^4]$ W/m/K and $\sigma_{\rho c} \in [1, 10^9]$ MJ/K/m^3. Ascent direction $\boldsymbol{\gamma}^k$, $\boldsymbol{\gamma}^{\rho c}$ (see Figure 4.1, Sections 2.2.1.3 and 2.2.3.3-2.2.3.4) is preconditioned with an always-positive constraint; the model tolerates negative steady surface temperature T_S^S on its progression to

convergence but negative k or ρc leads to divergence in the forward module. See Section 2.1.2.2 for a discussion of k and ρc related parameters in the model. The model shows similar behaviour to previous parameters where underestimated standard deviation σ_k, $\sigma_{\rho c}$ leads to instability.

An interesting behaviour emerging from the results is that the model is more effective at optimizing k from an initial estimate higher than the true value. Conversely, the model is more effective at optimizing ρc from an initial estimate lower than the true value. This is due to low k and/or high ρc inhibiting the range of temperatures that can be produced at depth within the medium.[9] This is behaviour can be traced back to the form of the Fréchet derivatives (Section 2.2.3.3) which rely on the temperatures throughout the entirety of the medium – not just at the boundaries. No temperature variation at depth means no gradients to calculate the Fréchet derivative from, so the update in those sections is essentially zero. As with previous parameters, a stable region can be defined by a stability ratio for each physical quantity such that $r_{\boldsymbol{d}}^{k} = \sigma_k/\sigma_{\boldsymbol{d}} \geq 10^4$ W/m/K^2 and $r_{\boldsymbol{d}}^{\rho c} = \sigma_{\rho c}/\sigma_{\boldsymbol{d}} \geq 10^5$ J/K/m^3.

Figure 4.15a shows that the optimized k is not smooth but tends to a distribution of values centred close to the true value – it may be smoothed by applying a mean or moving average filter at the preconditioning step of each iteration. Likewise, optimized ρc is not smooth (Figure 4.15b) but the model optimizes ρc to produce a temperature T^U which is close to ideal data measurement $\boldsymbol{d}_0$ (see Appendix 9.4.5 for the resulting profiles). Generally ρc tends to a distribution of values about the true value. For both optimized properties the misfit between the calculated subsurface unsteady temperature T^U and $\boldsymbol{d}_0$ is less than 10^{-4} %.

[9] Recall the effects of k and ρc as presented in Sections 3.2.2 and 3.4.2.

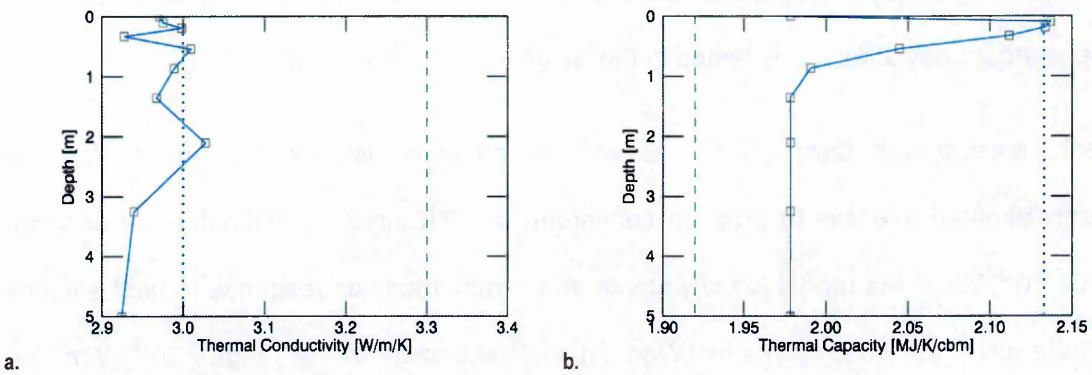

Figure 4.15. Conductivity k and thermal capacity ρc optimized from a temperature inversion at time $t = 23$ hr into a 24 hr sinusoidal temperature cycle. The dotted blue curves represent true profiles, the dashed green curves initial estimates, and the solid blue curves the optimized thermal properties where: a. is a plot of k and; b. is a plot of ρc. Grey squares represent sensor locations.

SD ratios of a posteriori to a priori standard deviations $r_{\sigma_k} = \sigma_{k^I}/\sigma_{k^0}$ and $r_{\sigma_{\rho c}} = \sigma_{\rho c^I}/\sigma_{\rho c^0}$ may be used to quantify the results as with the unsteady surface temperature T_S^U in Section 4.2.3. SD ratios show that k is more resolved towards the surface which can be deduced from Figure 4.15a, and ρc is better resolved towards the surface, which follows from most information on T^U being towards the surface. In optimizing k the model converges after 2 iterations in most instances, excepting those where k is low. In optimizing ρc the model can be terminated after 3-4 iterations. Generally it can be deduced that initializing the model with an initial k estimate higher than the true value or an initial ρc estimate lower than the true value, and appropriately large standard deviation σ_k, $\sigma_{\rho c}$ promotes convergence of the model. The SD ratios and convergence profiles of the result samples of Figure 4.15 are displayed in Appendix 9.4.5 along with the temperature profiles.

4.2.5 Heat Sources and Sinks S^S

Optimization of steady heat source or sink S^S is tested by inverting the ideal measurement profile of Figure 4.2 with a heat flow of 0.076 W/m^2. S^S is initialized with an even distribution of sources and sinks in the range $\pm[10^{-6},10^{-2}]$ W/m^3 about the true value of 0 W/m^3. The relatively large initial S^S estimates are used to ensure a discernible effect is

produced while the smaller values test the sensitivity of the model to small changes in S^S. The standard deviation σ_{S^S} is tested in the range $\sigma_{S^S} \in [10^{-9},1]$ W/m^3.

Ideal measurement tests on S^S, as with all previous parameters, indicate that an underestimated σ_{S^S} fails to produce convergence. With initial S^S estimates in the range $\pm[10^{-5},10^{-2}]$ W/m^3 the model is fairly stable and symmetric in its response to heat sources or heat sinks as initial estimates. With initial S^S estimates in the range $\pm10^{-6}$ W/m^3 the model is evidently more stable dealing with heat sources than heat sinks as initial estimates – the exact reason for this is unclear though it may be that the model is more stable optimising from high estimates with positive temperature residuals than low estimates with negative temperature residuals. Figure 4.16 shows typical good results.

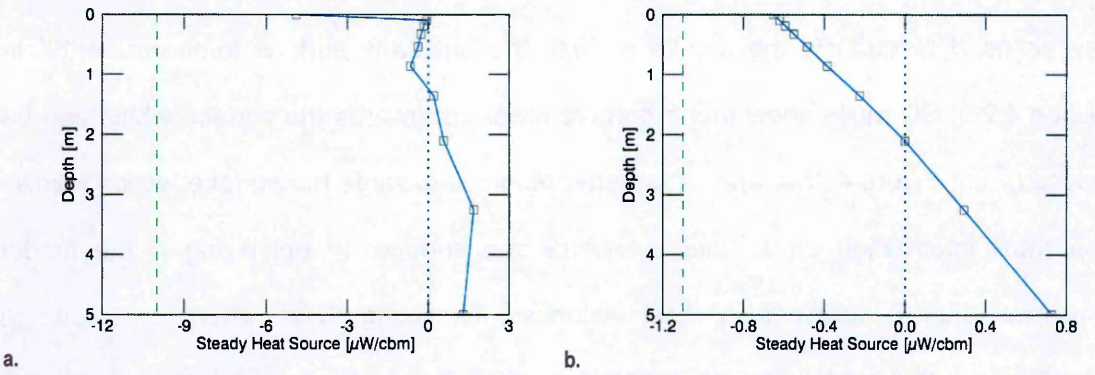

Figure 4.16. Optimization of heat sources and sinks S^S. The dotted curves are true S^S profiles, the dashed curves initial S^S estimates, and the solid curves optimized S^S. Plot: a. shows results from the range of relatively large initial S^S between -0.01 and 0.01 W/m^3; b. shows results from the range of relatively small initial S^S between -10^{-6} and 10^{-6} W/m^3. Grey squares are sensor locations.

In Figure 4.16 it can be seen that the optimized S^S tends to a distribution of values about the true value which is generally the case. The rough profile, as with the thermal properties, does not significantly influence the subsurface temperature profile (see Appendix 9.4.6). SD ratios of resolved (a posteriori) to initial (a priori) standard deviation $r_{\sigma_{S^S}} = \sigma_{S^{SI}}/\sigma_{S^{SO}}$ show that S^S is better resolved at depth (see Appendix 9.4.6). A stability ratio, identifying regions of good results, can be defined such that $r_d^{S^S} = \sigma_{S^S}/\sigma_d \geq 10$

W/m^3/K. The model generally converges after a single iteration, similar to the basal heat flow F_B^S, and steady surface temperature T_S^S (with stepping constant $\mu_i = 1$).[10]

4.3 Noisy Measurement

In reality the temperature measurement $\boldsymbol{d}_0$ may contain errors related to:

1. the precision of the sensors,
2. truncation of the temperature profile due to a finite number of sensors and/or model discretization,
3. potential uncertainty about the depth of a sensor and
4. model limitations in accounting for transient physical phenomena.

It is important to characterise how the model will deal with these. To this effect synthetic errors (Gaussian random noise η) are added to the ideal measurement of Figure 4.2 and the model benchmarked with these. As with the tests on the ideal measurement, a global view of the problem is considered the most informative and lends itself more readily to interpretation. Errors σ_η are tested in the range 1 mK to 1 K with the lower range of the order of instrument precision and the upper range relating to modelling errors such as unknown subsurface properties. Two forms of the data covariance matrix $\boldsymbol{C_d}$ are used in the tests such that $\boldsymbol{C_d} = \sigma_d^2 f_z$ where $f_z = [e^{-rz}, 1]$ representing exponentially decreasing and constant variance respectively. In all cases $r = 1$. Results of the ideal measurement tests are applied to ensure optimal stability of the model.

Noise related to sensor precision (1) and truncation of the temperature profile (2) η_s is modelled such that $|\eta_s| \leq \sigma_\eta e^{-z}$. This form reflects an exponential decrease in variance of

[10] This similarity in behaviour can be understood from the definition of the Fréchet derivatives $\hat{\boldsymbol{\gamma}}^d$ for F_B^S, T_S^S and S^S in the inverse model (see Figure 4.1) which are explicitly related to the dual steady temperature δT_S^D (see Section 2.2.3.3 and/or Equation 2–73).

$\boldsymbol{d}_0$ with depth[11]. The model is limited to dry conditions with regolith properties independent of temperature. Measurements which are influenced by single transient events involving advection, convection, flow and/or temperature dependent properties may therefore be considered in the sense of measurement errors[12]. Errors in sensor depth for an accurate temperature measurement are equivalent to errors in temperature for an accurate sensor depth. Model and location errors (3 and 4) are therefore modelled in the form of random sensor noise η_m such that $|\eta_m| \leq \sigma_\eta$, reflecting the fact that these effects are of unknown spatial distribution.

Figure 4.17 shows the ideal measurement of Figure 4.2 with heat flow $F_B^S = 0.076$ W/m^2, along with error bars for η_s and η_m, and four $\boldsymbol{d}_0$ profiles derived from each respective error regime – these are used for all parameters in the presentation which follows.

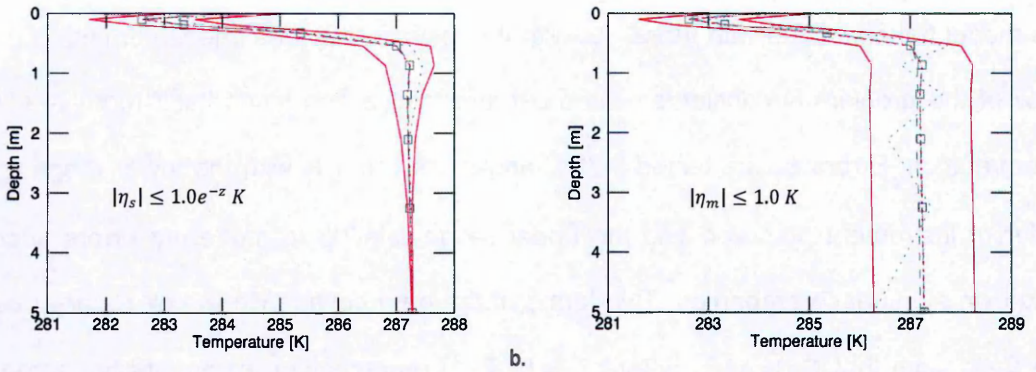

Figure 4.17. Temperature measurement from hr 23 of a 24 hr sinusoidal surface temperature cycle, with random errors (solid red curves illustrate upper and lower extremes) which: a. decrease with depth according to $|\eta_s| \leq \sigma_\eta e^{-z}$ K; b. are constant with depth according to $|\eta_m| \leq \sigma_\eta$. The grey curves are the profiles with errors defined by: double-dot-dashed ($\sigma_\eta = 1$ mK), dot-dashed ($\sigma_\eta = 10$ mK), dashed ($\sigma_\eta = 100$ mK), dotted ($\sigma_\eta = 1$ K). The grey squares are sensor locations which follow the true profile (red dotted curve; $\sigma_\eta = 0$ K).

[11] Noise is expected to decrease for sensors further from the surface as they tend to experience fewer transient phenomena providing a more reliable equilibrated temperature measurement.

[12] These are equivalent to unknown unsteady heat sources or sinks S^U.

4.3.1 Basal Heat Flow F_B^S

4.3.1.1 Instantaneous Measurement with Low Skin Depth (Diurnal)

As with the ideal measurement tests, F_B^S is initialized between 10-75 % inaccurate relative to the true value of 76 mW/m^2 while its standard deviation $\sigma_{F_B^S}$ is tested in the range $\sigma_{F_B^S} \in [10^{-5},10^3]$ W/m^2. The data standard deviation σ_d is tested in the range $\sigma_d \in [10^{-4},10]$ K. Tests are performed with the assumption of both exponential and constant uncertainties in data covariance $\boldsymbol{C_d}$ such that $\sigma_d e^{-z} = \sigma_\eta e^{-z}$ and $\sigma_d = \sigma_\eta$ K, respectively.

Figure 4.18 shows distributions of errors in the optimized F_B^S value for different noise levels (η_s and η_m) and assumptions (σ_d); the errors in the optimized data measurement follow a similar trend. With the exponential error model $|\eta_s| \leq \sigma_\eta e^{-z}$ the distribution of results is fairly similar for noise levels σ_η from 1 to 100 mK, though there is a gradual decrease in accuracy which is not resolved by the histograms (Table 4.1). There is a clear shift in accuracy when σ_η is 1 K. The assumption of exponential errors matching the model such that $\sigma_d e^{-z} = \sigma_\eta e^{-z}$ produces the most accurate results.

The model is less stable with the constant error model $|\eta_m| \leq \sigma_\eta$. The accuracy of the optimized F_B^S falls off relatively rapidly as σ_η increases. With σ_η at 100 mK there is some meaningful improvement (here considered 25 %) on most of the initial F_B^S estimates while $\sigma_\eta = 1$ K produces little meaningful improvement on the initial estimates (most diverge). The assumption of constant errors matching the model such that $\sigma_d = \sigma_\eta$ produces the most accurate results.

General trends in the results confirm that the accuracy of the optimized F_B^S decreases with increasing noise η in the data measurement indicating increasing difficulty for the model to find the true value of F_B^S. As noted earlier in the text, a stability ratio of standard deviations can be defined for an arbitrary model parameter m and data measurement $\boldsymbol{d}$ such that $r_d^m = \sigma_m/\sigma_d$. For the exponential noise model η_s, stability ratio $r_d^{F_B^S} = \sigma_{F_B^S}/\sigma_d \geq 1$, with the

most accurate results occurring at $r_d^{F_B^S} = 100$, assuming exponential uncertainties, and $r_d^{F_B^S} = 10$ assuming constant uncertainties. For the constant noise model η_m, $r_d^{F_B^S} \geq 1$, with the most accurate results occurring at $r_d^{F_B^S} = 10$. There are indications that larger stability ratios produce better results for smaller noise levels. Example plots of the stable regions are shown in Appendix 9.4.9.

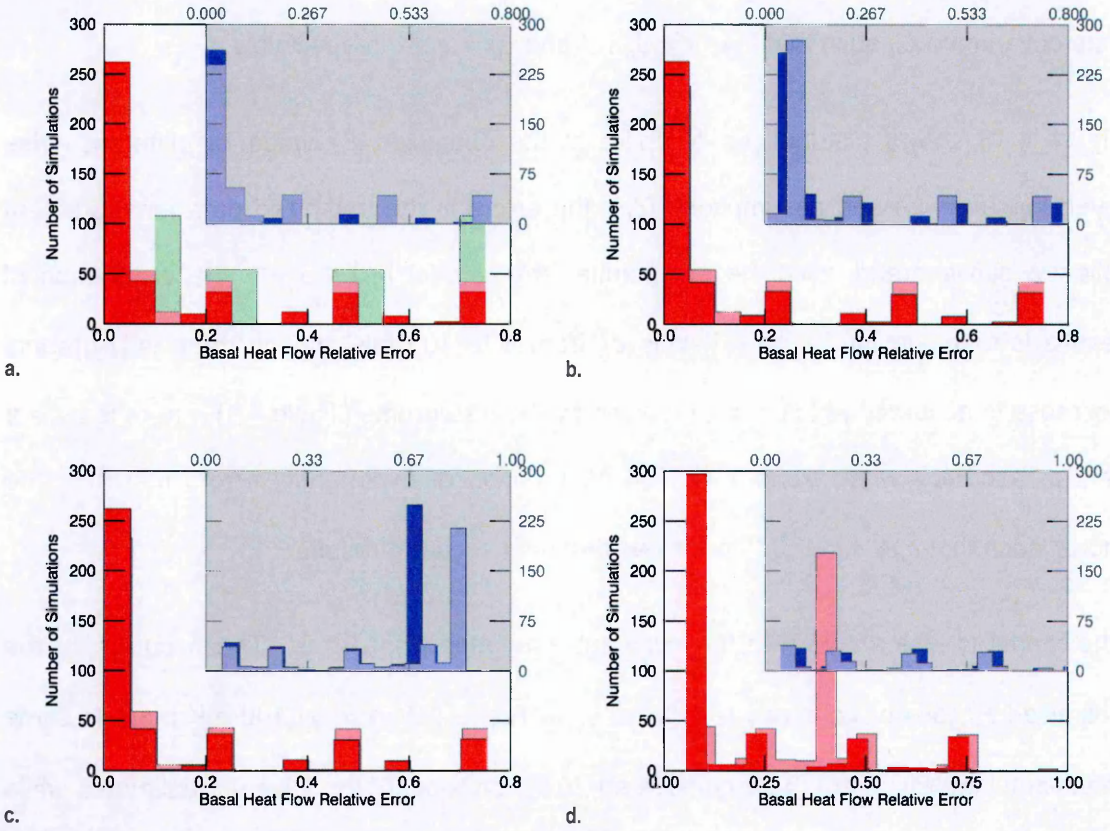

Figure 4.18. Accuracy of optimized $F_B^S - \left|\epsilon_{F_B^S}\right|$ – from inverting noisy subsurface temperature measurements generated by a sinusoidal surface temperature with a 24 hr period. The red plots are for noise model $|\eta_s| \leq \sigma_\eta e^{-z}$ while the inset plots are for noise model $|\eta_m| \leq \sigma_\eta$. Assumed noise profiles (represented by standard deviation σ_d) coordinate with colours according to bright red and indigo ($\sigma_d e^{-z} = \sigma_\eta e^{-z}$ K) and light red and indigo ($\sigma_d = \sigma_\eta$ K), σ_η being the maximum noise level. Plot: a. is for σ_η =1 mK; b. for σ_η =10 mK; c. for σ_η =100 mK and; d. for σ_η =1 K. Note that for d. the scale is cut off at $\left|\epsilon_{F_B^S}\right| = 1$ but the the inset values go beyond 1 – i.e. for those the model diverged. The histogram binsize is 0.05. The light green background histogram in plot a. is the intial distribution of F_B^S error used in all tests.

Most generally, the results indicate that applying the stability ratio conditions (along with skin depth, monitoring period and measurement frequency conditions highlighted in Section 4.2.1) creates an optimal setup for convergence of the model on the true value of F_B^S, if all other model parameters are correct. Of course, simultaneous optimization of F_B^S. with another unknown model parameter can be attempted.

Table 4.1. Minimum absolute value of optimized basal heat flow relative error $\epsilon_{F_B^S}$ from inversion tests with noisy data based on exponentially depth dependent η_s and constant η_m noise models with maximum error σ_η. Inversion tests are performed with assumed data error (standard deviation) σ_d.

F_B^S	$\lvert\eta_s\rvert \leq \sigma_\eta e^{-z}$				
σ_η [K]	1E-3	1E-2	1E-1	1E0	σ_d
$\lvert\epsilon_{F_B^S}\rvert$	7.50E-7	1.33E-6	2.23E-3	5.52E-2	$\sigma_\eta e^{-z}$
	6.15E-5	2.22E-3	4.95E-3	7.74E-2	σ_η
	$\lvert\eta_m\rvert \leq \sigma_\eta$				
	1.06E-5	3.49E-2	5.96E-2	8.59E-2	$\sigma_\eta e^{-z}$
	1.09E-4	6.59E-3	2.77E-3	5.15E-2	σ_η

4.3.1.2 Long-Period Measurements with High Skin Depth (Annual)

As with the ideal measurement tests, long-period measurement tests are performed with noisy measurements which: 1. cover the full period of a 360 d surface unsteady temperature T_S^U cycle with a measurement frequency of 1 per day (Figure 4.5); 2. are taken from the end of the 360 d T_S^U cycle as an instantaneous measurement (Figure 4.4). The measurements are taken on a 10 sensor grid with the constant noise model $\lvert\eta_m\rvert \leq \sigma_\eta$ used to add noise of standard deviation σ_η of 10 mK and 1 K at each sensor location (Figure 4.19; note that while one skin depth is shown, two are tested with $k = 0.3$ and 3 W/m/K).

F_B^S is initialized between 25-100 % inaccurate relative to the true value of 76 mW/m^2 while its standard deviation $\sigma_{F_B^S}$ is tested in the range $\sigma_{F_B^S} \in [10^{-3}, 10^3]$ W/m^2. The data standard

deviation σ_d is tested in the range $\sigma_d \in [10^{-4},10]$ K. Tests are performed with the assumption of constant uncertainties in data covariance $\boldsymbol{C}_d$ such that $\sigma_d = \sigma_\eta$ K.

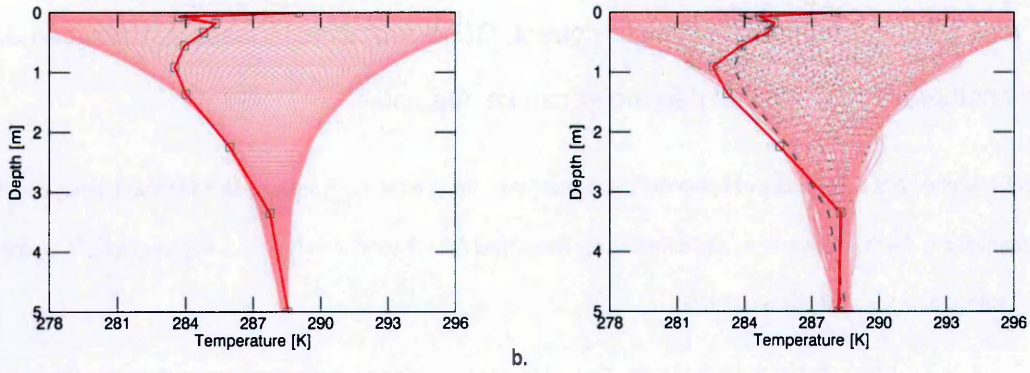

Figure 4.19. Noisy temperature measurements for a 360 d sinusoidal surface temperature cycle with conductivitity k of 0.3 W/m/K. The bright red profiles represent instantaneous noisy measurement at the end of the 360 d cycle (dashed grey plots are true profiles); the light red profiles represent daily measurements (displayed in 3.6 d increments) over the 360 d cycle (dotted grey contours are the true profiles). Contour: a. shows the measurements with standard deviation $\sigma_\eta = 10$ mK; b. shows the measurement with standard deviation $\sigma_\eta = 1$ K. The grey squares are sensor locations.[13] Note that parts of the true profiles may be hiddens by the measurements

The results demonstrate the optimization of the temperature measurement, essentially removing the noise from the data (Figure 4.20). F_B^S is less effectively optimized than the equivalent cases in Section 4.2.1.2.2 with the ideal measurement ($k = 0.3$ and 3 W/m/K), although the trends established with the frequency of temperature measurements are the same – more measurements give better results (Figure 4.21). Note, therefore, that results with $k = 3$ W/m/K are note illustrated (recall that those mostly diverged in the ideal

[13] The high frequency oscillations towards the surface show the penetration depth of the diurnal temperature fluctuations. To replicate them in the inversion a high density temporal grid is required to match the oscillation frequency of the diurnal temperature over 360 d which proves impractical with limited computing resources. Also, replicating the diurnal variations is unnecessary here as they play no major role in masking the basal heat flow F_B^S. This is overcome by ignoring the surface sensors which measure the diurnal temperature fluctuations, allowing the use of larger timesteps which effectively resolve the longer period changes over the 360 d period.

measurement tests of Section 4.2.1.2.2), they are mentioned only with relevance to general trends.

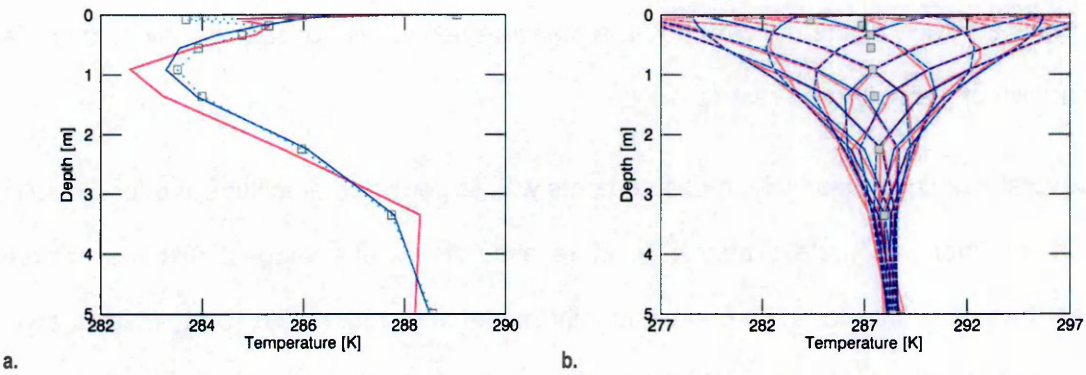

Figure 4.20. Temperature profiles for basal heat flow F_B^S, optimized from noisy measurements for a 360 d sinusoidal surface temperature cycle with conductivitity k of 0.3 W/m/K. The solid blue curves are optimized profiles, the solid red curves measurement profiles with standard deviation $\sigma_\eta = 1$ K and dotted grey curves the true profiles. Grey squares are sensor locations. Plot a. represents an instantaneous temperature profile at the end of the 360 d cycle; Countour b. represents a daily temperature record over the 360 d cycle (displayed at 30 d increments for visibility).

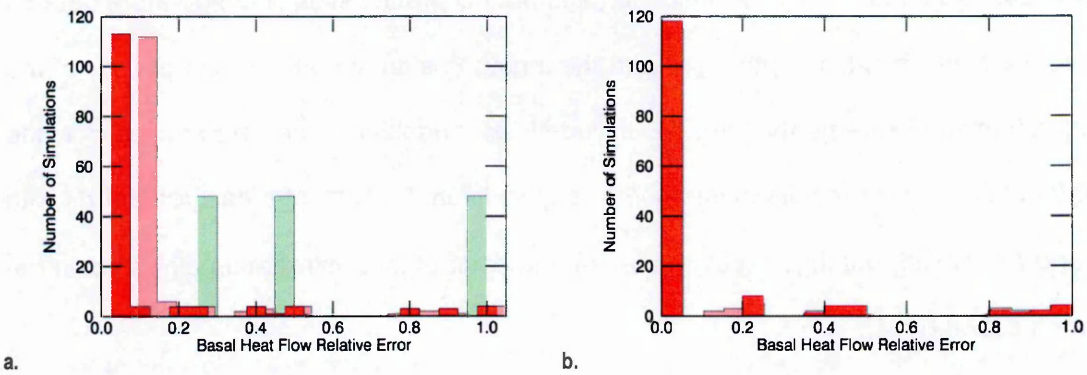

Figure 4.21. Distribution of the error $\left|\epsilon_{F_B^{SI}}\right|$ in basal heat flow F_B^S, optimized from noisy measurements for a 360 d sinusoidal surface temperature cycle with conductivitity k of 0.3 W/m/K. The bright red foreground represents the distribution of $\left|\epsilon_{F_B^{SI}}\right|$ for $\sigma_\eta = 10$ mK; the light red represents the distribution of $\left|\epsilon_{F_B^{SI}}\right|$ for $\sigma_\eta = 1$ K; the green represent the intial distribution of F_B^S error used in all tests. Histogram: a. represents the distribution of optimized F_B^S error for the instantaneous measurement; b. represents the distribution of optimized F_B^S error for the long-period measurement. The histogram binsize is 0.05.

Table 4.2 summarises the results in terms of the modal F_B^S accuracy encountered with measurements of different error and different measurement frequency. It is interesting to note that errors up to 10 mK give results very similar to the cases with no errors, suggesting having errors up to 10 mK in a measurement does not significantly deteriorate the quality of the optimized results.

In several cases, interestingly, measurements with larger noise amplitude produce results which are more accurate (Table 4.2). More accurate results suggest that the inverse model has more freedom to explore the joint model and data space $[\mathrm{D}, \mathrm{M}]$ (see Section 2.2); this is evidenced by trends in the results as data standard deviation σ_d is increased. However, σ_d and model standard deviation σ_m in covariances $\boldsymbol{C_d}$ and $\boldsymbol{C_m}$, which define $[\mathrm{D}, \mathrm{M}]$, are fixed in a number of cases, such that they don't play any role in the variation of optimized F_B^S accuracy.

The cases with fixed $\boldsymbol{C_d}$ and $\boldsymbol{C_m}$ effectively contain as variables the noise η_m and the initial basal heat flow accuracy F_B^{S0}. Additionally, if implicit characteristics of temperature data $\boldsymbol{d}_0$ are considered, the skin depth z_{SKIN} and the length (instantaneous or long-period) of the temperature measurements can be included as variables. The explanation for the counterintuitive noise results must, therefore, also lie in the form of measurement $\boldsymbol{d}_0$ with η_m and F_B^{S0} which, notably, stipulate the starting point of the optimization algorithm in the solution space $[\mathrm{D}, \mathrm{M}]$.

Correlating the frequency of the counterintuitive noise results with the variables noted above (Appendix 9.4.8) shows that the counterintuitive results are due to instabilities introduced by the large number of unique temperature gradients in the long-period measurement cases, and increased skin depth z_{SKIN} (also see Section 2.2). This conclusion is supported by the fact that no such counterintuitive result is found in the instantaneous, low skin depth cases presented in Section 4.3.1.1 (also see Appendix 9.4.9).

Increasing σ_d (relative to $\sigma_m = \sigma_{F_B^S}$), in the range of values tested, appears to stabilise the inverse model, reducing the number of counterintuitive cases. This happens because increasing the size of the data space D of [D, M], relative to model space M (see Section 8.2.3 for further discussion), allows for a larger solution set of estimates for optimal temperature data $\boldsymbol{d}$. Setting σ_d too large, however, results in the model returning F_B^{S0} as a solution, as all the weight is placed on this initial guess.

Table 4.2. Modal optimized basal heat flow relative error $\epsilon_{F_B^{SI}}$ where the improvement on the initial estimate is at least 25 %. This is from inversion tests with noisy data based on constant noise models $\eta_m \leq \sigma_\eta$ where σ_η. represents the maximum error in a measurement where m is the measurement frequency of the measurement.

F_B^S	$\lvert\eta_m\rvert \leq \sigma_\eta$		
m	1	360	σ_η [K]
MODAL $\lvert\epsilon_{F_B^{SI}}\rvert$	0.0686	7.223E-3	0
	0.0695	0.02694	0.01
	0.1426	0.01523	1

4.3.1.3 Thermal Property Errors

In Section 4.2.1.2.3 the results of optimization tests on ideal measurements with inaccurate thermal properties are presented. These illustrate positive correlation between the accuracy of k and the optimized basal heat flow F_B^S, and negative correlation between the accuracy of ρc and optimized F_B^S. It is more likely that a noisy data measurement will be accompanied by inaccurate thermal property estimates. Here, tests are performed on the same measurements presented in Figure 4.19 with inaccuracies in thermal properties.

F_B^S is initialized between 25-100 % inaccurate relative to the true value of 76 mW/m^2 while its standard deviation $\sigma_{F_B^S}$ is tested in the range $\sigma_{F_B^S} \in [10^{-3}, 10^3]$ W/m^2. Conductivity k and thermal capacity ρc are initialized within 25-90 % of their respective true values of 0.3 W/m/K and 2.133 MJ/K/m^3. The data standard deviation σ_d is tested in the range $\sigma_d \in [10^{-4}, 10]$ K. Tests are performed with the assumption of constant uncertainties in data covariance $\boldsymbol{C_d}$ such that $\sigma_d \leq \sigma_\eta$ K. Figure 4.22 shows representative results.

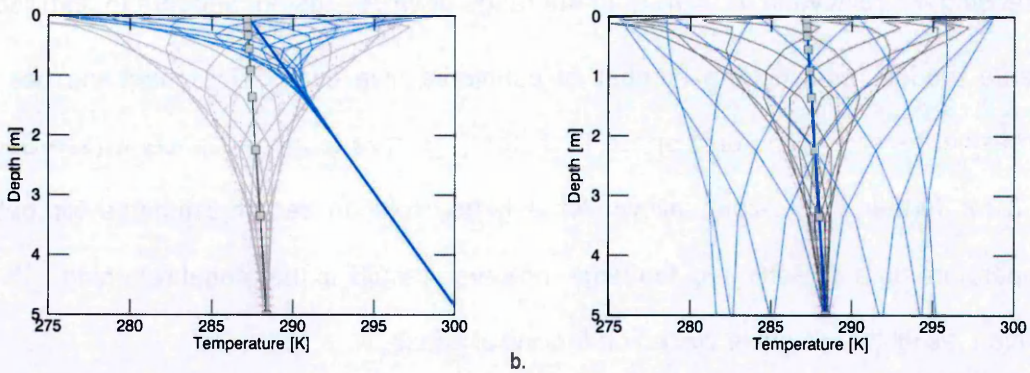

Figure 4.22. Temperature profiles at different times as a function of depth z with inaccurate thermal properties for basal heat flow F_B^S optimized from noisy data with standard deviation $\sigma_\eta = 1$ K. The measurements are generated by a 360 d sinusoidal surface temperature cycle. with true conductivitity k of 0.3 W/m/K and thermal capacity ρc of 2.133 MJ/K/m³. Plot: a. has innaccurate $k = 0.03$ W/m/K; b. has innacurate $\rho c = 0.2133$ MJ/K/m³. The solid blue curves are optimization results and the dotted red curves the inverted measurements. The solid grey curves represent the true profiles with grey squares representing sensor locations, and following the true steady temperature T_S^S profile.

It is clear that the inversion does not work well with inaccurate k and inaccurate ρc. The particular behaviour of each parameter is discussed in Section 4.2.1.2.3 with the ideal measurement. Of course, in practical situations results similar to those in Figure 4.22 are re-evaluated to reduce the misfit between temperature profiles, or equivalently, the thermal properties optimized. The results follow a similar trend to that highlighted in the related ideal measurement case in Section 4.2.1.2.3, with direct and inverse correlation between the relative errors in F_B^S, and the relative errors in k and ρc respectively. This is true, in particular, when the data standard deviation is constrained to $\sigma_d = 10^{-4}$ K. The higher values of tested σ_d produce significant scatter in the data, obscuring the parameter correlations. This confirms a need to constrain σ_d to small values relative to model standard deviation $\sigma_{F_B^S}$ (may include σ_k and $\sigma_{\rho c}$ in simultaneous optimization) when the error in thermal properties or boundary parameters is large. Making σ_d small gives the temperature measurement high weighting and effectively forces errant model parameters to conform to its values.

4.3.2 Steady Surface Temperature T_S^S

As with basal heat flow F_B^S, T_S^S is initialized between 10-75 % inaccurate relative to the true value of 287.15 K while its standard deviation $\sigma_{T_S^S}$ is tested in the range $\sigma_{T_S^S} \in [10^{-4},10^4]$ K. The data standard deviation σ_d is tested in the range $\sigma_d \in [10^{-4},10]$ K. Tests are performed with the assumption of both exponential and constant uncertainties in data covariance $\boldsymbol{C_d}$ such that $\sigma_d \leq \sigma_\eta e^{-z}$ and $\sigma_d \leq \sigma_\eta$ K, respectively.

Figure 4.23 shows distributions of errors in the optimized T_S^S value for different noise levels (η_s and η_m) and assumptions (σ_d) – they mirror the errors in the optimized data measurement. The distribution of optimized T_S^S remains noticeably unchanged across the different noise models (η_s and η_m) and different error assumptions with standard deviation σ_d. This can be understood in the sense that the optimization of T_S^S is mostly determined by the surface values of η_s and η_m and is therefore not directly affected by σ_d depth profile assumptions. Of course, in a simultaneous optimization case, T_S^S may be affected by other parameters which are influenced by depth profile assumptions (e.g. basal heat flow F_B^S and unsteady surface temperature T_S^U) There is increased inaccuracy in the optimized T_S^S as noise level η increases (Table 4.3), but these are not resolved by the histogram binsize.

Note that the case of η_m producing better results than η_s for $\sigma_\eta = 10^{-3}$ is a chance occurrence where the surface value of η_m is smaller than that of η_s. A stability ratio of standard deviations can be defined such that $r_d^{T_S^S} = \sigma_{F_B^S}/\sigma_d \geq 10^3$, with the most accurate results occurring at $r_d^{F_B^S} = 10^3$.

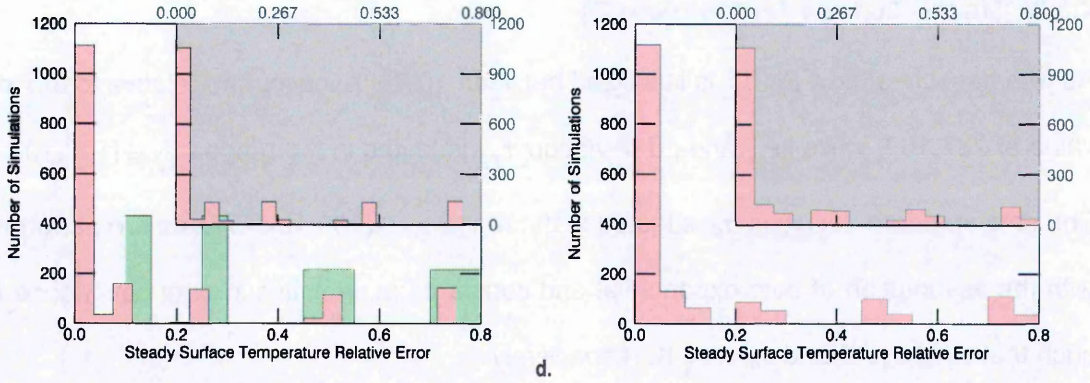

Figure 4.23. Accuracy of optimized T_S^S – $\left|\epsilon_{T_S^{SI}}\right|$ – from inverting noisy subsurface temperature measurements generated by a sinusoidal surface temperature with a 24 hr period. Plot: a. corresponds to noise model $|\eta_s| \leq \sigma_\eta e^{-z}$ while plot; b. corresponds to noise model $|\eta_s| \leq \sigma_\eta$. Green represents the apriori error distribution of $\left|\epsilon_{T_S^{S0}}\right|$ (applies to all case) while red represents the optimized distribution $\left|\epsilon_{T_S^{SI}}\right|$. The histogram binsize is 0.05.

Table 4.3. Minimum absolute value of optimized steady surface temperature relative error $\epsilon_{T_S^{SI}}$ from inversion tests with noisy data based on exponentially depth dependent η_s and constant η_m noise models with maximum error σ_η. Inversion tests are performed with assumed data error (standard deviation) σ_d.

T_S^S	$\lvert\eta_s\rvert \leq \sigma_\eta e^{-z}$				
σ_η K	1E-3	1E-2	1E-1	1E0	σ_d
$\left\lvert\epsilon_{T_S^{SI}}\right\rvert$	3.48E-8	2.09E-7	3.69E-6	8.36E-6	$\sigma_\eta e^{-z}$
	6.97E-8	4.53E-7	5.22E-7	2.11E-5	σ_η
	$\lvert\eta_m\rvert \leq \sigma_\eta$				
	0.00E0	1.99E-6	1.31E-5	8.73E-4	$\sigma_\eta e^{-z}$
	0.00E0	1.99E-6	1.51E-5	3.24E-5	σ_η

4.3.3 Unsteady Surface Temperature T_S^U

The behaviour of the model in optimizing T_S^U generally reflects increasing difficulty in finding the true T_S^U profile with increasing noise measurement η but as with the ideal case, is strongly dependent on a priori information. Here the model is initialised with the most stable results of tests in Section 4.2.3 with the ideal measurement – specifically a covariance $\boldsymbol{C}_{T_S^U}$ with an exponential or equivalent Hanning covariance function $f_\tau =$

$[e^{-r\tau}, 0.5e^{-r\tau}\left(1+\frac{cos\pi\tau}{\tau_c}\right)]$ respectively and $\tau_c = P$, the period of T_S^U where $T_S^U = T_S^{UA} sin\left(\frac{2\pi t}{P}+\varphi\right)+\beta K$ (see Appendix 9.1 for symbol definitions). Figure 4.24 shows typical good results of the optimization from both the exponential noise model η_s and the constant noise model η_m.

The most accurate fit is obtained when the initialization of $\boldsymbol{C_d}$, $\boldsymbol{C}_{T_S^U}$ and T_S^U allows the initial T_S^U estimate to evolve freely into the true T_S^U value. Relatively unconstrained $\boldsymbol{C_d}$ appears to have allowed an improved estimate of T_S^U towards $t = 0$. The results also illustrate the optimization of the noisy data measurement, most striking in the case of the constant noise model η_m. A stability ratio is evident in the data relative to σ_d and $\sigma_{T_S^U}$ where – consistent with the two other boundary parameters – $r_d^{T_S^U} \geq 10^2$.

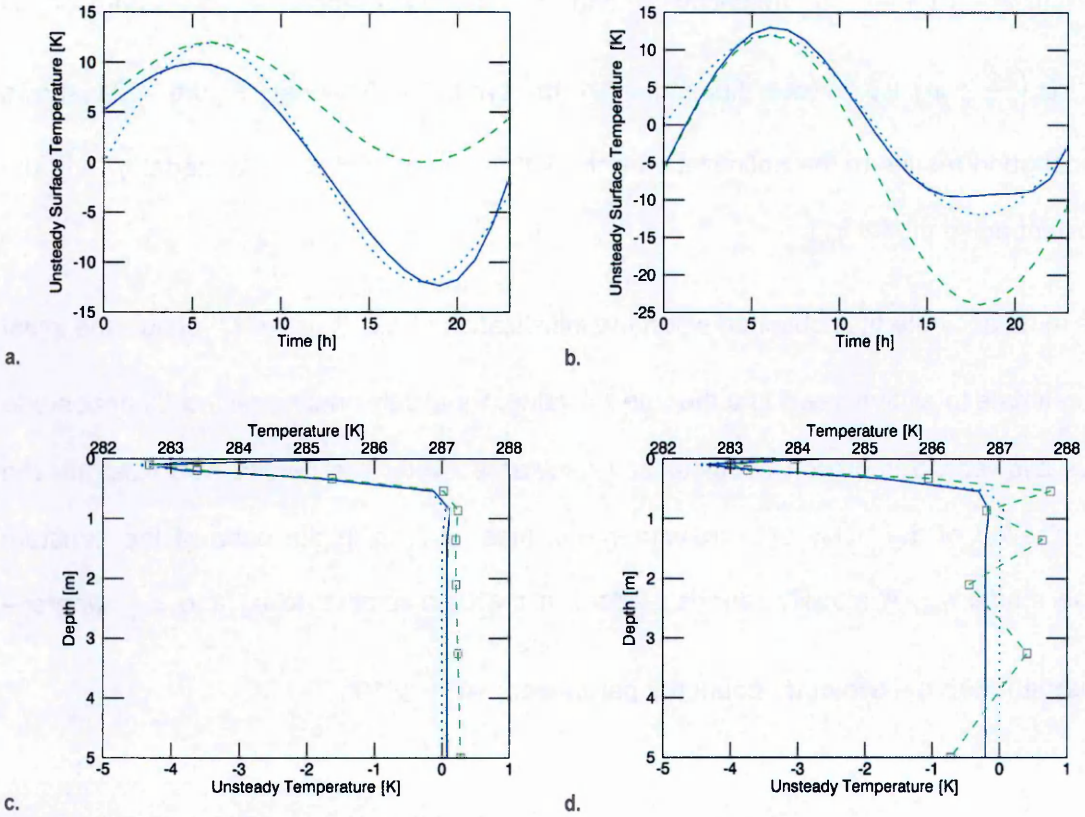

Figure 4.24. Optimization of unsteady surface temperature T_S^U from a noisy temperature measurement at time $t = 23$ hr into a sinusoidal T_S^U cycle. The blue dotted curves represent true profiles, the green dashed curves initial estimates (and measurements), and the blue solid curves the optimized profiles. Plots a. and c. are respective pairs of T_S^U and optimized unsteady subsurface temperature profiles T^U inverted from a noisy measurement T, with the exponential noise model $|\eta_s| \leq \sigma_\eta e^{-z}$. Plots b. and d. are respective pairs of T_S^U and T^U inverted from T with the constant noise model $|\eta_m| \leq \sigma_\eta$. The grey squares are sensor locations.

4.4 Summary

A model which inverts a data measurement $\boldsymbol{d}_0$ to optimize basal heat flow F_B^S, surface steady and unsteady temperatures T_S^S and T_S^U, conductivity k, thermal capacity ρc, and heat sources and sinks S^S is presented. The model is based on the theory outlined in Chapter 2, utilizing the forward model of Chapter 3 as a major component. The main parameter of interest is F_B^S and the presentation aims to illustrate how different model parameters $\boldsymbol{m}$ influence its optimization in an inversion.

The results show that the model optimizes F_B^S and other parameters to their true values when model and data covariance $\boldsymbol{C_m}$ and $\boldsymbol{C_d}$ satisfy specific characteristics. Ratios of standard deviations (stability ratios) – between two model parameters $r_{m_2}^{m_1}$ or model and data parameters r_d^m – are used to assist in quantifying the convergence characteristics of $\boldsymbol{C_m}$ and $\boldsymbol{C_d}$. Tests show that the $r_{m_2}^{m_1}$ and r_d^m are – to first order – consistent between optimized model parameters such that $r_{m_2}^{m_1} = r_{m_2}^{m_3}/r_{m_1}^{m_3}$ (see Appendix 9.4.7.3). They are related to the fundamental physical units of the model parameters being optimized and data being inverted, along with the conditioning of the dataset. This is indicated by results with basal heat flow F_B^S and steady surface temperature T_S^S (see Appendix 9.4.7.1). The analytical relationships involving $r_{m_2}^{m_1}$ and r_d^m are likely discoverable in the theory outlined in Section 2.2 (see Appendix 9.8.2 for a potential approach) or can be quantified after performing several analyses of the type done here with a diverse range of datasets.

When optimizing single parameters, improved optimized results (up to 99 % and better) are achieved from initial estimates between 10-100 % inaccurate. A more accurate initial estimate generally produces a more accurate optimized result in an idealised situation. For basal heat flow F_B^S, results are more accurate for shallower skin depth z_{SKIN} and longer monitoring periods with a minimum of 10 measurements over a surface temperature T_S cycle – see Section 4.2.1.2). For instantaneous or short period, low frequency measurements, F_B^S is more accurately optimized when the measurement is taken at a point where T_S is at a minimum. When F_B^S is optimized with inaccurate thermal properties the physical relationships between F_B^S and the unknown properties determine the accuracy of F_B^S and whether or not it is overestimated or underestimated (see Sections 4.2.1.2.3 and 4.3.1.3). F_B^S is less accurately optimized with increased data noise though results with long period high frequency measurements suggest random noise of large magnitude (1 K) may stabilize the result when skin depth z_{SKIN} is important (see Section 4.3.1.2). Noisy data is also optimized by the model, in the process of optimizing F_B^S and other parameters. Optimization of surface steady and unsteady temperatures T_S^S and T_S^U,

conductivity k, thermal capacity ρc and heat sources and sinks S^S is discussed in Sections 4.2.2-4.2.5 and 4.3.2-4.3.3.

When simultaneously optimizing two or more parameters accurate optimized results are obtained only when the initial model parameter estimates are constrained to within particular limits. The steady surface temperature T_S^S is the most stable in optimization either solely or with other parameters. The accuracy of optimized basal heat flow F_B^S correlates with other model parameters based on their physical relationships in the heat flow problem (see Appendix 9.4.7). When optimized with T_S^S or k, F_B^S is optimized to within 25 % of its true value when T_S^S and k are within 25 % of their true value. If F_B^S is optimized with inaccurate k or ρc, relative errors in the optimized F_B^S correlate directly with relative errors in k and inversely with the relative errors in ρc due to their roles in determining the steady temperature T^S gradient and the skin depth z_{SKIN} (see Sections 3.2.2 and 3.4.2).

The results presented here highlight principles which can be applied to optimize unknown parameters which affect the basal heat flow F_B^S, along with F_B^S itself. Applying these principles may require some experimentation (e.g. with the magnitude of standard deviations to design the most suitable covariances) to guarantee the most accurate optimized F_B^S from the data. These principles are applied to realistic datasets in Chapters 5-7.

4.5 References

SHEN, P. Y. & BECK, A. E. 1991. Least Squares Inversion of Borehole Temperature Measurements in Functional Space. *J. Geophys. Res.,* 96, 19965-19979.

SHEN, P. Y. & BECK, A. E. 1992. Paleoclimate change and heat flow density inferred from temperature data in the Superior Province of the Canadian sheild. *Palaeogeography, Palaeoclimatology, Palaeoecology,* 98, 143-165.

SHEN, P. Y., WANG, K., BELTRAMI, H. & MARESCHAL, J. C. 1992. A comparative study of inverse methods for estimating climatic history from borehole temperature data. *Palaeogeography, Palaeoclimatology, Palaeoecology,* 98, 113-127.

TARANTOLA, A. 2005. *Inverse problem theory and methods for model parameter estimation,* Philadelphia, PA, Society for Industrial and Applied Mathematics.

WANG, K. 1992. Estimation of Ground Surface Temperatures from Borehole Temperature Data. *J. Geophys. Res.,* 97, 2095-2106.

5 MARS

5.1 Heat Flow on Mars

5.1.1 Martian Thermal History and Models

An accurate estimate of planetary heat flow on Mars can place an important constraint on the numerous existing Martian thermal evolution models which predict its current thermal state. Combined with other measurements (see below), a Martian heat flow estimate can aid in answering important questions about Mars' remnant magnetic field (e.g. Stevenson et al., 1983; Nimmo and Stevenson, 2000), its present state of volcanism (e.g. Grott and Breuer, 2010), its surface cooling history (e.g. Spohn, 1991; Weizman et al., 2001) and its current internal state. Answering the former questions for Mars will also further the understanding of the thermal evolution of other planets (e.g. Kömle et al., 2011; Dehant et al., 2012).

Martian thermal models can broadly be classified into so-called plate cooling (e.g. Breuer and Spohn, 2003) and stagnant lid models (e.g. Weizman et al., 2001; Hauck and Phillips, 2002; Grott and Breuer, 2010; Morschhauser et al., 2011), though different models may include episodes of either of the former, piped volcanism (e.g. Spohn, 1991; Weizman et al., 2001) and dynamo activity (e.g. Spohn et al., 2001a) over their course.[1] Collectively, these thermal models typically predict current global heat flow in the range of 5-25 mW/m^2; plate cooling in the lower subrange and stagnant lid in the higher subrange, though some models predict global averages up to 45 mW/m^2 (Urquhart and Gulick, 2003).

Current heat flow predictions of the former models differ by only a few percent in several instances (see Spohn et al., 2001a for several examples); these are unlikely to be differentiated by a heat flow measurement, which may not achieve an accuracy below 10

[1] Plate cooling refers to crustal plate differentiation from a magma ocean, while stagnant lid accounts for a layered lithosphere which includes a crust and a rheological lithosphere, together forming an insulating 'stagnant lid,' atop a convecting mantle which contributes significant heat flow (e.g. Spohn, 1991).

% (e.g. Grott et al., 2007b). In the preceding cases, additional observable model parameters are required to select one particular thermal model over another (e.g. Grott et al., 2014).

Lithosphere thickness is one observable that attains different current states in tectonic plate cooling and stagnant lid models (e.g. Spohn et al., 2001a). Tectonic plates allow the mantle of a planet to cool more efficiently, leading to lower mantle temperatures and accelerated lithosphere growth. A stagnant lid, on the other hand, insulates the mantle, thereby increasing mantle temperatures and reducing lithosphere growth. Volcanism may complicate the interpretation of lithosphere thickness, as it can occur in both plate tectonics and stagnant lid regimes and increases the relative thickness of the lithosphere (e.g. Spohn, 1991; Weizman et al., 2001).

Interpretation of the planetary heat flow can be aided by decomposing it into a crustal component, produced by the decay of radioisotopes (e.g. Taylor et al., 2006; Boynton et al., 2007) and a mantle component[2], produced by mantle and core cooling (Grott and Breuer, 2010; Hahn et al., 2011). Determining the planetary heat flow along with the crustal distribution of radioisotopes, and mantle and core size from seismological studies (e.g. Spohn et al., 2001a; Dehant et al., 2012) can therefore go some way in determining crustal thickness, the thermal state of the sub-crustal interior, and consequently constraining the current thermal history model of Mars (e.g. Grott et al., 2014).

5.1.2 Martian Heat Flow Measurement

Mars' environment presents unique challenges for reliable planetary heat flow measurement due to its substantial, dusty atmosphere and potentially icy regolith. These can produce small-scale, short-term fluctuations in surface and shallow subsurface temperatures – and regolith properties – which may bias the result of any shallow, local

[2] The mantle heat flow component is known as reduced heat flow in Earth-based studies (e.g. Sclater et al., 1980; Jaupart et al., 1981).

heat flow measurement (e.g. Grott et al., 2007b). The former fluctuations are second order, with the variation in insolation causing the main fluctuations.

The Thermal and Electrical Conductivity Probe (TECP) of the Phoenix lander measured shallow subsurface conductivity, thermal capacity and temperature on Mars (Zent et al., 2010), integrated over 15 mm directly below the surface. However there are, to date, no in situ heat flow measurements – i.e. depth-resolved measurements of thermal properties and temperature. Current proposals with the latter capability include the Heat Flow and Physical Properties Package (HP^3) – a heat flow probe developed for deployment on terrestrial bodies (Spohn et al., 2001b; Spohn et al., 2010; Kömle et al., 2011; Dehant et al., 2012; Spohn et al., 2012). HP^3 is a planned payload on NASA's Interior Exploration using Seismic Investigations, Geodesy and Heat Transport (InSight) mission (Banerdt et al., 2012; Spohn et al., 2012; NASA, 2014). As HP^3 is designed to carry out the type of measurement investigated in this work, the model presented in Chapter 4 is applied to different Martian scenarios to assess the feasibility of returning a reliable planetary heat flow estimate from a HP^3 measurement on Mars.

There are estimates of Martian palaeo-heat flow from crustal deformation models (e.g. Grott et al., 2007a; Ruiz et al., 2011) and estimates of current global heat flow distribution from models of crustal thickness and radioelement distribution (Grott and Breuer, 2010; Hahn et al., 2011; Dehant et al., 2012). As noted in Section 5.1.1, stagnant lid and plate cooling Martian thermal models typically predict heat flows in the higher and lower sub ranges of 5-25 mW/m^2, respectively. There is also an expected variation of heat flow in relation to local crustal thickness and the abundance of heat producing elements (Figure 5.1 – after Dehant et al., 2012; also see Grott and Breuer, 2010). Hahn et al. (2011) produce a similarly featured crustal heat flow[3] map and calculate an average crustal heat

[3] The map of Hahn et al. (2011) presents only the crustal component of the heat flow as opposed to total surface heat flow which accounts for both the crustal, mantle and core components of heat flow.

flow component of 6.4 ±0.4 mW/m^2 which is similar to the crustal heat flow reported by Grott and Breuer (2010).[4]

Based on a global mean heat flow of 20 mW/m^2 from the stagnant lid regime, Grott et al. (2007b) estimate that Martian heat flow can be measured to an accuracy within 30 % given measurements over at least a Martian year, depths of 3-5 m and temperature measurement precision of 0.1 K. Dehant et al. (2012) demand a higher precision of 0.05 K for depths up to 2 m based on the same global mean heat flow. An accuracy of 30 % is not sufficient to corroborate the predicted heat flow difference between adjacent regions of Figure 5.1, save for, possibly, the Tharsis region with high heat flow (Figure 5.1b; ~30 % heat flow difference between green, yellow and red).[5] For a given heat flow situation (Figure 5.1a), a 30 % accurate heat flow estimate can resolve differences between say, the highest (red-orange; > 23 mW/m^2) and midddle (green; 17-21 mW/m^2) regions.

To get the most representative heat flow measurements, probes may be sent to sites at which the heat flow is expected to be close to the global mean, potentially adjusted for high heat flow at Olympus Mons (see Figure 5.1) or several representative sites where the relevant model parameters are well known. Sites with a minimal range of surface temperature variation are also ideal to avoid temperature dependent variation of thermal properties (see below), and minimise masking of the steady temperature by the unsteady temperature – such sites are, for example, close to the equator. Equatorial sites also minimise the chances of encountering icy deposits (e.g Boynton et al., 2002) which can diminish the usefulness of the measurement due to the relatively high conductivity of ice. Equatorial sites also minimise the effect of longer period (>1 M yr) temperature changes due to Mars obliquity cycle (Grott et al., 2007b). Thicker crust focuses heat flow; therefore

[4] The results are based on the same dataset, with similar methods.

[5] Dividing the regions by colour (mW/m^2) into red-orange (>23), yellow (21-23), green (17-21), light blue (15-17) and dark blue (<15); or respectively <40, 30-40, 17-30, 15-17 and <15 mW/m^2 for high Tharsis heat flow. Percentage differences are calculated by taking the means of the ranges and calculating the difference relative to a lower adjacent range.

planetary heat tends to escape from regions of lower elevation than regions of higher elevation. This means the heat flow measured in a relatively flat region is least likely to suffer from distortions due to topography dependent lateral heat flow (e.g. Wang, 1992) though unknown subsurface heterogeneities may still produce lateral heat flow.

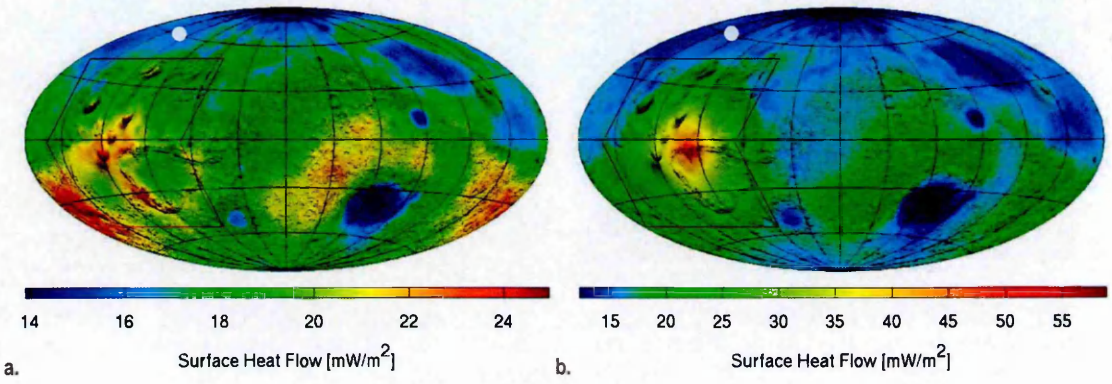

Figure 5.1. Expected surface heat flow distribution on Mars from surface crustal thickness and heat producing element abundance a. nominally and b: with active plume below the Tharsis region (red polygon). Credit: Dehant et al. (2012), based on the model of Morschhauser et al. (2011) – also see Grott and Breuer (2010). Hahn et al. (2011) obtain a crustal heat flow distribution similar to that on the right with values between 0–13 mW/m² (note that the distributions above take into account total surface heat flow, hence the higher values). The filled white circle indicates the approximate site of the Phoenix lander at ~234°E 68°N Zent et al., 2010.

Grott et al. (2007b) and Spohn et al. (2012) focus on the Elysium region of Mars for candidate landing sites (Figure 5.2, white ellipse). In this investigation, three sites (Figure 5.2, small squares) are investigated which are distinguished as middle (green ~17 mW/m/K), high (red ~22 or 40 mW/m/K) and low (blue ~15 mW/m/K) expected heat flows, as mapped in Figure 5.1. These sites include the site modelled in Grott et al. (2007b) which is located at 120°E 20°N – in the middle heat flow range, and the baseline landing site for the InSight mission Spohn et al., 2012 at 139°E 1°N – in the low heat flow range. The high heat flow site on the Tharsis plateau at 253°E 2°N is selected due to current unknowns regarding the peak heat flow from that area (Grott and Breuer (2010); also see Figure 5.1).

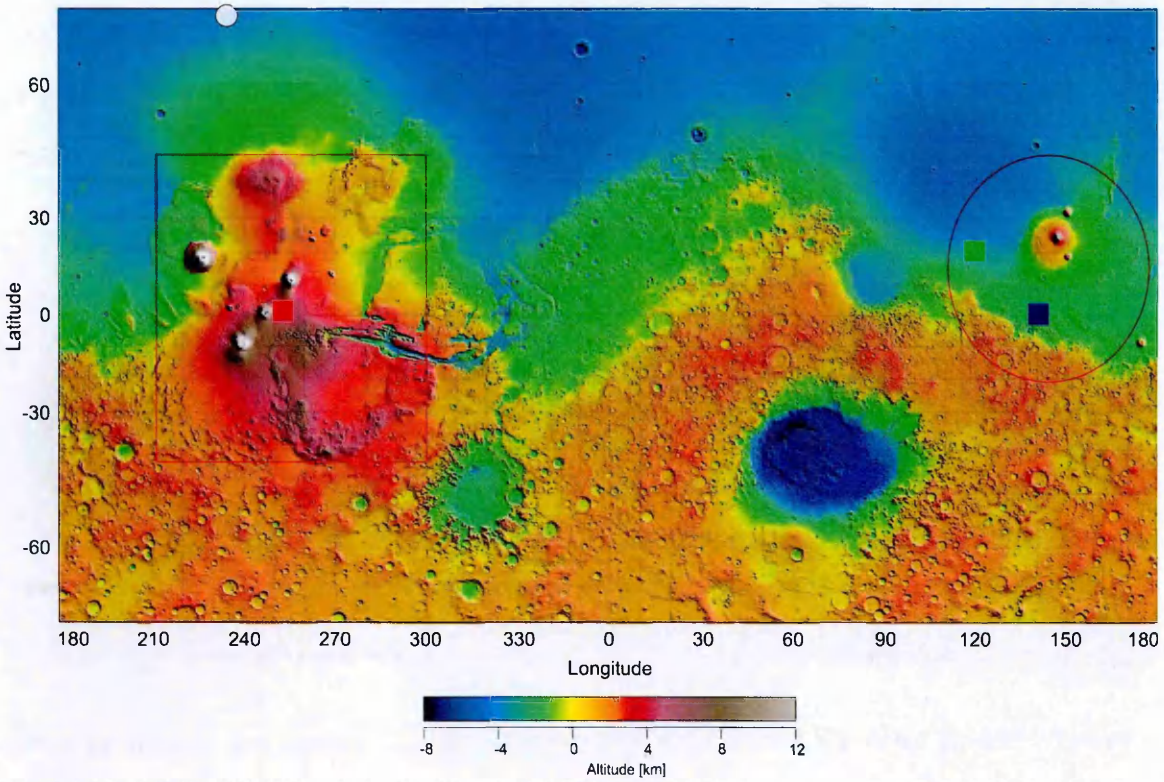

Figure 5.2. Potential heat flow probe landing sites (filled rectangles) identified on Mars Orbiter Laser Altimeter (MOLA) topographic map. The green rectangle (120°E 20°N, after Grott et al., 2007b) represents middle (~17 mW/m/K), the red rectangle (253°E 2°N) high (~22 or 40 mW/m/K) and the blue rectangle (139°E 1°N, after Spohn et al., 2012) low (~15 mW/m/K) heat flow regions as seen in Figure 5.1. The unfilled red rectangle identifies the Tharsis region, the unfilled red ellipse the Elysium region. The filled white circle indicates the approximate site of the Phoenix lander at ~234°E 68°N Zent et al., 2010. Topographic map credit: NASA

5.2 Further A Priori Information

The estimates of Martian basal heat flow discussed above form part of the a priori information available in an inversion. The quality of information on other Martian boundary parameters and regolith properties are assessed below.

5.2.1 Steady and Unsteady Surface Temperature

Typical seasonal and diurnal temperatures on Mars vary over 150-315 K (Piqueux and Christensen, 2011). Diurnal temperatures vary on the order of 100 K while seasonal temperatures vary on the order of 50 K (e.g. Grott et al. (2007b); Zent et al. (2010); also see Figure 5.3). While a measurement over a full Martian year is recommended for recovering the planetary heat flow (Grott et al., 2007b), this monitoring period may not be

achieved (due to premature instrument failure, for example). Mars is, however – apart from Earth – the most observed planet in the solar system: there is therefore abundant empirical information from orbiters, landers and rovers on climatic variations across its surface.

Large scale simulations such as the Mars Climate Database (MCD – Millour et al., 2012) and the Mars Global Reference Atmospheric Model (Mars-GRAM – Justh et al., 2011) integrate these empirical data to model Mars climate parameters. The model presented in Chapter 4 does not recover unsteady surface temperature to a precision or accuracy which would see any gains in surface temperature information above in situ measurements and estimates by MCD or Mars-GRAM. Also, in situ surface data may be available from the surface elements of a heat flow probe, following a long term monitoring period. Additionally results in Sections 3.4.1.2, 3.6 and 5.3.1 below show that the surface temperature becomes more sinusoidal with depth. This means that temperature measurements taken below unknown short period variations can be satisfactorily modelled by simple sinusoidal surface temperatures. Therefore, in this context, the Martian surface temperature may be considered known and/or knowable to a degree which would exclude it from the list of predictions in a temperature inversion.

Empirical measurements and outputs by MCD and Mars-GRAM are, however, limited to a superposed surface temperature while the model used here treats the unsteady and steady temperatures separately, in a partitioned solution. The steady temperature can be considered the mean of measurements made over at least a full Martian year; subtracting this from the superposed temperature then gives the unsteady temperature. Unknown longer term variations may contaminate the steady temperature in this sense, however Grott et al. (2007b) show that these should not perturb the heat flow beyond 15 %. The model is capable of simultaneously optimizing the steady and unsteady temperatures along with the basal (planetary) heat flow (see Appendix 9.4.7). This can isolate long term unsteady temperature variations as shown for Earth-focused studies (Beck et al., 1992; Shen and Beck, 1992; Shen et al., 1992; Wang, 1992). However the <5 m depth scales

proposed for heat flow probes like HP^3 are too shallow to effectively sample the effects of long term surface temperature variations.

The surface temperatures presented here (Figure 5.3) are simulated by Mars-GRAM, based on the measurement sites identified in Figure 5.2. Mars-GRAM surface temperatures are generated for each site using a nominal Martian climate scenario – the timings loosely coincide with the proposed timeline of the InSight mission which is slated to land on September 20, 2016 and begin taking measurements around 60 Sols later or after the heat flow probe reaches its maximum depth, continuing for at least 700 Sols to the end of mission (Spohn et al., 2012; NASA, 2013b).

Figure 5.3 shows that the annual mean surface temperature (blue curve) varies appreciably with location, indicating that it is not the best candidate for steady temperature on Mars, in estimating global planetary heat flow. Mean Martian heat flow is expected to remain constant over timescales of millions of years (e.g. Grott and Breuer, 2010), therefore estimating the steady temperature over a longer term leads to a more accurate heat flow estimate. In the case where there is only short term data or data from a single measurement, steady temperature may be estimated from a long term temperature average as output by a Martian Global Climate Model (GCM). For the demonstration purposes of this project, the simple case of the annual mean surface temperature as the steady surface temperature is considered sufficient.

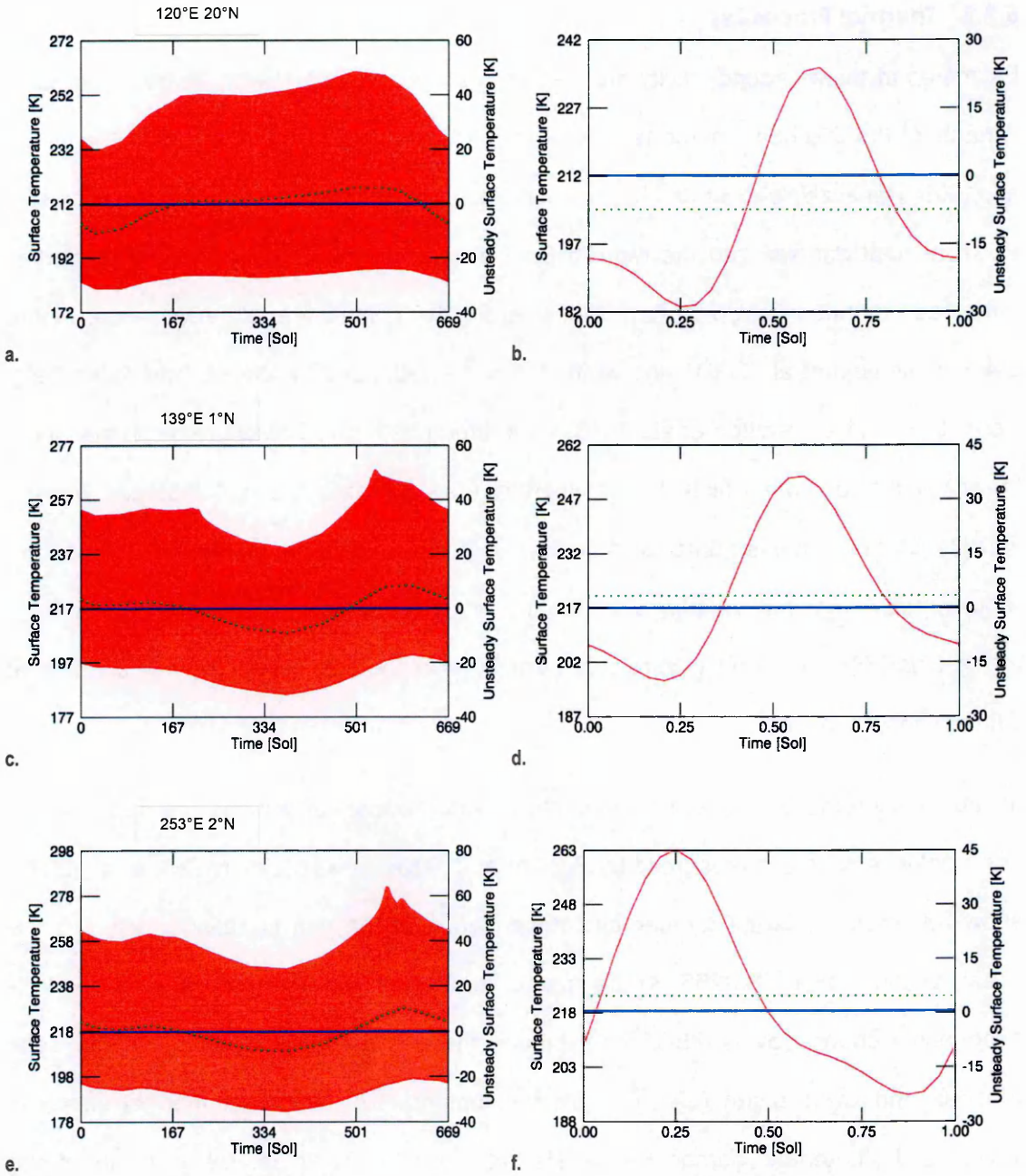

Figure 5.3. Surface temperatures T_S and T_S^U) used in simulations for measurement sites at 120°E 20°N (a, b), 139°E 1°N (c, d) and 253°E 2°N (e, f) as seen in Figure 5.1. The left plots are of Martian temperatures over one Martian year while the right plots show temperatures for the first Sol of the year. The solid red curves show diurnal temperature variation, the dotted green curve the diurnal mean, and the solid blue curve the annual mean. These temperatures were produced by Mars-GRAM time stepping over 1 Martian hour (see the Mars Climate Database (2013) for guidance on timings used).[6]

[6] The differences in diurnal variations at different sites are due to measurements starting at different local times. At 120°E 20°N (b), the local time is 22:42:21, at 139°E 1°N (d) the local time is

5.2.2 Thermal Properties

Estimates of thermal conductivity are derived from heat flow probe measurements using variants of the line heat source technique (or transient hotwire method – e.g. Seiferlin et al., 1996; Banaszkiewicz et al., 1997) where the conductivity is determined from the rate at which heat diffuses into the regolith from a heat source. Surface thermal properties have been mapped from orbit (e.g. Kieffer et al., 1977; Mellon et al., 2000 – see Figure 5.4; Christensen et al., 2001) and verified in some instances by landers and rovers (e.g. Zent et al., 2010; Hamilton et al., 2013). The referenced orbital measurements are in the thermal infrared, from which thermal inertias (see Sections 3.5 and 3.6) are derived. Results of these measurements indicate appreciable variation of thermal inertia with temperature. Regional variations in thermal inertia are associated with variations in regolith particle size, which correlates strongly with thermal conductivity (Piqueux and Christensen, 2009a,b).

In-situ measurements of thermal conductivity and thermal capacity by the TECP in the north polar regions are presented by Zent et al. (2010). The results in Zent et al. (2010) show relatively moderate temperature dependence of the thermal conductivity (~37 % linear change over 185-255 K) compared to that of the thermal capacity (~44 % exponential change over 185-255 K), though there is appreciable scatter in the data. Piqueux and Christensen (2011) model the temperature dependent thermal inertia of loose, and cemented homogeneous Martian regolith. Their results point to strong temperature dependence of the specific heat (75 % change over 150-315 K), and bulk (average) conductivity (30-50 % over 150-315 K for loose regolith, being largely controlled by the pore filling gas conductivity; lower percentage for cemented regolith where pore filling gas conductivity is less important). The Martian atmosphere is predominantly CO_2, the thermal conductivity of which is strongly temperature dependent, as noted by Piqueux and Christensen (2011).

23:58:21 and at and 253°E 2°N (f) the local time is 07:22:21 – all times Local Mean Solar Time (LMST – see Appendix 9.5.1).

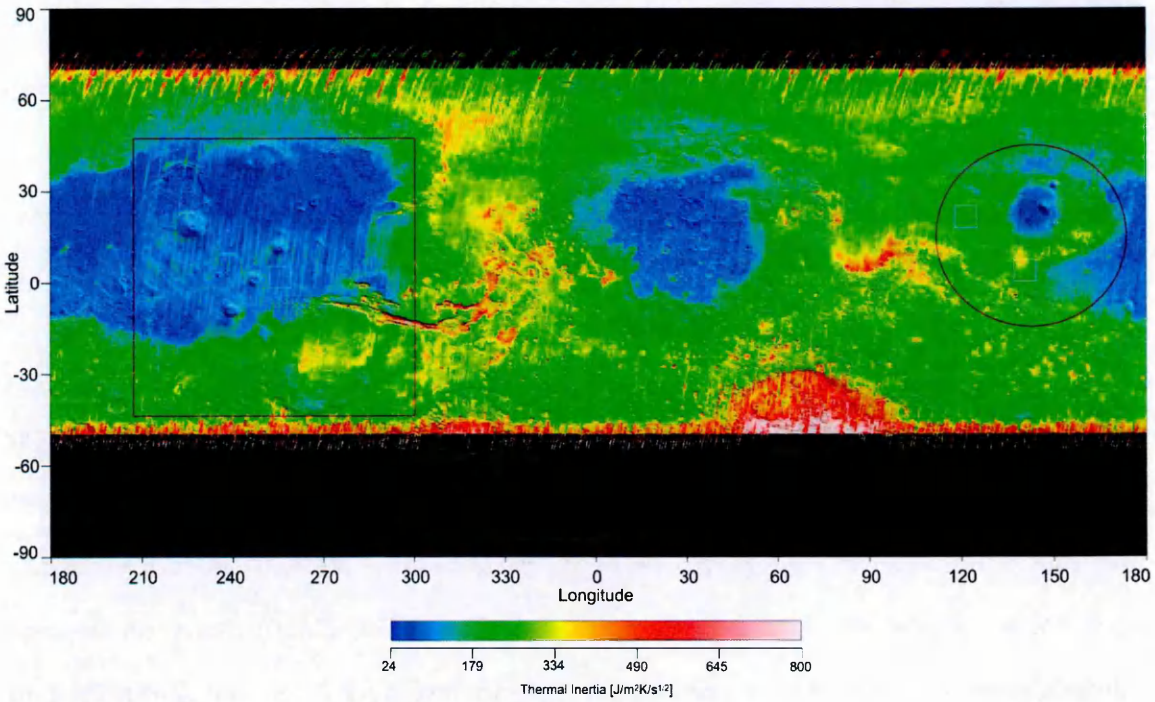

Figure 5.4. Nighttime thermal inertia mapped by the Thermal Emission Spectrometer (TES) projected onto a Mars Orbiter Laser Altimeter (MOLA) topographic map. Both instruments are aboard the now defunct Mars Global Surveyor orbiter. The rectangles show sites at 120°E 20°N, 253°E 2°N and 139°E 1°N as seen in Figure 5.2. The red rectangle identifies the Tharsis region, the red ellipse the Elysium region. The small white circle indicates the approximate site of the Phoenix lander at ~234°E 68°N Zent et al., 2010. TES map after Mellon et al. (2000). MOLA projection credit NASA, Ames Research Center.

The model of Chapter 4 is not capable of simulating temperature dependent thermal properties; however, the largest (diurnal) variations of temperature are confined to the upper few cm of Martian regolith while seasonal effects are mitigated by the smaller variation in temperature. These effects are reduced with depth and as the temperature amplitude is damped. Therefore, at greater depth, the model's limitations become less important in recovering the basal heat flow. Additionally the variation of the unsteady temperature about the steady (mean) value means that temperature dependent thermal properties will also vary about a mean value which can be associated with the steady temperature. Effectively this means that temperature averaged thermal properties (associated with the steady temperature) can be used in determining the heat flow. Therefore here, depth-dependent, annual temperature averaged thermal properties are

used.[7] Additionally, shallow subsurface depths, in which most of the temperature variation occurs, can be ignored, providing the number of heat flow probe sensors that access depths below this variation (at least two) is sufficient. Nonlinearities in the temperature dependence of the thermal conductivity can further lead to increases in the mean (steady) temperature – any such increase can be captured by surface temperature measurements of the heat flow probe.

Grott et al. (2007b) model depth-dependent thermal conductivities which monotonically increase from ~0.01 W/m/K (the thermal conductivity of CO_2 gas at the temperatures considered) to 0.02 and 0.1 W/m/K respectively, at depth – the same model is used to present the model simulations in Section 3.3.3. Zent et al. (2010) derive an average thermal conductivity of 0.08 W/m/K for the dust mantle layer (~15 mm) at the Phoenix landing site fitting better to the high conductivity model of the former. The aforementioned conductivities are consistent with the thermal inertias of Figure 5.4. Piqueux and Christensen (2011) model thermal conductivities up to 0.15 W/m/K at a typical Martian pressure of 530 Pa and typical Martian temperatures of 150-315 K. Grott et al. (2007b) use a specific heat capacity of 600 J/kg/K and an monotonic density model analogous to the conductivity model from a surface value of 1000 increasing monotonically to 1750 kg/m^3. Piqueux and Christensen (2011) note the results of Robie et al. (1970) which present measurements for specific heats of Apollo lunar samples – these show an almost linear variation of ~430-730 J/kg/K, over 150-315 K while density varies little with temperature. Zent et al. (2010) measure an average thermal capacity of 1.05 $MJ/m^3/K$ for the Phoenix landing site dust mantle layer – which equals the asymptotic value of Grott et al. (2005) and is compatible with results in Piqueux and Christensen (2011).

[7] The validity of the use of temperature averaged thermal properties is reduced for instantaneous measurements, or measurements which fall well short of a seasonal or diurnal temperature cycle associated with the skin depth.

The mean annual surface temperatures from the measurement sites (Figure 5.3) along with the thermal inertia model of Piqueux and Christensen (2011) for uncemented regolith are used to derive regolith grain sizes. Mars-GRAM simulations also show appreciable variation of annual mean surface pressure between the measurement sites (789, 709 and 340 Pa for 120°E 20°N, 139°E 1°N and 253°E 2°N[8] respectively) – the annual mean pressure from each site is used, along with the measurements of Presley and Christensen (1997a,b), and the derived grain sizes to estimate associated surface thermal conductivity values. The specific heats and surface densities are reasonable estimates consistent with the former where smaller particle sizes are associated with lower densities. The derivations are summarised in Table 5.1.

Table 5.1. Derived regolith surface thermal properties at selected measurement sites based on the thermal conductivity-temperature relationships of Piqueux and Christensen (2011) and the thermal conductivity-pressure relationships of Presley and Christensen (1997a),1997b). The regolith is assumed uncemented. φ_E is the location, T_S^S is the annual mean temperature, P_S^S the annual mean pressure, I the mapped thermal inertia, l the derived particle size, k the derived temperature and pressure averaged surface thermal conductivity, ρ derived surface density and c the calculated specific heats.

φ_E [+°E +°N]	T_S^S [K]	P_S^S [Pa]	I [J/m^2/K/s$^{1/2}$]	l [μm]	k [W/m/K]	ρ [kg/m^3]	c [J/kg/K]
120°E 20°N	212	789	234	800	0.060	1100	830
139°E 1°N	217	709	234	1000	0.065	1200	702
253°E 2°N	218	340	76	30	0.008	1000	722

Hypothetical depth profiles are plotted in Figure 5.5. The regolith is assumed to be uncemented, due to the low thermal inertia, based on the results of Piqueux and Christensen (2011). The results of Bridges et al. (2010) suggest some degree of cementation may be possible at the Tharsis site though the results of Nowicki and Christensen (2004) support a fine grained, uncemented material, as used here. The upper

[8] Note the high altitude of the Tharsis site (253°E 2°N) from Figure 5.2, hence the low pressure.

5 m of regolith can have complex stratigraphy and lithology, as suggested by the results of Stack et al. (2013) – the range of errors used in the measurements of Section 5.3.2 account for unexpected temperature gradients which may occur in arbitrarily layered regolith. The lunar-like parameterizations of depth variation used in Grott et al. (2007b) are adapted here for thermal conductivity and density depth profiles. The results of Fountain and West (1970) and Presley and Christensen (1997a,b) indicate a linear relationship between conductivity and density, which is adopted in the profiles of Figure 5.5. Here, the depth variation represents an idealised, thick dust mantle which is compressed at depth to the point of sedimentation. Asymptotic values of thermal conductivity and density are within the range of values discussed by Clifford and Fanale (1985) and are compatible with the values present in Piqueux and Christensen (2011). The thermal property values at depth are arbitrarily chosen to mirror the relative magnitudes of the surface values, given the fact that the depth variation of Martian thermal properties is currently unknown. The specific heat capacity is held constant with depth. Table 5.2 lists the resulting thermal property values at 20 m depth.

Table 5.2. Hypothetical regolith 'high' and 'low' subsurface thermal properties at selected measurement sites guided by the surface thermal properties listed in Table 5.1. These are in line with the analyses of Clifford and Fanale (1985) and compatible with values present in Piqueux and Christensen (2011). The latitude and east longitude are represented by φ_E, k_{20} is the thermal conductivity and ρ_{20} the density at 20 m.

φ_E [+°E +°N]	k_{20} [W/m/K]		ρ_{20} [kg/m^3]	
	LOW	HIGH	LOW	HIGH
120°E 20°N	0.1	1.0	1500	1800
139°E 1°N	0.2	2.0	1700	2200
253°E 2°N	0.02	0.2	1200	1500

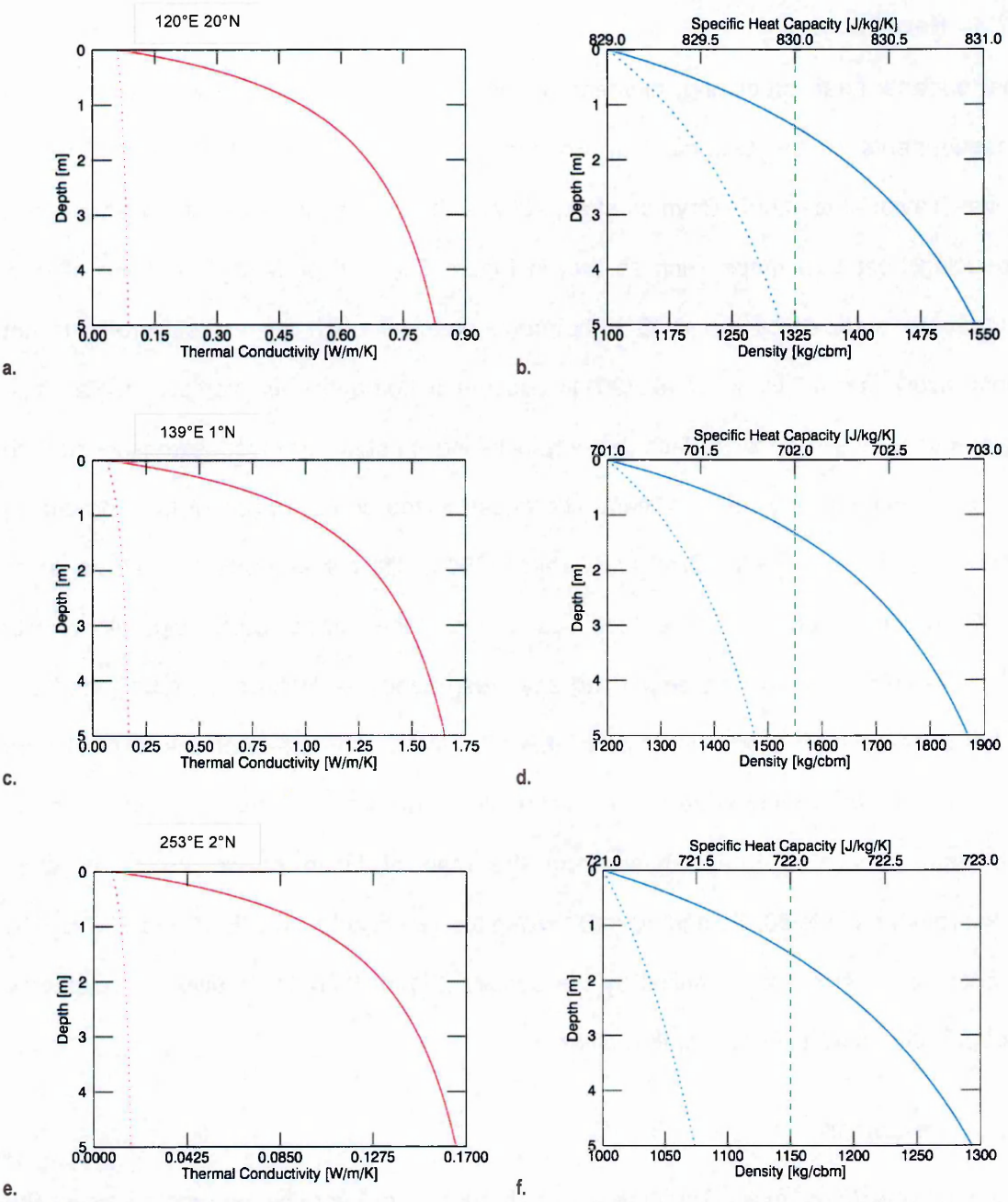

Figure 5.5. Derived hypothetical conductivity k, density ρ and specific heat capacity c for measurement sites at 120°E 20°N (a-b), 139°E 1°N (c-d) and 253°E 2°N (e-f) as seen in Figure 5.1. The red curves show conductivity variation, the blue curves the density variation and the green curves the constant specific heat. The dotted and solid curves indicate associated thermal conductivities and densities.

5.2.3 Heat Sources

The surface heat producing element distribution on Mars has been derived from measurements by the Gamma Ray Spectrometer (GRS) on the 2001 Mars Odyssey orbiter (Taylor et al., 2006; Boynton et al., 2007) – these measurements are in fact used in producing heat flow maps such as that in Figure 5.1. The surface distribution of heat sources as mapped by the GRS is heterogeneous although the vertical profile is not conclusively known. Hahn et al. (2011) assume a homogeneous vertical profile citing several lines of evidence (or lack thereof) including no plate tectonics, extensive surface impact gardening, and no significant differences in the concentration of heat producing elements in impact ejecta. Grott and Breuer (2010) cite the arguments of Taylor et al. (2006) which include no plate tectonics and surface impact gardening, along with extensive volcanic intrusions smoothing any heterogeneities. Hahn et al. (2011) derive a global average heat production rate of 4.9×10^{-11} W/kg. The effect of this level of heat production on the temperature is not discernible at the precision being considered here. The heat production rate derived from the map of Hahn et al. (2011) for each measurement site is 60, 55 and 50 $\times10^{-11}$ W/kg for 120°E 20°N, 139°E 1° and 253°E 2°N, respectively. These are multiplied by the density (Figure 5.5b,d,f) to give the volumetric heat production with similar depth profiles.

5.3 Scenarios

The main questions arising from the above discussion of heat flow parameters cover the measurement precision and accuracy required for relatively low versus high heat flows and low versus high thermal diffusivities. Low heat flow is more difficult to measure while high thermal diffusivity reduces the damping of the unsteady heat flow, resulting in greater masking of the planetary heat flow. A shortened monitoring period or too-shallow measurement depth will compound these difficulties. Scenarios are presented below which attempt to address these questions. Unknown inaccuracies in the thermal diffusivity contribute to inaccuracies in the basal heat flow estimate. The effects of these are studied

in Sections 4.2.1.2.3 and 4.3.1.3 – the results can be applied here and are therefore not investigated in the scenarios.

5.3.1 Forward Models

Hypothetical temperature profiles are generated based on 'high' (stagnant lid) and 'low' (plate cooling) heat flow regimes (as identified in Section 5.1; also see Dehant et al., 2012), and high and low conductivity models (Figure 5.5), for each measurement site. Representative temperature profiles generated by the forward model for the measurement sites are shown in Figure 5.6 (high conductivity) through Figure 5.7 (low conductivity) below – both in the 'high' heat flow, stagnant lid regime.

Evidently, at the high conductivities the unsteady surface heat flow is present at non-negligible magnitudes from 2-5 m, but to varying extents. The relatively high conductivities at the Elysium sites (120°E 20°N, 139°E 1°N) result in greater masking of the steady basal heat flow with the unsteady surface heat flow compared to the Tharsis site (253°E 2°N). Results of Section 4.2.1.2 indicate that several measurements, over a monitoring period of at least a seasonal cycle, are necessary to derive a robust estimate of the steady basal heat flow for the Elysium sites. Conversely, the former results suggest that one or two measurements over a monitoring period only a fraction of the seasonal cycle may suffice for the Tharsis site.

At low conductivities the unsteady surface heat flow is still universally present from 2-5 m at the Elysium sites (Figure 5.7a-d) but at much smaller amplitudes than the high conductivity scenarios. They are comparable to the high conductivity case at the Tharsis site (Figure 5.6e-f) – similar measurement requirements can be deduced. The steady basal heat flow is accessible towards 5 m at the Tharsis site for low conductivities (Figure 5.7e-f).

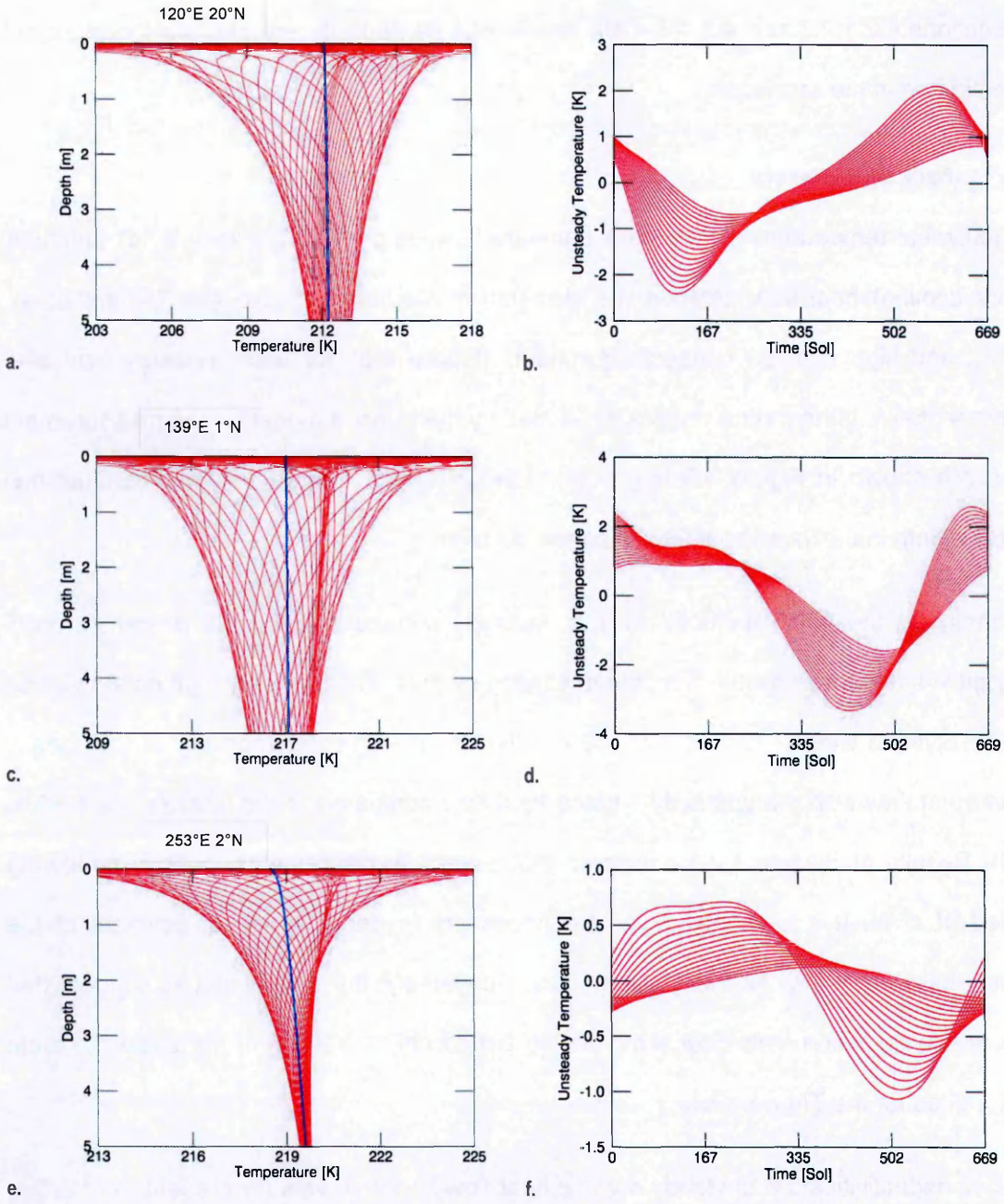

Figure 5.6. Forward modelled temperature profiles for measurement sites. The left contours are overlays of depth-dependent temperature T over time t of 669 Sol in ~13 Sol steps (overlapping contours indicate periods of relatively constant diurnal mean temperatures); the right contours are overlays of time-dependent temperature T^U over depth z of 2.3-4.7 m in 0.3 m steps (larger amplitudes towards the surface). These are from the respective high conductivity models of Figure 5.5 based on the 'high' heat flows of the stagnant lid regime where at 120°E 20°N (a-b), 139°E 1°N (c-d) and 253°E 2°N (e-f) the heat flow is 17, 15 and 22 mW/m/K respectively.

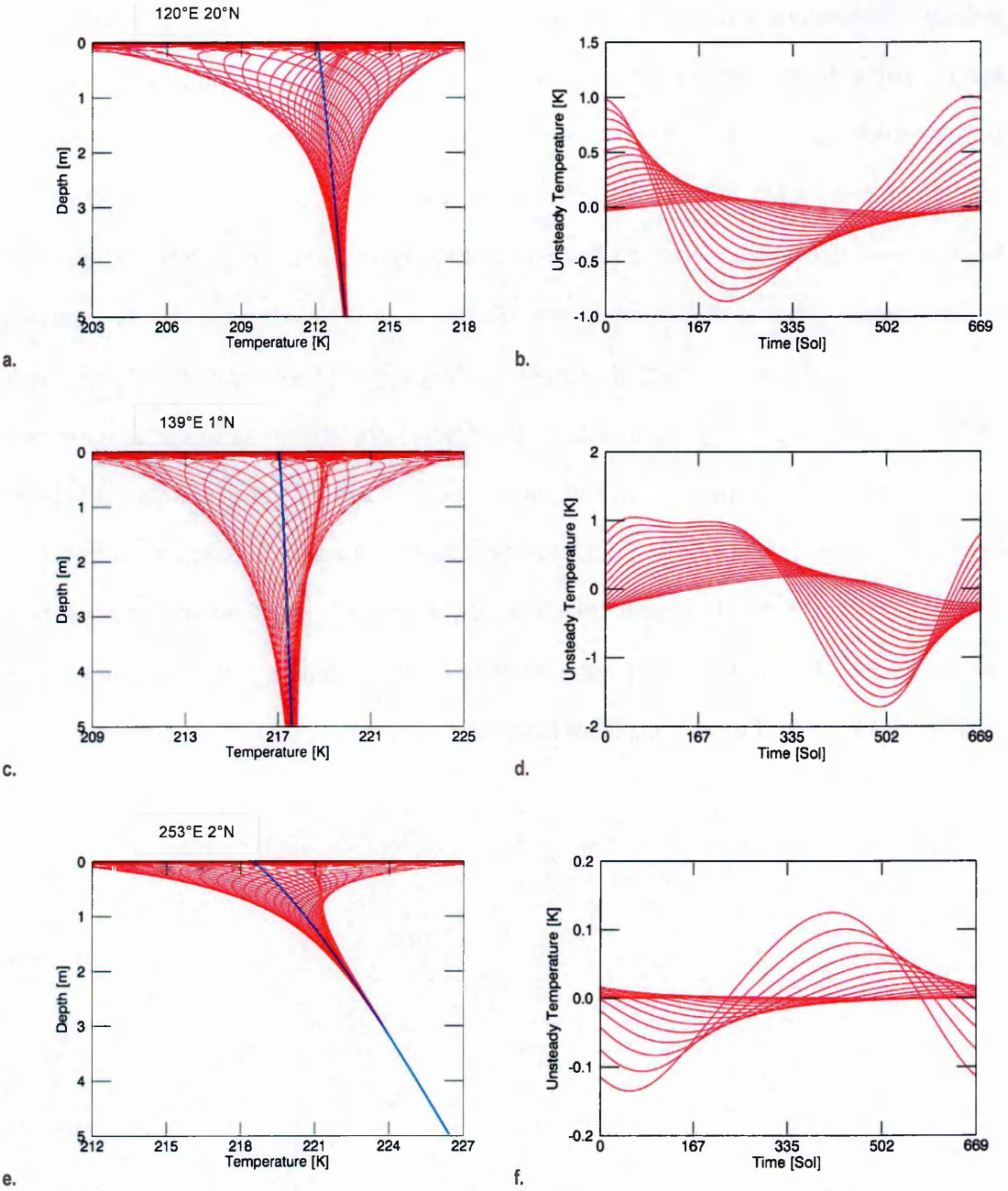

Figure 5.7. Forward modelled temperature profiles for measurement sites. The left contours are overlays of depth-dependent temperature T over time t of 669 Sol in ~13 Sol steps (overlapping contours indicate periods of relatively constant diurnal mean temperatures); the right contours are overlays of time-dependent temperature T^U over depth z of 2.3-4.7 m in 0.3 m steps (larger amplitudes towards the surface). These are from the respective low conductivity models of Figure 5.5 based on the 'high' heat flows of the stagnant lid regime where at 120°E 20°N (a-b), 139°E 1°N (c-d) and 253°E 2°N (e-f) the heat flow is 17, 15 and 22 mW/m/K respectively.

In an ideal situation an inversion is unnecessary for the Tharsis site with low conductivity, as the steady temperature gradient is between 0.65-1.45 K/m which dominates the

unsteady temperature envelope of between 1-30 mK (Table 5.3). Measurements are, however, likely to contain noise of unknown amplitude due to unknown subsurface heterogeneities and transient temperature perturbations[9]. Random noise with an amplitude of 1 K would obscure all temperature variation at 3-5 m for all the modelled scenarios, except the high conductivity cases at the Elysium sites (Figure 5.6a-d) and the low conductivity case at the Tharsis site (Figure 5.7e-f). Illustrations for the forward modelled results of the 'low' heat flow plate cooling regime (here, simply half the 'high' heat flow) can be found in Appendix 9.5.2 – the profiles are similar, as would be expected, save for a smaller temperature gradient, which requires greater measurement precision. Generally, low conductivity, and high heat flow which promote a steeper temperature gradient, and high thermal capacity which rapidly attenuates the unsteady surface heat flow with depth, are beneficial for basal heat flow measurement. This, of course, also follows from the forward model results of Chapter 3.

[9] For example due to volatiles.

Table 5.3. Unsteady temperature amplitudes and steady temperature gradients at depths z of 2, 3 and 5 m, along with heat flows and bulk conductivity; φ_E is the location, k_{BULK} the bulk thermal conductivity down to 20 m, F_B^S the basal heat flow, T_A^U the annual unsteady temperature amplitude and $\frac{dT^S}{dz}$ the steady temperature gradient at depth.

φ_E [+°E +°N]	k_{BULK} [W/m/K]	F_B^S [mW/m^2]	z [m] 2		3		5	
			T_A^U [K]	$\frac{dT^S}{dz}$ [K/m]	T_A^U [K]	$\frac{dT^S}{dz}$ [K/m]	T_A^U [K]	$\frac{dT^S}{dz}$ [K/m]
120°E 20°N	0.517	17	2.37	0.026	1.63	0.023	0.81	0.020
		8.5		0.013		0.011		0.010
	0.073	17	1.05	0.222	0.42	0.211	0.07	0.199
		8.5		0.111		0.106		0.099
139°E 1°N	1.02	15	3.06	0.011	2.30	0.010	1.35	0.009
		7.4		0.006		0.005		0.005
	0.122	15	1.52	0.107	0.81	0.098	0.24	0.089
		7.4		0.054		0.049		0.045
253°E 2°N	0.102	22	0.96	0.167	0.53	0.148	0.17	0.133
		11		0.026		0.020		0.015
	0.013	22	0.16	1.54	0.03	1.42	0.001	1.31
		11		0.770		0.710		0.653

5.3.2 Measurements

Measurement profiles are derived from the temperature profiles in Figure 5.6-Figure 5.7, with Gaussian noise of varying amplitudes as with the scenarios in Section 4.3. The noise considered here is of amplitude 10 mK, 100 mK and 1 K. These amplitudes are constant with depth[10] and reflect potential errors related to forward model limitations in simulating unknown subsurface heterogeneities and transient phenomena. Noise of the amplitude

[10] It may be the case that the noise decreases because transient insolation and atmospheric effects are restricted to the upper subsurface in nominal scenarios, or instrument precision increases with depth due to larger sensors being used, averaging temperatures over an increased depth range. These cases are tested in Section 4.3.1 and the results can be applied here.

used here is likely to obscure noise based on instrument precision which should be of the order of 1 mK (Grott et al., 2007b; Dehant et al., 2012), leading, in principle, to a temperature gradient error of the order of 1.5 mK/m. Fifteen sensors are used in the hypothetical heat flow probe based on the HP^3 description of Spohn et al. (2001b).[11] Measurement scenarios are tested both with accurate and inaccurate sensor locations, where the inaccuracies tend to increase with depth (Figure 5.8).[12]

Independent of the noise (error) level, several measurement scenarios are considered including a successful measurement down to 5 m over the course of a Martian year at high (1 Sol) time resolution[13] – here considered an ideal measurement. In other measurement scenarios the measurement is made for only a fraction of a Martian year (0.25, 0.5 and 0.75, for example due to instrument failure) and a fraction of the desired depth (2, 3 and 5 m, for example due to obstacles such as sedimented layers and/or large rocks, or instrument failure). A grid of the 36 resulting measurement scenarios for each of the 4 site scenarios is shown in Table 5.4. Representative profiles are shown in Figure 5.9 for the low conductivity, high heat flow (stagnant lid) measurement scenario. Equivalent profiles for the high conductivity scenario are shown in Appendix 9.5.3.

---

[11] Recall that in Section 4.2.1.2.2 no consistent trends in accuracy are observed when inverting a heat flow probe measurement to obtain the heat flow, using 10, 15, 20 or 25 sensors for a given measurement depth.

[12] A heat flow probe's position is known less accurately the further it travels into the regolith and is dependent on the accuracy and precision of its accelerometers. Encounters with material of varying density may also affect the positional accuracy.

[13] Here the measurement frequency is limited to 1 Sol where the diurnal mean is used for the unsteady surface temperature – considered reasonable as, here, the diurnal skin depth is less than 25 cm and does not play a part in masking the planetary heat flow. The temperature envelope down to 25 cm does affect the determined steady surface temperature, but a local mean surface temperature over 1 Martian year is not a true representation of the long term steady temperature, as pointed out in Section 5.2.1.

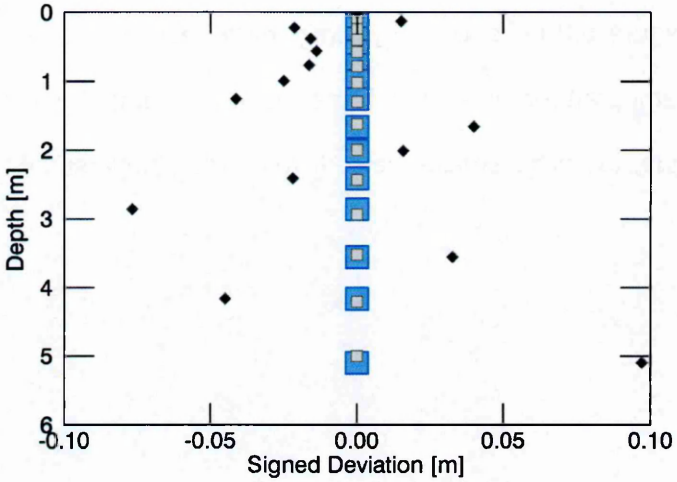

Figure 5.8. Errors in sensor depth z. The large blue squares represent the accurate sensor locations, the small grey squares the inaccurate sensor locations. The black diamonds represent signed deviations Δz of inaccurate from accurate sensor locations. An accompanying table can be found in Appendix 9.5.3.

Table 5.4. Grid of measurement scenarios (36 in total per scenario) simulated for each of the forward modeled scenarios of Section 5.3.1 and Appendix 9.5.2.

DEPTH [m]	MONITORING PERIOD [~MARTIAN YEARS]				ERROR [K]
	0.25	0.5	0.75	1.0	
2.0					0.01-1.0
3.0					
5.0				OPTIMAL	
	168 (1)	334 (1)	501 (1)	669 (1)	
	NUMBER OF MEASUREMENTS (TIME RESOLUTION [SOL][14])				

All other measurement scenarios can be visualised using those plotted in Figure 5.9 (c, d, f): measurements which fall short of one Martian year are more constrained in the range

[14] For monitoring periods of 0.25, 0.5 and 0.75 Martian years simulations were run with measurement frequencies (timer resolution) of 3.91, 1.99 and 1.33 Sol. The results follow those in Section 4.2.1.2.2 such that the denser measurements produce more accurate optimized heat flows, particularly at shallower sensor depths.

of temperatures; measurements which fall short of the desired depth are cut off at 2, 3 or 5 m as shown in Figure 5.9 (a, c, e – physically interpreted as the failure of the lowest sensors to record temperatures or approach the required depth). 1 K noise is considered a worst case scenario; therefore smaller noise levels simply have smaller deviations from the true profiles.

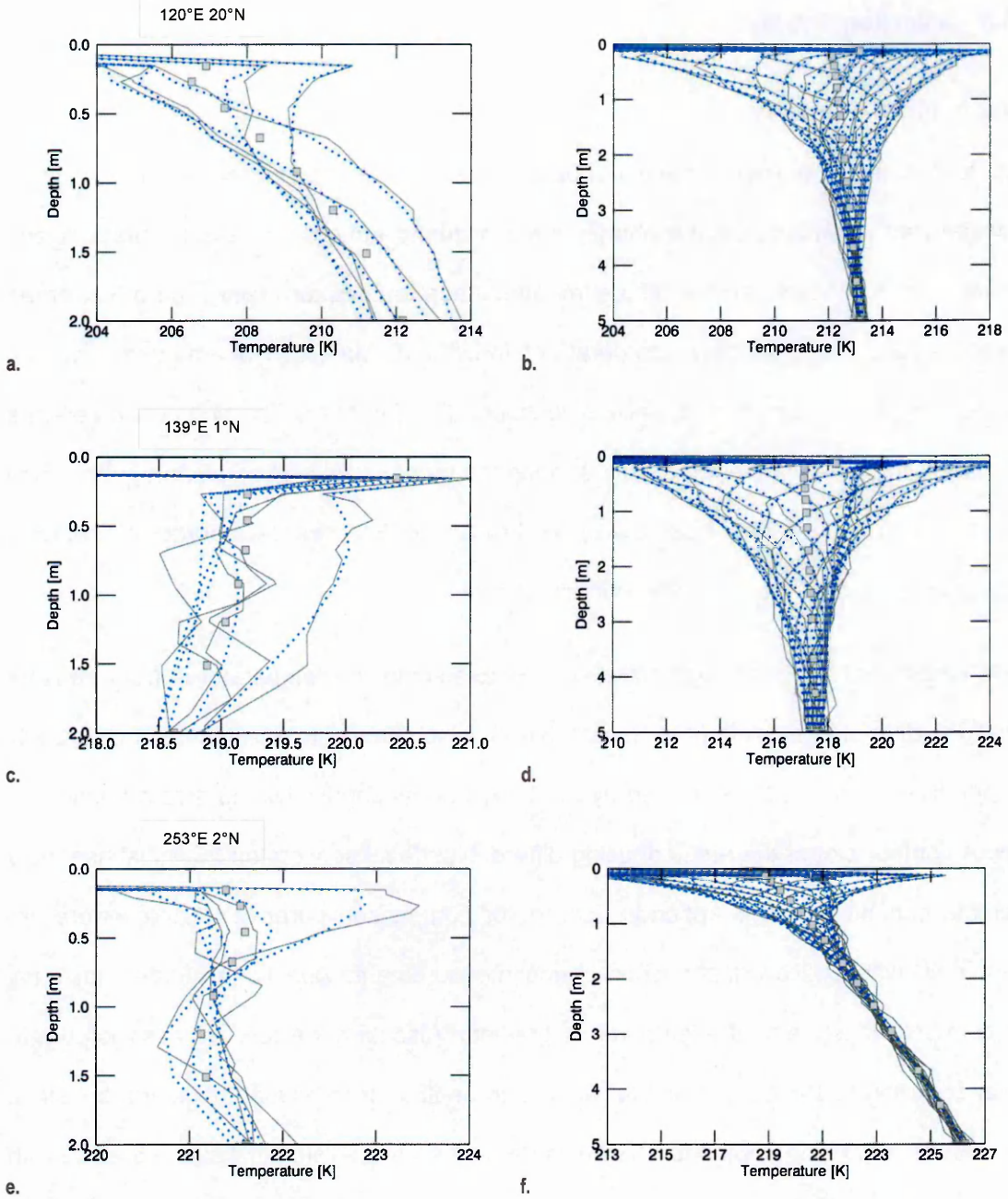

Figure 5.9. Representative profiles for measurements with 1 K additive noise for sites at 120°E 20°N (a-b), 139°E 1°N (c-d) and 253°E 2°N (e-f) for the low conductivity, high heat flow scenario. The plots are overlays of temperature-depth profiles in ~33 Sol steps over a monitoring period of: (a, c, e) 168 Sol down to 2 m depth; (b, d, f) 669 Sol down to 5 m depth. The solid grey curves represent the noisy measurement while the dotted blue curves illustrate the true profiles. The grey squares are sensor locations (innacurate) plotted at the true mean temperature at a particular depth – the surface sensor is not representative due to the high amplitude, high frequency diurnal variation of surface temperature

5.3.3 Inversion Results

5.3.3.1 Initial Estimates

Due to the large diurnal surface temperature amplitude, the larger the time interval between measurements, or the shorter the monitoring period, the less accurate is any derivation of the diurnal and/or annual mean surface temperature (see Figure 5.3, green dotted curves). Therefore here, temperatures forecast by Mars-GRAM are used to ensure reliable results. In practical situations without MCD or Mars-GRAM the temperature measurement may be inverted for the surface temperature as well as planetary heat flow (see Sections 4.2.2-4.2.3). Also, the upper few cm of data can be ignored, as noted in Section 5.2.1 – here, the surface sensor is ignored.

Initial basal heat flows are estimated by first averaging the temperatures from sensors below the diurnal skin depth (see Section 3.4.2), which provides an estimate of the steady temperature. This is then multiplied by the bulk thermal conductivity to give a basal heat flow. A contour plot of the result of using different 'surface' sensors on the initial heat flow estimate can be found in Appendix 9.5.4.1 for comparison purposes. Large errors are associated with shallow-depth, short-period measurements due to the larger unsteady temperature influence on the temperature gradient. Also, larger errors are associated with larger bulk conductivities and annual wave skin depths for individual measurement sites. The annual wave skin depths for the measurement sites are listed in Table 5.5 along with bulk conductivity. [15]

[15] The averaging method provides an efficient standard procedure to use in calculating initial heat flows across the large number of scenarios. It leads to large inaccuracies in some cases, as evidenced by the numbers in Table 5.6-Table 5.8 and Appendix 9.5.4.1. In practice, other a priori information is necessary for a reasonably accurate first estimate of the heat flow.

Table 5.5. Measured skin depths of the annual unsteady temperature z_{SKIN} of the forward modelled site scenarios along with bulk conductivity k_{BULK} down to 20 m[16]

LOCATION [+°E +°N]	k_{BULK} [W/m/K]	z_{SKIN} [m]
120°E 20°N	0.517	1.45
	0.073	0.91
139°E 1°N	1.02	1.89
	0.122	1.07
253°E 2°N	0.102	0.56
	0.013	0.44

For the Elysium site at 120°E 20°N (see Table 5.6 and Appendix 9.5.4.1) only 18 of the 144 initial estimates fall within 10 % of the true value ($\epsilon_{F_B^{S0}} \leq 0.1$) – these are nearly all low conductivity ($k_{BULK} = 0.073$ W/m/K) site scenarios where the monitoring period is 1 Martian year with 2 high conductivity ($k_{BULK} = 0.517$ W/m/K) exceptions. All sensor depths (2-5 m) and both high (17 mW/m^2) and low (8.5 mW/m^2) heat flow scenarios are represented.

Only 13 of the initial estimates fall between 10-25 % of the true value ($0.1 < \epsilon_{F_B^{S0}} \leq 0.25$) – these are nearly all high conductivity site scenarios where the monitoring period is 1 Martian year, with 2 low conductivity exceptions. All sensor depths and both high and low heat flow scenarios are represented.

Just 5 of the initial estimates fall between 26-50 % of the true value ($0.25 < \epsilon_{F_B^{S0}} \leq 0.5$) – these are high conductivity site scenarios monitored over 1 Martian year, nearly all with sensor depths down to 5 m, and high and low heat flows. There is one exception with a sensor depth of 3 m.

[16] These skin depth estimates are therefore high and are to be considered in a relative sense.

The 108 other initial estimates range between 50-8233 %[15] inaccurate ($0.50 < \epsilon_{F_B^{So}} \leq 82.33$). They include all measurement and site scenarios except those where the monitoring period is 1 Martian year. Of the preceding estimates: low conductivity site scenarios with longer monitoring periods and deeper sensor depths tend to be in the more accurate sub-range; high conductivity site scenarios with shorter monitoring periods and shallower sensor depths tend to be in the least accurate sub-range.

Table 5.6. Grid of initial heat flow estimate relative error magnitudes $\epsilon_{F_B^{So}} = \left|\frac{F_B^{So}}{F_B^{ST}} - 1\right|$ (green borders – see Appendix 9.1 for symbol definitions) at Elysium site 120°E 20°N for the low conductivity k scenario with a heat flow F_B^{ST} of 17 mW/m². The shaded cells show values which are not improved by the algorithm. The bulk conductivity down to 20 m is k_{BULK} [W/m/K] and z_{SKIN} [m] is the skin depth.

$k_{BULK} = 0.073$		MONITORING PERIOD [~MARTIAN YEARS]				$F_B^{ST} = 0.017$
		0.25	0.5	0.75	1.0	
DEPTH [m]	2.0	11.37	4.98	1.45	0.00	1.0
		11.59	5.04	1.49	0.05	0.1
		11.60	5.04	1.49	0.05	0.01
	3.0	7.61	3.85	1.32	0.03	1.0
		7.65	3.86	1.33	0.05	0.1
		7.65	3.86	1.33	0.05	0.01
	5.0	3.72	2.04	0.74	0.10	1.0
		3.71	2.02	0.73	0.10	0.1
		3.71	2.02	0.73	0.10	0.01
z_{SKIN} =0.91 m		168 (1)	334 (1)	501 (1)	669 (1)	120°E 20°N
		NUMBER OF MEASUREMENTS (TIME RESOLUTION [SOL])				

ERROR [K]

For the Elysium site at 139°E 1°N (see Table 5.7 and Appendix 9.5.4.1) just 5 of the 144 initial estimates fall within 10 % of the true value ($\epsilon_{F_B^{So}} \leq 0.1$) – these are all low conductivity ($k_{BULK} = 0.122$ W/m/K) site scenarios, nearly all with monitoring period of 1

Martian year with 1 exception over 0.5 Martian years. Interestingly, only sensor depths (2-3 m) are represented while both high (15 mW/m^2) and low (7.4 mW/m^2) heat flow scenarios are represented.

Only 16 of the initial estimates fall between 10-25 % of the true value ($0.1 < \epsilon_{F_B^{So}} \leq 0.25$) – these are nearly all low conductivity site scenarios where the monitoring period is 1 Martian year, with 1 high conductivity ($k_{BULK} = 1.02$ W/m/K) exception and 2 exception where the monitoring period is 0.5 Martian years. All sensor depths and both high and low heat flow scenarios are represented.

Similarly, 15 of the initial estimates fall between 26-50 % of the true value ($0.25 < \epsilon_{F_B^{So}} \leq 0.5$) – these are mostly high conductivity site scenarios monitored over 1 Martian year, with 2 exception monitored over 0.5 Martian years. All sensor depths and both high and low heat flow scenarios are represented.

The 108 other initial estimates range between 50-4839 %[15] inaccurate ($0.50 < \epsilon_{F_B^{So}} \leq 48.39$). They include all measurement and site scenarios with low conductivity site scenarios tending to be in the more accurate sub-range and high conductivity site scenarios tending to be in the least accurate sub-range.

Table 5.7. Grid of initial heat flow estimate relative error magnitudes $\epsilon_{F_B^{S0}} = \left|\frac{F_B^{S0}}{F_B^{ST}} - 1\right|$ (green borders – see Appendix 9.1 for symbol definitions) at Elysium site 139°E 1°N for the low conductivity k scenario with a heat flow F_B^{ST} of 15 mW/m². The shaded cells show values which are not improved by the algorithm. The bulk conductivity down to 20 m is k_{BULK} [W/m/K] and z_{SKIN} [m] is the skin depth.

$k_{BULK} = 0.122$		MONITORING PERIOD [~MARTIAN YEARS]				$F_B^{ST} = 0.015$
		0.25	0.5	0.75	1.0	
DEPTH [m]	2.0	5.20	0.04	5.26	0.03	1.0
		5.50	0.17	5.20	0.10	0.1
		5.48	0.19	5.20	0.11	0.01
	3.0	5.76	1.40	3.23	0.02	1.0
		5.71	1.40	3.23	0.13	0.1
		5.71	1.38	3.23	0.12	0.01
	5.0	4.30	1.81	1.25	0.19	1.0
		4.19	1.83	1.22	0.19	0.1
		4.19	1.82	1.22	0.19	0.01
z_{SKIN} =1.07		168 (1)	334 (1)	501 (1)	669 (1)	139°E 1°N
		NUMBER OF MEASUREMENTS (TIME RESOLUTION [SOL])				

ERROR [K]

For the Tharsis site (see Table 5.8 and Appendix 9.5.4.1), 29 of the 144 initial estimates fall within 10 % of the true value ($\epsilon_{F_B^{S0}} \leq 0.1$) – these are all over monitoring periods of 0.75-1 Martian year. All sensor depths (2-5 m), high ($k_{BULK} = 0.102$ W/m/K) and low ($k_{BULK} = 0.013$ W/m/K) conductivity and both high (22 mW/m^2) and low (11 mW/m^2) heat flow scenarios are represented.

Further, 22 of the initial estimates fall between 10-25 % of the true value ($0.1 < \epsilon_{F_B^{S0}} \leq 0.25$) – a similar range of scenarios as with the preceding more accurate estimates is represented, though with the inclusion of 0.5 Martian year monitoring periods.

Additionally 24 of the initial estimates fall between 26-50 % of the true value ($0.25 < \epsilon_{F_B^{So}} \leq 0.5$) – again, all scenarios are represented except measurements covering a 1 Martian year monitoring period.

A total of 69 other initial estimates range between 50-744 %[15] inaccurate ($0.50 < \epsilon_{F_B^{So}} \leq 7.44$). They include all measurement and site scenarios except those where the monitoring period is 1 Martian year. Of the former estimates, high conductivity site scenarios tend to occupy the least accurate sub-range.

Table 5.8. Grid of initial heat flow estimate relative error magnitudes $\epsilon_{F_B^{So}} = \left|\frac{F_B^{So}}{F_B^{ST}} - 1\right|$ (green borders – see Appendix 9.1 for symbol definitions) at Tharsis site 253°E 2°N for the low conductivity k scenario with a heat flow F_B^{ST} of 22 mW/m². The shaded cells show values which are not improved by the algorithm. The bulk conductivity down to 20 m is k_{BULK} [W/m/K] and z_{SKIN} [m] is the skin depth.

$k_{BULK} = 0.013$		MONITORING PERIOD [~MARTIAN YEARS]				$F_B^{ST} = 0.022$
		0.25	0.5	0.75	1.0	
DEPTH [m]	2.0	0.86	0.28	0.30	0.00	1.0
		0.86	0.28	0.31	0.01	0.1
		0.86	0.28	0.32	0.01	0.01
	3.0	0.57	0.21	0.16	0.04	1.0
		0.57	0.22	0.16	0.03	0.1
		0.57	0.22	0.16	0.03	0.01
	5.0	0.42	0.22	0.01	0.12	1.0
		0.42	0.22	0.01	0.12	0.1
		0.42	0.22	0.01	0.12	0.01
		168 (1)	334 (1)	501 (1)	669 (1)	ERROR [K]
z_{SKIN} =0.44		NUMBER OF MEASUREMENTS (TIME RESOLUTION [SOL])				253°E 2°N

The results above indicate a more strict sensitivity to monitoring period than to measurement depth which is confirmed in a general trend analysis. The initial heat flow

estimate accuracy negatively correlates with the measurement noise level though the effect is negligible.[17]. Generally, the initial heat flow estimates are more accurate for shallower skin depth, higher true heat flow, deeper sensor penetration and longer monitoring period, all else being equal. This explains why the initial estimates for the Tharsis site are generally better than those for the Elysium sites. Notably, the relative accuracy of initial estimates is approximately inversely proportional to the heat flow magnitude – i.e. when the true heat flow doubles, the error in the initial estimate is approximately halved, all else being equal. Figure 5.10 illustrates trends in the initial heat flow estimate accuracy, using the averaging method, arising from 3D interpolation of data points – the small effect of the measurement noise level is not visible.

Inaccurate sensor locations lead to inaccuracies in thermal properties and temperature, at depth, which in turn lead to inaccurate heat flow estimates. However, in most cases the location inaccuracies used here do not perturb the errors in initial or optimized heat flows by more than 1-3 %. The 2-3 % errors occur towards the surface (2 m) while the 1 % errors occur at 3-5 m, despite the fact that location inaccuracies tend to be smaller towards the surface. The difference is due to the larger temperature gradients towards the surface where location accuracy is more important.

[17] The initial estimate accuracy is also affected by the accuracy of the conductivity (see Grott, et al., 2007 for an analysis). In particular, the non-linear conductivity gradient results in a nonlinear temperature gradient which is not assumed in any heat flow estimate using bulk conductivity and two (surface and basal) temperature sensors.

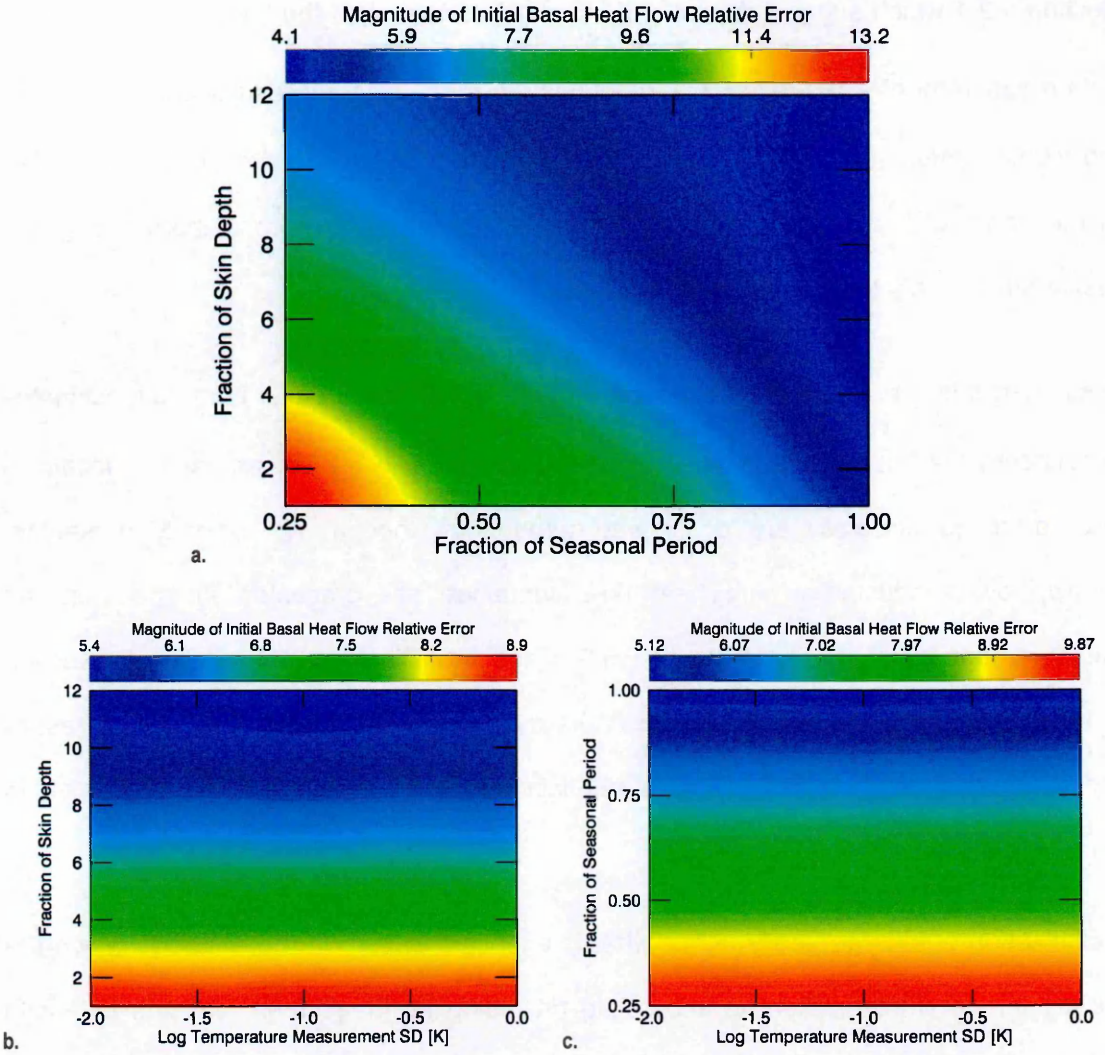

Figure 5.10. Trends $\overline{\epsilon_{F_B^{S0}}}$ in relative error $\epsilon_{F_B^{S0}} = \left|\frac{F_B^{S0}}{F_B^{ST}} - 1\right|$ of initial heat flow estimates F_B^{S0} to the true value F_B^{ST} across all measurement scenarios, interpolated from 3D scatterplots. The $\overline{\epsilon_{F_B^{S0}}}$ can be considered as central estimators of the heat flow distribution at particular postions defined by the axes. Contour: a. shows $\overline{\epsilon_{F_B^{S0}}}$ as a function of the ratio of basal sensor depth to annual skin depth r_z, and the ratio of monitoring period to seasonal period r_t; b. shows $\overline{\epsilon_{F_B^{S0}}}$ as a function of r_z and measurement noise amplitude σ_d (the standard deviation); c. shows $\overline{\epsilon_{F_B^{S0}}}$ as a function of r_t and σ_d. Note that $\epsilon_{F_B^{S0}}$ values for each σ_d, r_t and r_z are respectively stacked in a., b. and c., accounting for the differences in $\overline{\epsilon_{F_B^{S0}}}$ extrema.

5.3.3.2 *Optimized Heat Flow*

In optimizing the heat flow F_B^S, the assumed error in the temperature data measurement $\boldsymbol{d}$ – the standard deviation $\sigma_{\boldsymbol{d}}$ – is set to the added noise levels of 10 mK, 100 mK and 1 K. The error in the initial basal heat flow estimate – the standard deviation $\sigma_{F_B^S}$ – is set an order of magnitude greater than the data error. This is consistent with the results of

Section 4.2.1 which suggest the ratio of standard deviations of the basal heat flow to the data measurement – SD ratio $r_d^{F_B^S}$ – produces the most accurate results at $r_d^{F_B^S} = 10$. For the measurement scenarios which fall short of the ideal depth, the simulations are limited to the depth of the deepest sensor. This is because heat flow probe thermal property measurements are limited to the same depth.

Data from additional sets of simulations with $r_d^{F_B^S} = 100$, initial basal heat flow estimates consistently inaccurate by a factor of 2, recording frequency <1 Sol, and sensor locations with improved accuracy are considered throughout, though not explicitly presented. Below, low conductivity, high heat flow scenarios are presented in line with the measurement plots shown in Section 5.3.2 and the initial estimate tables in Section 5.3.3.1. This is done to limit the length of the main text presentation. However, all results are discussed and – specific results not included in the main text are presented in Appendix 9.5.4.2.

Optimization results generally mirror what is expected based on the extent to which the steady temperature gradient is accessible (including its magnitude), and the extent to which the unsteady surface heat flow can be characterised and essentially removed in the inversion. Having low thermal capacity, high conductivity, or failing to access the planetary heat flow at the target depth all have the effect of increasing the amplitude of the unsteady temperature measured by the sensors. Having an incomplete measurement of the seasonal cycle reduces the in situ information available on the unsteady temperature, impairing the accuracy of a derived steady temperature. Figure 5.11 illustrates trends in the accuracy of the optimized heat flow.

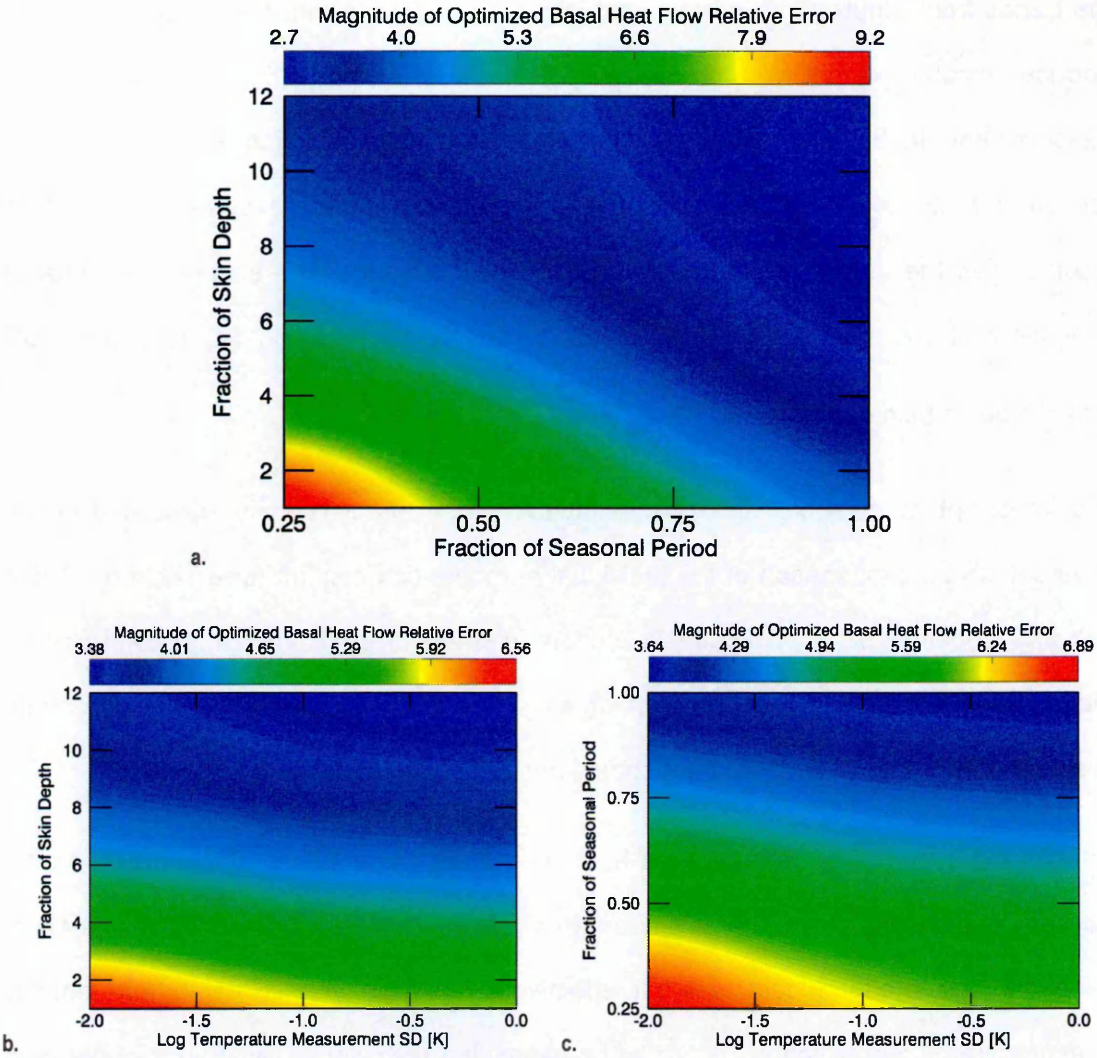

Figure 5.11. Trends $\overline{\epsilon_{F_B^{SI}}}$ in relative erro$\epsilon_{F_B^{SI}} = \left|\frac{F_B^{SI}}{F_B^{ST}} - 1\right|$r of optimized heat flow estimates F_B^{SI} to the true value F_B^{ST} across all measurement scenarios, interpolated from 3D scatterplots. The $\overline{\epsilon_{F_B^{SI}}}$ can be considered as central estimators of the heat flow distribution at particular postions defined by the axes. Contour: a. shows $\overline{\epsilon_{F_B^{SI}}}$ as a function of the ratio of basal sensor depth to annual skin depth r_z, and the ratio of monitoring period to seasonal period r_t; b. shows $\overline{\epsilon_{F_B^{SI}}}$ as a function of r_z and measurement noise amplitude σ_d (the standard deviation); c. shows $\overline{\epsilon_{F_B^{SI}}}$ as a function of r_t and σ_d. Note that $\epsilon_{F_B^{SI}}$ values for each σ_d, r_t and r_z are respectively stacked in a., b. and c., accounting for the differences in $\overline{\epsilon_{F_B^{SI}}}$ extrema.

Comparing the central estimators $\overline{\epsilon_{F_B^{SI}}}$ of Figure 5.11 to $\overline{\epsilon_{F_B^{So}}}$ of Figure 5.10 shows that there is some improvement on initial estimates. The $\overline{\epsilon_{F_B^{SI}}}$ are still fairly large, mostly due to large errors in optimized heat flow for the high conductivity, low heat flow scenarios at the 139°E 1°N Elysium site (see Table 5.9-Table 5.11 and Appendix 9.5.4.2).

The trends from Figure 5.11 indicate that larger errors in the data measurement tend to produce smaller errors in the optimized heat flow, particularly at non-optimal measurement depths and periods.[18] This counterintuitive result follows from those of Section 4.3.1.2 (also see Appendix 9.4.8): the larger standard deviation σ_d which accompanies the noisier measurements increases the size of the space of acceptable solutions of the algorithm such that it finds a more acceptable solution, despite the SD ratio $r_d^{F_B^S}$ being held constant.

It is important to note that the counterintuitive noise effect is fairly small and is not universal, as an examination of the individual numbers can confirm (see Table 5.9-Table 5.11 and Appendix 9.5.4.2). The most prudent inference from this result is that a one-to-one correlation between the precision of an instrument and other associated random noise in a temperature measurement should not be assumed.

Notably, the accuracy of the optimized heat flows show no significant dependence on the accuracy of the initial value, which is consistent with the results of Section 4.2.1 and 4.3.1. Generally, the model functions most effectively for large sensor depth and shorter measurement times, which is confirmed by examining the ratio of initial error of the heat flows to the final error (see Appendix 9.5.4.2).

More specifically, for the Elysium site at 120°E 20°N (see Table 5.9 and Appendix 9.5.4.2) only 21 of the 144 optimized heat flows fall within 10 % of the true value ($\epsilon_{F_B^{S0}} \leq 0.1$) – these are all low conductivity ($k_{BULK} = 0.073$ W/m/K) site scenarios. The full range of sensor depths (2-5 m) and monitoring periods are represented with mostly high (17 mW/m^2) and 2 low (8.5 mW/m^2) heat flow scenarios.

A total of 30 of the optimized heat flows fall between 10-25 % of the true value ($0.1 < \epsilon_{F_B^{S0}} \leq 0.25$) – these are nearly all low conductivity site scenarios with 3 high conductivity ($k_{BULK} = 0.517$ W/m/K) exceptions. All sensor depths, monitoring periods and both high

[18] Recall this effect from Section 4.3.1.2 (Table 4.2).

and low heat flow scenarios are represented. The high conductivity scenarios only associate with the 1 Martian year monitoring period.

Only 18 of the optimized heat flows fall between 26-50 % of the true value ($0.25 < \epsilon_{F_B^{So}} \leq 0.5$) – these include all scenarios where the monitoring period is greater than 0.25 Martian years.

A total of 75 other optimized heat flows range between 50-4172 %[19] inaccurate ($0.50 < \epsilon_{F_B^{So}} \leq 41.72$). They include mostly high conductivity site scenarios and all measurement scenarios. Of the former estimates: low conductivity site scenarios tend to be in the more accurate sub-range; high conductivity site scenarios tend to be in the least accurate sub-range.

The preceding results show statistical improvement on the initial estimate and largely follow the trends illustrated in Figure 5.11. However there are outliers: some where the heat flow is found to relatively high accuracy in non-optimal scenarios (e.g. Table 5.9 at 2.0 m and 0.5 Martian years); others where the heat flow estimate is not improved in optimal measurement scenarios (e.g. at 1 Martian year). These are discussed towards the end of this section.

[19] Even for the wildly inaccurate optimized heat flows, there is some improvement on the even more inaccurate initial estimates in several cases. Still, the large inaccuracies involved render these cases useless in practice.

Table 5.9. Grid of optimized heat flow relative error magnitudes $\epsilon_{F_B^{SI}} = \left|\frac{F_B^{SI}}{F_B^{ST}} - 1\right|$ (green borders – see Appendix 9.1 for symbol definitions) at Elysium 120°E 20°N for the low conductivity k scenario with a heat flow F_B^{ST} of 17 mW/m². The shaded cells show values where there is no improvement on the initial estimate (divergence). The bulk conductivity down to 20 m is k_{BULK} [W/m/K] and z_{SKIN} [m] is the skin depth.

$k_{BULK} = 0.073$		MONITORING PERIOD [~MARTIAN YEARS]				$F_B^{ST} = 0.017$
		0.25	0.5	0.75	1.0	
DEPTH [m]	2.0	1.49	0.07	0.29	0.12	1.0
		1.45	0.03	0.29	0.13	0.1
		1.45	0.03	0.29	0.13	0.01
	3.0	0.63	0.35	0.11	0.10	1.0
		0.64	0.35	0.12	0.10	0.1
		0.64	0.35	0.12	0.10	0.01
	5.0	0.05	0.09	0.09	0.07	1.0
		0.07	0.09	0.09	0.07	0.1
		0.07	0.09	0.09	0.07	0.01
z_{SKIN} =0.91		168 (1)	334 (1)	501 (1)	669 (1)	120°E 20°N
		NUMBER OF MEASUREMENTS (TIME RESOLUTION [SOL])				

ERROR [K]

For the Elysium site at 139°E 1°N (see Table 5.10 and Appendix 9.5.4.2) none of the 144 optimized heat flows fall within 10 % of the true value ($\epsilon_{F_B^{SO}} \leq 0.1$).

Just 9 of the optimized heat flows fall between 10-25 % of the true value ($0.1 < \epsilon_{F_B^{SO}} \leq 0.25$) – these are all low conductivity ($k_{BULK} = 0.122$ W/m/K), and mostly high heat flow (15 mW/m^2) site scenarios with 3 low heat flow (7.4 mW/m^2) exceptions. Interestingly, only sensor depths of 3 m and monitoring periods between 0.5-0.75 Martian years are represented.

Only 14 of the optimized heat flows fall between 26-50 % of the true value ($0.25 < \epsilon_{F_B^{S0}} \leq 0.5$) – these include the same range of scenarios as the latter, more accurate case.

A total of 121 other optimized heat flows range between 50-12969 %[20] inaccurate ($0.50 < \epsilon_{F_B^{S0}} \leq 129.69$). They include the entire range of site and measurement scenario with low conductivity site scenarios tending to be in the more accurate sub-range and high conductivity site scenarios tending to be in the least accurate sub-range.

The preceding results are statistically worse than the initial estimates, despite there being improvements in several cases. It shows that the Elysium site measurement scenarios at 139°E 1°N are appreciably more pathological to invert for the heat flow, than the 120°E 20°N site.

[20] Even for the wildly inaccurate optimized heat flows, there is some improvement on the even more inaccurate initial estimates in several cases. Still, the large inaccuracies involved render these cases useless in practice.

Table 5.10. Grid of optimized heat flow relative error magnitudes $\epsilon_{F_B^{SI}} = \left|\frac{F_B^{SI}}{F_B^{ST}} - 1\right|$ (green borders – see Appendix 9.1 for symbol definitions) at Elysium site 139°E 1°N for the low conductivity k scenario with a heat flow F_B^{ST} of 15 mW/m². The shaded cells show values where there is no improvement on the initial estimate (divergence). The bulk conductivity down to 20 m is k_{BULK} [W/m/K] and z_{SKIN} [m] is the skin depth.

$k_{BULK} = 0.122$		MONITORING PERIOD [~MARTIAN YEARS]				$F_B^{ST} = 0.015$
		0.25	0.5	0.75	1.0	
DEPTH [m]	2.0	3.37	2.86	0.27	1.13	1.0
		3.36	2.88	0.26	1.13	0.1
		3.37	2.88	0.26	1.13	0.01
	3.0	0.42	0.19	0.14	0.82	1.0
		0.43	0.19	0.10	0.81	0.1
		0.43	0.18	0.11	0.81	0.01
	5.0	0.69	0.64	0.49	0.51	1.0
		0.74	0.60	0.49	0.51	0.1
		0.74	0.60	0.49	0.51	0.01
$z_{SKIN} = 1.07$		168 (1)	334 (1)	501 (1)	669 (1)	139°E 1°N
		NUMBER OF MEASUREMENTS (TIME RESOLUTION [SOL])				

ERROR [K]

For the Tharsis site (253°E 2°N – see Table 5.11 and Appendix 9.5.4.2) a respectable 51 of the 144 optimized heat flows fall within 10 % of the true value ($\epsilon_{F_B^{SO}} \leq 0.1$) – these are mostly low conductivity ($k_{BULK} = 0.013$ W/m/K) site scenarios with 6 high conductivity ($k_{BULK} = 0.102$ W/m/K) exceptions. The full range of sensor depths (2-5 m) and monitoring periods (0.25-1 Martian year) are represented with mostly high (22 mW/m^2) and several low (11 mW/m^2) heat flow scenarios.

A total of 39 of the optimized heat flows fall between 10-25 % of the true value ($0.1 < \epsilon_{F_B^{SO}} \leq 0.25$) – all site and measurement scenarios are represented while, interestingly,

sensor depths of 5 m are in the least accurate of the range. Notably, though, the latter consistently associate with high conductivity scenarios.

Only 27 of the optimized heat flows fall between 26-50 % of the true value ($0.25 < \epsilon_{F_B^{So}} \leq 0.5$) – these are all high conductivity site scenarios, mostly with high heat flows. All monitoring periods and sensor depths are represented. Notably, the low heat flow scenarios fall towards the least accurate end of the range.

A relatively small 27 of the optimized heat flows range between 50-114 %[21] inaccurate ($0.50 < \epsilon_{F_B^{So}} \leq 1.14$) – they include high conductivity, mostly low heat flow site scenarios. All sensor depths and monitoring periods are represented.

The preceding results show statistical improvement on the initial estimate and largely follow the trends illustrated in Figure 5.11. However there are outliers: some where the heat flow is found to relatively high accuracy in non-optimal scenarios (e.g. Table 5.9 at 2.0 m and 0.5 Martian years); others where the heat flow estimate is not improved in optimal measurement scenarios (e.g. at 1 Martian year). These are discussed towards the end of this section.

The preceding results show appreciable improvement on initial estimates in most cases, except where the monitoring period is 1 Martian year – the reason for the ineffectiveness of the model at 1 Martian year is explored in the next paragraph. A Tharsis scenario with exceptionally high heat flow of the order of 40 mW/m^2 is not tested but the trend analyses point to such a scenario being more effectively optimized by the model, if at all optimization is necessary.

[21] Even for the wildly inaccurate optimized heat flows, there is some improvement on the even more inaccurate initial estimates in several cases. Still, the large inaccuracies involved render these cases useless in practice.

Table 5.11. Grid of optimized heat flow relative error magnitudes $\epsilon_{F_B^{SI}} = \left|\frac{F_B^{SI}}{F_B^{ST}} - 1\right|$ (green borders – see Appendix 9.1 for symbol definitions) at Tharsis site 253°E 2°N for the low conductivity k scenario with a heat flow F_B^{ST} of 22 mW/m². The shaded cells show values where there is no improvement on the initial estimate (divergence). The bulk conductivity down to 20 m is k_{BULK} [W/m/K] and z_{SKIN} [m] is the skin depth.

$k_{BULK} = 0.013$		MONITORING PERIOD [~MARTIAN YEARS]				$F_B^{ST} = 0.022$	
		0.25	0.5	0.75	1.0		
DEPTH [m]	2.0	0.11	0.10	0.08	0.08	1.0	ERROR [K]
		0.11	0.10	0.08	0.08	0.1	
		0.11	0.10	0.08	0.08	0.01	
	3.0	0.06	0.06	0.06	0.06	1.0	
		0.06	0.06	0.06	0.06	0.1	
		0.06	0.06	0.06	0.06	0.01	
	5.0	0.03	0.03	0.03	0.03	1.0	
		0.03	0.03	0.03	0.03	0.1	
		0.03	0.03	0.03	0.03	0.01	
z_{SKIN} =0.44		168 (1)	334 (1)	501 (1)	669 (1)	253°E 2°N	
		NUMBER OF MEASUREMENTS (TIME RESOLUTION [SOL])					

The shaded cells show that in some instances simpler methods (see Section 5.3.3.1) may be more suited to estimating the basal heat flow, in particular when the monitoring period is 1 Martian year. Examination of the tables show that nearly all scenarios indicated by the shaded cells have the most accurate initial heat flow estimates for the particular site, skin depth, and true heat flow. Interestingly, tests carried out with initial estimates consistently inaccurate by a factor of 2 ($\epsilon_{F_B^{SI}} = 1$) show very similar results, confirming that the algorithm is fairly insensitive to the accuracy of the initial estimate of the basal heat flow. This is because the assumed error in the heat flow is set large enough to decrease the sensitivity of the algorithm to the initial estimate (also see Section 4.2.1.1). The algorithm is, however, sensitive to the sign of the relative error, as tabulated in Appendix 9.4.2 such

that a low initial estimate produces a low optimized heat flow and a high initial estimate produces a high optimized heat flow. The shaded cell results are therefore not dependent on the initial heat flow estimate. The results point to instabilities introduced by temperature residuals caused by truncation errors coupled with the high frequency variation of the surface temperature (see Section 8.2.1). Truncation errors lead to increased data residuals for a measurement with multiple recordings over a monitoring period, versus those for an instantaneous measurement. This is because there are more temperature profiles within each of the former, with which data residuals are calculated and summed. This can be mitigated by ignoring more[22] affected sensors (close to the surface) and/or scaling the standard deviation of the temperature measurement to higher values within the bounds noted in Section 4.2.1.2.2.

The non-shaded cells all show marginal to substantial improvement on the initial basal heat flow estimate based on the skin depth, sensor depth, monitoring period, and magnitude of the true basal heat flow – they follow the trends established in Figure 5.11 and Figure 9.4-6 in Appendix 9.5.4.2. A substantial number of the tested scenarios result in optimized heat flows which are inaccurate by a factor of at least 2 ($\epsilon_{F_B^{SI}} \geq 1$) where the skin depth is large and the heat flow is low – the Elysium site at 139°E 1°N presents the most difficult measurement scenarios. The model is likely inapplicable to scenarios involving similarly large skin depth and shallow sensor depth. The heat flow is most measureable at the Tharsis site where the skin depth is shallow and the heat flow is high. There are some non-optimal scenarios in which the heat flow is found to relatively high accuracy – these are effectively due to chance where, for example, the unsteady temperature amplitude over the monitoring period is not large. The lack of diurnal variations due to the use of the diurnal mean surface temperature in the inversion also

[22] Recall that the surface sensor is ignored in the simulations.

plays an increasing role at shallower sensor depths.[23] See Appendix 9.5.4.2 for an example with the Elysium site at 139°E 1°N at 2 m sensor depth.

Figure 5.12 shows examples of the inputs and outputs of the model for the least and most optimal measurement scenarios, as tabulated above. The effects of the use of the diurnal mean temperatures over the monitoring period are most evident for the shallow measurements up to 2 m. For the Elysium site at 120°E 20°N the basal heat flow is underestimated ($\epsilon_{F_B^{SI}} = |\text{-}1.45|$, see Table 5.9) to counteract the highly positive (from surface) temperature gradients introduced by the unsteady temperature ($\epsilon_{F_B^{So}} = 11.37$, see Table 5.6). For the Elysium site at 139°E 1°N the unsteady surface heat flow introduces a negative temperature gradient ($\epsilon_{F_B^{So}} = |\text{-}5.20|$, see Table 5.7) which is coupled with high heat content introduced by the large diurnal surface temperature amplitude. The diurnal mean surface temperature used in the inversion underestimates the surface heat input over the monitoring period. The basal heat flow is therefore underestimated but still increased from the initial estimate ($\epsilon_{F_B^{SI}} = |\text{-}3.37|$, see Table 5.10). Shorter monitoring periods therefore require more accurate surface temperature estimates. The unsteady temperature amplitude is significantly reduced at 2 m for the Tharsis site at 253°E 2°N, therefore allowing a fairly accurate estimate of the heat flow ($\epsilon_{F_B^{SI}} = 0.11$, see Table 5.11), improved from a low initial estimate ($\epsilon_{F_B^{So}} = |\text{-}0.86|$, see Table 5.8). For the longer monitoring periods, with high recording frequency, and deeper penetration of sensors, the influence of the unsteady surface heat flow on the optimization is smaller. For the Tharsis scenarios, the basal heat flow can therefore be recovered with relatively high reliability.

[23] This effect is also an artefact of the 1 Sol timestep used in the simulations. Shorter timesteps, with a surface temperature of equivalent resolution, can more accurately reproduce the higher frequency components at shallow depth, where these cannot be ignored. However, the effect is increased demand for computing power or longer simulation time.

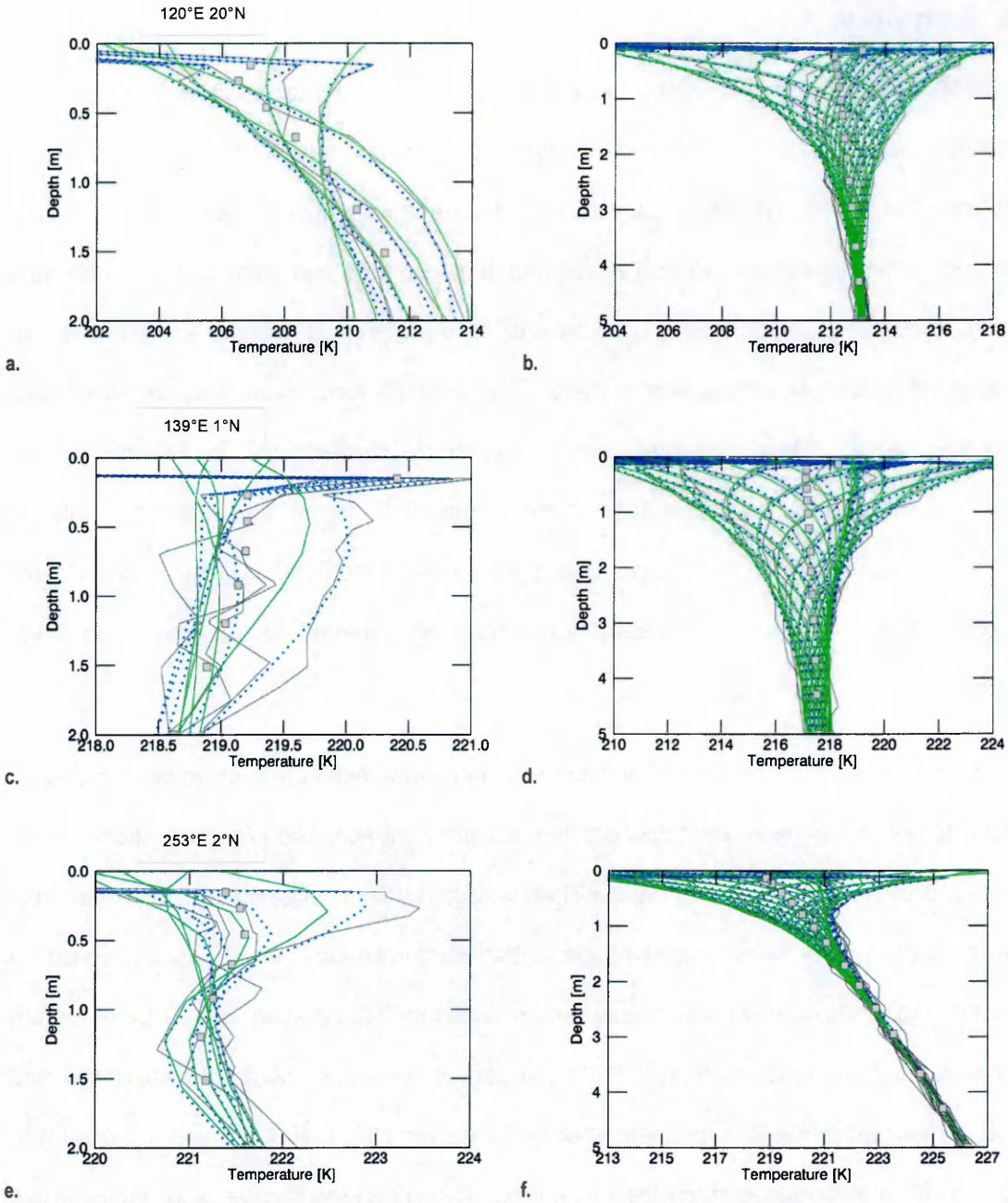

Figure 5.12. Representative profiles for temperature inversions at sites at 120°E 20°N (a-b), 139°E 1°N (c-d) and 253°E 2°N (e-f) for the low conductivity, high heat flow scenarios with noise of 1 K amplitude. The plots are overlays of temperature-depth profiles over time where the dotted blue curves represent the true profiles, the solid grey curves the profiles with 1 K error and the solid green curves represent the optimized temperature profiles. The plots on the left (a, c, e) cover a monitoring period of ~168 Sols in 1 Sol steps. The plots on the right (b, d, f) cover a monitoring period of ~669 Sol in 1 Sol steps. The steps are displayed every ~33 Sol for visibility. The grey squares are sensor locations and are plotted at the mean of the true temperature profile at a particular depth – the surface sensor is not representative due to the high amplitude, high frequency variation of the diurnal surface temperature

5.4 Summary

A heat flow measurement on Mars can aid in the selection of thermal models which most accurately describe Martian thermal evolution. Different models predict global averaged heat flows from 5-45 mW/m^2, and a variation of surface heat flow between 14-55 mW/m^2. With such large differences, even a crude heat flow estimate can invalidate some thermal models, though high accuracy of typically <10 % is required to validate estimates of the variation of heat flow across the surface. The achievement of an accurate heat flow measurement on Mars (in situ), while potentially challenging, is feasible if the measurement is restricted to the drier, dustier equatorial regions, and specific conditions are met in terms of the depth and time period over which the regolith is monitored. Inversion of the temperature measurement has the potential to improve upon initial Martian heat flow estimates.

To test the potential of inversion for improving heat flow estimates, an inverse model is applied to several feasible heat flow probe measurement scenarios for three locations on Mars. One of these locations is on the Tharsis region with its potential for high heat flow relative to the global mean, and two are in the Elysium region, which is considered an ideal landing site and heat flow measurement location. These scenarios include surface temperatures from NASA's Mars-GRAM Martian atmospheric model. Temperature and pressure averaged, depth-dependent shallow subsurface thermal properties are used with guidance from observed surface thermal inertia. The scenarios involve both relatively low and high heat flows as predicted by different thermal models. The derived measurements have noise of the order of 10 mK to 1 K added to account for potential modelling and measurement uncertainties. Monitoring periods cover 0.25-1 Martian year with different measurement frequencies and maximum sensor depths fall between 2-5 m.

Results show that in cases where the monitoring period is at least 1 Martian year, inversion may not be necessary as the heat flow can be initially determined to an accuracy (typically <20 %) which the algorithm does not improve upon. In cases where

the skin depth is particularly large (1.89 m) even crude estimates, ~50% inaccurate and larger, are not improved. For monitoring periods less than 1 Martian year, sensor depths at least 1.3 times the skin depth allow for a heat flow estimate within 20 % of the true value, providing the unsteady surface temperature amplitude is not too large. A higher frequency of measurements over a monitoring period improve optimized heat flow accuracy – more so at shallower sensor depths. Unique features of the unsteady surface temperature over the monitoring period also affect the accuracy of the optimized heat flow, more so, again, for shallower measurements. For example, if measurements are restricted to high temperature or low temperature periods in the cycle, respective negative or positive biases are introduced into the steady temperature gradient. Larger steady temperature gradients therefore lead to more accurate optimized heat flows.

Heat flow optimized from noisy data shows trends of marginally improved accuracy, though this is traced back to the larger assumed temperature data standard deviations used to initialise the inverse model. It appears to be most prudent to assume large temperature data standard deviation to avoid inverse model instabilities, even where the noise level appears to be low (e.g. with high heat flow probe precision; also see Section 4.3.1.2). Inaccurate thermal properties also affect the accuracy of the optimized heat flow. These are not investigated here but approximate one to one correlation in accuracy between underestimated bulk conductivity and heat flow is observed in the results of Sections 4.2.1.2.3 and 4.3.1.3.

Measurement depth relative to the skin depth and the measurement time are confirmed as additional primary factors which determine the accuracy of the optimized heat flow. It is found that measurement depths at least twice the skin depth and monitoring periods of at least 0.5 Martian years, or measurement depths at least 5 times the skin depth and monitoring periods of at least 0.25 Martian years, are required for the model to improve an initial heat flow estimate to within 10 % of the true value. Outside these bounds the model tends to be ineffective (or diverges), in particular with shallow skin depth and a long monitoring period approaching a full seasonal cycle (a product of truncation errors due to

large timesteps – Section 8.2.1). The latter may require some experimentation with the a priori standard deviation of the affected sensors, to improve the accuracy of the optimized heat flow.

5.5 References

BANASZKIEWICZ, M., SEIFERLIN, K., SPOHN, T., KARGL, G. & KÖMLE, N. 1997. A new method for the determination of thermal conductivity and thermal diffusivity from linear heat source measurements. *Review of Scientific Instruments,* 68, 4184-4190.

BANERDT, W. B., SMREKAR, S., ALKALAI, L., HOFFMAN, T., WARWICK, R., HURST, K., FOLKNER, W., LOGNONNÉ, P., SPOHN, T., ASMAR, S., BANFIELD, D., BOSCHI, L., CHRISTENSEN, U., DEHANT, V., GIARDINI, D., GOETZ, W., GOLOMBEK, M., GROTT, M., HUDSON, T., JOHNSON, C., KARGL, G., KOBAYASHI, N., MAKI, J., MIMOUN, D., MOCQUET, A., MORGAN, P., PANNING, M., PIKE, W. T., TROMP, J., VAN ZOEST, T., WEBER, R., WIECZOREK, M. & TEAM, I. 2012. InSight: An Integrated Exploration of the Interior of Mars. *In:* Lunar and Planetary Institute Science Conference Abstracts, March 1, 2012 2012. 43, 2838.

BECK, A. E., SHEN, P. Y., BELTRAMI, H., MARESCHAL, J. C., ŠAFANDA, J., SEBAGENZI, M. N., VASSEUR, G. & WANG, K. 1992. A comparison of five different analyses in the interpretation of five borehole temperature data sets. *Palaeogeography, Palaeoclimatology, Palaeoecology,* 98, 101-112.

BOYNTON, W. V., FELDMAN, W. C., SQUYRES, S. W., PRETTYMAN, T. H., BRÜCKNER, J., EVANS, L. G., REEDY, R. C., STARR, R., ARNOLD, J. R., DRAKE, D. M., ENGLERT, P. A. J., METZGER, A. E., MITROFANOV, I., TROMBKA, J. I., D'USTON, C., WÄNKE, H., GASNAULT, O., HAMARA, D. K., JANES, D. M., MARCIALIS, R. L., MAURICE, S., MIKHEEVA, I., TAYLOR, G. J., TOKAR, R. & SHINOHARA, C. 2002. Distribution of Hydrogen in the Near Surface of Mars: Evidence for Subsurface Ice Deposits. *Science,* 297, 81-85.

BOYNTON, W. V., TAYLOR, G. J., EVANS, L. G., REEDY, R. C., STARR, R., JANES, D. M., KERRY, K. E., DRAKE, D. M., KIM, K. J., WILLIAMS, R. M. S., CROMBIE, M. K., DOHM, J. M., BAKER, V., METZGER, A. E., KARUNATILLAKE, S., KELLER, J. M., NEWSOM, H. E., ARNOLD, J. R., BRÜCKNER, J., ENGLERT, P. A. J., GASNAULT, O., SPRAGUE, A. L., MITROFANOV, I., SQUYRES, S. W., TROMBKA, J. I., D'USTON, L., WÄNKE, H. & HAMARA, D. K. 2007. Concentration of H, Si, Cl, K, Fe, and Th in the low- and mid-latitude regions of Mars. *Journal of Geophysical Research (Planets),* 112, E12S99.

BREUER, D. & SPOHN, T. 2003. Early plate tectonics versus single-plate tectonics on Mars: Evidence from magnetic field history and crust evolution. *Journal of Geophysical Research (Planets),* 108, 5072.

BRIDGES, N. T., BANKS, M. E., BEYER, R. A., CHUANG, F. C., NOE DOBREA, E. Z., HERKENHOFF, K. E., KESZTHELYI, L. P., FISHBAUGH, K. E., MCEWEN, A. S., MICHAELS, T. I., THOMSON, B. J. & WRAY, J. J. 2010. Aeolian bedforms, yardangs, and indurated surfaces in the Tharsis Montes as seen by the HiRISE Camera: Evidence for dust aggregates. *Icarus,* 205, 165-182.

CHRISTENSEN, P. R., BANDFIELD, J. L., HAMILTON, V. E., RUFF, S. W., KIEFFER, H. H., TITUS, T. N., MALIN, M. C., MORRIS, R. V., LANE, M. D., CLARK, R. L., JAKOSKY, B. M., MELLON, M. T., PEARL, J. C., CONRATH, B. J., SMITH, M. D., CLANCY, R. T., KUZMIN, R. O., ROUSH, T., MEHALL, G. L., GORELICK, N., BENDER, K., MURRAY, K., DASON, S., GREENE, E., SILVERMAN, S. & GREENFIELD, M. 2001. Mars Global Surveyor Thermal Emission Spectrometer experiment: Investigation description and surface science results. *Journal of Geophysical Research,* 106, 23823-23872.

CLIFFORD, S. M. & FANALE, F. P. 1985. The Thermal Conductivity of the Martian Crust. *In:* Lunar and Planetary Institute Science Conference, March 1 1985. 16, 144-145.

DEHANT, V., BANERDT, B., LOGNONNÉ, P., GROTT, M., ASMAR, S., BIELE, J., BREUER, D., FORGET, F., JAUMANN, R., JOHNSON, C., KNAPMEYER, M., LANGLAIS, B., LE FEUVRE, M., MIMOUN, D., MOCQUET, A., READ, P., RIVOLDINI, A., ROMBERG, O., SCHUBERT, G., SMREKAR, S., SPOHN, T., TORTORA, P., ULAMEC, S. & VENNERSTRØM, S. 2012. Future Mars geophysical observatories for understanding its internal structure, rotation, and evolution. *Planetary and Space Science,* 68, 123-145.

FOUNTAIN, J. A. & WEST, E. A. 1970. Thermal conductivity of particulate basalt as a function of density in simulated lunar and Martian environments. *Journal of Geophysical Research,* 75, 4063-4069.

GROTT, M. & BREUER, D. A. A. 2010. On the spatial variability of the Martian elastic lithosphere thickness: Evidence for mantle plumes? *Journal of Geophysical Research (Planets),* 115, 3005.

GROTT, M., HAUBER, E., WERNER, S. C., KRONBERG, P. & NEUKUM, G. 2005. High heat flux on ancient Mars: Evidence from rift flank uplift at Coracis Fossae. *Geophysical Research Letters,* 32, L21201.

GROTT, M., HAUBER, E., WERNER, S. C., KRONBERG, P. & NEUKUM, G. 2007a. Mechanical modeling of thrust faults in the Thaumasia region, Mars, and implications for the Noachian heat flux. *Icarus,* 186, 517-526.

GROTT, M., HELBERT, J. & NADALINI, R. 2007b. Thermal structure of Martian soil and the measurability of the planetary heat flow. *J. Geophys. Res.,* 112, E09004.

GROTT, M., PLESA, A.-C., TOSI, N. & BREUER, D. 2014. Constraining the amount of radiogenic elements in the interior of Mars from the HP3 heat flow measurement. *In:* EGU General Assembly Conference Abstracts, May 1, 2014 2014. 16, 15053.

HAHN, B. C., MCLENNAN, S. M. & KLEIN, E. C. 2011. Martian surface heat production and crustal heat flow from Mars Odyssey Gamma-Ray spectrometry. *Geophysical Research Letters,* 38, 14203.

HAMILTON, V., VASAVADA, A., HABERLE, R., DE LA TORRE JUÁREZ, M., ZORZANO-MIER, M.-P., MARTIN-TORRES, J., ARMIENS, C., SEBASTIÁN-MARTÍNEZ, E., MARTÍNEZ-FRÍAS, J., HERNÁNDEZ, M. D. P., RAMOS, M., RODRÍGUEZ-MANFREDI, J., GÓMEZ-ELVIRA, J. & TEAM, M. S. 2013. Initial Results from the MSL REMS Ground Temperature Sensor at Rocknest. *In:* EGU General Assembly Conference Abstracts, April 1, 2013 2013. 15, 2502.

HAUCK, S. A. & PHILLIPS, R. J. 2002. Thermal and crustal evolution of Mars. *Journal of Geophysical Research (Planets),* 107, 5052.

JAUPART, C., SCLATER, J. G. & SIMMONS, G. 1981. Heat flow studies: Constraints on the distribution of uranium, thorium and potassium in the continental crust. *Earth and Planetary Science Letters,* 52, 328-344.

JUSTH, H. L., JUSTUS, C. G., RAMEY, H. S. & MILLOUR, E. 2011. Mars-Gram 2010: Improving the precison of Mars-Gram. *In:* FORGET, F., ed. Mars Atmosphere: Modelling and observation, February 1, 2011 2011. 265-267.

KIEFFER, H. H., MARTIN, T. Z., PETERFREUND, A. R., JAKOSKY, B. M., MINER, E. D. & PALLUCONI, F. D. 1977. Thermal and albedo mapping of Mars during the Viking primary mission. *Journal of Geophysical Research,* 82, 4249-4291.

KÖMLE, N. I., HÜTTER, E. S., MACHER, W., KAUFMANN, E., KARGL, G., KNOLLENBERG, J., GROTT, M., SPOHN, T., WAWRZASZEK, R., BANASZKIEWICZ, M., SEWERYN, K. & HAGERMANN, A. 2011. In situ methods for measuring thermal properties and heat flux on planetary bodies. *Planetary and Space Science,* 59, 639-660.

MARS CLIMATE DATABASE. 2013. *Martian Seasons and Solar Longitude* [Online]. Available: http://www-mars.lmd.jussieu.fr/mars/time/solar_longitude.html [Accessed 13/09/2013 2013].

MELLON, M. T., JAKOSKY, B. M., KIEFFER, H. H. & CHRISTENSEN, P. R. 2000. High-Resolution Thermal Inertia Mapping from the Mars Global Surveyor Thermal Emission Spectrometer. *Icarus,* 148, 437-455.

MILLOUR, E., SPIGA, A., COLAITIS, A., NAVARRO, T., MADELEINE, J.-B., CHAUFFRAY, J.-Y., MONTABONE, L., LOPEZ-VALVERDE, M. A., GONZALEZ-GALINDO, F., LEFÈVRE, F., MONTMESSIN, F., LEWIS, S. R., READ, L. P., DESJEAN, M.-C. & HUOT, J.-P. 2012. Mars Climate Database Version 5. *In:* European Planetary Science Congress 2012, September 1, 2012 2012. 302.

MORSCHHAUSER, A., GROTT, M. & BREUER, D. 2011. Crustal recycling, mantle dehydration, and the thermal evolution of Mars. *Icarus,* 212, 541-558.

NASA, A. R. C. 2013a. *Interactive Mars Data Maps* [Online]. Available: http://marsoweb.nas.nasa.gov/globalData/ [Accessed 13/09/2013 2013].

NASA, A. R. C. D. T. 2014. NASA App. *Missions.* 1.43 ed. Google Play Store: National Aeronautics and Space Administration.

NASA, J. P. L. 2013b. *InSight: Mission* [Online]. Available: http://insight.jpl.nasa.gov/overview.cfm [Accessed 13/09/2013 2013].

NIMMO, F. & STEVENSON, D. J. 2000. Influence of early plate tectonics on the thermal evolution and magnetic field of Mars. *Journal of Geophysical Research,* 105, 11969-11980.

NOWICKI, S. A. & CHRISTENSEN, P. R. 2004. Thermophysical Characterization of the Tharsis Plateau Low-Inertia Layer from TES and THEMIS Observations. *AGU Fall Meeting Abstracts,* 11, 0960.

PIQUEUX, S. & CHRISTENSEN, P. R. 2009a. A model of thermal conductivity for planetary soils: 1. Theory for unconsolidated soils. *Journal of Geophysical Research (Planets),* 114, 9005.

PIQUEUX, S. & CHRISTENSEN, P. R. 2009b. A model of thermal conductivity for planetary soils: 2. Theory for cemented soils. *Journal of Geophysical Research (Planets),* 114, 9006.

PIQUEUX, S. & CHRISTENSEN, P. R. 2011. Temperature-dependent thermal inertia of homogeneous Martian regolith. *Journal of Geophysical Research (Planets),* 116, 7004.

PRESLEY, M. A. & CHRISTENSEN, P. R. 1997a. Thermal conductivity measurements of particulate materials 1. A review. *Journal of Geophysical Research,* 102, 6535-6550.

PRESLEY, M. A. & CHRISTENSEN, P. R. 1997b. Thermal conductivity measurements of particulate materials 2. results. *Journal of Geophysical Research,* 102, 6551-6566.

ROBIE, R. A., HEMINGWAY, B. S. & WILSON, W. H. 1970. Specific heats of lunar surface materials from 90° to 350°K. *In:* LEVINSON, A. A., ed. Lunar and Planetary Science Conference Proceedings, March 4 1970. 3, 2361-2367.

RUIZ, J., MCGOVERN, P. J., JIMÉNEZ-DÍAZ, A., LÓPEZ, V., WILLIAMS, J.-P., HAHN, B. C. & TEJERO, R. 2011. The thermal evolution of Mars as constrained by paleo-heat flows. *Icarus,* 215, 508-517.

SCLATER, J. G., JAUPART, C. & GALSON, D. 1980. The heat flow through oceanic and continental crust and the heat loss of the earth. *Reviews of Geophysics and Space Physics,* 18, 269-311.

SEIFERLIN, K., KÖMLE, N. I., KARGL, G. & SPOHN, T. 1996. Line heat-source measurements of the thermal conductivity of porous H_2O ice, CO_2 ice and mineral powders under space conditions. *Planetary and Space Science,* 44, 691-704.

SHEN, P. Y. & BECK, A. E. 1992. Paleoclimate change and heat flow density inferred from temperature data in the Superior Province of the Canadian sheild. *Palaeogeography, Palaeoclimatology, Palaeoecology,* 98, 143-165.

SHEN, P. Y., WANG, K., BELTRAMI, H. & MARESCHAL, J. C. 1992. A comparative study of inverse methods for estimating climatic history from borehole temperature data. *Palaeogeography, Palaeoclimatology, Palaeoecology,* 98, 113-127.

SPOHN, T. 1991. Mantle differentiation and thermal evolution of Mars, Mercury, and Venus. *Icarus,* 90, 222-236.

SPOHN, T., ACUÑA, M. H., BREUER, D., GOLOMBEK, M., GREELEY, R., HALLIDAY, A., HAUBER, E., JAUMANN, R. & SOHL, F. 2001a. Geophysical Constraints on the Evolution of Mars. *Space Science Reviews,* 96, 231-262.

SPOHN, T., BALL, A. J., SEIFERLIN, K., CONZELMANN, V., HAGERMANN, A., ÖMLE, N. I. & KARGL, G. 2001b. A heat flow and physical properties package for the surface of Mercury. *Planetary and Space Science,* 49, 1571-1577.

SPOHN, T., GROTT, M., KNOLLENBERG, J., VAN ZOEST, T., KARGL, G., SMREKAR, S. E., BANERDT, W. B., HUDSON, T. L. & TEAM, H. I. 2012. INSIGHT: Measuring the Martian Heat Flow Using the Heat Flow and Physical Properties Package (HP^3). *In:* Lunar and Planetary Institute Science Conference, 2012. 43, 1445.

SPOHN, T., GROTT, M., RICHTER, L., KNOLLENBERG, J., SMREKAR, S. E. & TEAM, H. I. 2010. Measuring Heat Flow on the Moon -- The Heat Flow and Physical Properties Package HP^3. *LPI Contributions,* 1530, 3016.

STACK, K. M., GROTZINGER, J. P., SUMNER, D. Y., EHLMANN, B. L., MILLIKEN, R. E., EIGENBRODE, J. L., GUPTA, S., WILLIAMS, R. M. E., KAH, L. C., LEWIS, K. W. & TEAM, M. S. 2013. Using Outcrop Exposures on the Road to Yellowknife Bay to Build a Stratigraphic Column, Gale Crater, Mars. *In:* Lunar and Planetary Institute Science Conference Abstracts, March 1 2013. 44, 1431.

STEVENSON, D. J., SPOHN, T. & SCHUBERT, G. 1983. Magnetism and thermal evolution of the terrestrial planets. *Icarus,* 54, 466-489.

TAYLOR, G. J., STOPAR, J. D., BOYNTON, W. V., KARUNATILLAKE, S., KELLER, J. M., BRÜCKNER, J., WÄNKE, H., DREIBUS, G., KERRY, K. E., REEDY, R. C., EVANS, L. G., STARR, R. D., MARTEL, L. M. V., SQUYRES, S. W., GASNAULT, O., MAURICE, S., D'USTON, C., ENGLERT, P., DOHM, J. M., BAKER, V. R., HAMARA, D., JANES, D., SPRAGUE, A. L., KIM, K. J., DRAKE, D. M., MCLENNAN, S. M. & HAHN, B. C. 2006. Variations in K/Th on Mars. *Journal of Geophysical Research (Planets),* 111, E03S06.

URQUHART, M. L. & GULICK, V. C. 2003. Plausibility of the ``White Mars'' hypothesis based upon the thermal nature of the Martian subsurface. *Geophysical Research Letters,* 30, 1622.

WANG, K. 1992. Estimation of Ground Surface Temperatures from Borehole Temperature Data. *J. Geophys. Res.,* 97, 2095-2106.

WEIZMAN, A., STEVENSON, D. J., PRIALNIK, D. & PODOLAK, M. 2001. Modeling the Volcanism on Mars. *Icarus,* 150, 195-205.

ZENT, A. P., HECHT, M. H., COBOS, D. R., WOOD, S. E., HUDSON, T. L., MILKOVICH, S. M., DEFLORES, L. P. & MELLON, M. T. 2010. Initial results from the thermal and electrical

conductivity probe (TECP) on Phoenix. *Journal of Geophysical Research (Planets),* 115, E00E14.

6 MERCURY

6.1 Heat Flow on Mercury

6.1.1 Mercurian Thermal History

Mercury's bulk density is the highest of the planets suggesting a large metallic core >75 % of the diameter of the planet. Its small size points to relatively rapid cooling from its time of formation, however it has been observed to have a magnetic field which may be due to remnant magnetism (e.g. Purucker et al., 2009), or an active dynamo pointing to an at least partially molten core. A fluid core is contrary to the perception that a large metal core should, given the time since Mercury's formation, be frozen. Lobate scarps, have been observed across the Mercurian surface; these have been interpreted as thrust faults suggesting global contraction of the planet by ~1-2 km, significantly smaller than that predicted by simple cooling models with a large metallic core (also see e.g. Stevenson et al., 1983; Breuer et al., 2007; Zuber et al., 2007; Michel et al., 2013 and references therein).

The former observations raise important questions about the history of Mercury's heat loss, which appears to be smaller than its size suggests. Observational evidence supports a variety of thermal evolution models of Mercury, which provide a number of potential solutions to the enigma. These range from an insulating crust (Grott et al., 2011), through a mainly conductive mantle (e.g. Zuber et al., 2007; Head et al., 2012; Smith et al., 2012) to a large metallic core alloyed with light elements such as Si and S (e.g. Smith et al., 2012; Hauck et al., 2013). These models predict current global heat flow in the range 10-40 mW/m^2, therefore a heat flow measurement with <50 % uncertainty can help to eliminate less plausible models.

A heat flow measurement will provide a constraint on the depth of the crust and an upper limit on the distribution of radioisotopes at depth. The MErcury Surface, Space ENvironment, GEochemistry and Ranging (MESSENGER) orbiter Gamma-Ray Spectrometer (GRS) has measured gamma ray abundances at Mercury and allowed estimates of radiogenic heat production at its surface (down to a few 10s of cm – e.g.

Evans et al., 2012).[1] An in situ heat flow measurement can help to verify these while potentially avoiding many of the complexities associated with orbital measurement, as discussed further in Section 6.1.2 (also see Peplowski et al., 2012).

With the concentration of radioisotopes in the crust determined, the crustal component of the heat flow can be removed from the surface value, thereby allowing an estimate of the heat flow out of the mantle.[2] This will provide consequent insights into the thermal state of the mantle and core (e.g. Spohn et al., 2001). Therefore, considered with evidence noted above and other observations such as gravity field measurements (Smith et al., 2012), the heat flow can provide robust constraints on existing Mercurian thermal evolution models.

6.1.2 Mercurian Heat Flow Measurement

Keihm (1984) discusses microwave (5-30 cm) mapping of heat flow from orbit, citing several surface scattering effects which complicate the interpretation of brightness temperatures. The Mercury Thermal Imaging Spectrometer (MERTIS) instrument is due to arrive at Mercury aboard the BepiColumbo Planetary Orbiter in 2024 (Benkhoff and Helbert, 2006; ESA, 2013). MERTIS will attempt to map the surface heat flow from the night side of Mercury. Howett et al. (2011) use similar observations from the Cassini Composite Infrared Spectrometer (CIRS) to determine the heat flow at Enceladus south polar hot spot. The methods used by Howett et al. (2011) and those discussed in Keihm (1984) involve the same base principle as with an in situ heat flow probe measurement – the removal of the surface unsteady heat flow signal to reveal the subsurface steady heat flow signal. Orbital measurements, however, require the characterisation of several surface processes which include the electrical properties of the regolith, and assumptions are necessary about subsurface thermal properties. A heat flow probe has direct access

[1] This involves various methods of removing background signals from the gamma ray spectra. Models with varying elemental abundances are then fitted to the resulting spectra.

[2] As discussed throughout Section 1 (also see Section 5.1.1) the surface (planetary) heat flow is the sum of crustal heat flow due to radioisotope decay and cooling of the mantle and core.

to the subsurface and depth dependent thermal properties and in principle, therefore, does not suffer from the former limitations. The Heat Flow and Physical Properties Package (HP^3), as mentioned in Chapters 1 and 5 is a heat flow probe developed for deployment on terrestrial bodies (Spohn et al., 2001; Spohn et al., 2010; Kömle et al., 2011; Dehant et al., 2012; Spohn et al., 2012). Here, the model of Chapter 4 is applied to Mercury as an airless terrestrial planet to assess the characteristics of a potential HP^3 measurement.

Keihm (1984) suggests a nominal heat flow for Mercury of 40 mW/m^2 as suitable for orbital microwave measurements while the models of Spohn (1991) give values between 22-30 mW/m^2. Watters et al. (2002) use crustal faulting studies to estimate the heat flow of Mercury to be 10-43 mW/m^2, about 4 billion years ago. Ruiz et al. (2013) use similar studies of the Northern Rise (centred on ~30°E 68°N) and Kuiper regions (centred on 324°E 0°N) of Mercury (see Figure 6.1) to estimate palaeo-heat flows between ~27-36 mW/m^2 and current values between ~15-30 mW/m^2. The thermal evolution models of Breuer et al. (2007) are compatible with the former estimates and suggest present day values of the order of 12 mW/m^2. Egea-Gonzalez and Ruiz (2013) obtain a lower limit of 6 mW/m^2 by comparing the Mercurian regolith layer to the more insulating lunar megaregolith layer. Spohn et al. (2001) note the widely varying estimates of Mercurian heat flow of the order of 10-30 mW/m^2 due to different assumptions. They also note that heat flow on Mercury is expected to show less surface variation than on Earth due to a thin mantle – the MESSENGER results of Michel et al. (2013) suggest a thinner mantle than previous estimates. Despite this, the heat flow is likely to vary appreciably across the Mercurian surface based on the crustal thickness findings of Smith et al. (2012).

Crustal thickness largely correlates with surface altitude, the northern half of which is shown in Figure 6.1 along with potential heat flow measurement sites at 80°E 38°N, 160°E 25°N and 272°E 85°N. The selection of the sites is discussed in Section 6.2. Here, the heat flow is investigated in the context of low, intermediate and high estimates of 10, 20 and 30 mW/m^2, respectively. These are not associated with any specific heat flow

measurement site: this is because at the sites chosen – based on crustal thickness estimates and the assumption of uniform volumetric heat production throughout the crust – the heat flow should not vary by more than a few percent. The heat flow estimates, combined with conductivity estimates, allow for a broad analysis of the various steady temperature gradients which may be encountered on the Mercurian surface.

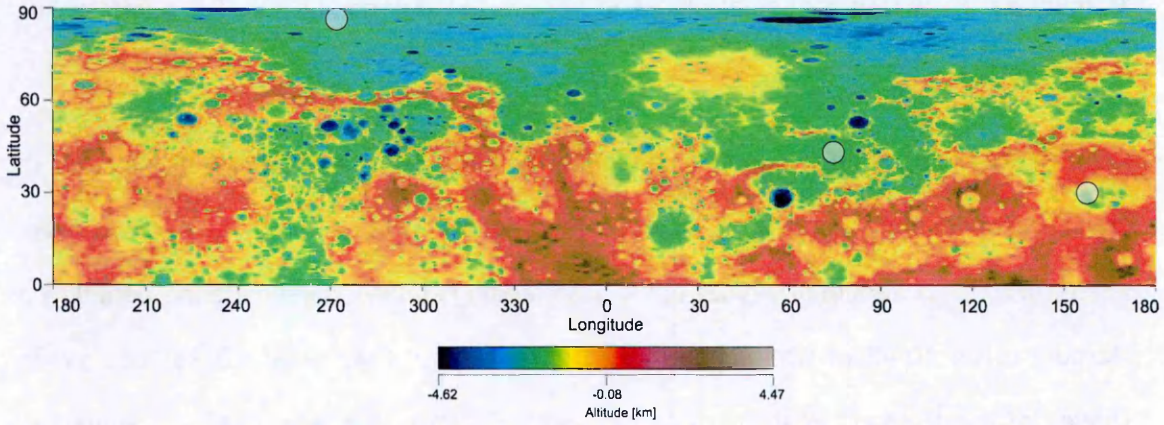

Figure 6.1. Mercury Laser Altimeter (MLA) map of the northern half of Mercury from Johns Hopkins University (2013). The map altitudes largely correlate with the crustal thickness estimates of Smith et al. (2012) and the map shows heat flow measurement sites (circled) at 80°E 38°N, 160°E, 25°N and, 272°E 85°N used in further in the text.

6.2 Further A Priori Information

Mercury is often compared to the Moon due to their similar sizes and surface geology (e.g. Linsky, 1966; Campbell and Taylor, 1983; Ernst et al., 2010). Chase Jr et al. (1976) find thermal properties similar to lunar values, in analysing data from the Mariner 10 flyby. Because Mercury is an airless body, its surface temperature can effectively be modelled similar to that of the Moon (see Section 3.6). The quality of these and other pieces of a priori information is discussed below to further assess the constraints on a reliable heat flow probe measurement.

6.2.1 Surface Temperature

Being the closest planet to the Sun, Mercurian surface temperatures are high with solar flux varying between 6290-14490 W/m^2 from aphelion to perihelion (Spohn et al., 2001). Mercurian surface temperature has been modelled and analysed in several investigations

using sophisticated surface energy balance models (e.g. Chase Jr et al., 1976; Vasavada et al., 1999; Yan et al., 2006). Chase Jr et al. (1976) compare modelled diurnal surface temperatures to measurements returned by Mariner 10. They also discuss the uniqueness of the surface temperature profiles at different longitudes due to the 3:2 Mercurian spin-orbit resonance. This results in a bimodal distribution of surface temperatures where longitudes 0°E and 180°E, in turn, face the Sun at perihelion and longitudes 90°E and 270°E, in turn, face the Sun at aphelion. The effect of this is a solar day which is twice the orbital period – about 176 Earth days (Vasavada et al., 1999; Spohn et al., 2001). This bimodal distribution can be seen in Peplowski et al. (2012), which uses the model of Vasavada et al. (1999). Vasavada et al. (1999) and Yan et al. (2006) show how near surface layering can affect the night time temperature, which is controlled by the shallow subsurface thermal properties. Generally the temperatures of the preceding studies range from a little over 100 to 600 (Vasavada et al., 1999) and 700 (Yan et al., 2006) K.

The surface energy balance model presented in Sections 2.1.2.2.2 and 3.6 is not as sophisticated as the preceding examples but replicates major features of the Mercurian surface temperature, similar to those presented in Vasavada et al. (1999) and Yan et al. (2006). The temperatures are presented in Section 6.3.1. As discussed in Section 5.2.1 a reliable determination of steady surface temperature involves long term and global averages, the length of which depend on data availability. The simple approach of Section 5.2.1 is adopted here: the steady surface temperature is taken as the local average over a Mercurian solar day. Surface temperatures are modelled at both the perihelion and aphelion facing latitudes to determine their effect on a heat flow probe measurement. The exact latitudes and longitudes are informed by further consideration of the surface geophysics, as discussed below.

6.2.2 Thermal Properties

Surface energy balance (see Sections 2.1.2.2.2 and 3.6), which determines the surface temperature, is affected by the albedo A and emittance ε at the surface of Mercury. A common value of emittance used throughout the investigations referenced here is 0.9

while assumed global albedo varies between 0.10-0.2. The albedo at individual locations, of course, varies where high albedo features correlate with impact craters and ejecta and low albedo features with older, space weathered terrain (Robinson et al., 2008; Hughes and Vaughan, 2012; Riner and Lucey, 2012). Taking into account the results of Hagermann and Tanaka (2006) (see Section 6.2.3) it may be prudent to avoid high albedo areas, however the heavily cratered Mercurian surface coupled with the map of Hughes and Vaughan (2012) suggest this may be challenging. Mercury does have smooth plains which cover ~27 % of the surface (>65 % being volcanic in origin) according to the finding of Denevi et al. (2013), mostly in the northern half (Figure 6.2). Taking a heat flow measurement on smooth plains avoids focusing effects by rough surface terrain, therefore simplifying interpretation of the measurement. These and former considerations lead to locating three potential heat flow measurements sites at: 80°E, 38°N where equatorial temperatures are close to a global minimum; 160°E, 25°N inside the Caloris basin where temperatures approach the global maximum and; 272°E, 85°N in the low temperature polar regions (Figure 6.2).

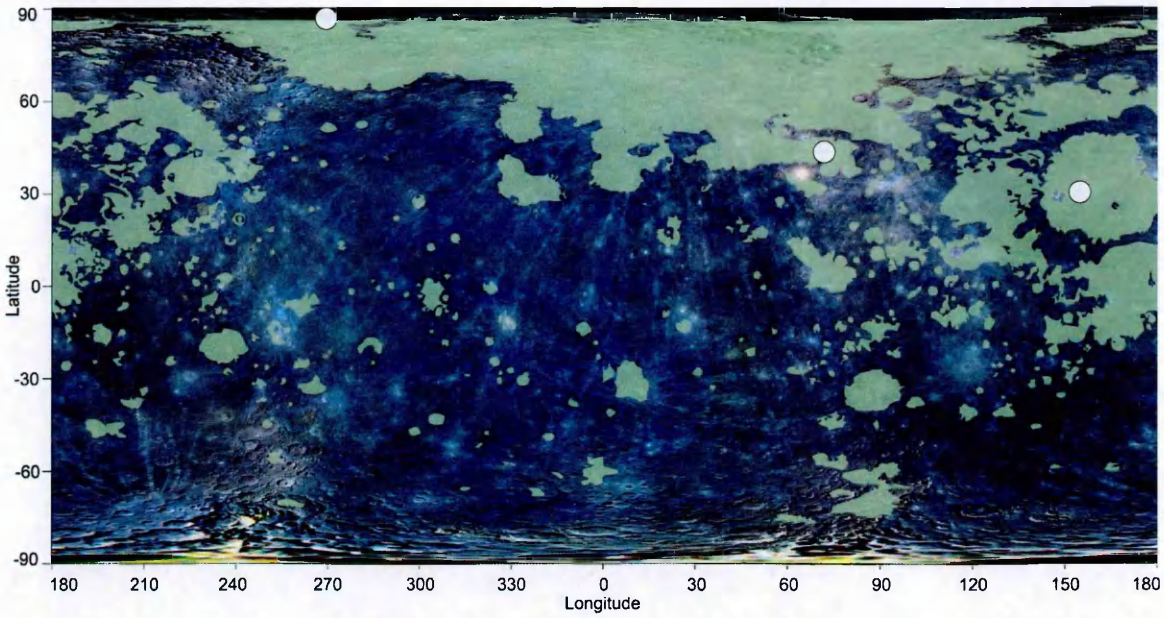

Figure 6.2. Potential heat flow measurements sites shown on MESSENGER Mercury Dual Imaging System (MDIS) colour mosaic with cyllindrical projection Johns Hopkins University, 2013. The colour mosaic is overlaid on a grayscale mosaic to elliminate some lack of coverage northward of 30° Latitude. The green areas identify smooth planes as identified by Denevi et al. (2013). Potential heat flow measurements sites (white circles) are shown at: 80°E, 38°N where equatorial temperature are close to a global minimum; 160°E, 25°N inside the Caloris basin where temperatures approach the global maximum and; 272°E, 85°N in the low temperature polar regions.

Chase Jr et al. (1976) used Mariner 10 TIR data to calculate the thermal inertia along the ground track ranging from 62.76 to 129.704 $J/m^2/s^{1/2}/K$, which is noted as being similar to lunar values. These values are consistent with small grain sizes and low thermal conductivity k with extrapolation of the results of Presley and Christensen (1997). Values of conductivity used in other investigations range from lows of ~1 mW/m/K (Chase Jr et al., 1976; Yan et al., 2006) for the shallow subsurface to highs of ~10 mW/m/K (Vasavada et al., 1999; Spohn et al., 2001) throughout the whole column, or at depth (assuming a mean surface temperature of 400 K) – they are adopted here. Vasavada et al. (1999) and Yan et al. (2006) use 2-layer depth profiles consistent with a thin (< 0.5 m) dust mantle over a basalt bed. A 2-layer model is also used here, though parameterizations similar to those in Section 5.2.2 (also see Grott et al., 2007) are used. Two conductivity profiles are assumed: one a heterogeneous profile with continuously varying thermal properties (1-layered), the other a 2-layered profile (see Section 3.3). As in Section 5.2.2 the profile for

density ρ is correlated with the conductivity profile, and the specific heat capacity c is held constant. Densities used in other investigations include Lunar values of 1300 kg/m^3 at the surface, with an exponential increase to 1920 kg/m^3 (Spohn et al., 2001), at depth or 1800 kg/m^3 in a lower layer (Vasavada et al., 1999; Yan et al., 2006). The specific heat is calculated via the mean surface thermal inertia $I = \sqrt{k\rho c} = 96.232$ J/m^2/K/s$^{1/2}$ from the results of Chase Jr et al. (1976), using bulk thermal conductivity k and density ρ. The calculated surface value of c is then held constant with depth. The profiles are shown in Figure 6.3 with associated numbers shown in Table 6.1.

Table 6.1. Derived regolith properties for 1-layered and 2-layered regolith models on Mercury based on a mean surface thermal inertia $I = \sqrt{k\rho c} = 96.232$ J/m^2/K/s$^{1/2}$. The same two models are used for all measurement sites. The thermal conductivity is k and ρ is the density at select depth z.

MODEL	z [m]	k [W/m/K]	ρ [kg/m^3]	c [kg/m^3]
1-LAYERED	0	0.001	1050	859.577
MODEL	0.5	0.0095	1852.5	859.577
2-LAYERED	0	0.005	1350	768.765
MODEL	0.5	0.01	1950	768.765

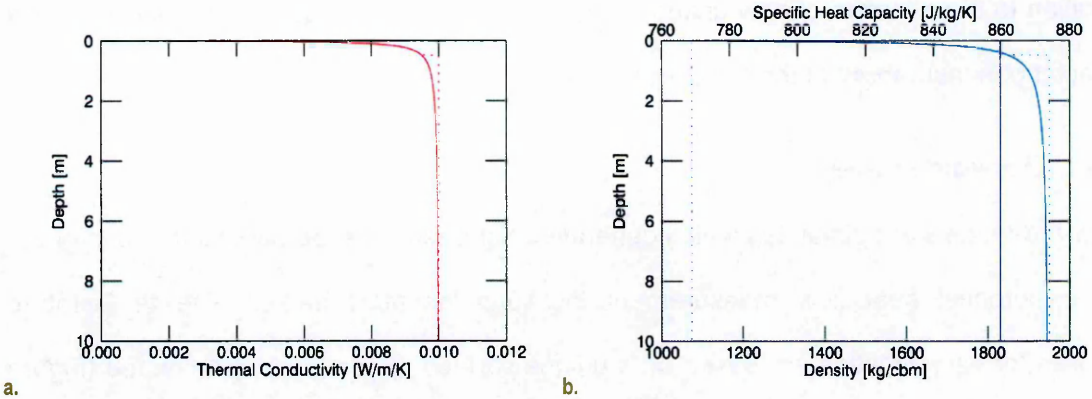

Figure 6.3. Hypothetical conductivity k, density ρ and specific heat capacity c depth profiles for potential heat flow measurement sites. In: a. the solid and dotted red curves show conductivity variation; b. the solid and dotted blue curves the density variation and the solid and dotted purple lines the constant specific heat. The dotted and solid curves indicate thermal properties respectively associated with the 1-layered and 2-layered regolith models. The pofiles overlap in the surface layer (0-50 cm).

6.2.3 Heat Sources

MESSENGER results of Peplowski et al. (2012) indicate some variation of potassium (K) across the surface of Mercury – the variation of thorium (Th) being relatively insignificant – with the implication that the K/Th ratio varies across the surface. The high K deposits can be associated with the northern volcanic plains though the Caloris basin appears to be an area of low K. The working hypothesis is that the K is transported by surface processes (e.g. due to high temperatures) and redeposited or lost to Mercury's exosphere which would suggest that the K enriched deposits are fairly thin. However, if the K enriched deposits are fairly thick, the analysis of Hagermann and Tanaka (2006) may need to be applied.

6.3 Scenarios

The thermal properties derived in Section 6.2.2 suggest shallow skin depths, allowing access to the unmasked steady basal heat flow at relatively shallow depths. Still, a heat flow probe may not penetrate to desired depths, therefore the question of how the temperature amplitudes affect measurements above the target is important. This is in

addition to the question of how unknown layering and different heat flow magnitudes may affect the measurability of the basal heat flow.

6.3.1 Forward Models

Forward models are simulated which generate unique temperature profiles for each of the three potential heat flow measurement locations identified earlier. The temperature profiles for each location are based on a unique surface temperature, a 1-layered (Figure 6.4) and 2-layered (see Appendix 9.6.1)[3] Mercurian regolith, and three basal heat flow estimates, as discussed in Section 6.1. Therefore, a total of 6 unique profiles are simulated for each location. Only the highest heat flow scenarios (highest temperature gradient) are presented in figures – the differences caused by the change in temperature gradient are nearly indistinguishable and therefore do not offer any new visual information.

The temperature-depth profiles show that the skin depths for the relatively low conductivities used here are shallow, meaning the basal heat flow can be accessed at a depth of ~1.25 m. For the 2-layered model, the higher conductivity of the lower layer results in a small reduction in the magnitude of the temperature gradient and a slight increase in skin depth.[3] The low conductivity upper layer attenuates most of the surface heat. Previous results in Sections 4.2.1, 4.3.1 and 5.3.3 (Tharsis site on Mars) illustrate what can be expected for scenarios with shallow skin depth and low heat flow. For example, the dependence of optimized heat flow accuracy on random error amplitude is found, in Section 5.3.3, to be small. Therefore themes related to the amplitude of random errors in measurements are not explored here. Systematic errors are discussed in Section 7.3. The relationship between skin depth and optimized heat flow accuracy is established in Sections 4.2.1, 4.3.1 and 5.3.3, therefore neither is that theme explored here.

[3] Despite the increase in skin depth between the 1-layered and 2-layered models being small, and visually indistinguishable at the scales shown in Figure 6.4 (also see Appendix 9.6.1), the inversion results do show a non-negligible response of the algorithm to the change.

The temperature-time profiles illustrate the results of the Mercurian bi-modal temperature distribution, with peak temperatures of ~660 K close to the 180°E hot pole and ~550 K close to the 90°E 'cool' region (see Appendix 9.6.1 for relevant surface energy balance parameters). The prominent 'second sunrises' respectively at 80°E 38°N and 272°E 85°N are because of retrograde motion of the Sun as Mercury's orbital velocity at perihelion outpaces its angular velocity (e.g. Vasavada et al., 1999). It is important to note that the surface energy balance calculation provides a first order estimate of the Mercurian surface temperature, which serves the purposes of this work. In practice, more sophistication may be introduced into the model, or more sophisticated models used to achieve more accurate surface temperature predictions.

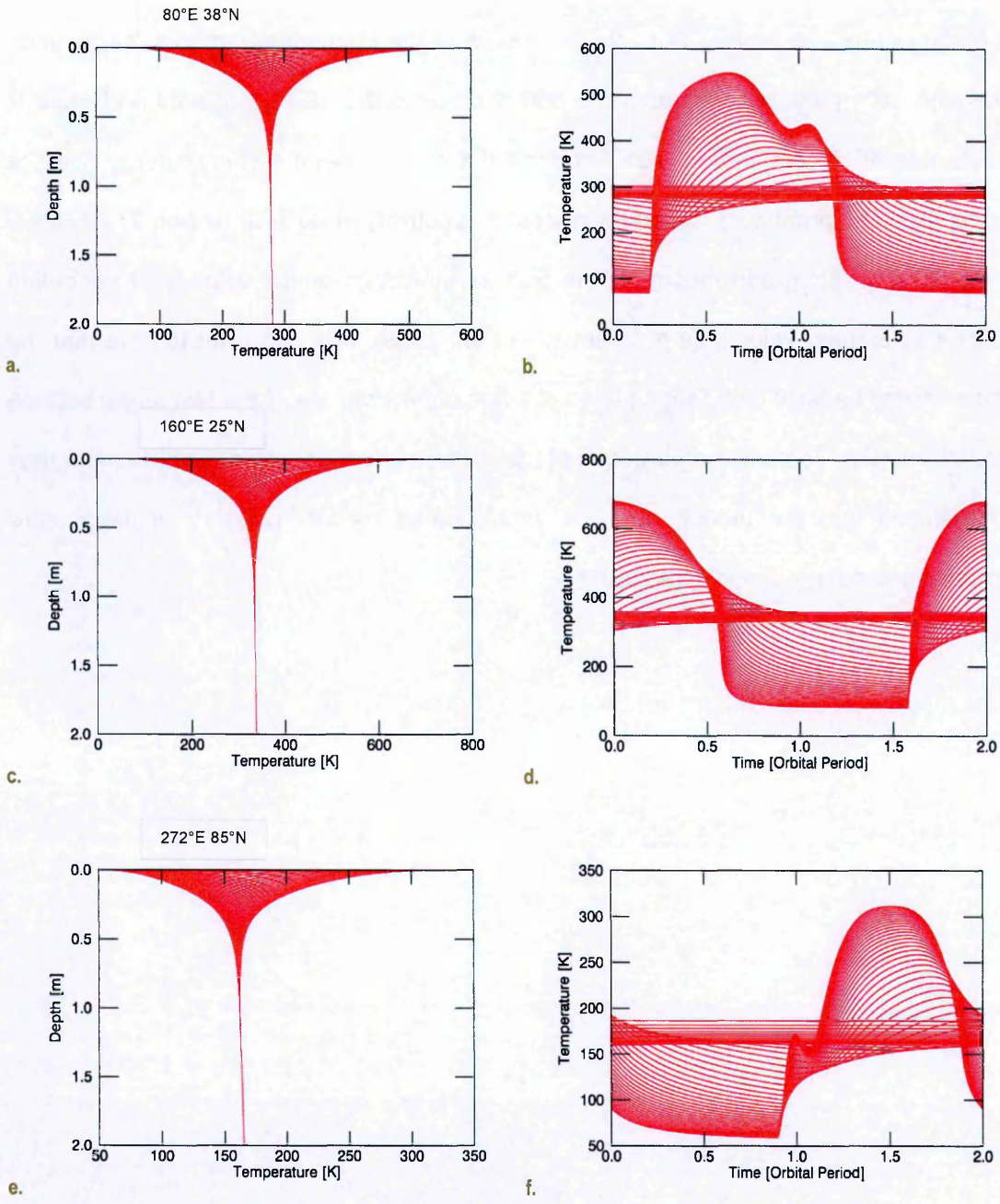

Figure 6.4. Forward modelled temperature profiles for measurement sites. These are from the respective 1-layered models (see Figure 6.3) with the 'high' heat flow (30 mW/m²) regime at 80°E 38°N (a-b), 160°E 25°N (c-d) and 272°E 85°N (e-f). The left contours are overlays of depth-dependent temperature T over time t of 2 orbital periods in ~3.5 d steps; the right contours are overlays of time-dependent temperature T over depth z of 5 m (larger amplitudes towards the surface). All simulations are run over the same time period from midnight at perihelion (also see Appendix 9.6.1).[4]

[4] The forward models with lower heat flow are visually indistinguishable from that presented in Figure 6.4 and are therefore not shown.

6.3.2 Measurements

Since some themes are explored in other chapters, the most relevant questions arising from the discussion above are how: 1. the geographic location (and therefore temperature amplitude); 2. the time of an instantaneous measurement (considering the steep dayside and flat night-side temperature-time gradients) and its effectiveness compared to longer time periods; 3. assumptions about subsurface layering, affect a heat flow probe measurement.

Noise of amplitude 100 mK is applied to each measurement, constant with depth. Instantaneous measurements are included, because it is likely that the harsh surface thermal conditions on Mercury will shorten the lifetime of any instrument – these are at peak daytime, transitional heating and cooling, and minimum night-time temperatures. A monitoring period of 1 Mercurian solar day is also included to assess any benefits of longer monitoring periods. A maximum of 15 sensors are used with maximum sensor depths of 0.5 (7 sensors) and 2 m (15 sensors). This leads to 10 measurement scenarios per site scenario – a grid of which is shown in Table 6.2. Representative measurements are shown in Figure 6.5 for the 1-layered model (2-layered model measurements are presented in Appendix 9.6.2).

Table 6.2. Grid of measurement scenarios (10 in total per site scenario) simulated for each of the forward modeled scenarios of Section 6.3.1 and Appendix 9.6.1.

		MONITORING PERIOD [~SOLAR DAY]					
		0.0	0.0	0.0	0.0	1	
DEPTH [m]	0.5	PEAK	HEATING	COOLING	MINIMUM		ERROR [K]
	2.0	PEAK	HEATING	COOLING	MINIMUM	OPTIMAL	0.1
		1 (-)	1 (-)	1 (-)	1 (-)	176 (1.0)	
		NUMBER OF MEASUREMENTS (TIME RESOLUTION [DAY])					

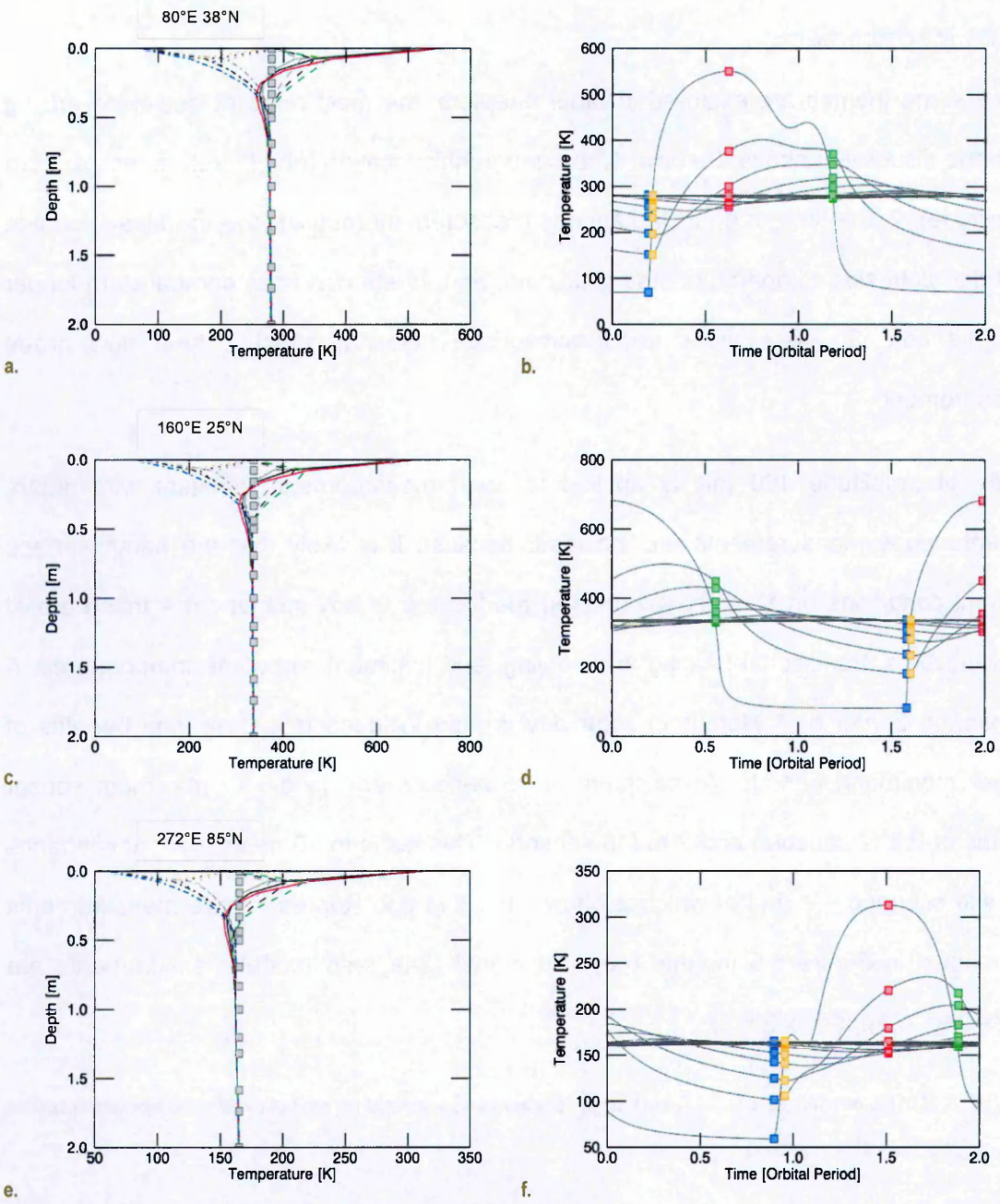

Figure 6.5. Temperature profiles for measurements at sites at 80°E 38°N (a-b), 160°E 25°N (c-d) and 272°E 85°N (e-f) for the 1-layered regolith model with a heat flow of 30 mW/m². The plots are overlays of: (a, c, e) temperature-depth profiles for instantaneous measurements at peak daytime, (solid red), transitional heating (dotted orange) and cooling (dashed green) and, minimum nightime (dot-dashed blue) temperatures and; (b, d, f) temperature-time profiles for measurements covering 1 Mercurian solar day. The squares represent sensor locations: in space (a, c, e, plotted at the basal temperature value); and time (b, d, f, plotted at the times and temperatures of, and colour coordinated with the instantaneous measurements).

6.3.3 Inversion Results

The inversion tests are carried out by assuming initial basal heat flows which are inaccurate by a factor of two – considered reasonable because current estimates vary by a factor of 3 or less.[5] Initial heat flows are also estimated using bulk conductivity, and the temperature gradient of the two lowest sensors of a measurement, to facilitate comparison to the more complicated optimization estimates (Table 6.3 to Table 6.5; also see Appendix 9.6.3.1).

The error in the temperature measurement is assumed to be additive noise of 0.1 K amplitude, constant with depth, which is consistent with the noise model used to synthesise the measurement errors (see Section 6.3.2).

The steady surface temperature is taken as the mean of the simulated surface temperature (see Sections 6.2.1 and 6.3.1) used for each measurement site. The unsteady surface temperature is taken as the difference between the simulated surface temperature and the mean.

To assess the effect of layering assumptions, all the optimizations are performed with assumed 2-layered and 1-layered regolith (conductivity and density) scenarios independent of the true regolith profile. This results in overestimated skin depth for the 1-layered regolith model and underestimated skin depth for the 2-layered regolith model (red bordered cells, Table 6.3 to Table 6.8; also see Appendix 9.6.3).

6.3.3.1 Initial Estimates

Errors in the initial heat flow estimates (Table 6.3 to Table 6.5; also see Appendix 9.6.3.1 – the grey shaded cells indicate initial estimates using bulk conductivity, which are not improved by optimization) show that, for a sensor penetration depth of 0.5 m, where the

[5] This is an academic note as it is already established that the magnitude of errors in the optimized heat flows show no significant dependence on the magnitude of the initial error (there is dependence on the sign of the error such that low estimates are optimized to a low value – Sections 4.2.1.1 and 4.3.1.1, and Appendix 9.4.2)

unsteady perturbations of the subsurface heat flow are still significant, the higher heat flow site scenarios (with steeper temperature gradients) produce more accurate results (though still inaccurate by factors between 8-125). At 2 m the dependence of the initial heat flow estimate accuracy on the magnitude of the true heat flow is lost, as the unsteady heat flow from the surface is damped to negligible values, and the precision errors present in the measurements become more significant (accuracies between 0-63 % of the true values).[6]

An interesting trend emerges in terms of the accuracy of the assumed regolith profiles: for nearly all instantaneous measurements, up to 0.5 m sensor penetration depth, the assumption of a 1-layered regolith (conductivity) model produces the most accurate heat flow estimates, regardless of the true regolith model; for nearly all measurements covering a full Mercurian solar day – and also instantaneous measurements at 2 m sensor penetration depth – the 2-layered regolith model produces the most accurate results.

The preceding result is because, above 0.5 m, the conductivity is lowest; therefore the low 1-layered bulk estimate is closer to the true bulk value. Up to 2 m, the conductivity is highest, meaning the high 2-layered bulk estimate fits better to the true values. Additionally, at 0.5 m sensor penetration depth, the instantaneous measurements have steep temperature gradients due to the unsteady heat flow, which overestimates the magnitude of the basal heat flow. A low conductivity estimate mitigates the former overestimate. For the measurements over a full solar day, the gradients are averaged: this, while avoiding the biasing effect of an instantaneous measurement, tends to hide (underestimate) the underlying steady temperature gradient. Therefore the high bulk

[6] This is important as it demonstrates the consistency of results between those in Section 4.2.1.1, where the ideal heat flow results show no significant dependence on heat flow magnitude, and those in Section 5.3.3.1 which show direct dependence on heat flow magnitude. This is further evidence for the conclusion that, once the role of the unsteady heat flow is damped out, the heat flow magnitude has a less significant impact on optimized heat flow accuracy.

conductivity estimate of the 2-layered assumption results in more accurate estimates as it produces higher heat flows with the (low) steady temperature gradient estimates.

At 0.5 m, the most accurate initial estimates are obtained from the sites with the smallest temperature amplitudes. These are, in turn from the sites at 272°E 85°N (127 K), 80°E 38°N (241 K) and 160°E 25°N (301 K). At 2 m the unsteady temperature variations are damped to negligible values, therefore there is no dependence on the temperature amplitudes, with most estimates falling within 40 % accuracy. For the instantaneous measurements, there are no consistent trends in accuracy in terms of the point in the cycle where the measurement is taken. The most accurate estimates are from the monitoring periods over a full Mercurian solar day (accurate to within 12 %).

Table 6.3. Grid of initial heat flow estimate relative error magnitudes $\epsilon_{F_B^{SO}} = \left|\frac{F_B^{SO}}{F_B^{ST}} - 1\right|$ (green borders – see Appendix 9.1 for symbol definitions) from measurement sited at 80°E 38°N on Mercury. This is for the 1-layered site scenario where the red shaded cells indicate a (incorrect) 2-layered regolith assumption. The bulk conductivity down to 10 m is k_{BULK} [W/m/K] and z_{SKIN} [m] is the skin depth. The shaded cells show values which are not improved by optimization.

80°E 38°N	MONITORING PERIOD [~SOLAR DAY]					1-LAYERED
	0.0 (PEAK DAYTIME)	0.0 (TRANSITIONAL HEATING)	0.0 (TRANSITIONAL COOLING)	0.0 (MINIMUM NIGHTIME)	1	
0.5	68.91	64.95	73.06	65.32	0.02	0.01
	34.78	33.50	36.70	32.72	0.02	0.02
	23.00	21.47	23.74	21.69	0.07	0.03
	70.70	66.63	74.90	67.02	0.01	0.01
	35.69	34.38	37.61	33.59	0.01	0.02
	23.62	22.04	24.32	22.27	0.05	0.03
2.0	0.35	0.63	0.05	0.18	0.11	0.01
	0.03	0.10	0.36	0.20	0.09	0.02
	0.10	0.11	0.09	0.05	0.11	0.03
	0.33	0.62	0.08	0.16	0.09	0.01
	0.01	0.08	0.34	0.18	0.07	0.02
	0.07	0.08	0.07	0.03	0.09	0.03
k_{BULK} = 6.62E-3	1 (-)	1 (-)	1 (-)	1 (-)	176 (1.0)	z_{SKIN} =0.15
	NUMBER OF MEASUREMENTS (TIME RESOLUTION [DAY])					

DEPTH [m]

HEAT FLOW [W/m^2]

Table 6.4. Grid of initial heat flow estimate relative error magnitudes $\epsilon_{F_B^{SO}} = \left|\frac{F_B^{SO}}{F_B^{ST}} - 1\right|$ (green borders – see Appendix 9.1 for symbol definitions) from measurement sited at 160°E 25°N on Mercury. This is for the 1-layered site scenario where the red shaded cells indicate a (incorrect) 2-layered regolith assumption. The bulk conductivity down to 10 m is k_{BULK} [W/m/K] and z_{SKIN} [m] is the skin depth. The shaded cells show values which are not improved by optimization.

160°E 25°N	MONITORING PERIOD [~SOLAR DAY]					1-LAYERED	
	0.0 (PEAK DAYTIME)	0.0 (TRANSITIONAL HEATING)	0.0 (TRANSITIONAL COOLING)	0.0 (MINIMUM NIGHTIME)	1		
DEPTH [m]	91.58	83.57	93.34	77.82	0.04	0.01	HEAT FLOW [W/m^2]
	45.90	41.34	46.48	38.53	0.05	0.02	
	30.95	27.94	30.58	25.53	0.09	0.03	
0.5	93.95	85.73	95.70	79.84	0.01	0.01	
	47.10	42.42	47.65	39.54	0.02	0.02	
	31.77	28.69	31.34	26.21	0.07	0.03	
	0.21	0.01	0.23	0.35	0.08	0.01	
	0.14	0.18	0.21	0.16	0.11	0.02	
2.0	0.17	0.05	0.07	0.13	0.11	0.03	
	0.19	0.01	0.21	0.33	0.06	0.01	
	0.12	0.16	0.19	0.13	0.09	0.02	
	0.15	0.08	0.05	0.11	0.09	0.03	
k_{BULK} = 6.62E-3	1 (-)	1 (-)	1 (-)	1 (-)	176 (1.0)	z_{SKIN} =0.15	
	NUMBER OF MEASUREMENTS (TIME RESOLUTION [DAY])						

Table 6.5. Grid of initial heat flow estimate relative error magnitudes $\epsilon_{F_B^{S0}} = \left|\frac{F_B^{S0}}{F_B^{S7}} - 1\right|$ (green borders – see Appendix 9.1 for symbol definitions) from measurement sited at 272°E 85°N on Mercury. This is for the 1-layered site scenario where the red shaded cells indicate a (incorrect) 2-layered regolith assumption. The bulk conductivity down to 10 m is k_{BULK} [W/m/K] and z_{SKIN} [m] is the skin depth. The shaded cells show values which are not improved by optimization.

272°E 85°N	MONITORING PERIOD [~SOLAR DAY]					1-LAYERED
	0.0 (PEAK DAYTIME)	0.0 (TRANSITIONAL HEATING)	0.0 (TRANSITIONAL COOLING)	0.0 (MINIMUM NIGHTIME)	1	
DEPTH [m] 0.5	27.14	29.22	28.95	23.28	0.10	0.01
	11.80	14.31	14.51	11.87	0.09	0.02
	7.81	10.07	10.04	7.95	0.05	0.03
	27.86	30.00	29.66	23.90	0.08	0.01
	12.12	14.70	14.86	12.20	0.07	0.02
	8.04	10.35	10.27	8.18	0.02	0.03
2.0	0.01	0.11	0.04	0.04	0.11	0.01
	0.20	0.34	0.05	0.11	0.11	0.02
	0.03	0.05	0.14	0.08	0.11	0.03
	0.01	0.14	0.02	0.01	0.08	0.01
	0.18	0.32	0.02	0.14	0.09	0.02
	0.05	0.03	0.11	0.05	0.09	0.03
k_{BULK} = 6.62E-3	1 (-)	1 (-)	1 (-)	1 (-)	176 (1.0)	z_{SKIN} =0.15
	NUMBER OF MEASUREMENTS (TIME RESOLUTION [DAY])					

HEAT FLOW [W/m^2]

6.3.3.2 *Optimized Heat Flow*

Optimization causes meaningful improvements on the initial estimates in several cases at shallow (0.5 m) penetration depth, in particular, and to a lesser degree, at 2 m (Table 6.6 to Table 6.8; also see Appendix 9.6.3.2 – the grey shaded cells indicate initial estimates using bulk conductivity that are not improved by optimization).

For the instantaneous measurements penetrating up to 0.5 m depth, errors in the optimized heat flows show that the higher heat flow site scenarios (with steeper steady temperature gradients) produce more accurate results. For measurements covering a full Mercurian solar day and/or measurements up to 2 m depth, the former trend is maintained at the 160°E 25°N site, but appears reversed at the 80°E 38°N and 272°E 85°N sites (though with values that differ by 0-4 %). The difference between sites is related to the relative temperature amplitudes, where 160°E 25°N has the largest, as noted in Section 6.3.3.1 (recall that as the unsteady temperature amplitude becomes negligible, dependence of the accuracy of optimized heat flow on heat flow magnitude diminishes).

At 0.5 m, the most accurate optimized heat flows are obtained from the sites with the smallest temperature amplitudes, similar to the case with the initial estimates. Also, for instantaneous measurements at 0.5 m, heat flows optimized from peak daytime temperatures are the most accurate (though still inaccurate by factors greater than 1). The peak daytime temperature measurements provide the most accurate optimized heat flows because the surface temperatures do not undergo rapid changes around the time of measurement. The transitional temperatures are taken at a time of rapid change, with sharp transitions in the subsurface temperature-depth gradient, and the minimum night-time temperatures occur just before the sharp transition to sunrise (see Figure 6.5 and Figure 6.6). These sharp transitions introduce ambiguities into the inverse model such that several surface temperatures can fit a temperature profile within a particular timestep. The most accurate estimates are from the monitoring periods over a full Mercurian solar day (most, accurate to within 50 %).

At 2 m the optimized heat flow accuracies display no explicit dependence on the location (amplitude) of the measurement, or the point in the cycle at which the measurement is taken. This follows from the damping of the surface heat flow to negligible values at depth.

Table 6.6. Grid of optimized heat flow relative error magnitudes $\epsilon_{F_B^{SI}} = \left|\frac{F_B^{SI}}{F_B^{ST}} - 1\right|$ (green borders – see Appendix 9.1 for symbol definitions) from measurement sited at 80°E 38°N onMercury. This is for the 1-layered site scenario where the red shaded cells indicate a (incorrect) 2-layered regolith assumption. The bulk conductivity down to 10 m is k_{BULK} [W/m/K] and z_{SKIN} [m] is the skin depth. The shaded cells show values which are not improved by optimization.

80°E 38°N		MONITORING PERIOD [~SOLAR DAY]					1-LAYERED
		0.0 (PEAK DAYTIME)	0.0 (TRANSITIONAL HEATING)	0.0 (TRANSITIONAL COOLING)	0.0 (MINIMUM NIGHTIME)	1	
DEPTH [m]	0.5	6.55	29.66	26.68	28.94	0.32	0.01
		3.07	15.05	13.20	14.68	0.35	0.02
		1.91	10.15	8.65	9.90	0.37	0.03
	2.0	3.78	17.63	17.20	16.82	0.07	0.01
		1.79	8.93	8.60	8.51	0.11	0.02
		1.13	5.98	5.65	5.70	0.12	0.03
		0.22	0.57	0.45	0.65	0.13	0.01
		0.19	0.36	0.14	0.39	0.14	0.02
		0.18	0.29	0.05	0.32	0.14	0.03
		0.15	0.03	0.17	0.09	0.00	0.01
		0.10	0.00	0.07	0.05	0.02	0.02
		0.08	0.01	0.04	0.05	0.02	0.03
k_{BULK} = 6.62E-3		1 (-)	1 (-)	1 (-)	1 (-)	176 (1.0)	z_{SKIN} =0.15
		NUMBER OF MEASUREMENTS (TIME RESOLUTION [DAY])					

HEAT FLOW [W/m^2]

Table 6.7. Grid of optimized heat flow relative error magnitudes $\epsilon_{F_B^{SI}} = \left|\frac{F_B^{SI}}{F_B^{ST}} - 1\right|$ (green borders – see Appendix 9.1 for symbol definitions) from measurement sited at 160°E 25°N onMercury. This is for the 1-layered site scenario where the red shaded cells indicate a (incorrect) 2-layered regolith assumption. The bulk conductivity down to 10 m is k_{BULK} [W/m/K] and z_{SKIN} [m] is the skin depth. The shaded cells show values which are not improved by optimization.

160°E 25°N	MONITORING PERIOD [~SOLAR DAY]					1-LAYERED
	0.0 (PEAK DAYTIME)	0.0 (TRANSITIONAL HEATING)	0.0 (TRANSITIONAL COOLING)	0.0 (MINIMUM NIGHTIME)	1	
DEPTH [m] 0.5	5.91	36.87	34.35	35.07	0.50	0.01
	2.77	18.65	16.96	17.72	0.44	0.02
	1.70	12.55	11.19	11.94	0.42	0.03
	3.84	22.51	22.22	20.12	0.30	0.01
	1.86	11.36	11.00	10.12	0.22	0.02
	1.16	7.60	7.30	6.80	0.20	0.03
2.0	0.38	0.79	0.41	0.72	0.20	0.01
	0.26	0.47	0.13	0.43	0.17	0.02
	0.22	0.37	0.04	0.34	0.17	0.03
	0.29	0.10	0.01	0.06	0.08	0.01
	0.16	0.06	0.01	0.04	0.06	0.02
	0.12	0.06	0.02	0.04	0.05	0.03
k_{BULK} = 6.62E-3	1 (-)	1 (-)	1 (-)	1 (-)	176 (1.0)	z_{SKIN} =0.15
	NUMBER OF MEASUREMENTS (TIME RESOLUTION [DAY])					

HEAT FLOW [W/m^2]

Table 6.8. Grid of optimized heat flow relative error magnitudes $\epsilon_{F_B^{SI}} = \left|\frac{F_B^{SI}}{F_B^{ST}} - 1\right|$ (green borders – see Appendix 9.1 for symbol definitions) from measurement sited at 272°E 85°N onMercury. This is for the 1-layered site scenario where the red shaded cells indicate a (incorrect) 2-layered regolith assumption. The bulk conductivity down to 10 m is k_{BULK} [W/m/K] and z_{SKIN} [m] is the skin depth. The shaded cells show values which are not improved by optimization.

272°E 85°N	MONITORING PERIOD [~SOLAR DAY]					1-LAYERED
	0.0 (PEAK DAYTIME)	0.0 (TRANSITIONAL HEATING)	0.0 (TRANSITIONAL COOLING)	0.0 (MINIMUM NIGHTIME)	1	
DEPTH [m] 0.5	5.99	14.05	15.09	13.11	0.36	0.01
	2.81	7.24	7.36	6.76	0.37	0.02
	1.75	4.92	4.79	4.64	0.38	0.03
	3.59	8.93	10.04	7.79	0.11	0.01
	1.73	4.57	4.96	3.98	0.13	0.02
	1.11	3.05	3.26	2.71	0.14	0.03
	0.14	0.42	0.11	0.34	0.15	0.01
	0.15	0.29	0.03	0.24	0.15	0.02
2.0	0.15	0.24	0.07	0.22	0.15	0.03
	0.09	0.10	0.00	0.04	0.02	0.01
	0.06	0.07	0.03	0.03	0.03	0.02
	0.05	0.05	0.03	0.03	0.03	0.03
k_{BULK} = 6.62E-3	1 (-)	1 (-)	1 (-)	1 (-)	176 (1.0)	z_{SKIN} =0.15
	NUMBER OF MEASUREMENTS (TIME RESOLUTION [DAY])					

HEAT FLOW [W/m^2]

In all scenarios, the 2-layer assumed regolith profiles produce more accurate optimized heat flows, which can be explained by the effects of the bulk conductivity on the temperature amplitude and gradient at depth and truncation errors due to the low sampling of the surface and subsurface temperatures.[7]

Towards the surface, above ~0.5 m, truncation errors cause the temperatures to be underestimated for peak daytime and transitional heating measurements, and overestimated for transitional cooling and minimum night-time measurements (see Figure 6.6 for the 1-layered regolith model and Appendix 9.6.3.2 for equivalent 2-layered model examples, examples with maximum penetration depths of 0.5 m, and examples for a full solar day measurement). The inverse model therefore compensates for the surface inaccuracies by producing high heat flows in the case of underestimates, and low heat flows in the case of overestimates. Assuming the 1-layer (lower conductivity) model increases the magnitude of the preceding effects relative to the 2-layer model assumption (effects of conductivity are discussed in Sections 3.2.2 and 3.4.2). The rapid changes in the transitional temperatures also exacerbate the effect which explains why the peak daytime temperatures produce the most accurate results.

[7] Truncation errors are caused by the use of relatively large control volumes such that the thermal capacity coefficient (see Section 3.4.1.1) becomes large, reducing the efficiency of unsteady heat transfer between control volumes. This arises in the use of implicit time discretization, which is the case here; however, tests using explicit time discretization produce equivalent results. In practice, a trade-off is necessary between time and depth resolution, and computer processing time. Because of the theoretical context of this presentation and the appreciable number of scenarios being tested, minimum processing time is given priority.

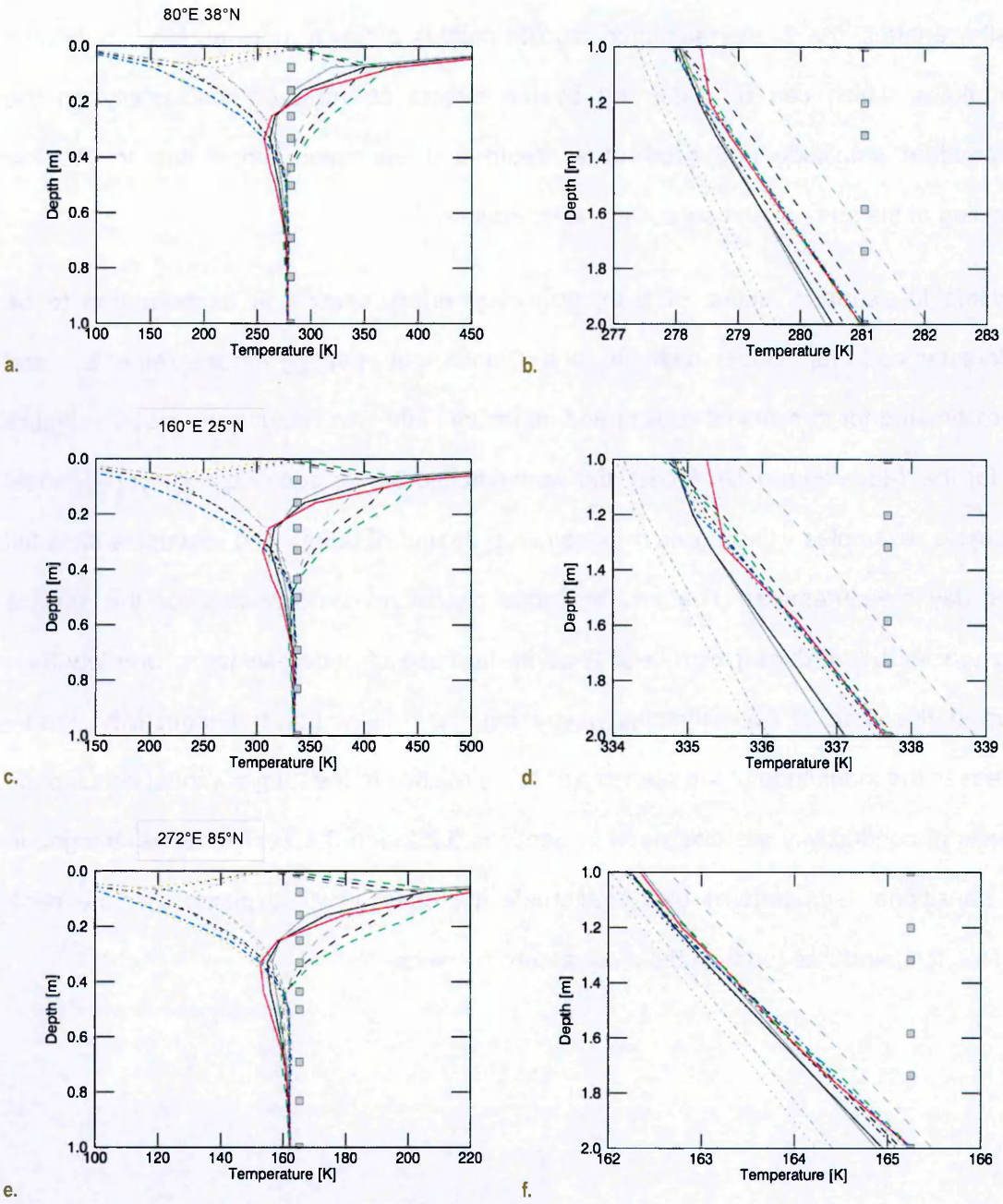

Figure 6.6. Temperature profiles for optimized heat flows, compared to true profiles, for sites at 80°E 38°N (a-b), 160°E 25°N (c-d) and 272°E 85°N (e-f) for the 1-layered instantaneous measurement scenario with a heat flow of 30 mW/m^2. The left plots (a, c, e) highlight the effects of the unsteady surface heat flow down to depth $z = 1$ m. The right plots (b, d, f) show the temperature gradients between 1-2 m depth where the unsteady surface heat flow becomes negligible. The curves are associated with measurement times according to: solid (peak daytime); dotted (transitional heating) and, dashed (cooling) and; dot-dashed (minimum nightime). The colored curves (red, orange, green, blue) are measured profiles, the grayscale curves are the optimized profiles where medium greys and dark greys respectively represent correct (1-layer) and incorrect (2-layer) layering assumptions. The grey squares are sensor locations and are plotted at the true basal temperature.

6.4 Summary

Mercury is an enigmatic planet: its small size, which suggests a rapid cooling history, is coupled with a high density and a magnetic field, which points to it having a large, metallic, at least partially fluid core. Its surface features lobate scarps, the extent of which suggests smaller global contraction than that expected from the cooling of a large metallic core. The former observations require a mechanism which slows Mercury's cooling. A variety of thermal models exist which seek to provide insight into the processes that have influenced Mercury's current state; these predict current global heat flow in the range of 10-40 mW/m^2. A planetary heat flow measurement, accurate to within 50 %, can therefore aid in the selection of the most plausible of these models.

To test the viability of a Mercurian heat flow measurement, an inverse model is applied to several feasible heat flow probe measurement scenarios for three locations on Mercury: one close to one of the hot poles at 160°E 25°N, and two in the cooler regions at low (80°E 38°N) and high (272°E 85°N) latitudes. The Mercurian surface temperature is estimated using a surface energy balance model. Surface thermal properties are derived from observed surface thermal inertia; these are extrapolated downwards with 1-layer and 2-layer (with a high density, high conductivity layer below 0.5 m) regolith models. The scenarios are forward modelled with a range of heat flows between 10-30 mW/m^2.

Instantaneous measurements are derived from the different forward models at peak daytime, transitional heating and cooling, and minimum night-time temperatures. Measurements are also derived which cover a full Mercurian solar day, to quantify the potential of longer term measurements. The measurement scenarios involve sensor penetration depths of 0.5 m (with appreciable unsteady temperature variation) and 2 m (where the unsteady temperature is negligible). They have noise of the order of 100 mK added to account for expected measurement uncertainties due to instrument precision.

The measurements are inverted with assumed initial heat flows inaccurate by a factor of 2; however, simple estimates are calculated, using bulk conductivity and the temperature

gradient at the lowest 2 sensors, to quantify the potential effect of inversion on heat flow accuracy. The true surface temperature profiles are used in the inversion, while inaccurate and accurate regolith model assumptions (1-layer and 2-layer) are applied in turn to the 1-layer and 2-layer regolith models to test the effect of inaccurate layering assumptions.

The forward models have shallow skin depth (0.15-0.16 m) such that inversion may not be necessary given the target depths of proposed heat flow probes. Below 1 m, the basal heat flow is largely accessible and can be initially determined to within 50 % in nearly all cases, and 20 % in most cases. Optimisation improves approximately half of these (by between 1-98 %) to within 10 % in most cases.

For penetration depths up to 0.5 m, long monitoring periods (1 Mercurian solar day tested) are required to derive accurate heat flow estimates without optimization (most fall within 10 %). Optimization, while improving nearly all of the initial heat flow estimates (inaccurate by factors >7) for instantaneous measurements by large factors, provides marginally useful results (still inaccurate by factors >1) in only a few cases. Low (inaccurate) conductivity estimates tend to mitigate the steep temperature gradient biases present in shallow measurements.

Significant truncation errors are present in the inverted temperature results because of the use of large control volumes in the inverse model, matching the number of measurement sensors – these complicate the interpretation of results with respect to incorrect layering assumptions. Conductivity overestimates appear to mitigate the effects of the use of large control volumes. Despite the former, optimization improves upon initial estimates, using bulk conductivity, in many instances, as noted above.

More accurate heat flows are optimized from measurements at Mercurian locations with lower temperature amplitudes; in order of decreasing accuracy these are 272°E 85°N (127 K), 80°E 38°N (241 K) and 160°E 25°N (301 K). The basal heat flows are most accurate, optimized from a peak daytime temperature, when the variation in the unsteady surface temperature is small. Taking instantaneous measurements where there are rapid, or

sharp temperature transitions exacerbates the problem with truncation errors and makes it more difficult for the inverse model to find a unique temperature solution at a particular timestep.

These results show that inversion of instantaneous temperature measurements at Mercury produces improvements on initial heat flow estimates where a heat flow probe does not penetrate far enough below the skin depth (and does not persist over a Mercurian solar day). These, though inaccurate by factors >1, can still provide useful constraints on thermal models which predict heat flows varying by up to a factor of 4. Inversion can also improve upon measurements at ideal depths (2 m tested) and an ideal monitoring period of 1 Mercurian solar day, producing highly accurate heat flow estimates. To maximise the chances of success it is best to seek out sites with the lowest temperature amplitudes and take measurements at times when the rate of change of the surface temperature is slow.

6.5 References

BENKHOFF, J. & HELBERT, J. 2006. Thermal infrared spectroscopy to investigate the composition of mercury – The MERTIS instrument on BepiColombo. *Advances in Space Research,* 38, 647-658.

BREUER, D., HAUCK, S., II, BUSKE, M., PAUER, M. & SPOHN, T. 2007. Interior Evolution of Mercury. *Space Science Reviews,* 132, 229-260.

CAMPBELL, I. H. & TAYLOR, S. R. 1983. No water, no granites-no oceans, no continents. *Geophysical Research Letters,* 10, 1061-1064.

CHASE JR, S. C., MINER, E. D., MORRISON, D., MÜNCH, G. & NEUGEBAUER, G. 1976. Mariner 10 infrared radiometer results: Temperatures and thermal properties of the surface of Mercury. *Icarus,* 28, 565-578.

DEHANT, V., BANERDT, B., LOGNONNÉ, P., GROTT, M., ASMAR, S., BIELE, J., BREUER, D., FORGET, F., JAUMANN, R., JOHNSON, C., KNAPMEYER, M., LANGLAIS, B., LE FEUVRE, M., MIMOUN, D., MOCQUET, A., READ, P., RIVOLDINI, A., ROMBERG, O., SCHUBERT, G., SMREKAR, S., SPOHN, T., TORTORA, P., ULAMEC, S. & VENNERSTRØM, S. 2012. Future Mars geophysical observatories for understanding its internal structure, rotation, and evolution. *Planetary and Space Science,* 68, 123-145.

DENEVI, B. W., ERNST, C. M., MEYER, H. M., ROBINSON, M. S., MURCHIE, S. L., WHITTEN, J. L., HEAD, J. W., WATTERS, T. R., SOLOMON, S. C., OSTRACH, L. R., CHAPMAN, C. R., BYRNE, P. K., KLIMCZAK, C. & PEPLOWSKI, P. N. 2013. The distribution and origin of smooth plains on Mercury. *Journal of Geophysical Research: Planets,* 118, 891-907.

EGEA-GONZALEZ, I. & RUIZ, J. 2013. Mercurian megaregolith layer and surface heat flows constraints. *In:* EGU General Assembly Conference Abstracts, April 1, 2013 2013. 15, 1788.

ERNST, C. M., MURCHIE, S. L., BARNOUIN, O. S., ROBINSON, M. S., DENEVI, B. W., BLEWETT, D. T., HEAD, J. W., IZENBERG, N. R., SOLOMON, S. C. & ROBERTS, J. H. 2010. Exposure of spectrally distinct material by impact craters on Mercury: Implications for global stratigraphy. *Icarus,* 209, 210-223.

ESA. 2013. *BepiColumbo* [Online]. ESA. Available: http://sci.esa.int/bepicolombo/ [Accessed 15/12/2013 2013].

EVANS, L. G., PEPLOWSKI, P. N., RHODES, E. A., LAWRENCE, D. J., MCCOY, T. J., NITTLER, L. R., SOLOMON, S. C., SPRAGUE, A. L., STOCKSTILL-CAHILL, K. R., STARR, R. D., WEIDER, S. Z., BOYNTON, W. V., HAMARA, D. K. & GOLDSTEN, J. O. 2012. Major-element abundances on the surface of Mercury: Results from the MESSENGER Gamma-Ray Spectrometer. *Journal of Geophysical Research (Planets),* 117.

GROTT, M., BREUER, D. & LANEUVILLE, M. 2011. Thermo-chemical evolution and global contraction of mercury. *Earth and Planetary Science Letters,* 307, 135-146.

GROTT, M., HELBERT, J. & NADALINI, R. 2007. Thermal structure of Martian soil and the measurability of the planetary heat flow. *J. Geophys. Res.,* 112, E09004.

HAGERMANN, A. & TANAKA, S. 2006. Ejecta deposit thickness, heat flow, and a critical ambiguity on the Moon. *Geophysical Research Letters,* 33, L19203.

HAUCK, S. A., MARGOT, J.-L., SOLOMON, S. C., PHILLIPS, R. J., JOHNSON, C. L., LEMOINE, F. G., MAZARICO, E., MCCOY, T. J., PADOVAN, S., PEALE, S. J., PERRY, M. E., SMITH, D. E. & ZUBER, M. T. 2013. The curious case of Mercury's internal structure. *Journal of Geophysical Research (Planets),* 118, 1204-1220.

HEAD, J. W., SOLOMON, S. C., FASSETT, C. I., MURCHIE, S. L., PROCKTER, L. M., ROBINSON, M. S., BLEWETT, D. T., DENEVI, B. W., WATTERS, T. R., WHITTEN, J. L., GOUDGE, T. A., BAKER, D. M. H., HURWITZ, D. M., BYRNE, P. K. & KLIMCZAK, C. 2012. Effusive Volcanism on Mercury from MESSENGER Mission Data: Nature and Significance for Lithospheric Stress State and Mantle Convection. *In:* Lunar and Planetary Science Conference, March 1, 2012 2012. 43, 1451.

HOWETT, C. J. A., SPENCER, J. R., PEARL, J. & SEGURA, M. 2011. High heat flow from Enceladus' south polar region measured using 10–600 cm−1 Cassini/CIRS data. *Journal of Geophysical Research: Planets,* 116, E03003.

HUGHES, E. T. & VAUGHAN, W. M. 2012. Albedo Features of Mercury. *In:* Lunar and Planetary Institute Science Conference Abstracts, March 1, 2012 2012. 43, 2151.

JOHNS HOPKINS UNIVERSITY, A. P. L. 2013. *Global Mosaics of Mercury* [Online]. Available: http://messenger.jhuapl.edu/the_mission/mosaics.html [Accessed 18/12/2013 2013].

KEIHM, S. J. 1984. Interpretation of the lunar microwave brightness temperature spectrum: Feasibility of orbital heat flow mapping. *Icarus,* 60, 568-589.

KÖMLE, N. I., HÜTTER, E. S., MACHER, W., KAUFMANN, E., KARGL, G., KNOLLENBERG, J., GROTT, M., SPOHN, T., WAWRZASZEK, R., BANASZKIEWICZ, M., SEWERYN, K. & HAGERMANN, A. 2011. In situ methods for measuring thermal properties and heat flux on planetary bodies. *Planetary and Space Science,* 59, 639-660.

LINSKY, J. L. 1966. Models of the Lunar Surface Including Temperature-Dependent Thermal Properties. *Icarus,* 5, 606-634.

MICHEL, N. C., HAUCK, S. A., SOLOMON, S. C., PHILLIPS, R. J., ROBERTS, J. H. & ZUBER, M. T. 2013. Thermal evolution of Mercury as constrained by MESSENGER observations. *Journal of Geophysical Research: Planets,* 118, 1033-1044.

PEPLOWSKI, P. N., LAWRENCE, D. J., RHODES, E. A., SPRAGUE, A. L., MCCOY, T. J., DENEVI, B. W., EVANS, L. G., HEAD, J. W., NITTLER, L. R., SOLOMON, S. C., STOCKSTILL-CAHILL, K. R. & WEIDER, S. Z. 2012. Variations in the abundances of potassium and thorium on the surface of Mercury: Results from the MESSENGER Gamma-Ray Spectrometer. *Journal of Geophysical Research: Planets,* 117, E00L04.

PRESLEY, M. A. & CHRISTENSEN, P. R. 1997. The effect of bulk density and particle size sorting on the thermal conductivity of particulate materials under Martian atmospheric pressures. *Journal of Geophysical Research,* 102, 9221-9230.

PURUCKER, M. E., SABAKA, T. J., SOLOMON, S. C., ANDERSON, B. J., KORTH, H., ZUBER, M. T. & NEUMANN, G. A. 2009. Mercury's internal magnetic field: Constraints on large- and small-scale fields of crustal origin. *Earth and Planetary Science Letters,* 285, 340-346.

RINER, M. A. & LUCEY, P. G. 2012. Spectral effects of space weathering on Mercury: The role of composition and environment. *Geophysical Research Letters,* 39, 12201.

ROBINSON, M. S., CHAPMAN, C. R., DOMINGUE, D. L., HAWKINS, S. E., HEAD, J. W., HOLSCLAW, G. M., MCCLINTOCK, W. E., MCNUTT, R. L., MURCHIE, S. L., PROCKTER, L. M., STROM, R. G., WATTERS, T. R., BLEWETT, D. T., GILLIS-DAVIS, J. J., SOLOMON, S. C. & MESSENGER. 2008. Mercury Color and Albedo: New Insights from MESSENGER. *In:* Lunar and Planetary Institute Science Conference Abstracts, March 1, 2008 2008. 39, 1187.

RUIZ, J., LÓPEZ, V. & EGEA-GONZÁLEZ, I. 2013. Paleo-heat flows, radioactive heat generation, and the cooling and deformation history of Mercury. *Icarus,* 225, 86-92.

SMITH, D. E., ZUBER, M. T., PHILLIPS, R. J., SOLOMON, S. C., HAUCK, S. A., LEMOINE, F. G., MAZARICO, E., NEUMANN, G. A., PEALE, S. J., MARGOT, J.-L., JOHNSON, C. L., TORRENCE, M. H., PERRY, M. E., ROWLANDS, D. D., GOOSSENS, S., HEAD, J. W. & TAYLOR, A. H. 2012. Gravity Field and Internal Structure of Mercury from MESSENGER. *Science,* 336, 214-.

SPOHN, T. 1991. Mantle differentiation and thermal evolution of Mars, Mercury, and Venus. *Icarus,* 90, 222-236.

SPOHN, T., BALL, A. J., SEIFERLIN, K., CONZELMANN, V., HAGERMANN, A., ÖMLE, N. I. & KARGL, G. 2001. A heat flow and physical properties package for the surface of Mercury. *Planetary and Space Science,* 49, 1571-1577.

SPOHN, T., GROTT, M., KNOLLENBERG, J., VAN ZOEST, T., KARGL, G., SMREKAR, S. E., BANERDT, W. B., HUDSON, T. L. & TEAM, H. I. 2012. INSIGHT: Measuring the Martian Heat Flow Using the Heat Flow and Physical Properties Package (HP^3). *In:* Lunar and Planetary Institute Science Conference, 2012. 43, 1445.

SPOHN, T., GROTT, M., RICHTER, L., KNOLLENBERG, J., SMREKAR, S. E. & TEAM, H. I. 2010. Measuring Heat Flow on the Moon -- The Heat Flow and Physical Properties Package HP^3. *LPI Contributions,* 1530, 3016.

STEVENSON, D. J., SPOHN, T. & SCHUBERT, G. 1983. Magnetism and thermal evolution of the terrestrial planets. *Icarus,* 54, 466-489.

VASAVADA, A. R., PAIGE, D. A. & WOOD, S. E. 1999. Near-Surface Temperatures on Mercury and the Moon and the Stability of Polar Ice Deposits. *Icarus,* 141, 179-193.

WATTERS, T. R., SCHULTZ, R. A., ROBINSON, M. S. & COOK, A. C. 2002. The mechanical and thermal structure of Mercury's early lithosphere. *Geophysical Research Letters,* 29, 1542.

YAN, N., CHASSEFIÈRE, E., LEBLANC, F. & SARKISSIAN, A. 2006. Thermal model of Mercury's surface and subsurface: Impact of subsurface physical heterogeneities on the surface temperature. *Advances in Space Research,* 38, 583-588.

ZUBER, M. T., AHARONSON, O., AURNOU, J. M., CHENG, A. F., HAUCK, S. A., HEIMPEL, M. H., NEUMANN, G. A., PEALE, S. J., PHILLIPS, R. J., SMITH, D. E., SOLOMON, S. C. & STANLEY, S. 2007. The Geophysics of Mercury: Current Status and Anticipated Insights from the MESSENGER Mission. *Space Science Reviews,* 131, 105-132.

7 VESTA

7.1 Heat Flow on Vesta

7.1.1 Thermal Evolution of Vesta

Asteroid (4) Vesta, while differentiated is not in hydrostatic equilibrium (e.g. Neumann et al., 2013; Russell et al., 2013; Rayman and Mase, 2014). Vesta, like the dwarf planet (1) Ceres, is classed as a protoplanet (e.g. Reddy et al., 2012). It is thought to have formed during the first million years of Solar System history (e.g. O'Brien and Sykes, 2011; Pieters et al., 2011; Formisano et al., 2013), its accretion towards a larger mass likely stopped by the disruptive effects of Jupiter (e.g Coradini et al., 2011; Zuber et al., 2011).

Vesta, as a differentiated asteroid, raises important questions about the sources of heat in the early Solar System which facilitated its melting and its subsequent cooling history (e.g. Zuber et al., 2011). These are currently thought to be short-lived radio isotopes such as ^{26}Al and ^{60}Fe, as confirmed by studies of so-called HED (Howardite, Eucrite and Diogenite) meteorites, where evidence points to Vesta being their parent body (e.g. Bogard and Garrison, 2003; Coradini et al., 2011; Cloutis et al., 2013; Formisano et al., 2013; Russell et al., 2013).

Vesta is therefore a unique repository of information on the early Solar System, even though substantial thermal and impact evolution since its formation may have erased much of its primordial features (Coradini et al., 2011). The observation of pitted terrain on its surface, associated with low albedo, hydrogen rich area, for example, points to an active surface potentially rich in volatiles (e.g De Sanctis et al., 2012; Prettyman et al., 2012; Russell et al., 2013). Understanding the nature of the pitted terrain can lead to a better understanding of Vesta's impact and thermal history.

The planetary heat flow from the Vestan surface is expected to very low if not, possibly, reversed; its interior is likely frozen and internal heating mechanisms extinct (e.g. Formisano et al., 2013; Elkins-Tanton et al., 2014). While this may be the case an in situ heat flow measurement can provide an important confirmation of the expected thermal

state of the Vestan interior, as well as useful information on properties affecting its surface energy balance, as is proposed for other small Solar System bodies (e.g. Spohn et al., 2007; Jaumann et al., 2014).

7.1.2 Measuring Heat Flow on Vesta

The first in-situ measurement of heat flow on a minor solar system body is planned for the Multi-Purpose Sensors for Surface and Subsurface Science Penetrator (MUPUS PEN), scheduled for a landing on comet 67P/Churyumov-Gerasimenko (67P/CG) in late 2014. It is part of the MUPUS payload on the Rosetta space probe lander, Philae (Spohn et al., 2007; Kömle et al., 2011; Kargl et al., 2012; ESA, 2013), which is designed to measure the temperature gradient of the upper 30 cm of the subsurface. The focus of MUPUS is the surface energy balance, which is primarily driven by processes related to coma formation (Hagermann, 2014).

A basal heat flow measurement on Vesta likely requires thermal sensor penetration below 30 cm to access the steady temperature gradient which allows the basal heat flow to be determined. There are almost no published estimates of the heat flow on Vesta – a zero value is used in the models of Formisano et al. (2013) while Stubbs and Wang (2012) do not explicitly consider it. Here arbitrary thermal conductivities (see Section 7.2.2), the internal temperatures of Formisano et al. (2013) (200 K at 270 km from centre) and equatorial surface temperatures of Stubbs and Wang (2012) (see Figure 7.2) are used to produce nominal equatorial values of 0.33-3.33 $\mu W/m^2$.

As noted in Section 5.1 planetary heat preferentially escapes from thinner crust, as thicker crust forms an insulating lid. This suggests that the crustal thickness of Vesta may be used to select measurement locations where the heat flow is expected to be relatively high, and therefore most resolvable. Figure 7.1 shows surface topography and gravity of Vesta determined from observations of the NASA Dawn mission to the asteroids. These can be used to infer crustal thickness (e.g. Asmar et al., 2012; Ermakov et al., 2012) and

are used to guide the selection of the identified measurement location at 120°E 20°N, which is also informed by further a priori information, discussed below.

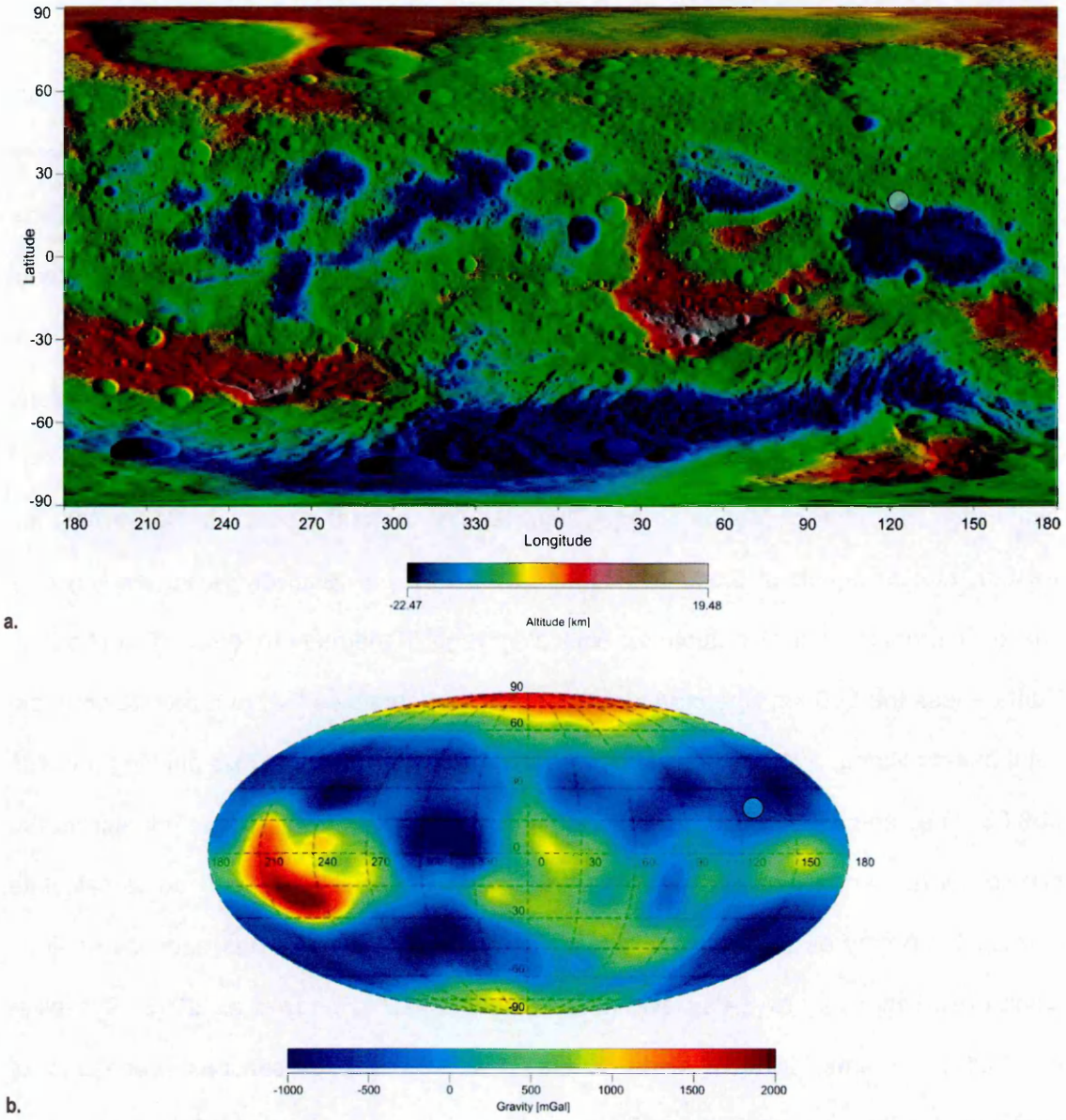

Figure 7.1. a. Surface topography of Vesta, relative to an ellipsoid of 285 kilometers by 285 kilometers by 229 kilometers. The topographic map is constructed from the analysis of more than 17,000 images from Dawn's framing camera that were taken with varying sun and viewing angles (after NASA, 2013c); b. Gravity of Vesta derived from results of Dawn's gravity experiment (after NASA, 2013b). The white circles identify a potential heat flow measurement location at 120°E 20°N based on an expected low crustal thickness (e.g. Asmar et al., 2012; Ermakov et al., 2012), and relatively high heat flow (also see further discussions in the text).

7.2 Further A Priori Information

7.2.1 Surface Temperature

The surface temperature on Vesta varies between 50 and 275 K (Titus et al., 2013 and references therein). These temperatures depend on its orbital parameters and thermal properties as discussed in Section 2.2.5. The orbit of Vesta lies beyond any significant tidal influences in the asteroid belt between Mars and Jupiter therefore no such effects should significantly affect its surface temperature. The Solar Constant at the orbit of Vesta varies of the order of 200-287 W/m^2 between aphelion and perihelion. The amplitude of the annual temperature variation is therefore expected to be small, though its particularly long orbital period of 3.63 Earth yr (Williams, 2014a) suggests deeper annual thermal skin depth than for Lunar or Mercurian equivalent regolith thermal properties. Conversely the Vestan rotation period of 5.342 hr (Reddy et al., 2013) is relatively rapid, leading to a shallow diurnal thermal skin depth for equivalent regolith thermal properties. The shape of Vesta – less the 500 km Rheasilvia impact basin – approaches that of a prolate spheroid (Stubbs and Wang, 2012).[1] It has simple rotation with the rotational axis pointing towards 309.03° R.A. and 42.24° Dec. (Reddy et al., 2013; Russell et al., 2013). This allows the simple surface energy balance model presented in Section 3.6 to be used to calculate surface temperatures (see Section 7.3.1). The obliquity of Vesta has been determined using observations by NASA's Dawn mission to be 27.46° (Reddy et al., 2013; Russell et al., 2013; Williams, 2014a) which is expected to result in seasonal variations of temperature, like on Mars (Section 5.2.1) and unlike Mercury (Section 6.3.1). Stubbs and Wang (2012) use a sophisticated thermal model to calculate mean (steady) temperatures across the Vestan surface and use them to determine the stability of water ice (Figure

[1] Vesta has a J_2 gravitational moment of 0.0317799 (Russell et al., 2013), compared to 0.00108263 for Earth (Williams, 2014b), 6×10^{-5} for Mercury (Williams, 2014d) and 0.00196045 for Mars (Williams, 2014c).

7.2). The findings of Stubbs and Wang (2012) are used to guide the choice of measurement location (Section 7.3).

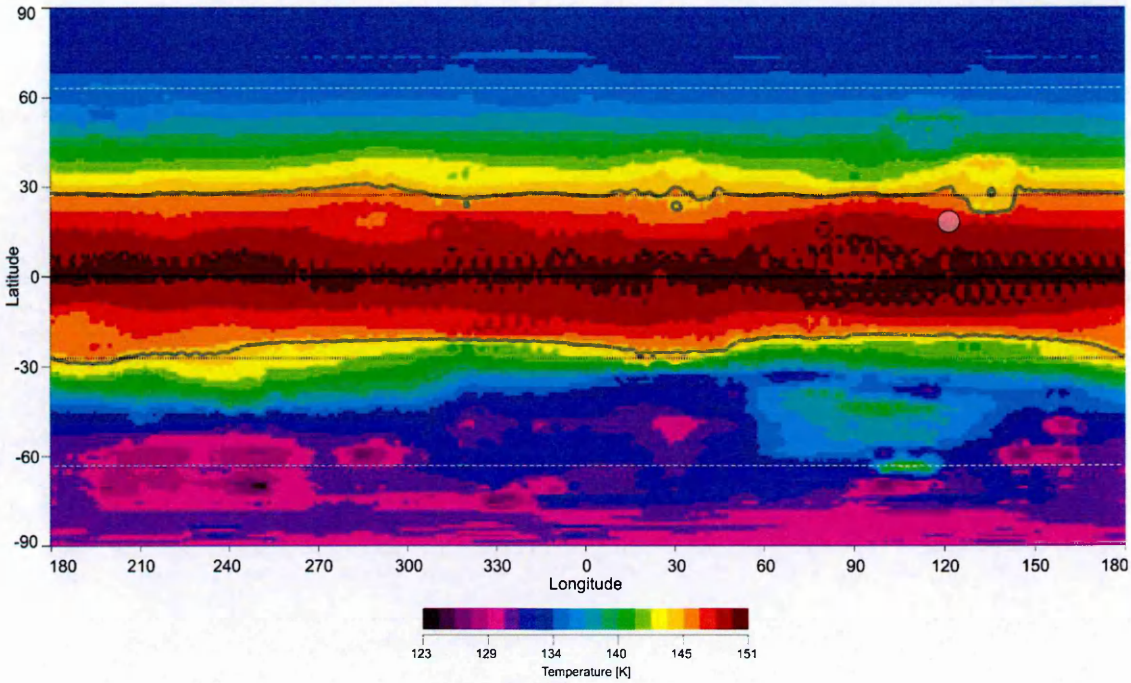

Figure 7.2. Mean surface temperatures across the Vestan surface. Latitudes poleward of the grey lines denote areas where the average surface temperatures allows for the existence of stable water ice (after NASA et al., 2012). The dashed black line is the equator, the dotted black lines at ±27.2° the tropical circles, and the white dashed lines at ±62.8° the polar circles (Stubbs and Wang, 2012). The white circle identifies a potential heat flow measurement location at 120°E 20°N chosen based on the high mean temperature lowering the likelihood of stable water existing at that site (also see futher discussions in the text).

7.2.2 Thermal Properties

The thermal properties of Vesta determine the temperature of the surface and subsurface. Vestan (Bond) albedo and thermal inertia determine the surface temperature due to solar irradiation via a surface energy balance relationship (see Section 2.2.5). Albedo has been observed to vary over a relatively large range across Vesta (e.g. Reddy et al., 2012; Titus et al., 2013) with low albedo areas associated with the presence of hydrated minerals (e.g. De Sanctis et al., 2012; Prettyman et al., 2012; Russell et al., 2013; also see Figure 7.3). Low albedo areas are therefore avoided, although the unsteady surface temperature amplitude is smaller in these areas, therefore minimising masking of the steady

temperature. In any event, the inverse model of Chapter 4 is limited to simulating dry regolith; therefore avoiding low albedo area simplifies the interpretation of results.

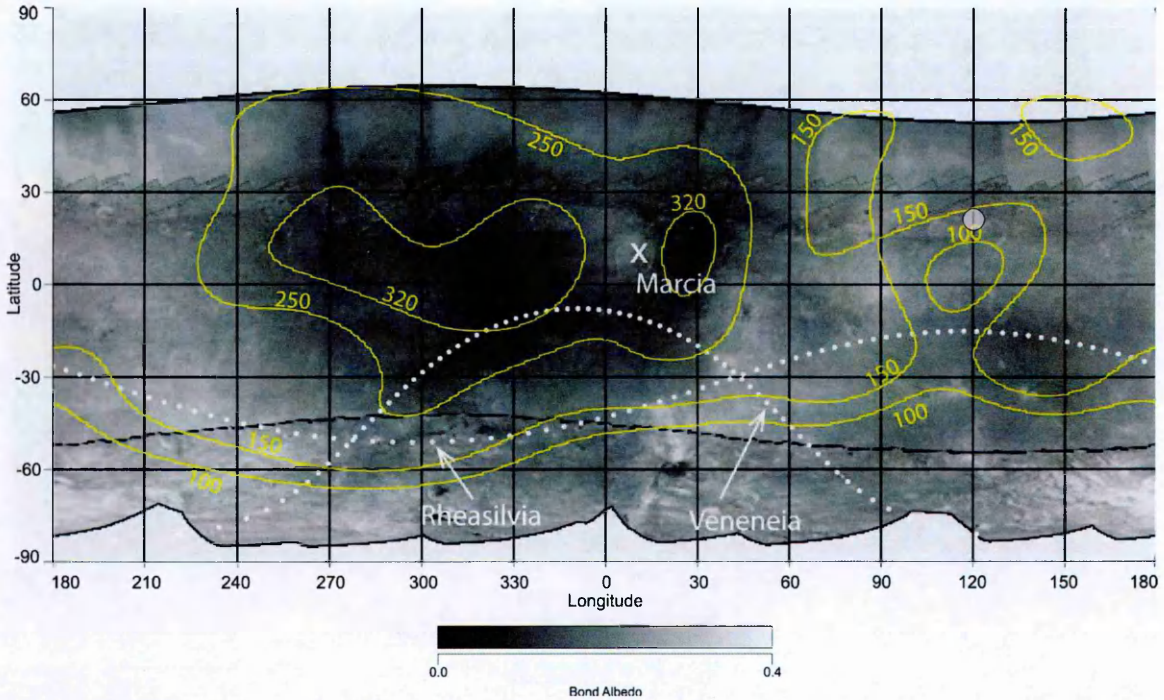

Figure 7.3. Bond albedo and hydrogen (H) abundance across the surface of Vesta. Areas poleward of ~60° and between -75° to -90° latitude are unmapped. The yellow countours show H abundance, with units of µg/g of surface material. The dotted white curves indicate the outlines of the largest and second largest impact basins on Vesta, Rheasilvia and Veneneia. Marcia crater is indicated with an X (after NASA, 2013a). The white circle identifies a potential heat flow measurement location at 120°E 20°N chosen based on the relatively high albedo (low volatile content) and lowered H abundance (also see futher discussions in the text).

Thermal inertia has been preliminarily calculated from Dawn Visible Infrared Imaging Spectrometer (VIR) data to vary across the surface of Vesta from 25-35 $J/m^2/K/s^{1/2}$ (e.g. Capria et al., 2012; Palmer et al., 2013). Leyrat et al. (2012) use Herschel IR observations to produce a lower global estimate of 20 $J/m^2/K/s^{1/2}$ with large uncertainties (+20, -10 $J/m^2/K/s^{1/2}$). This agrees with the optimized global value of 10-20 $J/m^2/K/s^{1/2}$ by Mueller and Lagerros (1998), using far IR observations of the imaging photopolarimeter ISOPHOT on board the Infrared Space Observatory (ISO). Gundlach and Blum (2013) use a less optimal result of Mueller and Lagerros (1998) (25±13 $J/m^2/K/s^{1/2}$) to derive average Vestan grain sizes of the order of 54 µm. The results of Piqueux and Christensen (2011) can be

applied to the former range of Vestan thermal inertia estimates (10-35 $J/m^2/K/s^{1/2}$) by extrapolation to vacuum pressures, using the results in Presley and Christensen (1997). This leads to particle sizes between 1-50 μm, consistent with thermal conductivities of the order of 10^{-4}-10^{-3} W/m/K – these are consistent with a seasonal skin depth of 0.148 m used in the models of Stubbs and Wang (2012). Surface thermal capacities of the order of 1-1.225 $MJ/K/m^3$ can be derived from the thermal inertia and thermal conductivity values. These are arbitrarily split into surface densities between 1100-1250 kg/m^3 – less than the surface value used on Mercury in Section 6.2.2. – and specific heat capacities of 909-980 J/kg/K. The lunar-like thermal property depth variation models used in Chapter 5 and 6 are used here with end member scenarios at the limits of the identified thermal property value ranges. Thangjam et al. (2013) identify the site at 120° E 20° N as Howardite rich – Burbine et al. (2001) study Howardite EET 87503 and estimate particle sizes of <63 μm and 106-150 μm, consistent with preceding estimates. Arbitrarily, then, a particle size of 106-150 μm is assumed, at depth 5 m, corresponding to thermal conductivities of ~10^{-3} W/m/K (Presley and Christensen, 1997). Models of Vesta in Zuber et al. (2011) use an upper crustal density of 2800 kg/m^3 – this value is adopted at 5 m. Specific numbers are shown in Table 7.1. Figure 7.4 shows the profiles.

Table 7.1. Regolith properties for high and low conductivity regolith models on Vesta based on a mean surface thermal inertia $I = \sqrt{k\rho c} =$ 10-35 $J/m^2/K/s^{1/2}$. The thermal conductivity is k and ρ is the density at select depth z in metres

REGOLITH MODEL	z [m]	k [W/m/K]	ρ [kg/m^3]	c [J/kg/K]
LOW CONDUCTIVITY	0	0.0001	1100	980
	5	0.0005	2800	980
HIGH CONDUCTIVITY	0	0.001	1250	909.09
	5	0.005	2800	909.09

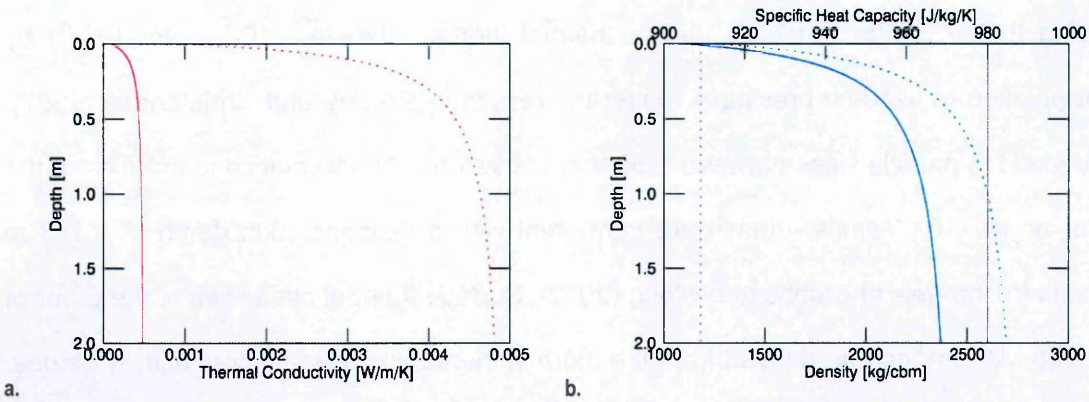

Figure 7.4. Hypothetical conductivity k, and thermal capacity ρc depth profiles for a potential heat flow measurement site on Vesta at latitude 120° E 20° N. In: a. the solid and dotted red curves respectively show low and high conductivity variation; b. the solid and dotted blue curves respectively show low and high density variation; the solid and dotted purple lines represent the specific heat capacity. The dotted and solid curves indicate associated thermal properties.

7.2.3 Heat Sources and Sinks

The heating of Vesta is thought to have been dominated by short lived radioisotopes as discussed in Section 7.1, it is therefore expected that the current heat production rate is negligible. This is also suggested by the results of the models of Formisano et al. (2013). Radiosotope heat sources are therefore not considered. However, due to the potential for degassing events (e.g. Denevi et al., 2012), heat source solutions are used to model systematic noise which may result from volatiles being released or transported in the regolith close to the axis along which a heat flow measurement is taken (see Appendix 9.7.2 for plots). The heat source solutions provide scenarios which allow a first order assessment of the effects of volatile degassing on a heat flow measurement.

7.3 Scenarios

The primary question arising from the discussion above is the measurability of heat flow in the shallow subsurface of Vesta, considering it is likely very low and what, if any, other useful information can be extracted from the measurement. Forward models are therefore produced to check the skin depth of the Vestan annual temperature and determine the scenarios which may present a challenge to a heat flow measurement.

7.3.1 Forward Models

Forward models are generated based on the surface and subsurface thermal properties presented in Section 7.2.2 and heat flows of Section 7.1. The surface energy balance relationship of Section 2.2.5 is used to generate surface temperatures. Four models are therefore simulated with two end member thermal property profiles, and two end member heat flows. Figure 7.5 and Figure 7.6 show the resulting temperature profiles – relevant model parameters are tabulated in Appendix 9.7.1.

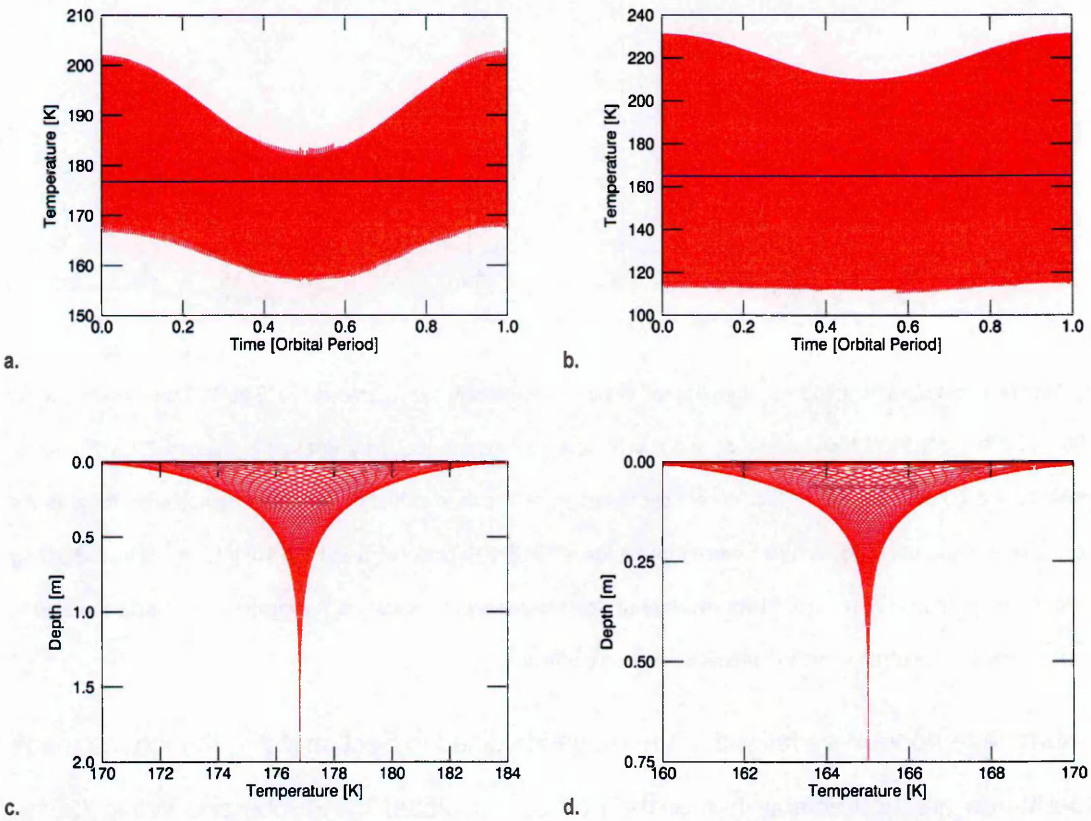

Figure 7.5. Forward modelled temperature profiles for Vestan measurement site located at 120°E 20°N. These are with a 'high' heat flow of 3.33 μW/m² and high (a. and c.) and low (b. and d.) conductivities as presented in Section 7.2.2. The red upper contours (a. and b.) are overlays of time-dependent temperature T over depth z of 2 m (larger amplitudes towards the surface). The blue line shows the annual mean temperatures of 176.819 K for the high and 165.010 K for the low conductivity scenario; the lower contours (c. and d.) are overlays of depth-dependent temperature T over time t of 1 orbital period in ~26.5 day steps. The simulations are run from high noon at perihelion.

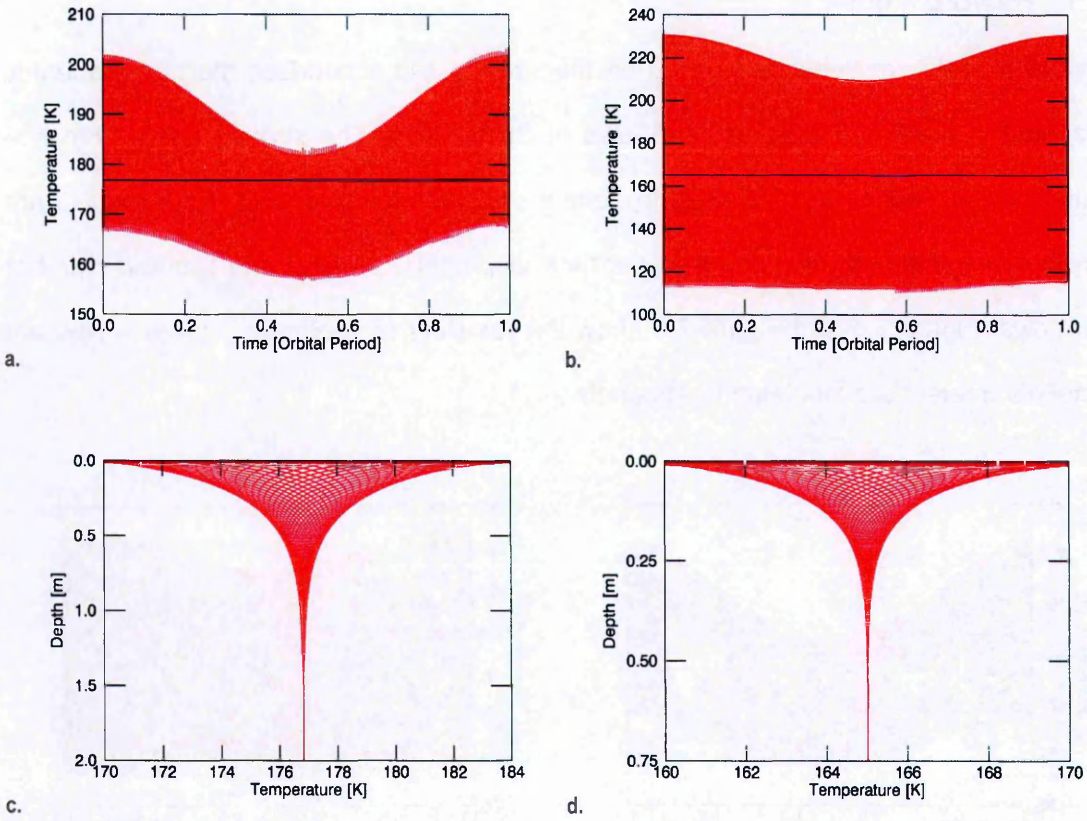

Figure 7.6. Forward modelled temperature profiles for Vestan measurement site located at 120°E 20°N. These are with a low heat flow of 0.33 μW/m² and high (a. and c.) and low (b. and d.) conductivities as presented in Section 7.2.2. The upper contours (a. and b.) are overlays of time-dependent temperature T over depth z of 2 m (larger amplitudes towards the surface). The blue line shows the annual mean temperatures of 176.819 K for the high and 165.010 K for the low conductivity scenario; the lower contours (c. and d.) are overlays of depth-dependent temperature T over time t of 1 orbital period in ~26.5 day steps. The simulations are run from high noon at perihelion.

The surface temperatures fall within the range identified in Section 7.2.1, though the mean temperatures are appreciably higher than those calculated by Stubbs and Wang (2012) (Figure 7.2). There are several possible reasons for the difference as the code of Stubbs and Wang (2012) is appreciably more sophisticated – the current model uses: a solar constant which is 3 W/m^2 higher; higher magnitude thermal properties in the topmost control volume leading to greater skin depth and; a simple shape model such that Vesta is assumed to have a smooth spherical surface. Also, the appreciable difference of 10 K between the mean temperatures of the low and high conductivity models is unusual and

appears to be due to rounding errors in the integration of the topmost control volume.[2] Notably the high heat flow models have slightly higher mean surface temperatures, illustrating the effect of the heat flow on the surface energy balance. The diurnal variation in surface temperature at the high conductivity site (Figure 7.6a) is appreciably smaller than at the low conductivity site (Figure 7.6b). This is because the high conductivity site has higher thermal diffusivity[3] (see Section 3.4) which allows heat to diffuse more readily into the subsurface, limiting the increase in surface temperature.

There is a clear distinction between high conductivity and low conductivity models. The annual skin depth[4] of the high conductivity model (1.06 m; 0.12 m for low conductivity) is relatively high – substantially higher than the case for Mercury in Section 6.3.1 where the surface temperature cycle is a relatively short 176 d. The low and high heat flow models are visually indistinguishable, though there are differences in the temperature at depth, as illustrated by Figure 7.7.

---

[2] Note that the surface energy balance temperatures are calculated separately, then read into the forward models to calculate the subsurface temperatures. Therefore any inaccuracies in the calculation of surface temperatures are unlikely to affect the conclusions of this study with regard to the subsurface temperature profiles.

[3] The thermal diffusivity for the high conductivity scenarios is 8.16E-10 m^2/s. For the low conductivity scenarios the thermal diffusivity is 1E-10 m^2/s.

[4] The skin depth is calculated using depth-averaged thermal properties.

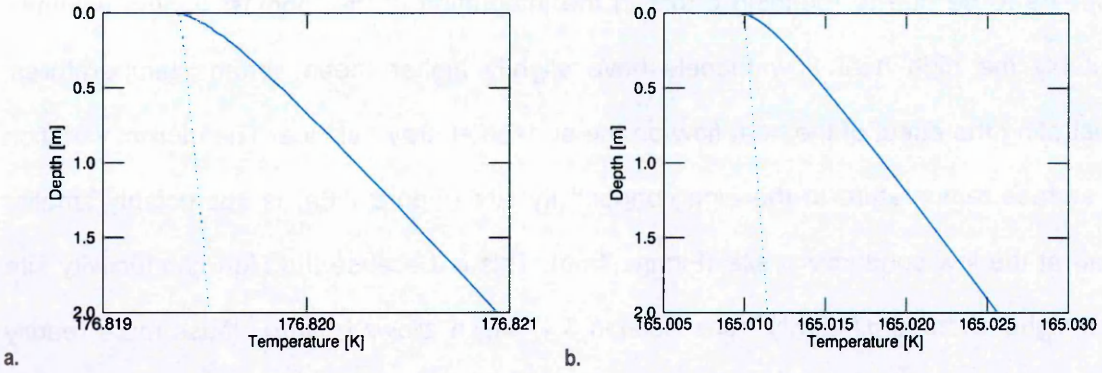

Figure 7.7. Steady temperature T^S for forward modelled temperature profiles at Vestan measurement site located at 120°E 20°N. Plot: a. shows T^S for the high conductivity model; b. shows T^S for the low conductivity model – with respective heat flows of 3.33 (solid lines) and 0.33 (dotted lines) μW/m².

The basal heat flow is accessible from ~1.5 m for the high conductivity scenario, with the temperature gradient between 1.5-2 m being ~0.75 mK/m for high heat flow. The same for the low conductivity scenarios are ~0.5 m and ~12 mK/m. With a penetration depth of 2 m the steady temperature gradient is accessible over 0.5 m for the high conductivity case and 1.5 m for the low conductivity case. For a heat flow probe with precision of the order of 1 mK (the required precision of some proposed heat flow probes – e.g. Grott et al., 2007; Dehant et al., 2012): the steady temperature gradient is, in principle resolvable in the low conductivity, high heat flow case, over 1.5 m – i.e. 18 ±1.5 mK/m; while being completely unresolvable in the high conductivity, high heat flow case over 0.5 m – i.e. 0.375 ±1.5 mK/m. It is immediately clear that the temperature gradient in the low heat flow cases is completely unresolvable.

7.3.2 Measurements

Despite the clear immeasurability of the heat flow in the high conductivity and low heat flow models, tests are conducted with them to assess the response of the model to the minute heat flows and completely obscured temperature gradients. Two end member cases are considered: an instantaneous measurement, and one which extends over the full orbital period of Vesta. The instrument is assumed to penetrate to a depth of 2 m, enough to access the steady temperature gradient, and therefore the basal heat flow.

Gaussian noise of the order of 1 mK (expected instrument precision) is added to each measurement. Also, a series of 3 non-Gaussian noise profiles with amplitudes ranging from 10^{-6}-10^{-1} K is introduced into the measurements to quantify how the model handles systematic noise. The former are based on source solutions with regolith properties equivalent to the site scenarios they are applied to; they are designed to reflect (to first order) the effect of degassing events of varying magnitudes (see Section 7.2.3) – they are presented in Appendix 9.7.2. This leads to a total of 8 measurement scenarios per site scenario, a grid of which is shown in Table 7.2. Measurements for the high heat flow scenarios are shown with Gaussian error in Figure 7.8 and non-Gaussian errors in Figure 7.9 (similar plots for the low heat flow scenarios can be found in Appendix 9.7.2).

Table 7.2. Grid of measurement scenarios (8 in total per site scenario) simulated for each of the forward modeled scenarios of Section 7.3.1.

		MONITORING PERIOD [ORBITAL PERIOD]		NOISE AMPLITUDE	
		0.0	1.0		
DEPTH [m]	2		OPTIMAL	10^{-3}	GAUSSIAN [K]
				10^{-5}	LOW k
				10^{-3}	SYSTEMATIC
				10^{-1}	[K]
				10^{-6}	HIGH k
				10^{-4}	SYSTEMATIC
				10^{-2}	[K]
		1 (-)	1326 (~1.0)		
		NUMBER OF MEASUREMENTS (TIME RESOLUTION [DAY])			

With Gaussian noise of amplitude 10^{-3} K, the basal heat flow is accessible from 0.5 m in the low conductivity scenarios (in principle, to accuracies of the order of 0.4 %), as noted earlier; therefore, with a penetration depth of 2 m inversion may be unnecessary. However

the main questions being addressed here are the response of the model to non-Gaussian noise, and its sensitivity to such low heat flows (and steady temperature gradients).

With non-Gaussian noise of the order of 0.2 K there is a notable negative deflection of the temperature gradient, completely obscuring the steady temperature gradient in some cases (Figure 7.9). The former is expected to be the case for non-Gaussian noise of amplitudes greater than or of the order of the Gaussian noise amplitudes (10^{-3} K).

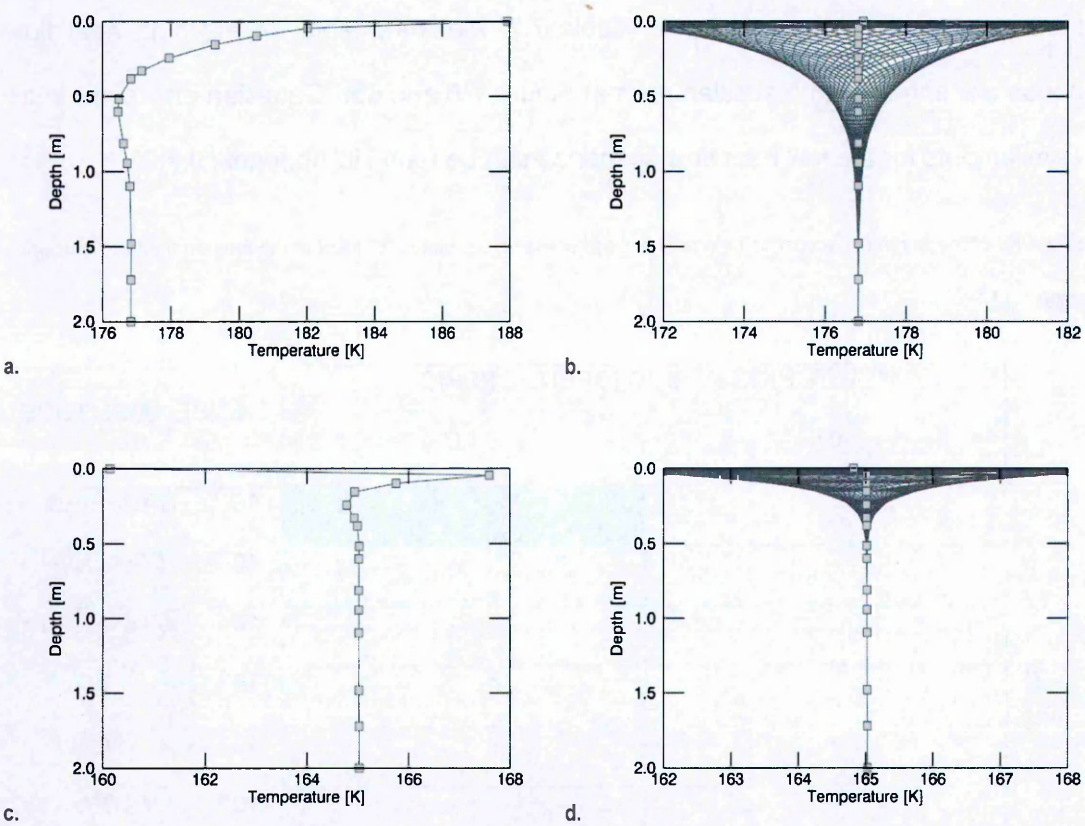

Figure 7.8. Temperature measurements for Vestan site located at 120°E 20°N. These are with a 'high' heat flow of 3.33 μW/m² and high (a. and b.) and low (c. and d.) conductivities as presented in Section 7.2.2. The plots show depth-dependent temperature T: for an instantaneous measurement (left); over time t of 1 orbital period in ~26.5 day steps (right). The grey squares are sensor locations.

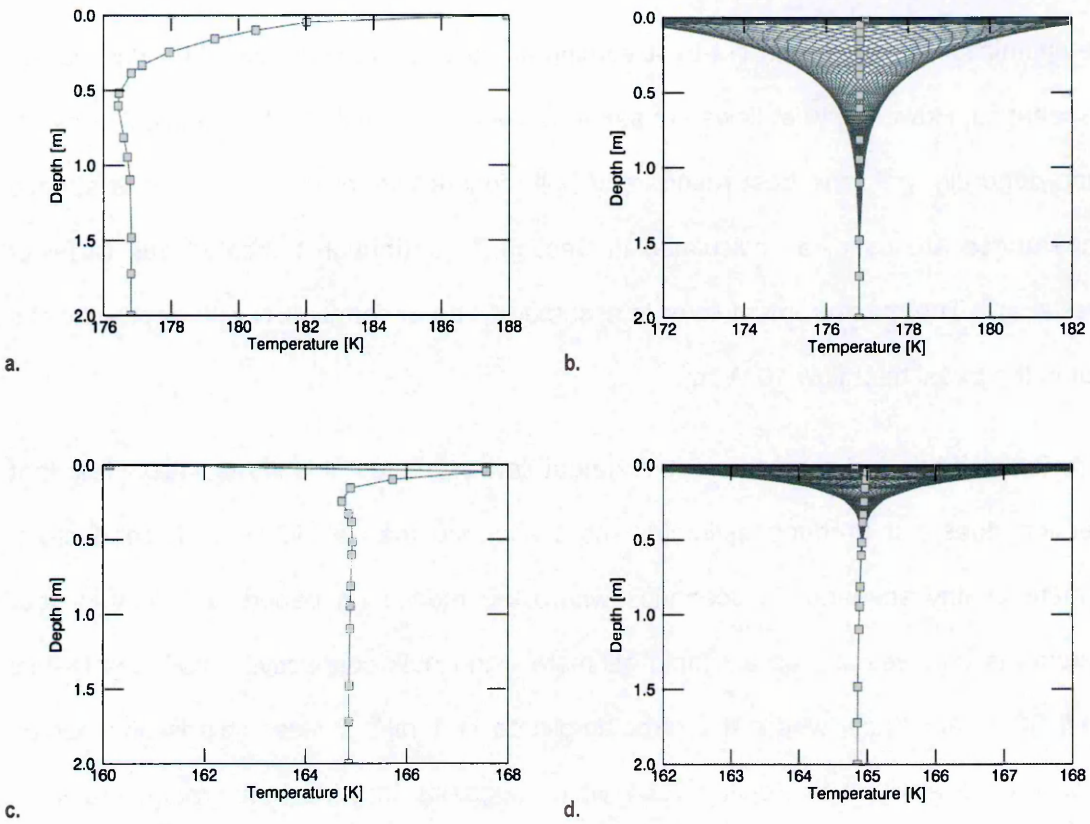

Figure 7.9. Temperature measurements for Vestan site located at 120°E 20°N with high systematic noise as shown in Appendix 9.7.2. These are with a 'high' heat flow of 3.33 μW/m^2 and high (a. and b.) and low (c. and d.) conductivities as presented in Section 7.2.2. The plots show depth-dependent temperature T: for an instantaneous measurement (left); over time t of 1 orbital period in ~26.5 day steps (right). The grey squares are sensor locations.

7.3.3 Inversion Results

The optimizations are carried out by assuming an initial basal heat flow of 0 W/m^2 across all scenarios. However, heat flows are separately estimated with the two deepest sensors, which generally yield the best results and bulk conductivity over 2 m. The true surface temperatures are used, as calculated in Section 7.3.1 (though truncated due to fewer timesteps) [5]. The measurement error is assumed to be uniformly 1 K with depth and the error in the basal heat flow 10 W/m^2.

Table 7.3 to Table 7.6 show the resulting heat flow estimates. It is immediately clear that inversion does not produce estimates more accurate than a simple bulk conductivity estimate in any scenario. In scenarios where the monitoring period is 1 Vestan year inversion is unnecessary as a simple estimate using bulk conductivity produces results within 30 % accuracy, where the error amplitude is 1 mK or less. This is unexpected based on the analysis in Section 7.3.1 which suggests that the temperature gradients should be completely masked in the high conductivity and low heat flow scenarios. It is likely the case that averaging the temperatures for multiple measurements tends to smooth out the effect of the Gaussian errors, such that they mutually cancel. Otherwise the bulk conductivity estimates are highly inaccurate except with an instantaneous measurement in the low conductivity, heat flow case, with error amplitude 1 mK, or less.

The high magnitudes of the heat flow relative error are due in part to the small magnitudes of the true heat flows being investigated (Figure 7.10 and Figure 7.11 show errors in the temperature measurement and inverted temperatures), and the use of the bulk conductivity to calculate the heat flow.[6] Also, in the inversion, there is a downward shift in the mean temperatures by ~0.4 K for the high conductivity scenarios and ~0.2 K for the

[5] The unsteady temperature used in the inversion is extracted from the higher (time) resolution version used to simulate the forward models.

[6] The accuracy of the initial estimates improve approximately 4-fold when the true conductivities at depth are used.

low conductivity scenarios. This is because the unsteady temperature used in the inversion is a truncated version of that in the forward model, such that more diurnal temperatures are selected below the annual mean, than above the annual mean. These shifts are not explicitly accounted for in the inversion (to do so involves simultaneously optimizing the surface temperature with the basal heat flow) therefore the inverse model overestimates the basal heat flow to mitigate the steady surface temperature underestimate.[7]

The preceding effect is balanced by the non-Gaussian noise due to heat sinks shown in Appendix 9.7.2. The heat sinks lower the gradient of the temperature measurement and therefore the apparent basal heat flow. The model then underestimates the basal heat flow to fit the errant temperature measurement. The net effect of the lowered steady temperature and decreased temperature gradient is smaller optimized heat flow errors for larger non-Gaussian noise magnitudes, as observed in Table 7.3 to Table 7.6.

The algorithm loses sensitivity to non-Gaussian noise at 10^{-6} K, when it is dominated by the Gaussian noise due to instrument imprecision. The sensitivity displayed to the non-Gaussian noise magnitude shows an effective positive correlation – i.e. the greater the magnitude of the non-Gaussian noise, the greater the response of the algorithm in underestimating the basal heat flow. This result can be compared to the cases with Mars in Section 5.3.3 and earlier in Section 4.3.1.2, which display positive correlation between optimized heat flow accuracy, and Gaussian noise amplitude. These results point to the model being robust in handling Gaussian noise relative to systematic noise with long tailed distributions.

Notably, the optimized heat flows are appreciably more accurate for the instantaneous measurements in the high conductivity scenarios and marginally more so in the low conductivity scenarios. This illustrates the instability caused by the truncation errors due to

[7] The result is analogous to results obtained in Appendices 9.4.7.1-9.4.7.3 where basal heat flow F_B^S is simultaneously optimized with steady T_S^S and unsteady T_S^U surface temperatures.

the larger timesteps coupled with the high frequency surface temperature variation, similar to the case on Mars. The small steady temperature gradient magnitudes compound the issue. For the low conductivity scenarios the temperature gradient is further from the sensitivity threshold of the model and the results are less affected by the destabilizing effect of the unsteady temperature profiles. Also, following from previous results in Sections 5.3.3 and 6.3.3, the relative accuracy of the heat flow estimates reflects the relative magnitudes of the true heat flows.

Figure 7.10 shows Gaussian and Figure 7.11 non-Gaussian errors in temperature measurements and inverted temperatures for the high heat flow scenarios presented in Figure 7.8 and Figure 7.9 (similar plots for the low heat flow scenarios are presented in Appendix 9.7.3). The errors in the inverted temperatures are reduced at depth but increase towards the surface, and away from the boundaries. Smaller error margins (instrument precision) are required at depth for more accurate optimized heat flow estimates. The increased errors towards the surface illustrate the destabilizing effect of the unsteady temperature, which cannot be precisely replicated with a truncated unsteady surface temperature. The non-Gaussian errors illustrate an appreciable negative shift in the subsurface temperatures in addition to the negative biasing of the temperature gradient, discussed earlier.

Table 7.3. Grid of initial $\epsilon_{F_B^{SO}} = \left|\frac{F_B^{SO}}{F_B^{ST}} - 1\right|$ and optimized $\epsilon_{F_B^{SI}} = \left|\frac{F_B^{SI}}{F_B^{ST}} - 1\right|$ (red shaded) heat flow estimate relative error magnitudes (green borders – see Appendix 9.1 for symbol definitions). This is at location 120°E 20°N for the high conductivity k scenario with a heat flow F of 3.33 µW/m². The bulk conductivity down to 2 m is k_{BULK} [W/m/K] and z_{SKIN} [m] is the skin depth.

F_B^{ST} =	MONITORING PERIOD [ORBITAL PERIOD]				k_{BULK} = 3.9E-4	
3.33E-6	0.0		1.0			
DEPTH [m]						
	14.16	29.19	0.17	36.53	1E-3	GAUSSIAN NOISE [K]
2	14.16	29.19	0.17	36.53	1.7E-6	SYSTEMATIC NOISE [K]
	14.16	29.06	0.18	36.40	1.7E-4	
	15.25	16.34	1.26	23.69	1.7E-2	
	1 (-)		1326 (~1.0)			
120°E 20°N	NUMBER OF MEASUREMENTS (TIME RESOLUTION [DAY])				z_{SKIN} = 1.06	

Table 7.4. Grid of initial $\epsilon_{F_B^{SO}} = \left|\frac{F_B^{SO}}{F_B^{ST}} - 1\right|$ and optimized $\epsilon_{F_B^{SI}} = \left|\frac{F_B^{SI}}{F_B^{ST}} - 1\right|$ (red shaded) heat flow estimate relative error magnitudes (green borders – see Appendix 9.1 for symbol definitions). This is at location 120°E 20°N for the low conductivity k scenario with a heat flow F of 3.33 µW/m². The bulk conductivity down to 2 m is k_{BULK} [W/m/K] and z_{SKIN} [m] is the skin depth.

F_B^{ST} =	MONITORING PERIOD [ORBITAL PERIOD]				k_{BULK} = 3.9E-5	
3.33E-6	0.0		1.0			
DEPTH [m]						
	0.05	17.27	0.18	17.87	1E-3	GAUSSIAN NOISE [K]
2	0.05	17.27	0.18	17.87	1.7E-5	SYSTEMATIC NOISE [K]
	0.04	17.15	0.19	17.74	1.7E-3	
	1.03	4.51	1.26	5.11	1.7E-1	
	1 (-)		1326 (~1.0)			
120°E 20°N	NUMBER OF MEASUREMENTS (TIME RESOLUTION [DAY])				z_{SKIN} = 0.12	

Table 7.5. Grid of initial $\epsilon_{F_B^{SO}} = \left|\frac{F_B^{SO}}{F_B^{ST}} - 1\right|$ and optimized $\epsilon_{F_B^{SI}} = \left|\frac{F_B^{SI}}{F_B^{ST}} - 1\right|$ (red shaded) heat flow estimate relative error magnitudes (green borders – see Appendix 9.1 for symbol definitions). This is at location 120°E 20°N for the high conductivity k scenario with a heat flow F of 0.33 μW/m². The bulk conductivity down to 2 m is k_{BULK} [W/m/K] and z_{SKIN} [m] is the skin depth.

F_B^{ST} =	MONITORING PERIOD [ORBITAL PERIOD]				k_{BULK} = 3.9E-4	
3.33E-7	0.0		1.0			
DEPTH [m]						
2	142.25	291.64	0.13	365.55	1E-3	GAUSSIAN NOISE [K]
	142.25	291.64	0.13	365.55	1.7E-6	SYSTEMATIC NOISE [K]
	142.25	290.34	0.01	364.26	1.7E-4	
	153.21	163.15	10.75	237.08	1.7E-2	
	1 (-)		1326 (~1.0)			
120°E 20°N	NUMBER OF MEASUREMENTS (TIME RESOLUTION [DAY])				z_{SKIN} = 1.06	

Table 7.6. Grid of initial $\epsilon_{F_B^{SO}} = \left|\frac{F_B^{SO}}{F_B^{ST}} - 1\right|$ and optimized $\epsilon_{F_B^{SI}} = \left|\frac{F_B^{SI}}{F_B^{ST}} - 1\right|$ (red shaded) heat flow estimate relative error magnitudes (green borders – see Appendix 9.1 for symbol definitions). This is at location 120°E 20°N for the low conductivity k scenario with a heat flow F of 0.33 μW/m². The bulk conductivity down to 2 m is k_{BULK} [W/m/K] and z_{SKIN} [m] is the skin depth.

F_B^{ST} =	MONITORING PERIOD [ORBITAL PERIOD]				k_{BULK} = 3.9E-5	
3.33E-7	0.0		1.0			
DEPTH [m]						
2	1.25	172.64	0.19	178.82	1E-3	GAUSSIAN NOISE [K]
	1.25	172.63	0.19	178.81	1.7E-5	SYSTEMATIC NOISE [K]
	1.34	171.36	0.30	177.54	1.7E-3	
	12.05	45.05	10.97	51.22	1.7E-1	
	1 (-)		1326 (~1.0)			
120°E 20°N	NUMBER OF MEASUREMENTS (TIME RESOLUTION [DAY])				z_{SKIN} = 0.12	

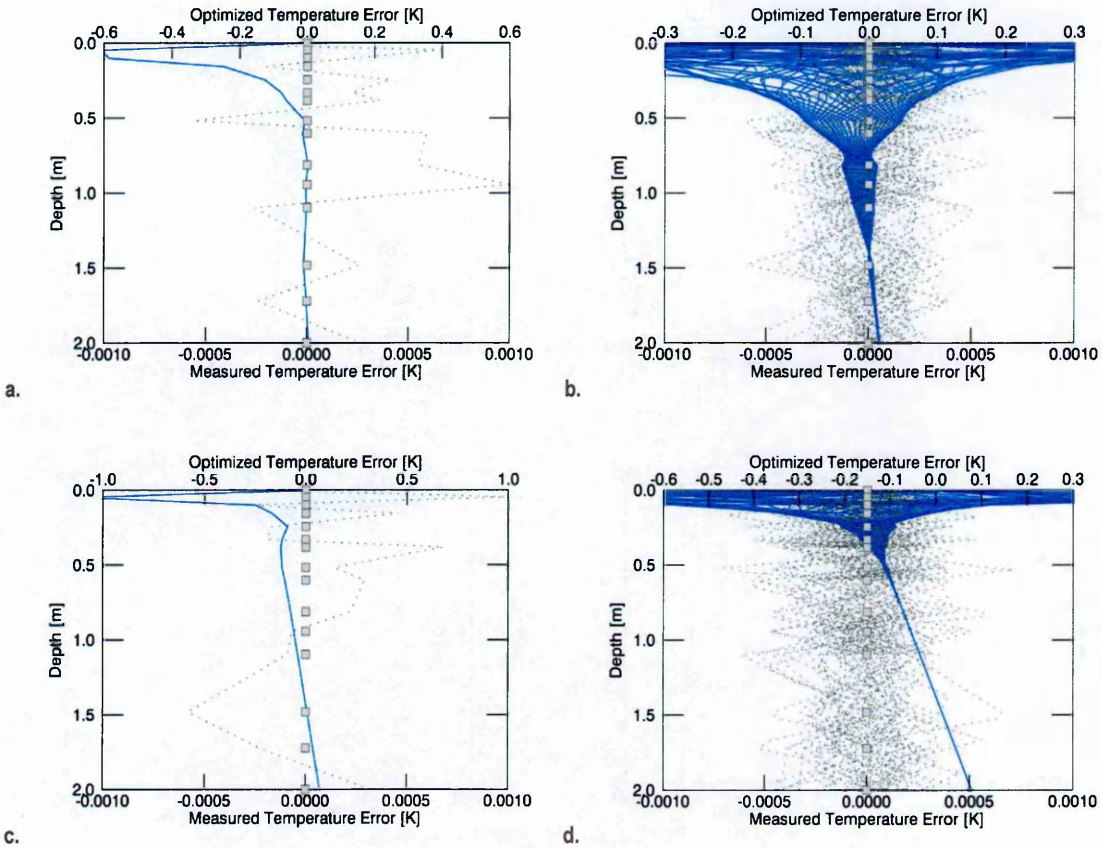

Figure 7.10. Errors in measurement (Gaussian ΔT^0 – dotted grey) and optimized (ΔT^I – solid blue) temperatures for Vestan site located at 120°E 20°N. These are with a high heat flow of 3.33 μW/m² and high (a. and b.) and low (c. and d.) conductivities as presented in Section 7.2.2. The plots show ΔT: for an instantaneous measurement (left); over time t of 1 orbital period in ~26.5 day steps (right). The grey squares are sensor locations.

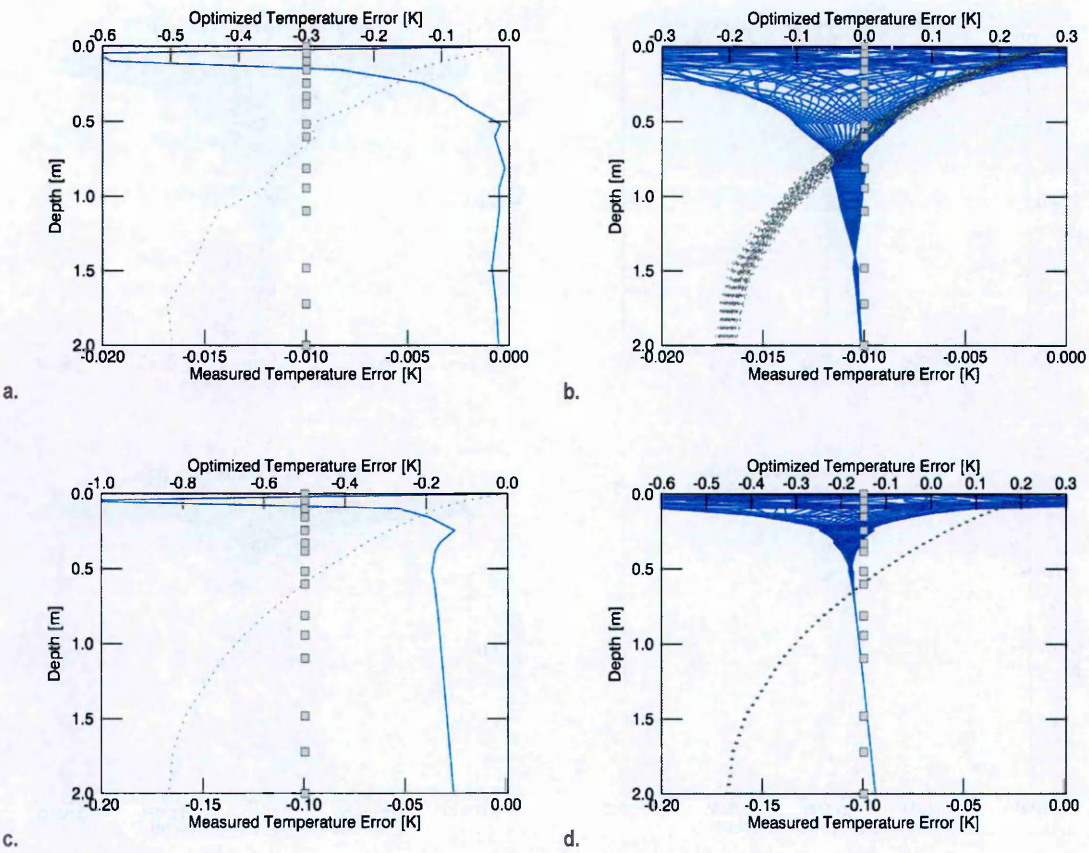

Figure 7.11. Errors in measurement (non-Gaussian ΔT^0 – dotted grey) and optimized (ΔT^I – solid blue) temperatures for Vestan site located at 120°E 20°N. These are with a high heat flow of 3.33 μW/m² and high (a. and b.) and low (c. and d.) conductivities as presented in Section 7.2.2. The plots show ΔT: for an instantaneous measurement (left); over time t of 1 orbital period in ~26.5 day steps (right). The grey squares are sensor locations.

7.4 Summary

Asteroid (4) Vesta, is an important repository of information on the early Solar System. Understanding the formation of its differentiated interior is important to theories of early Solar System formation and evolution. Its topographically heterogeneous, apparently volatile rich and active surface holds useful information on the type and nature of collisions of small planetary bodies in the early Solar System. While the heat flow on Vesta is likely very low, a measurement can provide important information on the thermal state of the Vestan interior and its surface energy balance, therefore assisting in constraining thermal and impact evolution theories of the early Solar System.

An inverse model is applied to a single measurement on Vesta, located at 120°E 20°N, to test the measurability of plausible values of planetary heat flow at its surface. The surface energy balance of the site is modelled with a Bond albedo of 0.2 and emittance of 0.9. High and low conductivity (10^{-3} and 10^{-4} W/m/K), and high and low heat flow (3.33 and 0.33 μW/m/K) end member models are simulated. Measurements are derived from these models with additive Gaussian and non-Gaussian noise – the non-Gaussian noise mirroring the effect of heat sinks. The measurements all cover a depth of 2 m and are either instantaneous or span a full Vestan year.

The temperature gradients produced by the forward models over 2 m are within the range of sensitivities for a heat flow probe with 1 mK precision. For the derived measurements, the larger the amplitude of the non-Gaussian noise (at least 1 mK modelled) the greater is the perturbation of the heat flow estimate from the true value, all else being equal. Downward shifts of 0.4 K and 0.2 K in mean surface temperature, which are not accounted for in the optimization, cause all the optimized heat flows to be overestimated (see Section 7.3.3). This is despite the presence of non-Gaussian noise, based on heat sinks, which deflects the temperature gradient to the left by decreasing temperatures (Figure 7.11; also see Appendix 9.7.2-9.7.3).

With temperature noise amplitude of ~3 mK and a monitoring period covering one Vestan year, simple heat flow estimates, using bulk conductivity and the temperature gradient at the deepest two sensors, are accurate to within 30 % of the true value. The latter is also the case for an instantaneous measurement with the low conductivity, high heat flow model. For instantaneous measurements where the conductivity is high and heat flow low and/or where the noise amplitude is above 3 mK, the heat flow estimates contain very large errors. The large inaccuracies are due, in part, to the use of bulk conductivity – using the (accurate) depth dependent conductivity improves the estimates approximately four-fold. Overall, however, these results demonstrate the feasibility of measuring a very low heat flow, given a long enough period of measurement.

While optimization works well for Mars (see Section 5.3.3) and Mercury (see Section 6.3.3), with heat flows of the order of mW/m^2, meaningful optimized estimates of heat flow which is of the order of $\mu W/m^2$ are not obtained in the Vestan application of the inverse model. Despite this, the model responds similarly to heat flows of different relative magnitudes such that true heat flows which differ by a given factor produce estimates which differ by the same factor, all else being equal – this result may be useful with a network of heat flow probes.

The most accurate heat flow estimate obtained by optimization is a little more than 4.5 times the true heat flow. The large errors in the optimization estimates are due in part to the high frequency variation of the surface temperature (and surface heat flow) which requires high recording frequencies (sampling rates) for an accurate representation of its variation and mean value. Also, the low heat flows of 0.33-3.33 $\mu W/m^2$ are equivalent to steady temperature gradients of 0.33-3.33 mK/m at a bulk conductivity of 1 mW/m/K; these are close to the sensitivity threshold of a heat flow probe with 1 mK precision.

7.5 References

ASMAR, S. W., KONOPLIV, A. S., PARK, R. S., RAYMOND, C. A., BILLS, B., GASKELL, R. W., RUSSELL, C. T., SMITH, D. E., TOPLIS, M. & ZUBER, M. T. 2012. The gravity field of Vesta from Dawn. *In:* European Planetary Science Congress 2012, September 1, 2012 2012. 814.

BOGARD, D. D. & GARRISON, D. H. 2003. 39Ar-40Ar ages of eucrites and thermal history of asteroid 4 Vesta. *Meteoritics and Planetary Science,* 38, 669-710.

BURBINE, T. H., BUCHANAN, P. C., BINZEL, R. P., BUS, S. J., HIROI, T., HINRICHS, J. L., MEIBOM, A. & MCCOY, T. J. 2001. Vesta, Vestoids, and the howardite, eucrite, diogenite group: Relationships and the origin of spectral differences. *Meteoritics and Planetary Science,* 36, 761-781.

CAPRIA, M. T., TOSI, F., CAPACCIONI, F., DE SANCTIS, M. C., PALOMBA, E., AMMANNITO, E., TITUS, T. N., COMBE, J.-P., TOPLIS, M., SUNSHINE, J., RUSSELL, C. T. & RAYMOND, C. A. 2012. Thermal Inertia Variations on the Surface of Vesta from the Dawn Data. *In:* Lunar and Planetary Institute Science Conference Abstracts, March 1, 2012 2012. 43, 1863.

CLOUTIS, E. A., IZAWA, M. R. M., POMPILIO, L., REDDY, V., HIESINGER, H., NATHUES, A., MANN, P., LE CORRE, L., PALOMBA, E. & BELL, J. F. 2013. Spectral reflectance properties of HED meteorites + CM2 carbonaceous chondrites: Comparison to HED grain size and compositional variations and implications for the nature of low-albedo features on Asteroid 4 Vesta. *Icarus,* 223, 850-877.

CORADINI, A., TURRINI, D., FEDERICO, C. & MAGNI, G. 2011. Vesta and Ceres: Crossing the History of the Solar System. *Space Science Reviews,* 163, 25-40.

DE SANCTIS, M. C., COMBE, J.-P., AMMANNITO, E., PALOMBA, E., LONGOBARDO, A., MCCORD, T. B., MARCHI, S., CAPACCIONI, F., CAPRIA, M. T., MITTLEFEHLDT, D. W., PIETERS, C. M., SUNSHINE, J., TOSI, F., ZAMBON, F., CARRARO, F., FONTE, S., FRIGERI, A., MAGNI, G., RAYMOND, C. A., RUSSELL, C. T. & TURRINI, D. 2012. Detection of Widespread Hydrated Materials on Vesta by the VIR Imaging Spectrometer on board the Dawn Mission. *The Astrophysical Journal Letters,* 758, L36.

DEHANT, V., BANERDT, B., LOGNONNÉ, P., GROTT, M., ASMAR, S., BIELE, J., BREUER, D., FORGET, F., JAUMANN, R., JOHNSON, C., KNAPMEYER, M., LANGLAIS, B., LE

FEUVRE, M., MIMOUN, D., MOCQUET, A., READ, P., RIVOLDINI, A., ROMBERG, O., SCHUBERT, G., SMREKAR, S., SPOHN, T., TORTORA, P., ULAMEC, S. & VENNERSTRØM, S. 2012. Future Mars geophysical observatories for understanding its internal structure, rotation, and evolution. *Planetary and Space Science,* 68, 123-145.

DENEVI, B. W., BLEWETT, D. T., BUCZKOWSKI, D. L., CAPACCIONI, F., CAPRIA, M. T., DE SANCTIS, M. C., GARRY, W. B., GASKELL, R. W., LE CORRE, L., LI, J.-Y., MARCHI, S., MCCOY, T. J., NATHUES, A., O'BRIEN, D. P., PETRO, N. E., PIETERS, C. M., PREUSKER, F., RAYMOND, C. A., REDDY, V., RUSSELL, C. T., SCHENK, P., SCULLY, J. E. C., SUNSHINE, J. M., TOSI, F., WILLIAMS, D. A. & WYRICK, D. 2012. Pitted Terrain on Vesta and Implications for the Presence of Volatiles. *Science,* 338, 246-.

ELKINS-TANTON, L. T., MANDLER, B. E. & FU, R. R. 2014. Placing Vesta in the Range of Planetesimal Differentiation Models. *LPI Contributions,* 1773, 2034.

ERMAKOV, A. I., ZUBER, M. T. & SMITH, D. E. 2012. Forward Modeling of Vesta's Interior Structure Using Gravity and Shape Models from the Dawn Mission. *In:* Lunar and Planetary Institute Science Conference Abstracts, March 1, 2012 2012. 43, 2382.

ESA. 2013. *Rosetta: Summary* [Online]. ESA. Available: http://sci.esa.int/jump.cfm?oid=2279 [Accessed 03/01/2014 2014].

FORMISANO, M., FEDERICO, C., TURRINI, D., CORADINI, A., CAPACCIONI, F., SANCTIS, M. C. & PAUSELLI, C. 2013. The heating history of Vesta and the onset of differentiation. *Meteoritics and Planetary Science,* 48, 2316-2332.

GROTT, M., HELBERT, J. & NADALINI, R. 2007. Thermal structure of Martian soil and the measurability of the planetary heat flow. *J. Geophys. Res.,* 112, E09004.

GUNDLACH, B. & BLUM, J. 2013. A new method to determine the grain size of planetary regolith. *Icarus,* 223, 479-492.

HAGERMANN, A. 30/01/2014 2014. *RE: Cometary Surface Energy Balance.* Type to CORNWALL, M.

JAUMANN, R., BIBRING, J. P., GLASSMEIER, K. H., GROTT, M., HO, T. M., ULAMEC, S., SCHMITZ, N., AUSTER, H. U., BIELE, J., KUNINAKA, H., OKADA, T., YOSHIKAWA, M., WATANABE, S., FUJIMOTO, M., SPOHN, T. & KONCZ, A. 2014. A Mobile Asteroid Surface Scout (MASCOT) for the Hayabusa 2 Mission. *In:* Lunar and Planetary Science Conference, March 1, 2014 2014. 45, 1817.

KARGL, G., KAUFMANN, E., KNOLLENBERG, J., KÖMLE, N. I., BENTLEY, M. S. & MACHER, W. 2012. Calibration Measurements of the MUPUS Thermal Probe. *In:* European Planetary Science Congress 2012, September 1, 2012 2012. 607.

KÖMLE, N. I., HÜTTER, E. S., MACHER, W., KAUFMANN, E., KARGL, G., KNOLLENBERG, J., GROTT, M., SPOHN, T., WAWRZASZEK, R., BANASZKIEWICZ, M., SEWERYN, K. & HAGERMANN, A. 2011. In situ methods for measuring thermal properties and heat flux on planetary bodies. *Planetary and Space Science,* 59, 639-660.

LEYRAT, C., BARUCCI, A., MUELLER, T., O'ROURKE, L., VALTCHANOV, I. & FORNASIER, S. 2012. Thermal properties of (4) Vesta derived from Herschel measurements. *Astronomy and Astrophysics,* 539, 154.

MUELLER, T. G. & LAGERROS, J. S. V. 1998. Asteroids as far-infrared photometric standards for ISOPHOT. *Astronomy and Astrophysics,* 338, 340-352.

NASA, J. P. L. 2013a. *Contour Map of Hydrogen on Vesta* [Online]. Online: NASA, Jet Propulsion Laboratory. Available: http://www.jpl.nasa.gov/spaceimages/details.php?id=PIA17037 [Accessed January 16 2014].

NASA, J. P. L. 2013b. *Shape and Gravity of Vesta* [Online]. Online: NASA, Jet Propulsion Laboratory. Available: http://dawn.jpl.nasa.gov/multimedia/shape_gravity_vesta.asp [Accessed 13/01/2014 2014].

NASA, J. P. L. 2013c. *Vesta Topography Map* [Online]. Online: NASA, Jet Propulsion Laboratory. Available: http://www.jpl.nasa.gov/spaceimages/details.php?id=PIA17037 [Accessed 13/01/2014 2014].

NASA, J. P. L., STUBBS, T. J. & WANG, Y. 2012. *Global Map of Average Surface Temperature* [Online]. Online: NASA, Jet Propulsion Laboratory. Available: http://dawn.jpl.nasa.gov/multimedia/vesta_global_map.asp [Accessed 12/01 2014].

NEUMANN, W., BREUER, D. & SPOHN, T. 2013. Early magma ocean and core formation on Vesta. *In:* EGU General Assembly Conference Abstracts, April 1, 2013 2013. 15, 13487.

O'BRIEN, D. & SYKES, M. 2011. The Origin and Evolution of the Asteroid Belt—Implications for Vesta and Ceres. *Space Science Reviews,* 163, 41-61.

PALMER, E. M., HEGGY, E., CAPRIA, M. T., TOSI, F. & RUSSELL, C. T. 2013. Dielectric Properties of the Surface of Asteroid Vesta from Dawn VIR Thermal Observations. *In:*

Lunar and Planetary Institute Science Conference Abstracts, March 1, 2013 2013. 44, 2476.

PIETERS, C., MCFADDEN, L., PRETTYMAN, T., SANCTIS, M. C., MCCORD, T., HIROI, T., KLIMA, R., LI, J.-Y. & JAUMANN, R. 2011. Surface Composition of Vesta: Issues and Integrated Approach. *Space Science Reviews,* 163, 117-139.

PIQUEUX, S. & CHRISTENSEN, P. R. 2011. Temperature-dependent thermal inertia of homogeneous Martian regolith. *Journal of Geophysical Research (Planets),* 116, 7004.

PRESLEY, M. A. & CHRISTENSEN, P. R. 1997. Thermal conductivity measurements of particulate materials 2. results. *Journal of Geophysical Research,* 102, 6551-6566.

PRETTYMAN, T. H., MITTLEFEHLDT, D. W., YAMASHITA, N., LAWRENCE, D. J., BECK, A. W., FELDMAN, W. C., MCCOY, T. J., MCSWEEN, H. Y., TOPLIS, M. J., TITUS, T. N., TRICARICO, P., REEDY, R. C., HENDRICKS, J. S., FORNI, O., LE CORRE, L., LI, J.-Y., MIZZON, H., REDDY, V., RAYMOND, C. A. & RUSSELL, C. T. 2012. Elemental Mapping by Dawn Reveals Exogenic H in Vesta's Regolith. *Science,* 338, 242-.

RAYMAN, M. D. & MASE, R. A. 2014. Dawn's exploration of Vesta. *Acta Astronautica,* 94, 159-167.

REDDY, V., LI, J.-Y., LE CORRE, L., SCULLY, J. E. C., GASKELL, R., RUSSELL, C. T., PARK, R. S., NATHUES, A., RAYMOND, C., GAFFEY, M. J., SIERKS, H., BECKER, K. J. & MCFADDEN, L. A. 2013. Comparing Dawn, Hubble Space Telescope, and ground-based interpretations of (4) Vesta. *Icarus,* 226, 1103-1114.

REDDY, V., NATHUES, A., LE CORRE, L., SIERKS, H., LI, J.-Y., GASKELL, R., MCCOY, T., BECK, A. W., SCHRÖDER, S. E., PIETERS, C. M., BECKER, K. J., BURATTI, B. J., DENEVI, B., BLEWETT, D. T., CHRISTENSEN, U., GAFFEY, M. J., GUTIERREZ-MARQUES, P., HICKS, M., KELLER, H. U., MAUE, T., MOTTOLA, S., MCFADDEN, L. A., MCSWEEN, H. Y., MITTLEFEHLDT, D., O'BRIEN, D. P., RAYMOND, C. & RUSSELL, C. 2012. Color and Albedo Heterogeneity of Vesta from Dawn. *Science,* 336, 700-.

RUSSELL, C. T., RAYMOND, C. A., JAUMANN, R., MCSWEEN, H. Y., SANCTIS, M. C., NATHUES, A., PRETTYMAN, T. H., AMMANNITO, E., REDDY, V., PREUSKER, F., O'BRIEN, D. P., MARCHI, S., DENEVI, B. W., BUCZKOWSKI, D. L., PIETERS, C. M., MCCORD, T. B., LI, J.-Y., MITTLEFEHLDT, D. W., COMBE, J.-P., WILLIAMS, D. A.,

HIESINGER, H., YINGST, R. A., POLANSKEY, C. A. & JOY, S. P. 2013. Dawn completes its mission at 4 Vesta. *Meteoritics and Planetary Science,* 48, 2076-2089.

SPOHN, T., SEIFERLIN, K., HAGERMANN, A., KNOLLENBERG, J., BALL, A. J., BANASZKIEWICZ, M., BENKHOFF, J., GADOMSKI, S., GREGORCZYK, W., GRYGORCZUK, J., HLOND, M., KARGL, G., KÜHRT, E., KÖMLE, N., KRASOWSKI, J., MARCZEWSKI, W. & ZARNECKI, J. C. 2007. Mupus A Thermal and Mechanical Properties Probe for the Rosetta Lander Philae. *Space Science Reviews,* 128, 339-362.

STUBBS, T. J. & WANG, Y. 2012. Illumination conditions at the Asteroid 4 Vesta: Implications for the presence of water ice. *Icarus,* 217, 272-276.

THANGJAM, G., REDDY, V., LE CORRE, L., NATHUES, A., SIERKS, H., HIESINGER, H., LI, J.-Y., SANCHEZ, J. A., RUSSELL, C. T., GASKELL, R. & RAYMOND, C. 2013. Lithologic mapping of HED terrains on Vesta using Dawn Framing Camera color data. *Meteoritics and Planetary Science,* 48, 2199-2210.

TITUS, T. N., BECKER, K. J., TOSI, F., CAPRIA, M. T., DE SANCTIS, M. C., PALOMBA, E., GRASSI, D., CAPACCIONI, F., AMMANNITO, E., COMBE, J.-P., MCCORD, T. B., LI, J.-Y., RUSSELL, C. T. & RAYMOND, C. A. 2013. Analysis of Temperature and Thermal Inertia of the Surface of Vesta Using Dawn VIR Survey Observations. *In:* Lunar and Planetary Institute Science Conference Abstracts, March 1, 2013 2013. 44, 2400.

WILLIAMS, D. R. 2014a. *Asteroid Fact Sheet* [Online]. Online: NASA. Available: http://nssdc.gsfc.nasa.gov/planetary/factsheet/asteroidfact.html [Accessed 12/01/2014 2014].

WILLIAMS, D. R. 2014b. *Earth Fact Sheet* [Online]. Online: NASA. Available: http://nssdc.gsfc.nasa.gov/planetary/factsheet/earthfact.html [Accessed 12/01/2014 2014].

WILLIAMS, D. R. 2014c. *Mars Fact Sheet* [Online]. Online: NASA. Available: http://nssdc.gsfc.nasa.gov/planetary/factsheet/marsfact.html [Accessed 12/01/2014 2014].

WILLIAMS, D. R. 2014d. *Mercury Fact Sheet* [Online]. Online: NASA. Available: http://nssdc.gsfc.nasa.gov/planetary/factsheet/mercuryfact.html [Accessed 12/01/2014 2014].

ZUBER, M., MCSWEEN, H., JR., BINZEL, R., ELKINS-TANTON, L., KONOPLIV, A., PIETERS, C. & SMITH, D. 2011. Origin, Internal Structure and Evolution of 4 Vesta. *Space Science Reviews,* 163, 77-93.

8 CONCLUSIONS

8.1 The Problem, Restated

The purpose of this study is to present a method by which planetary heat flow can be recovered from a shallow subsurface heat flow measurement on a terrestrial planet. The shallow subsurface heat flow is a superposition of planetary heat flow, and heat flow due to unsteady surface processes. The extent of superposition depends on the maximum depth covered by the heat flow measurement, coupled with the regolith skin depth (see Section 2.2). Deeper measurements access more of the pristine basal heat flow as the unsteady surface heat flow is damped to negligible levels below the skin depth.

An ideal heat flow measurement therefore depends on two or more sensors penetrating far enough below the skin depth to access the pristine basal heat flow. This may not happen for several reasons: the heat flow probe may encounter subsurface obstacles which stop its progress; some sensors may fail or return data that is unusable; the skin depth may be significantly deeper than expected, meaning the heat flow probe may not access the pristine basal heat flow, even at its target depth.

In the instance where the pristine basal heat flow is not accessed, the signal of the unsteady surface heat flow can be removed by monitoring the regolith over extended periods – at least one seasonal cycle over the skin depth is required, with at least ten measurements (see Section 4.2.1.2.2) to adequately characterise the unsteady heat flow so it can be removed. However, there is, naturally, no guarantee that a heat flow probe will function at full capacity throughout a seasonal cycle in the extreme thermal environments of the terrestrial planets.

To guarantee useful returns from any planetary heat flow probe measurement, a method is required which is capable of handling all the preceding

eventualities. The method of choice in this study is Function Specification Inversion (FSI), first applied to the deep borehole heat flow measurements on Earth (e.g. Shen and Beck, 1991,1992; Tarantola, 2005). FSI is the focus of this study through Chapters 2-7. In Chapter 2, the theory is presented; in Chapter 3, a forward model – an important element of FSI – is presented; in Chapter 4, FSI is parameterized and tested on synthetic scenarios; in Chapters 5-7 it is applied to realistic scenarios which may be encountered on select terrestrial planets – namely Mars, Mercury and Vesta. What follows is a discussion of results of the various applications of the FSI model.

8.2 Model Behaviour

The inverse model (Chapter 4) is essentially composed of a forward model[1] (Chapter 3 – based on the 1D Finite Control Volume (FCV) method of Patankar, 1980), solved iteratively with: primal and dual boundary conditions; dual heat sources which arise from the residuals between a calculated primal temperature and the measured temperature; and an optimization function which updates the forward model parameters (optionally, basal heat flow, steady and unsteady surface temperature, and thermal capacity). The model finds a best fit solution based on the a priori information supplied along with the temperature measurement.

8.2.1 Truncation Error

In this study, the temperature measurements are obtained from forward modelled simulations with relatively dense grids in space and time, at select gridpoints and timesteps.[2] These truncated versions of the densely gridded

[1] The calculations are partitioned into steady and unsteady states.

[2] Synthetic measurements generated by the FCV numerical forward model are verified against synthetic measurements generated by an analytical forward model in Appendix 9.4.9.

forward simulations have random or systematic errors added. The preceding procedure effectively replicates the measurement process of a heat flow probe.

In an inversion, then, the primal temperature calculations may contain truncation errors which increase with the size of the timesteps. The density of gridpoints has no significant impact on truncation errors (see Section 4.2.1.2.2). Therefore, timestep related truncation errors determine how well the temperature calculation fits the data measurement and consequently, impact the accuracy of the optimized heat flows.

Truncation errors are most evident when comparing the scenarios of Chapter 4 to the planetary scenarios of Chapters 5-7. In Chapter 4, the inversions are carried out with the same timesteps as the forward model simulations (~86400 s); in Chapters 5-7 the inversion timesteps are 86400 s in all cases, while the forward simulation timesteps are 3600 s. Additionally, comparing the results of Mars (Section 5.3.3.2), Mercury (Section 6.3.3.2) and Vesta (Section 7.3.3), truncation errors affect the results of Mars and Vesta substantially more so than they do those of Mercury. This is because the Mercurian surface temperature does not contain a large number of short period variations. On Mars, only the surface sensor is ignored, however it is likely that ignoring the first 2-3 sensors on Mars, and the first 2 on Vesta can produce more accurate optimized heat flow estimates.

The use of timesteps of the order of 3600 s require simulation times several times the equivalent cases with 86400 s timesteps (see Appendix 9.8.1 for a plot of simulation times for different grid spacing and timesteps). The appreciable number of inversion scenarios tested means there is a necessary trade-off between simulation time and accuracy. For the purposes of this study, calculation speed is given precedence over accuracy of the calculated

primal temperatures (and absolute accuracy of the optimized heat flows). Therefore, the heat flow optimization results of the planets must be taken in a relative to the presence of truncation errors. Reducing truncation errors will likely lead to better accuracy; however the effect of truncation errors is considered less important than errors related to skin depth, thermal properties, and instrument and systematic noise.

8.2.2 Convergence and Covariances

When optimizing basal heat flow only, the model converges[3] in a few iterations (usually less than 10), though there are some instances when the iterations pass a termination point of 50 iterations. Steady surface temperature, conductivity and heat source convergence is similar in behaviour to that with the basal heat flow. Convergence of thermal capacity requires a few more iterations than with the preceding parameters. The unsteady surface temperature requires several tens of iterations before the inverse model can be terminated (see Chapter 4 and Appendix 4 for example convergence plots). In cases of simultaneous optimization the number of iterations vary, though in most cases there is no significant improvement beyond the first few iterations. To allow for instances where the model covariance is too small, the model is allowed to progress beyond the minimum to a second stationary point, where it is terminated (see e.g. Appendix 9.4.6).

As discussed in Section 2.2.1.3.3, the path of optimization of the function S_m, is determined in large part by the design of the covariances. Model parameter covariances which are small tend to dictate the path of optimization. Therefore, the covariances are one of the key a priori parameters to

[3] In the referenced instances, the stepping factor is 1 (see Section 2.2 for details). Tests conducted with smaller stepping factors result in a greater number of iterations before convergence (see Appendix 9.2.1-9.2.2).

determine. The most natural inference is that the relative magnitudes of the model parameters are already accounted for by their fundamental unit relationships. However, there is some level of trial and error involved in designing the covariances (see Section 4.4).

Throughout Chapter 4 and Appendix 9.4.7, relationships between parameter standard deviations (SDs) are noted which guide the design of the relative magnitudes of the covariances (termed SD stability ratios), though the relationships are not analytical, and therefore not precise; this aspect of FSI warrants further investigation. A preliminary effort to establish analytical relationships is outlined in Appendix 9.8.2; it shows how a reduction of the covariance standard deviations to units analogous to energy densities predicts SD ratios consistent, to first order, with those identified in Chapter 4. If the analytical relationships hold true, the gridding plays a critical role in the values of the SD ratios; they must be evaluated at each unique spatiotemporal gridpoint.

8.2.3 Measurement Error

A counterintuitive result encountered in inverse model testing is more accurate optimization of heat flows with an increase of random noise in the temperature measurement (see Sections 4.3.1.2 and 5.3.3.2). As noted in Section 4.3.1.2, the result is mainly due to small assumed data standard deviations, relative to the model standard deviations in their respective covariance matrices. This is coupled with increased skin depth and length of measurement. These increase instabilities in the inverse problem (see Section 2.2) by, effectively, increasing the ill-determinacy of the problem for a given basal sensor depth (by increasing the number of different temperature gradients measured by any two sensors, to which the algorithm must match a single basal heat flow).

The results of Vesta (Section 7.3.3) show that the presence of systematic noise effectively perturbs the temperature gradient (and optimized heat flow) in a manner proportionate to the noise amplitude. The presence of any systematic noise which is above the random background (or instrument) noise, and affects the steady temperature gradient (such as the unknown heat sources or sinks with Vesta in Section 7.3; also see Wang, 1992), is likely to render optimized heat flows inaccurate. However, if other parameters are known with confidence, the systematic noise can be characterised and accounted for in the inversion or removed from the measurement pre-inversion.

8.2.4 A Priori Parameter Errors

While treated separately, a priori model parameter errors are not completely separate from measurement errors. For example, the systematic noise present in the Vesta simulations (Section 7.3) is due to heat sources. If these are accounted for in the a priori model then their presence in the temperature measurement does not adversely affect the optimized heat flow accuracy.

Overestimated or underestimated model parameters are accompanied by effects on the temperature distribution, similar to what would be seen with a simple increase or decrease of said parameters in the forward model (see Chapter 3). In the case where the heat flow is the only free parameter, the inverse model attempts to mitigate the effects of the incorrect parameters by overestimating or underestimating the heat flow. The effects are collated in Appendix 9.8.3[4] – effectively: overestimated conductivity and underestimated thermal capacity increase skin depth and lead to poorly constrained heat flows

[4] Results for thermal properties are described in Sections 4.2.1.2.3 and 4.3.1.3, while similar results for thermal properties, and also surface temperature and heat sources, can be deduced from the simultaneous optimization results of Appendix 9.4.7.

and vice versa; overestimated surface temperature amplitude decrease heat flow accuracy and vice versa; overestimated mean surface temperatures lead to high heat flow estimates and vice versa.

8.2.5 Interpretation of Results

Determining the accuracy of optimized heat flow results is probably the greatest challenge, given the numerous occasions in this study, where nearly equivalent measurement scenarios give largely divergent heat flow results (some accurate, some not). The resolution analyses of Section 2.2.3.5 may be applied in the case of simultaneous optimisation of parameters or inversion of different temperature measurements with the same a priori model. The analyses are strictly related to an equivalent linear problem but can give a sense of how resolved a parameters is, based on the a priori covariances. Of course, the a priori covariances may contain significant design flaws, as noted in Sections 8.2.2 and 8.2.4. To obtain accurate heat flows, with high confidence, the primal temperatures must be brought to acceptable agreement with the measured temperature. While being relatively accurate, optimized heat flows with high random noise (e.g. 1 K noise on Mars), can only be accepted with large error bars.

8.3 Heat Flow from the Planets

8.3.1 A Note on the Measurement

The synthetic measurements formulated here are considered at a post-processed stage, after the influence of the heat flow probe on the measurement environment has been accounted for. Prior to this a measurement effectively reflects the properties of the heat flow probe and its immediate environs as a combined thermal system. Physical effects such as soil compaction, which modifies the thermophysical properties of the regolith, as well as 'shunting' of the heat flow where the conductivity along the probe

axis is non-negligible are irreversible and must be accounted for to achieve accurate heat flow estimates (e.g. Langseth et al., 1972; Langseth et al., 1976; Hagermann and Spohn, 1999; Grott, 2009). These require further numerical modelling and are be beyond the scope of this project.

It is conceivable, for example, that the inverse model applied to the synthetic data herein can be applied to Apollo 15 and 17 ALSEP data (e.g. Langseth et al., 1976; also see Section 1.1.3.2); however, in addition to the processing required above, there are several practical issues to overcome. The data used in the preliminary Apollo lunar heat flow studies (e.g. Langseth et al., 1972; Langseth et al., 1976) is available from the National Space Science Data Center (NSSDC; NASA, 2015).

The NSSDC ALSEP data for Apollo 15 and 17 consist of absolute temperature data from four thermocouples and temperature difference, and average temperature data from two bridge temperature sensors on the two main probe sections (see e.g. Langseth et al., 1976; Nagihara et al., 2015 for probe configuration). The bridge sensor data are therefore not of the depth accuracy required for a reasonable determination of the heat flow.

A rudimentary application of the GPHLO1 inverse model to ALSEP data is shown in Appendix 9.8.4; the thermocouple temperature data has been used with the bridge sensors to increase the effective depth of the absolute temperature data. The results of Appendix 9.8.4 demonstrate the applicability of the inverse model to real-world data and illustrates its inherent limits with highly temperature-dependent thermal properties.

8.3.2 Mars

Simple initial (a priori) heat flow estimates[5] for Mars (Chapter 5) suggest that, in most cases, optimization is a requirement where the monitoring period is 0.75 Martian years, or less, and heat flow probe sensors penetrate up to 5 m. In most of these cases heat flows are inaccurate by factors of 0.5-83, generally in order of decreasing depth and monitoring period. There are a few instances with heat flows accurate to within 50 % at a skin depth[6] of 0.44 m. The initial heat flow estimates are accurate to within 20 % where the monitoring period is 1 Martian year. All the preceding estimates are improved with more accurate conductivity profiles.

Optimization improves upon most of the initial estimates. There are exceptions where the measurements are taken over 1 Martian year because of truncation errors (discussed in Section 8.2.1). There are also exceptions where the skin depth is below ~1 m and monitoring periods are at least 0.25 Martian years at 2 m sensor depth, or 0.75 Martian years at 3 m sensor depth. The exceptions are, also due to the increased ill-determinacy of the heat flow problem as monitoring period and skin depth are increased, as discussed in Section 8.2.3.

To minimise truncation errors (Section 8.2.1) in the case of the high frequency (~24 h), high amplitude (~40 K) Martian diurnal surface temperature variation, small model timesteps, or improvements in the accuracy of the model at larger timesteps, are required to accurately reproduce the associated temperatures. The relatively small amplitude of the annual temperature variation (~10 K) is

[5] The simple a priori heat flow estimates are calculated with the bulk conductivity over the measurement depth, and the temperature gradient at the two deepest sensors.

[6] The skin depths in this case are calculated using bulk thermal diffusivity and are therefore high estimates, to be considered in a relative sense.

beneficial below the diurnal skin depth (~1.5-7 cm), minimising masking of the steady temperature gradient.

The overall results suggest that heat flows can be optimized from a Martian temperature measurement – with thermal properties known – to within ~10 % accuracy where the measurement is taken at twice the skin depth over 0.5 Martian years or 5 times the skin depth over 0.25 Martian years. This is within the threshold required to correlate the measurement with estimates of the variation of heat flow across Mars surface and constrain the parameters of specific thermal evolution models.

8.3.3 Mercury

A sensor penetration depth of 2 m for Mercury (Chapter 6) is approximately 13 times the skin depth. Unsurprisingly, bulk conductivity estimates produce heat flows accurate to within 40 % in most cases – at these depths the dependence on monitoring period is largely lost as the unsteady surface temperature is damped to negligible values. Despite this, optimization does produce marginal improvements in some cases (substantial in a few), though the results (improvement or not) are largely unpredictable (likely a function of the 10 mK random errors). If heat flow probe sensors do not penetrate below 0.5 m, a measurement over a full Mercurian solar day can recover the heat flow to within 20 % – instantaneous measurements up to 0.5 m are inaccurate by large factors.

The special case of the Mercurian surface temperature has benefits and drawbacks in optimization. The lack of short period variations means truncation errors are kept to a relative minimum; however the steep transitions between terminator and peak daytime temperatures require high time resolution for accurate modelling. Notably, results show that instantaneous measurements are best taken at peak temperatures, where the variation in

surface temperature is slow. The shallow skin depths (0.15-0.16 m) mitigate the effects of the large surface temperature amplitudes (127-301 K). Below 0.5 m the amplitude of the temperature envelope is approximately the same as that at the Martian surface due to the Martian annual unsteady temperature variation (5-13 K). Therefore, where sensors penetrate below 5 m, results are expected to be on par with or better than results for Mars.

8.3.4 Vesta

The low heat flows at Vesta (~$\mu W/m^2$ modelled) are not successfully optimized by the model. Simple initial heat flow estimates are determined to within 20 % where there is minimal systematic noise, heat flow of the order of 3 $\mu W/m^2$ and bulk conductivity of the order of 10^{-5} W/m/K in the measurement. This is the case for instantaneous measurements, as well as measurements taken over a Vestan year. Heat flows are also found to within 20 % for Vestan year-long measurements with bulk conductivity of the order of 10^{-4} W/m/K and heat flows of the order of 0.3 $\mu W/m^2$.

The Vestan surface temperature has very short period diurnal variations (5.36 h; 17-115 K) coupled with long period annual variations (5-10 K). The use of smaller model timesteps and/or the reduction of truncation errors may therefore produce more accurate optimization results. The Vestan surface energy balance produces a negligible diurnal skin depth (less than ~1.4 cm) and relatively substantial annual skin depths of 1.06 m (higher than Mercury, and potentially Mars) and 0.12 m. Therefore for a reliable heat flow measurement penetration depths are required towards 2 m and monitoring periods approaching 1 Vestan year.

8.3.5 Estimating Planetary Heat Flow

The geology of the planetary measurement sites discussed above is described in the relevant Chapters. Sites are chosen primarily on their likelihood of being

dry. It is noteworthy that the high latitude site at Mercury (85° N) is one possible source of icy regolith, the high conductivity of which will bias a heat flow measurement; however the overriding focus at the site is the low temperature amplitude. A trade-off is necessary between: sites with low temperature amplitude, which are more likely in high latitude shadowed regions, with rough topography and icy regolith; and sites with high temperature amplitudes, which are more likely in low latitude areas, with smooth topography and dry regolith. The presented inverse model can only simulate dry regolith, therefore if icy conditions are met the model is inapplicable and/or further work may be necessary.

The preceding discussion shows that it is possible to obtain improved planetary heat flow estimates from a shallow subsurface measurement by optimization using the discussed FSI model. However, it is important that specific conditions are met. Where there are high frequency variations in surface temperature, it is best to ignore the affected surface sensors, or invert the measurements with high density grids. Where only short period measurements are likely, it is best to time those such that they are taken when the surface temperature is peaked, and relatively unchanging. It is important to accurately characterise errors in non-heat flow parameters, such that they can be optimized with the heat flow, either individually or simultaneously, otherwise the heat flow will contain related inaccuracies.

The improved estimates can further constrain current heat flow estimates for Mars and Mercury if the measurement is far enough below the skin depth (at least twice for Mars, and 3 times for Mercury), though this is dependent on monitoring periods: shorter monitoring periods require deeper sensor penetration. Optimization at the grid densities used here does not improve upon the low heat flows at Vesta even though a measurement is possible with the low conductivity models produced in this study. Even a single, short period

heat flow measurement, on a planetary body, is a critical first step; extrapolation to global heat flow estimates involve analyses of local and regional surface and subsurface geology. As noted earlier, and evidenced by studies mentioned in Chapter 1, appropriate site selection maximises a successful outcome.

8.4 Further Applications and Enhancements

8.4.1 Applications

The inverse model in this study is designed for application to a terrestrial planet, though limited to simulating dry regolith in 1D, and ignoring temperature dependence of regolith thermal properties. Mercury, Mars and Vesta are the focus of the current study, in part because of the abundance of scientific data and focus on these from numerous Martian space missions (the planned InSight mission, in particular), Mariner, MESSENGER, the planned Bepi-Colombo and Dawn. However, equally valid candidates for application are Venus, the Martian moons Phobos and Deimos, and the Moon (see Appendix 9.8.4 for a demonstration).

Venus is an interesting candidate because of its size similarity to Earth, with unique orbital characteristics and high surface temperatures coupled to a dynamic atmosphere, and potentially high heat flow (e.g. Ruiz, 2007). Important questions surround the origin of the Martian moons by accretion, capture or giant impact (e.g. Craddock, 2011; Rosenblatt and Charnoz, 2012; Murchie et al., 2014); a heat flow measurement can help to differentiate between these by providing information on the internal temperatures. The Apollo lunar heat flow measurements suffered from several ambiguities, and are still subject to refinement (e.g. Hagermann and Tanaka, 2006; Siegler et al., 2010). Lessons from the Apollo measurements are being applied to the design of future heat flow probes and measurement techniques because of

the high scientific priority of a reliable lunar heat flow measurement (e.g. Kiefer, 2012; Zacny et al., 2013).

8.4.2 Enhancements

8.4.2.1 Temperature Dependence

In applying the FSI model to airless bodies with short rotation periods, like the Moon, Phobos, Deimos or Vesta the non-linear effect of radiative thermal conductivity (~T^3 dependence) is non-negligible towards the surface regions. This results in a rise in mean temperatures[7] and may lead to a heat flow underestimate (e.g. Keihm and Langseth, 1973; 1975; Siegler et al., 2010). In cases where a heat flow probe penetrates only to shallow depths, temperature dependence must be taken into account where the affected sensors cannot be ignored. Along with the former, where the regolith monitoring period falls short of the seasonal cycle associated with the skin depth, accounting for the potential biases introduced by temperature dependence may lead to more accurate heat flows. For the lunar demonstration in Appendix 9.8.4, the internal heating effect of temperature dependent thermal conductivity is approximated with internal heat sources. Incorporating the non-linearity of temperature dependence into FSI requires an extensive, but potentially straight-forward re-work of the theory presented in Chapter 2.

8.4.2.2 Gas Diffusion

In applying FSI to bodies which may be volatile rich or bodies with atmospheres, it is useful to be able to account for gas diffusion (advection), which is not possible with the current model. Advection becomes important in volatile rich porous media where the volatile conductivity component is greater than that of the grain contact conductivity component (e.g. Piqueux and

[7] The ~T^3 dependence of conductivity causes more heat to enter the surface during that daytime than escapes during night time.

Christensen, 2011). Accounting for advection requires augmenting the current FSI model to include mass flow solutions coupled to the solution of the HFE as defined in Section 2.1, and modification of the inverse theory of Section 2.2 to account for the resulting non-linearities. The critical step in modifying the inverse theory is deriving an appropriate expression for the dual problem. Misfit functions capable of dealing with strong non-linearities in the inverse problem are discussed in Tarantola (2005).

8.4.2.3 3D

Hopcroft et al. (2009) show that more accurate inverse solutions are possible from 3D inversions, where lateral inhomogeneity in regolith thermal properties invalidates the assumption of isotropy in 1D modelling. 3D inversion effectively involves a 3D forward model, reduced to 1D in the inverse model by methods of Principal Components Analysis (e.g. Jolliffe, 1986), where in Hopcroft et al. (2009) the so-called Proper Orthogonal Decomposition method is used (e.g. Liang et al., 2002a,b ;Hosotani and Nishi, 2010). Patankar (1980) presents the extension of the FCV forward model to 3D. 3D modelling requires more simulation time and demands advanced computing resources. However, it may lead to longer term efficiencies in accounting for surface and subsurface topography, when extrapolating local heat flows to regional and global planetary estimates.

8.4.2.4 Simplicity

The former considered, it is important to keep in mind that time and resource limitations may demand the use of the simplest approach to solving the inverse problem. The FSI approach presented in this study is not the simplest of approaches, but it can provide useful information about the inverse problem solution, even where truncation errors are non-negligible. Rapid, low resolution simulations can be performed to loosely characterise the solution

space of the inverse problem, then higher resolution simulations can be run within the identified solution space, to improve accuracy (this is demonstrated in Appendix 9.8.4). The use of the dual problem introduces a layer of abstraction to the problem, which may take some amount of study to master; therefore it is important to weigh these considerations in choosing between FSI and more standard methods.

8.5 References

CRADDOCK, R. A. 2011. Are Phobos and Deimos the result of a giant impact? *Icarus,* 211, 1150-1161.

GROTT, M. 2009. Thermal disturbances caused by lander shadowing and the measurability of the martian planetary heat flow. *Planetary and Space Science,* 57, 71-77.

HAGERMANN, A. & SPOHN, T. 1999. A method to invert MUPUS temperature recordings for the subsurface temperature field of P/Wirtanen. *Advances in Space Research,* 23, 1333-1336.

HAGERMANN, A. & TANAKA, S. 2006. Ejecta deposit thickness, heat flow, and a critical ambiguity on the Moon. *Geophysical Research Letters,* 33, L19203.

HOPCROFT, P. O., GALLAGHER, K., PAIN, C. C. & FANG, F. 2009. Three-dimensional simulation and inversion of borehole temperatures for reconstructing past climate in complex settings. *Journal of Geophysical Research (Earth Surface),* 114, 2019.

HOSOTANI, K. & NISHI, R. 2010. Principal Component Analysis of the Tidal Current Vector Data Using the POD Method - Application to a Data Set of the Tidal Current in Kagoshima Bay Based on a Numerical Simulation. *Journal of the Japan Society for Marine Surveys and Technology,* 20.

JOLLIFFE, I. T. 1986. *Principal Component Analysis.*

KEIHM, S. J. & LANGSETH, M. G. 1975. Lunar microwave brightness temperature observations reevaluated in the light of Apollo program findings. *Icarus,* 24, 211-230.

KEIHM, S. J. & LANGSETH, M. G., JR. 1973. Surface brightness temperatures at the Apollo 17 heat flow site: Thermal conductivity of the upper 15 cm of regolith. *In:* Lunar and Planetary Science Conference Proceedings, n/a 1, 1973 1973. 4, 2503.

KIEFER, W. S. 2012. Lunar heat flow experiments: Science objectives and a strategy for minimizing the effects of lander-induced perturbations. *Planetary and Space Science,* 60, 155-165.

LANGSETH, M. G., JR., CLARK, S. P., JR., CHUTE, J. L., JR., KEIHM, S. J. & WECHSLER, A. E. 1972. The Apollo 15 Lunar Heat-Flow Measurement. *Moon,* 4, 390-410.

LANGSETH, M. G., KEIHM, S. & PETERS, K. 1976. The Revised Lunar Heat Flow Values. *In:* Lunar and Planetary Institute Science Conference Abstracts, March 1, 1976 1976. 7, 474.

LIANG, Y. C., LEE, H. P., LIM, S. P., LIN, W. Z., LEE, K. H. & WU, C. G. 2002a. Proper Orthogonal Decomposition and its Applications - Part I: Theory. *Journal of Sound Vibration,* 252, 527-544.

LIANG, Y. C., LIN, W. Z., LEE, H. P., LIM, S. P., LEE, K. H. & SUN, H. 2002b. Proper Orthogonal Decomposition and its Applications - Part II: Model Reduction for Mems Dynamical Analysis. *Journal of Sound Vibration,* 256, 515-532.

MURCHIE, S., ENG, D., CHABOT, N., GUO, Y., ARVIDSON, R., YEN, A., TREBI-OLLENNU, A., SEELOS, F., ADAMS, E. & FOUNTAIN, G. 2014. MERLIN: Mars-Moon Exploration, Reconnaissance and Landed Investigation. *Acta Astronautica,* 93, 475-482.

NAGIHARA, S., STEPHENS, M. K., TAYLOR, P. T., WILLIAMS, D. R., HILLS, H. K. & NAKAMURA, Y. 2015. Restoration of the Apollo Heat Flow Experiments Metadata. *In:* Lunar and Planetary Science Conference, March 1, 2015 2015. 46, 1243.

NASA, N. S. S. D. C. 2015. *National Space Science Data Center* [Online]. Online: NASA. Available: http://nssdc.gsfc.nasa.gov/ [Accessed 09/03/2015 2015].

PATANKAR, S. V. 1980. *Numerical Heat Transfer and Fluid Flow,* New York, NY, London, Hemisphere.

PIQUEUX, S. & CHRISTENSEN, P. R. 2011. Temperature-dependent thermal inertia of homogeneous Martian regolith. *Journal of Geophysical Research (Planets),* 116, 7004.

ROSENBLATT, P. & CHARNOZ, S. 2012. On the formation of the martian moons from a circum-martian accretion disk. *Icarus,* 221, 806-815.

RUIZ, J. 2007. The heat flow during the formation of ribbon terrains on Venus. *Planetary and Space Science,* 55, 2063-2070.

SHEN, P. Y. & BECK, A. E. 1991. Least Squares Inversion of Borehole Temperature Measurements in Functional Space. *J. Geophys. Res.,* 96, 19965-19979.

SHEN, P. Y. & BECK, A. E. 1992. Paleoclimate change and heat flow density inferred from temperature data in the Superior Province of the Canadian sheild. *Palaeogeography, Palaeoclimatology, Palaeoecology,* 98, 143-165.

SIEGLER, M. A., PAIGE, D. A., KEIHM, S. J., VASAVADA, A. R., GHENT, R. R., BANDFIELD, J. L. & SNOOK, K. J. 2010. Apollo Lunar Heat Flow Experiments and the LRO Diviner Radiometer. *In:* Lunar and Planetary Institute Science Conference Abstracts, March 1, 2010 2010. 41, 2650.

TARANTOLA, A. 2005. *Inverse problem theory and methods for model parameter estimation,* Philadelphia, PA, Society for Industrial and Applied Mathematics.

WANG, K. 1992. Estimation of Ground Surface Temperatures from Borehole Temperature Data. *J. Geophys. Res.,* 97, 2095-2106.

ZACNY, K., NAGIHARA, S., HEDLUND, M., PAULSEN, G., SHASHO, J., MUMM, E., KUMAR, N., SZWARC, T., CHU, P., CRAFT, J., TAYLOR, P. & MILAM, M. 2013. Pneumatic and Percussive Penetration Approaches for Heat Flow Probe Emplacement on Robotic Lunar Missions. *Earth, Moon, and Planets,* 111, 47-77.

9 APPENDIX

9.1 Introduction

9.1.1 General Formatting Notes

- Non-bold
  - $Italics$ reference any parameters
  - $\mathrm{Non-italics}$ (except the transpose mathematical operator $[\cdots]^{\mathrm{T}}$ reference a space
- **Bold**
  - ***Italics*** references a functional array operator
  - **Normal** references a discretized (array) operator
- Superscript^{s}
  - U and S reference unsteady and steady parameters
  - P and D reference primal and dual parameters
  - Others (except mathematical operators and GRID parameters) generally reference a time or iterative sequence
  - Superscript 0 refers to initial
- Subscript$_{s}$
  - S and B reference surface and basal parameters (except with independent parameter t where B references beginning (start) and E represents the end of a period)
  - Others generally reference a depth sequence or more generally, elements of vector parameters
  - See note for $\mathbf{m}$ (except with independent GRID parameter t where m references the number of timesteps)
- $\mathbf{m} \Leftrightarrow \boldsymbol{m} \ni m \Leftrightarrow [T_S^U, T_S^S, F_B, k, \rho, c, S]$
- In browsing the alphanumeric list, note that characters in parameter A_B^C take precedence in the order A, B, C.

9.1.2 Symbols: Alphanumeric List

A, B, A_S, B_S	Fourier constants
A_B	Bond albedo
A_i	Layer interface contact area
a_n	Current grid temperature coefficient
a_n^0	Previous grid temperature coefficient
b_n, c_n	Discretized heat flow equation conductance temperature coefficients
$c \Leftrightarrow c(z) \Leftrightarrow c_n$	Specific heat capacity
$\mathbf{C_d} \ni \mathbf{C}_{d_0}, \boldsymbol{C_d}$	Data covariance
$\mathbf{C}_{d_1 d_2}$	Data cross covariance
$\mathbf{C_m} \ni \mathbf{C}_m, \boldsymbol{C_m}$	Model covariance
$\mathbf{C}_{m_1 m_2}$	Model cross covariance
$\boldsymbol{C}_{m_I}$	A posteriori model covariance
$\delta \boldsymbol{d}$	Data residual
$\delta \widehat{\boldsymbol{d}}$	Dual of data residual
$\delta \boldsymbol{m}$	Model perturbation (update)
$\delta \widehat{\boldsymbol{m}}$	Dual of model update
$\delta z_i, \delta z_{i+}$	Node distance, right node-interface distance
$\delta_{z,z';t,t'}$	Identity operator
Δt_m	Timestep
Δz_n	Control volume size (interface distance)
$\mathbf{d} \ni \mathbf{d}_i, \boldsymbol{d} \ni \boldsymbol{d}_i$	Data vector
D	Data space
$\widehat{\boldsymbol{d}}$	Dual of data vector
$\widehat{\mathrm{D}}$	Data space dual
$\boldsymbol{d}^U, \boldsymbol{d}^S$	Unsteady, steady data vectors
$\mathbf{d}_I$	Data solution vector
d_n^m, d_n	Discretized heat flow equation source term

ε	Emittance
$\epsilon_d, \epsilon_{d_0}$	Mean relative error between data solution and true values
ϵ_m	Mean relative error between model solution and true value
$\overline{\epsilon_{F_B^{SI}}}$	Relative error between optimized and true basal heat flows interpolated from 3D scatterplots
$\overline{\epsilon_{F_B^{SO}}}$	Relative error between a priori and true basal heat flows interpolated from 3D scatterplots
$\mathbf{e}$	A vector element of a linear space
E	A linear space
e_p	A parameter of a linear space
F, F_S	Temperature Fourier (surface) components
$\mathbf{F}$	Tridiagonal system of temperature coefficients
$\boldsymbol{F}$	Linear forward differential operator
$\boldsymbol{F}^U, \boldsymbol{F}^S$	Unsteady, steady linear forward differential operators
$\boldsymbol{F}^*$	Non-linear forward differential operator
$F_B \Leftrightarrow F_B(t)$	Basal heat flow
F_B^S	Steady basal heat flow
$F_B^{SO}, F_B^{SI}, F_B^{ST}$	A priori, a posteriori, true steady basal heat flow
$F_B^U \Leftrightarrow F_B^U(t)$	Unsteady basal heat flow
f_i	Internode interface location
f_τ, f_z	Model parameter covariance function
$\boldsymbol{\gamma}_i, \boldsymbol{\gamma}, \boldsymbol{\gamma}_i$	Steepest ascent vector
$\hat{\boldsymbol{\gamma}}, \hat{\boldsymbol{\gamma}}_i$	Misfit function Fréchet derivative
$\hat{\boldsymbol{\gamma}}^d = [\hat{\boldsymbol{\gamma}}^{Ts}, \hat{\boldsymbol{\gamma}}^{F_B}, \hat{\boldsymbol{\gamma}}^k, \hat{\boldsymbol{\gamma}}^{pc}, \hat{\boldsymbol{\gamma}}^S], \hat{\boldsymbol{\gamma}}_i^d, \hat{\boldsymbol{\gamma}}^m, \hat{\boldsymbol{\gamma}}_i^m$	Misfit function Fréchet derivative data, model components
$\mathbf{g}, \boldsymbol{g}$	General inverse operator
G	General Green's function

$\mathbf{G}$	Linear inverse operator
$\boldsymbol{G}$	General Green's operator and data Fréchet derivative operator
$\boldsymbol{g}^U, \boldsymbol{g}^S$	Unsteady, steady inverse operator
$\boldsymbol{G}^U, \boldsymbol{G}^S$	Unsteady, steady Green's operators
$\mathbf{G}_i$	Data Fréchet derivative
$\boldsymbol{G}_I$	Data Fréchet derivative operator at maximum likelihood (solution) point
$\boldsymbol{G}_m$	Model resolution operator
$\widehat{\boldsymbol{G}}_{S*}, \widehat{\boldsymbol{G}}_{S*}^U, \widehat{\boldsymbol{G}}_{S*}^S$	General, steady, unsteady dual Green's operators
$\boldsymbol{G}_{S*}, \boldsymbol{G}_S, \boldsymbol{G}_B, \boldsymbol{G}^0$	Green's operators respectively associated with sources , surface boundary, basal boundary, initial temperature
$\boldsymbol{G}_S^U, \boldsymbol{G}_{S*}^S, \boldsymbol{G}_S^S, \boldsymbol{G}_B^S$	Unsteady surface and steady: source, surface, basal Green's operators
G_S^U, G^S, G_S^S, G_B^S	Unsteady surface and steady: source, surface, basal Green's functions
η_s, η_m	Sensor and modelling (or discretization) data noise
h, h_i	Hertz factor
H, H_i	Heat transfer coefficient (conductance)
$\widehat{\boldsymbol{H}}, \widehat{\boldsymbol{H}}_i$	Misfit function Hessian derivative
$\widehat{\boldsymbol{H}}^d = [\widehat{\boldsymbol{H}}^{Ts}, \widehat{\boldsymbol{H}}^{FB}, \widehat{\boldsymbol{H}}^k, \widehat{\boldsymbol{H}}^{pc}, \widehat{\boldsymbol{H}}^S], \widehat{\boldsymbol{H}}_i^d, \widehat{\boldsymbol{H}}^m, \widehat{\boldsymbol{H}}_i^m$	Misfit function Hessian derivative data, model components
i	Control volume interface; Iteration number
I	Thermal inertia
$\kappa \Leftrightarrow \kappa(z)$	Thermal diffusivity
$k \Leftrightarrow k(z)$	Conductivity
k^0, k^I, k^T	A priori, a posteriori, true conductivity

k_{BULK}	Bulk conductivity
k_i	Control volume interface conductivity
k_n	Layer (or discretized/nodal/grid) conductivity
l	Regolith particle size
$L_n \ni L_2 \equiv \|\mathbf{e}\|_n$	A norm of order n (not related to layer number)
μ	Fourier frequency multiple
μ, μ_i, μ_i	Stepping constant
m	Timestep/recording number
$\mathbf{m} \ni \mathbf{m}_i, \boldsymbol{m} \ni \boldsymbol{m}_i, \boldsymbol{m}_u$	Model vector
$\widehat{\boldsymbol{m}}$	Dual of model vector
M	Total number of timesteps
M	Model Space
$\widehat{\mathrm{M}}$	Model space dual
$\mathbf{m}_B$	Boundary parameter model vector
$\mathbf{m}_I$	Model solution vector
$\mathbf{M}_i, \boldsymbol{M}, \boldsymbol{M}_i$	Model distance quantifying metric
$\mathbf{M}_i^P$	Preconditioned model distance quantifying metric
$\mathbf{m}_P$	Property parameter model vector
n	Layer (or node/grid) number
N	Total number of layers (or nodes or gridpoints)
ω, ω_μ	Fourier frequency
ω_f	Temperature oscillation frequency
φ	Surface temperature phase
φ_E	Planetographic location (east longitude)
φ_i	Solar incidence angle
$\phi(\mathbf{d})$	Data probability density function
$\phi(\mathbf{d}, \mathbf{m})$	Joint probability density function
$\phi(\mathbf{m})$	Model probability density function

Φ_0	Probability density function constant
P	Period
$\mathbf{P}_i$	Preconditioner
P_S^S	Mean atmospheric pressure
$\rho \Leftrightarrow \rho(z) \Leftrightarrow \rho_n$	Density
$\rho c \Leftrightarrow \rho c(z)$	Thermal capacity
$\rho c^0, \rho c^I, \rho c^T$	A priori, a posteriori, true thermal capacity
$\rho_n c_n \Leftrightarrow \rho c_n$	Layer (or discretized/nodal/grid) thermal capacity
r	Exponential rate
R	Heliocentric distance
$\boldsymbol{R}_d$	Model sensitivity operator
r_d^m	Model:data standard deviation stability ratio
$r_{F_B^S}$	Ratio of optimized heat flow error to initial heat flow error
$r_{m_2}^{m_1}$	Model parameter standard deviation stability ratio
r_{S_m}	Ratio of the misfit function at the maximum likelihood point to the misfit function at initialization
r_t	Ratio of monitoring period to period of temperature variation
r_z	Ratio of maximum sensor penetration depth to skin depth
r_{zi}	Ratio of depths of surface to basal sensors used in estimating heat flow
σ	Stephan-Boltzmann constant
σ_d	Data standard deviation
σ_d^2	Data variance
σ_η	Standard deviation of data noise

σ_m	Model parameter standard deviation
σ_m^2	Model parameter variance
$\sigma_p{}^n$	Estimator of dispersion
$S \Leftrightarrow S(z,t)$	Source term
S	Source space
$\hat{\mathrm{S}}$	Dual of source space
$\mathbf{S}$	Array of source terms
$\boldsymbol{S}$	Primal source field
$\hat{\boldsymbol{S}}$	Dual source field
S^0, S^I, S^T	A priori, a posteriori, true source term
S^D	Dual source
S^o	Solar constant
S^P	Primal source
S^{DU}, S^{DS}	Unsteady, steady dual sources
$S^S \Leftrightarrow S^S(z)$	Steady sources
$S^U \Leftrightarrow S^U(z,t)$	Unsteady sources
$\boldsymbol{S}^U, \boldsymbol{S}^S$	Unsteady, steady primal source fields
$\hat{\boldsymbol{S}}^U, \hat{\boldsymbol{S}}^S$	Unsteady, steady dual source fields
$S_{\mathrm{m}}, S_m, S_{m_i}$	Misfit (objective, cost) function
S_{m_I}	Misfit function at maximum likelihood point
$\hat{S}_{\hat{m}}$	A dual misfit function
S_n^C	Layer (or discretized/nodal/grid) constant linearized source term component
S_n^T	Layer (or discretized/nodal/grid) temperature dependent linearized source term component
$S_{\|d\|}, S_{\|\mathrm{d}\|}$	Data residual norm
$S_{\|m\|}, S_{\|\mathrm{m}\|}$	Model misfit norm
τ	Time lag
τ_c	Correlation time

t, t_m	Time
t_{SIM}	Simulation time
$T \Leftrightarrow T(z,t)$	Temperature
T	Temperature space
$\widehat{\mathrm{T}}$	Dual of temperature space
$\mathbf{T}$	Array of temperatures
$T^0 \Leftrightarrow T^0(z)$	Initial temperature
$T^S \Leftrightarrow T^S(z)$	Steady temperature
$T^U \Leftrightarrow T^U(z,t)$	Unsteady temperature
t'	Time
T'	Arbitrary temperature
t_B, t_0	Begin
t_E, t_{M-1}	End
T_n	Layer (or discretized/nodal/grid) temperature
T_n^0	Initial (or previous) layer (or discretized/nodal/grid) temperature
T_n^m	Layer (or discretized/nodal/grid) time series of temperatures
$T_S \Leftrightarrow T_S(t)$	Surface temperature
T_S^S	Surface steady temperature
$T_S^U \Leftrightarrow T_S^U(t)$	Surface unsteady temperature
T_S^{UA}	Surface unsteady temperature amplitude
$\boldsymbol{T}$	Primal temperature field
$\widehat{\boldsymbol{T}}$	Dual temperature field
T^D	Dual temperature
T^{DU}, T^{DS}	Unsteady, steady dual temperatures
$\boldsymbol{T}^I$	A posteriori temperature field
T^P	Primal temperature
$\boldsymbol{T}^U, \boldsymbol{T}^S$	Unsteady, steady primal temperature fields

$\widehat{\boldsymbol{T}}^{U}, \widehat{\boldsymbol{T}}^{S}$	Unsteady, steady dual temperature fields
$T_S^{S0}, T_S^{SI}, T_S^{ST}$	A priori, a posteriori, true surface steady temperature
$T_S^{U0}, T_S^{UI}, T_S^{UT}$	A priori, a posteriori, true surface unsteady temperature
z, z_n	Depth
Z	Total depth
z'	Depth
z_{ACC}	Accurate sensor depth
z_B, z_N	Base
z_{ERR}	Inaccurate sensor depth
z_S, z_1	Surface
z_{SKIN}	Skin depth
∇	Divergence operator
[D, M]	Joint data and model space
$\langle e \rangle$	A linear space parameter mean
$\lvert\epsilon_d\rvert, \lvert\epsilon_{d_0}\rvert$	Absolute relative error between data solution and true values
$\lvert\epsilon_m\rvert$	Absolute relative error between model solution and true value

9.1.3 Symbols: Topical List

9.1.3.1 Forward Problem

GRID	
z, z_n	Depth
z_S, z_1	Surface
z_B, z_N	Base
Z	Total depth

Δz_n	Control volume size (interface distance)
δz_i, δz_{i+}	Node distance, right node-interface distance
f_i	Internode interface location
A_i	Layer interface contact area
n	Layer (or node/grid) number
N	Total number of layers (or nodes or gridpoints)
i	Control volume interface
t, t_m	Time
t_B, t_0	Begin
t_E, t_{M-1}	End
t_{SIM}	Simulation time
P	Period
Δt_m	Timestep
m	Timestep number
M	Total number of timesteps
BOUNDARY	
A	Bond albedo
ε	Emittance
φ_i	Solar incidence angle
R	Heliocentric distance
σ	Stephan-Boltzmann constant
S^o	Solar constant
$T \Leftrightarrow T(z,t)$	Temperature
T_n^m	Layer (or discretized/nodal/grid) time series of temperatures
T_n^0	Initial (or previous) layer (or discretized/nodal/grid) temperature
T_n	Layer (or discretized/nodal/grid) temperature
$T_S \Leftrightarrow T_S(t)$	Surface temperature

$T^0 \Leftrightarrow T^0(z)$	Initial temperature
$T^U \Leftrightarrow T^U(z,t)$	Unsteady temperature
$T_S^U \Leftrightarrow T_S^U(t)$	Surface unsteady temperature
T_S^{UA}	Surface unsteady temperature amplitude
ω_f	Temperature oscillation frequency
φ	Surface temperature phase
F, F_S	Temperature Fourier (surface) components
ω, ω_μ	Fourier frequency
μ	Fourier frequency multiple
A, B, A_S, B_S	Fourier constants
$T^S \Leftrightarrow T^S(z)$	Steady temperature
T_S^S	Surface steady temperature
$F_B \Leftrightarrow F_B(t)$	Basal heat flow
$F_B^U \Leftrightarrow F_B^U(t)$	Unsteady basal heat flow
F_B^S	Steady basal heat flow
PROPERTIES	
I	Thermal inertia
l	Regolith particle size
$\kappa \Leftrightarrow \kappa(z)$	Thermal diffusivity
$k \Leftrightarrow k(z)$	Conductivity
k_n	Layer (or discretized/nodal/grid) conductivity
k_i	Control volume interface conductivity
k_{BULK}	Bulk conductivity
H, H_i	Heat transfer coefficient (conductance)
h, h_i	Hertz factor
$\rho c \Leftrightarrow \rho c(z)$	Thermal capacity
$\rho_n c_n \Leftrightarrow \rho c_n$	Layer (or discretized/nodal/grid) thermal capacity
$\rho \Leftrightarrow \rho(z) \Leftrightarrow \rho_n$	Density

$c \Leftrightarrow c(z) \Leftrightarrow c_n$	Specific heat capacity
$S \Leftrightarrow S(z,t)$	Source term
$S^U \Leftrightarrow S^U(z,t)$	Unsteady sources
$S^S \Leftrightarrow S^S(z)$	Steady sources
S_n^C	Layer (or discretized/nodal/grid) constant linearized source term component
S_n^T	Layer (or discretized/nodal/grid) temperature dependent linearized source term component
z_{SKIN}	Skin depth
TDMA	
b_n, c_n	Discretized heat flow equation conductance temperature coefficients
d_n^m, d_n	Discretized heat flow equation source term
a_n	Current grid temperature coefficient
a_n^0	Previous grid temperature coefficient
$\mathbf{F}$	Tridiagonal system of temperature coefficients
$\mathbf{T}$	Array of temperatures
$\mathbf{S}$	Array of source terms

9.1.3.2 *Inverse Problem*

GENERAL	
τ	Time lag
r	Exponential rate
t'	Time
z'	Depth
T'	Arbitrary temperature
$S_{\mathbf{m}}, S_m, S_{m_i}$	Misfit (objective, cost) function
$S_{\mathbf{m}_I}$	Misfit function at maximum likelihood point
$S_{\|d\|}$, $S_{\|\mathbf{d}\|}, S_{\|m\|}, S_{\|\mathbf{m}\|}$	Data and model norms

$\hat{S}_{\hat{m}}$	A dual misfit function
$\phi(\mathbf{d}, \mathbf{m})$	Joint probability density function
ϕ_0	Probability density function constant
$L_n \ni L_2 \equiv \|\mathbf{e}\|_n$	A norm of order n (not related to layer number)
$\mathbf{e}$	A vector element of a linear space
e_p	A parameter of a linear space
$\langle e \rangle$	A linear space parameter mean
$\sigma_p{}^n$	Estimator of dispersion
SPACES	
E	A linear space
[D, M]	Joint data and model space
D	Data space
$\hat{\mathrm{D}}$	Data space dual
M	Model Space
$\hat{\mathrm{M}}$	Model space dual
T	Temperature space
$\hat{\mathrm{T}}$	Dual of temperature space
S	Source space
$\hat{\mathrm{S}}$	Dual of source space
OPERATORS	
$\mathbf{g}, \boldsymbol{g}$	General inverse operator
$\boldsymbol{g}^U, \boldsymbol{g}^S$	Unsteady, steady inverse operator
$\mathbf{G}$	Linear inverse operator
$\boldsymbol{G}$	General Green's operator and data Fréchet derivative operator
$\boldsymbol{G}_I$	Data Fréchet derivative operator at maximum likelihood (solution) point

G_{S*}, G_S, G_B, G^0	Green's operators respectively associated with sources , surface boundary, basal boundary, initial temperature
$G^U,\ G^S$	Unsteady, steady Green's operators
$G_S^U, G_{S*}^S, G_S^S, G_B^S$	Unsteady surface and steady: source, surface, basal Green's operators
$\widehat{G}_{S*}, \widehat{G}_{S*}^U, \widehat{G}_{S*}^S$	General, steady, unsteady dual Green's operators
$\delta_{z,z';t,t'}$	Identity operator
$\mathbf{C_d} \ni \mathbf{C}_{d_0}, \boldsymbol{C_d}$	Data covariance
$\mathbf{C_m} \ni \mathbf{C}_m, \boldsymbol{C_m}$	Model covariance
$\boldsymbol{C}_{m_I}$	A posteriori model covariance
$\boldsymbol{G_m}$	Model resolution operator
$\boldsymbol{R_d}$	Model sensitivity operator
$\mathbf{C}_{d_1 d_2}$	Data cross covariance
$\mathbf{C}_{m_1 m_2}$	Model cross covariance
$\mathbf{M}_i, \boldsymbol{M}, \boldsymbol{M}_i$	Model distance quantifying metric
$\mathbf{M}_i^P$	Preconditioned model distance quantifying metric
$\mathbf{P}_i$	Preconditioner
$\mathbf{G}_i$	Data Fréchet derivative
$\boldsymbol{F}$	Linear forward differential operator
$\boldsymbol{F}^U, \boldsymbol{F}^S$	Unsteady, steady linear forward differential operators
$\boldsymbol{F}^*$	Non-linear forward differential operator
$\boldsymbol{\nabla}$	Divergence operator
$\widehat{\boldsymbol{\gamma}}, \widehat{\boldsymbol{\gamma}}_i$	Misfit function Fréchet derivative
$\widehat{\boldsymbol{\gamma}}^d = [\widehat{\boldsymbol{\gamma}}^{Ts}, \widehat{\boldsymbol{\gamma}}^{F_B}, \widehat{\boldsymbol{\gamma}}^k, \widehat{\boldsymbol{\gamma}}^{pc}, \widehat{\boldsymbol{\gamma}}^S], \widehat{\boldsymbol{\gamma}}_i^d, \widehat{\boldsymbol{\gamma}}^m, \widehat{\boldsymbol{\gamma}}_i^m$	Misfit function Fréchet derivative data, model components

$\widehat{\boldsymbol{H}}, \widehat{\boldsymbol{H}}_i$	Misfit function Hessian derivative
$\widehat{\boldsymbol{H}}^d = \left[\widehat{\boldsymbol{H}}^{Ts}, \widehat{\boldsymbol{H}}^{F_B}, \widehat{\boldsymbol{H}}^k, \widehat{\boldsymbol{H}}^{pc}, \widehat{\boldsymbol{H}}^S\right], \widehat{\boldsymbol{H}}_i^d, \widehat{\boldsymbol{H}}^m, \widehat{\boldsymbol{H}}_i^m$	Misfit function Hessian derivative data, model components
DATA	
$\mathbf{d} \ni \mathbf{d}_i, \boldsymbol{d} \ni \boldsymbol{d}_i$	Data vector
$\boldsymbol{d}^U, \boldsymbol{d}^S$	Unsteady, steady data vectors
m	Number of recordings
$\delta \boldsymbol{d}$	Data residual
$\widehat{\boldsymbol{d}}$	Dual of data vector
$\delta \widehat{\boldsymbol{d}}$	Dual of data residual
$\mathbf{d}_I$	Data solution vector
$\phi(\mathbf{d})$	Data probability density function
σ_d^2	Data variance
σ_d	Data standard deviation
$\epsilon_d, \epsilon_{d_0}$	Mean relative error between data solution and true values
$\lvert\epsilon_d\rvert, \lvert\epsilon_{d_0}\rvert$	Absolute relative error between data solution and true values
$\overline{\epsilon_{F_B^{SI}}}$	Relative error between optimized and true basal heat flows interpolated from 3D scatterplots
$\overline{\epsilon_{F_B^{So}}}$	Relative error between a priori and true basal heat flows interpolated from 3D scatterplots
σ_η	Standard deviation of data noise
η_s, η_m	Sensor and modelling (or discretization) data noise
$S_{\lVert d \rVert}, S_{\lVert \mathbf{d} \rVert}$	Data residual norm
z_{ACC}	Accurate sensor depth
z_{ERR}	Inaccurate sensor depth
MODEL	
$\mathbf{m} \ni \mathbf{m}_i, \boldsymbol{m} \ni \boldsymbol{m}_i, \boldsymbol{m}_u$	Model vector

$\delta \boldsymbol{m}$	Model perturbation (update)
$\widehat{\boldsymbol{m}}$	Dual of model vector
$\delta \widehat{\boldsymbol{m}}$	Dual of model update
$\mathbf{m}_B$	Boundary parameter model vector
$\mathbf{m}_P$	Property parameter model vector
$\mathbf{m}_I$	Model solution vector
f_τ, f_z	Model parameter covariance function
τ_c	Correlation time
$\phi(\mathbf{m})$	Model probability density function
σ_m^2	Model parameter variance
σ_m	Model parameter standard deviation
ϵ_m	Mean relative error between model solution and true value
$\lvert\epsilon_m\rvert$	Absolute relative error between model solution and true value
$S_{\lVert m \rVert}, S_{\lVert \mathbf{m} \rVert}$	Model misfit norm
PRIMAL PROBLEM (also see Forward Problem)	
$\boldsymbol{T}$	Primal temperature field
T^P	Primal temperature
$\boldsymbol{T}^U, \boldsymbol{T}^S$	Unsteady, steady primal temperature fields
$\boldsymbol{S}$	Primal source field
S^P	Primal source
$\boldsymbol{S}^U, \boldsymbol{S}^S$	Unsteady, steady primal source fields
G	General Green's function
G_S, G^0, G_B	Surface, initial, basal Green's functions
G_S^U, G^S, G_S^S, G_B^S	Unsteady surface and steady: source, surface, basal Green's functions
DUAL PROBLEM	
$\widehat{\boldsymbol{T}}$	Dual temperature field

T^D	Dual temperature
$\hat{\boldsymbol{T}}^U, \hat{\boldsymbol{T}}^S$	Unsteady, steady dual temperature fields
T^{DU}, T^{DS}	Unsteady, steady dual temperatures
$\hat{\boldsymbol{S}}$	Dual source field
S^D	Dual source
$\hat{\boldsymbol{S}}^U, \hat{\boldsymbol{S}}^S$	Unsteady, steady dual source fields
S^{DU}, S^{DS}	Unsteady, steady dual sources
OPTIMIZATION	
i	Iteration number
μ, μ_i, μ_i	Stepping constant
$\boldsymbol{\gamma}_i, \boldsymbol{\gamma}, \boldsymbol{\gamma}_i$	Steepest ascent vector
$\mathbf{M}_i$	Model distance quantifying metric
$\boldsymbol{T}^I$	A posteriori temperature field
$F_B^{S0}, F_B^{SI}, F_B^{ST}$	A priori, a posteriori, true steady basal heat flow
$T_S^{S0}, T_S^{SI}, T_S^{ST}$	A priori, a posteriori, true surface steady temperature
$T_S^{U0}, T_S^{UI}, T_S^{UT}$	A priori, a posteriori, true surface unsteady temperature
k^0, k^I, k^T	A priori, a posteriori, true conductivity
$\rho c^0, \rho c^I, \rho c^T$	A priori, a posteriori, true thermal capacity
S^0, S^I, S^T	A priori, a posteriori, true source term
$S_{\mathbf{m}}, S_m, S_{m_i}$	Misfit (objective, cost) function
$S_{\mathbf{m}_I}$	Misfit function at maximum likelihood point
$S_{\|\boldsymbol{d}\|}, S_{\|\mathbf{d}\|}, S_{\|m\|}, S_{\|\mathbf{m}\|}$	Data and model norms
$r_{m_2}^{m_1}$	Model parameter standard deviation stability ratio
r_d^m	Model:data standard deviation stability ratio

r_{S_m}	Ratio of the misfit function at the maximum likelihood point to the misfit function at initialization
$r_{F_B^S}$	Ratio of optimized heat flow error to initial heat flow error
r_t	Ratio of monitoring period to period of temperature variation
r_z	Ratio of maximum sensor penetration depth to skin depth
r_{zi}	Ratio of depths of surface to basal sensors used in estimating heat flow

9.2 Theory

9.2.1 Forward Problem

9.2.1.1 *Unsteady Analytical Solution (Fourier Transform)*

For a homogeneous isotropic medium with thermal properties constant in each layer over M time intervals (see Appendix 9.1 for symbol definitions).

$$\frac{\partial T^U}{\partial t} = \kappa \frac{\partial^2 T^U}{\partial z^2}, \; z \in [z_S, z_B), t \in (t_0, t_{M-1}], \tag{9.2.1}$$

where $S^U = 0$. The surface and lower boundary are characterized by a surface temperature, T_S^U, with heat propagating into the regolith and vanishing at depth:

$$T^U = T_S^U, \quad z = z_S, t \in (t_0, t_{M-1}]; \tag{9.2.2}$$

$$T^U = 0, \quad z \to \infty, t \in (t_0, t_{M-1}]. \tag{9.2.3}$$

The initial temperature is constant and zero,

$$T^U = 0, \quad z \in [z_S, z_B), t = t_0. \tag{9.2.4}$$

Applying the discrete Fourier transform (DFT) due to the arbitrary nature of T_S^U (e.g. Arfken and Weber, 2005), temperature $T^U(z,t)$, becomes $F(z,\omega)$

$$F(z,\omega) \Leftrightarrow F = \frac{1}{M}\sum_{m=0}^{M-1} \frac{\partial^2 T^U}{\partial z^2} - \frac{1}{\kappa}\frac{\partial T^U}{\partial t} e^{-i\omega t_m}, \tag{9.2.5}$$
$$z \in [z_S, z_B), m \in [0, M-1], t \in (t_0, t_{M-1}].$$

The Fourier frequency ω with M components is defined by

$$\omega = \frac{2\pi\mu}{P}, \quad \mu \in [0, M-1], \tag{9.2.6}$$

where P is the period. The Fourier components are characterised by a fundamental frequency ω_f at $\mu = 1$, all other components being integer multiples of ω_f.

This transform leads to a differential equation in the variable z (Carslaw and Jaeger, 1973; Lindqvist, 1984)

$$\frac{\partial^2 F}{\partial z^2} = \frac{i\omega}{\kappa} F, \qquad z \in [z_S, z_B), \tag{9.2.7}$$

with converted boundary conditions

$$F = F_S = \frac{1}{M} \sum_{m=0}^{M-1} T_S^U e^{-i\omega t_m}, \qquad m \in [0, M-1], t \in (t_0, t_{M-1}]; \tag{9.2.8}$$

$$F = CONSTANT, \qquad z \in (z_S, z_B); \tag{9.2.9}$$

$$F = 0, \qquad z \to \infty. \tag{9.2.10}$$

This yields a Fourier domain solution which can be expressed as

$$F = A(\omega) e^{z\sqrt{i\omega/\kappa}} + B(\omega) e^{-z\sqrt{i\omega/\kappa}}, \qquad z \in [z_S, z_B). \tag{9.2.11}$$

The term $F_S(\omega) = A_S + B_S$ at $z = 0$ corresponds to an input function. Upon converting F back to the time domain via the inverse DFT

$$T^U = \frac{1}{M} \sum_{\mu=0}^{M-1} \left(A(\omega_\mu) e^{z\sqrt{i\omega_\mu/\kappa}} + B(\omega_\mu) e^{-z\sqrt{i\omega_\mu/\kappa}} \right) e^{i\omega_\mu t}, \tag{9.2.12}$$

$$z \in [z_S, z_B), \mu \in [0, M-1], t \in (t_0, t_{M-1}],$$

the solution is (Carslaw and Jaeger, 1973)

$$T^U = T_S^0 e^{-z\sqrt{\omega_f/2\kappa}} \cos\left(\omega_f t - \varphi - z\sqrt{\omega_f/2\kappa}\right), \quad z \in [z_S, z_B), t \in (t_0, t_{M-1}] \tag{9.2.13}$$

where T_S^0 is the amplitude of the surface temperature corresponding to $|F_S|$, ω_f is the frequency of temperature oscillations and φ indicates the phase of the surface boundary temperature, the leftmost term being the phase shift with depth.

9.2.1.2 Steady Analytical Solution

The steady state analytical solution for a homogeneous, isotropic semi-infinite solid can be found from (see Appendix 9.1 for symbol definitions)

$$-k\frac{d^2T^S}{dz^2} = S^S, \qquad z \in [z_S, z_B), \tag{9.2.14}$$

with boundaries

$$T^S = T_S^S, \qquad z = z_S, \tag{9.2.15}$$

$$-k\frac{dT^S}{dz} = F_B^S, \qquad z = z_B. \tag{9.2.16}$$

Dividing both sides of Equation 9.2.14 by k, integrating and applying the boundary conditions gives

$$T^S = T_S^S - \frac{F_B^S}{k}z + \frac{S^S}{2k}z^2, \qquad z \in [z_S, z_B). \tag{9.2.17}$$

9.2.1.3 1D Finite Control Volume Discretization

The 1D FCV discretization described here is adapted from Patankar (1980). Here the general HFE is discretized where the steady and unsteady variants emerge as special cases. The HFE is first integrated across the 1D control volume $\Delta z_n \times 1 \times 1$, anchored by central node n of N nodes in Figure 9.2.1, and over timestep Δt_m of M timesteps such that

$$\rho c \int_i^{i+1} dz \int_t^{t+\Delta t_m} dt \frac{\partial T}{\partial t} = \int_t^{t+\Delta t_m} dt \int_i^{i+1} dz \frac{\partial}{\partial z}\left(k\frac{\partial T}{\partial z}\right) + S. \tag{9.2.18}$$

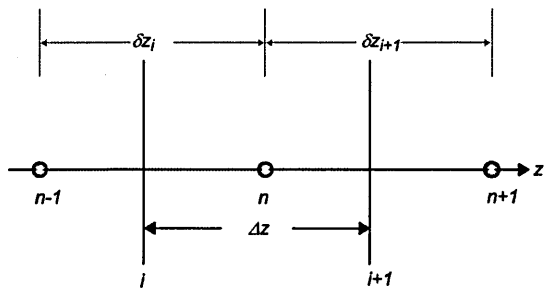

Figure 9.2.1. Discretization of the domain into 1D control volumes $\Delta z \times 1 \times 1$ with interfaces i. The full control volume illustrated is anchored by central node n. After Patankar (1980).

Integrating along the spatial dimension (z) different profile assumptions can be made to make calculations easier (Patankar, 1980). Here a linear variation is assumed for the variation of temperature between each node n, resulting in a piecewise-linear profile across the N control volumes as shown in Figure 9.2.2.

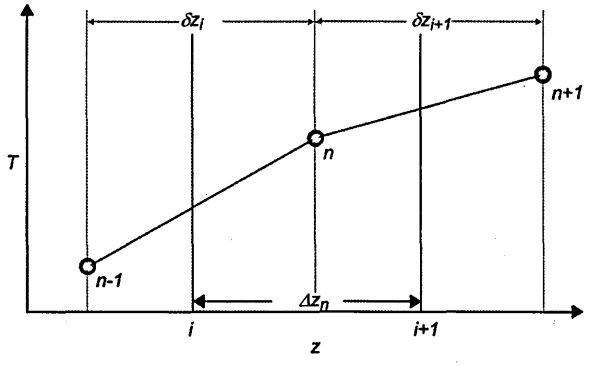

Figure 9.2.2. Linear variation of temperature between nodes. After Patankar (1980).

Therefore, integrating Equation 9.2.18 across control volume n from interface i to interface $i+1$ using Figure 9.2.2:

a. LHS

$$\rho c \int_i^{i+1} dz \int_t^{t+\Delta t_m} dt \frac{\partial T}{\partial t} = \rho c \Delta z_n \int_t^{t+\Delta t_m} dt \frac{\partial T}{\partial t};$$

b. RHS

$$\int_t^{t+\Delta t_m} dt \int_i^{i+1} dz \frac{\partial}{\partial z}\left(k\frac{\partial T}{\partial z}\right) + S = \int_t^{t+\Delta t_m} dt \left[\left(k\frac{\partial T}{\partial z}\right)_{i+1} - \left(k\frac{\partial T}{\partial z}\right)_i + \int_i^{i+1} dz\, S\right], \quad 9.2.19$$

$$\overset{\Delta_{dis}}{\Longrightarrow} \int_t^{t+\Delta t_m} dt \left[k_{i+1}\frac{(T_{n+1}-T_n)}{\delta z_{i+1}} - k_i \frac{(T_n - T_{n-1})}{\delta z_i} + S_n \Delta z_n\right].$$

The interface conductivities k_i are derived from the assumed variation between nodal conductivities k_n defined earlier. The most useful representation, as suggested in Patankar (1980) is the previously stated interpolation

a. $$k_i = \left(\frac{1-f_i}{k_{n-1}} + \frac{f_i}{k_n}\right)^{-1},$$ 9.2.20

b. $$f_i = \frac{\delta z_{i+}}{\delta z_i}.$$

This is derived from the consideration of the heat flowing across the interface i. The interpolation factor ($f_i \in [0,1]$) is defined by the location of the interfaces between the nodes – i.e. the nodal spacing δz_i, as illustrated in Figure 9.2.3 below. This representation of the interface conductivity in Equation 9.2.21 leads to the harmonic mean when the interface is located exactly halfway between the nodes ($f_i = 0.5$). This representation of interface conductivity will give more desirable results than, say, a linear representation, particularly in composite media where there may be abrupt changes in conductivity at the interface.

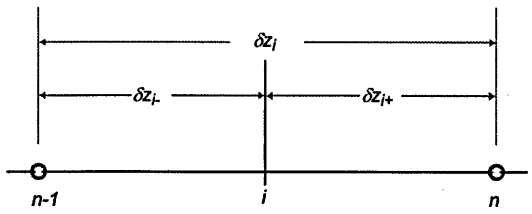

Figure 9.2.3. Locating the interfaces.

The integral source term of Equation 9.2.19b ($\int_i^{i+1} dz\, S$) is cast in discretized form as $S_n \Delta z_n$. Here S_n represents the average source contribution to the heat flowing out of control volume n. Various representations of S_n, which is often temperature dependent, are possible – a general representation of a linearized S_n is as noted earlier is

$$S_n = S_n^C + S_n^T T_n \qquad 9.2.21$$

where S_n^C represents a constant component of the source term while S_n^T is a temperature dependent component. For numerical stability in the forward problem, any heat sinks

(negative components of S_n) are absorbed into S_n^T while respective positive components are absorbed into S_n^C.

Many assumptions are also possible for the variation from time t to $t+\Delta t$ of the nodal temperatures (T_{n-1}, T_n, T_{n+1}). Many of these can be generalized to the interpolation formula (Patankar, 1980)

$$\int_t^{t+\Delta t_m} dt T_n = [f_t T_n + (1-f_t)T_n^0]\Delta t_m, \qquad 9.2.22$$

where $0 \leq f_t \leq 1$ is a weighting factor. Factor f_t determines whether the time discretization results in an implicit ($f_t = 1$), Crank-Nicholson ($f_t = 0.5$), explicit ($f_t = 0$) or other ($0 < f_t < 1$; $f_t \neq 0.5$) scheme for solving the discretization equations (Figure 9.2.4). The implicit scheme, which assumes that the final temperature T_n prevails across the whole timestep, is the most numerically stable of these and is used to evaluate the integral.

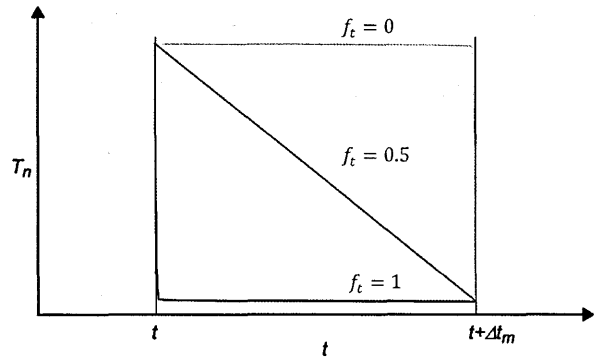

Figure 9.2.4. Variation of temperature over timestep Δt_m. After Patankar (1980).

Therefore using the implicit scheme, integrating the temperature (T) of Equation 9.2.18 in control volume n of Figure 9.2.4 along one timestep Δt_m:

a. RHS

$$\rho c \Delta z_n \int_t^{t+\Delta t_m} dt \frac{\partial T}{\partial t} = \rho c \Delta z_n (T_n - T_n^0);$$

$$\overset{\Delta}{\Rightarrow} \int_t^{t+\Delta t_m} dt \left[k_{i+1} \frac{(T_{n+1} - T_n)}{\delta z_{i+1}} - k_i \frac{(T_n - T_{n-1})}{\delta z_i} + S_n \Delta z_n \right] \quad 9.2.23$$

b. LHS

$$= \left[1 \cdot \left(k_{i+1} \frac{(T_{n+1} - T_n)}{\delta z_{i+1}} - k_i \frac{(T_n - T_{n-1})}{\delta z_i} \right) + S_n \Delta z_n \right] \Delta t_m.$$

With the interfaces and source terms dealt with Equation 9.2.23 can be restated as

a. $$a_n T_n - b_n T_{n+1} - c_n T_{n-1} = d_n,$$

b. $$b_n = \frac{k_{i+1}}{\delta z_{i+1}},$$

c. $$c_n = \frac{k_i}{\delta z_i},$$

d. $$a_n^0 = \rho_n c_n \frac{\Delta z_n}{\Delta t_m},$$

e. $$d_n = S_n^C \Delta z_n + a_n^0 T_n^0,$$

f. $$a_n = b_n + c_n + a_n^0 - S_n^T \Delta z_n,$$

$$n \in [1, N], \quad i \in [1, N-1], \quad z \in [z_1, z_N), \quad m \in [0, M-1], \quad t \in (t_0, t_{M-1}]. \quad 9.2.24$$

Finally the boundary conditions must be incorporated. These can take the form of temperature, temperature gradient, heat flow, heat source, or heat transfer coefficient. In cases where the boundary temperature is not provided, the same procedure as in Equations 9.2.19 and 9.2.23 is carried out, except – due to the special nature of the boundary points – the integration takes place across a half-control volume (Figure 9.2.3).

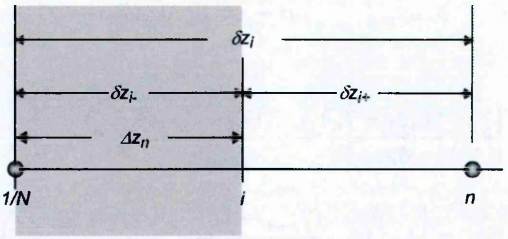

Figure 9.2.5. Half-control volume of the boundary point (shaded area).

Therefore

a. RHS
$$\rho c \Delta z_n \int_t^{t+\Delta t_m} dt \frac{\partial T}{\partial t} = \rho c \Delta z_n (T_n - T_n^0),$$

9.2.25

b. LHS
$$\overset{\Delta}{\Rightarrow} \int_t^{t+\Delta t_m} dt \left[k_i \frac{(T_{n+1} - T_n)}{\delta z_i} + F_n + S_n \Delta z_n \right] = \left[k_i \frac{(T_{n+1} - T_n)}{\delta z_i} + F_n + S_n \Delta z_n \right] \Delta t_m,$$

where F_n is the boundary heat flowing from node n towards node $n+1$. This leads to

a.
$$a_n T_n = b_n T_{n+1} + d_n,$$

b.
$$b_n = \frac{k_{i+1}}{\delta z_{i+1}},$$

c.
$$a_n^0 = \rho_n c_n \frac{\Delta z_n}{\Delta t_m},$$

9.2.26

d.
$$d_n = S_n^C \Delta z_n + a_n^0 T_n^0 + F_n,$$

e.
$$a_n = b_n + a_n^0 - S_n^T \Delta z_n.$$

The boundary coefficients c_1 and b_N are respectively zero. In matrix form:

$$\begin{bmatrix} a_1 & -b_1 & 0 & \cdots & 0 \\ -c_2 & a_2 & -b_2 & 0 & \vdots \\ 0 & -c_3 & a_3 & \ddots & 0 \\ \vdots & 0 & \ddots & \ddots & -b_{N-1} \\ 0 & \cdots & 0 & -c_N & a_N \end{bmatrix} \begin{bmatrix} T_1 \\ T_2 \\ T_3 \\ \vdots \\ T_N \end{bmatrix} = \begin{bmatrix} d_1 \\ d_2 \\ d_3 \\ \vdots \\ d \end{bmatrix},$$

9.2.27

or

$$\mathbf{FT} = \mathbf{S}$$

9.2.28

where $\mathbf{F}$[1] is a tridiagonal system of coefficients, $\mathbf{T}$ an vector of temperatures, and $\mathbf{S}$ a vector of source associated terms. The solution can therefore be represented by

$$\mathbf{T} = \mathbf{F}^{-1}\mathbf{S}. \tag{9.2.29}$$

The system can be solved using standard numerical methods.

9.2.2 Inverse Problem

9.2.2.1 Dual of the Forward Differential Operator

Restating the forward problem and the dual problem in terms of the differential equations and with operator notation

$$\rho c\frac{\partial T}{\partial t} - \frac{\partial}{\partial z}\left(k\frac{\partial T}{\partial z}\right) = S \equiv \boldsymbol{FT} = \boldsymbol{S}, \qquad z \in [z_S, z_B], t \in [t_B, t_E], \tag{9.2.30}$$

and

$$-\rho c\frac{\partial T^D}{\partial t} - \frac{\partial}{\partial z}\left(k\frac{\partial T^D}{\partial z}\right) = S^D \equiv \boldsymbol{F}^{\mathrm{T}}\widehat{\boldsymbol{S}} = \widehat{\boldsymbol{T}} \Leftrightarrow \boldsymbol{F}^{\mathrm{T}}T^D = S^D, \qquad z \in [z_S, z_B], t \in [t_E, t_B]. \tag{9.2.31}$$

The spaces T and S associated with Equation 9.2.30 have respective duals $\widehat{\mathrm{T}}$ and $\widehat{\mathrm{S}}$ such that $\langle \hat{T}, T\rangle_{\mathrm{T}} = \langle \hat{S}, S\rangle_{\mathrm{S}}$ or $\langle \boldsymbol{F}^{\mathrm{T}}\hat{S}, T\rangle_{\mathrm{T}} = \langle \hat{S}, \boldsymbol{F}T\rangle_{\mathrm{S}}$. Shen and Beck (1991) and Tarantola (2005) show that in the particular case where S can be identified with $\widehat{\mathrm{T}}$ such that $\mathrm{S} \subseteq \widehat{\mathrm{T}}$ and $\mathrm{T} \subseteq \widehat{\mathrm{S}}$, $\boldsymbol{F}$ and $\boldsymbol{F}^{\mathrm{T}}$ map T into $\widehat{\mathrm{T}}$ according to duality relations $\langle \boldsymbol{F}^{\mathrm{T}}T^D, T^P\rangle_{\mathrm{T}} = \langle T^D, \boldsymbol{F}T^P\rangle_{\widehat{\mathrm{T}}}$ where $[T^P, T^D] \in \mathrm{T}$ and are appropriately termed the primal (P) and dual (D) temperatures. The scalars from the duality relation between S and T can then be defined such that

$$\langle S^D, T^P\rangle_{\mathrm{T}} = \langle T^D, S^P\rangle_{\mathrm{S}} = \int_{z_S}^{z_B} dz \int_{t_B}^{t_E} dt\, TS, \tag{9.2.32}$$

where $[S^P, S^D] \in \mathrm{S}$.

---

[1] The matrix $\mathbf{F}$ is usually denoted $\mathbf{A}$ in the literature but the convention has been broken here to allow certain notation conventions further along in the text.

Reintroducing the primal and dual operators it is seen that

$$\langle \boldsymbol{F}^{\mathrm{T}} T^{D}, T^{P} \rangle_{\mathrm{T}} - \langle T^{D}, \boldsymbol{F} T^{P} \rangle_{\mathrm{S}} = \int_{z_S}^{z_B} dz \int_{t_B}^{t_E} dt\, \boldsymbol{F}^{\mathrm{T}} T^{D} T^{P} - T^{D} \boldsymbol{F} T^{P}, \qquad 9.2.33$$

$$z \in [z_S, z_B], t \in [t_B, t_E].$$

Tarantola (2005) shows that the transpose of the gradient operator is the negative of the divergence operator ($\nabla^{\mathrm{T}} = -\nabla$); likewise, in Shen and Beck (1991) $\boldsymbol{F}^{\mathrm{T}}$, the transpose of the differential operator in Equation 9.2.30, is shown to take the form of Equation 9.2.31.

To show this, Equations 9.2.30 and 9.2.31 are substituted into Equation 9.2.33 to give (integrating by parts)

a.

$$\langle \boldsymbol{F}^{\mathrm{T}} T^{D}, T^{P} \rangle_{\mathrm{T}} - \langle T^{D}, \boldsymbol{F} T^{P} \rangle_{\mathrm{S}}$$

$$= \int_{z_S}^{z_B} dz \int_{t_B}^{t_E} dt \left\{ \left[-\rho c \frac{\partial T^{D}}{\partial t} - \frac{\partial}{\partial z}\left(k \frac{\partial T^{D}}{\partial z} \right) \right] T^{P} - T^{D} \left[\rho c \frac{\partial T^{P}}{\partial t} - \frac{\partial}{\partial z}\left(k \frac{\partial T^{P}}{\partial z} \right) \right] \right\}.$$

b.

$$\Rightarrow \langle \boldsymbol{F}^{\mathrm{T}} T^{D}, T^{P} \rangle_{\mathrm{T}} - \langle T^{D}, \boldsymbol{F} T^{P} \rangle_{\mathrm{S}}$$

$$= -\int_{z_S}^{z_B} dz \int_{t_B}^{t_E} dt\, \rho c \left(\frac{\partial T^{D}}{\partial t} T^{P} + T^{D} \frac{\partial T^{P}}{\partial t} \right) + \int_{t_B}^{t_E} dt \int_{z_S}^{z_B} dz \left[-\frac{\partial}{\partial z}\left(k \frac{\partial T^{D}}{\partial z} \right) T^{P} + T^{D} \frac{\partial}{\partial z}\left(k \frac{\partial T^{P}}{\partial z} \right) \right] \qquad 9.2.34$$

c.

$$\therefore \langle \boldsymbol{F}^{\mathrm{T}} T^{D}, T^{P} \rangle_{\mathrm{T}} - \langle T^{D}, \boldsymbol{F} T^{P} \rangle_{\mathrm{S}} = -\int_{z_S}^{z_B} dz\, \rho c T^{P} T^{D} \Big|_{t_B}^{t_E} + \int_{t_B}^{t_E} dt\, T^{D} k \frac{\partial T^{P}}{\partial z} - k \frac{\partial T^{D}}{\partial z} T^{P} \Big|_{z_S}^{z_B}$$

$$z \in [z_S, z_B], t \in [t_E, t_B]$$

Therefore, by applying boundary and initial conditions such that

$$T^{P} = T^{D} = 0, \qquad z = z_S, t \in [t_B, t_E], \qquad 9.2.35$$

$$k \frac{\partial T^{P}}{\partial z} = k \frac{\partial T^{D}}{\partial z} = 0, \qquad z = z_B, t \in [t_B, t_E], \qquad 9.2.36$$

and

$$T^P = T^D = 0, \qquad z \in [z_S, z_B], t = t_B = t_E, \tag{9.2.37}$$

the RHS of Equation 9.2.34 vanishes to satisfy the definition of the transpose. Equations 9.2.35-9.2.37 are the dual boundary conditions mentioned in Section 2.2.2.2.2.

The final result in Equation 9.2.34 shows that for $\boldsymbol{F}^{\mathrm{T}}$ to be the transpose of $\boldsymbol{F}$, $\hat{\mathrm{S}}$ is defined to be the bidual of T (the dual of $\hat{\mathrm{T}}$) therefore restricting the domains of both $\boldsymbol{F}$ and $\boldsymbol{F}^{\mathrm{T}}$ to the subspaces of T such that $[\mathrm{T}^P \ni T^P, \mathrm{T}^D \ni T^D] \subseteq \mathrm{T}$. This restriction serves a practical role in optimization – the gradient of the misfit function is shown to occupy a dual parameter space and therefore requires finding the gradients of dual parameters. Once this is done the form of $\boldsymbol{F}^{\mathrm{T}}$ is deduced by applying the formal definition of transpose (Equations 9.2.33-9.2.34) and imposing dual boundary conditions (Equations 9.2.35-9.2.37).

The form of the respective unsteady and steady transpose operators (dual problems) can be obtained by a similar procedure.

9.2.2.2 *Greens Function Solution to the Dual Problem*

This derivation is after the more involved presentation in Shen and Beck (1991). For an arbitrary field of temperatures T' over the space T the Green's function solution for an unspecified (primal or dual) problem can be written explicitly as

$$T' = \int_{z_S}^{z_B} dz \int_{t_B}^{t_E} dt\, \delta_{z,z';t,t'} T = \int_{z_S}^{z_B} dz \int_{t_B}^{t_E} dt\, FGT, \qquad z, z' \in [z_S, z_B], t, t' \in [t_B, t_E], \tag{9.2.38}$$

G being a general Green's function. Substituting the explicit forms of both the primal $\boldsymbol{F}$ (upper algebraic operators) and dual $\boldsymbol{F}^{\mathrm{T}}$ (lower algebraic operators) problem operators into Equation 9.2.38, integrating by parts and grouping terms results in a general representation for an arbitrary transient field

a.
$$T' = \int_{z_S}^{z_B} dz \int_{t_B}^{t_E} dt \left[\pm \rho c \frac{\partial G}{\partial t} - \frac{\partial}{\partial z}\left(k \frac{\partial G}{\partial z} \right) \right] T$$

$$\Rightarrow T' = \int_{z_S}^{z_B} dz \int_{t_B}^{t_E} dt\, G \left[\mp \rho c \frac{\partial T}{\partial t} - \frac{\partial}{\partial z}\left(k \frac{\partial T}{\partial z} \right) \right] + \int_{t_B}^{t_E} dt\, k \left[G \frac{\partial T}{\partial z} - \frac{\partial G}{\partial z} T \right] \Big|_{z_S}^{z_B} \qquad 9.2.39$$

b.
$$\pm \int_{z_S}^{z_B} dz\, \rho c G T \Big|_{t_B}^{t_E}, \qquad z, z' \in [z_S, z_B], t, t' \in [t_B, t_E].$$

Choosing a particular temperature field (dual or primal) and applying the relevant Green's operator ($\boldsymbol{FG} = \boldsymbol{G}^{\mathrm{T}}\boldsymbol{F}^{\mathrm{T}} = \boldsymbol{I}$) with appropriate boundary conditions produces a unique solution. The form of the first term on the RHS of Equation 9.2.39b suggests that choosing the Green's operator $\boldsymbol{G}$ associated with the primal problem (Equation 9.2.39a upper operator) selects the dual temperature field $\widehat{\boldsymbol{T}}$ while choosing the Green's operator $\boldsymbol{G}^{\mathrm{T}}$ associated with the dual problem (Equation 9.2.39a lower operator) selects the primal temperature field $\boldsymbol{T}$. To solve for the primal field the dual Green's operator is selected in Equation 9.2.39a and the primal HFE substituted into Equation 9.2.39b. The primal and homogeneous boundary conditions are applied and variables transposed using $\boldsymbol{G} = \boldsymbol{G}(z, t; z', t') = \boldsymbol{G}^{\mathrm{T}} = \boldsymbol{G}(z', t'; z, t)$ giving

$$T = \int_{z_S}^{z_B} dz' \int_{t_B}^{t_E} dt'\, GS + \int_{t_B}^{t_E} dt' k_S \frac{\partial G_S}{\partial z'} T_S - \int_{t_B}^{t_E} dt'\, G_B F_B + \int_{z_S}^{z_B} dz'\, \rho c G^0 T^0, \qquad 9.2.40$$
$$z, z' \in [z_S, z_B], t, t' \in [t_B, t_E],$$

written more compactly as $\boldsymbol{T} = \boldsymbol{GS}$ giving the structure of the Green's operator as $\boldsymbol{G} = [\boldsymbol{G}_{S*}, \boldsymbol{G}_S, \boldsymbol{G}_B, \boldsymbol{G}^0]$ and the source as $\boldsymbol{S} = [S, T_S, F_B, T^0]$. It is clear then that the Green's solution corresponds to the inverse problem $\boldsymbol{d} = \boldsymbol{g}(\boldsymbol{m})$. The field $\boldsymbol{S}$ can therefore be considered as a generalised field of sources which generate the temperature field $\boldsymbol{T}$. Equations 9.2.39 and 9.2.40 show that the temperature field solution can be written $\boldsymbol{T} = \boldsymbol{G}[\boldsymbol{F}^*\boldsymbol{T}]\boldsymbol{m}$ where $\boldsymbol{S}$ is a nonlinear function of $\boldsymbol{T} = T = T^U + T^S$ and model parameters $\boldsymbol{m} = [T_S^U, T_S^S, F_B, k, \rho, c, S]$. This new form is useful in obtaining the form of the gradient.

To solve for the dual field the primal Green's operator is selected in Equation 9.2.39a and the dual HFE substituted into Equation 9.2.39b. The dual boundary conditions are applied giving

$$T^D = \int_{z_S}^{z_B} dz' \int_{t_B}^{t_E} dt'\, G^{\mathrm{T}} S^D, \qquad z, z' \in [z_S, z_B], t, t' \in [t_B, t_E], \tag{9.2.41}$$

recalling that spaces $\mathrm{S} \ni \boldsymbol{S} \subseteq \hat{\mathrm{T}}$ and $\hat{\mathrm{S}} \ni \hat{\boldsymbol{S}} \subseteq \mathrm{T}$ (S and T are mutual duals) with $T^D \in \mathrm{T}$ and $S^D \in \mathrm{S}$. This is written more compactly as $\hat{\boldsymbol{S}} = \boldsymbol{G}^{\mathrm{T}} \hat{\boldsymbol{T}}$ giving the structure of the dual Green's operator as $\boldsymbol{G}^{\mathrm{T}} = \hat{\boldsymbol{G}}_{S*}$ and the source as $\hat{\boldsymbol{T}} = S^D$.

9.2.2.3 *Model Residual*

9.2.2.3.1 Residual Heat Flow Equation

The model residual $\delta \boldsymbol{m}$ is caused by a perturbation in the data parameters $\boldsymbol{d} = T = T^U + T^S$ as well as model parameters $\boldsymbol{m} = [T_S^U, T_S^S, F_B, k, \rho, c, S]$ such that $\delta \boldsymbol{d} = \delta T = \delta T^U + \delta T^S$ and $\delta \boldsymbol{m} = [\delta T_S^U, \delta T_S^S, \delta F_B, \delta k, \delta \rho, \delta c, \delta S]$. This can be written

$$\delta \boldsymbol{d} = \boldsymbol{g}(\boldsymbol{m}) - \boldsymbol{d} = \boldsymbol{g}(\delta \boldsymbol{m}). \tag{9.2.42}$$

The explicit form of $\delta \boldsymbol{d}$ is obtained by applying the Green's function solutions and substituting in the parameter residuals according to $\delta \boldsymbol{T} = \boldsymbol{G} \delta \boldsymbol{S}$. To do this for the primal problem the perturbations are substituted into the general HFE to produce

$$(\rho + \delta\rho)(c + \delta c)\frac{\partial (T + \delta T)}{\partial t} = \frac{\partial}{\partial z}\left((k + \delta k)\frac{\partial (T + \delta T)}{\partial z}\right) + S + \delta S, \tag{9.2.43}$$
$$z \in [z_S, z_B], t \in (t_B, t_E].$$

This leads to

a. $$(\rho c + \delta\rho c)\frac{\partial T}{\partial t} + (\rho c + \delta\rho c)\frac{\partial \delta T}{\partial t} = \frac{\partial}{\partial z}\left(k\frac{\partial T}{\partial z} + k\frac{\partial \delta T}{\partial z} + \delta k\frac{\partial T}{\partial z} + \delta k\frac{\partial \delta T}{\partial z}\right) + S + \delta S$$

$$\Rightarrow \rho c\frac{\partial T}{\partial t} + \delta\rho c\frac{\partial \delta T}{\partial t} - \frac{\partial}{\partial z}\left(k\frac{\partial T}{\partial z} + \delta k\frac{\partial \delta T}{\partial z}\right) - S \qquad 9.2.44$$

b. $$= -\delta\rho c\frac{\partial T}{\partial t} - \rho c\frac{\partial \delta T}{\partial t} + \frac{\partial}{\partial z}\left(k\frac{\partial \delta T}{\partial z} + \delta k\frac{\partial T}{\partial z}\right) + \delta S,$$

$$z \in [z_S, z_B], t \in (t_B, t_E].$$

The LHS of Equation 9.2.44b is approximately equal to zero, therefore – keeping the first order terms – the equation for δT can be written

$$\rho c\frac{\partial \delta T}{\partial t} - \frac{\partial}{\partial z}\left(k\frac{\partial \delta T}{\partial z}\right) = -\delta\rho c\frac{\partial T}{\partial t} + \frac{\partial}{\partial z}\left(\delta k\frac{\partial T}{\partial z}\right) + \delta S, \qquad z \in [z_S, z_B], t \in (t_B, t_E], \qquad 9.2.45$$

or $\boldsymbol{F\delta T = \delta S}$ with boundary conditions

$$\delta T = \delta T_S, \qquad z = z_S, t \in (t_B, t_E] \qquad 9.2.46$$

$$-k\frac{\partial \delta T}{\partial z} = \delta k_B\frac{\partial T_B}{\partial z} + \delta F_B, \qquad z = z_B, t \in (t_B, t_E], \qquad 9.2.47$$

where T_B is the basal temperature, and initial condition

$$\delta T = \delta T^0, \qquad z \in [z_S, z_B], t = t_B. \qquad 9.2.48$$

Equation 9.2.45 is the residual form of the HFE.

This result leads to analogous results for the superposed problem as

$$\rho c\frac{\partial \delta T^U}{\partial t} - \frac{\partial}{\partial z}\left(k\frac{\partial \delta T^U}{\partial z}\right) = -\delta\rho c\frac{\partial T^U}{\partial t} + \frac{\partial}{\partial z}\left(\delta k\frac{\partial T^U}{\partial z}\right) + \delta S^U, \qquad 9.2.49$$

$$z \in [z_S, z_B], t \in (t_B, t_E],$$

or $\boldsymbol{F^U\delta T^U = \delta S^U}$ for the unsteady with boundary conditions

$$\delta T^U = \delta T_S^U, \qquad z = z_S, t \in (t_B, t_E] \qquad 9.2.50$$

$$-k\frac{\partial \delta T^U}{\partial z} = \delta k_B\frac{\partial T_B^U}{\partial z} + \delta F_B^U, \qquad z = z_B, t \in (t_B, t_E], \qquad 9.2.51$$

where T_B^U is the basal temperature, and initial condition

$$\delta T^U = 0, \qquad z \in [z_S, z_B], t = t_B. \tag{9.2.52}$$

For the steady residual

$$-\frac{\partial}{\partial z}\left(k\frac{\partial \delta T^S}{\partial z}\right) = \frac{\partial}{\partial z}\left(\delta k\frac{\partial T^S}{\partial z}\right) + \delta S^S, \qquad z \in [z_S, z_B], \tag{9.2.53}$$

or $\boldsymbol{F}^S\delta\boldsymbol{T}^S = \delta\boldsymbol{S}^S$ for the unsteady with boundary conditions

$$\delta T^S = \delta T_S^S, \qquad z = z_S, \tag{9.2.54}$$

$$-k\frac{\partial \delta T^S}{\partial z} = \delta k_B\frac{\partial T_B^S}{\partial z} + \delta F_B^S, \qquad z = z_B, \tag{9.2.55}$$

where T_B^S is the basal temperature.

9.2.2.3.2 Residual Heat Flow Equation Primal Green's Function Solution

The solution of the residual HFE is found by carrying out the Green's function procedure applied to the nominal HFE in Section 9.2.2.2 (also see Section 2.2.3.1) – i.e. substituting 9.2.45-9.2.55 into the Green's function solution. This reveals the explicit form of the solution $\delta\boldsymbol{T} = \boldsymbol{G}\delta\boldsymbol{S}$ analogous to the form of $\delta\boldsymbol{d} = \boldsymbol{g}(\delta\boldsymbol{m})$ such that

$$\begin{aligned}\delta T = &\int_{z_S}^{z_B} dz' \int_{t_B}^{t_E} dt'\, G\left[-\delta\rho c\frac{\partial T}{\partial t} + \frac{\partial}{\partial z}\left(\delta k\frac{\partial T}{\partial z}\right) + \delta S\right] + \int_{t_B}^{t_E} dt' k_S \frac{\partial G_S}{\partial z'}\delta T_S \\ &- \int_{t_B}^{t_E} dt'\, G_B\left[\delta k_B\frac{\partial T_B}{\partial z} + \delta F_B\right] + \int_{z_S}^{z_B} dz'\, \rho c G^0 \delta T^0, \\ &z, z' \in [z_S, z_B], t, t' \in [t_B, t_E],\end{aligned} \tag{9.2.56}$$

with the same Green's operator $\boldsymbol{G} = [\boldsymbol{G}_{S*}, \boldsymbol{G}_S, \boldsymbol{G}_B, \boldsymbol{G}^0]$ as the unperturbed solution and source $\delta\boldsymbol{S} = \left[-\delta\rho c\frac{\partial T}{\partial t} + \frac{\partial}{\partial z}\left(\delta k\frac{\partial T}{\partial z}\right) + \delta S, \delta T_S, \delta k_B\frac{\partial T_B}{\partial z} + \delta F_B, \rho c\delta T^0\right]$. As before, the Green's function solution and inverse problem can be combined to give $\delta\boldsymbol{T} = \boldsymbol{G}[\boldsymbol{F}^*\boldsymbol{T}]\delta\boldsymbol{m}$ showing that the term $\boldsymbol{G}[\boldsymbol{F}^*\boldsymbol{T}]$ corresponds to $\mathbf{G} = \frac{\partial \mathbf{d}}{\partial \mathbf{m}}$, the data Fréchet derivative introduced in Section 2.3.1 for the general discrete theory. The unsteady residual solution follows as

$$\delta T^U = \int_{z_S}^{z_B} dz' \int_{t_B}^{t_E} dt' \, G^U \left[-\delta\rho c \frac{\partial T^U}{\partial t} + \frac{\partial}{\partial z}\left(\delta k \frac{\partial T^U}{\partial z} \right) \right]$$

$$+ \int_{t_B}^{t_E} dt' k_S \frac{\partial G_S^U}{\partial z'} \delta T_S^U - \int_{t_B}^{t_E} dt' \, G_B^U \delta k_B \frac{\partial T_B^U}{\partial z} + \int_{z_S}^{z_B} dz' \, \rho c G^{U0} \delta T^{U0}, \qquad 9.2.57$$

$$z, z' \in [z_S, z_B], t, t' \in [t_B, t_E],$$

written more compactly as $\delta \boldsymbol{T}^U = \boldsymbol{G}^U \delta \boldsymbol{S}^U$ or $\boldsymbol{T}^U = \boldsymbol{G}^U [\boldsymbol{F}^{*U} \boldsymbol{T}^U] \delta \boldsymbol{m}$ giving the structure of the perturbing unsteady Green's operator as $\boldsymbol{G}^U = [\boldsymbol{G}_{S*}^U, \boldsymbol{G}_S^U, \boldsymbol{G}_B^U, , \boldsymbol{G}^{U0}]$ and the source as $\boldsymbol{S}^U = \left[-\delta\rho c \frac{\partial T^U}{\partial t} + \frac{\partial}{\partial z}\left(\delta k \frac{\partial T^U}{\partial z} \right), \delta T_S^U, \delta k_B \frac{\partial T_B^U}{\partial z}, \delta T^{U0} \right]$. The steady is

$$\delta T^S = \int_{z_S}^{z_B} dz' \, G^S \left[\frac{\partial}{\partial z}\left(\delta k \frac{\partial T^S}{\partial z} \right) + \delta S^S \right] + k_S \frac{\partial G_S^S}{\partial z'} \delta T_S^S - G_B^S \left[\delta k_B \frac{\partial T_B^S}{\partial z} + \delta F_B^S \right] \qquad 9.2.58$$

$$z, z' \in [z_S, z_B],$$

written more compactly as $\delta \boldsymbol{T}^S = \boldsymbol{G}^S \delta \boldsymbol{S}^S$ or $\delta \boldsymbol{T}^S = \boldsymbol{G}^S [\boldsymbol{F}^{*S} \boldsymbol{T}^S] \delta \boldsymbol{m}$ giving the structure of the steady Green's operator as $\boldsymbol{G}^S = [\boldsymbol{G}_{S*}^S, \boldsymbol{G}_S^S, \boldsymbol{G}_B^S]$ as with the unperturbed case and the source as $\boldsymbol{S}^S = \left[\frac{\partial}{\partial z}\left(\delta k \frac{\partial T^S}{\partial z} \right) + \delta S^S, \delta T_S^S, \delta k_B \frac{\partial T_B^S}{\partial z} \right]$.

9.2.2.3.3 Residual Heat Flow Equation Dual Green's Function Solution

Applying the procedure to the analogous dual equations reveals the forms of the dual residual solutions to be

$$\delta T^D = \int_{z_S}^{z_B} dz' \int_{t_B}^{t_E} dt' \, G^{\mathrm{T}} \left[\delta\rho c \frac{\partial T^D}{\partial t} + \frac{\partial}{\partial z}\left(\delta k \frac{\partial T^D}{\partial z} \right) + \delta S^D \right], \qquad 9.2.59$$

$$z, z' \in [z_S, z_B], t, t' \in [t_B, t_E],$$

or $\delta \widehat{\boldsymbol{S}} = \boldsymbol{G}^{\mathrm{T}} \delta \widehat{\boldsymbol{T}} \equiv \boldsymbol{G}^{\mathrm{T}} [\boldsymbol{F}^{*\mathrm{T}} \widehat{\boldsymbol{S}}] \delta \widehat{\boldsymbol{m}}$ for the unpartitioned problem with Green's operator $\boldsymbol{G}^{\mathrm{T}} = \widehat{\boldsymbol{G}}_{S*}$ and dual source[2] $\delta \widehat{\boldsymbol{T}} = \delta\rho c \frac{\partial T^D}{\partial t} + \frac{\partial}{\partial z}\left(\delta k \frac{\partial T^D}{\partial z} \right) + \delta S^D$.

[2] Recall that spaces T and S are mutual duals therefore $\mathrm{S} \ni S^P \subseteq \widehat{\mathrm{T}} \ni T^D$ and $\mathrm{T} \ni T^P \subseteq \widehat{\mathrm{S}} \ni S^D$.

$$\delta T^{DU} = \int_{z_S}^{z_B} dz' \int_{t_B}^{t_E} dt' \, G^{U^{\mathrm{T}}} \left[-\delta\rho c \frac{\partial T^{DU}}{\partial t} + \frac{\partial}{\partial z}\left(\delta k \frac{\partial T^{DU}}{\partial z} \right) + \delta S^{DU} \right], \qquad 9.2.60$$

$$z, z' \in [z_S, z_B], t, t' \in [t_B, t_E],$$

or $\delta \widehat{\boldsymbol{S}}^U = \boldsymbol{G}^{U^{\mathrm{T}}} \delta \widehat{\boldsymbol{T}}^U \equiv \boldsymbol{G}^{U^{\mathrm{T}}} \left[\boldsymbol{F}^{*U^{\mathrm{T}}} \widehat{\boldsymbol{S}}^U \right] \delta \widehat{\boldsymbol{m}}$ for the unsteady with Green's operator $\boldsymbol{G}^{U^{\mathrm{T}}} = \widehat{\boldsymbol{G}}^U_{S*}$ and dual source $\delta \widehat{\boldsymbol{T}}^U = \delta\rho c \frac{\partial T^{DU}}{\partial t} + \frac{\partial}{\partial z}\left(\delta k \frac{\partial T^{DU}}{\partial z} \right) + \delta S^{DU}$ and

$$\delta T^{DS} = \int_{z_S}^{z_B} dz' \, G^{S^{\mathrm{T}}} \left[\frac{\partial}{\partial z}\left(\delta k \frac{\partial T^{DS}}{\partial z} \right) + \delta S^{DS} \right] \qquad 9.2.61$$

$$z, z' \in [z_S, z_B],$$

or $\delta \widehat{\boldsymbol{S}}^S = \boldsymbol{G}^{S^{\mathrm{T}}} \delta \widehat{\boldsymbol{T}}^S \equiv \boldsymbol{G}^{S^{\mathrm{T}}} \left[\boldsymbol{F}^{*S^{\mathrm{T}}} \widehat{\boldsymbol{S}}^S \right] \delta \widehat{\boldsymbol{m}}$ for the steady with Green's operator $\boldsymbol{G}^{S^{\mathrm{T}}} = \widehat{\boldsymbol{G}}^S_{S*}$ and dual source $\delta \widehat{\boldsymbol{T}}^S = \delta\rho c \frac{\partial T^{DS}}{\partial t} + \frac{\partial}{\partial z}\left(\delta k \frac{\partial T^{DS}}{\partial z} \right) + \delta S^{DS}$.

With these results a data residual $\delta \boldsymbol{d}$ is used to obtain an associated model residual $\delta \boldsymbol{m}$ which is used to iteratively update a primal temperature $T \Leftrightarrow T^P$, reducing $\delta \boldsymbol{d}$ in accordance with the dual boundary conditions.[3] These residual solutions are elements of the misfit function gradient according to $\boldsymbol{G} = \frac{\partial \boldsymbol{d}}{\partial \boldsymbol{m}}$ which is the data Fréchet derivative used in optimizing the parameters with the least squares misfit function $S_{\boldsymbol{m}}$ (see Sections 2.2.1.3.2 and 2.2.3.3). Their role in the Fréchet and Hessian derivatives is outlined below.

9.2.2.4 *Fréchet and Hessian Derivatives*

The misfit function can be represented functionally by (Tarantola, 2005)

[3] Shen and Beck (1991) state that residual heat flow Equations 9.2.45-9.2.55 are best used to obtain $\delta \boldsymbol{d} \triangleq \delta \boldsymbol{T}$. The FSI algorithm allows the option to either update T using the former equations to obtain $\delta \boldsymbol{T}$ or update T using $\boldsymbol{m}$ updated with $\delta \boldsymbol{m}$. Here the simpler latter approach is preferred.

$$S_m = \frac{1}{2}\left[[\boldsymbol{d}-\boldsymbol{d}_0]^{\mathrm{T}}\boldsymbol{C_d}^{-1}[\boldsymbol{d}-\boldsymbol{d}_0] + [\boldsymbol{m}-\boldsymbol{m}_0]^{\mathrm{T}}\boldsymbol{C_m}^{-1}[\boldsymbol{m}-\boldsymbol{m}_0]\right]$$
$$\equiv \frac{1}{2}\left[\langle \delta\hat{\boldsymbol{d}}, \delta\boldsymbol{d}\rangle_{\mathrm{D}} + \langle \delta\hat{\boldsymbol{m}}, \delta\boldsymbol{m}\rangle_{\mathrm{M}}\right] \quad 9.2.62$$

A series expansion of S_m about a point $\boldsymbol{m}_0$ corresponding to model perturbation $\boldsymbol{m}_0 + \delta\boldsymbol{m}$ gives

$$S_{m_0+\delta m} = S_{m_0} + \langle \hat{\boldsymbol{\gamma}}, \delta\boldsymbol{m}\rangle_{\mathrm{M}} + \frac{1}{2}\langle \hat{\boldsymbol{H}}\delta\boldsymbol{m}, \delta\boldsymbol{m}\rangle_{\mathrm{M}} + O(\delta\boldsymbol{m}^3), \quad 9.2.63$$

where $O(\delta\boldsymbol{m}^3) \approx 0$, $\hat{\boldsymbol{H}}$ is the Hessian and $\hat{\boldsymbol{\gamma}}$ the Fréchet derivative. The operator $\hat{\boldsymbol{\gamma}} \in \hat{\mathrm{M}}$ is the dual of the steepest ascent vector $\boldsymbol{\gamma} \in \mathrm{M}$ which maps the model space M into the space of real numbers R according to

$$\boldsymbol{\gamma} = \boldsymbol{M}\left[\frac{\partial S_m}{\partial \boldsymbol{m}}\right] = \boldsymbol{M}\hat{\boldsymbol{\gamma}}. \quad 9.2.64$$

The Hessian $\hat{\boldsymbol{H}} = \frac{\partial \hat{\boldsymbol{\gamma}}}{\partial \boldsymbol{m}}$ and (in Newtonian descent optimization) its inverse metric $\boldsymbol{M}$ are a part of the dual space $\hat{\mathrm{M}}$ and also map M into $\hat{\mathrm{M}}$. It then follows that $\boldsymbol{G}^{\mathrm{T}}$ the transpose of $\boldsymbol{G} = \frac{\partial \boldsymbol{d}}{\partial \boldsymbol{m}}$ the data Fréchet derivative is also a member of $\hat{\mathrm{M}}$ according to $\hat{\boldsymbol{m}} = \boldsymbol{G}^{\mathrm{T}}\hat{\boldsymbol{d}}$

The explicit form of $\delta\boldsymbol{d} \triangleq \delta\boldsymbol{T}$ (Equation 9.2.56) can be used to derive the form of $\hat{\boldsymbol{\gamma}}$ and $\hat{\boldsymbol{H}}$. To achieve this Equation 9.2.62 is differentiated and compared to Equation 9.2.63. This leads to the Fréchet derivative

$$\frac{\partial S_m}{\partial \boldsymbol{m}} = \hat{\boldsymbol{\gamma}} = \frac{1}{2}\left[\frac{\partial \boldsymbol{d}^{\mathrm{T}}}{\partial \boldsymbol{m}}\boldsymbol{C_d}^{-1}[\boldsymbol{d}-\boldsymbol{d}_0] + [\boldsymbol{d}-\boldsymbol{d}_0]^{\mathrm{T}}\boldsymbol{C_d}^{-1}\frac{\partial \boldsymbol{d}}{\partial \boldsymbol{m}} + \boldsymbol{C_m}^{-1}[\boldsymbol{m}-\boldsymbol{m}_0]\right.$$
$$\left. + [\boldsymbol{m}-\boldsymbol{m}_0]^{\mathrm{T}}\boldsymbol{C_m}^{-1}\right]$$
$$= \frac{1}{2}\left[\langle \frac{\delta\boldsymbol{d}}{\delta\boldsymbol{m}}, \delta\hat{\boldsymbol{d}}\rangle_{\hat{\mathrm{D}}} + \langle \delta\boldsymbol{d}, \frac{\delta\hat{\boldsymbol{d}}}{\delta\boldsymbol{m}}\rangle_{\hat{\mathrm{D}}} + 2\langle \delta\hat{\boldsymbol{m}}\rangle_{\hat{\mathrm{M}}}\right] \quad 9.2.65$$
$$\equiv \frac{1}{2}\left[\langle \delta\hat{\boldsymbol{d}}, \frac{\delta\boldsymbol{d}}{\delta\boldsymbol{m}}\rangle_{\mathrm{D}} + \langle \frac{\delta\hat{\boldsymbol{d}}}{\delta\boldsymbol{m}}, \delta\boldsymbol{d}\rangle_{\mathrm{D}} + 2\langle \delta\hat{\boldsymbol{m}}\rangle_{\hat{\mathrm{M}}}\right].$$

Therefore the first order terms of $S_{m+\delta m}$ are

$$\langle \hat{\gamma}, \delta m\rangle_{\mathrm{M}} = \frac{1}{2}\left[\langle \delta\hat{d}, \delta d\rangle_{\mathrm{D}} + \langle \delta\hat{d}, \delta d\rangle_{\mathrm{D}} + 2\langle \delta\hat{m}, \delta m\rangle_{\mathrm{M}}\right] = \langle \delta\hat{d}, \delta d\rangle_{\mathrm{D}} + \langle \delta\hat{m}, \delta m\rangle_{\mathrm{M}}. \quad 9.2.66$$

Accordingly, the Hessian is

$$\begin{aligned}\frac{\partial^2 S_m}{\partial m^2} = \frac{\partial \hat{\gamma}}{\partial m} = \frac{1}{2}\Bigg[&\frac{\partial^2 d^{\mathrm{T}}}{\partial m^2} C_d^{-1}[d - d_0] + \frac{\partial d^{\mathrm{T}}}{\partial m} C_d^{-1}\frac{\partial d}{\partial m} + \frac{\partial d^{\mathrm{T}}}{\partial m} C_d^{-1}\frac{\partial d}{\partial m} \\ &+ [d - d_0]^{\mathrm{T}} C_d^{-1}\frac{\partial^2 d}{\partial m^2} + 2C_m^{-1}\Bigg] \\ \equiv \frac{1}{2}\Bigg[&\langle \delta\hat{d}, \frac{\delta^2 d}{\delta m^2}\rangle_{\mathrm{D}} + \langle \frac{\delta\hat{d}}{\delta m}, \frac{\delta d}{\delta m}\rangle_{\mathrm{D}} + \langle \frac{\delta\hat{d}}{\delta m}, \frac{\delta d}{\delta m}\rangle_{\mathrm{D}} + \langle \frac{\delta^2\hat{d}}{\delta m^2}, \delta d\rangle_{\mathrm{D}} \\ &+ 2C_m^{-1}\Bigg].\end{aligned} \quad 9.2.67$$

Therefore the second order terms of $S_{m+\delta m}$ are

$$\begin{aligned}\frac{1}{2}\langle \hat{H}\delta m, \delta m\rangle_{\mathrm{M}} &= \frac{1}{2}\left[\langle \delta\hat{d}, \delta^2 d\rangle_{\mathrm{D}} + \langle \delta\hat{d}, \delta d\rangle_{\mathrm{D}} + \langle \delta\hat{d}, \delta d\rangle_{\mathrm{D}} + \langle \delta^2\hat{d}, \delta d\rangle_{\mathrm{D}} + 2\langle \delta\hat{m}\rangle_{\mathrm{M}}\right] \\ &= \langle \delta\hat{d}, \delta d\rangle_{\mathrm{D}} + \langle \delta\hat{d}, \delta^2 d\rangle_{\mathrm{D}} + \langle \delta\hat{m}\rangle_{\mathrm{M}},\end{aligned} \quad 9.2.68$$

and $S_{m_0+\delta m}$ can be represented by

$$\begin{aligned}S_{m_0+\delta m} = S_m &+ \langle \delta\hat{d}, \delta T\rangle_{\mathrm{D}} + \langle \delta\hat{m}, \delta m\rangle_{\mathrm{M}} + \langle \delta\hat{d}, \delta T\rangle_{\mathrm{D}} + \langle \delta\hat{d}, \delta^2 T\rangle_{\mathrm{D}} + \langle \delta\hat{m}\rangle_{\mathrm{M}} \\ &+ O(\delta m^3).\end{aligned} \quad 9.2.69$$

Taking the terms in the data space D the aim is to get the function expressed in only the model space M as with Equation 9.2.63, therefore

a. $$\langle \delta\hat{d}, \delta T\rangle_{\mathrm{D}} = \langle \delta\hat{d}, G[F^*T]\delta m\rangle_{\mathrm{T}} = \langle G^{\mathrm{T}}\delta\hat{d}, [F^*T]\delta m\rangle_{\mathrm{S}} = \langle [F^*T]^{\mathrm{T}} G^{\mathrm{T}}\delta\hat{d}, \delta m\rangle_{\mathrm{M}},$$

b. $$\langle \delta\hat{d}, \delta T\rangle_{\mathrm{D}} = \langle [F^*T]^{\mathrm{T}} G^{\mathrm{T}} C_d^{-1}\delta T, \delta m\rangle_{\mathrm{M}} = \langle [F^*T]^{\mathrm{T}} G^{\mathrm{T}} C_d^{-1} G[F^*T]\delta m, \delta m\rangle_{\mathrm{M}}, \quad 9.2.70$$

c. $$\langle \delta\hat{d}, \delta^2 T\rangle_{\mathrm{D}} = \langle \delta\hat{d}, \delta G[F^*T]\delta m\rangle_{\mathrm{T}} = \langle \delta[F^*T]^{\mathrm{T}} G^{\mathrm{T}}\delta\hat{d}, \delta m\rangle_{\mathrm{M}},$$

where the terms have been transformed through different spaces using relevant operators explored earlier. This shows that $\hat{\boldsymbol{\gamma}}$ and $\hat{\boldsymbol{H}}$ can be written as

a. $$\hat{\boldsymbol{\gamma}} = \hat{\boldsymbol{\gamma}}^{d} + \hat{\boldsymbol{\gamma}}^{m} = [\boldsymbol{F}^{*}\boldsymbol{T}]^{\mathrm{T}}\boldsymbol{G}^{\mathrm{T}}\delta\hat{\boldsymbol{d}} + \delta\hat{\boldsymbol{m}},$$

b. $$\hat{\boldsymbol{H}} = \hat{\boldsymbol{H}}^{d} + \hat{\boldsymbol{H}}^{m} = [\boldsymbol{F}^{*}\boldsymbol{T}]^{\mathrm{T}}\boldsymbol{G}^{\mathrm{T}}\boldsymbol{C}_{\boldsymbol{d}}{}^{-1}\boldsymbol{G}[\boldsymbol{F}^{*}\boldsymbol{T}] + \frac{\delta[\boldsymbol{F}^{*}\boldsymbol{T}]^{\mathrm{T}}\boldsymbol{G}^{\mathrm{T}}}{\delta\boldsymbol{m}}\delta\hat{\boldsymbol{d}} + \boldsymbol{C}_{\boldsymbol{m}}{}^{-1}, \quad 9.2.71$$

which corresponds to the discrete form in Section 2.2.1.3.3 (Equation 2.38). The form of $\hat{\boldsymbol{\gamma}}^{m}$, the component of the gradient dictated explicitly by the model parameters is $\hat{\boldsymbol{\gamma}}^{m} = \delta\hat{\boldsymbol{m}} = \boldsymbol{C}_{\boldsymbol{m}}{}^{-1}[\boldsymbol{m} - \boldsymbol{m}_{\boldsymbol{0}}]$ and for the Hessian $\hat{\boldsymbol{H}}^{m} = \boldsymbol{C}_{\boldsymbol{m}}{}^{-1}$.

The explicit forms of the Green's operators $\boldsymbol{G}$ and $\boldsymbol{G}^{\mathrm{T}}$ are not obvious, therefore further spatial transformations are performed to get their explicit forms and consequently the explicit forms of $\hat{\boldsymbol{\gamma}}^{d}$ and $\hat{\boldsymbol{H}}^{d}$. To do this the spatial relationships of spaces $\langle \hat{\mathrm{M}}, \mathrm{M} \rangle$ and $\langle \hat{\mathrm{D}}, \mathrm{D} \rangle$ to spaces $\langle \hat{\mathrm{S}}, \mathrm{S} \rangle$ and $\langle \hat{\mathrm{T}}, \mathrm{T} \rangle$ are utilized. With the dual source space $\hat{\mathrm{S}} \subset \mathrm{D} \subset \hat{\mathrm{D}}$ a temperature perturbation $\delta\boldsymbol{T} \triangleq \delta\boldsymbol{d}$ in D has a dual field corresponding to a source $\delta\hat{\boldsymbol{T}} \triangleq \delta\hat{\boldsymbol{d}} = \boldsymbol{C}_{\boldsymbol{d}}{}^{-1}\delta\boldsymbol{d}$ in $\hat{\mathrm{D}}$ which generates a dual temperature field $\delta\hat{\boldsymbol{S}}$ in $\hat{\mathrm{S}}$ such that $\delta\hat{\boldsymbol{S}} = \boldsymbol{G}^{\mathrm{T}}\delta\hat{\boldsymbol{T}} \equiv \delta T^{D} = \boldsymbol{G}^{\mathrm{T}}\delta S^{D}$. With this particular case of the data perturbation $\hat{\boldsymbol{\gamma}}^{d}$ and $\hat{\boldsymbol{H}}^{d}$ can be presented as

a. $$\hat{\boldsymbol{\gamma}}^{d} = [\boldsymbol{F}^{*}\boldsymbol{T}]^{\mathrm{T}}\delta T^{D} = [\boldsymbol{F}^{*U}\boldsymbol{T}^{U}]^{\mathrm{T}}\delta T^{DU} + [\boldsymbol{F}^{*S}\boldsymbol{T}^{S}]^{\mathrm{T}}\delta T^{DS},$$

b. $$\hat{\boldsymbol{H}}^{d} = [\boldsymbol{F}^{*}\boldsymbol{T}]^{\mathrm{T}}\boldsymbol{G}^{\mathrm{T}}\boldsymbol{C}_{\boldsymbol{d}}{}^{-1}\boldsymbol{G}[\boldsymbol{F}^{*}\boldsymbol{T}] + \frac{\delta[\boldsymbol{F}^{*}\boldsymbol{T}]^{\mathrm{T}}}{\delta\boldsymbol{m}}\delta T^{D}. \quad 9.2.72$$

Taking these new representations, noting that $\hat{\boldsymbol{\gamma}}^{d} = [\hat{\boldsymbol{\gamma}}^{T_S}, \hat{\boldsymbol{\gamma}}^{F_B}, \hat{\boldsymbol{\gamma}}^{k}, \hat{\boldsymbol{\gamma}}^{\rho c}, \hat{\boldsymbol{\gamma}}^{S}]$ and $\hat{\boldsymbol{H}}^{d} = [\hat{\boldsymbol{H}}^{T_S}, \hat{\boldsymbol{H}}^{F_B}, \hat{\boldsymbol{H}}^{k}, \hat{\boldsymbol{H}}^{\rho c}, \hat{\boldsymbol{H}}^{S}]$ corresponding to the analogous model residuals $\delta\boldsymbol{m} = [\delta T_S, \delta F_B, \delta k, \delta\rho c, \delta S]$ and again transforming spaces produces

a. $$\langle [\boldsymbol{F^*T}]^{\mathrm{T}} \delta T^D, \delta \boldsymbol{m} \rangle_{\mathrm{M}} = \langle \boldsymbol{G}^{\mathrm{T}} \delta S^D, [\boldsymbol{F^*T}] \delta \boldsymbol{m} \rangle_{\mathrm{S}} = \langle \delta S^D, \boldsymbol{G}[\boldsymbol{F^*T}] \delta \boldsymbol{m} \rangle_{\mathrm{T}} = \langle \delta S^D, \delta \boldsymbol{T} \rangle_{\mathrm{T}},$$

b. $$\begin{aligned} \langle [\boldsymbol{F^*T}]^{\mathrm{T}} \boldsymbol{G}^{\mathrm{T}} \boldsymbol{C_d}^{-1} \boldsymbol{G}[\boldsymbol{F^*T}] \delta \boldsymbol{m}, \delta \boldsymbol{m} \rangle_{\mathrm{M}} &= \langle \boldsymbol{C_d}^{-1} \boldsymbol{G}[\boldsymbol{F^*T}] \delta \boldsymbol{m}, \boldsymbol{G}[\boldsymbol{F^*T}] \delta \boldsymbol{m} \rangle_{\mathrm{T}} = \langle \delta \widehat{\boldsymbol{T}}, \delta \boldsymbol{T} \rangle_{\mathrm{T}} \\ &= \langle \delta S^D, \delta \boldsymbol{T} \rangle_{\mathrm{T}}, \end{aligned} \quad 9.2.73$$

c. $$\langle \frac{\delta [\boldsymbol{F^*T}]^{\mathrm{T}}}{\delta \boldsymbol{m}} \delta T^D, \delta \boldsymbol{m} \rangle_{\mathrm{M}} = \langle \frac{\delta S^D}{\delta \boldsymbol{m}}, \delta \boldsymbol{T} \rangle_{\mathrm{T}}.$$

Explicitly for $\widehat{\boldsymbol{\gamma}}^{\boldsymbol{d}}$: substituting the primal temperature residual solution (Equation 9.2.56) gives

$$\begin{aligned} \langle \delta S^D, \delta \boldsymbol{T} \rangle_{\mathrm{T}} = &\int_{z_S}^{z_B} dz' \int_{t_B}^{t_E} dt'\, G \delta S^D \left[-\delta \rho c \frac{\partial T}{\partial t} + \frac{\partial}{\partial z} \left(\delta k \frac{\partial T}{\partial z'} \right) + \delta S \right] \\ &+ \int_{t_B}^{t_E} dt' k_S \frac{\partial G_S \delta S_S^D}{\partial z'} \delta T_S - \int_{t_B}^{t_E} dt'\, G_B \delta S_B^D \left[\delta k_B \frac{\partial T_B}{\partial z} + \delta F_B \right] \\ &+ \int_{z_S}^{z_B} dz'\, \rho c G^0 \delta S^{D0} \delta T^0, \qquad z, z' \in [z_S, z_B], t, t' \in [t_B, t_E]; \end{aligned} \quad 9.2.74$$

and substituting the Green's function solution to the dual residual problem (Equation 9.2.59) noting $G = G^{\mathrm{T}}$ and, for the particular case of mutual duality, the boundary and initial conditions are quiescent gives

$$\begin{aligned} \langle \delta S^D, \delta \boldsymbol{T} \rangle_{\mathrm{T}} = &\int_{z_S}^{z_B} dz \int_{t_B}^{t_E} dt\, \delta T^D \left[-\delta \rho c \frac{\partial T}{\partial t} + \frac{\partial}{\partial z} \left(\delta k \frac{\partial T}{\partial z} \right) + \delta S \right] + \int_{t_B}^{t_E} dt k_S \frac{\partial \delta T_S^D}{\partial z} \delta T_S \\ &- \int_{t_B}^{t_E} dt\, \delta T_B^D \left[\delta k_B \frac{\partial T_B}{\partial z} + \delta F_B \right] + \int_{z_S}^{z_B} dz\, \rho c \delta T^{D0} \delta T^0, \\ &z \in [z_S, z_B], t \in [t_B, t_E]. \end{aligned} \quad 9.2.75$$

Expanding and integrating gives

$$\begin{aligned}\langle \delta S^D, \delta \boldsymbol{T} \rangle_{\mathrm{T}} = &- \int_{z_S}^{z_B} dz \int_{t_B}^{t_E} dt \frac{\partial \delta T^D}{\partial z} \frac{\partial T}{\partial z} \delta k - \int_{z_S}^{z_B} dz \int_{t_B}^{t_E} dt\, \delta T^D \frac{\partial T}{\partial t} \delta \rho c \\ &- \delta S \int_{z_S}^{z_B} dz \int_{t_B}^{t_E} dt \frac{\partial^2 \delta T^D}{\partial z \partial t} + \int_{z_S}^{z_B} dz \int_{t_B}^{t_E} dt\, \delta T^D \delta S \\ &+ \int_{t_B}^{t_E} dt k_S \frac{\partial \delta T_S^D}{\partial z} \delta T_S - \int_{t_B}^{t_E} dt\, \delta T_B^D \delta F_B + \int_{z_S}^{z_B} dz\, \rho c \delta T^{D0} \delta T^0, \\ &z \in [z_S, z_B], t \in [t_B, t_E]\end{aligned} \qquad 9.2.76$$

which – comparing with the misfit function of Equation 9.2.63 – may be recognised as a superposition of Fredholm equations where $\langle \hat{\boldsymbol{\gamma}}^{\boldsymbol{d}}, \delta \boldsymbol{m} \rangle_{\mathrm{M}} \Leftrightarrow \int_{z_S|t_B}^{z_B|t_E} dz|dt\, \hat{\gamma}^d(z,t) \delta m(z|t)$. On the RHS, rightmost terms in the products are components of $\delta \boldsymbol{m}$ and therefore the expressions on the left represent the kernels of $\hat{\boldsymbol{\gamma}}^{\boldsymbol{d}}$ such that

$$\begin{aligned}\hat{\gamma}^{T_S} &= k_S \frac{\partial \delta T_S^D}{\partial z} \\ \hat{\gamma}^{F_B} &= -\delta T_B^D \\ \hat{\gamma}^{k} &= -\int_{t_B}^{t_E} dt \frac{\partial T}{\partial z} \frac{\partial \delta T^D}{\partial z} \\ \hat{\gamma}^{pc} &= -\int_{t_B}^{t_E} dt\, \delta T^D \frac{\partial T}{\partial t} \\ \hat{\gamma}^{S} &= \int_{t_B}^{t_E} dt\, \delta T^D, \qquad z \in [z_S, z_B], t \in [t_B, t_E].\end{aligned} \qquad 9.2.77$$

Elements of this derivation are taken from an alternative and more involved derivation in Shen and Beck (1991). It should be noted that $\hat{\gamma}^{T_S}$, $\hat{\gamma}^{F_B}$ and $\hat{\gamma}^{S}$ are separated into steady and unsteady components in the superposed problem where with steady $\hat{\gamma}^{S^S}$ the integration collapses.

A similar process reveals $\widehat{\boldsymbol{H}}^{\boldsymbol{d}}$ as

$$\langle[\boldsymbol{F}^{*\mathrm{T}}\widehat{\boldsymbol{S}}]\delta\widehat{\boldsymbol{m}},\delta\boldsymbol{T}\rangle_{\mathrm{T}} = \langle\delta S^{D},\delta\boldsymbol{T}\rangle_{\mathrm{T}}$$

$$= \int_{z_S}^{z_B} dz' \int_{t_B}^{t_E} dt'\, G\delta S^{D}\left[-\delta\rho c\frac{\partial T}{\partial t} + \frac{\partial}{\partial z}\left(\delta k\frac{\partial T}{\partial z'}\right) + \delta S\right]$$

a.

$$+ \int_{t_B}^{t_E} dt' k_S \frac{\partial G_S \delta S_S^{D}}{\partial z'}\delta T_S - \int_{t_B}^{t_E} dt'\, G_B \delta S_B^{D}\left[\delta k_B\frac{\partial T_B}{\partial z} + \delta F_B\right],$$

$$z, z' \in [z_S, z_B], t, t' \in [t_B, t_E], \qquad 9.2.78$$

$$\langle\frac{\delta S^{D}}{\delta\boldsymbol{m}},\delta\boldsymbol{T}\rangle_{\mathrm{T}} = \int_{z_S}^{z_B} dz \int_{t_B}^{t_E} dt \frac{\delta T^{D}(z,t)}{\delta\boldsymbol{m}}\left[-\delta\rho c\frac{\partial T}{\partial t} + \frac{\partial}{\partial z}\left(\delta k\frac{\partial T}{\partial z'}\right) + \delta S\right]$$

b.

$$+ \int_{t_B}^{t_E} dt' k_S \frac{\partial \delta T_S^{D}}{\partial z'\delta\boldsymbol{m}}\delta T_S + \int_{t_B}^{t_E} dt \frac{\delta T_B^{D}}{\delta\boldsymbol{m}}\left[\delta k_B\frac{\partial T_B}{\partial z} + \delta F_B\right],$$

$$z \in [z_S, z_B], t \in [t_B, t_E],$$

As noted earlier the second order term (Equation 9.2.78b) is small and can lead to instabilities. Additionally taking the calculation any further appears cumbersome. It is therefore left at this stage and the optimization is further developed in quasi-Newtonian fashion involving only Equation 9.2.78a. Therefore, the first order Hessian term, as with the Fréchet term is

$$\langle\delta S^{D},\delta\boldsymbol{T}\rangle_{\mathrm{T}} = \langle\widehat{\boldsymbol{H}}^{\boldsymbol{d}}\delta\boldsymbol{m},\delta\boldsymbol{m}\rangle_{\mathrm{M}}$$

$$= -\int_{z_S}^{z_B} dz \int_{t_B}^{t_E} dt \frac{\partial\delta T^{D}}{\partial z}\frac{\partial T}{\partial z}\delta k - \int_{z_S}^{z_B} dz \int_{t_B}^{t_E} dt\, \delta T^{D}\frac{\partial T}{\partial t}\delta\rho c$$

$$- \delta S\int_{z_S}^{z_B} dz \int_{t_B}^{t_E} dt \frac{\partial^2\delta T^{D}}{\partial z\partial t} + \int_{z_S}^{z_B} dz \int_{t_B}^{t_E} dt\, \delta T^{D}\delta S \qquad 9.2.79$$

$$+ \int_{t_B}^{t_E} dt k_S \frac{\partial\delta T_S^{D}}{\partial z}\delta T_S - \int_{t_B}^{t_E} dt\, \delta T_B^{D}\delta F_B, \qquad z \in [z_S, z_B], t \in [t_B, t_E].$$

On the RHS, all the rightmost terms in the products are components of $\delta\boldsymbol{m}$ and therefore the expressions on the left represent $\widehat{\boldsymbol{H}}^{\boldsymbol{d}}\delta\boldsymbol{m}$ giving the kernels as

$$\widehat{\boldsymbol{H}}^{Ts} = -\frac{\partial}{\delta T_S}\left(k_S \frac{\partial \delta T_S^D}{\partial z}\right) \equiv \frac{\partial \widehat{\boldsymbol{\gamma}}^{Ts}}{\delta T_S}$$

$$\widehat{\boldsymbol{H}}^{F_B} = -\frac{\partial \delta T_B^D}{\delta F_B} \equiv \frac{\partial \widehat{\boldsymbol{\gamma}}^{F_B}}{\delta F_B}$$

$$\widehat{\boldsymbol{H}}^{k} = -\int_{t_B}^{t_E} dt \frac{\partial}{\delta k}\left(\frac{\partial T}{\partial z}\frac{\partial \delta T^D}{\partial z}\right) \equiv \frac{\partial \widehat{\boldsymbol{\gamma}}^{k}}{\delta k} \qquad \textbf{9.2.80}$$

$$\widehat{\boldsymbol{H}}^{pc} = -\int_{t_B}^{t_E} dt \frac{\partial}{\delta \rho c}\left(\delta T^D \frac{\partial T}{\partial t}\right) \equiv \frac{\partial \widehat{\boldsymbol{\gamma}}^{pc}}{\delta \rho c}$$

$$\widehat{\boldsymbol{H}}^{S} = \int_{t_B}^{t_E} dt \frac{\partial \delta T^D}{\delta S} \equiv \frac{\partial \widehat{\boldsymbol{\gamma}}^{S}}{\delta S}, \qquad z \in [z_S, z_B], t \in [t_B, t_E].$$

As with the Fréchet derivative $\widehat{\boldsymbol{H}}^{Ts}$, $\widehat{\boldsymbol{H}}^{F_B}$ and $\widehat{\boldsymbol{H}}^{S}$ are separated into steady and unsteady components in the superposed problem where steady $\widehat{\boldsymbol{H}}^{S^S}$ the integrations collapses.

9.2.3 References

ARFKEN, G. B. & WEBER, H.-J. 2005. *Mathematical Methods for Physicists,* Amsterdam ; London, Elsevier Academic.

CARSLAW, H. S. & JAEGER, J. C. 1973. *Conduction of Heat in Solids,* Oxford, Clarendon.

LINDQVIST, J. G. 1984. Heat flow density measurements in the sediments of three lakes in Northern Sweden. *Tectonophysics,* 103, 121-140.

PATANKAR, S. V. 1980. *Numerical Heat Transfer and Fluid Flow,* New York, NY; London, Hemisphere.

SHEN, P. Y. & BECK, A. E. 1991. Least Squares Inversion of Borehole Temperature Measurements in Functional Space. *J. Geophys. Res.,* 96, 19965-19979.

TARANTOLA, A. 2005. *Inverse problem theory and methods for model parameter estimation,* Philadelphia, PA, Society for Industrial and Applied Mathematics.

9.3 Forward Models

9.3.1 Perfect Layer Contact Parameters

Table 9.3.1 shows the parameters used to simulate the steady temperature for the layered medium with perfect contact, in Section 3.3.1, with derived steady heat flow for each layer.

Table 9.3.1. Parameters used to simulate temperature in a layered medium with perfect contact with derived steady heat flow F^S. Parameter z is depth, k conductivity, T^S the steady temperature, $\frac{\Delta T^S}{\Delta z}$ the steady temperature gradient.

	LAYER	z [m]	k [W/m/K]	T^S [K]	$\frac{\Delta T^S}{\Delta z}$ [K/m]	F^S [W/m^2]
1	SURFACE	0.00	0.03	287.15	-2.49	0.075
	BASE	1.52		290.93		
2	SURFACE		0.30		-0.25	0.075
	BASE	3.03		291.31		
3	SURFACE		3.00		-0.025	0.076
	BASE	5.00		291.36		

Note that as k increases by factors of ten, $\frac{\Delta T^S}{\Delta z}$ decreases by factors of ten such that F^S remains (approximately, given the numerical errors) constant.

9.3.2 Imperfect Layer Contact Parameters

Table 9.3.2 shows the parameters used to simulate the steady temperature for the layered medium with imperfect contact, in Section 3.3.2, with derived steady heat flow for each layer.

Table 9.3.2. Parameters used to simulate temperature in a layered medium with perfect contact with derived steady heat flow F^S. Parameter z is depth, h_i the Hertz factor, k conductivity, T^S the steady temperature, $\frac{\Delta T^S}{\Delta z}$ the steady temperature gradient.

	LAYER	z [m]	h_i[W/k]	k [W/m/K]	T^S [K]	$\frac{\Delta T^S}{\Delta z}$ [K/m]	F^S [W/m^2]
1	SURFACE	0.00		0.03	287.15	-2.50	0.075
	BASE	1.53	0.5		290.97		
2	SURFACE			0.30	293.76	-0.25	0.075
	BASE	3.05	0.75		294.14		
3	SURFACE			3.00	294.32	-0.026	0.077
	BASE	5.00			294.37		

Note that the interface conductivities can be stated as $k_i^{1,2} = 0.0545$ and $k_i^{2,3} = 0.545$ W/m/K (Section 2.1.2.2.1), modified by the Hertz factors to contact conductivities $k_c^{1,2} = 0.0273$ and $k_c^{2,3} = 0.409$ W/m/K. The resulting temperature differences give heat transfer coefficients of $H^{1,2} = 0.027$ and $H^{2,3} = 0.42$ (Section 2.1.2.3), approximately equal to the contact conductivities – this indicates that for any interface i, $H_i = h_i k_i$.

9.3.3 Lunar Surface Energy Balance Parameters

The parameters used in the lunar surface energy balance calculations of Section 3.6 are listed in Table 9.3.3 (see Section 2.2.5 for discussion and Appendix 9.1 for symbol definitions).

Table 9.3.3. Surface energy balance parameters used to calculate the surface temperature for lunar site at the sub-solar point.

PARAMETER	VALUE
Solar Constant S^o [W/m^2]	1370
Bond albedo A	0.12
Emissivity ε	0.92
Heliocentric Orbit	
Aphelion [m]	1.52098E11
Perihelion [m]	1.47099E11
Eccentricity	0.016710219
Geocentric Orbit	
Aphelion [m]	4.05696E8
Perihelion [m]	3.63104E8
Eccentricity	0.0549

Thermal properties conductivity k and density ρ are plotted in Figure 9.3.1. The specific heat capacity c is 600 J/kg/K and constant with depth.

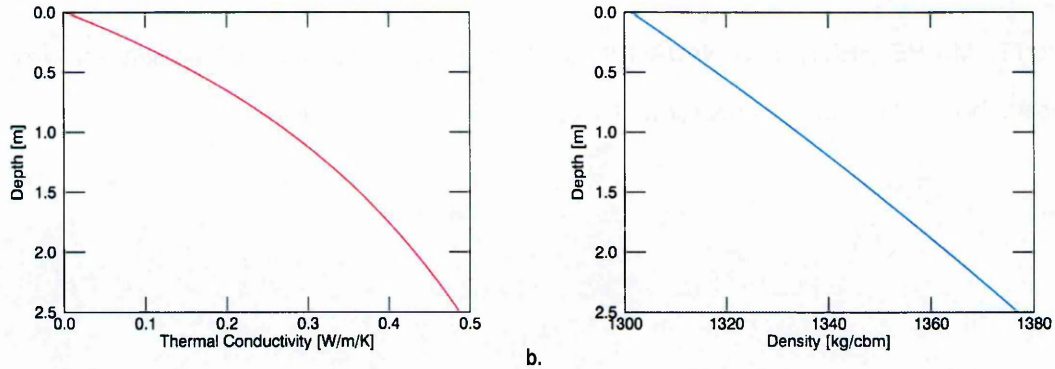

Figure 9.3.1. Conductivity k and density ρ used in lunar surface energy balance calculations. These are calculated on a 1000 point grid and are based on the formulas presented in Grott et al. (2007).

9.3.4 References

GROTT, M., HELBERT, J. & NADALINI, R. 2007. Thermal structure of Martian soil and the measurability of the planetary heat flow. *J. Geophys. Res.*, 112, E09004.

9.4 Misfit Function Optimization

9.4.1 Notation

Before presenting the test results, it is prudent to outline the general principles underlying the notation used. Model parameters $\boldsymbol{m}$ are defined such that $\boldsymbol{m} \ni m \Leftrightarrow [T_S^U, T_S^S, F_B, k, \rho, c, S]$. Using A_B^C to represent an arbitrary model parameter: A_B^{CT} is the true value, A_B^{C0} the initial guess and A_B^{CI} the optimized value (the value at which the algorithm is terminated). Therefore superscripts T, 0 and I always reference true, initial (a priori) and final (a posteriori) parameter values, respectively. Likewise, arbitrary measure a_m is associated with model parameter $m \Leftrightarrow A_B^C$. Specific measures used below include ϵ_m, a measure of relative error between model parameter estimates and true values. As a general rule, $|\epsilon_m| < 1$ indicates improvements in the estimate of a model parameter: the smaller the value of $|\epsilon_m|$, the more accurate is the improved value of the model parameter.

The measures mentioned above are based on the results of optimization tests involving a range of initial model parameter estimates, and associated errors. The results lead to a 'space' of different parameters (e.g. see tables in Appendix) which, collectively, measure how effectively a particular initialization of the inverse model optimizes a model parameter. These parameter results may be distributions of a few 10s or 100s or 1000s of data points which are presentable in 3D scatter plots. These points are interpolated using different 3D interpolation methods[1], to highlight particular trends within the dataset, and presented as contour plots. Some methods of interpolation work better than others for different datasets, therefore different methods are used based on which method best reproduces the distribution as shown in the scatter plots. Results are also confirmed using the tabulated data.

[1] The 3D interpolation methods used are Inverse Distance, Minimum Curvature, Quintic and Linear.

Here results are presented which complement those presented in Chapter 3. Some results are tabulated to allow direct comparison of figures and numbers – the quantity σ_{m^I} is the standard deviation of the solution, which is interpreted relative to the standard deviation σ_{m^0} of the a priori model.

9.4.2 Basal Heat Flow

Figure 9.4.1 shows the delta distribution of relative error in optimized basal heat flow F_B^S for tests where stepsize $\mu = 1$ and 0.5. The two distributions are essentially identical though the convergence at large $\epsilon_{F_B^S}$ is marginally better for the case with $\mu = 0.5$. The values far from $\epsilon_{F_B^S} = 0$ are where the F_B^S standard deviation $\sigma_{F_B^S}$ is underestimated relative to the standard deviation σ_d of the inverted temperature measurement.

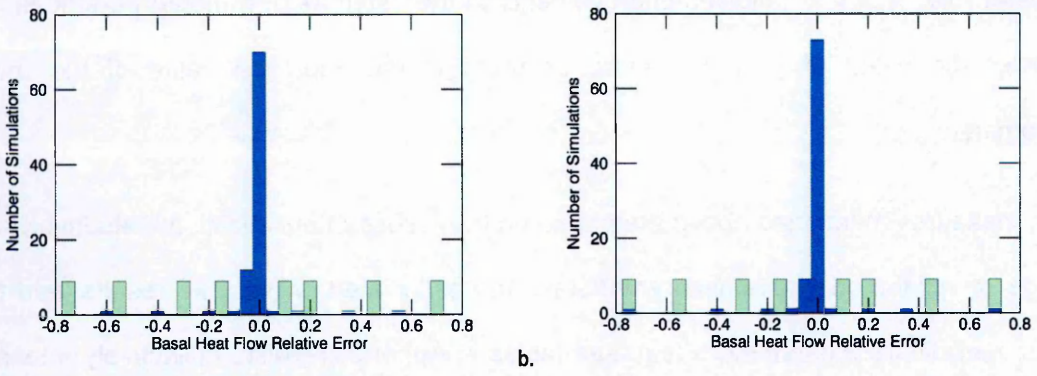

Figure 9.4.1. Accuracy of optimized basal heat flow $\epsilon_{F_B^S}$ (blue histogram) from inversion of subsurface temperature measurement generated by a sinusoidal surface temperature with a 360 d period. The light green background histogram is the initial distribution of F_B^S error. Plot: a. is run with stepsize $\mu = 1$ while; b. is run with stepsize $\mu = 0.5$. The histogram binsize is 0.05.

Figure 9.4.2 shows general trends in the results highlighting the likelihood of convergence in different regions of the solution space when $\mu = 0.5$. The contours are interpolated from 3D scatterplots – the values can be considered as central estimators and are not exclusively associated with any single data point.

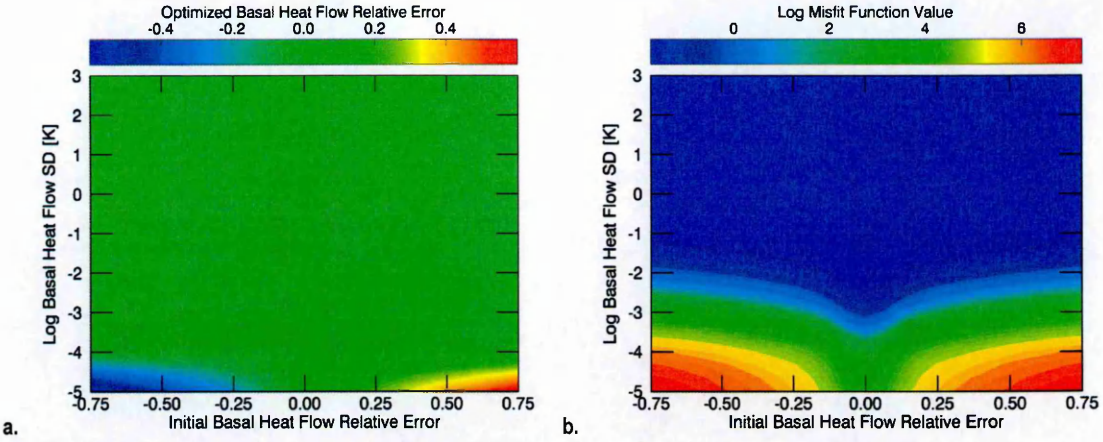

Figure 9.4.2. Trends in the optimization of basal heat flow F_B^S from ideal data with stepsize $\mu_l = 0.5$. Contour: a. shows trends in the relative error $\epsilon_{F_B^{SI}} = \frac{F_B^{SI}}{F_B^{ST}} - 1$ of optimal estimates F_B^{SI} to the true value F_B^{ST}, with respect to initial relative error $\epsilon_{F_B^{S0}} = \frac{F_B^{S0}}{F_B^{ST}} - 1$ of initial estimates F_B^{S0} to the true value F_B^{ST}, and standard deviation $\sigma_{F_B^S}$; b. shows trends in the misfit function value ($\log_{10} S_{m_l}$) at the optimal point. Symbol are defined in the text and Appendix 9.1.

The trends show that the case with $\mu = 0.5$ produces marginally smaller errors in the optimized F_B^S than the equivalent case with $\mu = 1$ discussed in Section 4.2.1.1.

Figure 9.4.3 shows an example of the progression of the algorithm to convergence. The results are essentially similar to the case with $\mu = 1$, except that the smaller stepsize means the space defined by $\boldsymbol{C_d}$ and $\boldsymbol{C_m}$ is explored in more detail requiring more iterations to get to S_{m_l}. This typical illustration shows that the model can be terminated after 2-4 iterations.

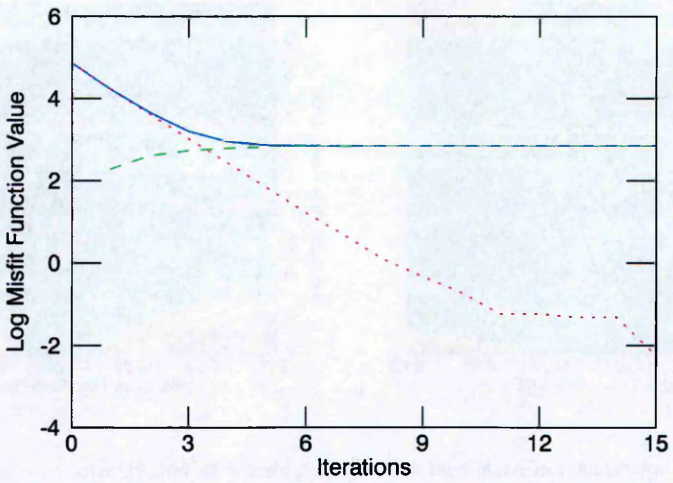

Figure 9.4.3. Convergence of the model in optimizing F_B^S. The base 10 logarithm of the misfit function S_m (solid blue) and its component data $S_{\|d\|}$ (dotted red) and model $S_{\|m\|}$ (dashed green) parameter norms are used to highlight small changes over the number of iterations i. In this simulation standard deviation $\sigma_{F_B^S}$ = 1E-3 W/m², initial relative error $\epsilon_{F_B^{S0}}$ = -0.10 and optimized F_B^S relative error $\epsilon_{F_B^{SI}}$ = 1.11E-5. The general behaviour is similar in other convergent simulations.

The raw numbers from the optimization tests are tabulated below.

Table 9.4.1. Convergence of algorithm for different F_B^S initializations with stepsize $\mu_i = 1$ (also see Section 4.2.1.1). Symbols are defined in Appendix 9.1.

S_{m_0}	S_{m_I}	i	$\epsilon_{F_B^{S0}}$	$\epsilon_{F_B^{SI}}$	$\sigma_{F_B^{S0}}$ [W/m^2]	$\sigma_{F_B^{SI}}$ [W/m^2]
4.31E+06	4.30E+06	2	-0.75	-7.49E-01	1.00E-05	8.93E-06
4.31E+06	3.62E+06	2	-0.75	-2.78E-02	1.00E-04	1.94E-05
4.31E+06	3.90E+04	2	-0.75	-1.25E-04	0.001	1.98E-05
4.31E+06	3.90E+02	2	-0.75	9.23E-05	0.01	1.98E-05
4.31E+06	3.94E+00	2	-0.75	9.86E-05	0.1	1.98E-05
4.31E+06	7.73E-02	2	-0.75	9.84E-05	1	1.98E-05
4.31E+06	3.87E-02	2	-0.75	9.85E-05	10	1.98E-05
4.31E+06	3.83E-02	2	-0.75	9.85E-05	100	1.98E-05
4.31E+06	3.83E-02	2	-0.75	9.85E-05	1000	1.98E-05
1.91E+06	8.39E+06	3	-0.50	-3.98E-01	1.00E-05	8.92E-06
1.91E+06	1.61E+06	2	-0.50	-1.86E-02	1.00E-04	1.94E-05
1.91E+06	1.73E+04	2	-0.50	-9.40E-05	0.001	1.98E-05

1.91E+06	1.73E+02	2	-0.50	7.42E-05	0.01	1.98E-05
1.91E+06	1.78E+00	2	-0.50	8.03E-05	0.1	1.98E-05
1.91E+06	6.12E-02	2	-0.50	8.03E-05	1	1.98E-05
1.91E+06	4.41E-02	2	-0.50	8.04E-05	10	1.98E-05
1.91E+06	4.39E-02	2	-0.50	8.04E-05	100	1.98E-05
1.91E+06	4.39E-02	2	-0.50	8.04E-05	1000	1.98E-05
4.79E+05	2.10E+06	3	-0.25	-1.99E-01	1.00E-05	8.92E-06
4.79E+05	3.98E+05	3	-0.25	-1.07E-02	1.00E-04	1.94E-05
4.79E+05	4.33E+03	20	-0.25	-1.57E-05	0.001	1.98E-05
4.79E+05	4.34E+01	2	-0.25	1.00E-04	0.01	1.98E-05
4.79E+05	4.77E-01	3	-0.25	6.45E-05	0.1	1.98E-05
4.79E+05	4.82E-02	3	-0.25	6.59E-05	1	1.98E-05
4.79E+05	4.40E-02	3	-0.25	6.60E-05	10	1.98E-05
4.79E+05	4.39E-02	3	-0.25	6.60E-05	100	1.98E-05
4.79E+05	4.39E-02	3	-0.25	6.60E-05	1000	1.98E-05
7.67E+04	3.36E+05	3	-0.10	-7.96E-02	1.00E-05	8.92E-06
7.67E+04	6.44E+04	3	-0.10	-3.69E-03	1.00E-04	1.94E-05
7.67E+04	6.93E+02	4	-0.10	1.25E-05	0.001	1.98E-05
7.67E+04	6.98E+00	2	-0.10	1.00E-04	0.01	1.98E-05
7.67E+04	1.08E-01	2	-0.10	1.02E-04	0.1	1.98E-05
7.67E+04	3.90E-02	2	-0.10	1.02E-04	1	1.98E-05
7.67E+04	3.83E-02	2	-0.10	1.02E-04	10	1.98E-05
7.67E+04	3.83E-02	2	-0.10	1.02E-04	100	1.98E-05
7.67E+04	3.83E-02	2	-0.10	1.02E-04	1000	1.98E-05
1.92E+04	1.91E+04	2	-0.05	-4.90E-02	1.00E-05	8.94E-06
1.92E+04	1.28E+04	2	-0.05	-3.96E-02	1.00E-04	1.94E-05
1.92E+04	1.74E+02	5	-0.05	3.00E-05	0.001	1.98E-05
1.92E+04	1.78E+00	2	-0.05	5.84E-05	0.01	1.98E-05
1.92E+04	6.13E-02	2	-0.05	5.83E-05	0.1	1.98E-05
1.92E+04	4.41E-02	2	-0.05	5.82E-05	1	1.98E-05
1.92E+04	4.39E-02	2	-0.05	5.82E-05	10	1.98E-05

1.92E+04	4.39E-02	2	-0.05	5.82E-05	100	1.98E-05
1.92E+04	4.39E-02	2	-0.05	5.82E-05	1000	1.98E-05
1.91E+04	1.90E+04	2	0.05	4.90E-02	1.00E-05	8.94E-06
1.91E+04	1.27E+04	2	0.05	3.96E-02	1.00E-04	1.94E-05
1.91E+04	1.73E+02	2	0.05	1.18E-04	0.001	1.98E-05
1.91E+04	1.76E+00	3	0.05	1.09E-04	0.01	1.98E-05
1.91E+04	5.56E-02	3	0.05	1.09E-04	0.1	1.98E-05
1.91E+04	3.85E-02	3	0.05	1.09E-04	1	1.98E-05
1.91E+04	3.83E-02	3	0.05	1.09E-04	10	1.98E-05
1.91E+04	3.83E-02	3	0.05	1.09E-04	100	1.98E-05
1.91E+04	3.83E-02	3	0.05	1.09E-04	1000	1.98E-05
7.65E+04	3.35E+05	20	0.10	7.97E-02	1.00E-05	8.92E-06
7.65E+04	6.42E+04	7	0.10	3.82E-03	1.00E-04	1.94E-05
7.65E+04	6.91E+02	2	0.10	1.32E-04	0.001	1.98E-05
7.65E+04	6.95E+00	7	0.10	1.13E-04	0.01	1.98E-05
7.65E+04	1.07E-01	7	0.10	1.10E-04	0.1	1.98E-05
7.65E+04	3.90E-02	7	0.10	1.10E-04	1	1.98E-05
7.65E+04	3.83E-02	7	0.10	1.10E-04	10	1.98E-05
7.65E+04	3.83E-02	7	0.10	1.10E-04	100	1.98E-05
7.65E+04	3.83E-02	7	0.10	1.10E-04	1000	1.98E-05
4.78E+05	4.75E+05	2	0.25	2.49E-01	1.00E-05	8.94E-06
4.78E+05	4.03E+05	2	0.25	8.96E-03	1.00E-04	1.94E-05
4.78E+05	4.33E+03	2	0.25	1.13E-04	0.001	1.98E-05
4.78E+05	4.33E+01	6	0.25	1.11E-04	0.01	1.98E-05
4.78E+05	4.71E-01	6	0.25	1.12E-04	0.1	1.98E-05
4.78E+05	4.27E-02	6	0.25	1.13E-04	1	1.98E-05
4.78E+05	3.84E-02	6	0.25	1.13E-04	10	1.98E-05
4.78E+05	3.83E-02	6	0.25	1.13E-04	100	1.98E-05
4.78E+05	3.83E-02	6	0.25	1.13E-04	1000	1.98E-05
1.91E+06	8.39E+06	20	0.50	3.98E-01	1.00E-05	8.93E-06
1.91E+06	1.61E+06	2	0.50	1.88E-02	1.00E-04	1.94E-05

1.91E+06	1.73E+04	2	0.50	2.62E-04	0.001	1.98E-05
1.91E+06	1.73E+02	5	0.50	1.14E-04	0.01	1.98E-05
1.91E+06	1.77E+00	6	0.50	1.10E-04	0.1	1.98E-05
1.91E+06	5.57E-02	6	0.50	1.10E-04	1	1.98E-05
1.91E+06	3.85E-02	6	0.50	1.10E-04	10	1.98E-05
1.91E+06	3.83E-02	6	0.50	1.10E-04	100	1.98E-05
1.91E+06	3.83E-02	6	0.50	1.10E-04	1000	1.98E-05
4.31E+06	4.29E+06	2	0.75	7.49E-01	1.00E-05	8.93E-06
4.31E+06	3.62E+06	2	0.75	2.80E-02	1.00E-04	1.94E-05
4.31E+06	3.90E+04	2	0.75	2.95E-04	0.001	1.98E-05
4.31E+06	3.90E+02	5	0.75	1.07E-04	0.01	1.98E-05
4.31E+06	3.94E+00	7	0.75	1.13E-04	0.1	1.98E-05
4.31E+06	7.73E-02	7	0.75	1.13E-04	1	1.98E-05
4.31E+06	3.87E-02	7	0.75	1.13E-04	10	1.98E-05
4.31E+06	3.83E-02	7	0.75	1.13E-04	100	1.98E-05
4.31E+06	3.83E-02	7	0.75	1.13E-04	1000	1.98E-05

Table 9.4.2. Convergence of algorithm for different F_B^S initializations with stepsize $\mu_i = 0.5$ (symbols are defined in Appendix 9.1).

S_{m_0}	S_{m_I}	i	$\epsilon_{F_B^{S0}}$	$\epsilon_{F_B^{SI}}$	$\sigma_{F_B^{S0}}$ [W/m^2]	$\sigma_{F_B^{SI}}$ [W/m^2]
4.23E+06	1.84E+07	68	-0.75	-6.00E-01	1.00E-05	8.94E-06
4.23E+06	3.61E+06	17	-0.75	-2.87E-02	1.00E-04	1.96E-05
4.23E+06	3.90E+04	41	-0.75	-2.51E-04	0.001	2.00E-05
4.23E+06	3.90E+02	14	-0.75	-3.49E-05	0.01	2.00E-05
4.23E+06	3.92E+00	19	-0.75	4.30E-05	0.1	2.00E-05
4.23E+06	5.80E-02	22	-0.75	3.48E-05	1	2.00E-05
4.23E+06	1.94E-02	26	-0.75	3.82E-05	10	2.00E-05
4.23E+06	1.90E-02	29	-0.75	4.04E-05	100	2.00E-05
4.23E+06	1.90E-02	32	-0.75	3.83E-05	1000	2.00E-05
1.88E+06	8.17E+06	65	-0.50	-4.00E-01	1.00E-05	8.94E-06

1.88E+06	1.61E+06	18	-0.50	-1.91E-02	1.00E-04	1.96E-05
1.88E+06	1.73E+04	20	-0.50	-1.66E-04	0.001	2.00E-05
1.88E+06	1.73E+02	11	-0.50	2.51E-05	0.01	2.00E-05
1.88E+06	1.75E+00	18	-0.50	4.00E-05	0.1	2.00E-05
1.88E+06	3.63E-02	22	-0.50	2.83E-05	1	2.00E-05
1.88E+06	1.92E-02	25	-0.50	4.53E-05	10	2.00E-05
1.88E+06	1.90E-02	28	-0.50	4.86E-05	100	2.00E-05
1.88E+06	1.90E-02	32	-0.50	3.98E-05	1000	2.00E-05
4.70E+05	2.04E+06	66	-0.25	-2.00E-01	1.00E-05	8.94E-06
4.70E+05	4.01E+05	15	-0.25	-9.55E-03	1.00E-04	1.96E-05
4.70E+05	4.33E+03	15	-0.25	-8.10E-05	0.001	2.00E-05
4.70E+05	4.34E+01	14	-0.25	4.19E-05	0.01	2.00E-05
4.70E+05	4.52E-01	18	-0.25	4.40E-05	0.1	2.00E-05
4.70E+05	2.33E-02	22	-0.25	3.59E-05	1	2.00E-05
4.70E+05	1.91E-02	26	-0.25	4.05E-05	10	2.00E-05
4.70E+05	1.90E-02	29	-0.25	4.35E-05	100	2.00E-05
4.70E+05	1.90E-02	32	-0.25	3.59E-05	1000	2.00E-05
7.52E+04	3.27E+05	62	-0.10	-7.99E-02	1.00E-05	8.94E-06
7.52E+04	6.43E+04	17	-0.10	-3.80E-03	1.00E-04	1.96E-05
7.52E+04	6.93E+02	15	-0.10	-1.11E-05	0.001	2.00E-05
7.52E+04	6.95E+00	15	-0.10	2.98E-05	0.01	2.00E-05
7.52E+04	8.84E-02	18	-0.10	4.56E-05	0.1	2.00E-05
7.52E+04	1.97E-02	22	-0.10	2.72E-05	1	2.00E-05
7.52E+04	1.90E-02	26	-0.10	4.38E-05	10	2.00E-05
7.52E+04	1.90E-02	29	-0.10	4.04E-05	100	2.00E-05
7.52E+04	1.90E-02	32	-0.10	3.84E-05	1000	2.00E-05
1.88E+04	8.19E+04	18	-0.05	-4.00E-02	1.00E-05	8.94E-06
1.88E+04	1.61E+04	200	-0.05	-1.90E-03	1.00E-04	1.96E-05
1.88E+04	1.73E+02	12	-0.05	-1.55E-05	0.001	2.00E-05
1.88E+04	1.75E+00	15	-0.05	2.77E-05	0.01	2.00E-05
1.88E+04	3.64E-02	19	-0.05	4.25E-05	0.1	2.00E-05

1.88E+04	1.92E-02	22	-0.05	3.53E-05	1	2.00E-05
1.88E+04	1.90E-02	26	-0.05	4.06E-05	10	2.00E-05
1.88E+04	1.90E-02	29	-0.05	4.31E-05	100	2.00E-05
1.88E+04	1.90E-02	32	-0.05	5.14E-05	1000	2.00E-05
1.88E+04	8.16E+04	61	0.05	4.00E-02	1.00E-05	8.94E-06
1.88E+04	1.60E+04	12	0.05	1.98E-03	1.00E-04	1.96E-05
1.88E+04	1.73E+02	12	0.05	5.87E-05	0.001	2.00E-05
1.88E+04	1.75E+00	62	0.05	5.09E-05	0.01	2.00E-05
1.88E+04	3.63E-02	57	0.05	5.11E-05	0.1	2.00E-05
1.88E+04	1.92E-02	64	0.05	5.05E-05	1	2.00E-05
1.88E+04	1.90E-02	80	0.05	5.14E-05	10	2.00E-05
1.88E+04	1.90E-02	77	0.05	5.11E-05	100	2.00E-05
1.88E+04	1.90E-02	75	0.05	5.05E-05	1000	2.00E-05
7.51E+04	3.27E+05	61	0.10	7.99E-02	1.00E-05	8.94E-06
7.51E+04	6.42E+04	14	0.10	3.85E-03	1.00E-04	1.96E-05
7.51E+04	6.92E+02	14	0.10	5.03E-05	0.001	2.00E-05
7.51E+04	6.94E+00	54	0.10	5.13E-05	0.01	2.00E-05
7.51E+04	8.83E-02	64	0.10	5.06E-05	0.1	2.00E-05
7.51E+04	1.97E-02	65	0.10	5.08E-05	1	2.00E-05
7.51E+04	1.90E-02	68	0.10	5.07E-05	10	2.00E-05
7.51E+04	1.90E-02	74	0.10	5.07E-05	100	2.00E-05
7.51E+04	1.90E-02	80	0.10	5.13E-05	1000	2.00E-05
4.69E+05	2.04E+06	63	0.25	2.00E-01	1.00E-05	8.94E-06
4.69E+05	4.01E+05	15	0.25	9.62E-03	1.00E-04	1.96E-05
4.69E+05	4.33E+03	14	0.25	1.38E-04	0.001	2.00E-05
4.69E+05	4.33E+01	48	0.25	5.03E-05	0.01	2.00E-05
4.69E+05	4.52E-01	68	0.25	5.04E-05	0.1	2.00E-05
4.69E+05	2.33E-02	70	0.25	5.15E-05	1	2.00E-05
4.69E+05	1.91E-02	67	0.25	5.04E-05	10	2.00E-05
4.69E+05	1.90E-02	73	0.25	5.12E-05	100	2.00E-05
4.69E+05	1.90E-02	73	0.25	5.05E-05	1000	2.00E-05

1.88E+06	8.17E+06	64	0.50	4.00E-01	1.00E-05	8.94E-06
1.88E+06	1.61E+06	21	0.50	1.92E-02	1.00E-04	1.96E-05
1.88E+06	1.73E+04	18	0.50	2.09E-04	0.001	2.00E-05
1.88E+06	1.73E+02	32	0.50	5.07E-05	0.01	2.00E-05
1.88E+06	1.75E+00	55	0.50	5.08E-05	0.1	2.00E-05
1.88E+06	3.63E-02	72	0.50	5.05E-05	1	2.00E-05
1.88E+06	1.92E-02	71	0.50	5.07E-05	10	2.00E-05
1.88E+06	1.90E-02	73	0.50	5.04E-05	100	2.00E-05
1.88E+06	1.90E-02	69	0.50	5.12E-05	1000	2.00E-05
4.23E+06	1.84E+07	65	0.75	6.00E-01	1.00E-05	8.94E-06
4.23E+06	3.61E+06	16	0.75	2.88E-02	1.00E-04	1.96E-05
4.23E+06	3.90E+04	21	0.75	3.00E-04	0.001	2.00E-05
4.23E+06	3.90E+02	14	0.75	7.83E-05	0.01	2.00E-05
4.23E+06	3.92E+00	59	0.75	5.08E-05	0.1	2.00E-05
4.23E+06	5.80E-02	69	0.75	5.09E-05	1	2.00E-05
4.23E+06	1.94E-02	78	0.75	5.06E-05	10	2.00E-05
4.23E+06	1.90E-02	75	0.75	5.14E-05	100	2.00E-05
4.23E+06	1.90E-02	74	0.75	5.07E-05	1000	2.00E-05

9.4.3 Steady Surface Temperature

Figure 9.4.4 shows the delta distribution of relative error in optimized steady surface temperature T_S^S for tests where stepsize $\mu = 1$ and 0.5. As with F_B^S the two distributions are similar though with more instability at $\mu = 0.5$ as evidenced by initializations which fail to converge. Figure 9.4.6 shows the progression of the algorithm to convergence.

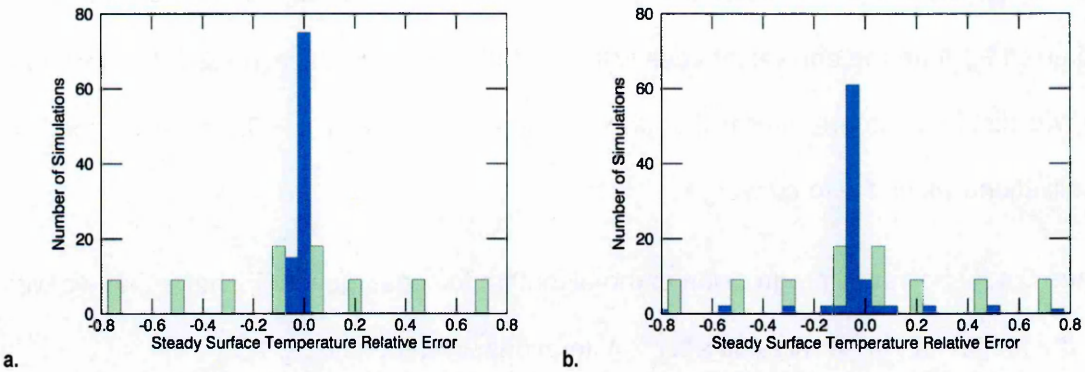

Figure 9.4.4. Accuracy of optimized steady surface temperature $\epsilon_{T_S^S}$ (blue histogram) from inversion of subsurface temperature measurement generated by a sinusoidal surface temperature with a 360 d period. The light green background histogram is the initial distribution of T_S^S error. Plot: a. is run with stepsize $\mu = 1$ while; b. is run with stepsize $\mu = 0.5$. The histogram binsize is 0.05.

Figure 9.4.2 shows general trends in the results highlighting the likelihood of convergence in different regions of the solution space when $\mu = 0.5$. The contours are interpolated from 3D scatterplots – the values can be considered as central estimators and are not exclusively associated with any single data point.

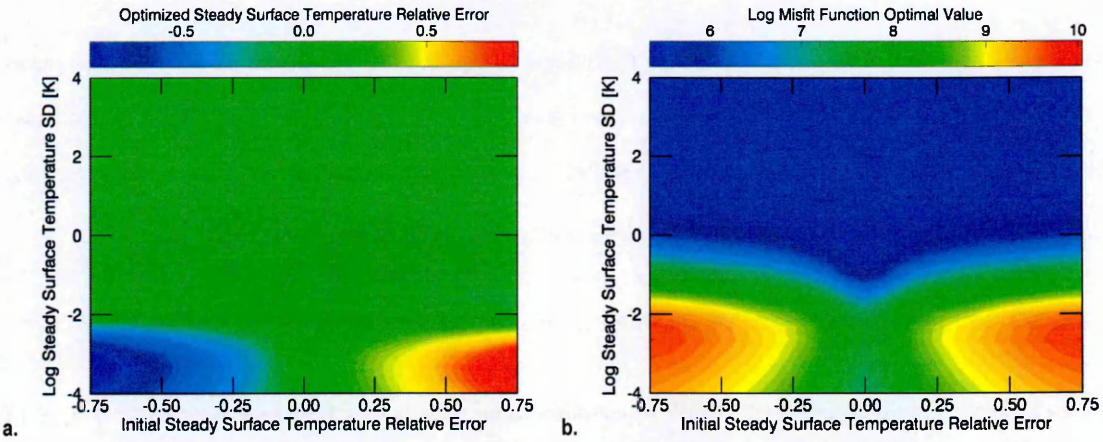

Figure 9.4.5. Trends in the optimization of steady surface temperature T_S^S from ideal data with stepsize $\mu_i = 0.5$. Contour: a. shows trends in the relative error $\epsilon_{T_S^{SI}} = \frac{T_S^{SI}}{T_S^{ST}} - 1$ of optimal estimates T_S^{SI} to the true value T_S^{ST}, with respect to initial relative error $\epsilon_{T_S^{S0}} = \frac{T_S^{S0}}{T_S^{ST}} - 1$ of initial estimates T_S^{S0} to the true value T_S^{ST}, and standard deviation $\sigma_{T_S^S}$; b. shows trends in the optimizal misfit function value $\log_{10} S_{m_f}$. Symbol are defined in the text and Appendix 9.1.

The trends show that the case with $\mu = 0.5$ produces marginally smaller errors in the optimized F_B^S than the equivalent case with $\mu = 1$ discussed in Section 4.2.2.1. As with F_B^S the two distributions are similar though with more instability at $\mu = 0.5$ as evidenced by initializations which fail to converge.

Figure 9.4.6 shows the progression of the algorithm to convergence. It shows that, as with F_B^S, the model can be terminated after 2-4 iterations when optimizing T_S^S.

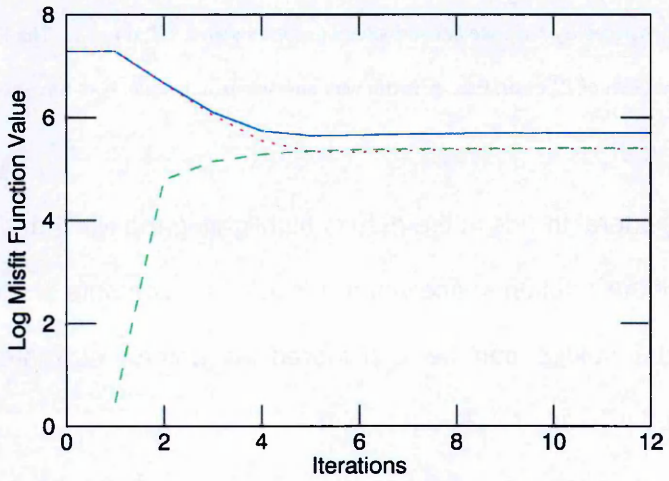

Figure 9.4.6. Convergence of the model in optimizing T_S^S. The base 10 logarithm of the misfit function S_m (solid blue) and its component data $S_{\|d\|}$ (dotted red) and model $S_{\|m\|}$ (dashed green) parameter norms are used to highlight small changes over the number of iterations i. In this simulation standard deviation $\sigma_{T_S^S} = 0.1$ K, initial relative error $\epsilon_{T_S^{S0}} =$ -0.05 and optimized T_S^S relative error $\epsilon_{T_S^{SI}} =$ -9.4E-6. The general behaviour is similar in other convergent simulations.

The raw numbers from the optimization tests are tabulated below.

Table 9.4.3. Convergence of algorithm for different T_S^S initializations for stepsize $\mu_i = 1$ (also see Section 4.2.2.1). Symbols are defined in Appendix 9.1.

S_{m_0}	S_{m_I}	i	$\epsilon_{T_S^{S0}}$	$\epsilon_{T_S^{SI}}$	$\sigma_{T_S^{S0}}$ [K]	$\sigma_{T_S^{SI}}$ [K]
5.11E+13	5.55E+11	3	-0.75	-1.03E-03	0.001	2.47E-05
5.11E+13	5.57E+09	3	-0.75	-9.43E-05	0.01	2.47E-05
5.11E+13	5.58E+07	2	-0.75	4.04E-05	0.1	2.47E-05
5.11E+13	5.57E+05	3	-0.75	0.00E+00	1	2.47E-05

5.11E+13	5.57E+03	3	-0.75	0.00E+00	10	2.47E-05
5.11E+13	5.57E+01	3	-0.75	0.00E+00	100	2.47E-05
5.11E+13	5.86E-01	3	-0.75	0.00E+00	1000	2.47E-05
5.11E+13	3.53E-02	3	-0.75	0.00E+00	10000	2.47E-05
5.11E+13	4.31E-02	3	-0.75	0.00E+00	100000	2.47E-05
2.27E+13	2.48E+11	3	-0.50	2.40E-04	0.001	2.47E-05
2.27E+13	2.47E+09	2	-0.50	2.99E-05	0.01	2.47E-05
2.27E+13	2.47E+07	3	-0.50	-9.05E-07	0.1	2.47E-05
2.27E+13	2.47E+05	2	-0.50	0.00E+00	1	2.47E-05
2.27E+13	2.47E+03	2	-0.50	0.00E+00	10	2.47E-05
2.27E+13	2.48E+01	2	-0.50	3.48E-08	100	2.47E-05
2.27E+13	2.77E-01	2	-0.50	0.00E+00	1000	2.47E-05
2.27E+13	3.22E-02	2	-0.50	0.00E+00	10000	2.47E-05
2.27E+13	4.30E-02	2	-0.50	0.00E+00	100000	2.47E-05
5.67E+12	6.19E+10	3	-0.25	1.20E-04	0.001	2.47E-05
5.67E+12	6.18E+08	3	-0.25	-3.14E-05	0.01	2.47E-05
5.67E+12	6.18E+06	3	-0.25	-4.53E-07	0.1	2.47E-05
5.67E+12	6.18E+04	2	-0.25	0.00E+00	1	2.47E-05
5.67E+12	6.18E+02	2	-0.25	0.00E+00	10	2.47E-05
5.67E+12	6.21E+00	2	-0.25	0.00E+00	100	2.47E-05
5.67E+12	8.36E-02	2	-0.25	0.00E+00	1000	2.47E-05
5.67E+12	3.04E-02	2	-0.25	0.00E+00	10000	2.47E-05
5.67E+12	2.98E-02	2	-0.25	0.00E+00	100000	2.47E-05
9.08E+11	9.90E+09	3	-0.10	4.79E-05	0.001	2.47E-05
9.08E+11	9.89E+07	3	-0.10	-1.26E-05	0.01	2.47E-05
9.08E+11	9.89E+05	3	-0.10	-1.74E-07	0.1	2.47E-05
9.08E+11	9.89E+03	2	-0.10	0.00E+00	1	2.47E-05
9.08E+11	9.90E+01	2	-0.10	0.00E+00	10	2.47E-05
9.08E+11	1.01E+00	2	-0.10	0.00E+00	100	2.47E-05
9.08E+11	3.16E-02	2	-0.10	0.00E+00	1000	2.47E-05
9.08E+11	2.98E-02	2	-0.10	0.00E+00	10000	2.47E-05

9.08E+11	2.97E-02	2	-0.10	0.00E+00	100000	2.47E-05
2.27E+11	2.48E+09	3	-0.05	2.40E-05	0.001	2.47E-05
2.27E+11	2.47E+07	3	-0.05	2.09E-07	0.01	2.47E-05
2.27E+11	2.47E+05	5	-0.05	3.48E-08	0.1	2.47E-05
2.27E+11	2.47E+03	4	-0.05	0.00E+00	1	2.47E-05
2.27E+11	2.48E+01	2	-0.05	0.00E+00	10	2.47E-05
2.27E+11	2.66E-01	2	-0.05	0.00E+00	100	2.47E-05
2.27E+11	2.14E-02	2	-0.05	0.00E+00	1000	2.47E-05
2.27E+11	5.71E-03	3	-0.05	0.00E+00	10000	2.47E-05
2.27E+11	1.89E-02	2	-0.05	0.00E+00	100000	2.47E-05
2.27E+11	2.48E+09	3	0.05	-2.40E-05	0.001	2.47E-05
2.27E+11	2.47E+07	3	0.05	-2.09E-07	0.01	2.47E-05
2.27E+11	2.47E+05	4	0.05	0.00E+00	0.1	2.47E-05
2.27E+11	2.47E+03	16	0.05	0.00E+00	1	2.47E-05
2.27E+11	2.47E+01	16	0.05	0.00E+00	10	2.47E-05
2.27E+11	2.77E-01	2	0.05	0.00E+00	100	2.47E-05
2.27E+11	3.22E-02	2	0.05	0.00E+00	1000	2.47E-05
2.27E+11	2.98E-02	2	0.05	0.00E+00	10000	2.47E-05
2.27E+11	2.97E-02	2	0.05	0.00E+00	100000	2.47E-05
9.08E+11	9.90E+09	3	0.10	-4.79E-05	0.001	2.47E-05
9.08E+11	9.89E+07	3	0.10	1.26E-05	0.01	2.47E-05
9.08E+11	9.89E+05	3	0.10	1.74E-07	0.1	2.47E-05
9.08E+11	9.89E+03	2	0.10	0.00E+00	1	2.47E-05
9.08E+11	9.90E+01	2	0.10	0.00E+00	10	2.47E-05
9.08E+11	9.95E-01	7	0.10	0.00E+00	100	2.47E-05
9.08E+11	1.56E-02	6	0.10	0.00E+00	1000	2.47E-05
9.08E+11	5.78E-03	8	0.10	0.00E+00	10000	2.47E-05
9.08E+11	5.68E-03	9	0.10	0.00E+00	100000	2.47E-05
5.67E+12	6.19E+10	3	0.25	-1.20E-04	0.001	2.47E-05
5.67E+12	6.18E+08	3	0.25	3.14E-05	0.01	2.47E-05
5.67E+12	6.18E+06	3	0.25	4.53E-07	0.1	2.47E-05

5.67E+12	6.18E+04	5	0.25	0.00E+00	1	2.47E-05
5.67E+12	6.18E+02	7	0.25	0.00E+00	10	2.47E-05
5.67E+12	6.19E+00	5	0.25	0.00E+00	100	2.47E-05
5.67E+12	6.75E-02	9	0.25	0.00E+00	1000	2.47E-05
5.67E+12	6.30E-03	7	0.25	0.00E+00	10000	2.47E-05
5.67E+12	1.13E-02	3	0.25	0.00E+00	100000	2.47E-05
2.27E+13	2.48E+11	3	0.50	-2.40E-04	0.001	2.47E-05
2.27E+13	2.47E+09	2	0.50	-2.99E-05	0.01	2.47E-05
2.27E+13	2.47E+07	3	0.50	9.05E-07	0.1	2.47E-05
2.27E+13	2.47E+05	7	0.50	0.00E+00	1	2.47E-05
2.27E+13	2.47E+03	11	0.50	0.00E+00	10	2.47E-05
2.27E+13	2.48E+01	14	0.50	0.00E+00	100	2.47E-05
2.27E+13	2.69E-01	2	0.50	0.00E+00	1000	2.47E-05
2.27E+13	2.42E-02	2	0.50	0.00E+00	10000	2.47E-05
2.27E+13	2.18E-02	2	0.50	0.00E+00	100000	2.47E-05
5.11E+13	5.55E+11	3	0.75	1.03E-03	0.001	2.47E-05
5.11E+13	5.57E+09	3	0.75	9.43E-05	0.01	2.47E-05
5.11E+13	5.58E+07	2	0.75	-4.04E-05	0.1	2.47E-05
5.11E+13	5.57E+05	6	0.75	0.00E+00	1	2.47E-05
5.11E+13	5.57E+03	13	0.75	0.00E+00	10	2.47E-05
5.11E+13	5.58E+01	2	0.75	-3.48E-08	100	2.47E-05
5.11E+13	6.00E-01	2	0.75	0.00E+00	1000	2.47E-05
5.11E+13	5.99E-02	2	0.75	3.48E-08	10000	2.47E-05
5.11E+13	1.15E-01	2	0.75	3.48E-08	100000	2.47E-05

Table 9.4.4. Convergence of algorithm for different T_S^S initializations for stepsize $\mu_I = 0.5$ (symbols are defined in Appendix 9.1).

S_{m_0}	S_{m_I}	i	$\epsilon_{T_S^{S0}}$	$\epsilon_{T_S^{SI}}$	$\sigma_{T_S^{S0}}$ [K]	$\sigma_{T_S^{SI}}$ [K]
4.72E+09	4.76E+09	7	-0.75	-7.51E-01	1.00E-04	1.00E-04
4.72E+09	9.43E+09	200	-0.75	-8.13E-01	0.001	1.09E-03

4.72E+09	6.21E+09	6	-0.75	4.12E-02	0.01	2.63E-03
4.72E+09	5.60E+07	12	-0.75	5.54E-04	0.1	2.55E-03
4.72E+09	8.02E+05	19	-0.75	-4.27E-05	1	2.55E-03
4.72E+09	2.51E+05	25	-0.75	-4.95E-05	10	2.55E-03
4.72E+09	2.45E+05	30	-0.75	-4.95E-05	100	2.55E-03
4.72E+09	2.45E+05	32	-0.75	-4.95E-05	1000	2.55E-03
4.72E+09	2.45E+05	35	-0.75	-4.96E-05	10000	2.55E-03
2.09E+09	2.11E+09	7	-0.50	-5.00E-01	1.00E-04	1.00E-04
2.09E+09	4.18E+09	200	-0.50	-5.42E-01	0.001	1.09E-03
2.09E+09	2.76E+09	6	-0.50	2.75E-02	0.01	2.63E-03
2.09E+09	2.50E+07	12	-0.50	3.53E-04	0.1	2.55E-03
2.09E+09	4.93E+05	19	-0.50	-4.50E-05	1	2.55E-03
2.09E+09	2.48E+05	26	-0.50	-4.95E-05	10	2.55E-03
2.09E+09	2.45E+05	30	-0.50	-4.95E-05	100	2.55E-03
2.09E+09	2.45E+05	31	-0.50	-4.96E-05	1000	2.55E-03
2.09E+09	2.45E+05	35	-0.50	-4.95E-05	10000	2.55E-03
5.18E+08	5.23E+08	7	-0.25	-2.50E-01	1.00E-04	1.00E-04
5.18E+08	1.04E+09	19	-0.25	-2.71E-01	0.001	1.09E-03
5.18E+08	6.90E+08	6	-0.25	1.37E-02	0.01	2.63E-03
5.18E+08	6.44E+06	12	-0.25	1.52E-04	0.1	2.55E-03
5.18E+08	3.07E+05	19	-0.25	-4.73E-05	1	2.55E-03
5.18E+08	2.46E+05	25	-0.25	-4.95E-05	10	2.55E-03
5.18E+08	2.45E+05	29	-0.25	-4.96E-05	100	2.55E-03
5.18E+08	2.45E+05	30	-0.25	-4.96E-05	1000	2.55E-03
5.18E+08	2.45E+05	35	-0.25	-4.95E-05	10000	2.55E-03
8.10E+07	8.17E+07	7	-0.10	-1.00E-01	1.00E-04	1.00E-04
8.10E+07	1.64E+08	200	-0.10	-1.08E-01	0.001	1.09E-03
8.10E+07	1.11E+08	6	-0.10	5.45E-03	0.01	2.63E-03
8.10E+07	1.24E+06	12	-0.10	3.09E-05	0.1	2.55E-03
8.10E+07	2.55E+05	19	-0.10	-4.86E-05	1	2.55E-03
8.10E+07	2.45E+05	27	-0.10	-4.95E-05	10	2.55E-03

8.10E+07	2.45E+05	29	-0.10	-4.95E-05	100	2.55E-03
8.10E+07	2.45E+05	31	-0.10	-4.96E-05	1000	2.55E-03
8.10E+07	2.45E+05	35	-0.10	-4.96E-05	10000	2.55E-03
1.95E+07	1.97E+07	7	-0.05	-5.00E-02	1.00E-04	1.00E-04
1.95E+07	4.03E+07	18	-0.05	-5.42E-02	0.001	1.09E-03
1.95E+07	2.79E+07	6	-0.05	2.70E-03	0.01	2.63E-03
1.95E+07	4.94E+05	12	-0.05	-9.40E-06	0.1	2.55E-03
1.95E+07	2.48E+05	19	-0.05	-4.91E-05	1	2.55E-03
1.95E+07	2.45E+05	31	-0.05	-4.95E-05	10	2.55E-03
1.95E+07	2.45E+05	28	-0.05	-4.96E-05	100	2.55E-03
1.95E+07	2.45E+05	31	-0.05	-4.96E-05	1000	2.55E-03
1.95E+07	2.45E+05	35	-0.05	-4.95E-05	10000	2.55E-03
2.31E+07	2.33E+07	6	0.05	5.00E-02	1.00E-04	1.00E-04
2.31E+07	4.43E+07	19	0.05	5.42E-02	0.001	1.09E-03
2.31E+07	2.78E+07	6	0.05	-2.81E-03	0.01	2.63E-03
2.31E+07	4.92E+05	12	0.05	-9.00E-05	0.1	2.55E-03
2.31E+07	2.48E+05	19	0.05	-5.00E-05	1	2.55E-03
2.31E+07	2.45E+05	23	0.05	-4.96E-05	10	2.55E-03
2.31E+07	2.45E+05	27	0.05	-4.96E-05	100	2.55E-03
2.31E+07	2.45E+05	31	0.05	-4.96E-05	1000	2.55E-03
2.31E+07	2.45E+05	35	0.05	-4.96E-05	10000	2.55E-03
8.81E+07	8.89E+07	6	0.10	1.00E-01	1.00E-04	1.00E-04
8.81E+07	1.72E+08	19	0.10	1.08E-01	0.001	1.09E-03
8.81E+07	1.11E+08	6	0.10	-5.56E-03	0.01	2.63E-03
8.81E+07	1.23E+06	12	0.10	-1.30E-04	0.1	2.55E-03
8.81E+07	2.55E+05	19	0.10	-5.05E-05	1	2.55E-03
8.81E+07	2.45E+05	24	0.10	-4.96E-05	10	2.55E-03
8.81E+07	2.45E+05	28	0.10	-4.95E-05	100	2.55E-03
8.81E+07	2.45E+05	30	0.10	-4.96E-05	1000	2.55E-03
8.81E+07	2.45E+05	33	0.10	-4.96E-05	10000	2.55E-03
5.36E+08	5.41E+08	7	0.25	2.50E-01	1.00E-04	1.00E-04

5.36E+08	1.06E+09	19	0.25	2.71E-01	0.001	1.09E-03
5.36E+08	6.90E+08	6	0.25	-1.38E-02	0.01	2.63E-03
5.36E+08	6.44E+06	12	0.25	-2.51E-04	0.1	2.55E-03
5.36E+08	3.07E+05	19	0.25	-5.18E-05	1	2.55E-03
5.36E+08	2.46E+05	26	0.25	-4.96E-05	10	2.55E-03
5.36E+08	2.45E+05	29	0.25	-4.96E-05	100	2.55E-03
5.36E+08	2.45E+05	30	0.25	-4.96E-05	1000	2.55E-03
5.36E+08	2.45E+05	34	0.25	-4.95E-05	10000	2.55E-03
2.13E+09	2.14E+09	7	0.50	5.00E-01	1.00E-04	1.00E-04
2.13E+09	4.22E+09	19	0.50	5.42E-01	0.001	1.09E-03
2.13E+09	2.76E+09	6	0.50	-2.76E-02	0.01	2.63E-03
2.13E+09	2.50E+07	12	0.50	-4.52E-04	0.1	2.55E-03
2.13E+09	4.93E+05	19	0.50	-5.41E-05	1	2.55E-03
2.13E+09	2.48E+05	25	0.50	-4.96E-05	10	2.55E-03
2.13E+09	2.45E+05	30	0.50	-4.96E-05	100	2.55E-03
2.13E+09	2.45E+05	31	0.50	-4.96E-05	1000	2.55E-03
2.13E+09	2.45E+05	34	0.50	-4.96E-05	10000	2.55E-03
4.77E+09	4.81E+09	7	0.75	7.51E-01	1.00E-04	1.00E-04
4.77E+09	9.49E+09	18	0.75	8.13E-01	0.001	1.09E-03
4.77E+09	6.21E+09	6	0.75	-4.13E-02	0.01	2.63E-03
4.77E+09	5.60E+07	12	0.75	-6.54E-04	0.1	2.55E-03
4.77E+09	8.02E+05	19	0.75	-5.64E-05	1	2.55E-03
4.77E+09	2.51E+05	26	0.75	-4.96E-05	10	2.55E-03
4.77E+09	2.45E+05	30	0.75	-4.96E-05	100	2.55E-03
4.77E+09	2.45E+05	31	0.75	-4.95E-05	1000	2.55E-03
4.77E+09	2.45E+05	33	0.75	-4.96E-05	10000	2.55E-03

9.4.4 Unsteady Surface Temperature

The optimization results presented here complement unsteady surface temperature T_S^U results discussed in Section 4.2.3.

Figure 9.4.7 shows the unsteady subsurface temperature profile T^U optimized from ideal data measurements. The measurements are generated by a diurnal sinusoidal temperature profile such that $T_S^U = 12\sin(2\pi t/86400)$ K, chosen at time $t = 23$, 17, 11 and 5 hr into the cycle. These correspond to the optimized T_S^U shown in Figure 4.14. The exponential covariance function $f_\tau = e^{-r\tau}$ where r is a real number provides the best qualitative fit to the sinusoidal T_S^U as discussed in Sections 4.2.3.2-4.2.3.3.

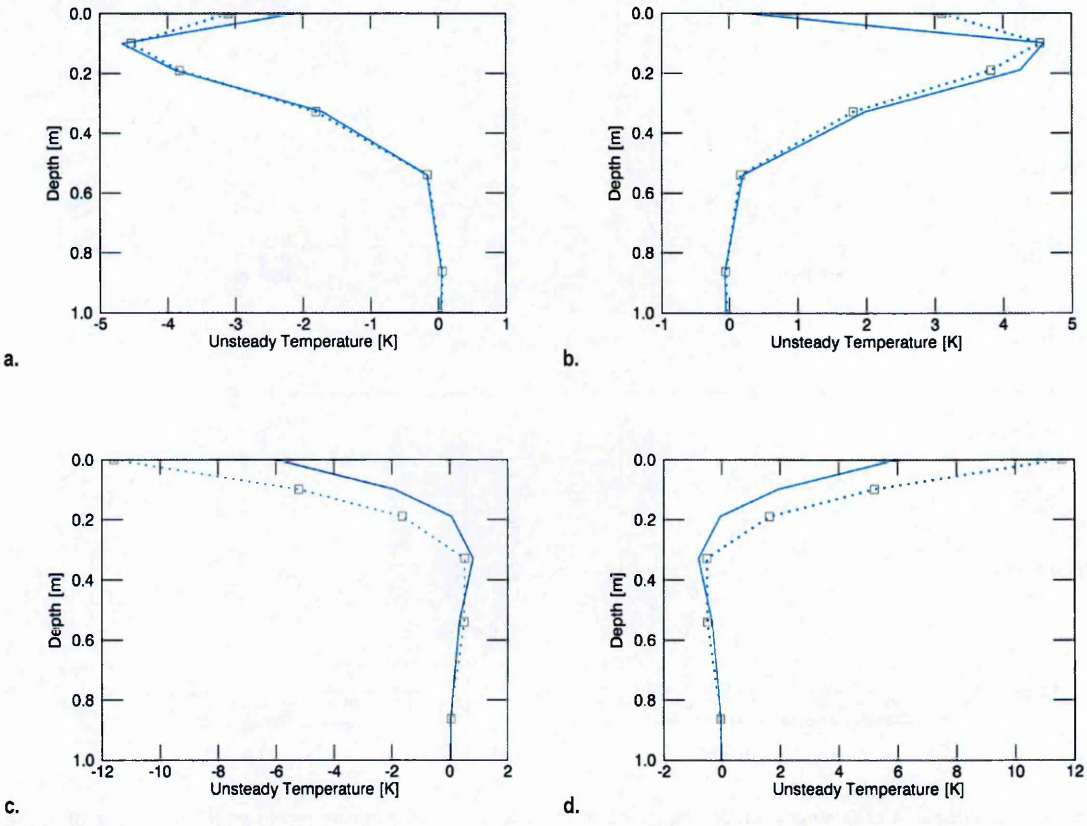

Figure 9.4.7. Optimization of unsteady surface temperature T_S^U. Each plot represents the profile of subsurface unsteady temperature T^U inverted from a measurement at: a. time $t = 23$ hr into a sinusoidal T_S^U cycle with a covariance function $f_\tau = e^{-4\tau}$; b. time $t = 11$ hr into a sinusoidal T_S^U cycle with $f_\tau = e^{-4\tau}$; c. time $t = 17$ hr into a sinusoidal T_S^U cycle with $f_\tau = 0.5e^{-4\tau}(1 - \frac{5cos\pi\tau}{P})$; d. time $t = 5$ hr into a sinusoidal T_S^U cycle with $f_\tau = 0.5e^{-4\tau}(1 - \frac{2cos\pi\tau}{P})$ where τ is the time lag and P is the period of T_S^U. The dotted blue curves represent the true T^U profile (and ideal measurement) and the solid blue curves the optimized T^U. Grey squares are sensor locations.

Figure 9.4.8 shows the results of introducing frequency information into the initial T_S^U estimate. The addition of frequency information to the initial T_S^U estimate minimises the

misfit between the optimized and true T_S^U profiles. This, of course, is subject to the frequency information reflecting the true nature of the T_S^U profile. The more accurate fit of T_S^U leads to a more accurate subsurface unsteady temperature T^U fit, though investigations confirm that, due to the damping of information, several possible T_S^U profiles can produce similar T^U profiles.

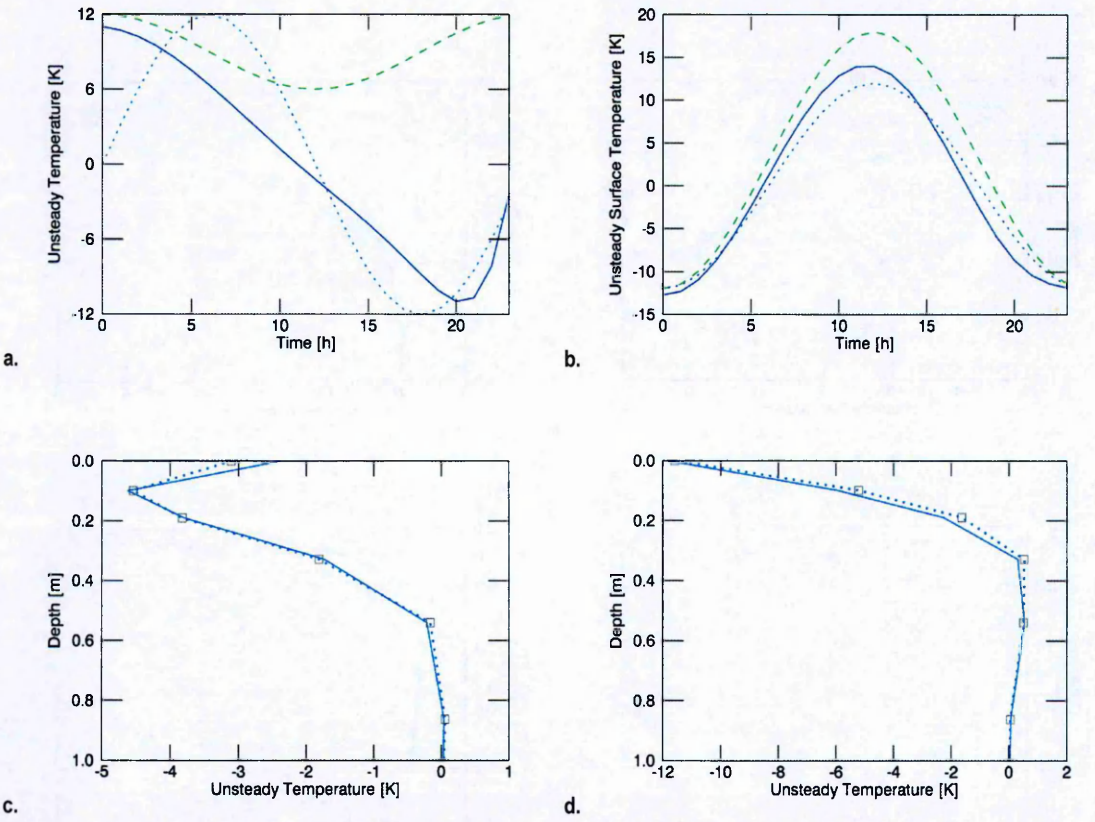

Figure 9.4.8. Optimization of unsteady surface temperature T_S^U. The dotted blue curves represent the true T_S^U profile, the dashed green curves constant initial T_S^U estimate, and the solid blue curves the optimized T_S^U. The upper plots represent a 24 hr profile of T_S^U leading up to a measurement at: a. time $t = 23$ hr into a sinusoidal T_S^U cycle with a covariance function $f_\tau = e^{-4\tau}$; b. time $t = 17$ hr into a sinusoidal T_S^U cycle with $f_\tau = 0.5e^{-4\tau}(1 - \frac{5cos\pi\tau}{P})$ where τ is the time lag and P is the period of T_S^U. The lower plots (c. and d.) represent the profile of subsurface unsteady temperature T^U due to each of the upper plots.

Figure 9.4.9 shows the ratio of a priori to a posteriori standard deviations (SD ratios) for the temperature profiles shown in Figure 9.4.7 (see Figure 4.14 along with Sections 2.3.8 and 4.2.3.2 for related discussions). The SD ratios effectively illustrate the relative

information gain by the optimized T_S^U where smaller values indicate more information gain (smaller errors). The similarity of the profiles from similar standard deviation profiles (a. and b., c. and d.) confirm that the relative information gain is highly dependent on the form of the initial data and model standard deviations. The smaller values towards later (more recent) times follow from the fact that the exponential data standard deviation used in the model (larger values towards the surface) allows larger changes to the initial T_S^U in recent times. The same follows for the initial T_S^U standard deviation $\sigma_{T_S^{U0}}$.

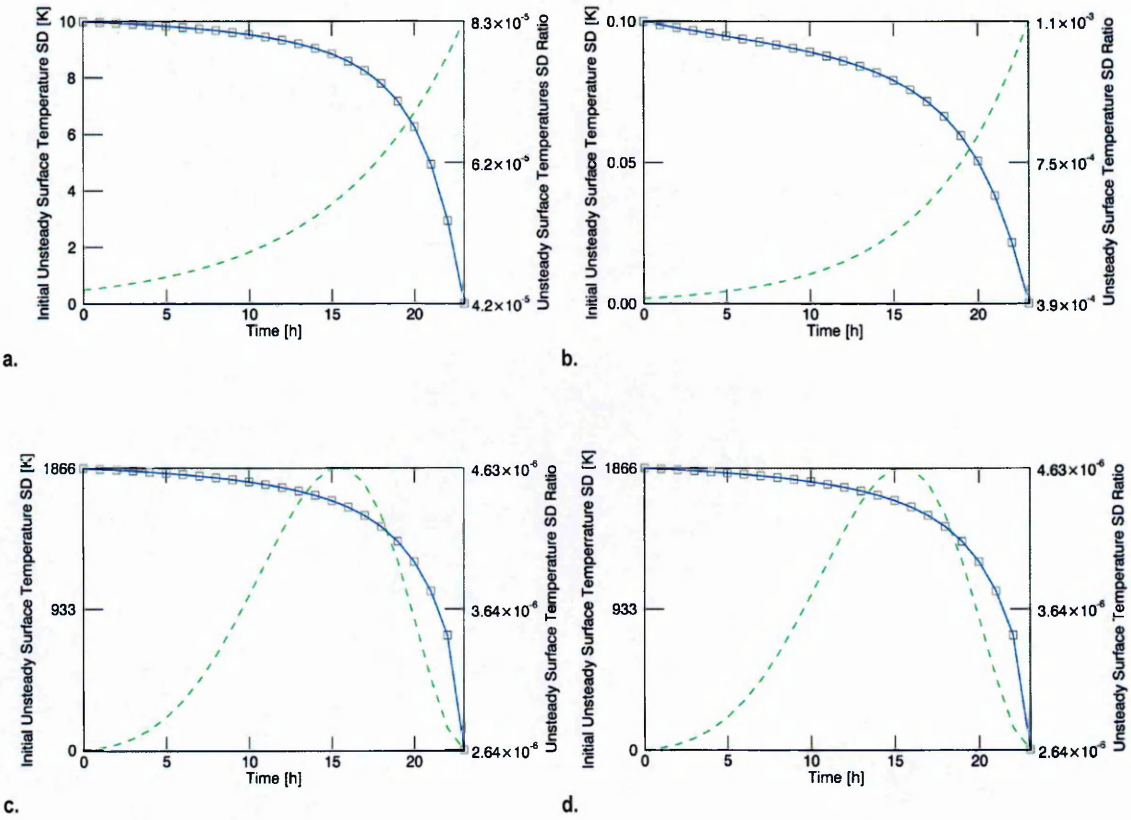

Figure 9.4.9. Each plot shows the ratio of a priori $\sigma_{T_S^{U0}}$ to a posteriori $\sigma_{T_S^{UI}}$ standard deviation (SD ratio) of unsteady surface temperature T_S^U inverted from a measurement at: a. time $t = 23$ hr into a sinusoidal T_S^U cycle with a covariance function $f_\tau = e^{-4\tau}$; b. time $t = 11$ hr into a sinusoidal T_S^U cycle with $f_\tau = e^{-4\tau}$; c. time $t = 17$ hr into a sinusoidal T_S^U cycle with $f_\tau = 0.5e^{-4\tau}(1 - \frac{5cos\pi\tau}{P})$; d. time $t = 5$ hr into a sinusoidal T_S^U cycle with $f_\tau = 0.5e^{-4\tau}(1 - \frac{2cos\pi\tau}{P})$ where τ is the time lag and P is the period of T_S^U. The solid blue curves represent the SD ratios and the dashed green curves the distribution of $\sigma_{T_S^{U0}}$. Grey squares separate the timesteps.

Figure 9.4.10 shows the convergence behaviour of the model when optimizing the temperature profiles shown in Figure 9.4.7 (also see Section 4.2.3.3 and Figure 4.14). T_S^U evidently takes much longer than the other parameters to converge, which follows from the ill-posed nature of the T_S^U optimization problem. The sharp changes at the start are due to the model establishing its location in the solution space $[\mathrm{D}, \mathrm{M}]$ (in other words, testing different general profiles of T_S^U). The algorithm then iteratively calculates an optimum path towards the optimum of the solution space – i.e. a particular T_S^U profile is settled on and small changes are made to the profile as the iterations progress towards convergence.

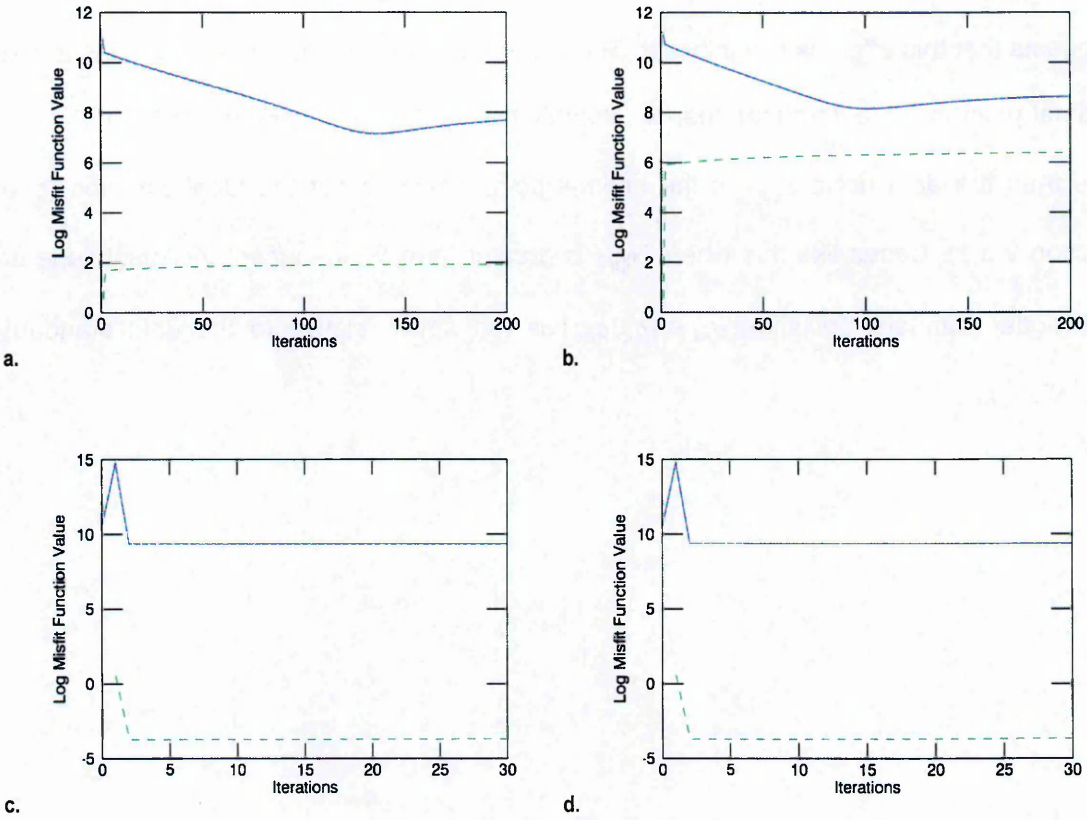

Figure 9.4.10. Convergence of the model in optimizing unsteady surface temperature T_S^U. The base 10 logarithm of the misfit function S_m (solid blue) and its component data $S_{\|d\|}$ (dotted red) and model $S_{\|m\|}$ (dashed green) parameter norms are used to highlight small changes over the number of iterations i. T_S^U is optimized from a measurement at: a. time $t = 23$ hr into a sinusoidal T_S^U cycle with a covariance function $f_\tau = e^{-4\tau}$; b. time $t = 11$ hr into a sinusoidal T_S^U cycle with $f_\tau = e^{-4\tau}$; c. time $t = 17$ hr into a sinusoidal T_S^U cycle with $f_\tau = 0.5e^{-4\tau}(1 - \frac{5cos\pi\tau}{P})$; d. time $t = 5$ hr into a sinusoidal T_S^U cycle with $f_\tau = 0.5e^{-4\tau}(1 - \frac{2cos\pi\tau}{P})$ where τ is the time lag and P is the period of T_S^U. The general behaviour is similar in other convergent simulations. Not that while plots c. and d. appear constant for $i \geq 2$, S_m continues to decrease with each iteration.

9.4.5 Thermal Properties

The optimization results presented here complement conductivity k and thermal capacity ρc results discussed in Section 4.2.4 (Figure 9.4.11).

The noisy optimized k and ρc profiles of Section 4.2.4 do not significantly affect the profiles of subsurface unsteady temperature T^U because the model effectively calculates a profile which optimizes the data norm $S_{\|d\|}$. The SD ratios show that both thermal

properties are more resolved towards the surface, though the small range of values suggests that this effect is insignificant. The convergence plots show that ρc arrives at the optimal point in more iterations than k. Notably the model norm in Figure 9.4.11f, $S_{\|m\|}$ is less than the data norm $S_{\|d\|}$ at the optimal point, which is not the ideal situation (see Section 2.3.1). Cases like this where $S_{\|d\|}$ is greater than $S_{\|m\|}$ suggest the magnitude of the model standard deviation $\sigma_{\boldsymbol{m}} \ni [\sigma_k, \sigma_{\rho c}]$ is too small relative to the data standard deviation $\sigma_{\boldsymbol{d}}$.

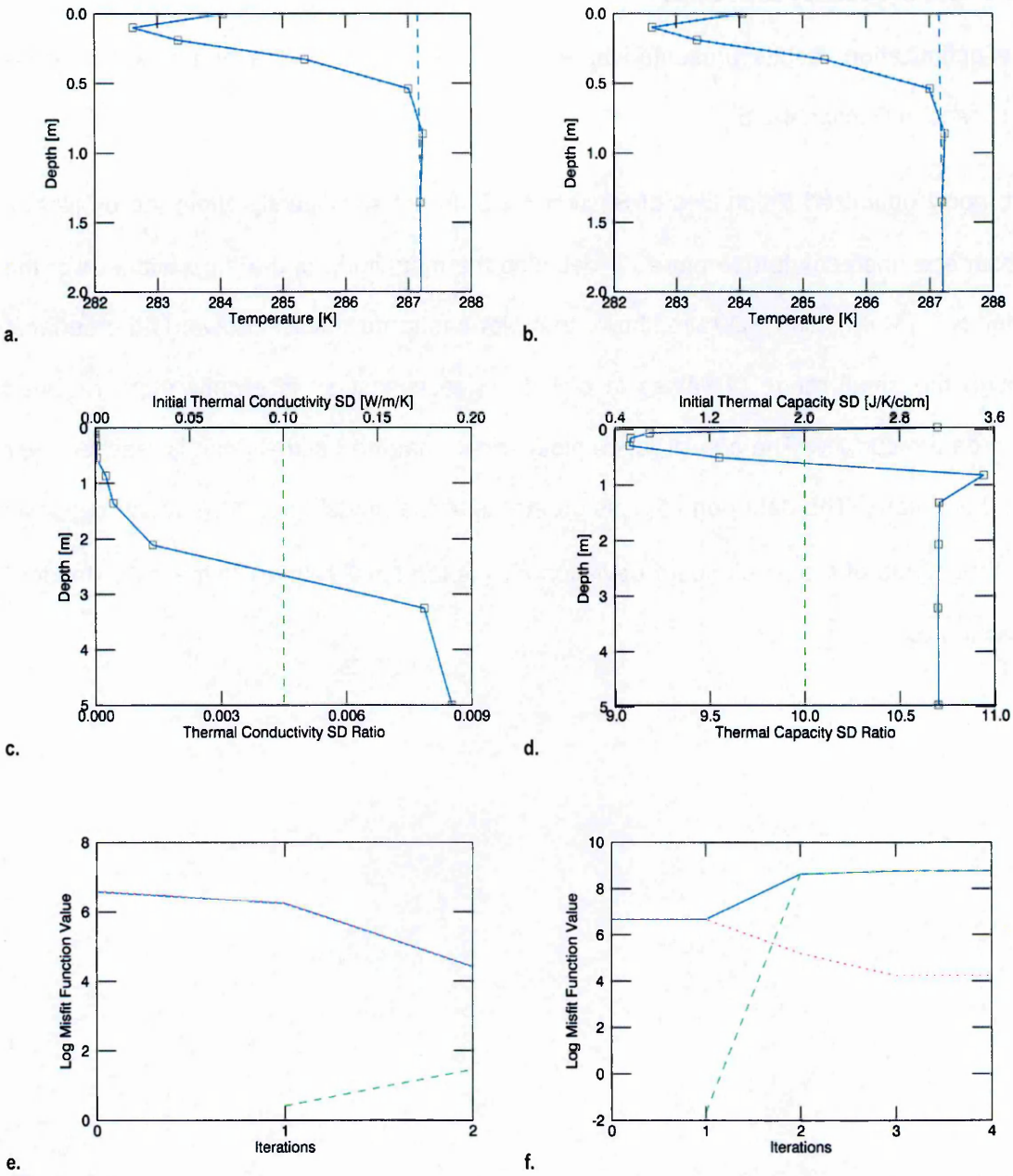

Figure 9.4.11. Optimization of thermal properties conductivity k and thermal capacity ρc from an inverted subsurface temperature measurement T taken at time time $t = 23$ hr into a sinusoidal T_S^U cycle. For optimized k and ρc, plots: a. and b. respectively show the temperature profiles (solid blue is the optimized T profile, dashed blue the optimized profile for steady subsurface temperature T^S and dotted blue the true T profile; c. and d. respectively show the ratio of a priori to a posteriori standard deviation (SD ratio $\sigma_{k^I}/\sigma_{k^0}$ and $\sigma_{\rho c^I}/\sigma_{\rho c^0}$– solid blue) along with the initial distribution of standard deviation with depth; e. and f. show the convergence profiles measured by the base 10 logarithm of misfit function S_m (solid blue) and its component data $S_{\|d\|}$ (dotted red) and model $S_{\|m\|}$ (dashed green) parameter norms.

9.4.6 Heat Sources and Sinks

The optimization results presented here complement heat source and sink S^S results discussed in Section 4.2.5.

The noisy optimized S^S profiles of Section 4.2.5 do not significantly affect the profiles of subsurface unsteady temperature T^U because the magnitude of the fluctuations is of the order of 1 μW/m^3. The SD ratio shows that plot c is more resolved towards the surface, though the small range of values in plot d suggests that S^S is slightly more resolved towards the surface. The convergence plots show what the optimal point is reached after just 2 iterations. The data norm $S_{\|d\|}$ is greater than the model norm $S_{\|m\|}$ which suggests the magnitude of the S^S standard deviation $\sigma_{S^{S0}}$ is too small relative to the data standard deviation σ_d.

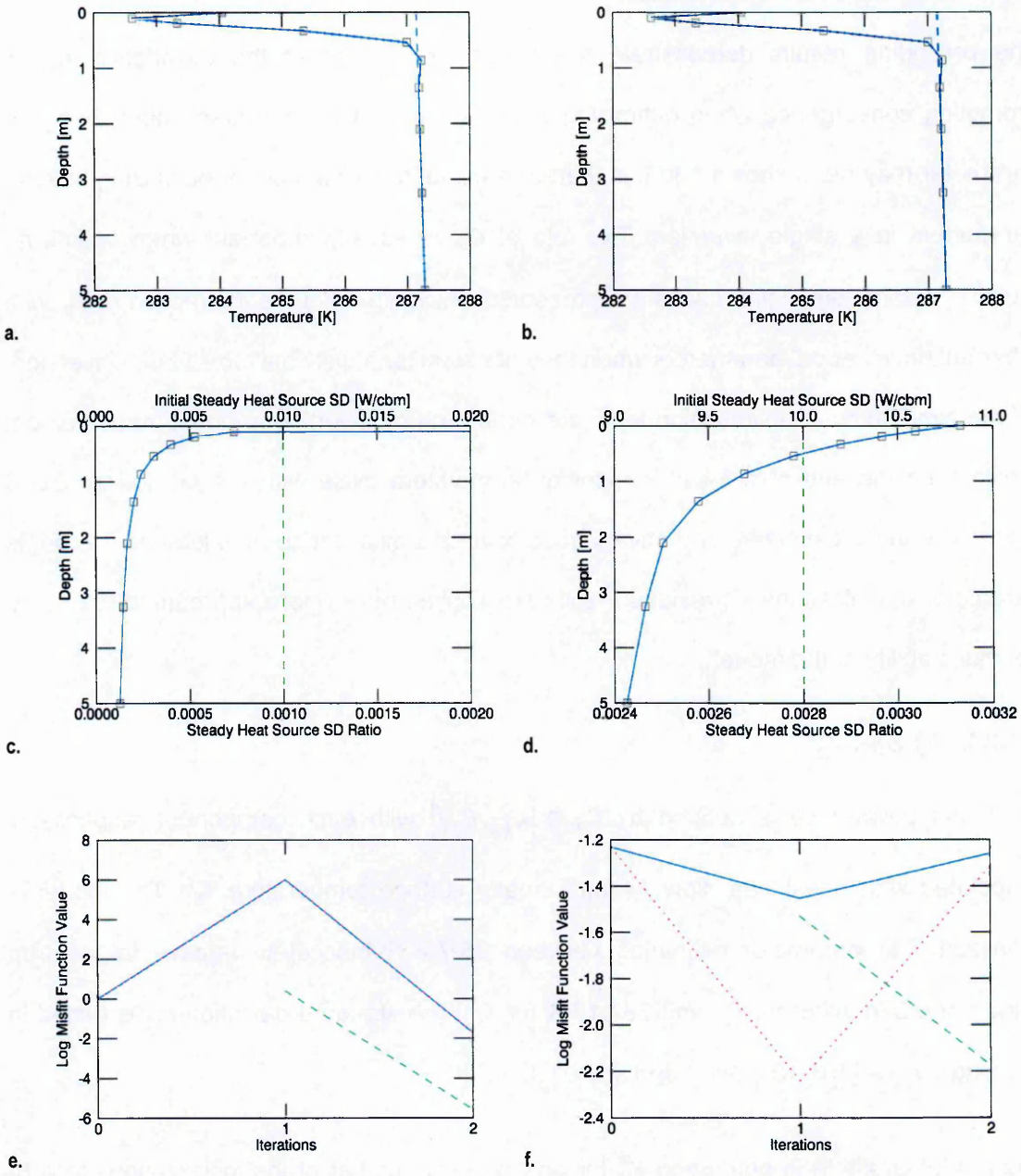

Figure 9.4.12. Optimization of steady heat sources and sinks S^S from an inverted subsurface temperature measurement T taken at time time $t = 23$ hr into a sinusoidal T_S^U cycle. For optimized S^S, plots: a. and b. respectively show the temperature profiles (solid blue is the optimized T profile, dashed blue the optimized profile for steady subsurface temperature T^S and dotted blue the true T profile; c. and d. respectively show the ratio of a priori to a posteriori standard deviation (SD ratio $\sigma_{S^{SI}}/\sigma_{S^{SO}}$ – solid blue) along with the initial distribution of standard deviation with depth; e. and f. show the convergence profiles measured by the base 10 logarithm of misfit function S_m (solid blue) and its component data $S_{\|d\|}$ (dotted red) and model $S_{\|m\|}$ (dashed green) parameter norms.

9.4.7 Simultaneous Optimization

The preceding results demonstrate the critical importance of the covariance C_m in promoting convergence when optimizing a single parameter. Of course, more than one parameter may be unknown and it is therefore useful to be capable of optimizing several parameters in a single inversion. The role of C_m is equally important when optimizing multiple parameters. Test results are presented which illustrate the interaction of F_B^S with other unknown model parameters when they are simultaneously optimized in an inversion. All the simultaneous optimization tests are performed by inverting an ideal measurement profile from the end of a 24 hr sinusoidal temperature cycle with a heat flow of 0.076 W/m^2. The initial estimates and covariances cover a similar range of values as the single parameter optimizations – previous results are applied here where appropriate to ensure optimal stability of the model.

9.4.7.1 F_B^S and T_S^S

Here, the covariance is defined by $C_m \ni \left[C_{F_B^S}, C_{T_S^S}\right]$ with each component respectively associated with basal heat flow F_B^S and steady surface temperature T_S^S. The model is initialized with parameter estimates between 25-75 % inaccurate relative to the true values of 0.076 W/m^2 for F_B^S and 287.15 K for T_S^S. The standard deviation σ_m is tested in the range $\sigma_{F_B^S} \in [10^{-2},10^2]$ W/m^2 and $\sigma_{T_S^S} \in [10,10^4]$ K.

The model is stable in optimizing F_B^S for only a small number of the initializations tested, while being fairly robust in optimizing T_S^S (with exact convergence on the true value in most stable cases). The relative error in optimized F_B^S is negatively correlated with the relative error in optimized T_S^S such that high optimized F_B^S accompanies low optimized T_S^S. This result can be understood in terms of the algorithm compensating for low T_S^S with high F_B^S and vice versa to cancel any data residuals. The same result is expected when F_B^S is solely optimized with inaccurate T_S^S. The best results (within 3 % accuracy) are obtained for both parameters when the total error in the initial estimates is 100 % and – introducing

ratio of standard deviations (stability ratio) $r_{T_S^S}^{F_B^S} = \sigma_{F_B^S}/\sigma_{T_S^S} - r_{T_S^S}^{F_B^S} \in [10^{-4},10^{-5}]$ W/m^2/K. Notably when the F_B^S error is 75 %, $r_{T_S^S}^{F_B^S} = 10^{-4}$ W/m^2/K and when the F_B^S error is 25 % $r_{T_S^S}^{F_B^S} = 10^{-5}$ W/m^2/K confirming that the stability ratio is at least partially related to the relative inaccuracies in the initial F_B^S and T_S^S estimates.

9.4.7.2 F_B^S and T_S^U

Here, the covariance is defined by $\boldsymbol{C_m} \ni \left[\boldsymbol{C}_{F_B^S}, \boldsymbol{C}_{T_S^U}\right]$ with each component respectively associated with basal heat flow F_B^S and unsteady surface temperature T_S^U. The model is initialized with F_B^S estimates between 25-75 % inaccurate relative to the true value of 0.076 W/m^2, and T_S^U estimates with 50 % inaccurate amplitudes relative to the true value of 12 K and phase ±π radians out of phase, or in phase, with the true phase of 2π radians. The standard deviation σ_m is tested in the range $\sigma_{F_B^S} \in [10^{-2},10^2]$ W/m^2 and $\sigma_{T_S^U} \in [10,10^4]$ K – the same as with steady surface temperature T_S^S.

Again the model is stable in optimizing F_B^S for only a small number of the initializations tested. The best optimized F_B^S (within 1 % accuracy) all occur when the initial T_S^U is in phase with, and its amplitude less than, that of the true T_S^U value. T_S^U with smaller amplitudes have a smaller masking effect on F_B^S which explains why the low amplitude T_S^U estimates produce more accurate results. Interestingly, a positive phase shift in T_S^U causes the optimized F_B^S to be underestimated while the opposite happens with a negative phase shift. This is because the positive phase shifted T_S^U produces substantially lower shallow subsurface temperatures than the negative phase shifted T_S^U at the time of measurement, therefore the model counterbalances the resulting low surface temperature residual by decreasing the F_B^S estimate. This produces a corresponding decrease in the steady temperature T^S gradient bringing it closer in line with that of the data measurement. The profiles are shown in Section 4.2.3.1 and can be compared to the ideal measurement at the beginning of Section 4.2.1.1.

The model follows previous results in optimizing T_S^U such that the solution is strongly dependent on the initial T_S^U estimate and the form of covariance $\boldsymbol{C}_{T_S^U}$ – in all cases $T_S^U = T_S^{UA}\sin\left(\frac{2\pi t}{P}+\varphi\right)+\beta\, K$ (see symbol definitions in Appendix 9.1) and $\boldsymbol{C}_{T_S^U} \ni \sigma^2_{T_S^U} f_\tau$ where $f_\tau = e^{-r\tau}$ (r adjusts the rate at which f_τ approaches the asymptote). In most cases the optimized T_S^U does not progress very far from the initial T_S^U estimate – this is because in all cases $\beta = 0$ which results in similar behaviour as when solely optimizing T_S^U. Also, the more positive the relative error in the initial F_B^S estimate, the better the optimized T_S^U fits the true profile. It should be noted that $\beta \equiv T_S^S$, the steady surface temperature, therefore setting $\beta \neq 0$ effectively introduces an error into T_S^S. In any event, investigations show that the model is most stable with the optimized F_B^S approaching the true value for $r_{T_S^U}^{F_B^S} \in [10^{-6},0.1]$ W/m^2/K, the best (within 1 % accuracy) results occurring at $r_{T_S^U}^{F_B^S} = 0.1$ W/m^2/K. Tests are presented in Section 9.4.7.4 which investigate the behaviour of the model when F_B^S, T_S^S and T_S^U are optimized simultaneously.

9.4.7.3 T_S^S and T_S^U

Here, the covariance is defined by $\boldsymbol{C}_{\boldsymbol{m}} \ni \left[\boldsymbol{C}_{T_S^S}, \boldsymbol{C}_{T_S^U}\right]$ with each component respectively associated with steady and unsteady surface temperatures T_S^S and T_S^U. The model is initialized with the same T_S^S and T_S^U estimates, and range of standard deviations σ_m as are used in simultaneous optimization with basal heat flow F_B^S above.

The model is fairly stable in optimizing T_S^S though less so simultaneously optimized with T_S^U than with F_B^S. A positive phase shift in T_S^U causes a high T_S^S estimate while a negative phase shift has the opposite effect. This is due to the shapes of the subsurface temperature profiles generated by the phase shifted T_S^U at the time of the instantaneous measurement. The positive phase shifted T_S^U produces substantially lower shallow subsurface temperatures than the negative phase shifted T_S^U at the time of measurement, therefore the model counterbalances the resulting low temperature residual by increasing

the T_S^S estimate. The profiles are shown in Section 4.2.3.1 and can be compared to the ideal measurement at the beginning of Section 4.2.1.1. Also, T_S^U estimates with a high amplitude result in less reliable optimized T_S^S estimates (greater scatter in the data), due to a larger shallow subsurface unsteady temperature T^U envelope. Note the related results with F_B^S in Section 9.4.7.2.

The model follows previous results in optimizing T_S^U such that the solution is strongly dependent on the initial T_S^U estimate and the form of $\boldsymbol{C}_{T_S^U}$ – the same initializations are used as in the optimization of unknown T_S^U and F_B^S above. Investigations show that the model is most stable with T_S^S converging on the true T_S^S value when the ratio of standard deviations $r_{T_S^U}^{T_S^S} = \sigma_{T_S^S}/\sigma_{T_S^U} \in [10,10^3]$ with progressively better results as $r_{T_S^U}^{T_S^S}$ increases. It should be noted that $r_{T_S^U}^{T_S^S}$ can be derived, to first order, from $r_{T_S^S}^{F_B^S}$ and $r_{T_S^U}^{F_B^S}$ which are discussed above, such that $r_{T_S^U}^{T_S^S} = r_{T_S^U}^{F_B^S} \Big/ r_{T_S^S}^{F_B^S}$ – generally $r_{m_2}^{m_1} = r_{m_2}^{m_3}/r_{m_1}^{m_3}$ where m_n refers to a particular optimized parameter.

9.4.7.4 F_B^S, T_S^S and T_S^U

The previous results show that using the appropriate ratio of standard deviations $r_{m_2}^{m_1}$ promotes convergence. Here, the results are applied to covariance $\boldsymbol{C_m} \ni \left[\boldsymbol{C}_{F_B^S}, \boldsymbol{C}_{T_S^S}, \boldsymbol{C}_{T_S^U}\right]$ where the standard deviation σ_m is tested in the range $\sigma_{F_B^S} \in [0.01,1]$ W/m^2, $\sigma_{T_S^S} \in [10^2,10^4]$ K and $\sigma_{T_S^U} \in [0.1,10]$ K such that stability ratio $r_{T_S^S}^{F_B^S} = 10^{-4}$ W/m^2/K, $r_{T_S^U}^{T_S^S} = 10^3$ and $r_{T_S^U}^{F_B^S} = 0.1$ W/m^2/K. The respective subscripts associate each parameter with the basal heat flow F_B^S, and steady and unsteady surface temperatures T_S^S and T_S^U. With the stability ratios constant the solutions display no dependence on the standard deviation σ_m of any model parameter m.

Previous relationships established between F_B^S, T_S^S and T_S^U are evident in the data (see Sections 9.4.7.1-9.4.7.3). Effectively the model adjusts free parameters in the optimization

to minimize the data misfit. Where F_B^S and T_S^S are free parameters, the algorithm adjusts them to match the steady temperature T^S gradient.[2] Here, F_B^S is optimized to within 25 % of the true value when the initial T_S^S estimate is within 25 % of its true value and the initial F_B^S estimate is 75 % inaccurate. T_S^S is optimized to within 3 % of the its value in all cases. The results show no significant correlation between the error in optimized F_B^S and the error in the initial T_S^U estimate. T_S^U does not progress in the optimization – i.e. optimized T_S^U in most cases is essentially the same as the initial T_S^U estimate. There are indications of non-optimal balances in $\boldsymbol{C_m}$ and $\boldsymbol{C_d}$ therefore better stability may be gained by refining estimates of the stability ratios $r_{m_2}^{m_1}$ and r_d^m.

9.4.7.5 F_B^S and k

Here, the covariance is defined by $\boldsymbol{C_m} \ni \left[\boldsymbol{C}_{F_B^S}, \boldsymbol{C}_k\right]$ with each component respectively associated with basal heat flow F_B^S and conductivity k. The model is initialized with parameter estimates between 25-75 % inaccurate, relative to the true values of 0.076 W/m^2 for F_B^S and 3 W/m/K for k. The standard deviation σ_m is tested in the range $\sigma_{F_B^S} \in$ [10^{-2},10^2] W/m^2 and $\sigma_k \in$ [1,10^3] W/m/K.

The model is stable in optimizing F_B^S and k for only a small number of the initializations tested. The optimized F_B^S falls within 25 % of the true value when the initial k estimate is within 25 % of its true value. There is positive correlation between the error in F_B^S and the error in k. This can be understood in the sense of the algorithm compensating for changes in the steady temperature T^S gradient where underestimated k (and overestimated F_B^S) causes it to increase and vice versa (see Section 3.2.2). The algorithm therefore overestimates k to counteract overestimated F_B^S and vice versa. No consistent trends emerge in terms of stability ratio $r_k^{F_B^S} = \sigma_{F_B^S}/\sigma_k$, though there are indications that high $r_k^{F_B^S}$

[2] This can be visualized in the sense of a lever in equilibrium with two balanced but opposing forces (F_B^S and T_S^S) acting on opposite ends. If an unbalanced force (data residual) acts on one end, a reaction (model optimization) force will act on the opposite end to regain equilibrium.

is more stable. Likewise, the convergence plots indicate non-optimal balances in C_m and C_d such that the standard deviations may need to be tested over a wider range of values.

9.4.7.6 F_B^S and ρc

Here, the covariance is defined by $C_m \ni \left[C_{F_B^S}, C_{\rho c}\right]$ with each component respectively associated with basal heat flow F_B^S and thermal capacity ρc. The model is initialized with parameter estimates between 25-75 % inaccurate, relative to the true values of 0.076 W/m^2 for F_B^S and 2.133 MJ/K/m^3 for k. The standard deviation σ_m is tested in the range $\sigma_{F_B^S} \in [10^{-2},10^{2}]$ W/m^2 and $\sigma_k \in [10^{2},10^{8}]$ MJ/K/m^3.

The model is fairly stable in optimizing F_B^S while ρc is not well optimized. Due to this the behaviour of the model is similar to that discussed in Section 4.2.1.2.3. F_B^S is optimized to within 5 % of its true value when the initial ρc estimate is 25 % inaccurate and to within 30 % of its true value when the initial ρc estimate is 75 % inaccurate. The accuracy of the optimized F_B^S is positively correlated with the accuracy of the initial ρc estimate while also having less accuracy with underestimated ρc. This can be understood in the sense of low ρc estimates causing more instability in the model by increasing the skin depth of the unsteady temperature. Related discussions are in Sections 3.4.2 (Forward Model), 4.2.1.2 and 4.3.1.3 (Inverse Model). In terms of the ratio of standard deviations $r_{\rho c}^{F_B^S} = \sigma_{F_B^S}/\sigma_{\rho c}$, the best results occur when $r_{\rho c}^{F_B^S} = 10^4$ mWK/MJ which is at the upper extreme of the range tested, so higher values may yield better results.

9.4.7.7 F_B^S and S^S

Here, the covariance is defined by $C_m \ni \left[C_{F_B^S}, C_{S^S}\right]$ with each component respectively associated with basal heat flow F_B^S and source term S^S. The model is initialized with estimates from 25 to 75 % above and below the true value of 0.076 W/m^2 for F_B^S while an even distribution of sources and sinks is used to supply initial S^S estimates in the range

$\pm[10^{-5},10^{-3}]$ W/m^3 about the true value of 0 W/m^3. The standard deviation σ_m is tested in the range $\sigma_{F_B^S} \in [10^{-2},10^{2}]$ W/m^2 and $\sigma_{S^S} \in [10^{-5},10]$ W/m^3.

Tests show that the model is fairly stable in optimizing both F_B^S and S^S with the most accurate (within 3 %) optimized F_B^S being obtained when the initial S^S estimate is most accurate. Negative correlation is observed between S^S and F_B^S which can be understood in the sense that overestimated S^S is compensated for by underestimated F_B^S as overestimated S^S increases the steady temperature T^S gradient (see Section 3.2.3). As with other parameters, a stability ratio can be defined such that $r_{S^S}^{F_B^S} = \sigma_{F_B^S}/\sigma_{S^S}$. Investigations show that the model is most stable with both parameters converging on their respective true values for $r_{S^S}^{F_B^S} \geq 10^3$ m with the best results occurring at $r_{S^S}^{F_B^S} = 10^3$ m.

9.4.8 Error Analysis of Counterintuitive Noise Results

Table 9.4.5 shows an example listing of counterintuitive error results for a series of inversions where basal heat flow standard deviation $\sigma_{F_B^{S0}} = 10$ W/m^2. These accompany the discussion in Section 4.3.1.2 regarding counterintuitive noise results. Note that, for this specific analysis, the data standard deviation σ_d is tested in the range $\sigma_d \in [10^{-4},10^{8}]$ K.

Table 9.4.5. Example listing of counterintuitive error results for basal heat flow standard deviation $\sigma_{F_B^{S0}} = 10$ W/m^2 (symbols are defined in Appendix 9.1).

σ_d [K]	$r_d^{F_B^S}$	$\epsilon_{F_B^{S0}}$	m	σ_η [K]	k [W/m/K]
100000	0.0001	R$^+$	1	[0.01,1]	3
10000	0.001	R$^+$	1	[0.01,1]	3
1000	0.01	R$^+$	1	[0.01,1]	3
100	0.1	R$^+$	1	[0.01,1]	3
10	1	R	1	[0.01,1]	3
0.1	100	R	1	[0.01,1]	3
0.01	1000	R	1	[0.01,1]	3
0.001	10000	R	1	[0.01,1]	3

0.0001	100000	R	1	[0.01,1]	3
100000	0.0001	R^+	1	[0.01,1]	0.3
10000	0.001	R^+	1	[0.01,1]	0.3
1000	0.01	R^+	1	[0.01,1]	0.3
10000	0.001	R^+	360	[0.01,1]	3
1000	0.01	R^+	360	[0.01,1]	3
100	0.1	R^+	360	[0.01,1]	3
10	1	R	360	[0.01,1]	3
0.1	100	R	360	[0.01,1]	3
0.01	1000	R	360	[0.01,1]	3
0.001	10000	R	360	[0.01,1]	3
0.0001	100000	R	360	[0.01,1]	3
100000	0.0001	R^+	360	[0.01,1]	0.3
10000	0.001	R^+	360	[0.01,1]	0.3
1000	0.01	R^+	360	[0.01,1]	0.3
100	0.1	R^+	360	[0.01,1]	0.3
10	1	R	360	[0.01,1]	0.3
0.1	100	R	360	[0.01,1]	0.3
0.01	1000	R	360	[0.01,1]	0.3
0.001	10000	R	360	[0.01,1]	0.3
0.0001	100000	R	360	[0.01,1]	0.3

Trends in the frequency of the counterintuitive noise results, correlated with the variables as illustrated in Table 9.4.5, are listed below.

Where $\boldsymbol{C_d}$ and $\boldsymbol{C_m}$ are fixed (and more generally) these trends are observed for the counterintuitive noise results:

1. significantly more cases occur with long-period measurements than with instantaneous measurements;
2. further to observation 1, the high skin depth scenarios ($k = 3$ W/m/K), account for most of the instantaneous measurements, while there is effectively an even split

between high and low ($k = 0.3$ W/m/K) skin depth scenarios for long-period measurements.

Likewise, where $\boldsymbol{C_d}$ and $\boldsymbol{C_m}$ are not fixed:

3. the number of cases decrease with an increase in σ_d for a given σ_m – i.e. as the stability (SD) ratio $r_d^{F_B^S}$ decreases;
4. further to observation 3, the cases remaining as σ_d increases, are mostly those in which F_B^{S0} is initialised with high estimates ($\epsilon_{F_B^{S0}} \in [R^+]$);
5. further to observation 4, the cases vanish as σ_d increases (or as $r_d^{F_B^S}$ decreases) beyond given values, though at these points σ_d is so high that the inverse model gives F_B^{S0} as a solution;
6. curiously, in the high skin depth scenarios, the cases vanish at lower values of σ_d (higher $r_d^{F_B^S}$) than with otherwise equivalent low skin depth scenarios.

Considering the preceding observations, it is reasonable to conclude that the counterintuitive results are due to instabilities introduced by the large number of unique temperature gradients in the long-period measurement cases, and increased skin depth z_{SKIN}, as noted in Section 4.3.1.2. Increasing σ_d, within limits, goes some way towards removing the counterintuitive results, though this must be considered within the context of the stability ratio $r_d^{F_B^S}$ discussed throughout Section 4.3.1 (also see Sections 9.4.7 and 9.4.9.3-0).

9.4.9 Inverse Model Verification

9.4.9.1 Forward Models

The inverse model is mainly presented in Chapters 2-4. As noted in the main text, it involves, iteratively, the solution of the primal problem (forward model) and the dual problem. The primal and dual problems utilize the same numerical IDL code (finite control volume (FCV) discretization solved by tri-diagonal matrix algorithm (TDMA), e.g.

Patankar, 1980) to solve the respective primal and dual linear systems. The synthetic measurements used herein are all generated by the forward model, therefore a potential conflict exists where the same code is used to generate the data and solve the problem.

In Section 3.4.1.1, the forward model numerical solutions, used in the IDL code, are compared to analytical solutions discussed in Section 2.1.2.1 (also see e.g. Carslaw and Jaeger, 1986), which can be considered a step towards mitigating the issue. Given the former, several tests are performed which seek to assess any divergence in behaviour of the inverse model, in recovering unknown basal heat flow from synthetic data generated by the numerical forward model, versus the analytical model of Sections 2.1.2.1 and 3.4.1.1. The tests involve end-member skin depth scenarios (four in total) with parameters similar to those tested in Chapters 3 and 4 (Table 9.4.6).[3]

Several important differences are observable between the numerical and analytical forward model calculations, which illustrate the limits of precision of the numerical model (Figure 9.4.13). Notably, where the modelled depth is not far enough below the skin depth (the basal boundary being too close to the surface – at least ~7× appears reasonable), such that the instability of the unsteady temperature variation is negligible, the numerical diverges significantly from the analytical model. This is an artefact of the numerical calculation where the unsteady temperature gradient approaches zero with no specified basal temperature at which it can be fixed.[4] Otherwise, the features highlighted in the grid convergence discussion of Section 2.1.2.1 can be observed.[5]

---

[3] For simplicity, control volume size is kept constant for the numerical and analytical solutions, as opposed to the cases presented in Chapter 4 where the control volume size increases with depth.

[4] The unsteady basal heat flow F_B^U is known as a Neumann (derivative) boundary condition while the unsteady basal temperature T_B^U is a Dirichlet boundary condition. Non-uniqueness is a known feature of Neumann boundary conditions, such that $F_B^U = -k\frac{\partial T_B^U}{\partial z} = -k\frac{\partial}{\partial z}(T_B^U + \epsilon)$, ϵ being a constant (e.g. Saad, 2003).

[5] Note that as grid convergence is approached the asymmetry of Figure 9.4.13c-f vanish.

Table 9.4.6. Parameters used to calculate two numerical and two analytical forward model solutions. Symbols are defined in Appendix 9.1. All quantities are in standard SI units, except times, which are in days.

PARAMETER	VALUE			
	DIURNAL		ANNUAL	
T_S^S	287.15		287.15	
T_S^U	$T_S^U = T_S^{UA} \sin(2\pi t/P)$		$T_S^U = T_S^{UA} \sin(2\pi t/P)$	
P	1		360	
T_S^{UA}	12		12	
F_B^S	0.075		0.075	
ρ	2000		2000	
c	700		700	
k	0.3	3	0.3	3
Z, z_N	1	2	10	20
Δz_N	1/24	2/24	10/24	20/24
t_E	1		360	
Δt	1/24		1	

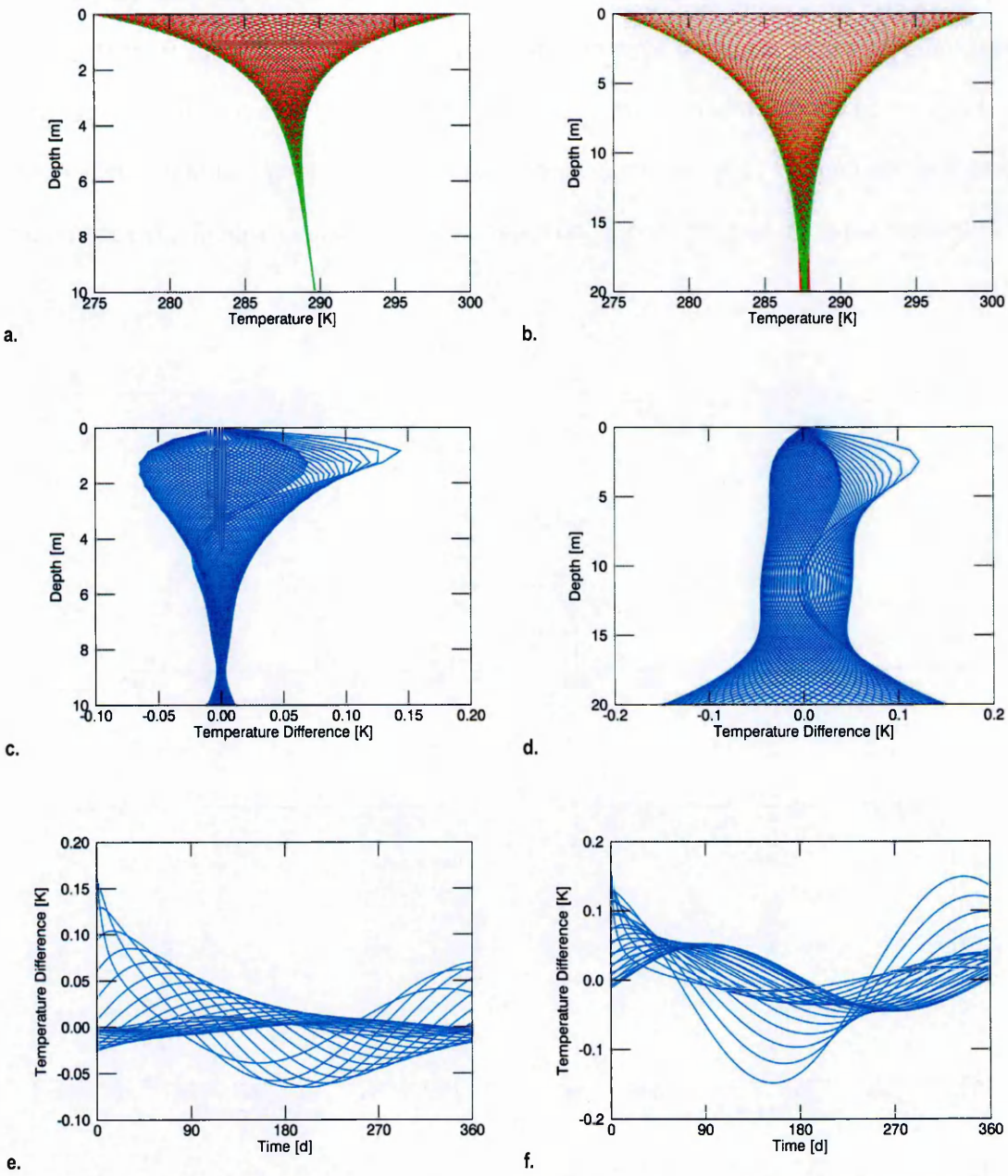

Figure 9.4.13. Forward modelled analytical and numerical temperatures based on the annual parameters of Table 9.4.6: the left plots show the low skin depth scenarios and the right plots the high skin depth scenarios. Plots: a and b show overlays of depth-dependent temperature at different times (the solid red curves represent the numerical temperatures and the dotted green curves the analytical temperatures; c and d show the depth-dependent temperature differences (numerical – analytical); e and f show overlays of time-dependent temperature differences at different depth.

9.4.9.2 Synthetic Measurements

Measurements are synthesised by adding four levels of Gaussian noise with amplitudes of $\sigma_\eta = 0.001\text{-}1.0$ K, with order-of-magnitude steps, to temperature profiles extracted from

the numerical and analytical forward model grids. Profiles are extracted as instantaneous measurements at the end of a simulated temperature cycle (e.g. Figure 9.4.14b and d) and long-period measurements with recordings throughout the temperature cycle (e.g. Figure 9.4.14a and c). To keep things simple the spatial and temporal grid densities are kept constant between forward model and measurement for the long-period measurement scenarios.

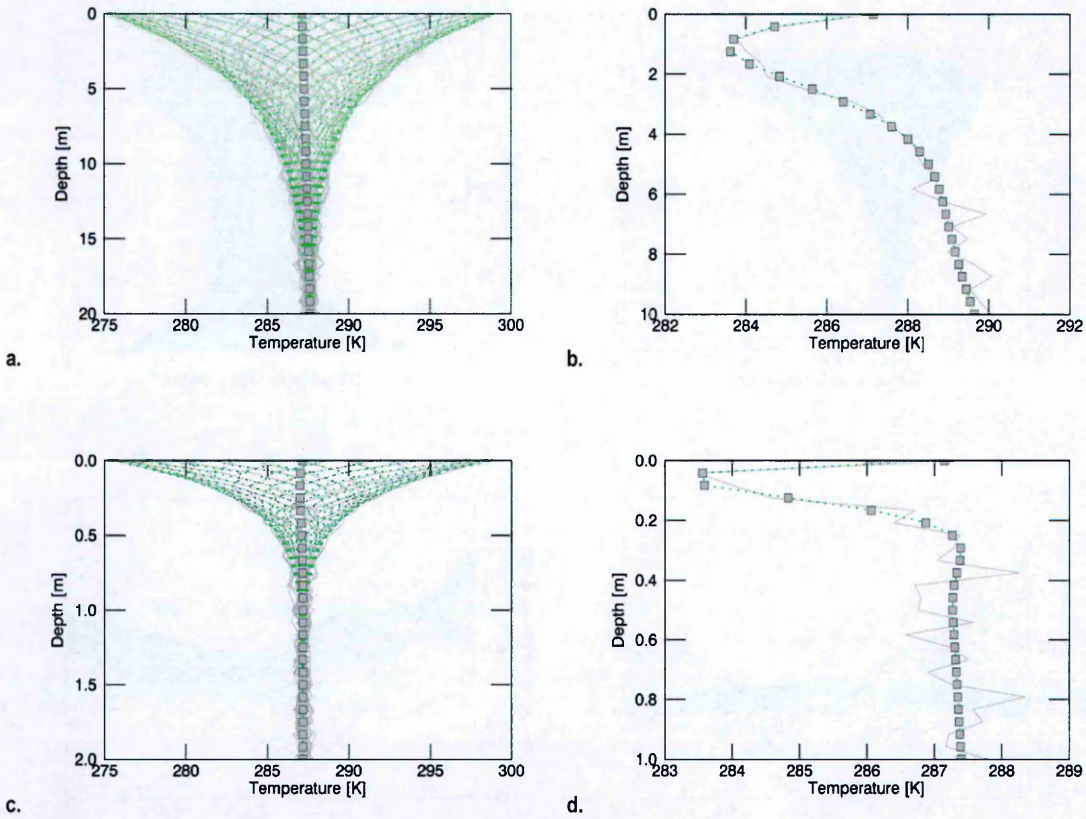

Figure 9.4.14. Representative synthetic temperature measurements from analytical temperatures based on the annual parameters of Table 9.4.6 with 1.0 K additive Gaussian noise. Plot: a is a long-period annual temperature measurement for the high skin depth scenario; b an instantaneous measurement for the low skin depth, annual scenario; c a long-period diurnal temperature measurement for the high skin depth scenario; d an instantaneous measurement for the low skin depth, diurnal scenario. The dotted green curves represent the pristine profile, the solid grey curves the noisy profile. Grey squares are sensor locations.

9.4.9.3 Inverse Model Results

The inverse model is applied to both the analytically derived (AD) and numerically derived (ND) synthetic measurements. For each measurement, the model is run with all boundary

parameters accurate, except heat flow, which is constantly inaccurate by a factor of two – i.e. $F_B^{S0} = 0.15$ W/m^2. The assumed data and model standard deviations σ_d and σ_m respectively span equivalent ranges from 0.1-1000 K and W/m^2, with order-of-magnitude steps.

While the general behaviour is the same, results show some divergence in the accuracy of basal heat flow optimized from AD versus ND synthetic measurements (Figure 9.4.15). This is the case, in particular, towards extremes of SD ratio $r_d^{F_B^S}$ and measurement noise amplitude σ_η. Interestingly, the results for the analytical are consistently more accurate than those for the numerical. Note that the SD stability ratio effectively defines a solution subspace within the inverse model space defined by data and model covariances $\boldsymbol{C_d}$ and $\boldsymbol{C_m}$ (Figure 9.4.16c and d, shaded green triangles).

The most pathological results are at the low extremes of $r_d^{F_B^S}$, as was established in previous tests, and where data noise amplitude σ_η is high. The range of accuracies achieved in the AD results is narrower than that achieved in the ND results such that ND results achieve greater accuracy in the well-behaved cases and greater inaccuracy in the pathological cases.[6]

Example profiles are shown in Figure 9.4.16 (to be compared to Figure 9.4.13). It is fairly evident in Figure 9.4.16a and b that the AD result closely matches the ND result. This is to be expected as the only differences between the AD and ND initialisations of the inverse model are the relatively small temperature differences exemplified by Figure 9.4.13 and random variation of the added Gaussian noise.

Most notably, misfits between the AD and ND results only occur in the steady temperature regime, which should be the case because the only free parameters are the subsurface steady temperatures T^S and the basal heat flow F_B^S. Figure 9.4.16c and d show that,

[6] These differences are not explicitly reflected in Figure 9.4.15 because the data points are centrally estimated.

generally, the derived F_B^S is more inaccurate with higher noise levels, however, as noted in Section 9.4.8, unexpected results do occur at high skin depth z_{SKIN} (e.g. Figure 9.4.16d at 0.1 K).

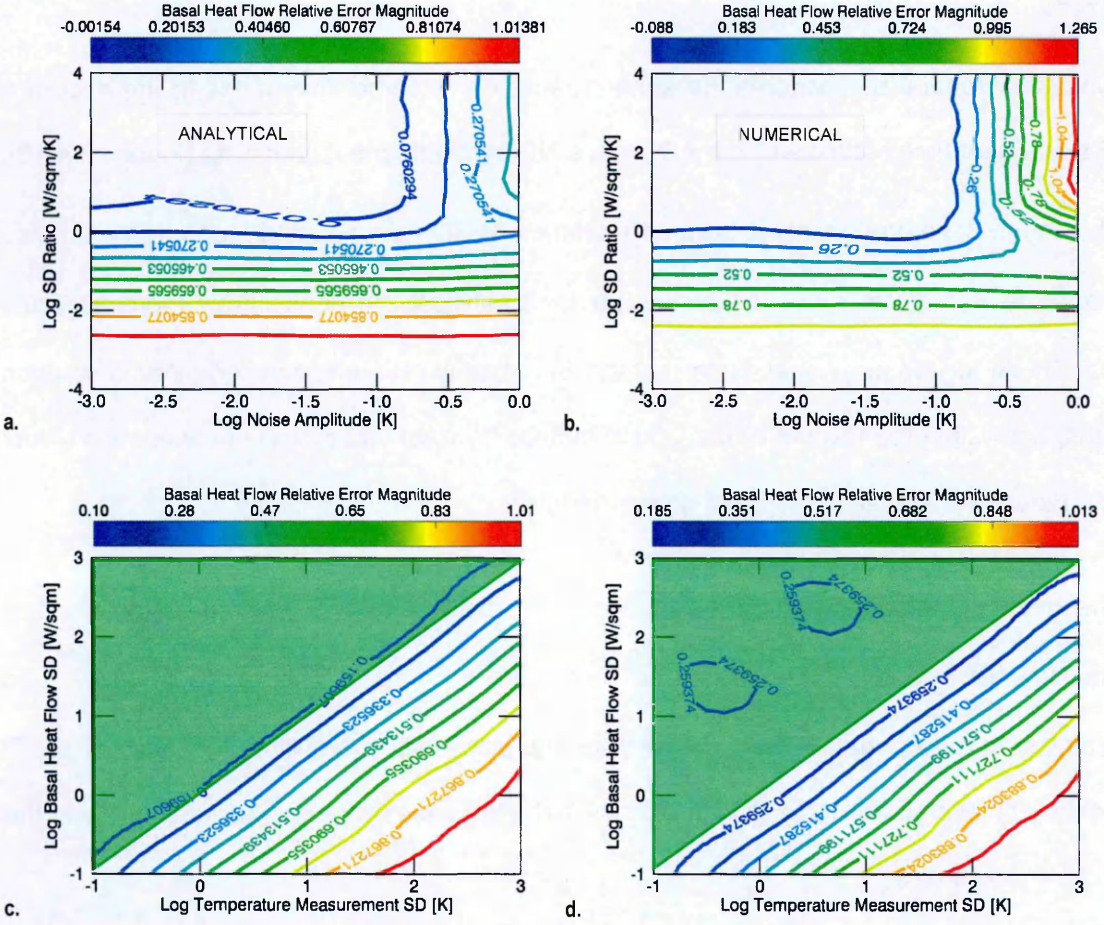

Figure 9.4.15. Results of optimization of analytical (left) and numerical (right) synthetic measurements as outlined in the text. These are interpolated from mean values across all other varied parameters discussed in the text.[7] The green triangles highlight the subspace, the border of which is defined by the ratio of standard deviation $r_d^{F_B^S}$, which can be explored for the most viable solutions.

It is important to observe that, in the numerical and analytical forward model calculations there are no differences between the calculated steady temperatures T^S; all differences occur in the unsteady temperatures T^U. In the inverse model, the T^U differences are

[7] Note that the negative numbers are an artefact of the Quintic interpolation method used in generating the contour lines from the scatter of data points.

propagated into differences between the derived F_B^S and attendant T^S, because of the fixing of unsteady temperature parameters.

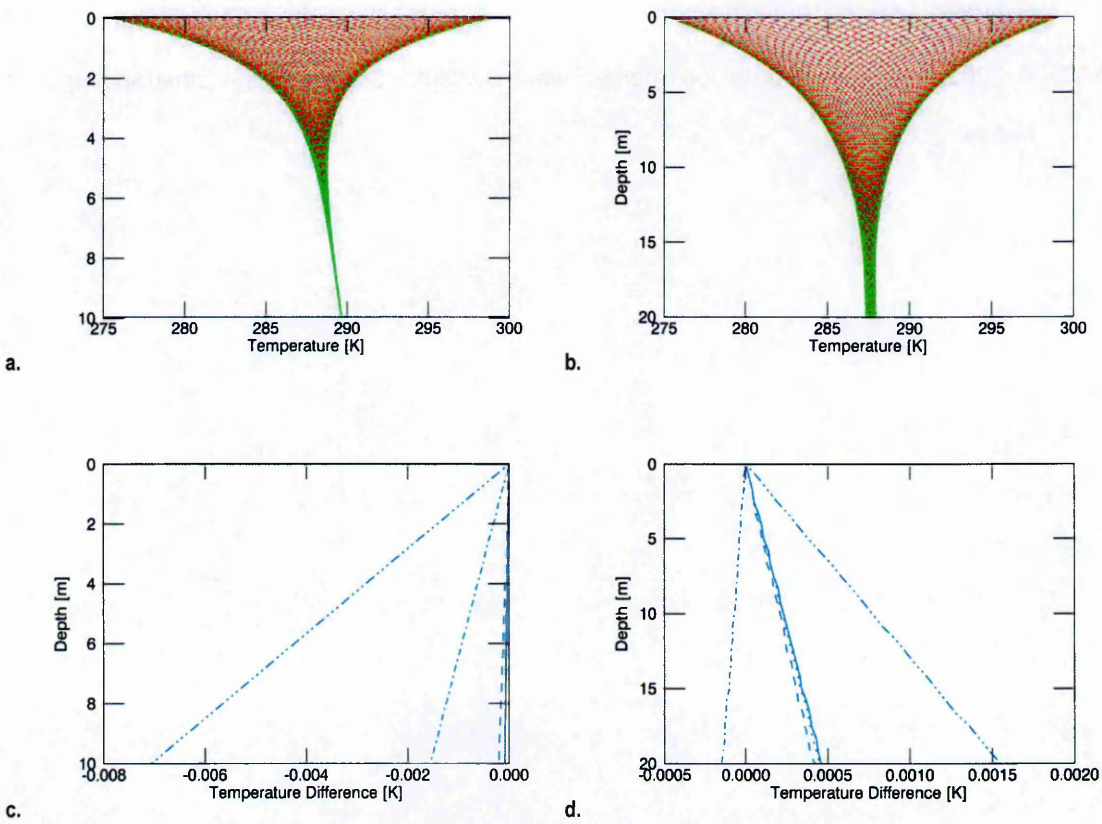

Figure 9.4.16. Inverse modelled analytical and numerical temperatures based on the annual parameters of Table 9.4.6: the left plots show the low skin depth scenarios and the right plots the high skin depth scenarios. Plots: a and b show overlays of depth-dependent temperature at different times (the solid red curves represent the numerical temperatures and the dotted green curves the analytical temperatures; c and d show the depth-dependent temperature differences (numerical – analytical) with noise amplitudes of 0-1 K in order-of-magnitude steps respectively represented (blue curves) by solid, dotted, dashed, dot-dashed and double dot-dashed lines. Compare to Figure 9.4.13.

9.4.10 References

CARSLAW, H. S. & JAEGER, J. C. 1986. *Conduction of heat in solids,* Oxford, Clarendon.

PATANKAR, S. V. 1980. *Numerical Heat Transfer and Fluid Flow,* New York, NY, London, Hemisphere.

SAAD, Y. 2003. *Iterative Methods for Sparse Linear Systems*, Society of Industrial and Applied Mathematics.

9.5 Mars

9.5.1 Local Mean Time on Mars

Figure 9.5.1 shows the local mean time for Mars on November 1, 2016, the time at which heat flow measurements commence in the scenarios investigated for Mars in Chapter 5 (see Sections 5.2.1, 5.3.1 and 5.3.2).

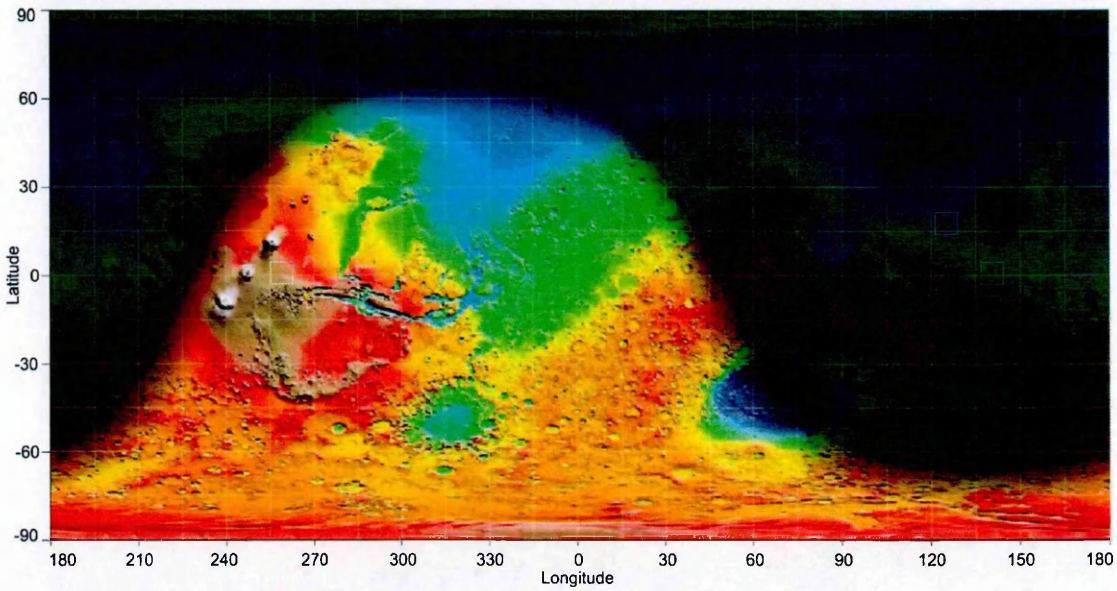

Figure 9.5.1. Mars map of Local Mean Solar Time produced by the Mars24 application of NASA GISS. The white rectangles represent landing sites at: 120°E 20°N, local time 22:42:21; 139°E 1°N, local time 23:58:21 and; 253°E 2°N, local time is 07:22:21.

9.5.2 Forward Models

Figure 9.5.2 and Figure 9.5.3 represent the respective high and low conductivity scenarios for the measurement sites investigated for Mars in Section 5.3.1 in the low heat flow, plate cooling regime. The only distinction between these low heat flow, plate cooling models and the high heat flow, stagnant lid models of Chapter 5 is a smaller steady temperature gradient for the former, A smaller temperature gradient requires greater measurement precision and – all else being equal – is subject to greater masking by the unsteady temperature.

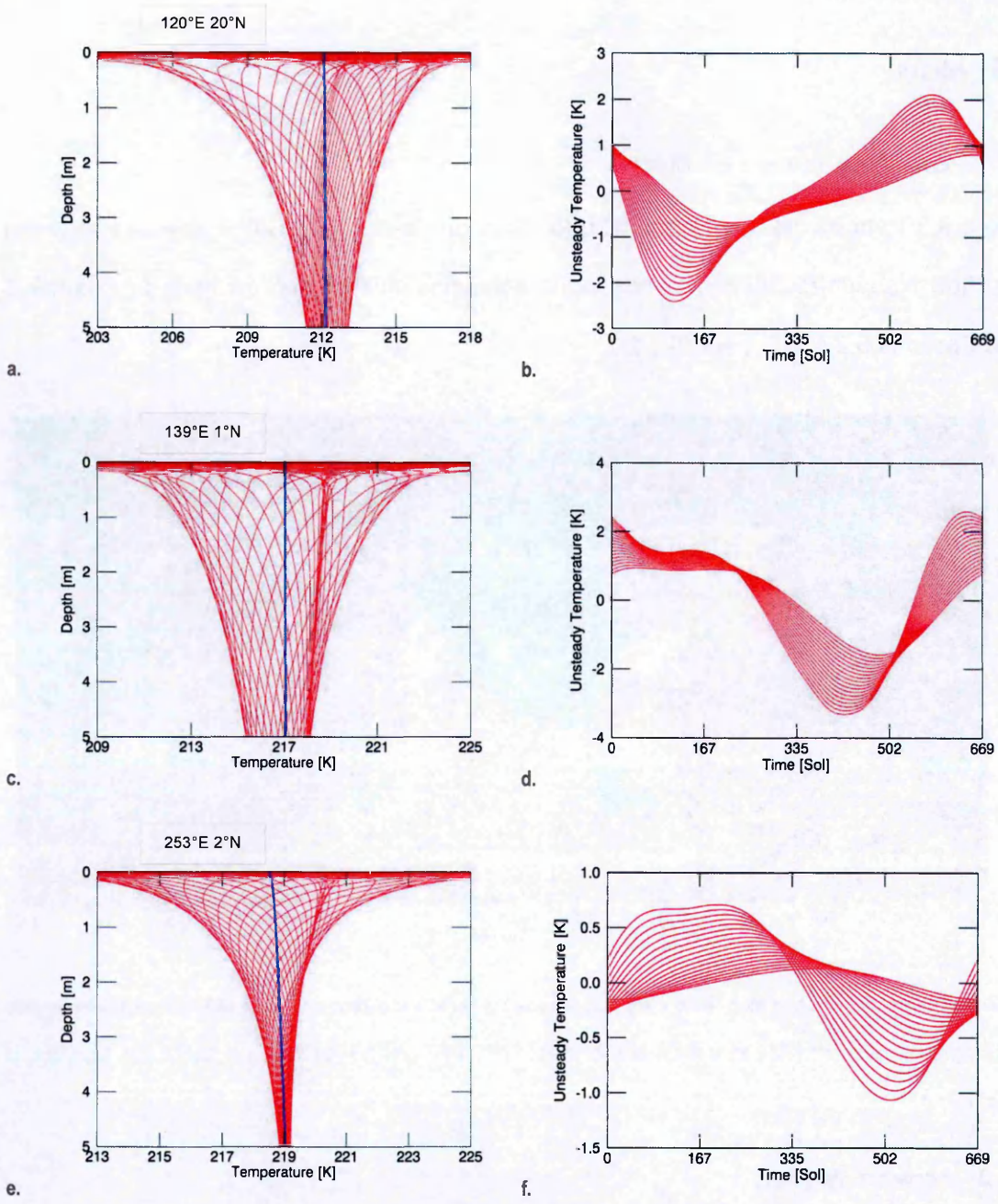

Figure 9.5.2. Forward modelled temperature profiles for measurement sites. The left contours are overlays of depth-dependent temperature T over time t of 669 Sol in ~13 Sol steps (overlapping contours indicate periods of relatively constant diurnal mean temperatures); the right contours are overlays of time-dependent temperature T^U over depth z of 3.2-4.8 m in 0.2 m steps (larger amplitudes towards the surface). These are from the respective high conductivity models of Section 5.2.2 based on the 'low' heat flows of the plate cooling regime where at 120°E 20°N (a-b), 139°E 1°N (c-d) and 253°E 2°N (e-f) the heat flow is 8.5, 6.5 and 11 mW/m/K respectively.

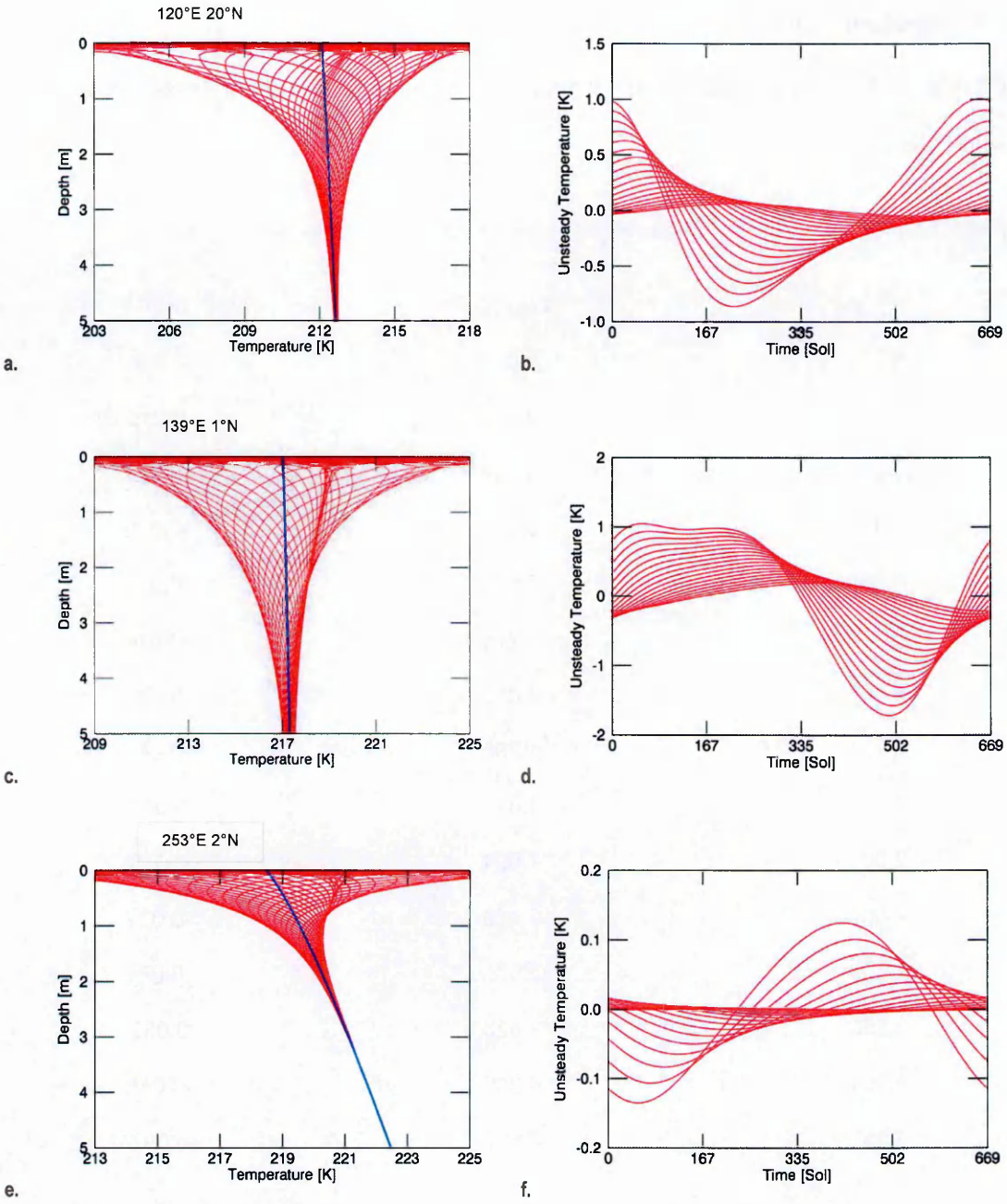

Figure 9.5.3. Forward modelled temperature profiles for measurement sites. The left contours are overlays of depth-dependent temperature T over time t of 669 Sol in ~13 Sol steps (overlapping contours indicate periods of relatively constant diurnal mean temperatures); the right contours are overlays of time-dependent temperature T^U over depth z of 3.2-4.8 m in 0.2 m steps (larger amplitudes towards the surface). These are from the respective low conductivity models for Mars in Chapter 5 based on the 'low' heat flows of the plate cooling regime where at 120°E 20°N (a-b), 139°E 1°N (c-d) and 253°E 2°N (e-f) the heat flow is 8.5, 6.5 and 11 mW/m/K respectively.

9.5.3 Measurements

Table 9.5.1 shows accurate versus inaccurate measurement sensor locations and the absolute deviation.

Table 9.5.1. Accurate z_{ACC} and inaccurate z_{ERR} sensor locations with absolute errors Δz.

z_{ACC} [m]	z_{ERR} [m]	Δz [m]
0.000	0.000	0.000
0.128	0.113	0.015
0.223	0.244	-0.021
0.381	0.397	-0.016
0.560	0.574	-0.014
0.763	0.779	-0.016
0.993	1.018	-0.025
1.255	1.296	-0.041
1.659	1.619	0.040
2.009	1.994	0.016
2.407	2.429	-0.022
2.859	2.935	-0.077
3.556	3.523	0.033
4.161	4.206	-0.045
5.097	5.000	0.097

Figure 9.5.4 shows representative measurement profiles for the high conductivity scenarios, to be compared to the equivalent low conductivity profiles illustrated in Section 5.3.2. Higher density, shorter period and/or shallower depth measurement profiles can be derived from those plotted in Figure 9.5.4 by respectively increasing the density of measurements, restricting the range of temperatures, or cutting off the measurement at shallower sensor depths.

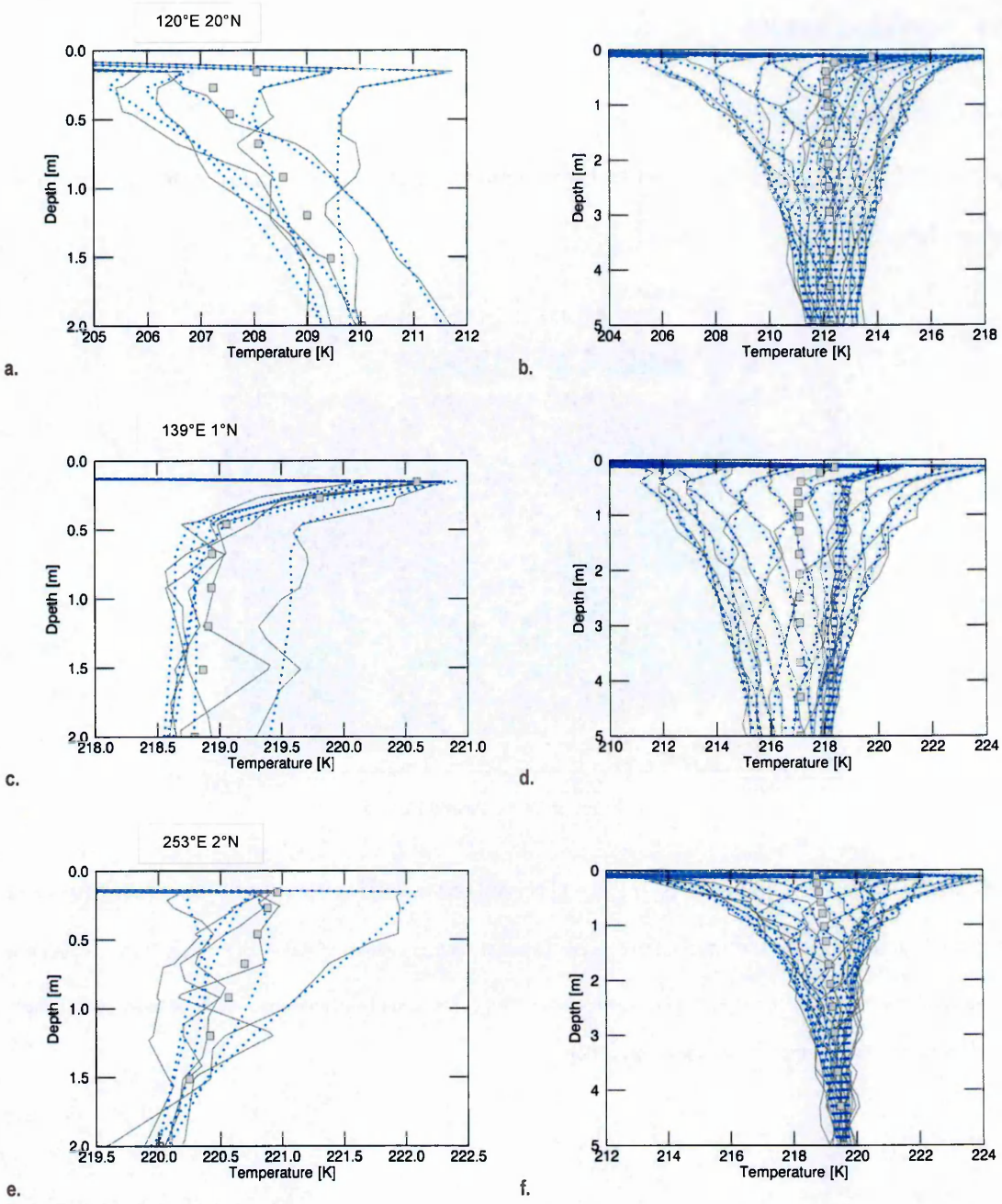

Figure 9.5.4. Representative profiles for measurements with 1 K additive noise at sites at 120°E 20°N (a-b), 139°E 1°N (c-d) and 253°E 2°N (e-f) for the high conductivity, high heat flow scenario. The plots are overlays of temperature-depth profiles in ~33 Sol steps over a monitoring period of: (a, c, e) 168 Sol down to 2 m depth; (c, d, f) 669 Sol down to 5 m depth. The solid grey curves represent the noisy measurement while the dotted blue curves illustrate the true profiles. The grey squares are sensor locations (inaccurate) plotted at the true mean temperature at a particular depth.

9.5.4 Inversion Results

9.5.4.1 *Initial Estimates*

Figure 9.5.5 shows trends in initial heat flow accuracy when using different 'surface' sensors to calculate it.

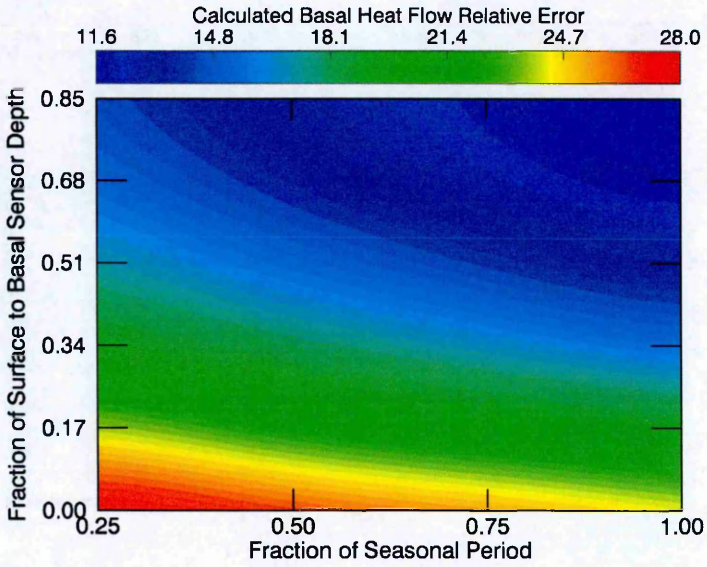

Figure 9.5.5. Trends $\overline{\epsilon_{F_B^{SO}}}$ in relative error $\epsilon_{F_B^{SO}} = \left|\frac{F_B^{SO}}{F_B^{ST}} - 1\right|$ of initial heat flow F_B^{SO} to true value F_B^{ST} across all measurement scenarios, interpolated from 3D scatterplots. The $\overline{\epsilon_{F_B^{SO}}}$ can be considered as central estimators of the heat flow distribution at particular postions defined by the axes and is shown as a function of the ratio of surface sensor depth to basal sensor depth r_{zl}, and the ratio of monitoring period to seasonal period r_t.

Table 9.5.2. Grid of initial heat flow estimate relative error magnitudes $\epsilon_{F_B^{SO}} = \left|\frac{F_B^{SO}}{F_B^{ST}} - 1\right|$ (green borders) at Elysium 120°E 20°N for the high conductivity k scenario with a heat flow F_B^{ST} of 17 mW/m². The shaded cells show values which are not improved by the algorithm. The bulk conductivity down to 20 m is k_{BULK} [W/m/K] and z_{SKIN} [m] is the skin depth.

$k_{BULK} = 0.517$	MONITORING PERIOD [~MARTIAN YEARS]				$F_B^{ST} = 0.017$
	0.25	0.5	0.75	1.0	
DEPTH [m] 2.0	40.37	15.97	2.95	0.25	1.0
	39.96	14.74	2.78	0.17	0.1
	40.08	14.68	2.79	0.16	0.01
3.0	35.70	13.66	3.20	0.05	1.0
	35.19	13.97	3.42	0.22	0.1
	35.16	13.97	3.41	0.19	0.01
5.0	24.18	10.91	3.33	0.22	1.0
	24.20	10.96	3.28	0.27	0.1
	24.20	10.96	3.29	0.28	0.01
$z_{SKIN} = 1.45$	168 (1)	334 (1)	501 (1)	669 (1)	120°E 20°N
	NUMBER OF MEASUREMENTS (TIME RESOLUTION [SOL])				ERROR [K]

Table 9.5.3. Grid of initial heat flow estimate relative error magnitudes $\epsilon_{F_B^{S0}} = \left|\frac{F_B^{S0}}{F_B^{ST}} - 1\right|$ (green borders) at Elysium 120°E 20°N for the low conductivity k scenario with a heat flow F_B^{ST} of 8.5 mW/m². The shaded cells show values which are not improved by the algorithm. The bulk conductivity down to 20 m is k_{BULK} [W/m/K] and z_{SKIN} [m] is the skin depth.

$k_{BULK} = 0.073$	MONITORING PERIOD [~MARTIAN YEARS]				$F_B^{ST} = 0.0085$	
	0.25	0.5	0.75	1.0		
DEPTH [m] 2.0	23.18	10.20	3.10	0.10	1.0	ERROR [K]
	23.30	10.13	3.04	0.04	0.1	
	23.26	10.13	3.03	0.04	0.01	
3.0	15.28	7.70	2.68	0.01	1.0	
	15.36	7.77	2.70	0.05	0.1	
	15.35	7.77	2.70	0.04	0.01	
5.0	7.47	4.08	1.52	0.11	1.0	
	7.52	4.14	1.55	0.10	0.1	
	7.51	4.15	1.55	0.10	0.01	
$z_{SKIN} = 0.91$	168 (1)	334 (1)	501 (1)	669 (1)	120°E 20°N	
	NUMBER OF MEASUREMENTS (TIME RESOLUTION [SOL])					

Table 9.5.4. Grid of initial heat flow estimate relative error magnitudes $\epsilon_{F_B^{S0}} = \left|\frac{F_E^{S0}}{F_B^{ST}} - 1\right|$ (green borders) at Elysium 120°E 20°N for the high conductivity k scenario with a heat flow F_B^{ST} of 8.5 mW/m². The shaded cells show values which are not improved by the algorithm. The bulk conductivity down to 20 m is k_{BULK} [W/m/K] and z_{SKIN} [m] is the skin depth.

$k_{BULK} = 0.517$		MONITORING PERIOD [~MARTIAN YEARS]				$F_B^{ST} = 0.0085$
		0.25	0.5	0.75	1.0	
DEPTH [m]	2.0	82.34	28.98	4.99	0.17	1.0
		80.57	29.69	5.79	0.11	0.1
		80.32	29.57	5.76	0.15	0.01
	3.0	71.12	29.37	7.67	0.04	1.0
		70.58	28.15	6.99	0.27	0.1
		70.53	28.15	7.03	0.18	0.01
	5.0	48.14	21.97	6.62	0.23	1.0
		48.72	22.23	6.87	0.27	0.1
		48.68	22.21	6.86	0.27	0.01
		168 (1)	334 (1)	501 (1)	669 (1)	ERROR [K]
$z_{SKIN} = 1.45$		NUMBER OF MEASUREMENTS (TIME RESOLUTION [SOL])				120°E 20°N

Table 9.5.5. Grid of initial heat flow estimate relative error magnitudes $\epsilon_{F_B^{SO}} = \left|\frac{F_B^{SO}}{F_B^{ST}} - 1\right|$ (green borders) at Elysium site 139°E 1°N for the high conductivity k scenario with a heat flow F_B^{ST} of 15 mW/m². The shaded cells show values which are not improved by the algorithm. The bulk conductivity down to 20 m is k_{BULK} [W/m/K] and z_{SKIN} [m] is the skin depth.

$k_{BULK} = 1.02$

		MONITORING PERIOD [~MARTIAN YEARS]				$F_B^{ST} = 0.015$
		0.25	0.5	0.75	1.0	
DEPTH [m]	2.0	4.03	12.91	21.71	3.02	1.0
		11.61	12.24	24.02	0.35	0.1
		11.78	12.18	24.04	0.29	0.01
	3.0	13.73	7.54	20.84	0.70	1.0
		13.35	8.02	21.22	0.33	0.1
		13.57	7.94	21.24	0.27	0.01
	5.0	15.11	1.60	14.60	0.38	1.0
		14.63	1.42	14.52	0.30	0.1
		14.66	1.45	14.52	0.34	0.01
		168 (1)	334 (1)	501 (1)	669 (1)	ERROR [K]

$z_{SKIN} = 1.89$

NUMBER OF MEASUREMENTS (TIME RESOLUTION [SOL])

139°E 1°N

Table 9.5.6. Grid of initial heat flow estimate relative error magnitudes $\epsilon_{F_B^{S0}} = \left|\frac{F_B^{S0}}{F_B^{ST}} - 1\right|$ (green borders) at Elysium site 139°E 1°N for the low conductivity k scenario with a heat flow F_B^{ST} of 7.4 mW/m². The shaded cells show values which are not improved by the algorithm. The bulk conductivity down to 20 m is k_{BULK} [W/m/K] and z_{SKIN} [m] is the skin depth.

$k_{BULK} = 0.122$

DEPTH [m]	MONITORING PERIOD [~MARTIAN YEARS] 0.25	0.5	0.75	1.0	ERROR [K]
2.0	11.51	0.64	11.19	0.43	1.0
	10.86	0.46	10.46	0.09	0.1
	10.87	0.47	10.49	0.11	0.01
3.0	11.39	2.52	6.59	0.04	1.0
	11.31	2.67	6.58	0.12	0.1
	11.30	2.65	6.57	0.13	0.01
5.0	8.35	3.44	2.64	0.20	1.0
	8.19	3.44	2.61	0.19	0.1
	8.18	3.45	2.62	0.20	0.01
	168 (1)	334 (1)	501 (1)	669 (1)	

$F_B^{ST} = 0.0074$

$z_{SKIN} = 1.07$

NUMBER OF MEASUREMENTS (TIME RESOLUTION [SOL])

139°E 1°N

Table 9.5.7. Grid of initial heat flow estimate relative error magnitudes $\epsilon_{F_B^{SO}} = \left|\frac{F_B^{SO}}{F_B^{ST}} - 1\right|$ (green borders) at Elysium site 139°E 1°N for the high conductivity k scenario with a heat flow F_B^{ST} of 7.4 mW/m². The shaded cells show values which are not improved by the algorithm. The bulk conductivity down to 20 m is k_{BULK} [W/m/K] and z_{SKIN} [m] is the skin depth.

$k_{BULK} = 1.02$		MONITORING PERIOD [~MARTIAN YEARS]				$F_B^{ST} = 0.0074$	
		0.25	0.5	0.75	1.0		
DEPTH [m]	2.0	25.60	25.82	47.67	2.45	1.0	ERROR [K]
		22.74	24.64	48.39	0.74	0.1	
		23.29	24.57	48.33	0.37	0.01	
	3.0	30.28	15.79	43.71	1.10	1.0	
		26.81	16.13	42.64	0.33	0.1	
		26.86	16.14	42.71	0.32	0.01	
	5.0	27.06	2.21	29.21	0.22	1.0	
		29.03	3.19	29.38	0.29	0.1	
		29.00	3.24	29.37	0.36	0.01	
$z_{SKIN} = 1.89$		168 (1)	334 (1)	501 (1)	669 (1)	139°E 1°N	
		NUMBER OF MEASUREMENTS (TIME RESOLUTION [SOL])					

Table 9.5.8. Grid of initial heat flow estimate relative error magnitudes $\epsilon_{F_B^{SO}} = \left|\frac{F_B^{SO}}{F_B^{ST}} - 1\right|$ (green borders) at Tharsis site 253°E 2°N for the high conductivity k scenario with a heat flow F_B^{ST} of 22 mW/m². The shaded cells show values which are not improved by the algorithm. The bulk conductivity down to 20 m is k_{BULK} [W/m/K] and z_{SKIN} [m] is the skin depth.

$k_{BULK} = 0.102$		MONITORING PERIOD [~MARTIAN YEARS]				$F_B^{ST} = 0.022$
		0.25	0.5	0.75	1.0	
DEPTH [m]	2.0	3.65	0.38	3.15	0.11	1.0
		3.64	0.47	3.17	0.08	0.1
		3.63	0.46	3.17	0.08	0.01
	3.0	3.29	0.35	1.94	0.00	1.0
		3.33	0.34	1.95	0.03	0.1
		3.33	0.34	1.95	0.03	0.01
	5.0	2.37	0.66	0.83	0.15	1.0
		2.37	0.68	0.81	0.18	0.1
		2.37	0.68	0.81	0.18	0.01
$z_{SKIN} = 0.56$		168 (1)	334 (1)	501 (1)	669 (1)	253°E 2°N
		NUMBER OF MEASUREMENTS (TIME RESOLUTION [SOL])				

ERROR [K]

Table 9.5.9. Grid of initial heat flow estimate relative error magnitudes $\epsilon_{F_B^{SO}} = \left|\frac{F_B^{SO}}{F_B^{ST}} - 1\right|$ (green borders) at Tharsis site 253°E 2°N for the low conductivity k scenario with a heat flow F_B^{ST} of 11 mW/m². The shaded cells show values which are not improved by the algorithm. The bulk conductivity down to 20 m is k_{BULK} [W/m/K] and z_{SKIN} [m] is the skin depth.

$k_{BULK} = 0.013$	MONITORING PERIOD [~MARTIAN YEARS]				$F_B^{ST} = 0.011$	
	0.25	0.5	0.75	1.0		
DEPTH [m] 2.0	1.72	0.56	0.62	0.00	1.0	ERROR [K]
	1.74	0.56	0.62	0.01	0.1	
	1.73	0.56	0.62	0.01	0.01	
3.0	1.08	0.41	0.35	0.04	1.0	
	1.11	0.40	0.35	0.03	0.1	
	1.11	0.40	0.35	0.03	0.01	
5.0	0.73	0.32	0.10	0.12	1.0	
	0.73	0.32	0.10	0.12	0.1	
	0.73	0.32	0.10	0.12	0.01	
$z_{SKIN} = 0.44$	168 (1)	334 (1)	501 (1)	669 (1)	253°E 2°N	
	NUMBER OF MEASUREMENTS (TIME RESOLUTION [SOL])					

Table 9.5.10. Grid of initial heat flow estimate relative error magnitudes $\epsilon_{F_B^{S0}} = \left|\frac{F_B^{S0}}{F_B^{ST}} - 1\right|$ (green borders) at Tharsis site 253°E 2°N for the high conductivity k scenario with a heat flow F_B^{ST} of 11 mW/m². The shaded cells show values which are not improved by the algorithm. The bulk conductivity down to 20 m is k_{BULK} [W/m/K] and z_{SKIN} [m] is the skin depth.

$k_{BULK} = 0.102$	MONITORING PERIOD [~MARTIAN YEARS]				$F_B^{ST} = 0.011$
	0.25	0.5	0.75	1.0	
DEPTH [m] 2.0	7.44	0.75	6.34	0.09	1.0
	7.38	0.83	6.25	0.06	0.1
	7.37	0.83	6.25	0.07	0.01
3.0	6.54	0.66	3.94	0.02	1.0
	6.65	0.67	3.93	0.04	0.1
	6.63	0.66	3.93	0.04	0.01
5.0	4.53	1.23	1.78	0.16	1.0
	4.57	1.19	1.80	0.19	0.1
	4.57	1.19	1.80	0.19	0.01 ERROR [K]
$z_{SKIN} = 0.56$	168 (1)	334 (1)	501 (1)	669 (1)	253°E 2°N
	NUMBER OF MEASUREMENTS (TIME RESOLUTION [SOL])				

9.5.4.2 Optimized Heat Flow

Figure 9.5.6 shows the effectiveness of the model in optimizing the heat flow based on the trivial (Section 5.3.3.1) and optimized (Section 5.3.3.2) estimates of Martian heat flow in Section 5.3.3.

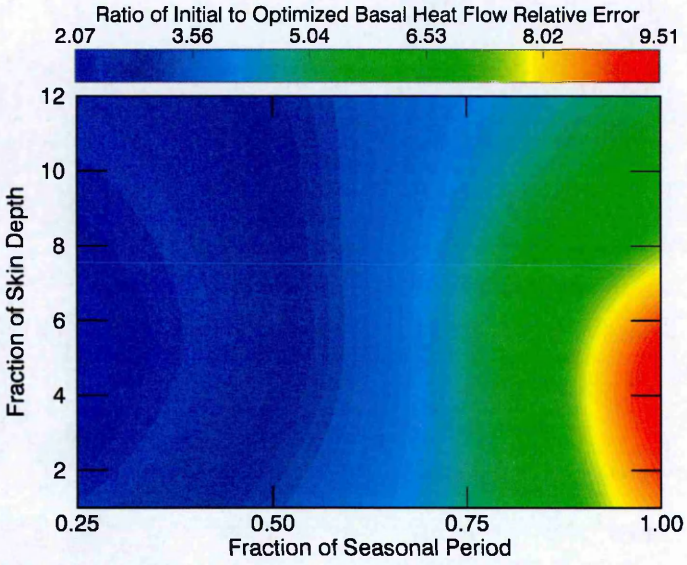

Figure 9.5.6. Trends in the ratio $r_{F_B^S} = \frac{\epsilon_{F_B^{SI}}}{\epsilon_{F_B^{SO}}}$ of optimized heat flow relative error $\epsilon_{F_B^{SI}}$ to initial heat flow relative error $\epsilon_{F_B^{SO}}$ across all measurement scenarios, interpolated from 3D scatterplots. The ratio $r_{F_B^S}$ is shown as a function of the ratio of basal sensor depth to annual skin depth r_z, and the ratio of measurement period to seasonal period r_t. The $r_{F_B^S}$ can be considered as central estimators of the heat flow distribution at particular postions defined by the axes, hence the very high values due to high errors associated with 1 K noise amplitude.

Figure 9.5.6 must be interpreted in line with the trends in initial estimates presented in Section 5.3.3.1, Figure 5-9.

The tables below supplement the results in Section 5.3.3.

Table 9.5.11. Grid of optimized heat flow relative error magnitudes $\epsilon_{F_B^{SI}} = \left|\frac{F_B^{SI}}{F_B^{ST}} - 1\right|$ (green borders) at Elysium 120°E 20°N for the high conductivity k scenario with a heat flow F_B^{ST} of 17 mW/m². The shaded cells show values where there is no improvement on the initial estimate (divergence). The bulk conductivity down to 20 m is k_{BULK} [W/m/K] and z_{SKIN} [m] is the skin depth.

$k_{BULK} = 0.517$	MONITORING PERIOD [~MARTIAN YEARS]				$F_B^{ST} = 0.017$
	0.25	0.5	0.75	1.0	
DEPTH [m] 2.0	20.89	15.76	7.76	0.21	1.0
	20.81	15.68	7.70	0.18	0.1
	6.94	15.68	7.71	0.19	0.01
3.0	2.19	6.45	4.40	0.39	1.0
	2.09	6.58	4.33	0.37	0.1
	11.89	33.04	4.33	0.37	0.01
5.0	3.89	0.74	0.36	0.42	1.0
	3.95	0.71	0.33	0.39	0.1
	3.95	0.70	0.33	0.39	0.01
$z_{SKIN} = 1.45$	168 (1)	334 (1)	501 (1)	669 (1)	120°E 20°N
	NUMBER OF MEASUREMENTS (TIME RESOLUTION [SOL])				

ERROR [K]

Table 9.5.12. Grid of optimized heat flow relative error magnitudes $\epsilon_{F_B^{SI}} = \left|\frac{F_B^{SI}}{F_B^{ST}} - 1\right|$ (green borders) at Elysium 120°E 20°N for the low conductivity k scenario with a heat flow F_B^{ST} of 8.5 mW/m². The shaded cells show values where there is no improvement on the initial estimate (divergence). The bulk conductivity down to 20 m is k_{BULK} [W/m/K] and z_{SKIN} [m] is the skin depth.

$k_{BULK} = 0.073$ | $F_B^{ST} = 0.0085$

DEPTH [m]	MONITORING PERIOD [~MARTIAN YEARS] 0.25	0.5	0.75	1.0	ERROR [K]
2.0	2.90	0.04	0.63	0.26	1.0
	2.88	0.04	0.59	0.25	0.1
	2.88	0.04	0.59	0.25	0.01
3.0	1.22	0.72	0.23	0.18	1.0
	1.27	0.69	0.23	0.18	0.1
	1.26	0.69	0.23	0.19	0.01
5.0	0.14	0.18	0.18	0.15	1.0
	0.13	0.18	0.16	0.12	0.1
	0.13	0.18	0.16	0.13	0.01
	168 (1)	334 (1)	501 (1)	669 (1)	

$z_{SKIN} = 0.91$ | 120°E 20°N

NUMBER OF MEASUREMENTS (TIME RESOLUTION [SOL])

Table 9.5.13. Grid of optimized heat flow relative error magnitudes $\epsilon_{F_B^{SI}} = \left|\frac{F_B^{SI}}{F_B^{ST}} - 1\right|$ (green borders) at Elysium 120°E 20°N for the high conductivity k scenario with a heat flow F_B^{ST} of 8.5 mW/m². The shaded cells show values where there is no improvement on the initial estimate (divergence). The bulk conductivity down to 20 m is k_{BULK} [W/m/K] and z_{SKIN} [m] is the skin depth.

$k_{BULK} = 0.517$	MONITORING PERIOD [~MARTIAN YEARS]				$F_B^{ST} = 0.0085$
	0.25	0.5	0.75	1.0	
DEPTH [m] 2.0	41.47	31.44	15.41	0.21	1.0
	41.72	31.42	15.48	0.32	0.1
	41.69	31.41	15.48	0.32	0.01
3.0	4.30	13.26	8.76	0.70	1.0
	4.21	13.21	8.70	0.69	0.1
	23.57	13.21	8.70	0.69	0.01
5.0	8.06	1.59	0.53	0.71	1.0
	7.84	1.36	0.70	0.74	0.1
	7.87	1.37	0.69	0.74	0.01
$z_{SKIN} = 1.45$	168 (1)	334 (1)	501 (1)	669 (1)	120°E 20°N
	NUMBER OF MEASUREMENTS (TIME RESOLUTION [SOL])				ERROR [K]

Table 9.5.14. Grid of optimized heat flow relative error magnitudes $\epsilon_{F_B^{SI}} = \left|\frac{F_B^{SI}}{F_B^{ST}} - 1\right|$ (green borders) at Elysium site 139°E 1°N for the high conductivity k scenario with a heat flow F_B^{ST} of 15 mW/m². The shaded cells show values where there is no improvement on the initial estimate (divergence). The bulk conductivity down to 20 m is k_{BULK} [W/m/K] and z_{SKIN} [m] is the skin depth.

$k_{BULK} = 1.02$	MONITORING PERIOD [~MARTIAN YEARS]				$F_B^{ST} = 0.015$
	0.25	0.5	0.75	1.0	
DEPTH [m] 2.0	28.87	5.21	19.46	6.94	1.0
	28.96	5.25	19.42	6.91	0.1
	64.98	5.26	28.80	6.91	0.01
3.0	29.77	15.18	5.85	5.20	1.0
	29.85	15.26	5.82	5.14	0.1
	29.84	45.34	5.82	5.15	0.01
5.0	7.81	7.93	1.28	3.55	1.0
	7.80	7.99	1.25	3.55	0.1
	7.81	7.97	1.24	3.55	0.01
$z_{SKIN} = 1.89$	168 (1)	334 (1)	501 (1)	669 (1)	139°E 1°N
	NUMBER OF MEASUREMENTS (TIME RESOLUTION [SOL])				

ERROR [K]

Table 9.5.15. Grid of optimized heat flow relative error magnitudes $\epsilon_{F_B^{SI}} = \left|\frac{F_B^{SI}}{F_B^{ST}} - 1\right|$ (green borders) at Elysium site 139°E 1°N for the low conductivity k scenario with a heat flow F_B^{ST} of 7.4 mW/m². The shaded cells show values where there is no improvement on the initial estimate (divergence). The bulk conductivity down to 20 m is k_{BULK} [W/m/K] and z_{SKIN} [m] is the skin depth.

$k_{BULK} = 0.122$	MONITORING PERIOD [~MARTIAN YEARS]				$F_B^{ST} = 0.0074$
	0.25	0.5	0.75	1.0	
DEPTH [m] 2.0	6.53	5.64	0.44	2.28	1.0
	6.72	5.75	0.50	2.28	0.1
	6.73	5.74	0.50	2.27	0.01
3.0	0.87	0.36	0.17	1.63	1.0
	0.88	0.36	0.23	1.62	0.1
	0.87	0.36	0.22	1.62	0.01
5.0	1.48	1.25	1.00	1.00	1.0
	1.48	1.21	0.98	1.03	0.1
	1.48	1.21	0.98	1.03	0.01
	168 (1)	334 (1)	501 (1)	669 (1)	ERROR [K]
$z_{SKIN} = 1.07$	NUMBER OF MEASUREMENTS (TIME RESOLUTION [SOL])				139°E 1°N

Table 9.5.16. Grid of optimized heat flow relative error magnitudes $\epsilon_{F_B^{SI}} = \left|\frac{F_B^{SI}}{F_B^{ST}} - 1\right|$ (green borders) at Elysium site 139°E 1°N for the high conductivity k scenario with a heat flow F_B^{ST} of 7.4 mW/m². The shaded cells show values where there is no improvement on the initial estimate (divergence). The bulk conductivity down to 20 m is k_{BULK} [W/m/K] and z_{SKIN} [m] is the skin depth.

$k_{BULK} = 1.02$ | MONITORING PERIOD [~MARTIAN YEARS] | $F_B^{ST} = 0.0074$

DEPTH [m]	0.25	0.5	0.75	1.0	ERROR [K]
2.0	57.93	10.61	39.22	14.11	1.0
	57.84	10.39	38.91	13.94	0.1
	129.69	10.41	57.36	13.93	0.01
3.0	59.49	30.31	11.59	9.99	1.0
	59.59	30.44	11.76	10.37	0.1
	59.59	30.44	11.73	10.39	0.01
5.0	15.61	15.80	2.46	7.19	1.0
	15.52	15.90	2.42	7.19	0.1
	15.53	15.87	2.41	7.17	0.01
	168 (1)	334 (1)	501 (1)	669 (1)	

$z_{SKIN} = 1.89$ | NUMBER OF MEASUREMENTS (TIME RESOLUTION [SOL]) | 139°E 1°N

Table 9.5.17. Grid of optimized heat flow relative error magnitudes $\epsilon_{F_B^{SI}} = \left|\frac{F_B^{SI}}{F_B^{ST}} - 1\right|$ (green borders) at Tharsis site 253°E 2°N for the high conductivity k scenario with a heat flow F_B^{ST} of 22 mW/m². The shaded cells show values where there is no improvement on the initial estimate (divergence). The bulk conductivity down to 20 m is k_{BULK} [W/m/K] and z_{SKIN} [m] is the skin depth.

$k_{BULK} = 0.102$	MONITORING PERIOD [~MARTIAN YEARS]				$F_B^{ST} = 0.022$
DEPTH [m]	0.25	0.5	0.75	1.0	ERROR [K]
2.0	3.65	0.38	3.15	0.11	1.0
	3.64	0.47	3.17	0.08	0.1
	3.63	0.46	3.17	0.08	0.01
3.0	3.29	0.35	1.94	0.00	1.0
	3.33	0.34	1.95	0.03	0.1
	3.33	0.34	1.95	0.03	0.01
5.0	2.37	0.66	0.83	0.15	1.0
	2.37	0.68	0.81	0.18	0.1
	2.37	0.68	0.81	0.18	0.01
$z_{SKIN} = 0.56$	168 (1)	334 (1)	501 (1)	669 (1)	253°E 2°N
	NUMBER OF MEASUREMENTS (TIME RESOLUTION [SOL])				

Table 9.5.18. Grid of optimized heat flow relative error magnitudes $\epsilon_{F_B^{SI}} = \left|\frac{F_B^{SI}}{F_B^{ST}} - 1\right|$ (green borders) at Tharsis site 253°E 2°N for the low conductivity k scenario with a heat flow F_B^{ST} of 11 mW/m². The shaded cells show values where there is no improvement on the initial estimate (divergence). The bulk conductivity down to 20 m is k_{BULK} [W/m/K] and z_{SKIN} [m] is the skin depth.

$k_{BULK} = 0.013$ | MONITORING PERIOD [~MARTIAN YEARS] | $F_B^{ST} = 0.011$

DEPTH [m]	0.25	0.5	0.75	1.0	ERROR [K]
2.0	1.72	0.56	0.62	0.00	1.0
	1.74	0.56	0.62	0.01	0.1
	1.73	0.56	0.62	0.01	0.01
3.0	1.08	0.41	0.35	0.04	1.0
	1.11	0.40	0.35	0.03	0.1
	1.11	0.40	0.35	0.03	0.01
5.0	0.73	0.32	0.10	0.12	1.0
	0.73	0.32	0.10	0.12	0.1
	0.73	0.32	0.10	0.12	0.01
	168 (1)	334 (1)	501 (1)	669 (1)	

$z_{SKIN} = 0.44$ | NUMBER OF MEASUREMENTS (TIME RESOLUTION [SOL]) | 253°E 2°N

Table 9.5.19. Grid of optimized heat flow relative error magnitudes $\epsilon_{F_B^{SI}} = \left|\frac{F_B^{SI}}{F_B^{ST}} - 1\right|$ (green borders) at Tharsis site 253°E 2°N for the high conductivity k scenario with a heat flow F_B^{ST} of 11 mW/m². The shaded cells show values where there is no improvement on the initial estimate (divergence). The bulk conductivity down to 20 m is k_{BULK} [W/m/K] and z_{SKIN} [m] is the skin depth.

$k_{BULK} = 0.102$		MONITORING PERIOD [~MARTIAN YEARS]				$F_B^{ST} = 0.011$
		0.25	0.5	0.75	1.0	
DEPTH [m]	2.0	7.44	0.75	6.34	0.09	1.0
		7.38	0.83	6.25	0.06	0.1
		7.37	0.83	6.25	0.07	0.01
	3.0	6.54	0.66	3.94	0.02	1.0
		6.65	0.67	3.93	0.04	0.1
		6.63	0.66	3.93	0.04	0.01
	5.0	4.53	1.23	1.78	0.16	1.0
		4.57	1.19	1.80	0.19	0.1
		4.57	1.19	1.80	0.19	0.01
$z_{SKIN} = 0.56$		168 (1)	334 (1)	501 (1)	669 (1)	253°E 2°N
		NUMBER OF MEASUREMENTS (TIME RESOLUTION [SOL])				

ERROR [K]

Figure 9.5.7 shows comparison plots of optimization results at 2 m for the Elysium site at 139°E 1°N where particular features of the unsteady temperature allow for accurate optimization of the basal heat flow. Examination of the related surface temperatures shown in Section 5.2.1 shows that, for monitoring periods shorter than 0.75 Martian years, only the lower temperatures of the cycle are measured, causing a positive shift in the mean temperature gradient measured by the sensors. At 0.75 Martian years and longer, the full range of unsteady temperature extrema is sampled reducing the biases introduced by the unsteady temperature variation – this follows results in Section 4.2.1.2.

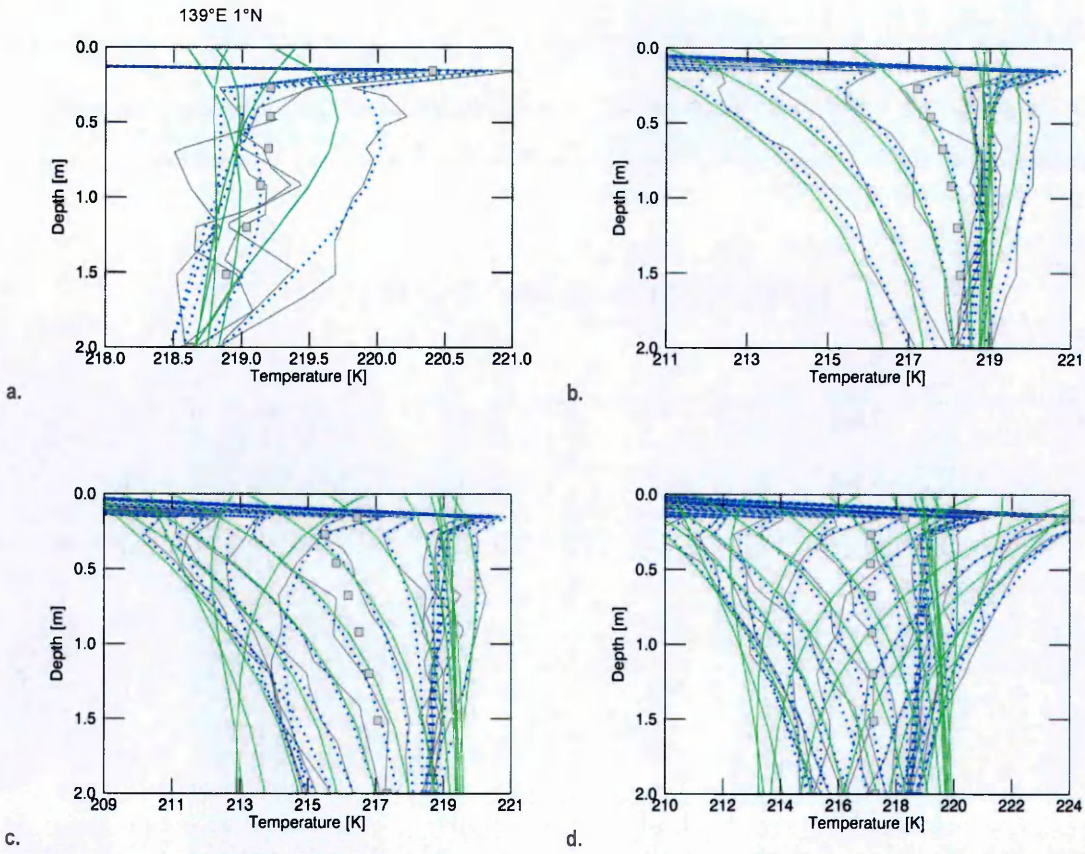

Figure 9.5.7. Representative profiles for temperature inversions at the Elysium site at 139°E 1°N for the low conductivity, high heat flow scenarios with noise of 1 K amplitude, measurement depth up to 2 m. The plots are overlays of temperature-depth profiles over time where the dotted blue curves represent the true profiles, the solid grey curves the profiles with 1 K error and the solid green curves represent the optimized temperature profiles. Plot: a. covers a monitoring period of 168 Sols in; b. 334 Sol; c. 501 Sol and; d. 669 Sol. The curves are shown in ~33 Sol steps though the calculations are carried out in 1 Sol steps. The grey squares are sensor locations and are plotted at the mean of the true temperature profile at a particular depth.

9.6 Mercury

9.6.1 Forward Models

Table 9.6.1 lists the critical parameters used to calculate the surface energy balance for the Mercurian scenarios presented in Section 6.3.1.

Table 9.6.1. Surface energy balance parameters used to calculate the surface temperature on Mercury.

PARAMETER	VALUE
Solar Constant S^o [W/m^2]	1370
Bond albedo A	0.1
Emissivity ε	0.9

Solar incidence angles are after JPL (2014) and cover the period from June 13, 2024 to December 06, 2024 (perihelion to perihelion).

Figure 9.6.1 shows the forward modelled temperature profiles for the 2-layered models discussed in Section 6.3.1.

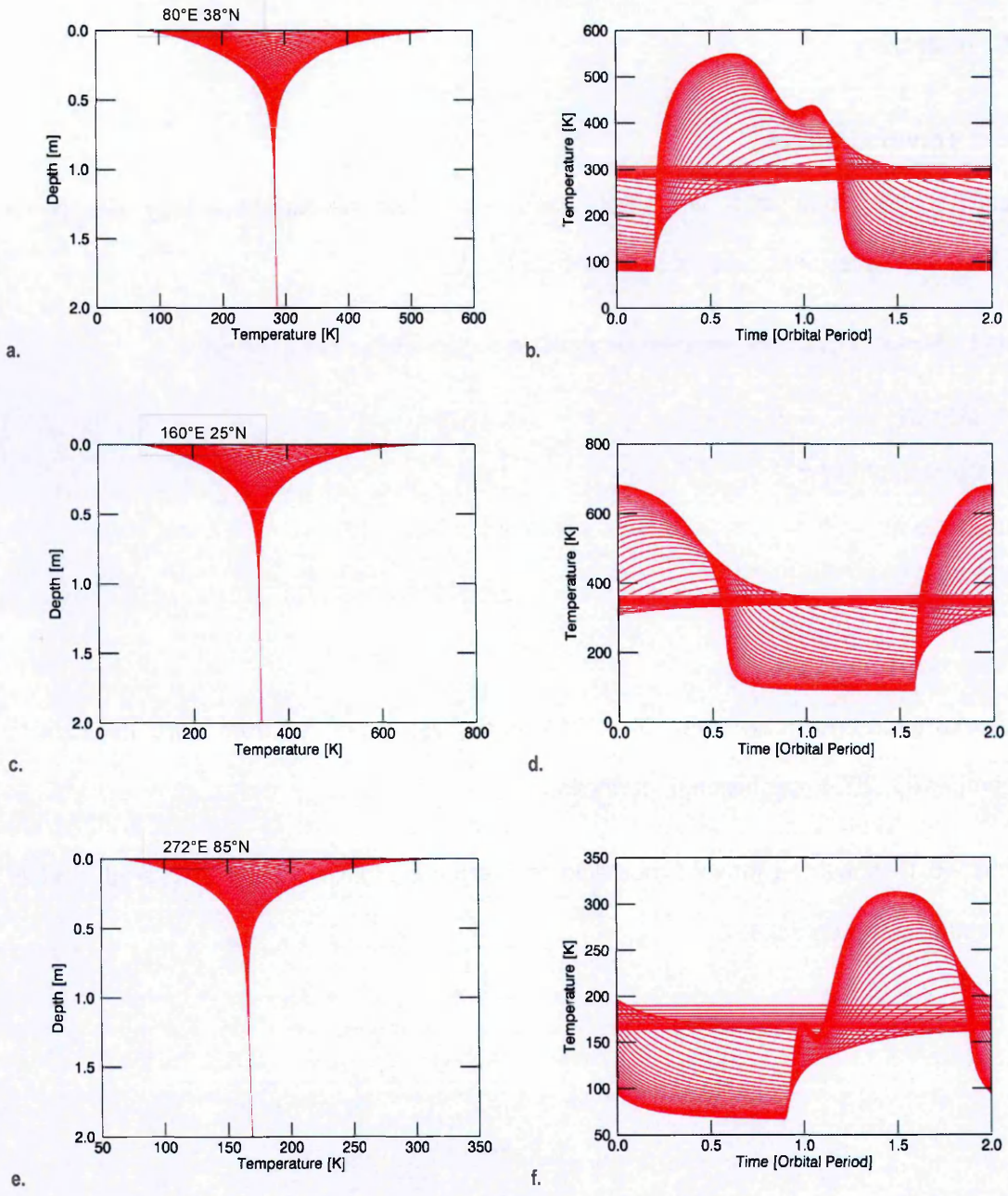

Figure 9.6.1. Forward modelled temperature profiles for measurement sites. These are from the respective 2-layered models (see Section 6.2.2) with the 'high' heat flow (30 mW/m²) regime at 80°E 38°N (a-b), 160°E 25°N (c-d) and 272°E 85°N (e-f). The left contours are overlays of depth-dependent temperature T over time t of 2 orbital periods in ~3.5 d steps; the right contours are overlays of time-dependent temperature T over depth z of 5 m (larger amplitudes towards the surface). All simulations are run over the same time period from midnight at perihelion (also see Appendix 9.6.1).[1]

[1] The forward models with lower heat flow are visually indistinguishable from that presented in Figure 9.6 1 and is therefore not shown.

9.6.2 Measurements

Figure 9.6.2 shows representative measurements for the 2-layered site scenarios, as discussed in Sections 6.2.2 and 6.3.1.

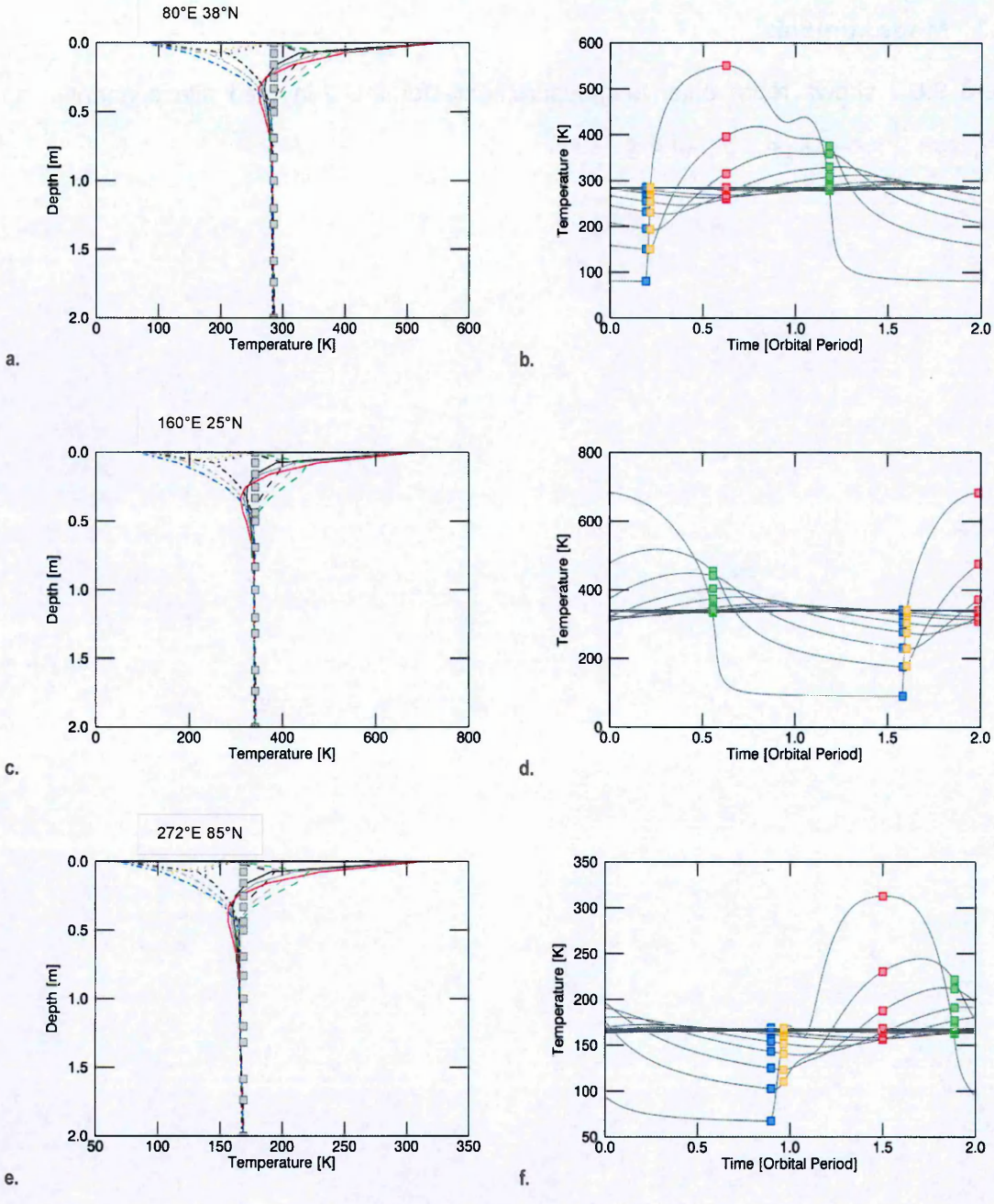

Figure 9.6.2. Temperature profiles for measurements at sites at 80°E 38°N (a-b), 160°E 25°N (c-d) and 272°E 85°N (e-f) for the 2-layered regolith model with a heat flow of 30 mW/m^2. The plots are overlays of: (a, c, e) temperature-depth profiles for instantaneous measurements at peak daytime, (solid red), transitional heating (dotted orange) and cooling (dashed green) and, minimum nightime (dot-dashed blue) temperatures and; (b, d, f) temperature-time profiles for measurements covering 1 Mercurian solar day. The squares represent sensor locations: in space (a, c, e, plotted at the basal temperature value); and time (b, d, f, plotted at the times and temperatures of, and colour coordinated with the instantaneous measurements).

9.6.3 Optimization Results

9.6.3.1 *Initial Estimates*

Table 9.6.2 to Table 9.6.4 show the errors in heat flow estimates, before optimization, using bulk conductivity (down to 10 m) and the temperature gradient at the 2 lowest sensors. These are discussed in Section 6.3.

Table 9.6.2. Grid of initial heat flow estimate relative error magnitudes $\epsilon_{F_B^{SO}} = \left|\frac{F_B^{SO}}{F_B^{ST}} - 1\right|$ (green borders – see Appendix 9.1 for symbol definitions) from measurement sited at 80°E 38°N on Mercury. This is for the 2-layered site scenario where the red shaded cells indicate a (incorrect) 2-layered regolith assumption. The bulk conductivity down to 10 m is k_{BULK} [W/m/K] and z_{SKIN} [m] is the skin depth. The shaded cells show values which are not improved by optimization.

80°E 38°N	MONITORING PERIOD [~SOLAR DAY]					2-LAYERED
DEPTH [m]	0.0 (PEAK DAYTIME)	0.0 (TRANSITIONAL HEATING)	0.0 (TRANSITIONAL COOLING)	0.0 (MINIMUM NIGHTIME)	1	HEAT FLOW [W/m^2]
0.5	66.43	84.95	94.33	83.62	0.02	0.01
	32.88	43.27	47.35	41.52	0.04	0.02
	22.13	28.70	30.96	27.68	0.09	0.03
	68.15	87.15	96.72	85.79	0.00	0.01
	33.74	44.40	48.54	42.61	0.02	0.02
	22.72	29.46	31.73	28.41	0.07	0.03
2.0	0.19	0.01	0.30	0.11	0.11	0.01
	0.12	0.23	0.05	0.23	0.11	0.02
	0.16	0.13	0.08	0.20	0.12	0.03
	0.17	0.03	0.29	0.09	0.08	0.01
	0.10	0.21	0.03	0.21	0.09	0.02
	0.14	0.10	0.05	0.18	0.10	0.03
k_{BULK} = 6.95E-3	1 (-)	1 (-)	1 (-)	1 (-)	176 (1.0)	z_{SKIN} =0.16
	NUMBER OF MEASUREMENTS (TIME RESOLUTION [DAY])					

Table 9.6.3. Grid of initial heat flow estimate relative error magnitudes $\epsilon_{F_B^{SO}} = \left|\frac{F_B^{SO}}{F_B^{ST}} - 1\right|$ (green borders – see Appendix 9.1 for symbol definitions) from measurement sited at 160°E 25°N on Mercury. This is for the 2-layered site scenario where the red shaded cells indicate a (incorrect) 2-layered regolith assumption. The bulk conductivity down to 10 m is k_{BULK} [W/m/K] and z_{SKIN} [m] is the skin depth. The shaded cells show values which are not improved by optimization.

160°E 25°N	MONITORING PERIOD [~SOLAR DAY]					2-LAYERED
	0.0 (PEAK DAYTIME)	0.0 (TRANSITIONAL HEATING)	0.0 (TRANSITIONAL COOLING)	0.0 (MINIMUM NIGHTIME)	1	
DEPTH [m] 0.5	91.81	108.64	121.04	102.99	0.01	0.01
	47.12	54.22	60.78	51.23	0.07	0.02
	30.83	35.25	40.47	34.05	0.10	0.03
	94.19	111.44	124.11	105.65	0.01	0.01
	48.36	55.63	62.31	52.57	0.05	0.02
	31.64	36.18	41.48	34.94	0.07	0.03
	0.04	0.20	0.18	0.26	0.12	0.01
	0.13	0.23	0.05	0.07	0.12	0.02
2.0	0.03	0.04	0.21	0.18	0.12	0.03
	0.01	0.23	0.21	0.24	0.10	0.01
	0.11	0.21	0.08	0.04	0.09	0.02
	0.01	0.01	0.19	0.16	0.09	0.03
k_{BULK} = 6.95E-3	1 (-)	1 (-)	1 (-)	1 (-)	176 (1.0)	z_{SKIN} =0.16
	NUMBER OF MEASUREMENTS (TIME RESOLUTION [DAY])					

HEAT FLOW [W/m^2]

Table 9.6.4. Grid of initial heat flow estimate relative error magnitudes $\epsilon_{F_B^{SO}} = \left|\frac{F_B^{SO}}{F_B^{ST}} - 1\right|$ (green borders – see Appendix 9.1 for symbol definitions) from measurement sited at 272°E 85°N on Mercury. This is for the 2-layered site scenario where the red shaded cells indicate a (incorrect) 2-layered regolith assumption. The bulk conductivity down to 10 m is k_{BULK} [W/m/K] and z_{SKIN} [m] is the skin depth. The shaded cells show values which are not improved by optimization.

272°E 85°N	MONITORING PERIOD [~SOLAR DAY]					2-LAYERED
	0.0 (PEAK DAYTIME)	0.0 (TRANSITIONAL HEATING)	0.0 (TRANSITIONAL COOLING)	0.0 (MINIMUM NIGHTIME)	1	
DEPTH [m] 0.5	24.07	37.67	40.89	30.39	0.12	0.01
	10.72	18.37	20.68	16.02	0.05	0.02
	7.14	12.85	14.92	11.14	0.07	0.03
	24.71	38.66	41.91	31.20	0.10	0.01
	11.02	18.86	21.19	16.45	0.03	0.02
	7.35	13.21	15.28	11.45	0.04	0.03
	0.19	0.18	0.00	0.46	0.12	0.01
	0.15	0.14	0.03	0.05	0.12	0.02
2.0	0.13	0.15	0.10	0.04	0.11	0.03
	0.22	0.16	0.02	0.44	0.09	0.01
	0.13	0.11	0.06	0.03	0.10	0.02
	0.11	0.12	0.08	0.07	0.09	0.03
k_{BULK} = 6.95E-3	1 (-)	1 (-)	1 (-)	1 (-)	176 (1.0)	z_{SKIN} =0.16
	NUMBER OF MEASUREMENTS (TIME RESOLUTION [DAY])					

HEAT FLOW [W/m^2]

9.6.3.2 *Optimized Heat Flow*

Table 9.6.5 to Table 9.6.7 show the errors in optimized heat flow estimates. These are discussed in Section 6.3.

Table 9.6.5. Grid of optimized heat flow relative error magnitudes $\epsilon_{F_B^{SI}} = \left|\frac{F_B^{SI}}{F_B^{ST}} - 1\right|$ (green borders – see Appendix 9.1 for symbol definitions) from measurement sited at 80°E 38°N onMercury. This is for the 2-layered site scenario where the red shaded cells indicate a (incorrect) 2-layered regolith assumption. The bulk conductivity down to 10 m is k_{BULK} [W/m/K] and z_{SKIN} [m] is the skin depth. The shaded cells show values which are not improved by optimization.

80°E 38°N	MONITORING PERIOD [~SOLAR DAY]					2-LAYERED
	0.0 (PEAK DAYTIME)	0.0 (TRANSITIONAL HEATING)	0.0 (TRANSITIONAL COOLING)	0.0 (MINIMUM NIGHTIME)	1	
0.5	8.65	23.75	22.04	22.53	0.14	0.01
	4.18	11.97	10.95	11.38	0.16	0.02
	2.75	8.03	7.23	7.67	0.17	0.03
	11.19	35.50	31.27	34.48	0.38	0.01
	5.35	17.95	15.45	17.46	0.40	0.02
	3.44	12.10	10.16	11.79	0.40	0.03
2.0	0.23	0.16	0.17	0.19	0.04	0.01
	0.14	0.10	0.06	0.13	0.05	0.02
	0.12	0.09	0.01	0.11	0.05	0.03
	0.24	0.82	0.51	0.81	0.16	0.01
	0.21	0.49	0.17	0.50	0.17	0.02
	0.20	0.39	0.05	0.39	0.17	0.03
k_{BULK} = 6.95E-3	1 (-)	1 (-)	1 (-)	1 (-)	176 (1.0)	z_{SKIN} =0.15
	NUMBER OF MEASUREMENTS (TIME RESOLUTION [DAY])					

DEPTH [m]

HEAT FLOW [W/m^2]

Table 9.6.6. Grid of optimized heat flow relative error magnitudes $\epsilon_{F_B^{SI}} = \left|\frac{F_B^{SI}}{F_B^{ST}} - 1\right|$ (green borders – see Appendix 9.1 for symbol definitions) from measurement sited at 160°E 25°N onMercury. This is for the 2-layered site scenario where the red shaded cells indicate a (incorrect) 2-layered regolith assumption. The bulk conductivity down to 10 m is k_{BULK} [W/m/K] and z_{SKIN} [m] Is the skin depth. The shaded cells show values which are not improved by optimization.

160°E 25°N	MONITORING PERIOD [~SOLAR DAY]					2-LAYERED
	0.0 (PEAK DAYTIME)	0.0 (TRANSITIONAL HEATING)	0.0 (TRANSITIONAL COOLING)	0.0 (MINIMUM NIGHTIME)	1	
0.5	10.57	29.86	28.90	27.52	0.33	0.01
	5.13	15.08	14.37	13.89	0.26	0.02
	3.35	10.10	9.53	9.30	0.24	0.03
	12.10	44.08	40.71	42.37	0.52	0.01
	5.79	22.29	20.15	21.42	0.47	0.02
	3.72	14.98	13.31	14.40	0.45	0.03
2.0	0.38	0.27	0.05	0.20	0.11	0.01
	0.21	0.17	0.01	0.12	0.09	0.02
	0.16	0.13	0.02	0.10	0.08	0.03
	0.39	1.04	0.54	0.94	0.22	0.01
	0.27	0.61	0.18	0.55	0.20	0.02
	0.24	0.47	0.06	0.43	0.19	0.03
k_{BULK} = 6.95E-3	1 (-)	1 (-)	1 (-)	1 (-)	176 (1.0)	z_{SKIN} =0.15
	NUMBER OF MEASUREMENTS (TIME RESOLUTION [DAY])					

DEPTH [m]

HEAT FLOW [W/m^2]

Table 9.6.7. Grid of optimized heat flow relative error magnitudes $\epsilon_{F_B^{SI}} = \left|\frac{F_B^{SI}}{F_B^{ST}} - 1\right|$ (green borders – see Appendix 9.1 for symbol definitions) from measurement sited at 272°E 85°N onMercury. This is for the 2-layered site scenario where the red shaded cells indicate a (incorrect) 2-layered regolith assumption. The bulk conductivity down to 10 m is k_{BULK} [W/m/K] and z_{SKIN} [m] is the skin depth. The shaded cells show values which are not improved by optimization.

272°E 85°N	MONITORING PERIOD [~SOLAR DAY]					2-LAYERED
	0.0 (PEAK DAYTIME)	0.0 (TRANSITIONAL HEATING)	0.0 (TRANSITIONAL COOLING)	0.0 (MINIMUM NIGHTIME)	1	
0.5	6.73	11.14	13.20	10.56	0.16	0.01
	3.28	5.71	6.46	5.37	0.17	0.02
	2.13	3.86	4.30	3.61	0.18	0.03
	8.65	16.02	17.97	15.62	0.39	0.01
	4.12	8.26	8.74	8.01	0.40	0.02
	2.62	5.63	5.73	5.46	0.41	0.03
2.0	0.11	0.12	0.00	0.11	0.05	0.01
	0.08	0.09	0.02	0.08	0.06	0.02
	0.08	0.09	0.04	0.08	0.06	0.03
	0.13	0.46	0.14	0.43	0.17	0.01
	0.15	0.32	0.01	0.30	0.18	0.02
	0.17	0.28	0.08	0.26	0.18	0.03
k_{BULK} = 6.95E-3	1 (-)	1 (-)	1 (-)	1 (-)	176 (1.0)	z_{SKIN} =0.15
	NUMBER OF MEASUREMENTS (TIME RESOLUTION [DAY])					

DEPTH [m] — HEAT FLOW [W/m^2]

Figure 9.6.3 shows example plots of optimization results with an instantaneous measurement for the 2-layered regolith model as discussed in Section 6.3.3.2, along with the 1-layered regolith model results.

Figure 9.6.4 shows 1 and 2-layered results with sensor penetration depths of up to 0.5 m, also discussed in Section 6.3.3.2.

Figure 9.6.5 and Figure 9.6.6 show the optimization results for measurements covering a full Mercurian solar day for the 1-layered, and 2-layered measurement scenarios, with different (correct, incorrect) layering assumptions.

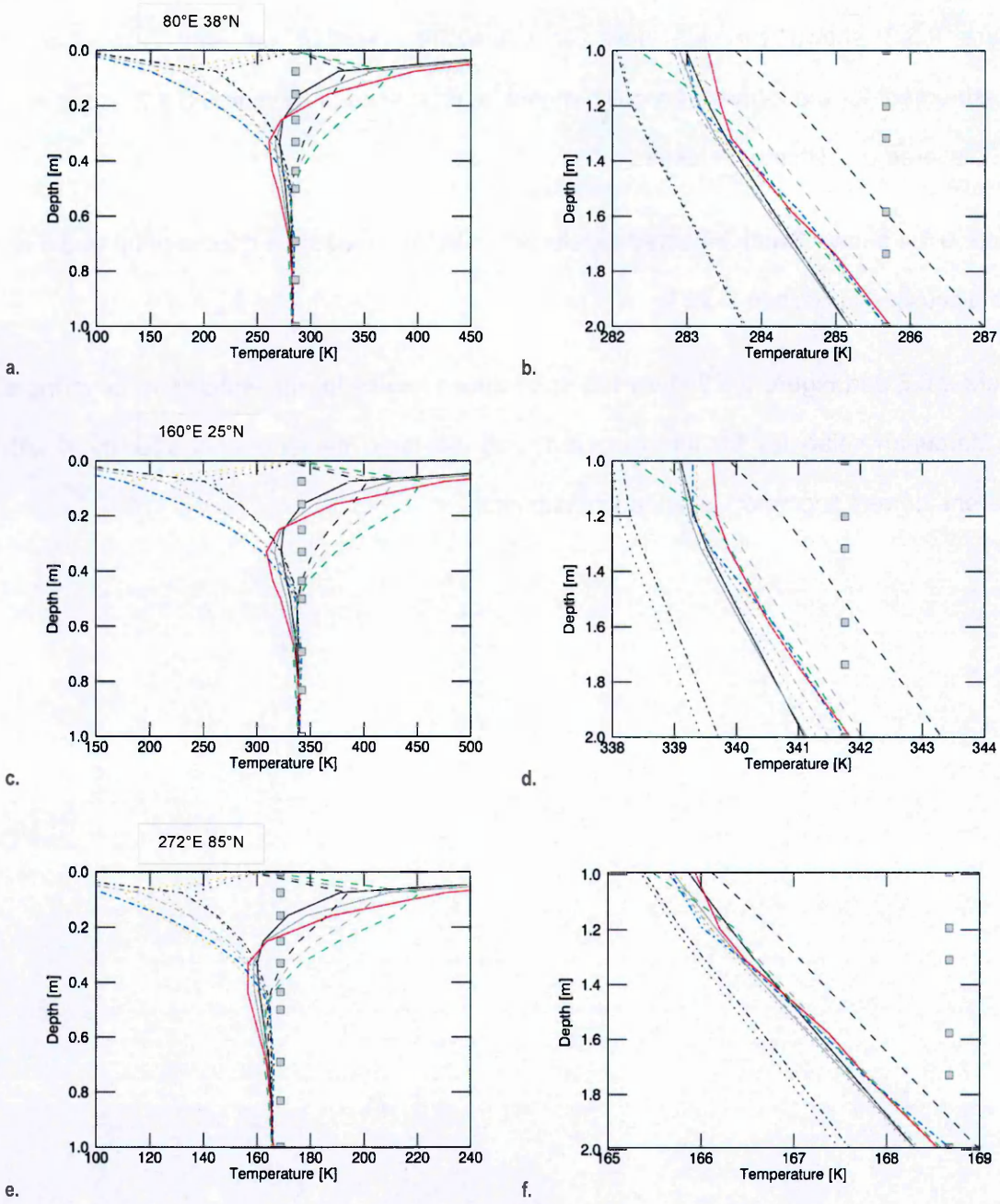

Figure 9.6.3. Temperature profiles for optimized heat flows, compared to true profiles, for sites at 80°E 38°N (a-b), 160°E 25°N (c-d) and 272°E 85°N (e-f) for the 2-layered instantaneous measurement scenario with a heat flow of 30 mW/m^2. The left plots (a, c, e) highlight the effects of the unsteady surface heat flow down to depth $z = 1$ m. The right plots (b, d, f) show the temperature gradients between 1-2 m depth where the unsteady surface heat flow becomes negligible. The curves are associated with measurement times according to: solid (peak daytime); dotted (transitional heating) and, dashed (cooling) and; dot-dashed (minimum nightime). The colored curves (red, orange, green, blue) are measured profiles, the grayscale curves are the optimized profiles where medium greys and dark greys respectively represent correct (2-layer) and incorrect (1-layer) layering assumptions. The grey squares are sensor locations and are plotted at the true basal temperature.

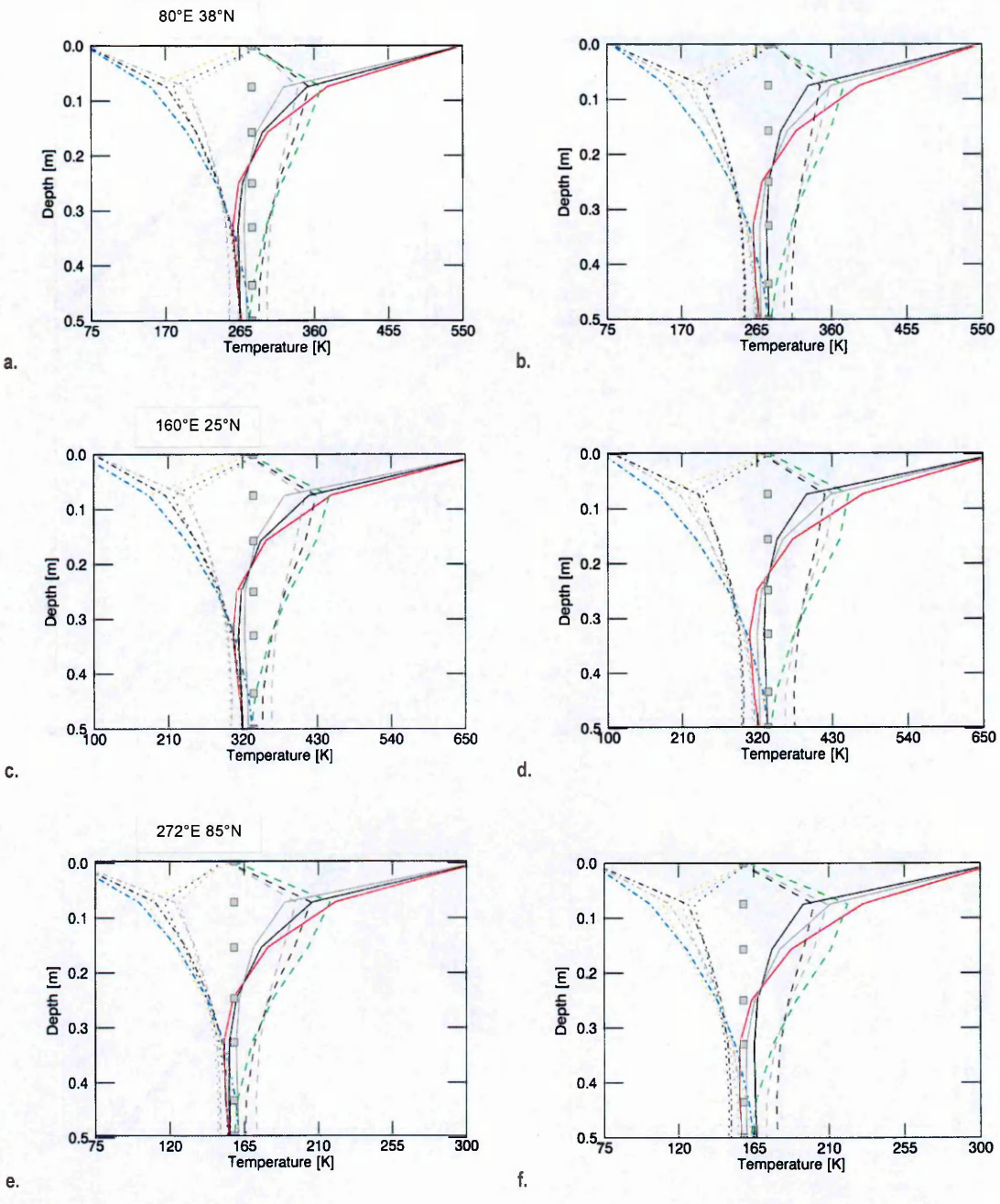

Figure 9.6.4. Temperature profiles for optimized heat flows, compared to true profiles, for sites at 80°E 38°N (a-b), 160°E 25°N (c-d) and 272°E 85°N (e-f) for the 1- and 2-layered (left and right, respectively) instantaneous measurement scenarios with a heat flow of 30 mW/m^2. The curves are associated with measurement times according to: solid (peak daytime); dotted (transitional heating) and, dashed (cooling) and; dot-dashed (minimum nightime). The colored curves (red, orange, green, blue) are measured profiles, the grayscale curves are the optimized profiles where medium greys and dark greys respectively represent correct and incorrect layering assumptions. The grey squares are sensor locations and are plotted close to the mean surface temperature.

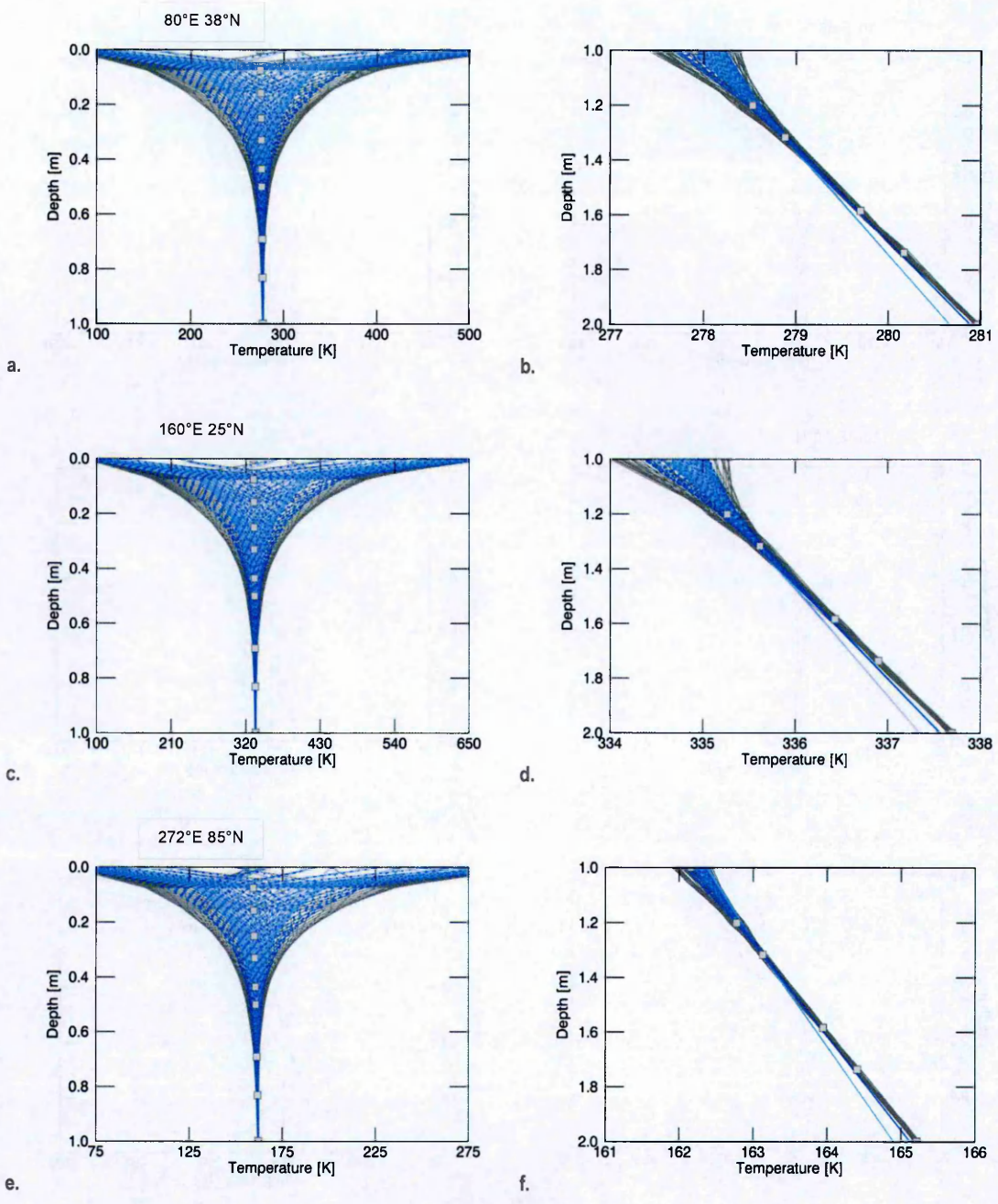

Figure 9.6.5. Temperature profiles for optimized heat flows, compared to true profiles, for sites at 80°E 38°N (a-b), 160°E 25°N (c-d) and 272°E 85°N (e-f) for the 1-layered measurement over 1 Mercurian solar day, with a heat flow of 30 mW/m². The left contours (a, c, e) highlight the effects of the unsteady surface heat flow down to depth $z = 1$ m. The right contours (b, d, f) show the temperature gradients between 1-2 m depth where the unsteady surface heat flow approaches negligible values. The curves are associated with regolith model assumptions according to: light blue solid (correct 1-layer assumption); dark blue dotted (incorrect 2-layer assumption). The grey squares are sensor locations and are plotted at the true steady temperature.

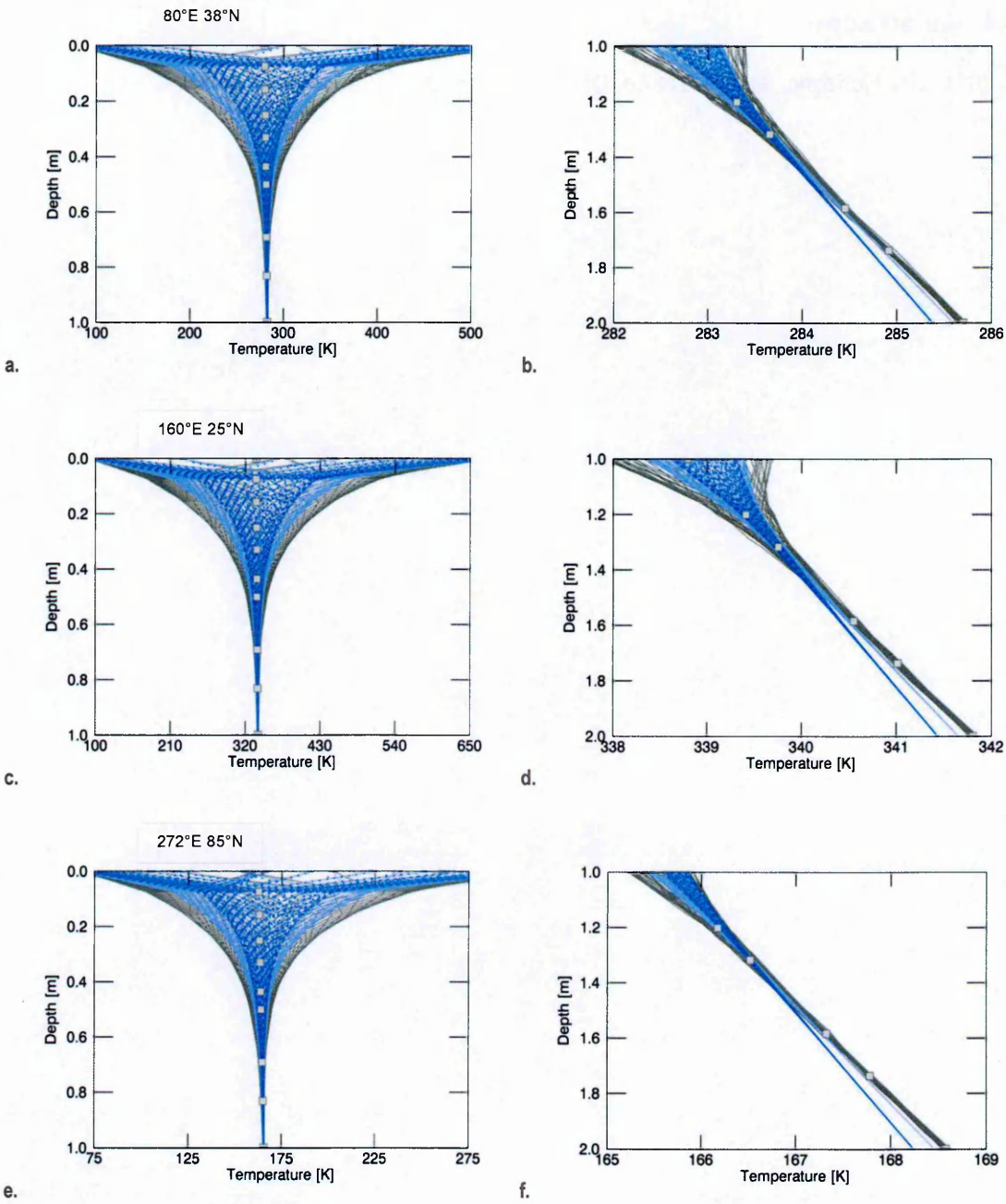

Figure 9.6.6. Temperature profiles for optimized heat flows, compared to true profiles, for sites at 80°E 38°N (a-b), 160°E 25°N (c-d) and 272°E 85°N (e-f) for the 2-layered measurement over 1 Mercurian solar day, with a heat flow of 30 mW/m^2. The left contours (a, c, e) highlight the effects of the unsteady surface heat flow down to depth $z = 1$ m. The right contours (b, d, f) show the temperature gradients between 1-2 m depth where the unsteady surface heat flow approaches negligible values. The curves are associated with regolith model assumptions according to: light blue solid (correct 2-layer assumption); dark blue dotted (incorrect 1-layer assumption). The grey squares are sensor locations and are plotted at the true steady temperature.

9.6.4 References

JPL 2014. JPL Horizons. 31/01/2014 ed. Online: Jet Propulsion Laboratory, NASA.

9.7 Vesta

9.7.1 Forward Models

Table 9.7.1 lists the critical parameters used to calculate the surface energy balance for a site on Vesta located at 120°E 20°N in Section 7.3.1.

Table 9.7.1. Surface energy balance parameters used to calculate the surface temperature for site located at 120°E 20°N on Vesta.

PARAMETER	VALUE
Solar Constant S^o [W/m^2]	1370
Bond albedo A	0.2
Emissivity ε	0.9
Heliocentric Orbit	
Aphelion [m]	3.84745E11
Perihelion [m]	3.21768E11
Eccentricity	0.08890
Shape	
x-axis [m]	2.85E5
y-axis [m]	2.85E5
z-axis [m]	2.85E5

9.7.2 Measurements

Figure 9.7.1 shows time dependent heat sources used to simulate the source solutions (Figure 9.7.2 and Figure 9.7.3) used to perturb the measurements of Section 7.3.2. These represent, to first order, the effect of OH bearing volatiles being released (e.g. Denevi et al., 2012; Russell et al., 2013) or transported in the regolith off the axis of the heat flow

probe (see e.g. Prialnik, 1992 for a discussion of gas transport in comets). The features are tied to the temperature-time plots of Section 7.3.1[1] and are explained below:

- $t = 0.0\text{-}0.25$

Volatiles are likely to sublimate at peak temperatures – when this happens heat energy is released, causing the temperature of the remaining regolith to fall. Assuming the regolith in which the probe is embedded (a cylinder of ~ 10s of cm radius, surrounding the probe, and roughly a cylinder radius longer than the probe length) is dry and experiences no degassing, a temperature gradient is created between the probe regolith, and the area of regolith were degassing occurred. This temperature gradient will be negative such that heat flows down the temperature gradient, away from the probe axis, towards the area of degassing. This is represented by the heat sinks, which starts at $t = 0$ when the temperature gradient is at a maximum. As heat flows from the probe regolith to the degassed regolith, the temperatures equilibrate until the heat sinks vanish at $t = 0.25$.

- $t = 0.25\text{-}0.75$

The regolith temperatures are assumed to remain in equilibrium[2] as temperatures are below a threshold value which triggers sublimation of volatiles.[3]

---

[1] The pristine peak temperatures of Vesta are not high enough to permit the sublimation of – e.g. H_2O, however heating may occur long after an impact event because of the low thermal diffusivity of Vestan regolith (e.g. Denevi et al., 2012).

[2] It is unlikely that the temperatures would equilibrate on such a short timescale, given Vesta's low thermal diffusivity, however, the exact profile of the heat sources are unlikely to affect the conclusions drawn from the presence of unknown heat source distributions in the regolith.

[3] It may be the case that more gas from adjacent volatile rich areas flows into the volatile depleted. This may cause condensation and a subsequent rise in temperature, but is assumed to remain below the threshold temperature, which is only achieved at peak surface temperatures.

- $t = 0.75\text{-}1.0$

As the temperatures begin to rise a threshold value is reached which triggers further degassing of regolith off the probe axis, which is left over from the earlier degassing event, or has built up in the interim. The degassing event re-establishes a negative temperature gradient between the probe regolith and volatile rich regolith such that heat flows away from the probe axis, towards the degassed regolith. The cycle is then repeated.

Figure 9.7.2 and Figure 9.7.3 show that with these specific heat source profiles (with accompanying assumptions and arguments), result in a temperature decrease at all modelled depths. The high conductivity model responds more to the variation in heat sinks than the low conductivity equivalents.

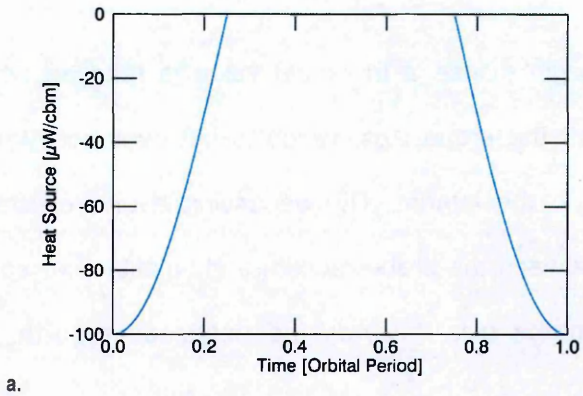

a.

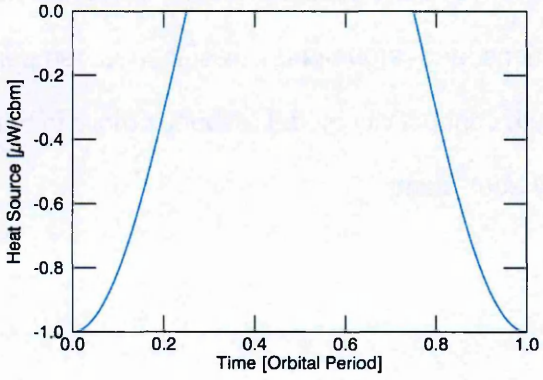

b.

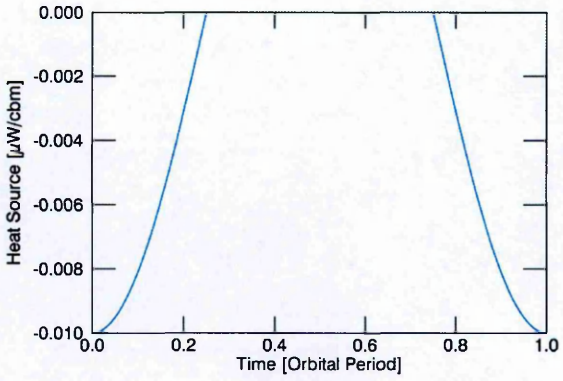

c.

Figure 9.7.1. Time dependent heat sinks used to model source solutions added as systematic errors to temperature measurements. They correspond, in time, with the forword modelled temperature of Section 7.3.1. These decrease in magnitude from a-c and correspond to degassing events of varying magnitude. These are applied at all depths.

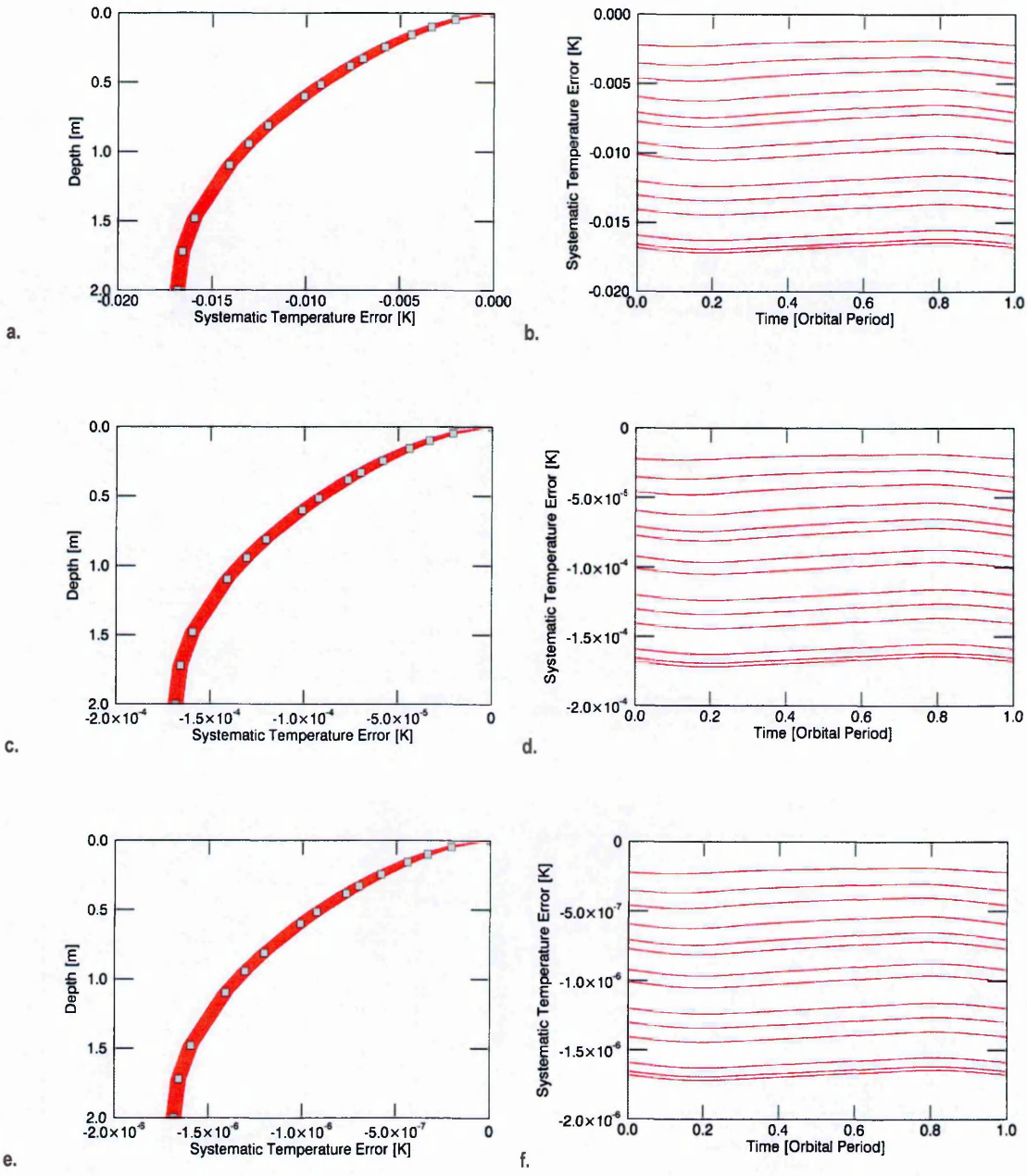

Figure 9.7.2. Forward modelled source solutions added as systematic errors to temperature measurements. These are based on the high conductivity models of Section 7.2.2 for Vesta. The left contours are overlays of depth-dependent temperature perturbation ΔT over time t of 1 orbital period in ~26.5 day steps; the right contours are overlays of time-dependent temperature T over depth z of 2 m (positive towards the surface). Grey squares represent sensor locations.

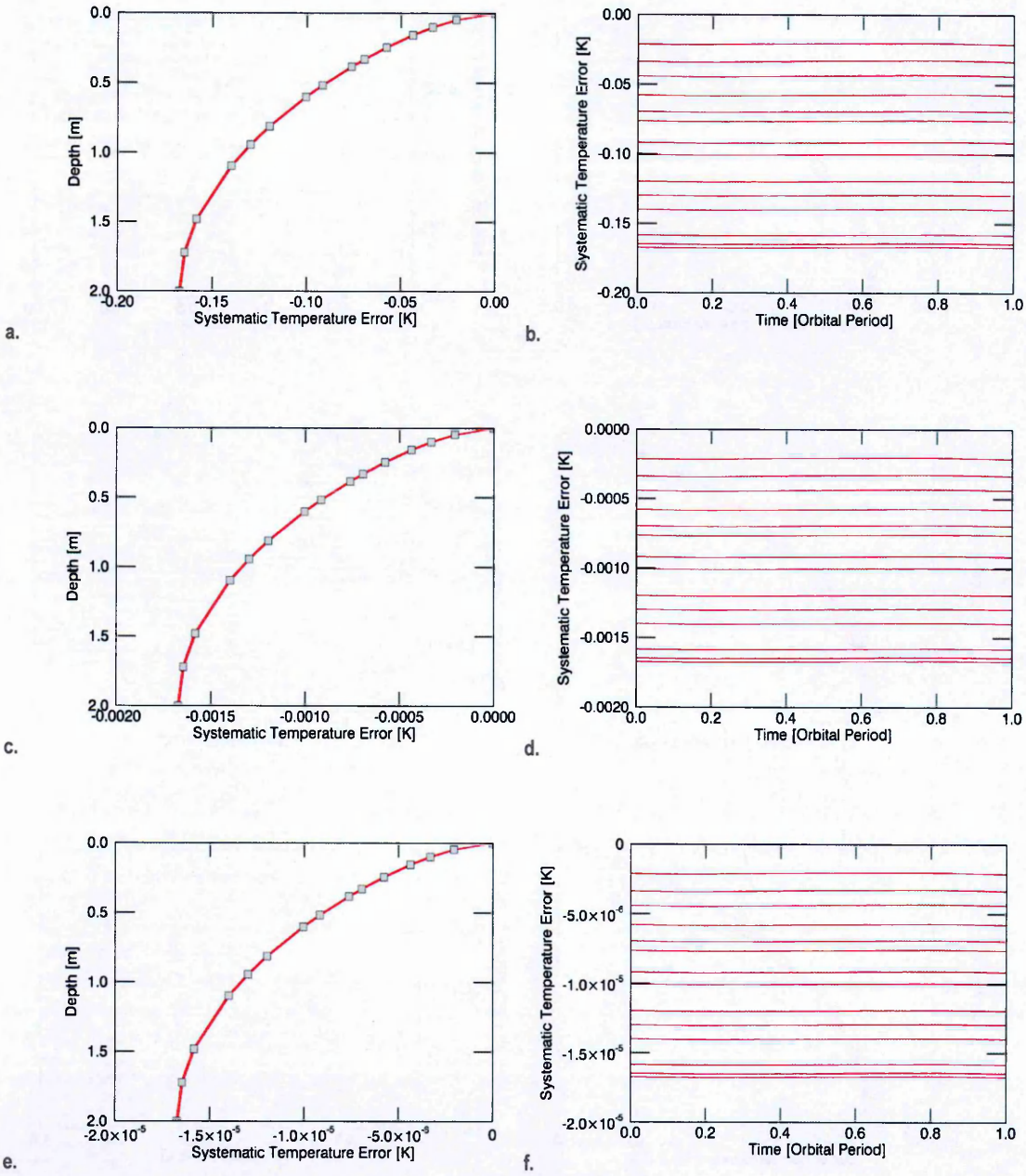

Figure 9.7.3. Forward modelled source solutions added as systematic errors to temperature measurements. These are based on the low conductivity models of Section 7.2.2 for Vesta. The left contours are overlays of depth-dependent temperature perturbation ΔT over time t of 1 orbital period in ~26.5 day steps; the right contours are overlays of time-dependent temperature T over depth z of 2 m (positive towards the surface). Grey squares represent sensor locations.

Figure 9.7.4 illustrate the temperature measurement profiles with the presence of the systematic noise shown in Figure 9.7.2 and Figure 9.7.3 for the highest noise amplitudes. The resulting negative temperature-depth gradient can clearly be seen in the low conductivity models. These can be compared to the case with Gaussian error in Figure 9.7.5.

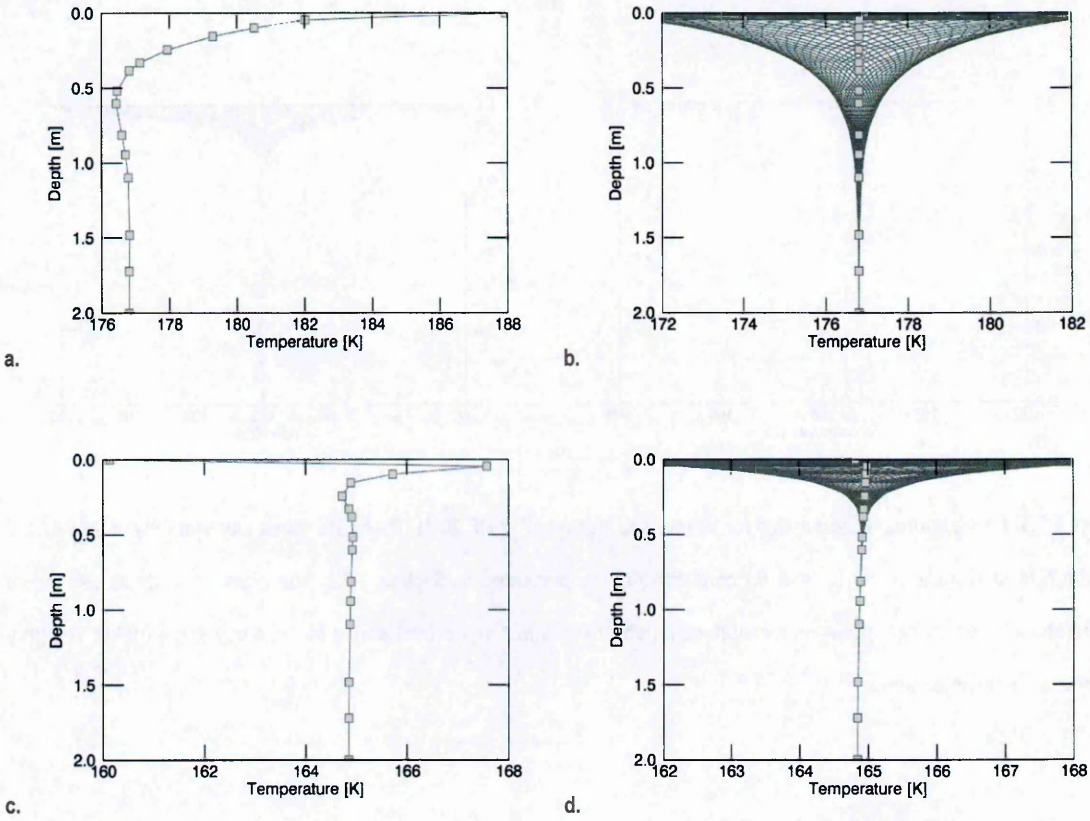

Figure 9.7.4. Temperature measurements for Vestan site located at 120°E 20°N with high systematic noise as shown in Figure 9.7.2 and Figure 9.7.3. These are with a low heat flow of 0.33 μW/m² and high (a. and b.) and low (c. and d.) conductivities as presented in Section 7.2.2. The plots show depth-dependent temperature T: for an instantaneous measurement (left); over time t of 1 orbital period in ~26.5 day steps (right). The grey squares are sensor locations.

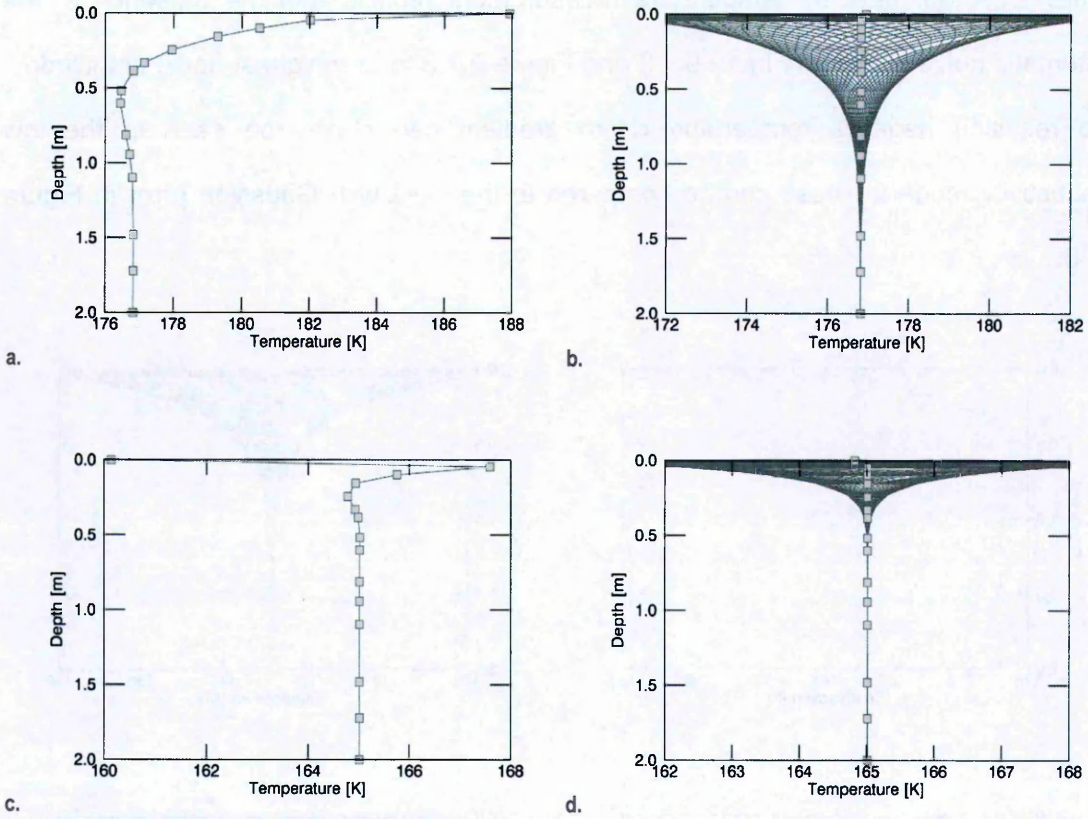

Figure 9.7.5. Temperature measurements for Vestan site located at 120°E 20°N. These are with a low heat flow of 0.33 μW/m^2 and high (a. and b.) and low (c. and d.) conductivities as presented in Section 7.2.2. The plots show depth-dependent temperature T: for an instantaneous measurement (left); over time t of 1 orbital period in ~26.5 day steps (right). The grey squares are sensor locations.

9.7.3 Optimization Results

Figure 9.7.6 and Figure 9.7.7 respectively show Gaussian and non-Gaussian temperature measurement errors and errors in the related optimized temperature profiles.

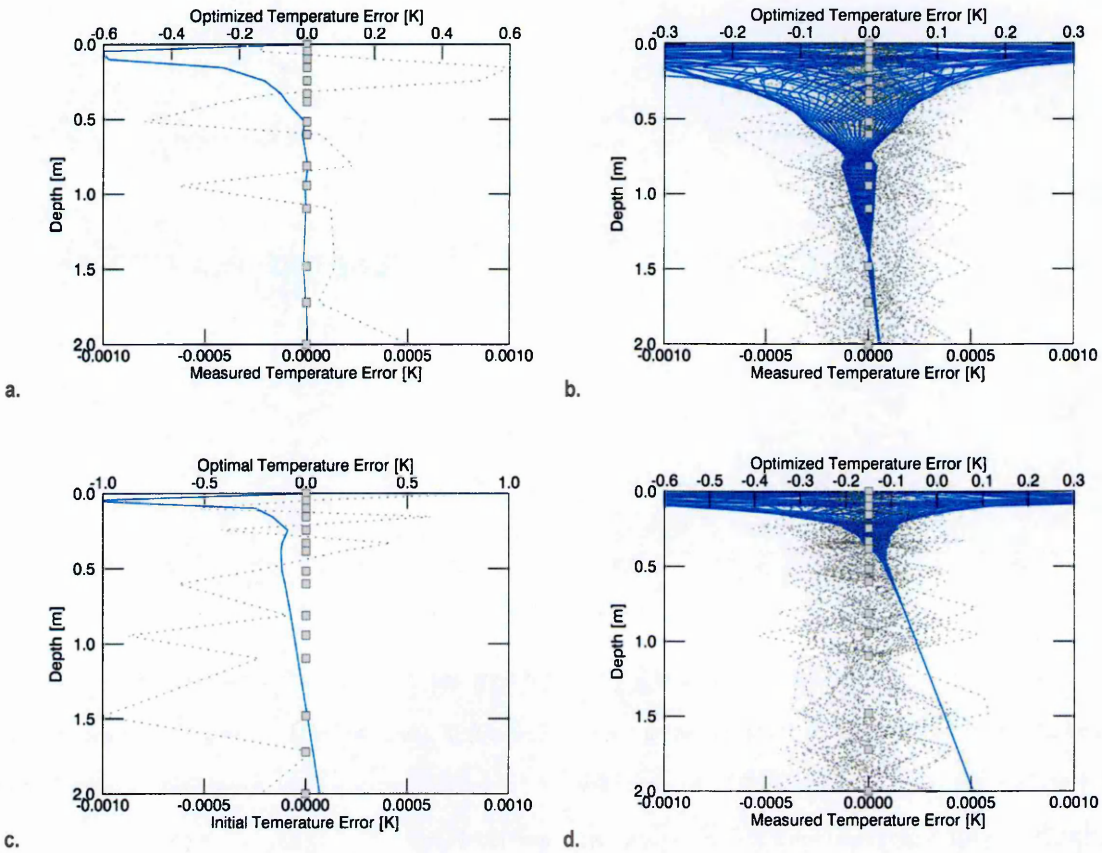

Figure 9.7.6. Errors in measurement (Gaussian ΔT^0 – dotted grey) and optimized (ΔT^I – solid blue) temperatures for Vestan site located at 120°E 20°N. These are with a high heat flow of 3.33 μW/m² and high (a. and b.) and low (c. and d.) conductivities as presented in Section 7.2.2. The plots show ΔT: for an instantaneous measurement (left); over time t of 1 orbital period in ~26.5 day steps (right). The grey squares are sensor locations.

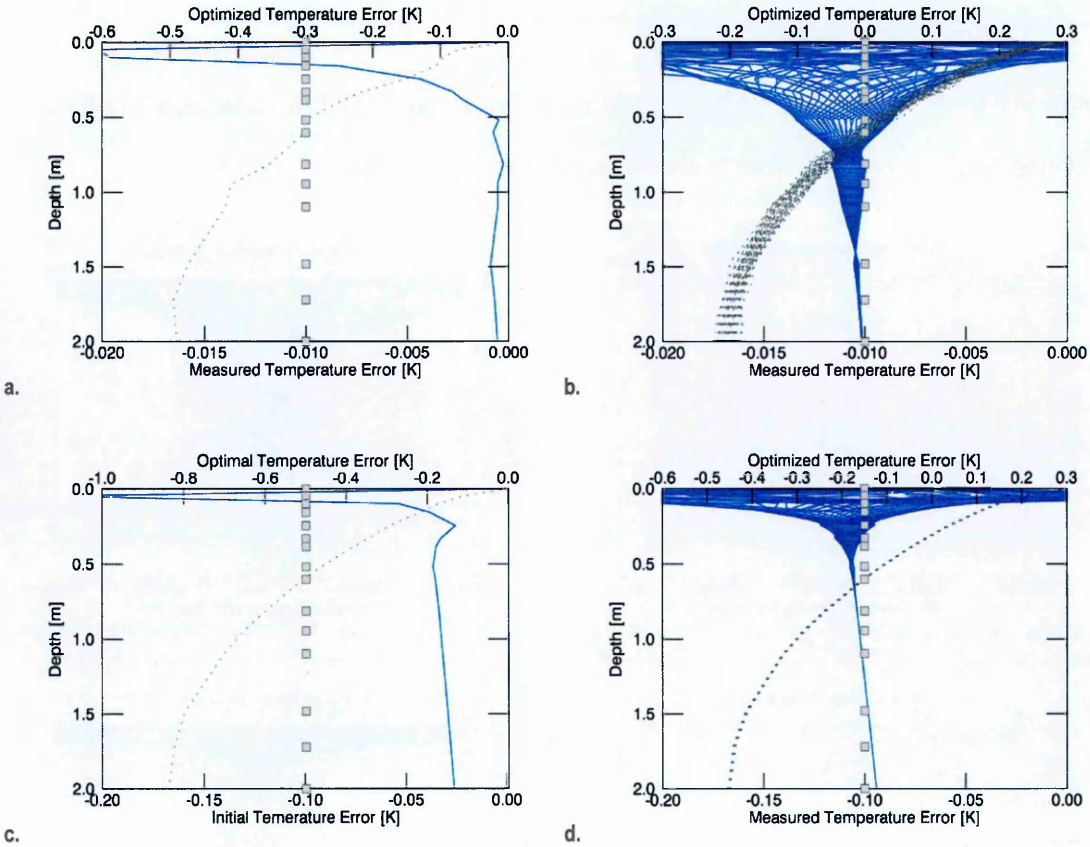

Figure 9.7.7. Errors in measurement (non-Gaussian ΔT^0 – dotted grey) and optimized (ΔT^I – solid blue) temperatures for Vestan site located at 120°E 20°N. These are with a low heat flow of 0.33 μW/m² and high (a. and b.) and low (c. and d.) conductivities as presented in Section 7.2.2. The plots show ΔT: for an instantaneous measurement (left); over time t of 1 orbital period in ~26.5 day steps (right). The grey squares are sensor locations.

9.7.4 References

DENEVI, B. W., BLEWETT, D. T., BUCZKOWSKI, D. L., CAPACCIONI, F., CAPRIA, M. T., DE SANCTIS, M. C., GARRY, W. B., GASKELL, R. W., LE CORRE, L., LI, J.-Y., MARCHI, S., MCCOY, T. J., NATHUES, A., O'BRIEN, D. P., PETRO, N. E., PIETERS, C. M., PREUSKER, F., RAYMOND, C. A., REDDY, V., RUSSELL, C. T., SCHENK, P., SCULLY, J. E. C., SUNSHINE, J. M., TOSI, F., WILLIAMS, D. A. & WYRICK, D. 2012. Pitted Terrain on Vesta and Implications for the Presence of Volatiles. *Science,* 338**,** 246-.

PRIALNIK, D. 1992. Crystallization, sublimation, and gas release in the interior of a porous comet nucleus. *The Astrophysical Journal,* 388**,** 196-202.

RUSSELL, C. T., RAYMOND, C. A., JAUMANN, R., MCSWEEN, H. Y., SANCTIS, M. C., NATHUES, A., PRETTYMAN, T. H., AMMANNITO, E., REDDY, V., PREUSKER, F., O'BRIEN, D. P., MARCHI, S., DENEVI, B. W., BUCZKOWSKI, D. L., PIETERS, C. M., MCCORD, T. B., LI, J.-Y., MITTLEFEHLDT, D. W., COMBE, J.-P., WILLIAMS, D. A., HIESINGER, H., YINGST, R. A., POLANSKEY, C. A. & JOY, S. P. 2013. Dawn completes its mission at 4 Vesta. *Meteoritics and Planetary Science,* 48**,** 2076-2089.

9.8 Conclusions

9.8.1 Simulation Times

Figure 9.8.1 shows the change in forward model simulation times as the grid spacing, and timesteps are refined. This data must be interpreted in a relative sense. Other factors, including the spatiotemporal grid size, inhomogeneity in grids and thermal properties, the shape of the surface unsteady temperature, and the presence of heat sources or sinks affect the simulation times.

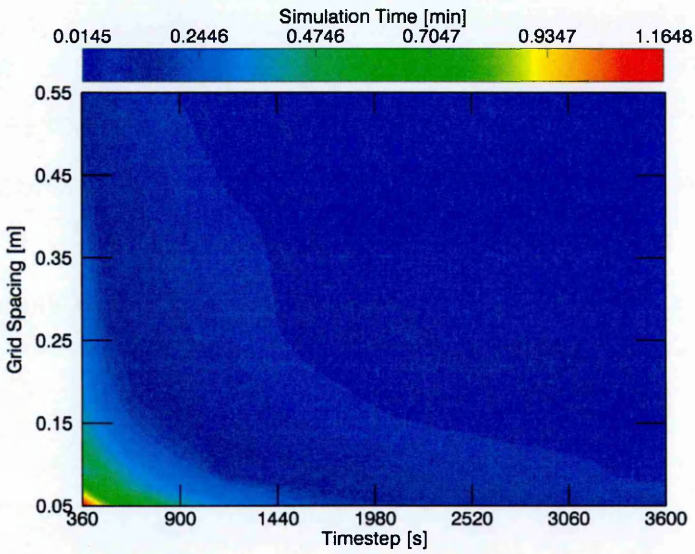

Figure 9.8.1. Forward model simulation times t_{SIM} [min] with respect to grid spacing Δz and timesteps Δt, for unsteady temperature due to $T_S^U = T_S^{UA} \sin(2\pi t/P)$ with amplitude $T_S^{UA} = 12$ K and period $P = 86400$ s in a homogeneous medium where: thermal conductivity $k = 3.0$ W/m/K; density $\rho = 2700$ kg/m^3 and; specific heat capacity $c = 790$ J/kg/K. This is based on the same data as the grid convergence study in Section 3.4.1.1.

9.8.2 Covariance Relationships

The units of the inverse model parameters can be reduced to achieve an idea of their relative magnitudes as listed in Table 9.8.1. Examining Table 9.8.1 shows that all the parameter units differ by factors involving length scale, time scale, and energy units. For example, the relative magnitudes of F_B^S and S^S differ by a length scale factor while, those of F_B^S and k differ by a factor of length × temperature. Therefore, in the inversion,

accounting for the differences may involve updating the covariances, at each iteration, based on temperature residuals, control volume sizes and timesteps.

Table 9.8.1. Reduction of inverse model paramters to basic energy units.

PARAMETER	UNIT
$T_S^S + T_S^U = T_S;\ T \equiv \boldsymbol{d}$	K
k	J/smK
ρc	J/m^{3}K
S^S	J/sm^3
F_B^S	J/sm^2

Taking the first order estimates outlined in Chapter 4 and Appendix 9.4 these can be gridded as shown in Table 9.8.2 (the numerical SD ratios for untested simultaneous optimizations [red borders] are discerned using the relation $r_{m_2}^{m_1} = r_{m_2}^{m_3}/r_{m_1}^{m_3}$). Assessing, for example, $r_{S^S}^{F_B^S}$ shows that the standard deviation for F_B^S is fundamentally larger than that for S^S, which is reflected in the first order estimate $r_{S^S}^{F_B^S} \geq 10^3$ ($r_{F_B^S}^{S^S} \leq 10^{-3}$). Interestingly, the relationship does not hold for the experimental values of $r_{\boldsymbol{d}}^{F_B^S}$ and $r_{\boldsymbol{d}}^{S^S}$ but it should be noted that $r_{\boldsymbol{d}}^{F_B^S}$ has been shown to be stable at values exceeding 10 (see Sections 4.2.1, 4.3.1 and Appendix 9.4.9.3); the discussion below sheds further light on this.

The other SD ratios are not easily compared, analytically, save for the dimensionless, temperature-related quantities. However, taking the time and length scale units as control volume size Δz and timestep Δt, these can be reduced to units involving J and K, analogous to energy densities. For example, taking Δz and Δt from the lower extremes of the range in Figure 9.8.1 such that $\Delta z = 0.05$ m and $\Delta t = 360$ s gives $r_{S^S}^{F_B^S} = 0.05$ m, $r_{S^S}^{\boldsymbol{d}} =$ 0.045 K/J and $r_{F_B^S}^{\boldsymbol{d}} = 0.9$ K/J, which are naturally consistent with the SD ratio relation. They are not entirely inconsistent with the experimentally derived minimum values (Table 9.8.2) of 10^3 m, 0.1 K/J and 1 K/J.

A comparison between the analytical and experimental results is nontrivial because control volume sizes (grid spacing) is inhomogeneous, increasing with depth from ~0.1-1.75 m (average 0.55 m) in the numerical experiments of Appendix 9.4.7.7. With $\Delta z < 1$ m the analytical approach suggests $r_d^{F_B^S} < r_d^{S^S}$ and with $\Delta z \geq 1$ m, $r_d^{F_B^S} \geq r_d^{S^S}$. Analytical, then, $r_d^{F_B^S}$ should be smaller than $r_d^{S^S}$ by a factor of about 20, with $\Delta z = 0.05$ m and $\Delta t = 360$ s, nominally consistent with the experimental value of ~10. As noted above, though, this is somewhat at odds with the experimental value of $r_{S^S}^{F_B^S}$.

Table 9.8.2. Grid of derived first order numerical values (lower triangle) of SD (stability) ratios (upper triangle/lower triangle) and associated SI units (upper triangle). Numerical values associated with particular units are read diagonally along lower left to upper right with associated cell shading colours (red, green or blue). Red-bordered cells are values derived analytically.

		UNITS $\left[\frac{ROW}{COLUMN}\right]$						
		T_S^S	T_S^U	k	ρc	S^S	F_B^S	$\boldsymbol{d}$
VALUES $\left[\frac{COLUMN}{ROW}\right]$	T_S^S			smK^2/J	m^3K^2/J	sm^3K/J	sm^2K/J	
	T_S^U	$\sim 10^4$		smK^2/J	m^3K^2/J	sm^3K/J	sm^2K/J	
	k	$\sim 10^7$	$\sim 10^3$		m^2/s	m^2/K	m/K	J/smK^2
	ρc	$\sim 10^9$	$\sim 10^5$	$\sim 10^2$		s/K	s/mK	J/m^3K^2
	S^S	$\sim 10^8$	$\sim 10^4$	~ 10	$\sim 10^{-1}$		$1/m$	J/sm^3K
	F_B^S	$\leq 10^5$	10	$< 10^{-2}$	$\leq 10^{-4}$	$\leq 10^{-3}$		J/sm^2K
	$\boldsymbol{d}$	$\geq 10^4$	~10	$\geq 10^4$	$\geq 10^5$	≥ 10	≥ 1	

The Function Specification Inverse (FSI) theory (Section 2.2.3) shows that the covariance plays a critical role in weighting the temperature residuals with data covariance $\boldsymbol{C_d}$ and weighting the model parameter updates with covariance $\boldsymbol{C_m}$. The preceding analysis shows how the inverse problem may be stabilised with a systematic approach to nominally defining the relative sizes of $\boldsymbol{C_d}$ and $\boldsymbol{C_m}$, as opposed to the trial and error approach used in the numerical experiments of Chapter 4 and Appendix 9.4. Of course,

these quantities are largely unknown in the inverse problem, therefore, some trial and error may still be necessary in establishing their precise values.

9.8.3 Unknown A Priori Model Parameter Errors

Table 9.8.3 lists the various effects of high and low estimates of a priori model parameters which are not accounted for in optimization. These can prove useful in cases where unexpected results are obtained to assess potential inaccuracies in the forward model.

Table 9.8.3. Relative effects of unaccounted for errors in a priori model paramters.

PARAMETER	ESTIMATE			
	HIGH	F_B^S EFFECT	LOW	F_B^S EFFECT
T_S^S	Low temperature gradient; high data residuals	Low	High temperature gradient; low data residuals	High
T_S^U	-High Amplitude -High Mean	-Less accurate -Low	-Low Amplitude -Low Mean	-More accurate -High
k	Increased skin depth; low temperature gradient	Less constrained; high	Decreased skin depth; high temperature gradient	More constrained; low
ρc	Decreased skin depth	More constrained; low	Increased skin depth	Less constrained; high
S^S	Increased internal temperatures and gradient	Low	Decreased internal temperatures and gradient	High

9.8.4 Apollo Lunar Probe Data Inversion

9.8.4.1 Data Format and Reduction

The Apollo 15 and 17 ALSEP probe data is available from the National Space Science Data Center (NSSDC; NASA, 2015). The data consists of absolute temperature data for four thermocouples and temperature difference and average temperature data for two Wheatstone bridge circuits on each of the two probes. The Wheatstone bridge sensors are respectively separated by 0.47 and 0.28 m on an upper and lower section of the probe (Figure 9.8.2); for the former reason, the average temperatures supplied in the inverse model, results in a large attendant depth inaccuracy, and heat flow inaccuracy. Since one thermocouple coincides with the uppermost gradient bridge sensor, that thermocouple temperature is combined with the gradient bridge temperature difference to calculate the temperature of the lowest gradient bridge sensor.

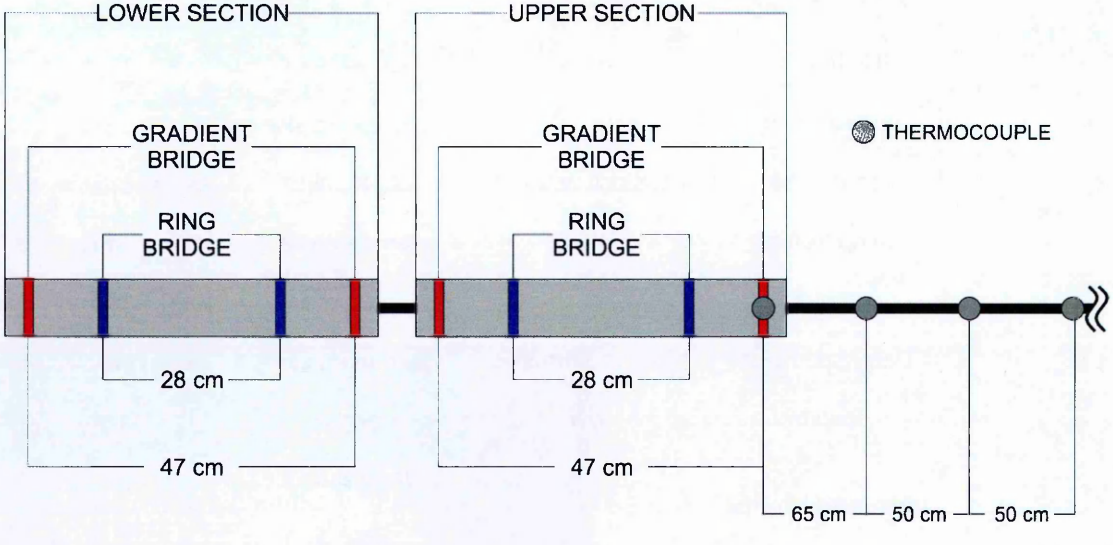

Figure 9.8.2. Schematic of ALSEP heat flow probe (after Langseth et al., 1972; Langseth et al., 1976).

The data show that the measurements by the thermocouples and the upper and lower sections of the probe are recorded at different times within intervals of 10 s to 10 min, such that finding measurements along the probe length that coincide in time is a non-trivial task. Additionally the thermocouples, naturally, take measurements at a higher

frequency than do the gradient bridge sensors, which are, nominally, below the skin depth.

To make things simpler, the former discrepancies are handled by creating a uniform temporal grid spanning a range of times which is shared by all sensors along each probe axis. The data is then projected onto the new, uniform temporal grid according to data times that most closely match those from the uniform temporal grid. The time discrepancies thus created are of the same order as those in the original data but are, in any event, associated at unique times along the probe axis.

The data contain several anomalous temperatures which have been associated with periods of heating by heaters incorporated into the probe axis (not shown in Figure 9.8.2), in line with thermal conductivity experiments. To keep the data as dense as possible, and given the variability in the data, the anomalous data is replaced with data equivalent to a boxcar average over $1/10^{th}$ of the span of data points. Data is assessed as anomalous if it lies outside of a given multiple of standard deviations (< 1 for bridge sensors, > 1 for thermocouples) of the data mean. This process effectively reduces the prevalence of large outliers in and maintains the statistical properties of the data.

Thus extracted, useful data is found in the first of the Apollo 15 and both Apollo 17 probes. The co-temporal data, as defined on the uniform temporal grid span: ~0.41 Lunations with two thermocouples adjacent to the lower gradient bridge sensor down to 0.82 m, in the case of the Apollo 15 probe; and ~0.2 Lunations with all four thermocouples and the lower gradient bridge sensor down to ~1.75 m in the case of the Apollo 17 probes. This is enough for the GPHLO1 inverse model, which, as has been demonstrated throughout Chapter 4 is effective with short duration or instantaneous heat flow measurements. An instantaneous measurement is derived from the end of the Apollo 15 span (Figure 9.8.3) while the full span of the Apollo 17 extracted data set is used (Figure 9.8.4).

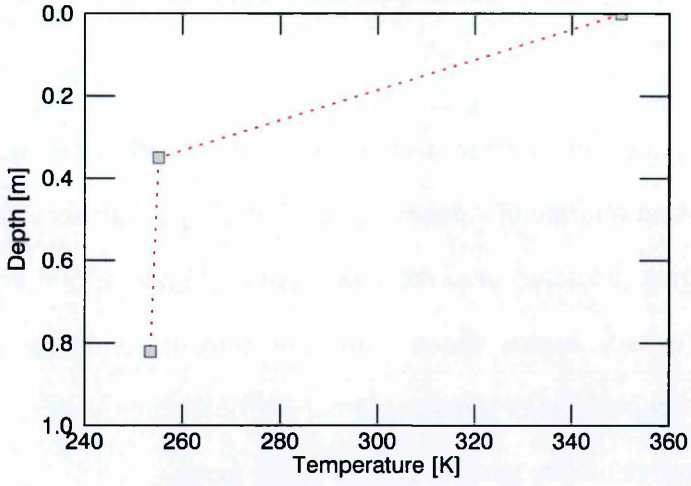

Figure 9.8.3. Apollo 15 Probe 1 derived instantaneous temperature measurement, taken towards lunar high noon at approximately 8.07099 Lunations after the start of 1971. Grey squares are sensor locations.

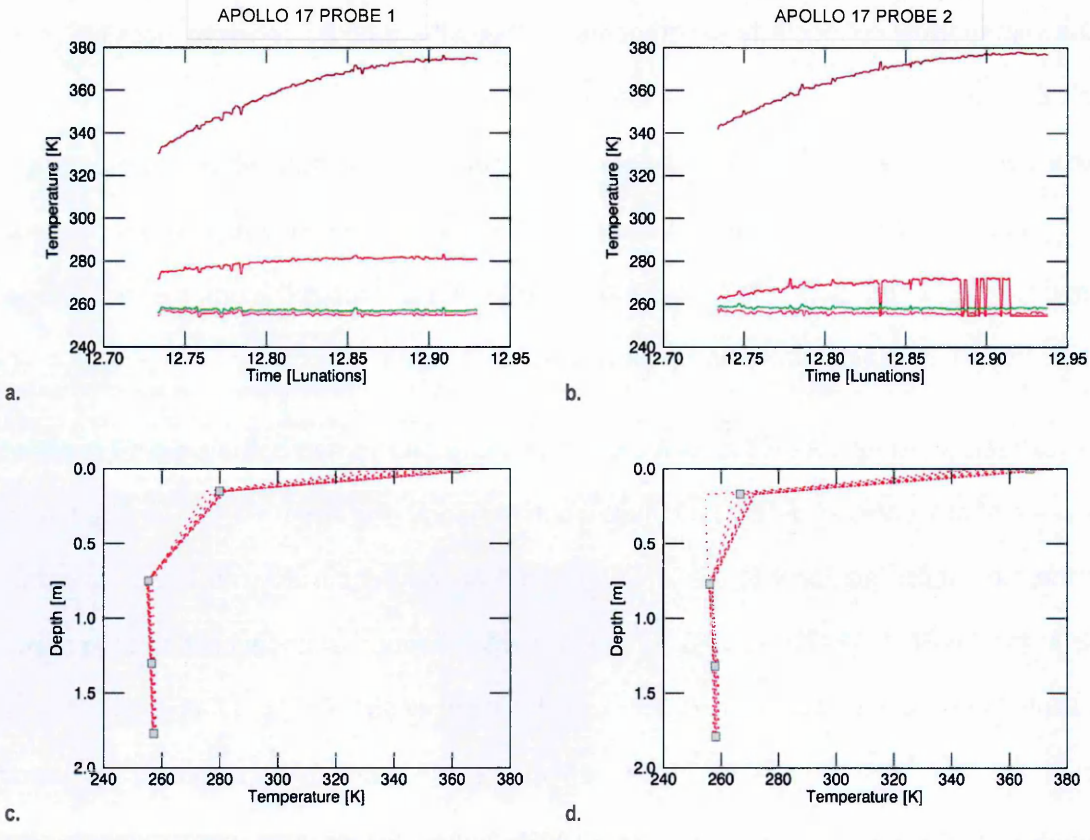

Figure 9.8.4. Apollo 17 derived heat flow probe measurements. The upper plots are overlays of time dependent temperatures at different depths, with smaller temperatures at depth (red are thermocouples while green is the lower of the upper gradient bridge sensors at > 1.5 m; times are measured in Lunations since that start of 1972). The lower plots are corresponding overlays of depth dependent temperature at different times with grey squares indicating sensor locations.

9.8.4.2 Data Inversion

The data extracted from the three probes are inverted independently. Surface boundary temperatures are taken from the surface temperatures measured by one surface thermocouple on each probe (Figure 9.8.5a-b). Thermal property data is not available from the NSSDC archive, therefore these are calculated using data presented in Langseth et al. (1976) and Heiken et al. (1991) (Figure 9.8.5c-d). Since the model is unable to handle temperature dependent thermal properties, the so-called "solid state greenhouse" effect on the Moon (e.g. Jones et al., 1975; Heiken et al., 1991) is approximated by a heat source distribution in the upper 10 cm of regolith (Figure 9.8.5e-f).[1]

The inverse model is run over a period of 12 Lunations in 24 h steps. The depth is restricted to that of the lowest sensor, which, due to the shallow lunar skin depth, experiences relatively small temperature variation at depth, over the period of measurement. The basal heat flow is initialised with values of 0.005, 0.010, 0.02, 0.03 and 0.06 W/m^2 per parameter set where, in select instances, the conductivity is included as an additional free parameter (the regions).

A range of covariances are used, as in tests throughout Chapter 4 and Appendix 9.4. The range involves basal heat flow and conductivity covariances in $\boldsymbol{C_m}$ where the temperature measurement standard deviations in $\boldsymbol{C_d}$ are multiplied by factors from 10^{-7} to 10^{7}, in order of magnitude steps. Optimization is performed with stepping factor $\mu \approx 1$ with variations of $\pm 10^{-2}$ or less.

[1] The lunar solid state greenhouse effect is an observed ~45 K rise of the mean temperature from the surface value to a depth of 0.35 m.

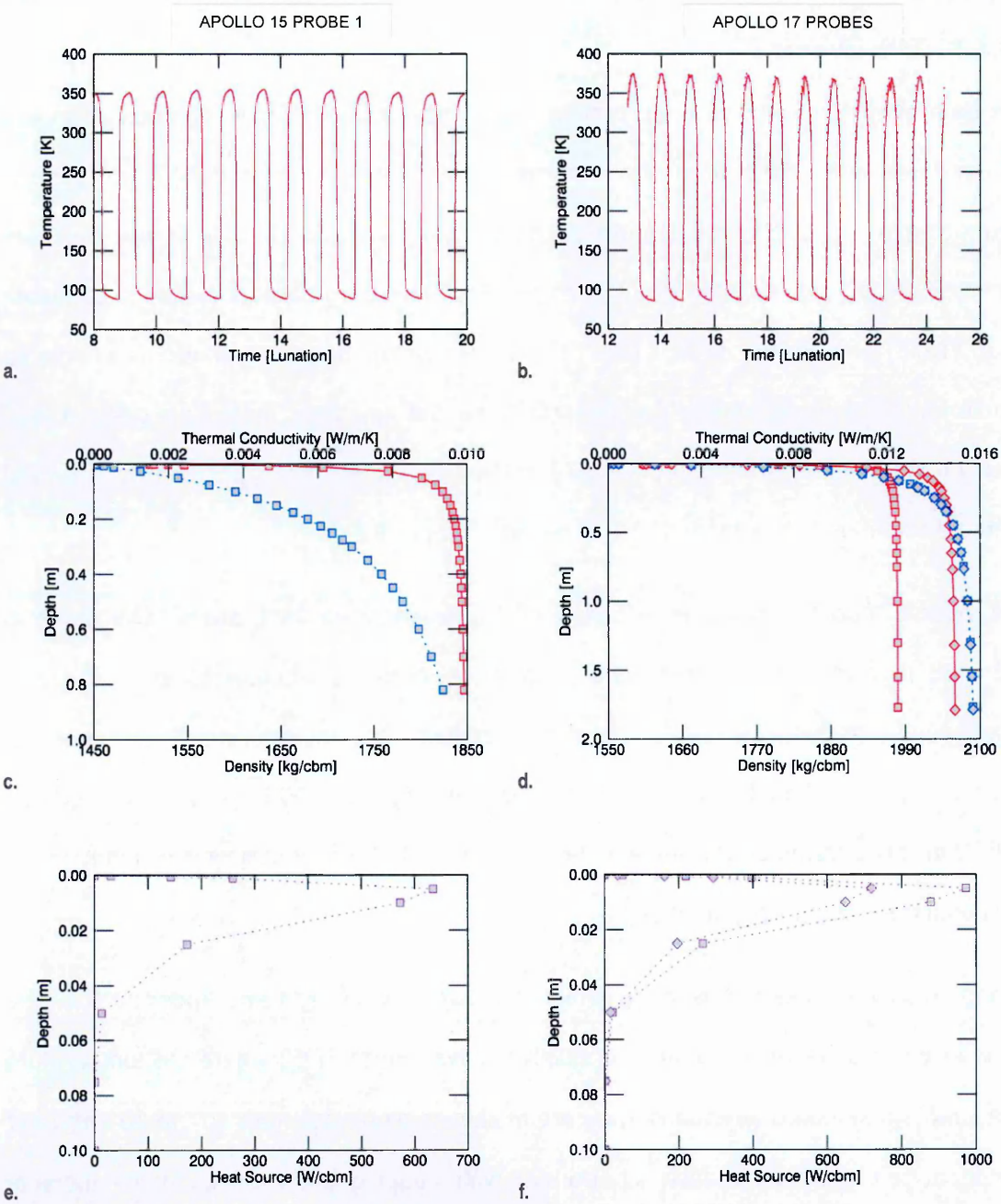

Figure 9.8.5. Derived model parameters for Apollo temperature data inversion. Plots a-b are surface temperatures (Apollo 15 times are measured in Lunations since that start of 1971 and, likewise, Apollo 17 since the start of 1972). Plots c-d are regolith thermal conductivity (solid red) and density (dotted blue). Plots e-f are heat source distributions. Note that, for Apollo 17, there is substantial overlap of the surface temperatures for Probe 1 (solid red) and Probe 2 (dotted red) and, likewise, the densities for Probe 1 (square symbols) and 2 (diamond symbols). The square and diamond symbols represent the spatial grids used for each probe.

The approach of exploring the solution space by varying the values of the standard deviations creates a multidimensional space with the standard deviations of the temperature measurements, basal heat flow and thermal conductivity along with all the relevant misfit function parameters and the stepping factor – i.e. a lookup table. The space associated with each probe is used to assess the most viable basal heat flow estimate in the range of returned values, and therefore a first order estimate of the lunar planetary heat flow.[2] Contours of the solution spaces for the misfit function values and heat flow estimates are shown for each probe in Figure 9.8.6.

A linear feature (along a minor diagonal), demarcating the SD ratio $r_d^{F_B^S}$ and solution region (green shaded polygon), can be observed in the misfit function spaces of Figure 9.8.6a, c and d. The feature is characterised by an oscillation in the misfit function value most visible along the basal heat flow standard deviation $\sigma_{F_B^S}$ axis. The green shaded areas highlight the regions from which viable solutions can be taken – outside these regions the heat flow is not modified significantly beyond its initial estimate.

Within the solution subspace defined by the standard deviations, there is a particular stepping factor at which the optimized basal heat flow and, in select instances, thermal conductivity provide a minimum misfit function value (Figure 9.8.6b, d and f). The plots in Figure 9.8.6 show inversions where only the basal heat flow is optimized (as opposed to simultaneous optimization with the thermal conductivity)[3]. A priori knowledge is used to select solutions from the entire pool of inversion results (the Apollo 15 Probe 1 results of Figure 9.8.6b, for example, can be considered as unlikely).

---

[2] Given the caveats of the data being unprocessed, and further processing being necessary to correct the values for topographic and other environmental factors, as discussed in Sections 1.1.3.2, 8.3.1 and 8.3.5.

[3] The equivalent plots for simultaneous optimization of thermal conductivity and basal heat flow are not smooth, and are best displayed in three dimensions: they are therefore not shown here. The minimum points are simply extracted from the lookup table.

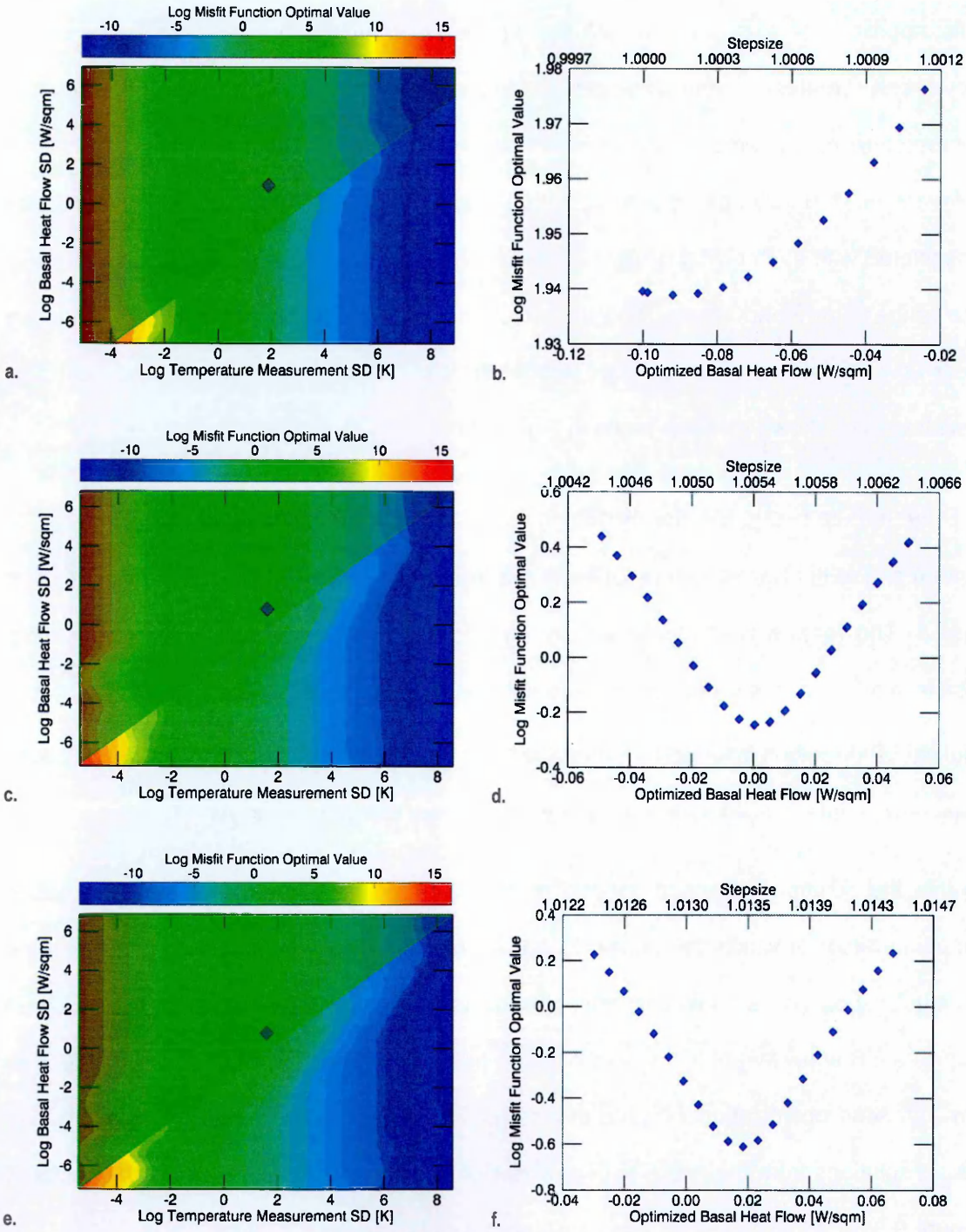

Figure 9.8.6. Select results for Apollo temperature data inversion. Contours a-b, c-d and e-f are respectively for Apollo 15 Probe 1, Apollo 17 Probe 1 and Apollo 17 Probe 2. The left contours are mean misfit function values over the range of initializations of basal heat flow and covariances (standard deviations) of the inverse model described in the text; the green shaded polygons highlight the areas that can be investigated for viable solutions. The right contours are misfit function values and optimized basal heat flows associated with select points (purple diamonds on left) in the space defined by the covariances, based on different stepsizes.

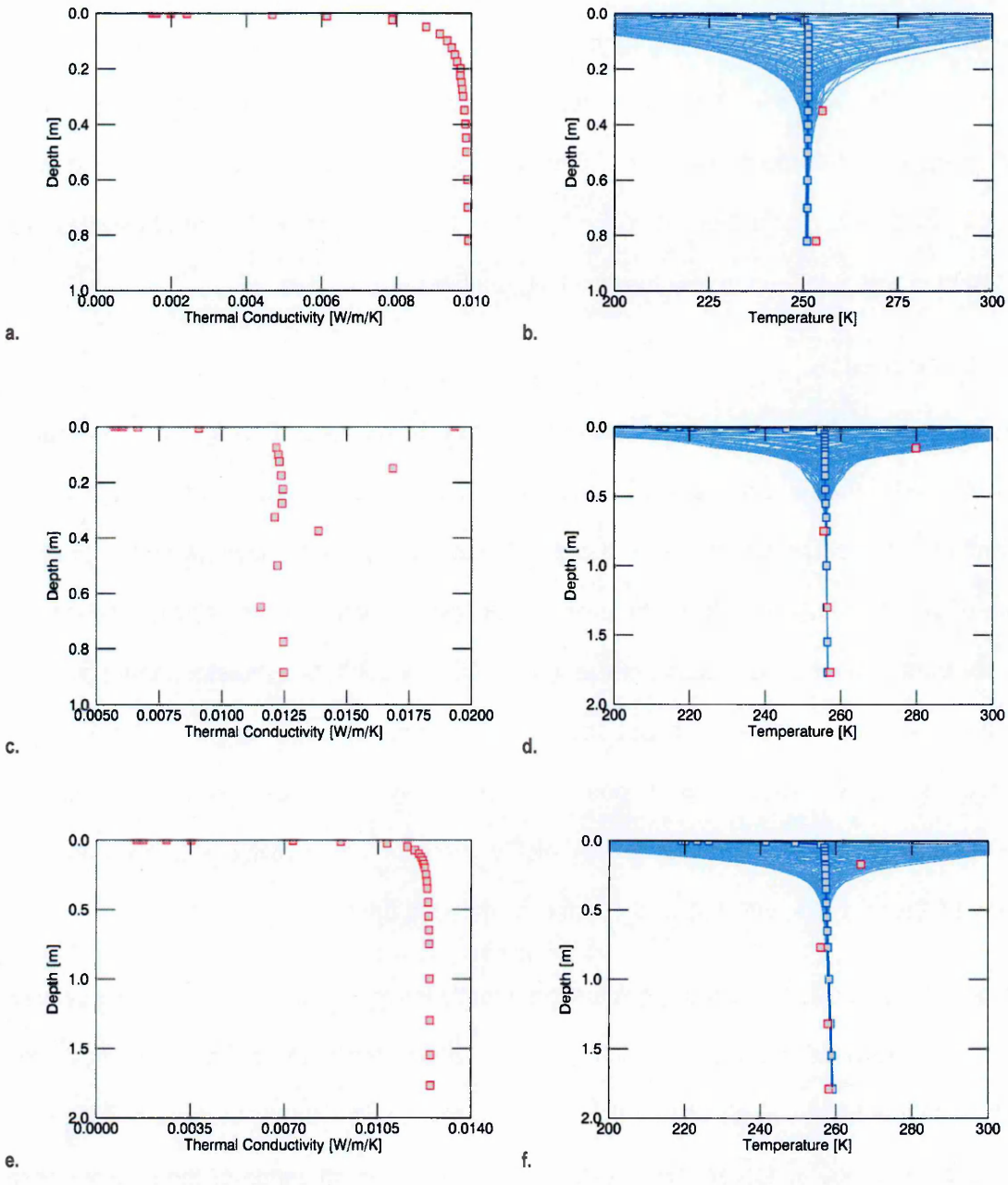

Figure 9.8.7. Select results for Apollo temperature data inversion. Contours a-b, c-d and e-f are respectively for Apollo 15 Probe 1, Apollo 17 Probe 1 and Apollo 17 Probe 2. The left contours are optimized conductivities (red squares are simulation gridpoints), while the right contours are optimized subsurface temperatures (blue squares are simulation gridpoints; red squares are sensor locations).

The value of the basal heat flow (and thermal conductivity where applicable) at the minimum point marks the optimal combination of thermal parameters for the given ALSEP probe data set. The heat flows thus determined are 13 mW/m^2 for Apollo 15 Probe 1 (optimized with thermal conductivity), 5 mW/m^2 for Apollo 17 Probe 1 (optimized with thermal conductivity) and 19 mW/m^2 for Apollo 17 Probe 2. The best fit conductivities are plotted in Figure 9.8.7 along with the resulting temperature profiles.

9.8.4.3 Discussion

The former results give a best estimate of the basal heat flow given the largely unprocessed data set extracted from the NSSDC archive. The temperature data is not equilibrated; therefore the estimated basal heat flows are probably lower than the pristine value of the planetary heat flow. The initial conductivity estimate for the Apollo 17 Probe 2 site appears to be the most stable of the three initial conductivity estimates, as it provided a stable heat flow solution without the need to simultaneously optimize the thermal conductivity. The Apollo 15 Probe 1 conductivity (or heat sources) appears underestimated towards the surface. A highly irregular conductivity is implied for the Apollo 17 Probe 1 site, which is likely underestimated at depth.

The primal (forward) temperature calculation directly influences the optimized conductivity estimates (see Section 2.2.3.3), which therefore means the latter is indirectly influenced by the shallow heat source distributions. Setting the shallow-depth thermal conductivity standard deviations σ_k to very small values ~0 reduces the influence of the shallow heat sources by maintaining the values of the initial conductivity estimates at the equivalent depths.

The heat flows obtained cannot be directly compared to estimates obtained by other authors because, as noted earlier, the temperature measurements have not been corrected for various effects. The purpose herein, is to demonstrate the application of the inverse model to a real-world data set.

9.8.5 References

HEIKEN, G. H., VANIMAN, D. T., FRENCH, B. M., VANIMAN, D. T. & FRENCH, B. M. 1991. *Lunar sourcebook - A user's guide to the moon.*

JONES, W. P., WATKINS, J. R. & CALVERT, T. A. 1975. Temperatures and thermophysical properties of the lunar outermost layer. *Moon,* 13, 475-494.

LANGSETH, M. G., JR., CLARK, S. P., JR., CHUTE, J. L., JR., KEIHM, S. J. & WECHSLER, A. E. 1972. The Apollo 15 Lunar Heat-Flow Measurement. *Moon,* 4, 390-410.

LANGSETH, M. G., KEIHM, S. & PETERS, K. 1976. The Revised Lunar Heat Flow Values. *In:* Lunar and Planetary Institute Science Conference Abstracts, March 1, 1976 1976. 7, 474.

NASA, N. S. S. D. C. 2015. *National Space Science Data Center* [Online]. Online: NASA. Available: http://nssdc.gsfc.nasa.gov/ [Accessed 09/03/2015 2015].

9.9 IDL Procedures and Functions (DVD)

This is a listing of the main IDL procedures and functions used in the FSI model. A complete listing, along with example data, can be found on the included optical disc, labelled GPHLO1.

Definitions:

1. **Procedure**: an IDL procedure is analogous to a mathematical operator. It can act on and return several parameters simultaneously, by reference.
2. **Function**: an IDL function is analogous to a mathematical equation. It returns one main parameter, though it may return others by reference.

PROCEDURES AND FUNCTIONS	DESCRIPTION
GPHLO1	Procedure: **G**eneral **P**lanetary **H**eat f**LO**w in **1** dimension (*pron. gee-flo one*). • Calculates forward model temperatures. • Optimizes boundary and initial conditions from a temperature distribution.
INITIALIZE_PARAMETER	Function: • Initializes regolith property, and heat sources and sink arrays used in running forward and inverse model simulations.
ERROR_GENERATE	Function: • Initializes inverse model parameter error (standard deviation) arrays, to be read in by COVARIANCE.

COVARIANCE	Function: • Creates covariance arrays from error arrays output by ERROR_GENERATE.
TDMA	Procedure: **T**ri-**D**iagonal **M**atrix **A**lgorithm • Calculates forward model temperatures using the TDMA at each timestep.
HEAT_SOURCE	Procedure: • Calculates heat sources from temperature residuals, and temperature measurement (data) covariance array. These are used in the TDMA calculation of the dual problem solution.
FRECHET_DERIVATE	Procedure: • Calculates Fréchet derivative(s) of parameters being optimized, using TDMA dual problem solution, a priori model parameters and covariances and current model parameter estimates. • Used in simple steepest, Newtonian and preconditioned descent optimization
HESSIAN_DERIVATIVE	Procedure: • Calculates Hessian derivative(s) of parameters being optimized, using Fréchet derivatives calculated by FRECHET_DERIVATE. • Used in Newtonian, or preconditioned

	descent optimization
ASCENT_DIRECTION	Procedure: • Calculates direction of steepest ascent of model parameters, using Hessian derivatives, Fréchet derivatives, current and a priori model parameters, and covariances.
MODEL_STEP	Procedure: • Optionally calculates optimal stepsize for model parameters to be updated with the direction of steepest ascent.
PRECONDITION	Procedure: • Optionally allows the inclusion of unique preconditioning operators to stabilize the optimization and/or accelerate convergence.
MISFIT_FUNCTION	Procedure: • Calculates misfit (objective) function using covariance weighted temperature residuals and model parameter updates.
TRACK	Procedure: • Monitors and records progress of optimization of misfit function and, optionally, other parameter specific variables (e.g. derivatives, directions of

steepest ascent).

OPTIMIZE	Procedure: • Checks progress of the model in optimizing the misfit function and determines termination of optimization (when the current point is assessed to be a stationary point). • Optionally: performed by comparing the misfit function shape to predetermined *analytical* function shapes; or using the *numerical* values of the function to determine the stationary point.
RESOLVE	Procedure: • Optionally calculates a posteriori covariance operator(s) to allow resolution analysis of the inverse model solution.
MODEL_UPDATE	Procedure: • Updates values of model parameters being optimized, which is then passed back to TDMA, if current point is not (or just past) a stationary point.